University of Sydney

Doctoral Thesis

Exploring Extended Scalar Sectors, Neutrinos and Flavour Anomalies

Author:
Shyam Balaji

Lead Supervisor:
Prof Kevin Varvell
Supervisor:
Prof Céline Bœhm

A thesis submitted in fulfillment of the requirements for the degree of Doctor of Philosophy

in the

Particle Physics Group
School of Physics
Faculty of Science

March, 2021

Declaration of Authorship

This doctoral thesis presents novel findings for a host of fundamental particle physics problems. These can be separated broadly into extended scalar sector searches, including direct searches for new Higgs particles at the CERN ATLAS experiment as well as calculating phase transitions that could arise from these beyond the Standard Model scalar potentials. As well as theoretical and phenomenological studies on the nature of CP violation, which is explored in the context of heavy neutrinos and other fermions. Finally, development of unified field theories that could resolve the strongest experimental tensions in the flavour sector. It is the culmination of my work that will go towards completion of my doctorate in particle physics at the University of Sydney.

Chapter 1 is an introductory chapter that aims to provide global context of this work and the requisite background for the subsequent chapters. It is based on several historical references and borrows many important technical details regarding the theoretical basis of the Standard Model and the current position and outlook of the field of particle physics. It also contains a section dedicated to the ATLAS experiment which provides an outline of the experimental setup and detector technology. This information is drawn from a mixture of technical reports, past theses and published articles. Even though this section borrows heavily from preceding works, it has been written and synthesised by myself with citations made to sources where appropriate.

Chapter 2 is based on work shown in Ref. [1],

[1] ATLAS collaboration, G. Aad et al., Search for a heavy Higgs boson decaying into a Z boson and another heavy Higgs boson in the $\ell\ell bb$ and $\ell\ell WW$ final states in pp collisions at $\sqrt{s} = 13$TeV with the ATLAS detector,

with minor stylistic modifications. It is by the ATLAS collaboration with minor stylistic modifications, note that the author list for ATLAS publications includes all members of the collaboration in alphabetical order as per convention of the experiment. It is currently in advanced review with the European Physics Journal C. It is the second iteration of a previous analysis which only considered the $\ell\ell bb$ final state. The approach taken in this analysis is similar, and hence, significant portions of the analysis methodology and code base were exported for reuse.

My main contribution was with regard to event selection optimisation in $\ell\ell bb$, large width signal modelling, narrow width signal modelling, modelling uncertainties and ancillary machine learning studies. There were signal modelling codes and frameworks developed in the previous analysis that I adapted and modified into the current version. My code was then adapted for use independently in the $\ell\ell WW$ channel as well. I also prepared the entire hepdata input for the analysis. The experimental data itself was collected by the ATLAS collaboration as a whole and my specific contributions included management of the data preparation and reconstruction software code at CERN as a Level 1 shifter. The simulated datasets were prepared by others in the collaboration. Each individual on our fourteen person exotic Higgs search team has contributed to different aspects of the work over time, this is typical for ATLAS since it is impractical for a single physicist to manage all of the technical details of the analysis and the experiment.

Chapter 3 is based on the published work in Ref. [2],

[2] S. Balaji, M. Spannowsky and C. Tamarit, *Cosmological bubble friction in local equilibrium, JCAP* 03 (2021) 051,

with minor stylistic modifications. My contribution was determining that a "friction effect" like the one we outline exists by studying the equations of motion of the scalar field and subsequently calculating the dynamic phase transitions by solving the resulting coupled partial differential equations. I also assisted in computing the field profiles in the static and planar limits but this was mainly performed by another member of the project. I developed the entire machine learning framework and numerical models for the time dependent solutions. All members of the project contributed to writing the final manuscript.

Chapter 4 is based on published work in Refs. [3–5],

[3] S. Balaji, M. Ramirez-Quezada and Y.-L. Zhou, *CP violation and circular polarisation in neutrino radiative decay, JHEP* 04 (2020) 178,

[4] S. Balaji, M. Ramirez-Quezada and Y.-L. Zhou, *CP violation in neutral lepton transition dipole moment, JHEP* 12 (2020) 090,

[5] S. Balaji, *CP asymmetries in the rare top decays* $t \to c\gamma$ *and* $t \to cg$*, Phys. Rev. D* 102 (2020) 113010,

with minor stylistic modifications. In Ref. [3], I calculated the kinetic terms in the loop for the transition dipole moment for the Yukawa model and cross–checked my results with another member of the project. All members of the project contributed to the manuscript. In Ref. [4], I suggested exploring the neutral lepton transition dipole moment as a source of CP violation, this became the central theme of the publication. I was involved in calculating all the loops, numerical results and performing the plots and cross–checked my results with another member of the project. Finally Ref. [5] was a single author study so I performed all the relevant theory calculations and numerical studies shown in the final publication.

Chapter 5 is based on published work in Refs. [6, 7],

[6] S. Balaji, R. Foot and M. A. Schmidt, *Chiral SU(4) explanation of the* $b \to s$ *anomalies, Phys. Rev. D* 99 (2019) 015029,

[7] S. Balaji and M. A. Schmidt, *Unified SU(4) theory for the* $R_{D^{(*)}}$ *and* $R_{K^{(*)}}$ *anomalies*, *Phys. Rev. D* 101 (2020) 015026,

with minor stylistic modifications. In both works I was involved in the model building, prediction of flavour physics observables, generating plots and performing the relevant calculations to determine allowable regions based on the available constraints. These results were cross-checked with other members of the project. In Ref. [7], along with the coauthor, I suggested extension of the neutrino spectrum and using the S_1 leptoquark from the scalar sector to explain one of the anomalies as a novelty over the model suggested in Ref. [6]. All members of the project contributed to the final manuscripts and results.

In addition to the statements above, in cases where I am not the corresponding author of a published item, permission to include the published material has been granted by the corresponding author.

Shyam Balaji
March 29, 2021

As supervisor for the candidature upon which this thesis is based, I can confirm that the authorship attribution statements above are correct.

Kevin Varvell
March 29, 2021

Statement of Originality

This is to certify that to the best of my knowledge, the content of this thesis is my own work. This thesis has not been submitted for any degree or other purposes.

I certify that the intellectual content of this thesis is the product of my own work and that all the assistance received in preparing this thesis and sources have been acknowledged.

Shyam Balaji
March 29, 2021

Abstract

Exploring Extended Scalar Sectors, Neutrinos and Flavour Anomalies

by Shyam Balaji

The best current theory describing the fundamental interactions of matter in our universe is the Standard Model of Particle Physics. However, it leaves many important physical questions unanswered. These include, providing a consistent explanation for the predominance of matter over antimatter, the origin of neutrino masses, unification of quantum gauge fields at high energy scales as well as flavour violation as hinted at by results of recent experiments. This thesis focuses on providing explanations for these questions whilst outlining solutions that predict phenomena that can be tested in collider searches and through cosmological observables.

The topics presented in this thesis can be separated into several categories including the potential existence of extended scalar sectors. This begins with a presentation of a dedicated search for new Higgs particles at the Large Hadron Collider. The physics analysis, performed with data drawn from the ATLAS experiment, focuses on Two-Higgs-Doublet models, which provide an elegant explanation for the abundance of matter over antimatter in our universe through an early universe cosmological phase transition. On a related note, we also explicitly calculate such a phase transition dynamically and the speed with which it propagates in the early universe plasma for a particular extended scalar potential. Such transitions produce compelling phenomenology such as gravitational waves that could be detected at interferometer experiments such as LIGO. Developing general techniques, like the ones outlined in this work, that determine how fast these transitions travel accurately, is of crucial importance in predicting experimental signatures that may result from such processes.

Beyond this, we explore the phenomenon of CP violation which is a necessary condition for the generation of matter–antimatter asymmetry. In this thesis, we calculate novel fundamental CP properties of fermions such as the CP asymmetry in the neutrino and top quark transition dipole moments. Such properties directly affect their respective decay rates for several interesting channels. Finally, we explore grand unified field theories that yield exotic low energy phenomenology and thereby provide UV complete explanations for tensions in the flavour sector. These tensions provide some of the most compelling experimental evidence yet for physics beyond the Standard Model.

Acknowledgements

First and foremost, I would like to express my immense gratitude to my lead supervisor, Kevin Varvell, for your continued support and guidance over my entire doctoral candidature. With your encouragement, I pursued my interests in all areas of particle physics, this has helped me grow and provided me with confidence as a young physicist. I would also like to thank my supervisor Céline Bœhm who has been a consistent source of support and advice, this has helped me pave my path as a scientific researcher and to realise that limitations in our field are often illusions.

I would also like to thank my many senior collaborators for indispensable physics learnings. Michael Schmidt, it was through our work that I developed and cultivated strong interests in unified field theories and flavour physics. Robert Foot, it was through our interactions that I gained exposure to beyond the Standard Model building. I would also like extend gratitude to Archil Kobakhidze for our many informative discussions on Higgs physics and dark matter.

I would also like to acknowledge my colleagues turned friends Neil Barrie, Suntharan Arunasalam, Matthew Talia, Cyril Lagger, Thomas Nommensen and Carl Suster as well as other occupants of Room 342, both past and present. Your many compelling and entertaining conversations over the years stimulated my curiosity and interest across a myriad of topics. I would also like to thank my overseas connections Ye–Ling Zhou and Carlos Tamarit for equally edifying scientific discussions. I would also like to especially thank my collaborator Maura Ramirez–Quezada, who has been a great source of support since our projects were initiated and someone I now consider one of my closest friends.

I would also like to thank my ATLAS experiment collaborators Daniel Neilsen, Wai Yuen (Alan) Chan, Xiaohu Sun, Nikolaos "Nikos" Rompotis, Jeff Shahinian, Flavia Dias and Troels Petersen. Without your combined efforts, completion of the new Higgs particles search presented in this work would not have been possible.

Finally, I would like to thank my friends and family. Mum and Dad, without your continued support, encouragement and belief in me, I would have never had the courage to commence this often challenging but ultimately inspiring and fulfilling voyage that is a doctorate. I would also like to thank my brother Arjun and my dearest Grandma (Patti) for your endless love and support on this journey. To all my other physics and non–physics related friends and family who's playful distraction or encouragement hindered or helped me, I thank you for both in equal measure.

Contents

Acronyms

A Toroidal LHC Apparatus	ATLAS
Big Bang Observer	BBO
Cabbibo–Kobayashi–Maskawa	CKM
Charge-Parity	CP
Compact Muon Solenoid	CMS
Dark Matter	DM
Deci–hertz Interferometer Gravitational Wave Observatory	DECIGO
Electromagnetic Dipole Moment	EDM
Final State Radiation	FSR
Flavour Changing Neutral Current	FCNC
Glashow–Iliopoulos–Maiani	GIM
High Level Trigger	HLT
Initial State Radiation	ISR
Inner Detector	ID
Insertable Barrel Layer	IBL
Large Hadron Collider	LHC
Leading Order	LO
Lepton Flavour Universality	LFU
Level 1	L1
Minimal Supersymmetric Standard Model	MSSM
Monte Carlo	MC
Multiple Parton Interactions	MPI
New Physics	NP
Next–to–Leading Order	NLO
Parton Distribution Function	PDF
Pontecorvo–Maki–Nakagawa–Sakata	PMNS
Quantum Chromodynamics	QCD
Quantum Electrodynamics	QED
Quantum Field Theory	QFT
Semiconductor Tracker	SCT
Standard Model	SM
Transition Radiation Tracker	TRT
Two–Higgs–Doublet Model	2HDM
Ultraviolet	UV
Vacuum Expectation Value	VEV
Vector–like Quark	VLQ

Chapter 1

Introduction

The best description of fundamental particles and their interactions in our universe is currently given by the Standard Model (SM). It was developed in the late 1960s, and it was within this framework that the Higgs mechanism was proposed. The Higgs mechanism itself was formulated in an attempt to explain why elementary particles have mass. In the same decade, CP violation was first discovered. Despite its remarkable success in describing known fundamental interactions to a very high degree of precision, there is strong evidence that the SM of particle physics in its current form is incomplete. The discovery of the Higgs boson in 2012 meant that an important piece of the SM was finally validated, but we are still far from the final picture of nature and several important questions remain unanswered. Among these are, why is there an asymmetry between matter and antimatter in our current universe, what is the mechanism by which neutrinos acquire mass, what is the nature of dark matter and is flavour universality violated for fermions. In this chapter we present an overview of the SM of particle physics, outline the aforementioned outstanding challenges the SM is facing and provide the requisite background to motivate and outline potential resolutions to these fundamental problems which will be covered in the following chapters.

In Chapter 2, we outline the search for a heavy CP odd Higgs boson, A, decaying to another heavy CP even Higgs boson, H, and a Z boson, which subsequently decay to $\ell\ell bb$ and $\ell\ell WW$ ($\ell\ell qqqq$) final states. The mass of the H boson is assumed to be larger than the SM-like Higgs of 125GeV discovered at CERN. The search for such Two-Higgs-Doublet models (2HDM) is motivated by the possibility that they provide a first–order phase transition in the early universe, necessary for electroweak baryogenesis. Electroweak baryogenesis will be explained further in Section 1.1.5 and Section 1.3. Using 13TeV proton–proton collision data collected with the ATLAS detector at the Large Hadron Collider (LHC) that corresponds to an integrated luminosity of 139fb^{-1}, the chapter focuses on mass ranges up to 800(700)GeV for the A (H) bosons respectively.

In Chapter 3, we explore first–order cosmological phase transitions, similar to the ones that arise from the scalar sector outlined in Chapter 2. This is an important area of study since the asymptotic velocity of expanding bubbles is of crucial relevance for predicting observables like the spectrum of stochastic gravitational waves, or for establishing the viability of mechanisms explaining fundamental properties of the universe, such as the observed baryon asymmetry. In these dynamic phase transitions, it is generally accepted that subluminal bubble expansion requires out-of-equilibrium interactions with the plasma. These are typically captured by friction terms in the equations of motion for the scalar field.

However, this has been disputed in works pointing out subluminal velocities in local equilibrium arising either from hydrodynamic effects in transitions of deflagration type or from the entropy change across the bubble wall in general situations. In this chapter, we aim to explore both effects and their relations which can be understood from the conservation of the entropy of the degrees of freedom in local equilibrium. This naturally leads to subluminal speeds for both deflagration and detonation type transitions which are of high phenomenological interest. The friction effects arising from the background field dependence of the plasma are studied and accounted for considering local conservation of stress-energy and by including field dependent thermal contributions to the effective scalar potential. Furthermore, we focus on illustrating these effects with explicit calculations of dynamic and static bubbles for a first–order electroweak transition in a SM extension with additional scalar fields. The results are compared and contrasted with recent analysis linking friction forces in local equilibrium with entropy changes across the bubble. We outline novel corrections from the temperature and velocity gradients.

In Chapter 4, we explore previously undiscovered sources of CP violation and potential signals of new physics. The radiative decay of charged and neutral fermions has been studied for decades but CP violation induced within such a paradigm has not been studied explicitly. CP violation in the radiative decay of fermions can produce an asymmetry between circularly polarised directions of the radiated light and creates an important source of net circular polarisation in particle and astroparticle physics observables.

We compute this in Section 4.1 and the results presented outline the general connection between CP violation and circular polarisation through conservation of angular momentum for both Dirac and Majorana fermions and can be used for any class of models that enable such radiative decays. The total CP violation is calculated based on a widely studied Yukawa interaction considered in both active and sterile neutrino radiative decay scenarios as well as searches for dark matter via direct detection and collider signatures. The phenomenological implications of the formalism on topical scenarios such as keV sterile neutrino decay, leptogenesis-induced right-handed neutrino radiative decay and IceCube-driven heavy dark matter decay are discussed.

In Section 4.2, the CP violation in the neutrino transition electromagnetic dipole moment is discussed in the context of the SM with an arbitrary number of right–handed singlet neutrinos. The transition dipole moment is a key electromagnetic property of the neutrino. A full one–loop calculation of the neutrino electromagnetic form factors is performed in the Feynman gauge. A non–zero CP asymmetry is generated by requiring threshold conditions for the neutrino masses along with non-vanishing CP violating phases in the lepton flavour mixing matrix. We apply the formalism to a minimal seesaw model with two heavy right–handed neutrinos denoted N_1 and N_2 and discuss the CP asymmetries for decays into light neutrinos $N \to \nu\gamma$ and the more experimentally interesting $N_2 \to N_1\gamma$ which can reach of order unity. We find that even if the Dirac CP phase δ is the only source of CP violation, a large CP asymmetry around 10^{-5}-10^{-3} is comfortably achieved.

In Section 4.3, we explore fundamental properties of the top quark through the CP properties of its flavour violating decays. The rare radiative flavour changing top decays $t \to c\gamma$ and $t \to cg$ (and the even rarer $t \to u\gamma$ and $t \to ug$) have been processes of interest for decades as they offer a key probe for studying top quark properties. However an explicit analytical study of the branching ratios and CP

asymmetries resulting from these loop level processes has thus far evaded attention. In this section, we provide the formulation for the CP asymmetry resulting from the total kinetic contribution of the loop integrals and their imaginary parts, as well as an updated numerical computation of the predicted SM branching fractions. These rare processes are suppressed in the SM by the Glashow-Iliopoulos-Maiani (GIM) mechanism.

The results presented in this chapter can easily be exported for use in minimal extensions of the SM including vector-like quarks (VLQs) or in 2HDMs such as the one described in Chapter 2. In these beyond the SM scenarios, radiative fermionic decay processes can be enhanced relative to the SM by several orders of magnitude. Such processes provide an experimentally clean signature for new fundamental physics and can potentially be tested by current collider experiments. These topical beyond the SM theories are an elegant means to provide improved global fits to the latest results emerging from flavour physics, Cabibbo–Kobayashi–Maskawa (CKM) and precision electroweak measurements.

In Chapter 5, we study the B physics anomalies which suggest a strong hint in favour of violation of lepton flavour universality (LFU) and possible beyond the SM explanations. We first discuss a variant of the famous unified Pati-Salam model, with gauge group $SU(4)_C \times SU(2)_L \times U(1)_{Y'}$ in Section 5.1, wherein chiral left–handed quarks and leptons are unified into a $\underline{4}$ of $SU(4)_C$, while the right–handed quarks and leptons have quite a distinct treatment. The model introduces particles that couple to both quarks and leptons called leptoquarks. The $SU(4)_C$ leptoquark gauge bosons can explain the measured deviation of lepton flavour universality in the rare decays $\bar{B} \to \bar{K}^{(*)}\bar{\ell}\ell$, $\ell = \mu, e$, which directly effect the measured R_K and R_{K^*} ratios.

Beyond this, we also present a theory based on gauge group $SU(4)_C \times SU(2)_L \times SU(2)_R$ in Section 5.2. The left–handed quarks and leptons are unified into the same fundamental representation of $SU(4)_C$ as in Section 5.1, while right–handed quarks and leptons have a separate treatment. The deviations measured in the rare semileptonic decays $B \to D^{(*)}\tau\bar{\nu}$, which effect the measured R_D and R_{D^*} ratios, are explained by a scalar leptoquark which couples to right–handed fields and is contained in the $SU(4)_C \times SU(2)_R$-breaking scalar multiplet. The measured deviation of lepton flavour universality in the rare decays $\bar{B} \to \bar{K}^{(*)}\ell^+\ell^-$, $\ell = \mu, e$ is explained via the $SU(4)_C$ leptoquark gauge boson. We also discuss a prediction of a new sub-GeV scale sterile neutrino which participates in the anomaly and can be searched for in upcoming neutrino experiments. Both theories satisfy the current most sensitive experimental constraints and their allowable parameter regions will be probed as more precise measurements from the LHCb and Belle II experiments become available.

1.1 The Standard Model of Particle Physics

The SM is an ensemble of quantum field theories (QFTs) that successfully describes all known particle properties and their interactions. More specifically, it has provided a consistent description of the electromagnetic, weak and strong forces using the principles of gauge theory. It was developed over several decades and remains the best available model to describe subatomic processes. The first pieces of the SM were born during the late 1920s when Paul Dirac applied QFT to the electromagnetic interaction, this established framework for the now well known Dirac equation. The Dirac equation describes the behaviour of half–integral spin particles called fermions. This development later gave rise to the theory of Quantum Electrodynamics (QED), which was further improved and formalised by Tomaga, Feynman and Schwinger [8–13]. The second major addition was the successful description of the weak interaction by Glashow, Weinberg and Salam in the 1960s who later showed that the electromagnetic and weak interactions could unified into a single electroweak theory [14,15]. The third and final addition was a consistent description of the strong forces which is now called Quantum Chromodynamics (QCD) [16].

Particle interactions can crudely be described as fermions exchanging gauge bosons. Fermions as mentioned earlier, carry half–integral spin while bosons carry integral spin. Fermionic particles have an additional requirement that they must satisfy the Pauli Exclusion principle which states that no two fermions can occupy the exact same quantum state. The fundamental fermions are viewed as quarks and leptons, which exhibit no internal structure down to scales of at least 10^{-18}m.

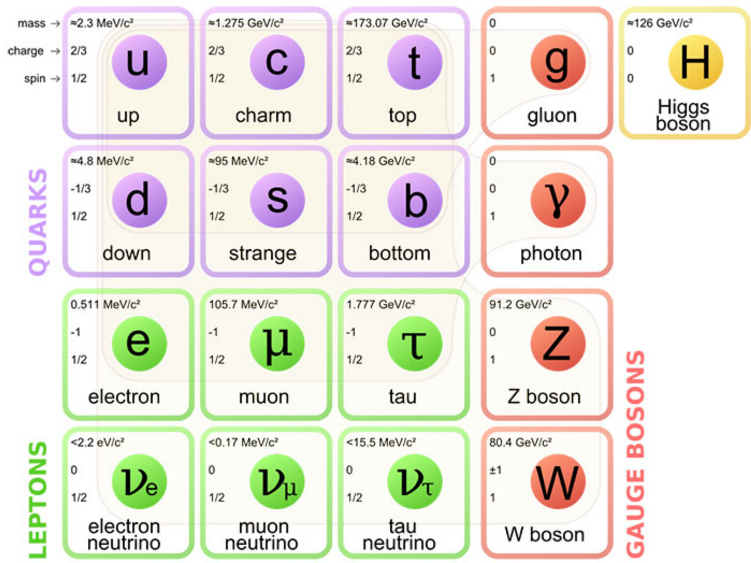

FIGURE 1.1: The Standard Model of particle physics depicted pictorially. The matter particles (first three columns) are displayed in purple for the quarks and green for the leptons. The bosons (last two columns) are given in red for the gauge bosons and yellow for the scalar Higgs boson. The interactions between the matter particles and the gauge bosons are indicated by the light grey lines with a beige background. The quarks are colour charged and therefore interact with the strong force (gluons), the quarks and leptons interact with the electromagnetic force (photons) and every matter particle interacts with the weak interactions (W and Z bosons) [17].

The SM, depicted visually in Figure 1.1, is based on the gauge group $SU(3)_C \times SU(2)_L \times U(1)_Y$ where $SU(3)_C$ corresponds to the strong interactions and the subscript C denotes the quantum number "colour". $SU(2)_L \times U(1)_Y$ corresponds to the combined gauge group describing the electroweak interactions, the subscript L denotes the "left–handedness" of the weak interactions and the subscript Y for the quantum number "weak hypercharge".

There are eight vector bosons (gluons) associated with the strong force, three vector bosons ($W^{\pm}$ and Z bosons) associated with the weak force and one vector boson (the photon) associated with the electromagnetic force. The photon and the gluons are massless while the $W^{\pm}$ and Z bosons are massive particles [18–21]. Apart from these gauge bosons, there is also one other boson called the "Higgs" boson with zero spin that corresponds to an excitation of the Higgs field. Gravity is a fundamental force that is not yet captured within the SM.

In order to properly generate the masses of the gauge bosons in the SM without violating gauge invariance, Guralnik, Hagen and Kibble [22], Brout and Englert [23] and, Higgs [24] proposed their novel Englert-Brout-Kibble-Guralnik-Hagen-Higgs mechanism. The mechanism introduced the aforementioned Higgs field, which acquires a nonzero vacuum expectation value (vev) because it is an energetically favourable configuration due to its quartic potential. The quartic structure itself is required to ensure the theory is renormalisable. As a consequence, when the W and Z bosons interact with this field, they acquire a mass. This will be elucidated further in the following section. The complete SM Lagrangian in its non-expanded form is given by

$$\begin{aligned}\mathcal{L}_{\mathrm{SM}} = &-\frac{1}{4}G^a_{\mu\nu}G^{a\mu\nu} - \frac{1}{4}W^a_{\mu\nu}W^{a\mu\nu} - \frac{1}{4}B^a_{\mu\nu}B^{a\mu\nu} \\ &+ i\overline{\psi}\not{D}\psi \\ &+ i\overline{\psi}_i y_{ij}\psi_j\phi \\ &+ |D_\mu\phi|^2 - V(\phi) + h.c.,\end{aligned} \tag{1.1}$$

where the gauge field strength terms are given in full generality by $F_{\mu\nu} = \partial_\mu A^a_\nu - \partial_\nu A^a_\mu + g\epsilon^{abc}A^b_\mu A^c_\nu$, ψ represents fermion fields, ϕ is the Higgs field, D_μ is the covariant derivative and y_{ij} the Yukawa couplings. Note we have used the Feynman slash notation where $\not{a} = \gamma_\mu a^\mu$.

The first line in Eq. (1.1) describes the kinetic and self-interactions of the gauge bosons while the second term describes the kinetic terms of fermions and their interaction with gauge bosons. The third describes the interactions of the fermions with the Higgs field. The last term contains the kinetic and self-interactions of the Higgs boson.

1.1.1 Electroweak Symmetry Breaking

Since some of the most relevant aspects of the SM Lagrangian given in Eq. (1.1) have been covered, we can now discuss the Higgs mechanism in the electroweak sector. The non–zero vacuum expectation of the Higgs field initiates spontaneous symmetry breaking of the electroweak sector

$$SU(3)_c \times SU(2)_L \times U(1)_Y \to SU(3)_c \times U(1)_Q. \tag{1.2}$$

Where Q represents the usual quantum number for electric charge. The gauge field dependent part of the Lagrangian is

$$\mathcal{L}_{gauge} = -\frac{1}{4}G^a_{\mu\nu}G^{a,\mu\nu} - \frac{1}{4}W^a_{\mu\nu}W^{a,\mu\nu} - \frac{1}{4}B_{\mu\nu}B^{\mu\nu} \tag{1.3}$$

where W_μ^a has $a = 1, 2, 3$ corresponding to three electroweak gauge bosons and G_μ^a has $a = 1, ..., 8$ corresponding to eight gluons, with the field strength tensors defined by

$$\begin{aligned} B_{\mu\nu} &= \partial_\mu B_\nu - \partial_\nu B_\mu, \\ W_{\mu\nu}^a &= \partial_\mu W_\nu^a - \partial_\nu W_\mu^a + g\epsilon^{abc} W_\mu^b W_\nu^c, \\ G_{\mu\nu}^a &= \partial_\mu G_\nu^a - \partial_\nu G_\mu^a + g_s f^{abc} G_\mu^b G_\nu^c, \end{aligned} \tag{1.4}$$

where B_μ is the hypercharge gauge boson, W_μ^a and g are the $SU(2)_L$ gauge boson and coupling respectively while g_s is the $SU(3)_C$ strong coupling constant. The terms ϵ^{abc} and f^{abc} are the structure constants of $SU(2)_L$ and $SU(3)_C$ respectively. The covariant derivative is defined

$$D_\mu = \partial_\mu - ig\frac{W_\mu^a \sigma^a}{2} - i\frac{g'}{2} B_\mu, \tag{1.5}$$

with σ^a ($a = 1, 2, 3$) being the Pauli matrices and g' denoting the $U(1)_Y$ hypercharge coupling. The Higgs potential requires inclusion of an $SU(2)$ doublet field $\Phi = (\phi^+ \phi^0)^T$ with Lagrangian

$$\mathcal{L}_{Higgs} = (D^\mu \Phi)^\dagger (D_\mu \Phi) + \mu^2 \Phi^\dagger \Phi - \lambda (\Phi^\dagger \Phi)^2, \tag{1.6}$$

where μ^2 and λ are free parameters. The quartic coupling requires $\lambda > 0$, since the potential must be Hermitian and positive-definite. The unique potential that facilitates the symmetry breaking as per (1.2) is

$$V(\Phi) = -\mu^2 |\Phi|^2 + \lambda |\Phi|^4. \tag{1.7}$$

This potential is minimised at $|\Phi| = \frac{v}{\sqrt{2}} = \sqrt{\frac{\mu^2}{2\lambda}}$, where v is the vev of the Higgs field. Since Φ is a two-component complex object, it has four degrees of freedom (two real and two imaginary), three of which will correspond to massless Goldstone modes π^a ($a = 1, 2, 3$) which eventually are consumed by the longitudinal modes of the W^+, W^- and Z bosons. The remaining degree of freedom is identified as the massive Higgs boson with real field h. Hence, a convenient parametrisation about the minimum becomes

$$\Phi = e^{i\frac{\xi^a \sigma^a}{v}} \begin{pmatrix} 0 \\ \frac{v+h}{\sqrt{2}} \end{pmatrix} \tag{1.8}$$

where the Goldstone boson fields π^a are associated with each broken generator σ^a corresponding to the Pauli matrices with $a = 1, 2, 3$. It is simpler to study this theory in unitary gauge, so we will proceed setting the rotation parameter $\xi^a = 0$.

Upon substitution of the expression (1.8), in the unitary gauge, into the covariant derivative (1.5) and the scalar potential (1.6), the mass terms associated with three massive gauge bosons can be obtained. When we diagonalise the resulting mass matrix, we obtain two linear combinations of the hypercharge gauge boson with one of the generators of $SU(2)$ corresponding to one massless and one massive eigenstate respectively. These are the well–known massless photon A_μ and the Z_μ gauge bosons

$$A_\mu = -W^3_\mu \sin\theta_w + B_\mu \cos\theta_w \,,$$
$$Z_\mu = W^3_\mu \cos\theta_w + B_\mu \sin\theta_w \,, \tag{1.9}$$

with the weak mixing angle defined by $\tan\theta_w = g'/g$. In the on-shell scheme this is calculated to be $\sin^2\theta_w = 0.2233$ [25]. Additionally, we also find the definition for the massive W bosons,

$$W^\pm_\mu = \frac{1}{\sqrt{2}}(W^1_\mu \mp iW^2_\mu) \tag{1.10}$$

and the mass terms in the SM Lagrangian are given by

$$m_W^2 = \frac{g^2}{4}v^2, \qquad m_Z^2 = \frac{g^2+g'^2}{4}v^2, \tag{1.11}$$

which directly relate the massive weak boson masses to the gauge coupling constants and the Higgs vev. Furthermore, we note that gauge invariance forbids terms like $\frac{1}{2}m^2 A^\mu A_\mu$, which would correspond to a massive photon. We also have the following useful relations between the gauge coupling constants

$$e = g\sin\theta_w = g'\cos\theta_w \tag{1.12}$$

Direct fermionic mass terms are not allowed in the SM Lagrangian shown in Eq. (1.1), since they break gauge invariance. However, the inclusion of the scalar field ϕ into the Lagrangian will also generate the missing fermion mass terms. This will be discussed in the following section.

On a phenomenological level, the electroweak vev can be determined from the measurements of the muon lifetime. This is because the Fermi constant $G_F = 1.1663787(6) \times 10^{-5}\text{GeV}^{-2}$ [26] can be determined from the muon lifetime and is related to the electroweak vev via the relation $v^2 = \frac{1}{\sqrt{2}G_F}$. This fixes $v \approx 246$GeV. The Higgs mass was found to be $m_h = 125.09(24)$GeV [26] and implies that the quartic coupling is $\lambda = m_h^2/(2v^2) \approx 0.13$ which is perturbative. This is consistent with the current experimental averages for the $W^\pm$ and Z bosons, masses which are [26]

$$m_W = 80.385(15)\text{GeV}, \qquad m_Z^2 = 91.1876(21)\text{GeV}. \tag{1.13}$$

1.1.2 Fermion Masses

We shall now turn our attention to how fermions in the SM acquire their masses. There are three generations of $SU(2)_L$ leptons and quarks in the SM

$$L_{Li} = \begin{pmatrix} \nu_{Li} \\ \ell_{Li} \end{pmatrix}, \quad Q_{Li} = \begin{pmatrix} u_{Li} \\ d_{Li} \end{pmatrix} \tag{1.14}$$

where the generation index is $i = e, \mu, \tau$ for the lepton doublet L and $i = (u, c, t)$ and $i = (d, s, b)$ for the up and down type quarks respectively. The right–handed fermions are written simply as ℓ_{Ri}, u_{Ri} and d_{Ri} respectively as they are gauge singlets.

Left– and right–handed fermions have different hypercharges. We can denote Y_Q and Y_L as the hypercharge of the left–handed quark and lepton fields respectively, while Y_e, Y_u, and Y_d denote the hypercharges of the right–handed fields. The field content and their representations under the different gauge groups in the SM are shown in Table 1.1, where the first two columns show the transformation properties under $SU(3)_C$ and $SU(2)_L$, while the last column shows the hypercharge of each field.

Name			$SU(3)_C, SU(2)_L, U(1)_Y$
Matter Fields (Spin-1/2)			
Quarks (3 Gen.)	Q	$(u_L \;\; d_L)$	$(\mathbf{3},\mathbf{2},\frac{1}{6})$
	$\overline{u}$	$u_R^\dagger$	$(\overline{3},\mathbf{1},-\frac{2}{3})$
	$\overline{d}$	$d_R^\dagger$	$(\overline{3},\mathbf{1},\frac{1}{3})$
Leptons (3 Gen.)	L	$(\nu_L \;\; \ell_L)$	$(\mathbf{1},\mathbf{2},-\frac{1}{2})$
	$\overline{e}$	$\ell_R^\dagger$	$(\mathbf{1},\mathbf{1},1)$
Gauge Fields (Spin-1)			
B Boson		B	$(\mathbf{1},\mathbf{1},0)$
W Bosons		W	$(\mathbf{1},\mathbf{3},0)$
Gluons		g	$(\mathbf{8},\mathbf{1},0)$
Scalar Fields (Spin-0)			
Higgs boson	Φ	$(\phi^+ \;\; \phi^0)$	$(\mathbf{1},\mathbf{2},\frac{1}{2})$

Table 1.1: The Standard Model matter and gauge field content with associated quantum numbers for each field. Quarks and leptons both have three families that transform the same under the SM gauge group.

A lepton mass term in the SM Lagrangian would have the form $m_\alpha[\overline{\ell}_{R\alpha}\ell_{L\alpha} + \overline{\ell}_{L\alpha}\ell_{R\alpha}]$ where L and R stand for left– and right–hand chiralities and α stands for generation. The left– and right–chiralities transform differently under $SU(2)_L$ and $U(1)_Y$. As a consequence, the explicit mass terms are forbidden in the SM Lagrangian since they violate gauge invariance. The resolution to this problem is achieved by means of the Higgs field and its interactions with fermions, known as *Yukawa interactions*. When the Higgs field acquires its vev v, the Yukawa interactions lead to fermion mass terms as well as mixing between different generations in the SM Lagrangian (1.1). For the fermions, the Yukawa interaction is given by

$$\mathcal{L}_{Yukawa} = -(y_\ell)_{ij}\overline{L}_i\Phi\ell_{Rj} - (y_d)_{ij}\overline{Q}_i\Phi d_{Rj} - (y_u)_{ij}\overline{Q}_i\widetilde{\Phi}u_{Rj} + h.c, \tag{1.15}$$

where the conjugate scalar doublet is defined $\widetilde{\Phi} = i\sigma_2\Phi^*$ while y_ℓ, y_d and y_u are the 3×3 lepton, down and up quark Yukawa coupling matrices in generation space respectively. This Lagrangian is gauge invariant and we note that both left–handed leptons and the Higgs field are $SU(2)$ doublets while the right–handed fields are $SU(2)$ singlets as shown in Table 1.1. After symmetry breaking, the Yukawa Lagrangian in the unitary gauge becomes

$$\mathcal{L}_{Yukawa} = -\left(\frac{h+v}{\sqrt{2}}\right)\left[(y_\ell)_{ij}\overline{\ell}_{Li}\ell_{Rj} + (y_u)_{ij}\overline{u}_{Li}u_{Rj} + (y_d)_{ij}\overline{d}_{Li}d_{Rj}\right] + h.c. \tag{1.16}$$

Hence we can see that the mass terms for charged fermions are of the form

$$m_f = \frac{y_f}{\sqrt{2}}v \tag{1.17}$$

where $f = \ell, u, d$ after symmetry breaking, while neutrinos remain massless. There are no right–handed neutrino states ν_R in the SM (since none have been experimentally observed yet), which would be required to produce a neutrino mass term via an interaction with the Higgs field.

The fermion mass matrices are non–diagonal and can be diagonalised to the mass matrix M_f^{diag} by the bi–unitary transformations

$$m_f = V_L^{f\dagger} M_f^{\text{diag}} V_R^f \tag{1.18}$$

where V_L^f and V_R^f are unitary rotation matices that can be absorbed by redefining the left- and right-handed fermion fields like

$$\psi_{fL} \to V_L^{f\dagger}\psi_{fL}, \qquad \psi_{fR} \to V_R^{f\dagger}\psi_{RL}. \tag{1.19}$$

The neutral currents remain diagonal under such a transformation, while the charged ones become flavour violating.

1.1.3 Cabbibo–Kobayashi–Maskawa Matrix

If the change of basis is performed as (1.19), the $W^\pm$ interactions couple to the physical left–handed quark field q_L, leading to a mixing between generations in the charged current interactions

$$\mathcal{L}_{kin} = -\frac{g}{\sqrt{2}}\overline{u}_{Li}\gamma^\mu V_{\text{CKM}} d_{Lj} W^+ + h.c, \tag{1.20}$$

where $V_{\text{CKM}} = V_L^u V_L^{d\dagger}$ is known as the CKM matrix [27]. The CKM matrix is a 3×3 unitary matrix that can be parameterised by three mixing angles and one phase [28],

$$V_{\text{CKM}} = \begin{pmatrix} c_{12}c_{13} & s_{12}c_{13} & s_{13}e^{-i\delta} \\ -s_{12}c_{23} - c_{12}s_{23}s_{13}e^{i\delta} & c_{12}c_{23} - s_{12}s_{23}s_{13}e^{i\delta} & s_{23}c_{13} \\ s_{12}s_{23} - c_{12}c_{23}s_{13}e^{i\delta} & -c_{12}s_{23} - s_{12}c_{23}s_{13}e^{i\delta} & c_{23}c_{13} \end{pmatrix}, \tag{1.21}$$

where $s_{ij} = \sin\theta_{ij}$ and $c_{ij} = \cos\theta_{ij}$ correspond to rotations in the (i,j) flavour planes and δ is the phase that accounts for CP violation in the SM.[1]

The three angles and one complex phase, must be extracted from experiment, similar to the fermion masses. To clarify this, we note that any $n\times n$ unitary matrix has n^2 parameters, from which $n(n-1)/2$ are real and $n(n+1)/2$ are complex. Some of the complex parameters can be absorbed by re–phasing the quark fields. More specifically, by redefining the n down type quarks and the n up type quarks and by imposing baryon number conservation, we can eliminate $2n-1$ phases (the relative phases of the quark fields) [29]. Therefore, by taking $n=3$ we obtain that the CKM matrix has $n(n-1)/2 = 3$ angles, and $(n-1)(n-2)/2 = 1$ phase. The observation that a third generation is needed in order to have CP violation in the SM is known as the Kobayashi–Maskawa mechanism [29]. We discuss what CP violation is in more detail in the following section.

[1] The necessary condition for CP invariance is that all elements of the CKM matrix are real. This is true for the three quark generation case, only if $\delta = 0$ or $\delta = \pi$. If δ differs from these two values, it means that the CKM matrix is a source of CP violation as observed in nature.

1.1.4 CP Violation in the Standard Model

Parity (P) and charge–conjugation (C) are two fundamental discrete operations which can be performed on a physical system. At one time, it was thought that nature was invariant under these operations. In other words, a parity-transformed or charge-conjugate system would be an equally viable system which could be observed in nature. In particle physics terms, the charge–conjugation parity (CP) symmetry signifies that the laws of physics should be the same if a particle is replaced with its antiparticle while its spatial coordinates are inverted. Hence, assuming that the evolution of the universe preserves the ratio between matter and antimatter components, the CP symmetry must have been violated in the early universe somehow to explain the overwhelming predominance of matter over antimatter in our current universe. This comprises one of the Sakharov's conditions as discussed in the following Section 1.1.5.

In the previous section, we explained how CP violation appears in weak interactions in the SM. This was observed for the first time in processes, such as neutral K_L decays [30], and established later in B and D decays. However, the amount of CP asymmetry generated during such weak interactions is simply not enough to explain the observed over abundance of matter over antimatter. This strongly suggests that, besides weak interactions in the quark sector there must exist some additional sources of CP violation, comprising physics beyond the SM.

1.1.5 Sakharov's Conditions

In 1967 Andrei Sakharov proposed three necessary conditions for a matter dominated universe [31]. In the quark sector, this process is referred to as *baryogenesis*.

- A mechanism for baryon number violation. Baryon number refers to the difference in the number of baryons B and anti–baryons $\overline{B}$: $n_B = B - \overline{B}$. Any theory that starts from a symmetric universe where $n_B = 0$ and transitions to a universe where $n_B \neq 0$ has to violate the conservation of baryon number [32].

- The presence of CP violation. This is required because otherwise the transition probabilities for a process generating a baryon asymmetry would be equivalent for the C or CP conjugate process producing the same asymmetry but with opposite charge. Therefore, even in the presence of baryon number violation there would be no net baryon number without C and CP violation.

  An intuitive way to understand this is by realising that a universe with zero net baryon number is symmetric under the exchange of particles with antiparticles (C symmetry) whereas a universe with finite net baryon number cannot be. Hence there has to be some source of C and CP violation in order to explain the $n_B > 0$, which we clearly observe with the significant presence of baryonic matter in our universe [32].

- A first–order phase transition. This is an out-of-equilibrium condition that can also be understood intuitively. In thermal equilibrium the expectation values of all observables are constant as equilibrium by definition is time translationally invariant. If we want to go from a universe with $n_B = 0$ to a universe with $n_B \neq 0$ there must be an out–of–equilibrium phase to overcome this. Since in equilibrium, the mass of a particle and its antiparticle are equal, the CPT theorem would mean equal numbers of particles and antiparticles are enforced [32].[2]

An extension to the SM known as the 2HDM introduces a new Higgs doublet where four new Higgs bosons are hypothesised. The 2HDM is able to produce the required phase transition and potentially generate the CP violation conditions in some regions of its parameter space. One specific case is the $A \to ZH$ decay, which may be considered the smoking gun for electroweak baryogenesis. We discuss this further in the following Section 1.2.

1.2 The Two Higgs Doublet Model

After the Big Bang, it is thought that baryonic matter was at equilibrium with photons $\gamma + \gamma \rightleftharpoons p + \overline{p}$. As the temperature of the universe dropped and it expanded, the forward direction into matter stopped. Then, with further expansion, the density of baryons and anti–baryons fell further, and the backwards process also fell, eventually freezing the number of baryons and anti–baryons with an experimentally measured number density ratio of $\frac{n_b - n_{\overline{b}}}{n_\gamma} \approx 10^{-9}$ [33]. As mentioned in Section 1.1.4, the experimentally observed matter–antimatter asymmetry today is not consistent with the limited CP violation induced by the CKM matrix. A successful extension of the SM must be invoked in order to properly explain the baryon asymmetry as the universe transitioned out of thermal equilibrium.

Simple extensions of the SM include adding one or two real scalar singlets or one or two complex singlets or doublets respectively. The 2HDMs [34, 35] are in the latter category. The scalar spectrum of the 2HDM introduces five new bosons and consists of several types, both of which will be introduced here. It is one of the most well known and well studied extensions, and can be used as a general benchmark for additional Higgs bosons or as part of the Minimal Supersymmetric SM [34]. 2HDMs may be used to explain the baryon asymmetry [36–39] through electroweak baryogenesis [40], and similar models with two complex Higgs doublets are also part of some dark matter [41] and neutrino mass models [42].

In the 2HDM, an additional complex $SU(2)$ doublet is added to the Higgs sector. After symmetry breaking, we get [34]

$$\langle \Phi_1 \rangle = \frac{1}{\sqrt{2}} \begin{pmatrix} 0 \\ v_1 \end{pmatrix}, \qquad \langle \Phi_2 \rangle = \frac{1}{\sqrt{2}} \begin{pmatrix} 0 \\ v_2 \end{pmatrix} \tag{1.22}$$

where v_1 and v_2 are the real valued vevs of the two doublets Φ_1 and Φ_2 respectively. We require $v_1^2 + v_2^2 = v^2$ to recover SM like Higgs phenomenology for the lightest neutral scalar in the model [35]. Complex and zero vev models are also possible but we shall focus on the real–valued case here for simplicity. The gauge invariant scalar potential can then be written

[2]The CPT theorem states that the laws of physics are invariant under a charge–conjugation, parity and time transformation. It is satisfied in all Lorentz invariant local quantum field theories.

$$V(\Phi_1,\Phi_2) = m_{11}^2\Phi_1^\dagger\Phi_1 + m_{22}^2\Phi_2^\dagger\Phi_2 - m_{12}^2(\Phi_1^\dagger\Phi_2 + \Phi_2^\dagger\Phi_1) + \frac{\lambda_1}{2}(\Phi_1^\dagger\Phi_1)^2 \\ + \frac{\lambda_2}{2}(\Phi_2^\dagger\Phi_2)^2 + \lambda_3\Phi_1^\dagger\Phi_1\Phi_2^\dagger\Phi_2 + \lambda_4\Phi_1^\dagger\Phi_2\Phi_2^\dagger\Phi_1 \\ + \frac{\lambda_5}{2}[(\Phi_1^\dagger\Phi_2)^2 + (\Phi_2^\dagger\Phi_1)^2]. \tag{1.23}$$

With two complex $SU(2)$ doublets, there are eight fields,

$$\Phi_a = \begin{pmatrix} \phi_a^+ \\ \frac{1}{\sqrt{2}}(v_a + \rho_a + i\eta_a) \end{pmatrix}. \tag{1.24}$$

Three of these get "eaten" to give mass to the $W^\pm$ and Z gauge bosons and the remaining five scalars are the physical Higgs fields. There is a charged scalar, two neutral scalars and one pseudoscalar. Substituting the minimisation condition (1.22) into the scalar potential (1.23), the mass terms in the Lagrangian for the charged scalars becomes

$$\mathcal{L}_{\phi^\pm} = [m_{12}^2 - (\lambda_4 + \lambda_5)v_1v_2]\begin{pmatrix}\phi_1^- & \phi_2^-\end{pmatrix}\begin{pmatrix} \frac{v_2}{v_1} & -1 \\ -1 & \frac{v_1}{v_2}\end{pmatrix}\begin{pmatrix}\phi_1^+ \\ \phi_2^+\end{pmatrix}. \tag{1.25}$$

There is a zero eigenvalue corresponding to the charged Goldstone mode $G^\pm$ which gets eaten by the $W^\pm$. Hence the mass of the charged Higgs is given by,

$$m_+^2 = \sqrt{\frac{m_{12}^2 v^2}{v_1v_2 - \lambda_4 - \lambda_5}}, \tag{1.26}$$

while for the neutral psuedoscalars, η, we get

$$\mathcal{L}_\eta = \frac{m_A^2}{v^2}\begin{pmatrix}\eta_1 & \eta_2\end{pmatrix}\begin{pmatrix} v_2^2 & -v_1v_2 \\ -v_1v_2 & v_1^2\end{pmatrix}\begin{pmatrix}\eta_1 \\ \eta_2\end{pmatrix}, \tag{1.27}$$

where $m_A^2 = \left[\frac{m_{12}^2}{v_1v_2} - 2\lambda_5\right]v^2$. in the limit $m_{12} \to 0$ and $\lambda_5 \to 0$ the physical pseudoscalar is massless. Constructing the squared mass matrix for the neutral scalars, ρ, we get

$$\mathcal{L}_\rho = -\begin{pmatrix}\rho_1 & \rho_2\end{pmatrix}\begin{pmatrix} m_{12}^2\frac{v_2}{v_1} + \lambda_1 v_1^2 & -m_{12}^2 + \lambda_{345}v_1v_2 \\ -m_{12}^2 + \lambda_{345}v_1v_2 & m_{12}^2\frac{v_1}{v_2} + \lambda_2 v_2^2\end{pmatrix}\begin{pmatrix}\rho_1 \\ \rho_2\end{pmatrix}, \tag{1.28}$$

with $\lambda_{345} = \lambda_3 + \lambda_4 + \lambda_5$. The squared mass matrix of the scalars can consequently be diagonalised with the angle α defined as the rotation from mass to interaction basis. One of the other important angles is the vev ratio $\tan\beta = \frac{v_2}{v_1}$, which is the rotation angle that diagonalises the squared mass matrices of the charged scalars and pseudoscalars. If we perform a field redefinition of the doublets,

$$H_1 = \cos\beta\Phi_1 + \sin\beta\Phi_2, \qquad H_2 = -\sin\beta\Phi_1 + \cos\beta\Phi_2, \tag{1.29}$$

it follows that the lower component of H_1 has a real and positive vev $v/\sqrt{2} =$

$\sqrt{v_1^2+v_2^2})/\sqrt{2}$ while H_2 has a zero vev. Therefore, the parameters α and β together, determine the interactions of the various Higgs fields with the gauge bosons and fermions. Hence, they are crucial when it comes to phenomenological predictions of the model.

1.2.1 Two-Higgs-Doublet Model Types and Flavour Conservation

One of the most serious problems 2HDMs face is the potential existence of tree level flavour-changing neutral currents (FCNC). For example, the Yukawa couplings of the down type quarks will be

$$\mathcal{L}_{Yukawa} = y_{1ij}\overline{\psi}_i\psi_j\Phi_1 + y_{2ij}\overline{\psi}_i\psi_j\Phi_2 \tag{1.30}$$

where i, j are quark generation indices. The mass matrix is then given by

$$M_{ij} = y_{1ij}\frac{v_1}{\sqrt{2}} + y_{2ij}\frac{v_2}{\sqrt{2}}\,. \tag{1.31}$$

In the SM, diagonalisation of the mass matrices automatically diagonalises the Yukawa interactions, therefore there is no tree level FCNC. However, in the 2HDM, simultaneous diagonalisation of the y_1 and y_2 matrices is not possible, as they correspond to couplings with different field doublets. We end up getting neutral Higgs scalars ϕ mediating FCNC of the form $d\bar{s}\phi$ and similar flavour violating operators.

It should be noted that such FCNC can predict many observables that are tightly constrained by experimental measurements. For example, it can induce K–$\overline{K}$ meson mixing at tree level. If the coupling is comparable to the b quark mass, then the exchanged scalar mass would have to be above 10TeV [35]. With reasonable assumptions, models with these FCNC may still be viable. In the 2HDM, FCNC at tree level can only be removed by the introduction of discrete or continuous symmetries.

Studying the quark sector of the 2HDM, there are two possibilities of interest in this work. In the *type–I* 2HDM, all quarks couple to just one of the Higgs doublets (convention dictates this to be Φ_2) [35]. In the *type–II* 2HDM, the $Q = 2/3$ right–handed quarks couple to one Higgs doublet (chosen to be Φ_2) and the $Q = -1/3$ right–handed quarks couple to the other (Φ_1) [35]. The type–I 2HDM can be enforced with a simple $\Phi_1 \to -\Phi_1$ discrete Z_2 symmetry, whereas the type–II 2HDM is enforced with a combined $\Phi_1 \to -\Phi_1$, $d_{Ri} \to -d_{Ri}$ discrete symmetry. The Z_2 symmetry is softly broken in the aforementioned potential by not setting m_{12}^2 to zero while otherwise keeping the Lagrangian invariant under the $\Phi_1 \to -\Phi_1$ interchange to ensure CP conservation. Note that the original Peccei–Quinn models [43] as well as supersymmetric models give the same Yukawa couplings as in a type–II 2HDM, but do so by using continuous symmetries.

For this discussion, we will consider the case where there is no CP violating phase in the vevs of the scalar doublets $\Phi_{1,2}$. This means that $v_{1,2}$ will be assumed to be both real and positive. Thus, we may write

$$\Phi_j = \begin{pmatrix} \phi_j^+ \\ \frac{v_j+\rho_j+i\eta_j}{\sqrt{2}} \end{pmatrix}, \tag{1.32}$$

with $v_1 = v\cos\beta$ and $v_2 = v\sin\beta$. The neutral Goldstone boson can be written as the linear combination $G^0 = \eta_1\cos\beta + \eta_2\sin\beta$. The orthogonal combination to G^0 is the physical pseudoscalar

$$A = \eta_1\sin\beta - \eta_2\cos\beta. \tag{1.33}$$

The physical scalars are a lighter h and a heavier H, which are orthogonal combinations of ρ_1 and ρ_2,

$$\begin{aligned} h &= \rho_1\sin\alpha - \rho_2\cos\alpha \\ H &= -\rho_1\cos\alpha - \rho_2\sin\alpha. \end{aligned} \tag{1.34}$$

In such a scenario, it turns out that the SM Higgs is given by

$$\begin{aligned} h_{SM} &= \rho_1\cos\beta + \rho_2\sin\beta \\ &= h\sin(\alpha-\beta). \end{aligned} \tag{1.35}$$

One can then, without loss of generality, assume that β is in the first quadrant i.e. $v_1, v_2 \geq 0$ and real, adding π to α which inverts the sign of both the h and H fields, without affecting any physics [44].

In the *lepton–specific* 2HDM, the right–handed quarks all couple to Φ_2 and the right–handed leptons couple to Φ_1 [35]. In the *flipped* 2HDM, one has the $Q = 2/3$ right–handed quarks coupling to Φ_2 and the $Q = -1/3$ right–handed quarks coupling to Φ_1, as in the type–II 2HDM, but now the right–handed leptons couple to Φ_2 as well [35]. We may characterise the various 2HDMs as

- Type-I, in which the right–handed up and down type quarks and the right–handed charged leptons couple to Φ_2.
- Type-II, in which only the right–handed up type quarks couple to Φ_2 and the right–handed down type quarks and the right–handed charged leptons couple to Φ_1.
- Lepton–specific, where the right–handed quarks couple to Φ_2 and the right–handed charged leptons to Φ_1.
- Flipped, where the right–handed up type quarks and the right–handed charged leptons couple to Φ_2 and right–handed down type quarks to Φ_1.

Model	u_{Ri}	d_{Ri}	e_{Ri}
Type-I	Φ_2	Φ_2	Φ_2
Type-II	Φ_2	Φ_1	Φ_1
Lepton–Specific	Φ_2	Φ_2	Φ_1
Flipped	Φ_2	Φ_1	Φ_2

TABLE 1.2: Summary of Two-Higgs-Doublet Model types by scalar–fermion interactions [35]

The coupling of H to a pair of vector bosons is the same as the SM but with an additional factor of $\cos(\beta-\alpha)$, and the physical pseudoscalar A couples to V and both the neutral scalars like [17]

$$g_{HVV} = \cos(\beta - \alpha) g^{SM}_{hVV},$$
$$g_{AZh} \propto \cos(\beta - \alpha) g^{SM}_{hVV}, \tag{1.36}$$
$$g_{AZh} \propto \sin(\beta - \alpha). \tag{1.37}$$

For type–I and lepton–specific models, the gluon-gluon fusion production for A dominates (as it does for the SM Higgs) in proton–proton collisions. While b-associated production (via fusion of b quarks) becomes important for the other two models for large values of $\tan\beta$ [35, 45].

The ability for a 2HDM to generate a strong first–order phase transition to induce baryogenesis is found through Monte Carlo (MC) simulations by scanning a wide range of m_A, m_H, $\tan\beta$ and $\alpha - \beta$ values [45]. Any points satisfying unitarity requirements, precision constraints and collider bounds are considered physical, while points also passing $v_c/T_c > 1$ (v_c being the magnitude of the broken vev at the critical temperature T_c) will lead to the required strong phase transition. The results are shown in Figure 1.2 as heat maps visualising the density of points passing the criteria. In general, models near the alignment limit ($\cos(\beta - \alpha) = 0$) are favoured, especially for larger m_H. A relatively large mass difference $m_A - m_H$ is also favoured with most points lying in for $m_A > m_H$.

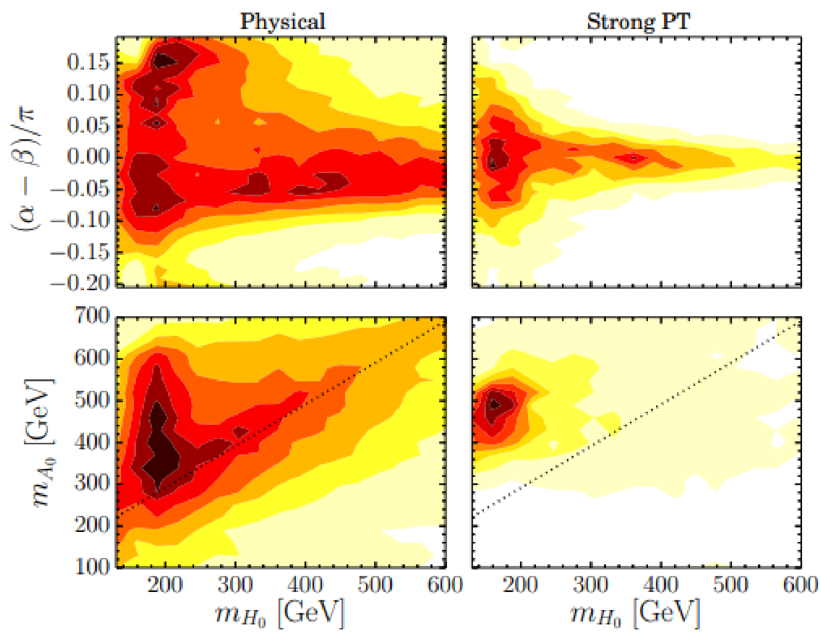

FIGURE 1.2: Heat maps for the physical region (left) and region with a strongly first–order electroweak phase transition (right). Top: $(m_H, \frac{\alpha-\beta}{\pi})$ plane. Bottom: (m_H, m_A) plane. The dotted black line corresponds to the resonance condition $m_A = m_H + m_Z$ [45].

In Figure 1.3 [45], we show the branching ratios for H and A close to and away from the alignment limit as a function of mass m_H. For the H decay, the WW final state dominates away from alignment. For the A decay, the branching ratio is less dependent on the alignment, and $A \to t\bar{t}$ becomes dominant at $m_H \gtrsim 250$GeV. These figures provide some preliminary indications on the expected sensitivity for the $A \to ZH \to \ell\ell bb(\ell\ell WW)$ decays. We expect falling sensitivity past $m_H = 250$GeV. There is one ATLAS study on the $A \to t\bar{t}$ channel using limited Run 1 data [46], but extra care has to be taken due to the interference with the SM $t\bar{t}$ decay. We shall make some more assumptions on the properties of the Higgs bosons to simplify the following analysis. The lightest CP even boson (h) is assumed to be the SM Higgs at $m_h = 125$GeV with $m_H > m_h$, the heavier CP even boson is lighter than the CP odd ($m_H < m_A$), and the charged bosons have the same mass as the CP odd ($m_{H^\pm} = m_A$).The parameter m_{12}^2 is defined as

$$m_{12}^2 = \frac{m_A^2 \tan\beta}{1 + \tan^2\beta}, \tag{1.38}$$

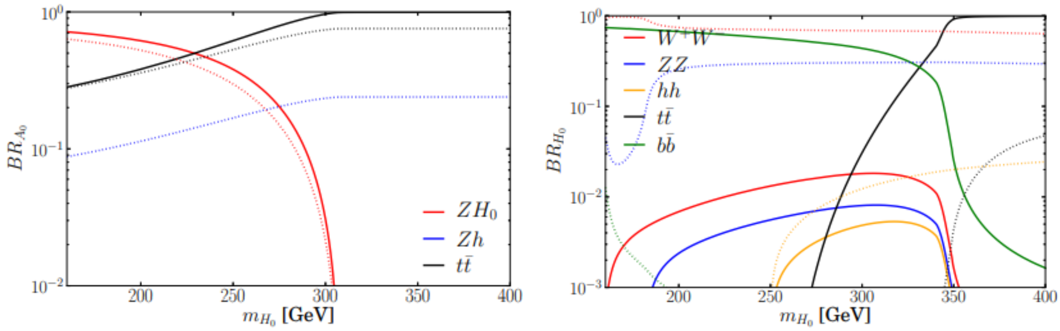

FIGURE 1.3: Left: Main Branching Ratios of the CP-odd scalar A as a function of m_H for $m_A = m_H^\pm = 400$GeV, $\tan\beta = 2, \mu = 100$GeV, $\alpha - \beta = 0.001\pi$ (solid lines) and $\alpha - \beta = 0.1\pi$ (dotted lines). Right: Main Branching Ratios of H as a function of m_H (same benchmark parameters as in the left panel) [45].

For the ATLAS analysis discussed in Chapter 2, production cross sections are calculated by SusHi 1.7.0 [47–53] using the parton distribution functions (PDFs) from the LHAPDF 6.3.0 [54] library, the partial decay widths and branching ratios are calculated by 2HDMC 1.7.0 [55]. These values have been calculated for $-1 \leq \cos(\beta - \alpha) \leq 1$ in steps of 0.1, $0.5 \leq \tan\beta \leq 3$ in steps of 0.5, and $(m_A, m_H) = (300, 200)$ to $(800, 700)$GeV in steps of 50GeV in the (m_A, m_H) plane with the previously mentioned condition that $m_A > m_H$. Under these constraints, the $A \to ZH$ decay dominates [52].

Current limits on α and β are shown in Figure 1.4. The result on the top left panel is made at the alignment limit. However, it should be noted that the results from the top right and bottom panels are not directly comparable to the top left panel and the results shown in this work. This is because they are indirect searches that assume very large masses for both A and H, making it possible to integrate out the heavy fields [45]. It should also be noted that no CMS results for type-I 2HDM currently exist.

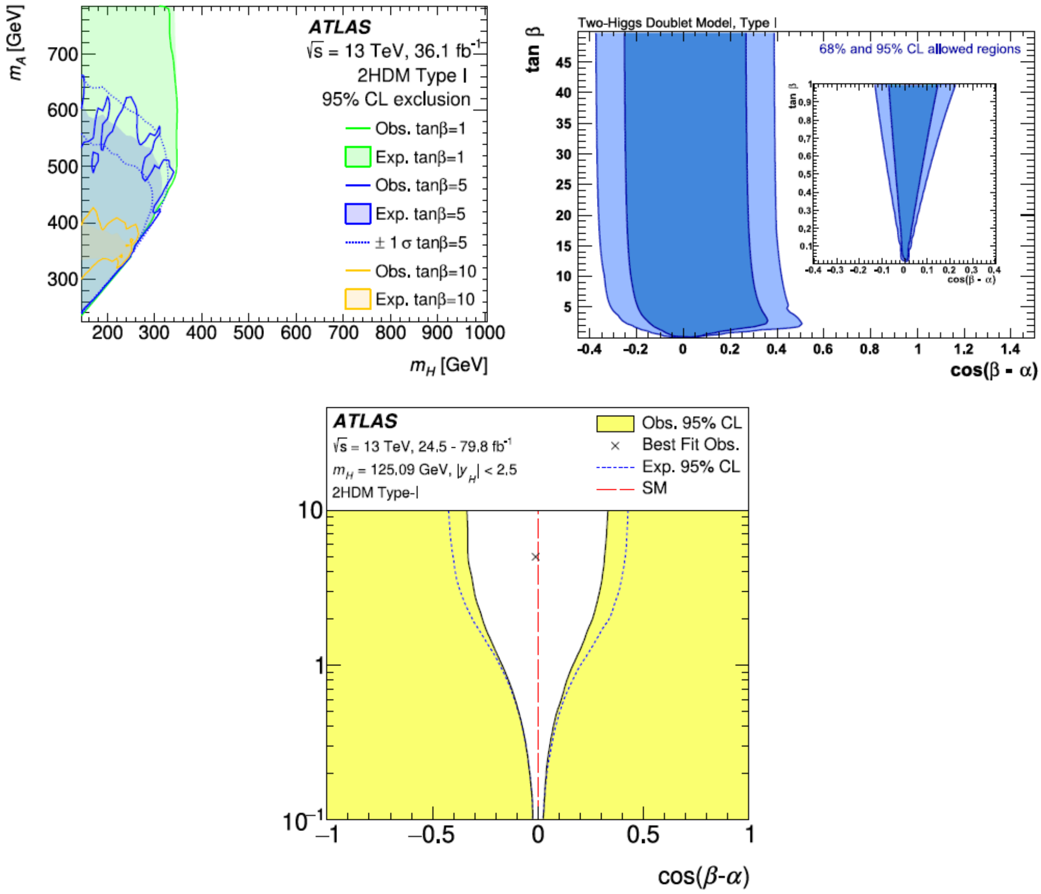

FIGURE 1.4: Top left: Exclusion bounds for type–I 2HDM from the previous iteration of the AZH analysis [56], Top right: combined results from ATLAS and CMS [57] and finally the, Bottom: latest ATLAS results [58].

1.3 Cosmological Phase Transitions and Baryogenesis

In Section 1.2, we have discussed the 2HDM and its searches at the ATLAS experiment. We also motivated the reason for its existence as it produces the correct scalar potential to enable a first–order phase transition in the early universe. As we mentioned in in Section 1.1.5, a phase–transition is a Sakharov condition that is required for baryogenesis to occur. The phase transition(s) themselves may give rise to a variety of physical processes with rich phenomenology, and some of their effects may be observable in our current universe, such as the production of a stochastic gravitational wave background [59, 60]. In these bubbles a meta–stable phase may exist alongside a stable one for some band of temperatures. For a very large system wherein the temperature is modulated at a very slow rate, the phase transition takes place at a temperature called the critical temperature T_c.

If the temperature reduction rate is finite, as would be the case in a universe that is expanding, the temperature of the phase transition differs from T_c. At T_c nothing of interest happens per se, the high temperature region simply moves into a super–cooled state. However, at a somewhat lower temperature, bubbles of the new phase begin to nucleate. The bubbles can then grow and convert the region of space with the old field value to the new field value. The new phase will have a lower energy density than the old one. Hence, in the phase transition the universe is heated up to a certain temperature lower than the critical temperature. After completions of the transition, the universe starts to cool again as usual. Such super–cooling is crucial for scenarios in electroweak scale baryogenesis [61].

Hence it is of crucial importance to study how these phase transitions propagate in the early universe plasma. Since first–order phase transitions occur via bubble nucleation and subsequent expansion, it is essential to understand the velocity of the expanding bubble wall v_w. This is because, for example, the electroweak baryogenesis is based on particle asymmetries diffusing into the plasma in front of the bubble wall [61]. Subsonic bubble walls are necessary to build up a large baryon asymmetry (note here that "sonic" refers to the speed of sound in the plasma of interest). However, fast moving walls are essential for the production of a sizeable amount of gravitational radiation by bubble collisions [60, 62, 63], turbulence [64] or magnetic fields [65]. Determining this wall velocity in a numerically accurate way comprises the main topic of investigation in Chapter 3.

The analysis of the bubble wall velocity generally assumes that after a short period of acceleration of order $\sim 1/T$, (where T represents the typical energy scale associated with the temperature or latent heat of the transition) the pressure difference that drives the bubble expansion is balanced by friction and the bubbles subsequently expand with a constant speed due to the net force being zero as shown in Figure 1.5. Determining the amount of friction requires solving a coupled system of Boltzmann equations for all particle species with a large coupling to the Higgs field. This type of calculation has thus far only been performed in the SM [66] and in the Minimal Supersymmetric Standard Model (MSSM) [67] under the assumption of small v_w. On the other hand, in the limit of $v_w \lesssim c$ it is found that the friction in the plasma approaches a constant value [68] (potentially up to $\log(\gamma_w)$ corrections where $\gamma_w = \frac{1}{\sqrt{1-\frac{v^2}{c^2}}}$). This enables the possibility of continuously accelerating "runaway" bubble walls where the pressure difference along the wall overcomes this threshold. This runaway behaviour is in fact realistic in many models, if no hydrodynamic obstruction prohibits the highly relativistic regime from being reached [61].

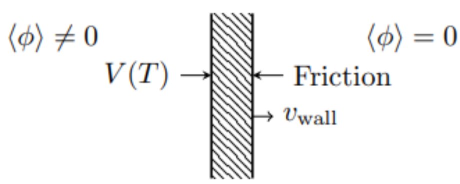

FIGURE 1.5: Force balance shown at the bubble wall. The latent heat released during the phase transition drives the bubble outwards, while its interaction with the plasma of light particles creates friction. When the two forces are balanced, the net force is zero and the wall ceases to accelerate [69].

Therefore an important analysis to perform is to identify and compute possible obstruction forces based on the plasma heating in front of the phase boundary during bubble expansion. Such an effect has previously been observed [66, 70], where finite

v_w were found with very small and even vanishing friction. More recently [71], this result was obtained under the assumption that the temperature in the Higgs wall is identified with the temperature in front of the bubble. Additionally, the study focused on models with a scalar potential similar to the SM.

What is preferable is to determine a simple criterion for the occurrence of such back reaction forces. If the criterion holds for specific cases, the v_w is subsonic and electroweak baryogenesis is possible. Such a heating effect only provides an upper bound and a more precise determination of the wall velocity still requires some knowledge of friction. However, if the friction is not too large (like in the SM) the resulting v_w are fairly accurate [61]. Furthermore, the baryon asymmetry in electroweak baryogenesis is not highly sensitive to the wall velocity, therefore, as long as it is significantly below the speed of sound and large enough to avoid a saturation of the sphaleron process.

1.3.1 The Nucleation Temperature

In a first–order phase transition, the nucleation of bubbles is governed by the three dimensional instanton action for field ϕ,

$$S_3 = 4\pi \int_0^\infty r^2 dr \left[\frac{1}{2} \left(\frac{d\phi}{dr} \right)^2 + V(\phi(r), T) \right], \tag{1.39}$$

where the potential is defined $V(\phi(r), T) = \mathcal{F}(\phi, T) - \mathcal{F}(0, T)$ and $\mathcal{F}$ is the free energy of the field and T is the temperature. The bounce solution of this action is obtained by extremising S_3. This yields the radial configuration of the nucleated bubble assuming that it is spherically symmetric [72]. The action for this bounce solution coincides with the free energy of a critical bubble, in other words, a bubble in an unstable equilibrium between states of expansion and contraction. Using the Euler–Lagrange equations, we find the bounce solution obeys the equation

$$\frac{d^2\phi}{dr^2} + \frac{2}{r}\frac{d\phi}{dr} = V'(\phi) \tag{1.40}$$

with the boundary conditions

$$\frac{d\phi}{dr}(0) = 0, \qquad \lim_{r\to\infty} \phi(r) = 0. \tag{1.41}$$

Then we may compute the tunneling probability for bubble nucleation per unit time and volume which is given by [72]

$$\Gamma(T) \simeq A(T) e^{-S_3(T)/T}, \tag{1.42}$$

where $A(T) = [S_3(T)/2\pi T]^{3/2}$. The nucleation temperature T_N is defined as the temperature at which the probability of finding a bubble in a causal volume is 1, so

$$\int_{t_c}^{t_N} dt \Gamma(T) V = 1, \tag{1.43}$$

where t_c is the time at which the universe reaches the critical temperature T_c and t_N is the time at which the first bubbles are nucleated in a causal volume V. The nucleation rate $\Gamma(T)$ can be calculated by numerically solving for the bubble profile from (1.40) and (1.41) before substituting back into the bounce action (1.39) integrating and finally computing (1.42).

1.3.2 Origin of the Friction Force

The combined "wall-plasma" system dynamics is described by the equations of motion of the Higgs field and the plasma. However, for the following discussion, it is advantageous to replace the equation of motion of the plasma (similar to a Boltzmann equation) by the assumption of local thermal equilibrium and energy–momentum conservation, leading to a hydrodynamic approximation [61]. The energy-momentum tensor of the Higgs field ϕ is then given by

$$T^{\phi}_{\mu\nu} = \partial_\mu\phi\partial_\nu\phi - g_{\mu\nu}\left[\frac{1}{2}\partial_\rho\phi\partial^\rho\phi - V_0(\phi)\right], \tag{1.44}$$

where $V_0(\phi)$ is the re–normalised vacuum potential. Since the field ϕ is a background field which interacts will all particle content: Higgs bosons, gauge fields, leptons and quarks), this combination of fields form a plasma. If one approximates the equilibrium distribution functions f_i for i particle species with four–momentum k^μ by a relativistic fluid u^μ, the stress-energy momentum tensor of the fluid is

$$T^{plasma}_{\mu\nu} = \sum_i \int \frac{d^3k}{(2\pi)^3 E_i} k_\mu k_\nu f_i(k), \tag{1.45}$$

if this plasma is in local equilibrium, this may then be conveniently written as

$$T^{plasma}_{\mu\nu} = w u_\mu u_\nu - g_{\mu\nu} p, \tag{1.46}$$

where w and p represent the enthalpy and pressure of the plasma respectively. The quantity u_μ is the four–velocity field of the plasma related to the usual three–velocity $\mathbf{v}$ by $u_\mu = (\gamma, \gamma\mathbf{v})$ where γ is the canonical Lorentz factor.

There is a contribution to the total pressure from the constant ϕ background, we may denote this total pressure as p. The enthalpy ω, the entropy density σ and the energy density E can then be defined by the relations

$$\omega = T\frac{\partial p}{\partial T}, \qquad \sigma = \frac{\partial p}{\partial T}, \qquad E = T\frac{\partial p}{\partial T} - p, \tag{1.47}$$

where T is the plasma temperature. It then follows that

$$w = E + p. \tag{1.48}$$

Energy-momentum conservation then yields

$$\partial^\mu T_{\mu\nu} = \partial^\mu T^{\phi}_{\mu\nu} + \partial^\mu T^{plasma}_{\mu\nu} = 0. \tag{1.49}$$

Since we want to analyse a system where the bounce propagates at a constant speed. Assuming there is no time–dependence i.e. in the static limit, (1.49) in the wall–frame (with the wall and fluid velocities aligned in the z direction), the above equation becomes

$$\partial_z T^{zz} = \partial_z T^{z0} = 0. \tag{1.50}$$

Integrating the above equations and denoting the fields in front of and behind the bubble wall by subscripts + and −, respectively, in the wall frame, we get

$$\omega_+ v_+^2 \gamma_+^2 + p_+ = \omega_- v_-^2 \gamma_-^2 + p_-, \qquad \omega_+ v_+ \gamma_+^2 = w_- v_- \gamma^2. \tag{1.51}$$

From here it follows that [61]

$$v_+ v_- = \frac{p_+ - p_-}{E_+ - E_-}, \qquad \frac{v_+}{v_-} = \frac{E_- + p_+}{E_+ + p_-}. \tag{1.52}$$

For a chosen model, the thermodynamic potentials can be calculated in the front and back sections of the wall and the temperature at which the phase transition begins can be determined using numerical techniques. Then, we are left with three unknown variables (T_-, v_+ and v_-) and only two equations, so the viable family of solutions are parametrised by one parameter. It is convenient to parametrise the solution by its wall velocity v_w, as this is the observable of interest.

The wall velocity is obtained from the equation of motion of the Higgs [61]

$$\Box\phi + \frac{\partial \mathcal{F}}{\partial \phi} - \mathcal{K}(\phi) = 0. \tag{1.53}$$

Where the bubble expansion is driven by the the free energy $\mathcal{F}$ and $\mathcal{K}(\phi)$ represents the friction term that arises from deviations of the particle distributions in the plasma from equilibrium. It was shown in Ref. [61] that a subsonic v_w could be reached even if the friction is vanishingly small. This is in contrast to the previous intuitive expectation of faster than sound velocity or runaway behaviour in the low friction limit. However, (1.40), shows that in steady state, the size of the bubble is large enough that a planar limit can be used wherein integration of the pressure field in the wall frame can yield the force driving the expansion

$$F_{dr} = \int dz \partial_z \phi \frac{\partial \mathcal{F}}{\partial \phi} = \int dz \partial_z \phi \mathcal{K} = F_{fr}. \tag{1.54}$$

This equation may be interpreted as showing that the pressure change in the wall driving the bubble expansion and this driving force F_{dr} is ultimately being balanced by the friction force F_{fr} in order to reach a constant v_w as shown before in Figure 1.5.

Without the bubble, the pressure change is always positive definite, since nucleation requires $T_+ < T_c$. However, a heating effect in front of the bubble wall may be created due to some particles being reflected at the wall. Hence a hydrodynamic obstruction force can occur and the temperature experienced by the wall is also increased. This means that the bubbles may accelerate while building up a compression wave in front of the Higgs wall [61]. At some wall velocity v_w, the average temperature in the wall might approach T_c, then $F_{dr} \to 0$ and the bubble cannot further accelerate even in the limit of zero friction.

1.3.3 Calculating the Wall Velocity

If we consider a system with the bag equation of state in the broken phase (behind the wall) we have

$$p_- = \frac{1}{3}a_- T_-^4 + \epsilon \qquad\qquad E_- = a_- T_-^4 - \epsilon \tag{1.55}$$

and in the symmetric phase (in front of the wall)

$$p_+ = \frac{1}{3}a_+ T_+^4, \qquad\qquad E_+ = a_+ T_+^4, \tag{1.56}$$

with a different number of light degrees of freedom across the wall and hence $a_+ \neq a_-$ and $a_+ > a_-$ and different temperatures on either side of the wall i.e. $T_+ \neq T_-$. In the above expression ϵ represents the false vacuum energy resulting from the Higgs potential. The above bag equation of state approximation is only applicable when the Higgs vev does not change significantly between T_c and zero. However a more accurate treatment for temperatures close to the critical one is [61]

$$\begin{aligned} p_- &\simeq \frac{1}{3}a_+ T_-^4 - \ell_c\left(\frac{T_-}{T_c} - 1\right), \qquad\qquad & p_+ &\simeq \frac{1}{3}a_+ T_+^4, \\ E_- &\simeq a_+ T_-^4 - \ell_c, & E_+ &\simeq a_+ T_+^4, \end{aligned} \tag{1.57}$$

where ℓ_c is the latent heat at T_c. Comparing with the bag case, one can write down

$$\ell_c = \frac{4}{3}(a_+ - a_-)T_c^4 = 4\epsilon \tag{1.58}$$

Using the bag equation of state (1.55) and (1.56) and substituting into (1.52) we get

$$v_+ v_- = \frac{1-(1-3\alpha_+)r}{3-3(1+\alpha_+)r}, \qquad\qquad \frac{v_+}{v_-} = \frac{3+(1-3\alpha_+)r}{1+3(1+\alpha_+)r}, \tag{1.59}$$

where we have made use of the convenient definitions

$$\alpha_+ = \frac{\epsilon}{a_+ T_+^4} = \frac{\ell_c}{4a_+ T_+^4}, \qquad\qquad r = \frac{a_+ T_+^4}{a_- T_-^4}. \tag{1.60}$$

The parameter α_+ is the vacuum energy to radiation energy density ratio and characterises the strength of the phase transition. We may now solve Eq. (1.59) simultaneously to obtain [61]

$$v_+ = \frac{1}{1+\alpha_+}\left[\left(\frac{v_-}{2} + \frac{1}{6v_-}\right) \pm \sqrt{\left(\frac{v_-}{2} + \frac{1}{6v_-}\right)^2 + \alpha_+^2 + \frac{2}{3}\alpha_+ - \frac{1}{3}}\right], \tag{1.61}$$

this results in three classes of solutions for the bulk fluid motion. These are commonly referred to as detonations, deflagrations and hybrid solutions [61]. In the case of detonations, the bubble wall expands at supersonic velocities and the vacuum energy of the Higgs leads to a rarefaction wave behind the bubble wall. This occurs while the plasma in front of the wall is at rest. In detonations the wall velocity is $v_w = v_+ > v_-$, and therefore they are identified with the positive branch of solutions in Eq. (1.61). For deflagrations, the plasma is dominantly affected by particles being reflected at the bubble wall and therefore a compression wave builds up in front of the wall while the plasma behind the wall is at rest. In this case, the wall velocity is identified with $v_w = v_- > v_+$. This corresponds to the negative branch of solutions. "Pure" deflagrations are subsonic, while the hybrid case corresponds to supersonic deflagrations where both compression and refraction waves are present. We may show this diagrammatically as in Figure 1.6.

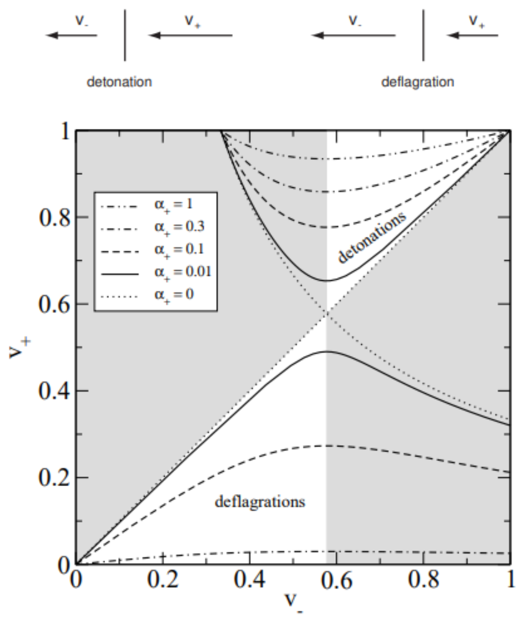

FIGURE 1.6: Top: Representation of the velocity vectors on each side of the wall, in the wall frame. Bottom: Contours of the fluid velocities v_+ and v_- in the wall frame for fixed α_+ values. In the shaded region in the top—left no consistent solutions to the hydrodynamic equations exist. Flow profiles in the shaded region in the bottom–right decay into hybrid solutions [71].

From Ref. [71], we have the central equation describing the velocity profile

$$2\frac{v}{v_w} = \gamma^2(1 - vv_w)\left[\frac{\mu^2}{c_s^2} - 1\right]\frac{\partial v}{\partial v_w}, \tag{1.62}$$

with the Lorentz transformed fluid velocity μ defined

$$\mu(v_w, v) = \frac{v_w - v}{1 - v_w v}, \tag{1.63}$$

in general, c_s is the speed of sound in the plasma and depends on its equation of state, in the bag case $c_s^2 = 1/3$. Most generally, c_s will be v_w dependent but will usually be around 1/3. Setting $c_s = 1/\sqrt{3}$ in Eq. (1.62), it is immediately clear that there are fixed points at $v_w = c_s$ and $v = 0$ and another for $v_w = v = 1$. By introducing a new quantity τ, we may rewrite (1.62) as

$$\frac{dv}{d\tau} = 2vc_s^2(1-v^2)(1-v_w v), \qquad \frac{dv_w}{d\tau} = v_w[(v_w - v)^2 - c_s^2(1-v_w v)^2] \tag{1.64}$$

The above region can be contour plotted as shown in Figure 1.7. In Chapter. 3 we

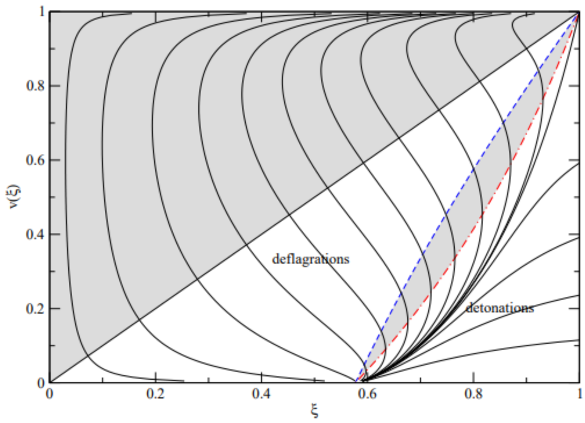

FIGURE 1.7: Contours of the fluid velocity $v(\xi)$ in the frame of the bubble centre (with $c_s^2 = 1/3$). Detonation curves start below $\mu(\xi, v) = c_s$ (dashed–dotted curve) and end at $(\xi, v) = (c_s, 0)$. Deflagration curves start below $v = \xi$ and end at $\mu(\xi, v)\xi = c_s^2$ (dashed curve) corresponding to the shock front. There are no consistent solutions in the shaded regions [71]. Note that in the above plot the variable assignment $\xi \equiv v_w$ is used.

aim to confirm that indeed local equilibrium is compatible with the above discussed subluminal bubble expansion, clarify the local origin of the friction forces and elucidate the relation to the hydrodynamic effects detailed above. Beyond this, we provide consistent estimates of bubble velocities. Rather than including additional terms in the scalar's equation of motion, the friction–like behaviour in the presence of local equilibrium is caused by the field dependence of the local entropy and enthalpy density itself, which enters into the hydrodynamic equations of the plasma similar to the heating effect discussed above.

1.4 Neutrino Physics

Neutrinos are half–integral spin electrically neutral particles which appear in three flavours ν_e (electron), ν_μ (muon) and ν_τ (tau).[3] Direct Dirac neutrino mass terms cannot be included in the SM Lagrangian due to violation of gauge invariance and as a consequence they are assumed to be massless. Nevertheless, many neutrino experiments have now shown that these particles do in fact possess nonzero, albeit very tiny masses since they can oscillate, changing from one flavour to another in flight $\nu_i \rightleftharpoons \nu_j$. Hence, a leptonic mixing matrix will appear analogous to the CKM matrix

[3] An example of electron–type neutrino production is in nuclear beta decay, particularly in neutron decay processes $n \to p + e^- + \overline{\nu}_e$, they are also produced in muon decays $\mu^\pm \to e^\pm + \overline{\nu}_\mu(\nu_\mu) + \nu_e(\overline{\nu}_e)$. Muon–type neutrinos and anti-neutrinos are produced in muon decays and pion decays $\pi^\pm \to \mu^\pm + \nu_\mu(\overline{\nu}_\mu)$. Tau–type neutrinos are produced in $\tau^\pm$ decays.

discussed in Section. 1.1.3. This gives rise to a leptonic charged current interaction of the form

$$\mathcal{L}_{kin} = \frac{g}{\sqrt{2}}\mathcal{U}_{\alpha\, i}\bar{\ell}_\alpha \gamma^\mu P_L \nu_i W^-_\mu + h.c. \tag{1.65}$$

with

$$\nu_\alpha = \mathcal{U}_{\alpha i}\nu_i \tag{1.66}$$

where $\alpha = e,\, \mu,\, \tau$ are the flavour eigenstates, $i = 1, 2, .., n$ are the mass eigenstates and $\mathcal{U}_{\alpha\, i}$ is a $3 \times n$ matrix that rotates mass eigenstates into flavour eigenstates. This matrix was introduced by Ziro Maki, Masami Nakagawa and Shoichi Sakata in 1962 [73] to describe neutrino oscillations. The idea of neutrino oscillation dates back to 1958 when Bruno Pontecorvo proposed the neutrino-antineutrino transition [74]. Today, the mixing matrix is known simply as the Pontecorvo-Maki-Nakagawa-Sakata (PMNS) matrix.

Studying neutrinos has deepened our understanding of nature for decades [75]. Even though their very tiny but nonzero masses (for two or more of their generations) and flavour mixing in the lepton sector has been observed and verified by neutrino oscillation experiments, some fundamental questions about neutrinos still exist. This includes understanding their exact electromagnetic properties, whether they are Dirac or Majorana fermions, whether there are additional sources of CP violation and if they have additional species existing in nature.

1.4.1 Dirac vs Majorana Neutrinos

In this section we will discuss the possible origins for neutrino masses. Since the nature of neutrinos being Dirac or Majorana is still an open question, both possibilities will be discussed.

Dirac Mass Term

In order to generate a Dirac neutrino mass, it is necessary to introduce additional right–handed neutrino singlets ν_R into the SM Lagrangian. This enables one to obtain neutrino mass terms through symmetry breaking and the Higgs mechanism, just like in the case of quarks and the charged leptons.

The right–handed neutrino fields are invariant under SM symmetry, since they don't transform under $SU(3)_C \times SU(2)_Y$ and have hypercharge $Y = 0$. Since they do not participate in weak interactions they are referred to as sterile neutrinos. The number of sterile neutrinos that can be introduced to extend the SM is not constrained by the theory. In the case where three sterile neutrinos, one for each flavour, are introduced to the SM, the extended Lagrangian mass term for leptons is now

$$\mathcal{L}_{Yukawa} = -(y_\ell)_{ij}\overline{L}_i \Phi e_{Rj} - (y_\nu)_{ij}\overline{L}_i \widetilde{\Phi}\nu_{Rj} + h.c., \tag{1.67}$$

where y_ℓ and y_ν are the Yukawa matrices and $\overline{L}$ is the lepton doublet given in Eq. (1.14) and

$$\nu_R = \begin{pmatrix} \nu_e \\ \nu_\mu \\ \nu_\tau \end{pmatrix}_R . \tag{1.68}$$

After electroweak symmetry breaking, the mass terms of neutrinos becomes

$$-m_D\overline{v}_L\nu_R + h.c. \tag{1.69}$$

To diagonalise the leptonic Lagrangian, we can make the field re–definitions in flavour space

$$\ell'_{L,R} = \begin{pmatrix} e' \\ \mu' \\ \tau' \end{pmatrix}_{L,R}, \qquad \nu'_{L,R} = \begin{pmatrix} \nu'_e \\ \nu'_\mu \\ \nu'_\tau \end{pmatrix}_{L,R}, \tag{1.70}$$

with $\ell_{L,R} = V^{\ell\dagger}_{L,R}\ell'_{L,R}$, $y^{\text{diag}}_\ell = V^{\ell\dagger} y_{\ell'} V^\ell_R$ for the charged leptons and $\nu_{L,R} = V^{\nu\dagger}_{L,R}\nu'_{L,R}$, $y^{\text{diag}}_\nu = V^{\nu\dagger} y_{\nu'} V^\nu_R$, where y^{diag}_ℓ and y^{diag}_ν are the diagonalised Yukawa matrices. It should be noted that the rotation matrices $V^\nu_{L,R}$ and $V^\ell_{L,R}$ are all unitary. The leptonic Lagragian can now be written

$$\mathcal{L}_{Yukawa} = -\left(\frac{v+h}{\sqrt{2}}\right)\left[(y_\ell)_{ij}\overline{\ell}'_{Li}\ell'_{Rj} - (y'_\nu)_{ij}\overline{\nu}'_{Li}\nu'_{Rj}\right] + h.c., \tag{1.71}$$

by rotating into the mass basis where the Yukawa coupling matrices y_ℓ and y_ν are diagonal, we then get the Dirac mass terms

$$\mathcal{L}^D_{mass} = -\frac{v}{\sqrt{2}}\left[y^{\text{diag}}_{\ell i}\overline{\ell}_{Li}\ell_{Ri} + y^{\text{diag}}_{\nu i}\overline{\nu}_{Li}\nu_{Ri}\right] + h.c. \tag{1.72}$$

Hence it is clear that the charged and neutral lepton masses are given by M_l is the diagonal mass matrix for charged leptons and

$$M_{li} = \frac{y^{\text{diag}}_{li} v}{\sqrt{2}}, \tag{1.73}$$

where l can be either ℓ or ν for the charged and neutral lepton case respectively.

The Yukawa matrix y_ν can be diagonalised in a similar way as the charged leptons, see Section 1.1.2, and this is

$$V^{\nu,\ell\dagger}_L y_{\nu,\ell} V^{\nu,\ell}_R = y^{\text{diag}}_\nu, \tag{1.74}$$

where $V^{\nu,\ell}_L$ and $V^{\nu,\ell}_R$ are the left and right hanged 3×3 unitary matrices and the right–hand side is the diagonalised Yukawa matrix. Hence when introducing this change of basis and the diagonalised mass matrix in Eq. (1.74) the Dirac neutrino masses terms are finally obtained in the Lagrangian given by

$$\mathcal{L}_{mass} = \frac{1}{2}\overline{\ell}_{Li}M_\ell\ell_{Ri} + \frac{1}{2}\overline{\nu}_{Li}M_\nu\nu_{Ri} + h.c. \tag{1.75}$$

where M_ℓ is the diagonalised mass matrix for charged leptons and

$$M_{\nu_i} = \frac{y^{\text{diag}}_{\nu i} v}{\sqrt{2}}. \tag{1.76}$$

The mass terms of leptons in the Lagrangian, including neutrino masses, is given in Eq. (1.75). Following a similar treatment as for the quarks as per (1.1.3), the change of basis for neutrinos shown above induces mixing between the lepton flavours. It is straightforward to show that for three Dirac neutrinos the change of basis is therefore given as

$$\mathcal{U}^D = V_L^{\nu\,\dagger} V_L^{\ell}. \tag{1.77}$$

It should be noted that the mass hierarchy problem remains and the Yukawa couplings have to be fine–tuned to explain the smallness of m_ν. The lepton numbers by generation L_e, L_μ and L_τ are violated, since charged currents do not conserve these quantities, but the total lepton number remains conserved. It is an exact global symmetry at the classical level like baryon number B. This kind of SM extension generates a mixing matrix in the leptonic sector analogous to the CKM matrix with the inclusion of the heavy neutrino species. For Dirac neutrinos the mixing matrix depends on three mixing angles and one CP violating phase. We will discuss this further in Section 1.4.2.

Majorana Mass Term

In 1937 Ettore Majorana established that a massive neutral fermion can be described by a real wave function rather than a complex one [76]. This implies that a Majorana fermion can be its own antiparticle. This led to the Majorana condition

$$\nu = \nu^c = \mathcal{C}\,\overline{\nu}^T \tag{1.78}$$

where $\mathcal{C}$ is the charge conjugation matrix defined according to $\mathcal{C}\gamma_\mu^T\mathcal{C}^{-1} = -\gamma_\mu$. By using the charge conjugated field for one generation of Majorana neutrino we may write the Majorana Lagrangian

$$\mathcal{L}^M = \frac{1}{2}\left(i\overline{\nu}_L\partial\!\!\!/\overline{\nu}_L + i\overline{\nu}_L^c\partial\!\!\!/\nu_L^c\right) - \underbrace{\frac{M_L}{2}(\overline{\nu}_L^c\nu_L + \overline{\nu}_L\nu_L^c)}_{\frac{M_L}{2}(\overline{\nu}_L^T\mathcal{C}^\dagger\nu_L + \nu_L^\dagger\mathcal{C}\nu_L^*)} \tag{1.79}$$

where the factor of $\frac{1}{2}$ in the mass term is included to avoid double counting since ν_L and ν_L^c are not independent fields. We note that we have not needed to introduce right-handed singlet fields since we used the Majorana field definitions where $\nu = \nu_L + \nu_L^C$ and $\nu^C \equiv \mathcal{C}\,\overline{\nu}^T$.

If three generations of Majorana neutrinos are considered the Majorana mass term becomes

$$\mathcal{L}^M_{mass} = -\frac{1}{2}\nu'^{\,T}_{\alpha\,L}\mathcal{C}^\dagger(M_L)_{\alpha\beta}\nu'_{\beta\,L} - \frac{1}{2}\nu'^{\,\dagger}_{\alpha\,L}\mathcal{C}(M_L)_{\alpha\beta}\nu^{*\prime}_{\beta\,L}. \tag{1.80}$$

As in the Dirac neutrino case, it is necessary to diagonalise the complex symmetric matrix M_L. This, as usual, is achieved by introducing the 3×3 unitary rotation matrix V_L^ν

$$(V_L^\nu)^T M^L V_L^\nu = M_\nu. \tag{1.81}$$

The diagonalisation is achieved by rotating from the interaction eigenstates into the mass eigenstates via the transformation $\nu_L = V_L^{\nu\,\dagger}\nu'_L$. Hence, the Majorana mass term can be written as

$$\mathcal{L}^M_{mass} = \frac{1}{2}m_i\overline{\nu}^c_{Li}\nu_{Li} + h.c. \tag{1.82}$$

As in the case of Dirac neutrinos, the leptonic Lagrangian with Majorana neutrinos can be written as (1.65) with the Majorana lepton mixing matrix $\mathcal{U}^M$. However, there is a crucial difference compared to the Dirac mixing matrix. The Majorana mass term is not invariant under the global $U(1)$ symmetry. Therefore there are three physical CP violating phases in the Majorana mixing matrix instead of one. The Majorana mixing matrix can be written in terms of the unitary Dirac mixing matrix in Eq. (1.77) and a diagonal matrix P_ν with two independent phases

$$\mathcal{U}^M = \mathcal{U}^D P_\nu \tag{1.83}$$

In the following section, we shall discuss exact parametrisations of the lepton mixing matrices further.

1.4.2 Pontecorvo–Maki–Nakagawa–Sakata Matrix

The PMNS matrix given in Eqs. (1.77) and (1.83) for Dirac and Majorana neutrinos, can generically be written as

$$\mathcal{U}_{\alpha i} = P_{\ell,\alpha\alpha} V^{\ell\,\dagger}_{\alpha\, j} V^{\nu}_{j\, i} P_{\nu,\, ii}, \tag{1.84}$$

where P_ℓ is a 3×3 phase matrix and P_ν a diagonal matrix, both introduced such that they reduce the number of phases in the PMNS matrix ($\mathcal{U}_{\text{PMNS}}$). In the standard PDG parametrisation of the $\mathcal{U}_{\text{PMNS}}$ [75], the matrix for three neutrinos is assumed to be unitary, this yields three flavour mixing angles θ_{12} , θ_{13} , θ_{23} and one (or three) CP violating phase(s) corresponding to Dirac (or Majorana) neutrinos. This parametrisation of (1.84) can be written explicitly as

$$\begin{aligned}
\mathcal{U}_{\text{PMNS}} &= \begin{pmatrix} 1 & 0 & 0 \\ 0 & c_{23} & s_{23} \\ 0 & -s_{23} & c_{23} \end{pmatrix} \begin{pmatrix} c_{13} & 0 & s_{13}e^{-i\delta_\nu} \\ 0 & 1 & 0 \\ -s_{13}e^{i\delta_\nu} & 0 & c_{13} \end{pmatrix} \begin{pmatrix} c_{12} & s_{12} & 0 \\ -s_{12} & c_{12} & 0 \\ 0 & 0 & 1 \end{pmatrix} P_\nu \\
&= \begin{pmatrix} c_{12}c_{13} & s_{12}c_{13} & s_{13}e^{-\delta_\nu} \\ -s_{12}c_{23} - c_{12}s_{13}s_{23}e^{\delta_\nu} & c_{12}c_{23} - s_{12}s_{13}s_{23}e^{\delta_\nu} & c_{13}s_{23} \\ s_{12}s_{23} - c_{12}s_{13}c_{23}e^{\delta_\nu} & -c_{12}s_{23} - s_{12}s_{13}c_{23}e^{\delta_\nu} & c_{13}c_{23} \end{pmatrix} P_\nu
\end{aligned} \tag{1.85}$$

where $c_{ij} \equiv \cos\theta_{ij}$ and $s_{ij} = \sin\theta_{ij}$. δ_ν is the CP violating phase which is referred to as Dirac phase. Analogous to the quark case discussed in Section 1.1.3 the mixing matrix for Dirac neutrinos depends on these four physical parameters. Therefore, the diagonal matrix P_ν will simply be a 3×3 identity matrix.

In the case where neutrinos are considered to be Majorana particles, the diagonal P_ν contains additional arbitrary phases, ρ and σ, called Majorana phases. As a consequence, there are three physical CP violating phases in the Majorana mixing matrix. This is because, as mentioned earlier, the Majorana mass term in Eq. (1.82) is not invariant under global $U(1)$ gauge transformations meaning there is additional freedom in selection of the phases.

1.4.3 Neutrino Oscillation

Neutrino flavour oscillations occur due to the mixing of different massive neutrinos [77, 78]. The probability of the neutrino to oscillate in a vacuum from one state to another will be discussed in this section [79].

A neutrino with flavour α created in a charged current interaction process from a charged lepton ℓ_α is described by the flavour state according to (1.66)

$$|\nu_\alpha\rangle = \sum_i \mathcal{U}^*_{\alpha\, i}|\nu_i\rangle. \tag{1.86}$$

the massive neutrino quantum states evolve in time as plane waves,

$$|\nu_i(t)\rangle = e^{-iE_it}|\nu_i\rangle, \tag{1.87}$$

where $E_i = \sqrt{\vec{p}^2 + m_i^2}$ is its relativistic energy. From (1.86) and (1.87) the time evolution of a neutrino state of flavour α is given by

$$|\nu_\alpha(t)\rangle = \sum_i \mathcal{U}^*_{\alpha\, i}e^{-iE_it}|\nu_i\rangle. \tag{1.88}$$

Using the unitarity relation, we can write the mass eigenstates in terms of the flavour eigenstates as follows

$$|\nu_i\rangle = \sum_\alpha \mathcal{U}_{\alpha\, i}|\nu_\alpha\rangle \tag{1.89}$$

and this result can be introduced into Eq. (1.88) to obtain

$$|\nu_\alpha(t)\rangle = \sum_\beta \sum_i \mathcal{U}^*_{\alpha\, i}e^{-iE_it}\mathcal{U}_{\beta\, i}|\nu_\beta\rangle \tag{1.90}$$

this means that the superposition of massive neutrino states $|\nu_\alpha(t)\rangle$, where $|\nu_\alpha(0)\rangle = |\nu_\alpha\rangle$, becomes a superposition of different flavour states if neutrino mixing is allowed. The amplitude of the transition $\nu_\alpha \to \nu_\beta$ as a function of time is then given by

$$A_{\nu_\alpha\to\nu_\beta}(t) = \sum_i \mathcal{U}^*_{\alpha\, i}\mathcal{U}_{\beta\, i}e^{-iE_it} \tag{1.91}$$

and the transition probability is given by $P_{\nu_\alpha\to\nu_\beta}(t) = |A_{\nu_\alpha\to\nu_\beta}(t)|^2$

$$P_{\nu_\alpha\to\nu_\beta}(t) = \sum_i \sum_j \mathcal{U}^*_{\alpha\, i}\mathcal{U}_{\beta\, i}\mathcal{U}_{\alpha\, j}\mathcal{U}^*_{\beta\, j}e^{-i(E_i-E_j)t} \tag{1.92}$$

In the case of ultra–relativistic neutrinos $m_i << |\vec{p}|$, the energy–momentum relation $E_i = \sqrt{\vec{p}^2 + m_i^2}$ can be approximated by

$$E_i \sim E + \frac{m_i^2}{2E}, \quad \text{with} \quad E = |\vec{p}| \tag{1.93}$$

then, the transition probability can be written in terms of the neutrino squared mass difference $\Delta m_{ij}^2 = m_i^2 - m_j^2$

$$P_{\nu_\alpha\to\nu_\beta}(t) = \sum_i \sum_j \mathcal{U}^*_{\alpha\, i}\mathcal{U}_{\beta\, i}\mathcal{U}_{\alpha\, j}\mathcal{U}^*_{\beta\, j}e^{-i\frac{\Delta m_{ij}^2 L}{2E}} \tag{1.94}$$

where we have approximated $t \simeq L$ and L is the distance from the neutrino source to the detector. From (1.94) we can conclude the following

- Neutrino oscillation measurements provide information on the values of the squared–mass differences Δm^2_{ij} and the elements of the $\mathcal{U}_{\mathrm{PMNS}}$ matrix
- It is only possible to obtain values of the squared–mass differences but not the absolute values of neutrino masses
- The oscillation probability depends on the elements of the mixing matrix $\mathcal{U}_{\mathrm{PMNS}}$ through the quartet
$$\mathcal{U}^*_{\alpha\, i}\mathcal{U}_{\beta\, i}\mathcal{U}_{\alpha\, j}\mathcal{U}^*_{\beta\, j}. \tag{1.95}$$
This does not depend on the choice of parametrisation and is invariant under re–phasing transformations.

  This means that it is independent of any phases that can be factorised. Therefore in the case of Majorana neutrinos, neutrino oscillations are independent of the Majorana phases ρ and σ, which can be factorised in a diagonal matrix on the right, see Eq. (1.85). Consequently, Majorana phases are inaccessible in neutrino oscillation experiments.

1.4.4 Seesaw Mechanism

We may now write the most general neutrino Lagrangian with both Dirac and Majorana mass terms

$$\mathcal{L}^{D+M}_{mass} = \mathcal{L}^{D}_{mass} + \mathcal{L}^{ML}_{mass} + \mathcal{L}^{MR}_{mass}, \tag{1.96}$$

where ML and MR denote left–and right–handed Majorana Lagrangians respectively, defined like

$$\mathcal{L}^{D}_{mass} = -m_D\overline{\nu}_R\nu_L + h.c., \qquad \mathcal{L}^{ML}_{mass} = -\frac{m_L}{2}\overline{\nu}^T_L\mathcal{C}^\dagger\nu_L + h.c.,$$
$$\mathcal{L}^{MR}_{mass} = -\frac{m_R}{2}\overline{\nu}^T_R\mathcal{C}^\dagger\nu_R + h.c., \tag{1.97}$$

in general we may consider m right-handed neutrinos

$$N'_L = \begin{pmatrix}\nu'_L\\ \nu'^c_R\end{pmatrix}, \qquad \nu'_L = \begin{pmatrix}\nu'_{eL}\\ \nu'_{\mu L}\\ \nu'_{\tau L}\end{pmatrix}, \qquad \nu'^c_R = \begin{pmatrix}\nu'^c_{1R}\\ \vdots\\ \nu'^c_{mR}\end{pmatrix}. \tag{1.98}$$

The mass term is then

$$\mathcal{L}^{D+M}_{mass} = \frac{1}{2}N'^T_L\mathcal{C}^\dagger M^{D+M}N'_L + h.c \tag{1.99}$$

where the total mass matrix

$$M^{D+M} = \begin{pmatrix} m_L & m_D^T\\ m_D & m_R\end{pmatrix}, \tag{1.100}$$

In general, m_D is a $3 \times m$ complex matrix and m_R and m_L are $m \times m$ symmetric matrices, in fact expansion of (1.99) yields

$$\mathcal{L}_{mass}^{D+M} = \frac{1}{2}\left[\nu_L'^T \mathcal{C}^\dagger m_L \nu_L' + \nu_L'^T \mathcal{C}^\dagger m_D^T \nu_R'^c + \nu_R'^{cT} \mathcal{C}^\dagger m_D \nu_L' + \nu_R'^{cT} \mathcal{C}^\dagger m_R \nu_R'^c\right]. \quad (1.101)$$

Hence the Dirac part of the Lagrangian above can be simplified with matrix indices like

$$\frac{1}{2}\left[\nu_{Li}'^T \mathcal{C}^\dagger (m_D)_{ij}^T \nu_{Rj}'^c + \nu_{Ri}'^{cT} \mathcal{C}^\dagger (m_D)_{ij} \nu_{Lj}'\right] = \overline{\nu}'_{Ri} (m_D)_{ij} \nu_{Lj}'. \quad (1.102)$$

We may diagonalise this matrix to the operator as usual to $\overline{\nu}_{Rj} m_{Dj}^{\mathrm{diag}} \nu_{Lj}$, where we procure three linear combinations

$$\overline{\nu}_{Rj} = \frac{\overline{\nu}'_R (m_D)_{ij}}{\sqrt{\sum_i |(m_D)_{ij}|^2}} \quad (1.103)$$

with mass m_{Dj}^{diag} in the basis $(\nu_{Li}, \nu_{Ri})^T$. There are $m-3$ remaining linear combinations of right–handed neutrinos that don't participate in the Dirac mass term.

In the special case that $m_L = 0$, we can diagonalise the Dirac-Majorana mass term M^{D+M} to obtain $m+3$ massive Majorana neutrinos and if $M_i \gg m_{Di}$, this yields the well known Seesaw formula for the light neutrinos

$$m_\nu \simeq -m_D (m_R)^{-1} m_D^T \quad (1.104)$$

where M_i corresponds to the eigenvalues of m_{Ri}. The matrices m_ν and m_R are in general complex so provide sources of CP violation. In order to illustrate the seesaw mechanism, we may study a toy model with a 2×2 matrix with real coefficents of the form

$$\begin{pmatrix} 0 & m \\ m & M \end{pmatrix}, \quad (1.105)$$

which has eigenvalues $m_{1,2} = \frac{1}{2}(M \pm \sqrt{M^2 + 4m})$. Where if $M >> m$ we find $m_1 \to M$ and $m_2 \to -\frac{m^2}{M}$. From here it is clear that the first mass eigenstate is very heavy and the second one is very light. The light neutrinos in such a scenario would correspond to the light neutrinos observed in nature. One can always introduce a phase matrix to produce positive masses.

If all the eigenvalues of the matrix m_R are much larger than the Higgs vev v this is considered to be the canonical Seesaw mechanism. In this scenario, sterile neutrinos are integrated out and at low energy and we have an effective theory with three light active Majorana neutrinos. If some eigenvalue of m_R is larger than or equal to v, the mass matrix diagonalisation yields more than three light Majorana neutrinos. If one of the eigenvalues of m_R equals zero, it is equivalent to imposing lepton number conservation. In this case we can identify three sterile neutrinos as the right–handed component of the left–handed Dirac fields [80].

1.4.5 Thermal Leptogenesis

Leptogenesis is scenario in which baryogenesis can be induced while also providing a viable mechanism for light active neutrinos [81]. When the seesaw mechanism is invoked, as described in the previous section, it is almost impossible to avoid leptogenesis. Indeed, the seesaw mechanism itself, requires lepton number violation by construction. It also introduces new general CP violating phases in the neutrino Yukawa interactions and for significant portions of the parameter space, predicts that new heavy singlet neutrinos may decay out of thermal equilibrium [81]. Hence, the three Sakharov conditions listed in Section 1.1.5 are naturally fulfilled. Therefore, the possibility of leptogenesis being the source of the observed baryon asymmetry in the universe is a consistent one within the seesaw framework.

There are several ways to produce a baryon asymmetry in seesaw models. They all require the introduction of singlet neutrinos N_I with masses M_I that are usually heavier than the electroweak breaking scale where $M_I \gg \nu_i$. However, they may diverge in the type of cosmological scenario and in the values of the seesaw parameters (as mentioned in the previous section, the number of seesaw parameters, particularly in the Majorana case, is much larger than the number of measured light neutrino parameters). A popular possibility, is "thermal leptogenesis" with hierarchical masses, $M_1 \ll M_{j>1}$ [81]. In this scenario, N_1 particles are produced by scattering in the thermal bath. This means that their number density can be calculated from the seesaw parameters and the reheating temperature of the universe.

If we consider the case with mass ordering $M_1 < M_2 < M_3$ and the relevant Yukawa operator

$$\mathcal{L} = y_{ij}\overline{N}_R^i \Phi^\dagger \ell_L^j + h.c. \tag{1.106}$$

the following decays for the right–handed neutrino can occur

$$N_R \to \ell_L + \overline{\phi}, \qquad\qquad N_R \to \ell_L + \phi, \tag{1.107}$$

where ϕ corresponds to the charged longitudinal component of the Higgs doublet that gets eaten by the $W^\pm$ bosons after symmetry breaking. The branching ratios of these

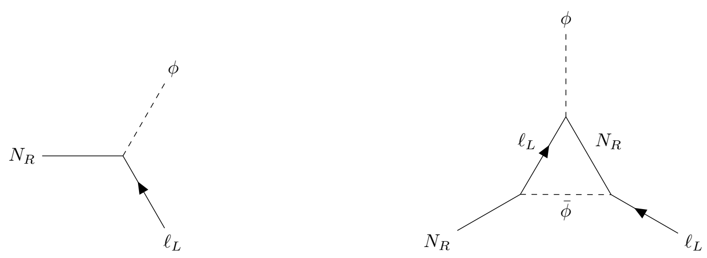

FIGURE 1.8: The simplest diagrams giving rise to a net lepton number production. Note that there is a Majorana mass insertion before the vertex in the left diagram and one inside the loop in the right diagram.

processes differ if CP is violated through the one-loop radiative correction with the

Higgs. The net lepton number production due to the decay of the lightest right–handed neutrino N_R^1 arises from the interference of the two diagrams in Figure 1.8, and its magnitude is calculated as [81]

$$\epsilon = \frac{9}{4\pi}\mathrm{Im}[y_{li}y^\dagger_{ij}y^\dagger_{jk}y_{kl}]\frac{I[m_j^2/M_i^2]}{(yy^\dagger)_{11}} \tag{1.108}$$

with the loop factor

$$I(x) = \sqrt{x}\left(1 + (1+x)\log\frac{x}{1+x}\right). \tag{1.109}$$

Hence the out–of–equilibrium Sakharov condition for baryon asymmetry is satisfied if the temperature T of the plasma is smaller than the mass M_1. This means that the inverse process is blocked at the time when the decay rate $\Gamma = \frac{(yy^\dagger)_{11}}{16\pi}$ is equal to the expansion rate of the universe $\frac{\dot{a}}{a} \sim \frac{1.7\sqrt{g}T^2}{m_{pl}}$, where g is the number of degrees of freedom and m_{pl} is the Planck mass, this can be simplified to the relation $\frac{\Gamma m_{pl}}{\sqrt{g}} < M_1^2$.

This provides us with a source of lepton number violation but we still need to explain the baryon number asymmetry. This occurs because the presence of instanton like electroweak processes effect the baryon asymmetry changes like [82]

$$\Delta B(t) = \frac{1}{2}\Delta(B-L)_i + \frac{1}{2}\Delta(B+L)_i e^{-\gamma t}, \tag{1.110}$$

with the factor $\gamma \sim T$. At electroweak symmetry breaking, the exponent is $\frac{m_{pl}}{T\sqrt{g}} \sim 10^{16}$ and hence the second term is heavily suppressed. This leads to a direct relation between the baryon asymmetry and the lepton asymmetry

$$\Delta B = -\frac{(\Delta L)_i}{2} \tag{1.111}$$

which survives till the present day.

Thus we have seen that the seesaw mechanism provides an elegant means for producing neutrino masses and the baryon and lepton asymmetry of the universe. Another process of significant interest that occurs in seesaw models is the radiative loop level decay $N_R \to \nu_L\gamma$. Furthermore, such a process occurs via the neutrino transition dipole moment which has additional sources of CP violation that produces an observable photon polarisation asymmetry in the final states. Computing this effect and studying the resulting phenomenology is one of the main topics of discussion in Chapter 4.

1.5 Lepton Flavour Universality Violation in B Decays

In the last two decades, the experimental study of B decays has been carried out at the LHC and at the B factories. Two related experiments, BaBar and Belle, finished operating in 2008 and 2010 respectively while the upgrade of Belle, Belle II, started collecting data in early 2018. At the LHC, three experiments are involved in the study of B physics, ATLAS, CMS and LHCb, where the latter was specially designed for studying the production and the decay of charm and beauty hadrons.

Over the past several years BaBar, LHCb, and Belle, have reported anomalies in decays associated with the $b \to c$ and $b \to s$ transitions. Violations of LFU, known to be theoretically clean probes of new physics, are of particular interest. We note that LFU is a striking prediction of some processes in the 2HDM models discussed in Chapter 2, variations of which are equipped to explain these anomalies. In the SM, LFU is only broken by the lepton masses. Hence, hints for additional sources of LFU violation have been observed in the ratios of branching ratios of flavour-changing charged current and neutral current decays of B mesons. The ratios of interest are commonly referred to as R_K, R_{K^*}, R_D and R_{D^*} where

$$R_{K^{(*)}} = \frac{\Gamma(\bar{B} \to \bar{K}^{(*)}\mu^+\mu^-)}{\Gamma(\bar{B} \to \bar{K}^{(*)}e^+e^-)}, \qquad R_{D^{(*)}} = \frac{\Gamma(\bar{B} \to \bar{D}^{(*)}\tau\nu)}{\Gamma(\bar{D} \to \bar{D}^{(*)}\ell\nu)} \tag{1.112}$$

and $\ell = e, \mu$. The experimental world averages of R_D and R_{D^*} from the heavy flavour averaging group (HFLAV) based on BaBar [83], Belle [84–86], and LHCb [87,88] read

$$R_D = 0.340 \pm 0.027 \pm 0.013 \text{ [89]}, \qquad R_{D^*} = 0.295 \pm 0.011 \pm 0.008 \text{ [89]}, \tag{1.113}$$

with a correlation error of $\rho = -38\%$. The corresponding SM theoretical predictions are known with high precision [90–92]. The values adopted by HFLAV are

$$R_D^{SM} = 0.299 \pm 0.003 \text{ [89]}, \qquad R_{D^*}^{SM} = 0.258 \pm 0.005 \text{ [89]}. \tag{1.114}$$

Therefore, the combined discrepancy between the SM prediction and experimental world averages of R_D and R_{D^*} is at the 3.1σ level. The most precise measurement to date of the LFU ratio R_K has been performed by LHCb

$$R_K = 0.846^{+0.060+0.016}_{-0.054-0.014} \qquad \text{for } 1.1\,\text{GeV}^2 < q^2 < 6\,\text{GeV}^2\,, \tag{1.115}$$

with q^2 denoting the squared invariant mass of the dilepton system in the final state. The SM predicts $R_K^{SM} \simeq 1$ with current theoretical uncertainties being held significantly below experimental ones [93]. It is important to note however that the above experimental value is now closer to the SM prediction than the Run-1 result [94]. However, the improved precision of the measurement still implies a notable tension between theory and experiment of 2.5σ.

The most precise measurement of the R_{K^*} ratio thus far is from the Run-1 LHCb analysis [94] that finds

	observed	q^2 range
R_{K^*}	$0.66^{+0.11}_{-0.07} \pm 0.03$	$0.045\text{GeV}^2 < q^2 < 1.1\text{GeV}^2$
	$0.69^{+0.11}_{-0.07} \pm 0.05$	$1.1\text{GeV}^2 < q^2 < 6\text{GeV}^2$

where both q^2 bins are in tension with the SM prediction [93], $R_{K^*}^{SM} \simeq 1$, by $\sim 2.5\sigma$. More recent measurements by Belle [95,96] are shown in Table.1.3 which are compatible with both the SM prediction and the LHCb results.

In Chapter 5 we propose Pati-Salam model variants that aim to resolve the anomalies. This is discussed in Section 5.1 by introducing a $SU(4)_C \times SU(2)_L \times U(1)_{Y'}$ gauge group in which the chiral left-handed quarks and leptons are unified into a $\underline{4}$ of $SU(4)_C$ while the right-handed quarks and leptons are treated differently. After

	observed	q^2 range
R_{K^*}	$0.90^{+0.27}_{-0.21} \pm 0.1$	$0.1\text{GeV}^2 < q^2 < 8\text{GeV}^2$
	$1.18^{+0.52}_{-0.32} \pm 0.1$	$15\text{GeV}^2 < q^2 < 19\text{GeV}^2$
R_K	$0.98^{+0.27}_{-0.23} \pm 0.06$	$1\text{GeV}^2 < q^2 < 6\text{GeV}^2$
	$1.11^{+0.29}_{-0.26} \pm 0.07$	$14.18\text{GeV}^2 < q^2\text{GeV}^2$

TABLE 1.3: Latest R_K and R_{K^*} measurements from the Belle experiment

symmetry breaking to the SM gauge group, a new $SU(4)_C$ gauge leptoquark can potentially explain the R_K and R_{K^*} measurements through new tree level contributions that interfere both positively and negatively with the SM processes.

Similarly in Section 5.2, we propose a Pati-Salam theory, but this time based on the gauge group $SU(4)_C \times SU(2)_L \times SU(2)_R$. The left–handed quarks and leptons are once again unified into a fundamental representation of $SU(4)_C$, however the R_D and R_{D^*} deviations are explained by a scalar leptoquark which couples to right–handed fields and is contained in the $SU(4)_C \times SU(2)_R$-breaking scalar multiplet. The measured deviation of lepton flavour universality in R_K and R_{K^*} can once again explained via the $SU(4)_C$ leptoquark gauge boson. The model predicts a new sub-GeV scale sterile neutrino which is involved in the process and can be searched for in new neutrino experiments.

1.6 Modelling of Proton Collisions

Hadrons are strong interaction bound states of quarks. While a proton can naively be considered as a composition of two up quarks and one down quark, this is only a crude approximation since quarks constantly radiate and reabsorb gluons that themselves further split into gluons and quarks [97]. The effective description of these interactions manifests as the "nuclear force" in the low energy regime. But at high energies, such as those at probed at the LHC, a more fundamental description of hadron interaction phenomenology must be adopted in order to make meaningful predictions [97].

High energy collisions between protons can be characterised as elastic collisions that result in two outgoing protons, or inelastic collisions in which constituents of one or both protons interact and create new particles. The probability of a given interaction occurring is related to its cross section, the equivalent target area presented by the proton under the interaction [97]. This is often quoted in barns ($1\text{b} = 10^{-28}\text{m}^2$). The probability of producing a pair of particles from a two-to-two ($1 + 2 \to 3 + 4$) process can be computed from the differential cross section $d\sigma$ that is determined using Fermi's golden rule, which may be expressed in the form

$$d\sigma = \frac{1}{64\pi^2} \frac{|\mathbf{p}_3|}{|\mathbf{p}_1|} |\mathcal{M}|^2 d\Omega. \tag{1.116}$$

Where $\mathcal{M}$ is the Lorentz invariant matrix element and $d\Omega$ is the differential solid angle element which must be integrated over in order to determine the total cross section σ. It should be noted that this is in the centre–of–mass frame where $|\mathbf{p}_1| = |\mathbf{p}_2|$ and $|\mathbf{p}_3| = |\mathbf{p}_4|$. At lowest order, the matrix elements are given by $\mathcal{M} \propto \langle f|\mathcal{H}_{int}|i\rangle$ where $\mathcal{H}_{int}$ is the interaction Hamiltonian. The expansion of the matrix elements can be expressed in terms of Feynman diagrams. Figure 1.9 describes a tree level process, which corresponds to the leading order (LO) term in $\mathcal{M}$ for two-to-two electron scattering. Higher order terms include an increasing number of vertices, are called next-to-leading order (NLO), next-next-to-leading order NNLO etc. An example of an NLO process is also shown in Figure 1.9.

Terms in the matrix elements contain coupling constants depending on the interaction between two particles. The coupling at four–momentum exchange q^2 is denoted $\alpha(q^2)$ and for electromagnetic interactions has approximately $\alpha(0) = \frac{1}{137}$ which is the fine–structure constant, and it only increases slowly for higher q^2. As each higher order term gains an additional factor of $\alpha(q^2)$ in the matrix element, additional terms in the perturbative expansion quickly become suppressed. The coupling $\alpha_s(q^2)$ for the strong interaction is around unity at low energies and non–perturbative (since the expansion of the matrix element will contain many significant terms), but $\alpha_s(q^2)$ decreases asymptotically for higher q^2 to about 0.1 at relevant energies (typically set to the pole mass of the Z boson), which makes QCD perturbative at higher energies. These higher–order terms are still significant and therefore must be included when making predictions.

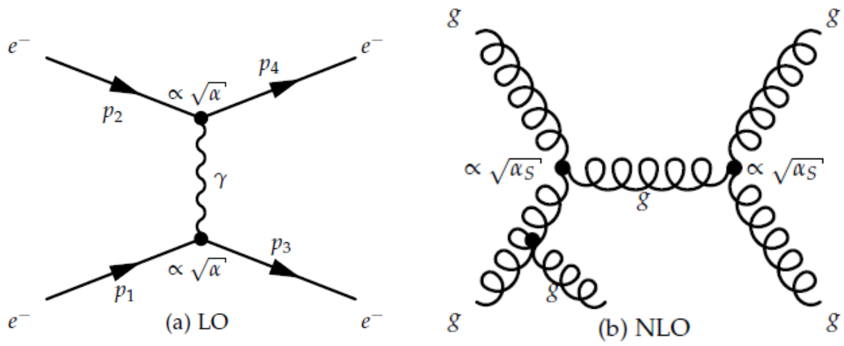

FIGURE 1.9: (a) Tree level Coulomb scattering between two electrons through the exchange of a photon. (b) NLO QCD process between gluons [17]

The decay width or decay rate of an unstable particle can be expressed in a similar way to the cross section, for example for a 2-body decay $P \to 1 + 2$

$$\Gamma_i = \frac{1}{32\pi^2 M^2} \int |\mathcal{M}_i|^2 |\mathbf{p}_1| d\Omega, \tag{1.117}$$

where momenta $|\mathbf{p}_1| = |\mathbf{p}_2|$ in the centre–of–mass frame and M is the mass of the decaying mother particle P. Since unstable particles may decay to numerous different final states, each with a unique amplitude, we require unique decay rates for each process i. The total decay width can then simply be computed by summing the individual widths Γ_i. The branching ratio $\mathcal{B} = \Gamma_i/\Gamma$ is the fraction of a particular decay channel relative to all possible channels. The decay width of a particle is intrinsically related to the particles mean lifetime $\tau = \frac{1}{\Gamma}$. The survival probability of a particle with $p^\mu = (E, \mathbf{p})$ in the lab-frame over a time t_0 is then given by

$$P(t_0) = e^{-Mt_0\Gamma/E}, \tag{1.118}$$

and the probability that it travels a distance x_0 or greater is

$$P(x_0) = e^{-Mx_0\Gamma/|\mathbf{p}|}. \tag{1.119}$$

The probability of extracting specific partons a and b (quarks and gluons) from the proton–proton collision and having these interact to form a new particle x can be calculated independently and is known as the factorisation theorem. This can be demonstrated mathematically like

$$\sigma_X = \sum_{a,b=q,g} \int_0^1 dx_1 dx_2 f_a(x_1, \mu_F^2) f_b(x_2, \mu_F^2) \hat{\sigma}_{ab\to X}, \tag{1.120}$$

where the functions f_a are the probability distributions of extracting a parton a with

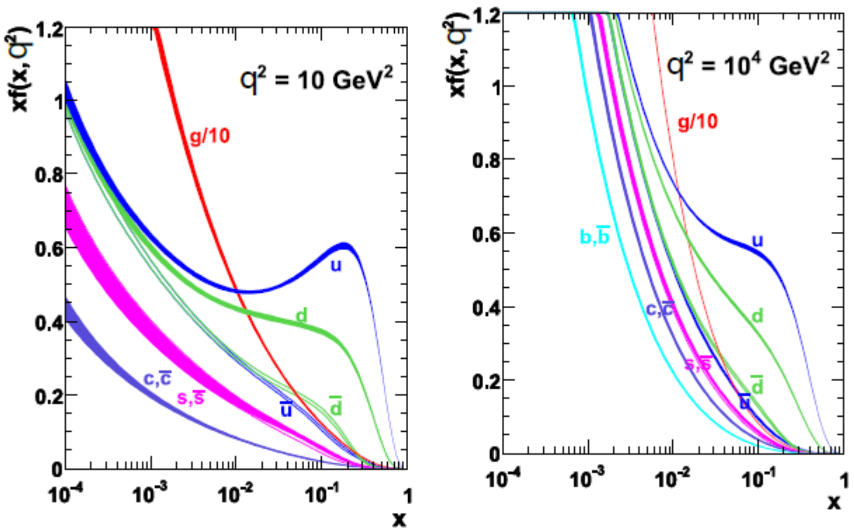

FIGURE 1.10: Parton distribution functions shown at two energy scales. We note that the vertical axis shows xf, the product of x and the PDF f for a given parton [98]

a fraction x of the momentum from the parent proton. These are the PDFs mentioned earlier. They can be visualised as follows at two distinct energy scales as shown in Figure 1.10.

The valence quarks of protons (uud) are more probable at high x than the virtual sea quarks. This signifies that the finer structure of the proton becomes relevant. Hence, it is most probable that very low momentum partons are extracted, particularly gluons and this is why most proton–proton collisions produce soft scatter events which are of little phenomenological interest.

The first term in Eq. (1.120) integrates the PDFs over all momentum fractions x_1 and x_2. The second term yields the cross section for forming particle X from the partons a and b, which contains the matrix elements for $\mathcal{M}(ab \to X)$. Finally, the full product is summed over for all gluons and quarks. The theorem depends on the factorisation μ_F and renormalisation μ_R scales, which are introduced to suppress divergences. The dependence on these unphysical scales decreases when including higher–order Feynman diagrams. The sum of cross sections for all possible processes,

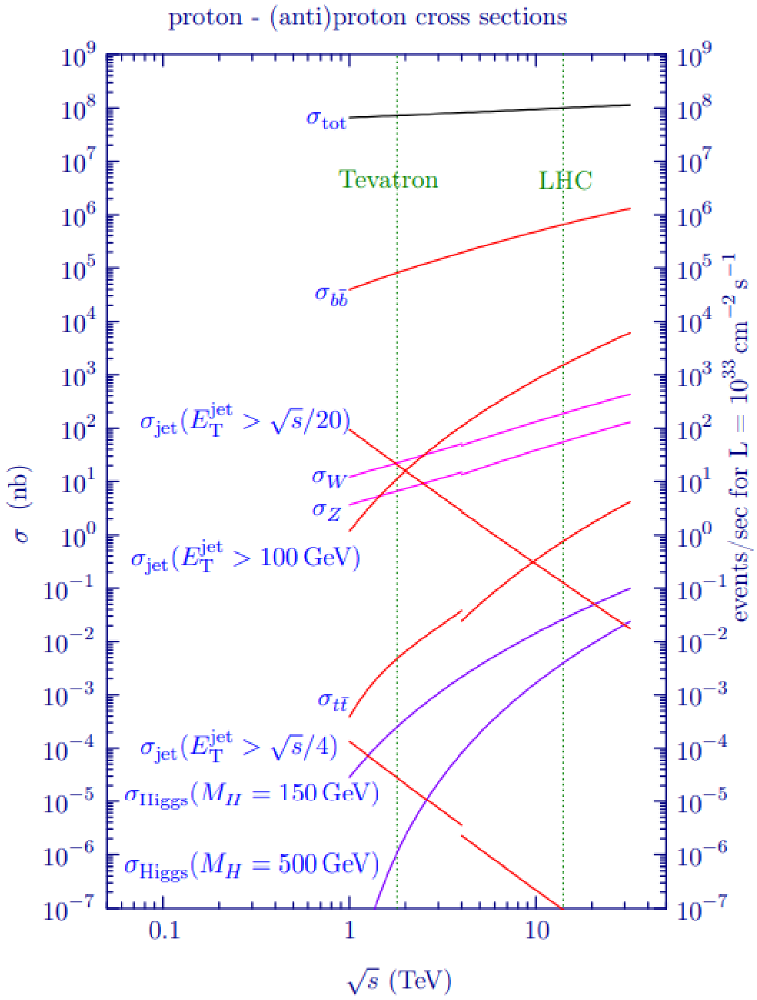

FIGURE 1.11: Predicted cross sections of various processes at the Tevatron and LHC hadron colliders over a range of collision energies. The right–hand axis shows the event rate corresponding to the cross-sections for a fixed luminosity. The discontinuity in the curves corresponds to a change in the choice of colliding particles from $p\bar{p}$ to pp [99]

including diffractive ones, gives the total cross section σ_{tot}.

The total event rate is related to the instantaneous luminosity $\mathcal{L}(t)$, which can be integrated over time to give the integrated luminosity $L = \int \mathcal{L}(t)dt$. From these, one can calculate the total number of interactions, $N = \sigma_{tot}L$. The instantaneous luminosity depends on many factors, including the collision frequency $f = 1/(25\text{ns}) = 40\text{MHz}$, the number of particles in the colliding bunches and the cross–sectional area of the beams. Using the equation for the total number of interactions, one can calculate the cross section of a given process by $s = N/(L\epsilon)$, where ϵ contains selection efficiencies as well as the detector acceptances. The total proton–proton cross section $\sigma_{tot} = \sigma_{el} + \sigma_{inel}$ can be thought of as the sum of the elastic and inelastic cross sections.

1.6.1 Components of Events

We may characterise the events at a hadron collider as shown in Figure 1.12 The

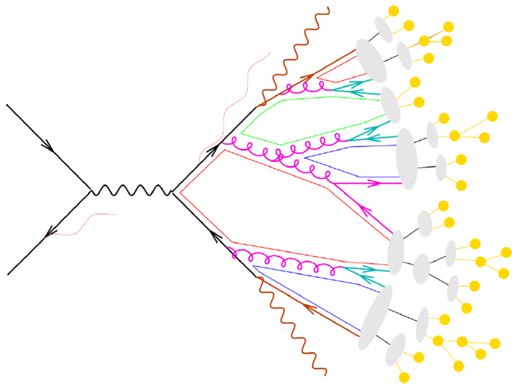

FIGURE 1.12: A pictorial representation of a hard scatter process including initial and final state radiation, particle showering (shown in grey), and hadronisation (grey and yellow) [17].

various types of events are

- The hard scatter/process is where a fraction of momentum x is carried by the partons from the colliding protons (left–most lines). These partons interact and form a virtual particle shown as a propagator (dark wavy line), which subsequently transforms into two on-shell (real) particles.

- Underlying event refers to the remnants of the protons after the hard scatter as well as soft particles produced in the QCD field between the hard scatter and the remnants. This includes photons or gluons radiated by the incoming particles, called initial state radiation (ISR) and outgoing particles, final state radiation (FSR) particles, shown in the illustration as light pink wavy lines. The underlying event may contain additional interactions between the partons, known as multiple parton interactions (MPI), which may produce additional high transverse momentum p_T particles.

- Minimum bias events refer to parton collisions with very loose trigger conditions. Most collisions are actually of this type. Multiple protons interact in ATLAS with upwards of 55 [100] interactions per bunch-crossing. These events are termed "pileup". Pileup also covers the average number of interactions per bunch–crossing $\langle\mu\rangle$. These interactions happen some distance from the location of the hard interaction and can be suppressed by requiring reconstruction of the coordinates of the individual proton–proton interactions. Minimum bias from an earlier or later collision may interfere with measurements in the detectors and are known as out-of-time pileup.

1.6.2 Particle Interactions With the Detector

As the particles traverse the detector volume, their interactions with the environment must be accurately captured. For example, due to their low mass, electrons, will primarily lose energy through bremsstrahlung radiation at $E > 7$MeV when passing through absorbing matter. This is shown for electrons travelling through lead in Figure 1.13 on the left panel. However, this mode of energy loss is approximately suppressed by a factor of $1/m^2$, where m is the particle mass, making it negligible for heavier particles, for example the heavier muon and tau leptons. The effect is negligible until they have much higher energy $\gtrsim \mathcal{O}(100)$GeV. This is shown for antimuons travelling through copper in the right panel of Figure 1.13.

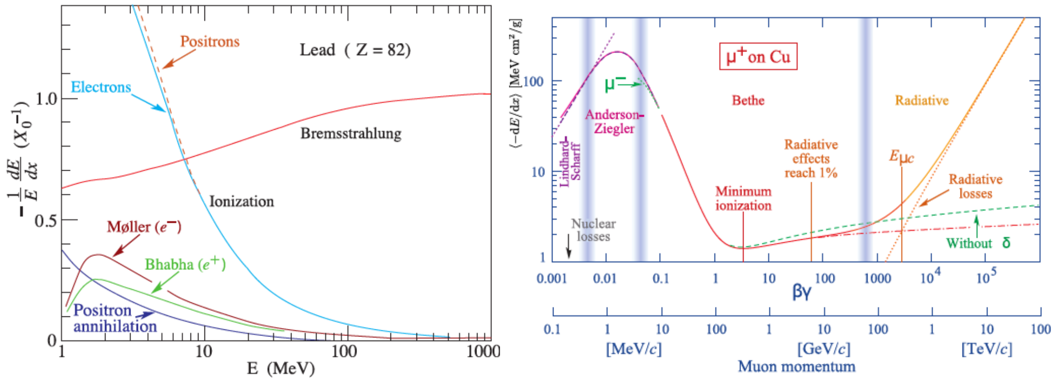

FIGURE 1.13: Left: Energy loss for electrons in lead, Right: Energy loss for antimuons in copper [25].

In general, the average energy loss per unit length for "intermediate energies" labelled in the Bethe band, can be described by the Bethe formula

$$-\left\langle \frac{dE}{dx} \right\rangle = \frac{4\pi}{m_e c^2} \frac{nz^2}{\beta^2} \left(\frac{e^2}{4\pi\epsilon_0} \right)^2 \left[\log\left(\frac{2m_e c^2 \beta^2}{I(1-\beta^2)} \right) - \beta^2 \right], \tag{1.121}$$

where v is the speed of the incident particle with charge z (in multiples of electron charge), and energy E, travelling a distance x into the target of electron number density n and an average excitation potential of I. It should be noted that c is the speed of light and ϵ_0 is the vacuum permittivity while $\beta = v/c$ is the usual relativistic velocity ratio.

We note that in this rather large range of approximately 100MeV to 100GeV, particles will pass through even dense detectors with minimal energy loss. At even higher momenta, muons will lose some energy via bremsstrahlung, but will then reach energies where they become minimum ionisation particles. However, at very low energies, particles quickly lose energy by ionising the traversed material [17].

A relevant property of a material is also its radiation length X_0, which is defined as the distance a particle travels in a material before having $1/e \simeq 0.37$ of its initial energy. For example, as electrons travel through sufficiently dense matter, they will radiate bremsstrahlung photons, which will again travel some distance before pair-producing an electron–positron pair from their matter interactions. Hence a successive cascade of pair–producing bremsstrahlung photons follows, which is the main mode of energy loss for the electrons. After travelling a distance of x radiation lengths, an electron will on average have an energy of $E/2x$ [17]. This continues repeatedly, until the energy of the electron is so low that it eventually loses all its remaining energy to ionisation.

In a detector such as ATLAS, the energy of these radiated Bremmstrahlung photons can be transferred by devices called scintillators to be measured by photomultiplier tubes [17]. For hadrons, the length scale is called the nuclear interaction length instead. Other sources of energy losses are delta rays coming from liberated matter electrons that ionise the matter and Coulomb scattering. Coulomb scattering only causes significant energy loss for electrons, but all particles will scatter randomly multiple times, which contributes significantly to the momentum uncertainty.

1.6.3 Jets and Jet Algorithms

When analysing high energy particle collisions, one has to often consider processes where quarks and gluons are produced in the final state. At the LHC, there is a number of such processes involving high energy QCD particles in the final state. This is because in proton collisions, a hard QCD parton can be radiated from the incoming partons. Then, other states that are created like the electroweak gauge bosons and Higgs bosons can themselves decay to QCD states like quarks and gluons. Finally, in new particle searches, decay chains with quarks and gluons resulting must often be considered.

The quarks and gluons at high energy mentioned above, are not directly observable in the final state of the interaction. This is because, as mentioned in the previous sections, they undergo successive collinear branchings, this produces a series of collimated quarks and gluons [101]. The resulting parton shower being collimated is due to the collinear divergence of QCD. Starting from a highly virtual parton (around the hard scale of the process), the parton shower will produce a sequence of branchings into further partons of decreasing virtuality, until one reaches a non–perturbative (hadronisation) scale, typically of order Λ_{QCD} or 1GeV [101].

At this stage, due to QCD confinement, these quarks and gluons undergo a process called "hadronisation", referring to the formation of hadrons as shown in Figure 1.12. Colour confinement itself refers to the phenomenon that colour charged particles (such as quarks and gluons) cannot be isolated into colour singlets, and therefore cannot be directly observed in conditions below the Hagedorn temperature of $\approx$ 2TK (corresponding to energies of approximately 130—140MeV per particle). Although some analytic approaches to model hadronisation exist, this process is non–perturbative and often relies on models implemented in MC event generators [101].

The produced high energy partons appear in the final state as a collimated collection of hadrons that are called collectively as jets. In principle they are collimated flows of hadrons and can be viewed as composite proxies to the fundamental quarks and gluons produced in the hard scatter [101].

The above discussion of jets is crude in a few respects. Firstly, because partons themselves are not well defined objects, for example due to higher–order QCD corrections where additional partons, real or virtual, have to be included [101]. Furthermore, whether two or more particles are part of the same jet or belong to two distinct jets is also somewhat ad hoc.

Hence the above oversimplified concept of a jet is insufficient to practically identify jets arising in an event. To do this, there must be a well defined procedure that demonstrates how to reconstruct the jets from the set of hadrons in the final state of the collision, commonly referred to as a "jet definition". A jet definition usually requires a "jet algorithm", which corresponds to a set of free parameters associated with the algorithm. A typical parameter example, is the jet radius which essentially provides a distance in the rapidity-azimuth (y, ϕ) plane above which two particles are considered as no longer part of the same jet [101].

In addition to this, a jet definition typically uses a recombination scheme which provides a specification about how the kinematic properties of the jet are obtained from its constituents. Most applications today use the so–called "E-scheme" recombination scheme which sums the components of the four–vectors.

Several jet substructure applications make use of the winner-take-all (WTA) recombination scheme [102] where the result of the recombination of two particles has the azimuth, rapidity and mass of the particle with the larger p_T, and a p_T equal to the sum of the two p_T values. The immediate advantage of this approach is that it reduces effects related to recoil of the jet axis when computing observables that share similarities with the event–shape broadening [101].

A number of jet algorithms have been proposed over the last few decades. These typically come under two major categories: cone algorithms and sequential recombination algorithms. A comprehensive review of jet algorithms can be found here Ref. [103].

1.6.4 Missing Transverse Energy

Neutral weakly interacting particles, such as neutrinos, escape from typical collider detectors without producing any visible signature in the detector elements. Hence, the presence of such "inert" particles must be inferred from the imbalance of total momentum in the event [104]. The vector momentum imbalance in the transverse direction is particularly useful in proton–proton colliders. This is known as missing transverse momentum denoted usually as p_T. Its energy equivalent is called missing transverse energy, and is denoted E_T^{miss}.

E_T^{miss} is one of the most important observables for discriminating several decays including leptonic decays of W bosons and top quarks from background events which do not contain neutrinos. It is also an important variable in searches for new weakly interacting long–lived particles. Many beyond the SM scenarios including dark matter, heavy neutrinos, Z' and supersymmetry searches predict events with large E_T^{miss}. Therefore the accurate reconstruction of this variable is very sensitive to particle mis–identification, momentum mis–measurements, detector malfunctions, cosmic ray backgrounds and beam halo particles, which may result in artificial E_T^{miss} [104].

1.6.5 Monte Carlo Event Generators

QFT calculations today must be performed at increasingly higher orders of perturbation theory in order to properly match the experimental precision that has been achieved at colliders. This means that the number of integrals that need to be computed for the increasingly complicated processes grows rapidly with each order [97]. These calculations generally require the assistance of computer programs using MC methods. MC generators are modular tools that perform parts of the QFT calculations required to describe the full hadronic interaction [97]. The interaction described by the MC is intrinsically random since specific partons that participate in the interaction have their momenta distributed according to their PDFs. Hence, even if the collision was hypothetically with monochromatic beams of protons with known momenta, the interaction would be inherently probabilistic [97].

The MC generators sample these possibilities according to theoretical and empirical descriptions of the underlying physics to produce numerous random events that each represent one possible outcome of the interaction. From the resulting events, physical observables that can be seen at detectors are constructed. Experimentally, such MC simulations are essential, since they enable direct comparison to experimental observables with these simulated predictions. The MC simulations also aid in the execution of the experiment itself. This is because every part of the experiment, from modelling of backgrounds, interpretations of results to calibration of detectors relies on comparisons of observed events to MC simulated events. The interdependence of MC simulation and experiment leads to an iterative process by which new experiments constrain modelling and identify inconsistencies in MC generators, and new predictions allow greater experimental precision [97].

1.6.6 Detector Simulation

In order to directly compare MC predictions with real observables, either the measurements or the simulation must be corrected to account for various discrepancies. A clear example is the finite resolution of physical detectors. Even in cases where the measurements are corrected, for a proper interpretation of results, fully reconstructed simulated events are used extensively for correction, calibration and validation throughout the reconstruction and analysis framework [97].

After matrix element generation as described in Section 1.6.5, events are said to be at parton level, containing descriptions of only the hard processes [97]. MC generators typically assign weights to each event such that a finite set of events can be used to efficiently sample the full kinematic phase space of the underlying particle physics process and scaled up or down based on the experimental luminosity. The parton shower generator can then be used to process the parton level events and decay unstable states into stable particles. After this is complete, the event status is changed to being at particle level.

The interaction of particles with the ATLAS detector, which we will cover in detail in Section 1.7.2, is simulated using the Geant4 toolkit [105]. Geant4 models a comprehensive set of physical processes over energies ranging all the way from $\mathcal{O}(100)$eV to TeV scale like at the LHC. It is configured using detailed cut out models of the detector material and geometry as well as the magnetic field in which it is situated and it simulates the trajectory and interactions of each type of particle. The individual detector element response can then be simulated by digitising the "hits" from Geant4 into voltages and other readout signals. This process takes into account detailed information about damaged modules or elements, as well as channel–dependent variations in the responses [97].

The effect from pileup is accounted for by simulation of additional collisions that are then overlaid onto the event along with samples of electronic noise and ambient background conditions [97]. We emphasise that the accuracy of these models depends on knowing both the condition of the detector and the operation conditions of the experiment (with particular importance being assigned to the pileup distribution). Furthermore, simulated samples typically need to be prepared well in advance of data taking for efficient allocation of computational resources. This is performed by preparing dedicated simulations for each specific dataset, and by re–weighting prepared simulated events to match the actual detector conditions.

In terms of computational resources, the most costly part of the outlined pipeline is the simulation of interactions with the calorimeters. However, For many applications it is sufficient to parametrise the response of the calorimeters to produce an approximately correct simulation, using a technique called the ATLAS fast calorimeter simulation (AtlfastII) [106] which is approximately 20 times faster than the full Geant4 modelling of the calorimeters.

1.7 The Experiment

The European Centre for Nuclear Physics (CERN) is a laboratory located on the outskirts of Geneva, Switzerland. It aims to uncover answers to many of the most fundamental unanswered questions in particle physics. The largest project in the laboratory is the LHC, a synchrotron 27km in circumference located underground (around 100m in depth) and extending into both France and Switzerland.

1.7.1 The Large Hadron Collider

The LHC experiment accelerates two collimated particle beams (either protons or atomic nuclei) in opposite directions around its circumference, and eventually collides them at four distinct interaction points where the beams are focused and crossed. Particle detectors are located at these four points to measure the outcome of these collisions. These four experiments are ATLAS, ALICE, CMS and LHCb [107–110]. The positions of the various detectors and accelerators across the CERN complex can be seen in Figure 1.14. ATLAS and CMS are designed to explore particle physics at the high energy frontier while ALICE is used for heavy ion collisions and the LHCb for heavy flavour studies.

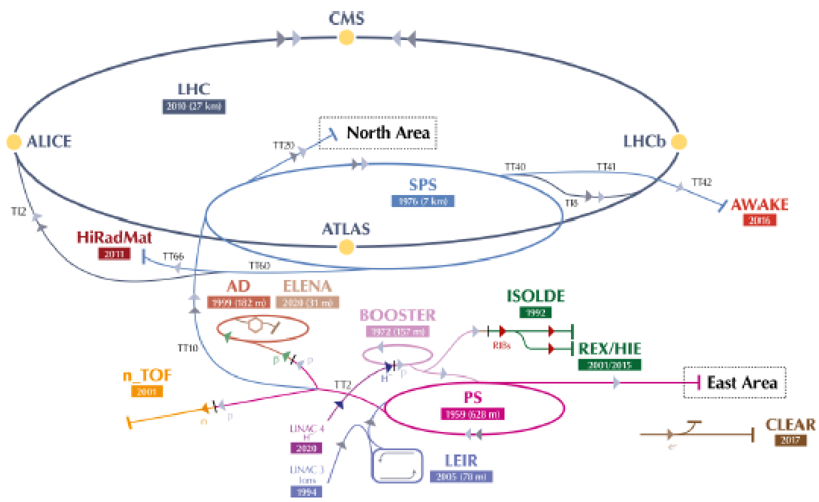

FIGURE 1.14: The CERN detector complex picturing the accelerators and connected experiments. The protons in the LHC ring are created in a linear accelerator and passed to several circular accelerators before entering the LHC [111].

The first run of the LHC gave rise to the first ever particle collisions at centre–of–mass energy of $\sqrt{s} = 7$TeV and $\sqrt{s} = 8$TeV between 2009 and 2013 [112, 113]. After a two year "long" shutdown, the LHC began a second run in 2015 and would continue until 2018. Over this period ATLAS collected data corresponding to an integrated luminosity of 139fb^{-1}. The LHC proton beams were each accelerated to 6.5TeV during Run 2, providing a collision centre–of–mass energy of $\sqrt{s} = 13$TeV. The main 2HDM search presented in Chapter 2 was conducted using proton–proton collision data gathered by the ATLAS experiment during Run 2 of the LHC.

Protons in the beam are separated into partitioned segments referred to as bunches, typically these will contain around 10^{11} protons each. When two bunches collide it is likely that multiple pairs of protons will interact, leading to several interactions per crossing. Inelastic hard scatter collisions of interest with high momentum transfer are considered the primary interaction (and will later be reconstructed as the primary vertex), while the other less energetic or diffractive interactions are called pileup.[4] The average number of interactions per bunch–crossing was 33.7 for the Run 2 dataset [114].

1.7.2 Overview of ATLAS

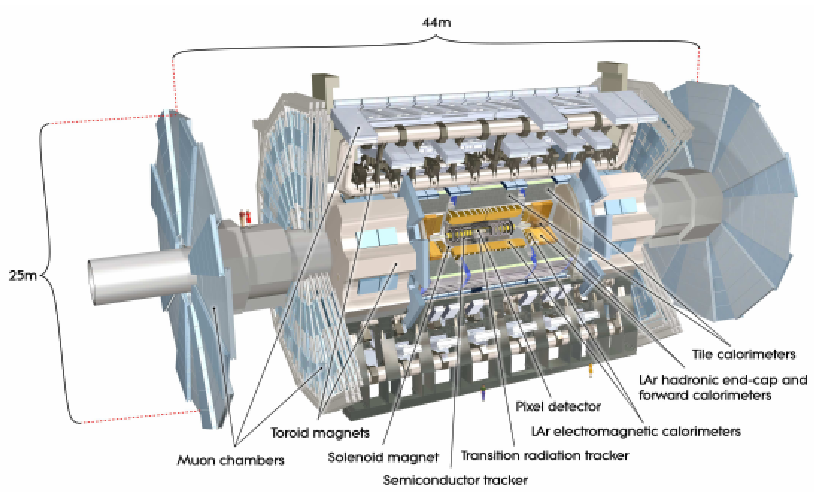

FIGURE 1.15: The ATLAS detector and its sub-detectors [107].

The ATLAS detector is 44m long and 25m high and is the largest of the LHC experiments. It is comprised of several subsystems surrounding the proton–proton interaction point in various concentric layers. Moving from inside to out these layers are [107]

- The Inner Detector (ID), dedicated to tracking charged particle trajectories and reconstrucing vertices.
- The calorimeter system, which measures the energy of a particle that interacts with it before absorbing it. Some particles can pass through the calorimeter system whilst only depositing part of their energy before escaping.

[4] See Section 1.6.1 for a more detailed explanation about event types

- The muon system, which measures a muon's momentum and tracks its trajectory.

The detector is approximately cylindrical and orientated along the direction of the beam axis, the round section is referred to as the barrel and the flat ends as the end–caps. A schematic of ATLAS is shown in Figure 1.15.

Powerful magnetic fields bend the trajectories of charged particles through Lorentz forces. By measuring the amount of curvature, the particles' momenta can be calculated, ATLAS has two superconducting magnet systems for exactly this purpose. One is a solenoid placed in between the ID and the calorimeters and provides a 2T field in the direction parallel to the beam [107]. Three other sets of magnets provide a toroidal magnetic field for the muon system, one wrapped around the barrel and two placed at its end–caps.

1.7.3 Coordinate System

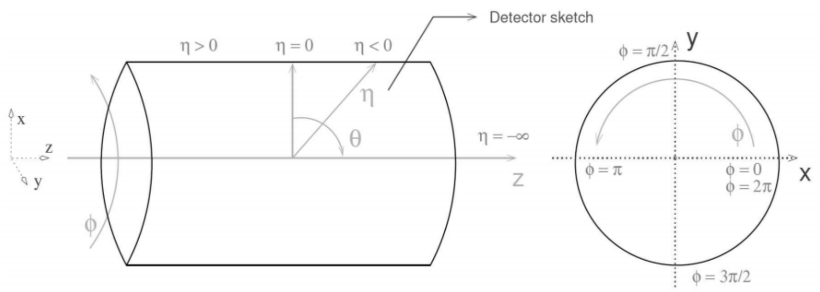

FIGURE 1.16: The ATLAS coordinate system [115].

The coordinate system used in ATLAS has the z-axis pointing along the beam direction. The x-axis points towards the centre of the LHC ring, and the y-axis points upwards. The positive direction of the z-axis is defined by the right–hand rule. Due to the cylindrical symmetry of collisions and the detector, it is convenient to use different coordinates. Points on a plane transverse to the beam are labelled using polar coordinates, the azimuthal angle ϕ, and the distance to the beam r. The position along the direction of the beam is marked by the polar angle θ (similar to how latitude is defined on a globe).

It is convention to use the pseudorapidity $\eta = -\log\left[\tan\frac{\theta}{2}\right]$ rather than the geometric angle θ since an angular separation in pseudorapidity is approximately invariant under Lorentz boosts in the direction of the beam. A visual representation can be seen in Figure 1.16. In the relativistic limit, pseudorapidity approximates rapidity defined as $y = \frac{1}{2}\log\left(\frac{E+p_L}{E-p_L}\right)$ where p_L is the longitudinal component of momentum. It is also beneficial to define the angular separation ΔR in the (η, ϕ) plane which can be written $\Delta R = \sqrt{\Delta\eta^2 + \Delta\phi^2}$. Typically the transverse projection of momentum and energy are of interest and these are defined $p_T = \sqrt{p_x^2 + p_y^2}$ and $E_T = \sqrt{p_T^2 + m^2}$ respectively.

1.7.4 Sub-detectors

ATLAS has various subsystems which are combinations of different detectors and devices exploiting various useful physical properties to perform measurements.

1.7.5 Inner Detector

The ID uses two technologies to track charged particle trajectories, silicon and transition radiation detectors respectively. The main characteristics of the ATLAS detector's ID subsystems are shown in Table 1.4. The ATLAS ID has a single track momentum resolution of around $\sigma(1/p_T) \approx 0.4\text{TeV}^{-1}$ for $p_T = 200\text{GeV}$, this starts to degrade in the forward regions ($|\eta| > 2$) [114].

The ID contains silicon detectors that utilise the semiconducting properties of silicon. Positively doped silicon is embedded on a negatively doped silicon substrate, creating a depleted zone of charge carriers in the boundary region. This depleted zone is then extended by applying a reverse bias voltage. Hence, when a charged particle travels through this zone it promotes electron–hole pairs to the conduction band. These pairs then drift in opposite directions due to the bias voltage. This generates a flow of charges which then registers as a signal on the detector's readout electronics [116].

Sub-System	Radius (mm)	Size (μm)	Resolution (μm)
Pixel	$5 - 12$	50×400	10×115
IBL	25.7	50×250	10×72
SCT	$30 - 52$	$80 \times 1.26 \times 10^5$	17
TRT	$56 - 107$	$4 \times 1.44 \times 10^6$	130

TABLE 1.4: The ATLAS ID system [115].

ATLAS uses silicon sensors in the ID, pixel and strip modules. Pixel modules have individual cells of $50\mu\text{m} \times 400\mu\text{m}$ in size [114]. These are oriented with the shorter side on the plane of the magnetic bending to maximise the momentum measurement resolution. The ID has pixel layers surrounding the interaction point, with four layers in the barrel and three discs covering the end–caps. The innermost layer of the barrel pixel detectors contains the the Insertable Barrel Layer (IBL) which was added after Run 1 to improve the detection of B hadron decays. This is because the precise resolution of the pixel sensors is optimal to find tracks pointing at a vertex away from the beam that can be left by long lived particles, such as B hadrons, decaying in the ID [117]. The improved granularity of this detector is also essential to avoid missing a particle's hit due to another particle's interaction with the sensor in conditions with high particle flow.

The Semiconductor Tracker (SCT) silicon strip modules work in the same way as the IBL, but they house long strips of silicon $\simeq 80\mu\text{m} \times 12\text{cm}$ rather than individual pixels [118]. Silicon strips are oriented the same way as the pixel strips i.e. with their short side along the magnetic bending plane. Resolution on the coordinate of the long side axis is improved by having two sensors with a small intermediate stereoangle. The system is formed by four layers of silicon strip modules in the barrel region and nine layers of disks at each end–cap.

The Transition Radiation Tracker (TRT) is the final piece of the ID and is made of long cylindrical wire chambers. Each chamber is filled with a mixture gases and has a tungsten wire running down its length [119]. As a charged particle passes through the chamber it can ionise the gas mixture causing electrons and ions to drift in opposite directions due to a voltage difference being produced across the cylinder and the wire. The signal measured in the cylinder depends on the amount of "transition" radiation generated, which in turn depends on the mass of the particle. This mass dependence is used to identify electrons in the tracker from other, heavier, charged particles commonly produced, for example pions.

1.7.6 Calorimeters

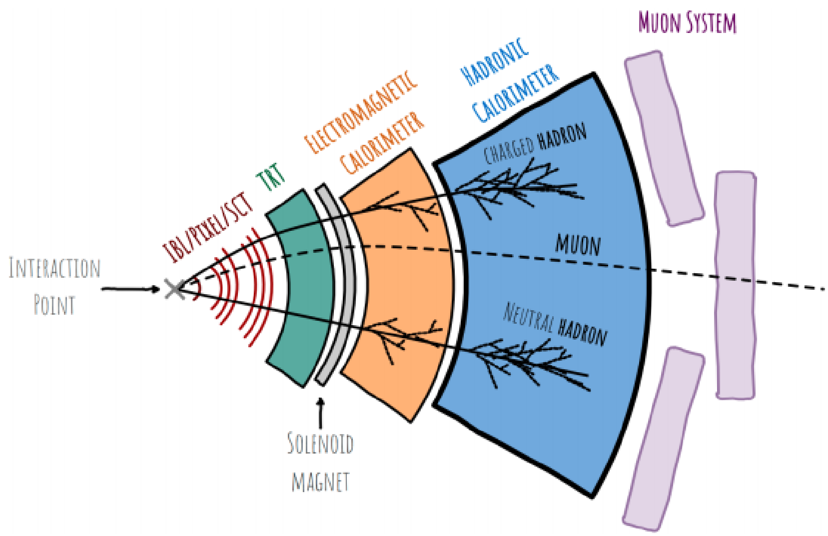

FIGURE 1.17: Schematic of the ATLAS subdetectors representing a slice in ϕ of the plane transverse to the beam. The signatures various particles would leave in each layer is also shown [117].

ATLAS has two main calorimeter systems, these are the electromagnetic and hadronic calorimeters. The electromagnetic calorimeter is optimised to measure energy deposited by electromagnetic showers of charged particles. Analogously, the hadronic calorimeters are optimised to measure hadronic shower energy. It is convenient to separate the calorimeters in this way since electromagnetic showers tend to be smaller in volume than hadronic ones. Hence, finer granularity is needed in the electromagnetic calorimeter to discern features of the smaller shower shapes, and a larger, denser, calorimeter is needed for the hadronic section to allow particles to deposit all their energy [117]. A visual representation of the showering is shown in Figure 1.17.

Electromagnetic Calorimeter

The electrogmagnetic calorimeter is utilised mainly for detection of electrons and photons. It is comprised of various liquid argon (LAr)-lead sampling calorimeters. The layers of each material are placed in alternating order. Since a travelling particle is likely to interact with the high density absorber material, lead, and produce a shower of particles, the products of this shower can then ionise the active material, LAr. This leads to drifting charges that can be measured by electrodes placed between the LAr and the lead absorber [117].

The barrel electromagnetic calorimeter is divided into three concentric sections in the radial direction. The absorber and active layers in each section are shown in the left panel of Figure. 1.18 with its "waves" oriented radially so so there is coverage of all zones with alternating material in ϕ. The end–cap LAr electromagnetic calorimeter has a similar geometry but it is arranged in two wheels per end–cap.

Hadronic Calorimeter

The hadronic calorimeter uses LAr-copper in the end–cap region and iron scintillating tiles in the barrel region. The LAr–Cu end–cap calorimeters are similar to the ones described in the electromagnetic calorimeter, except that the layers are shaped as planes as shown in the right panel of Figure. 1.18. The tile calorimeter uses the dense copper material to maximise the number of interactions a high energy particle has as it passes through the detector, but in this case, secondary particles from the shower will produce scintillation light when travelling through the active material, which can be gathered by wavelength shifting fibres and read out by photomultiplier tubes [120].

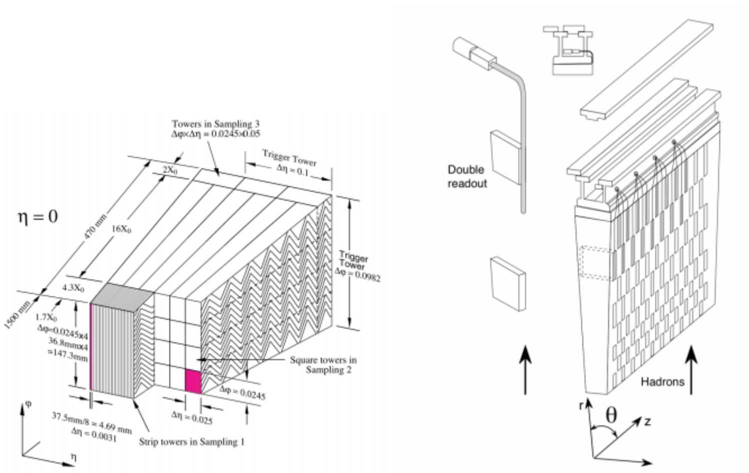

Figure 1.18: Left: liquid argon calorimeter section [121]. Right: tile calorimeter section of the ATLAS detector [120].

1.7.7 The Muon Spectrometer

The muon spectrometer is the outermost system of the ATLAS detector. The magnetic field for these detectors is provided by the toroidal superconducting magnets (the large barrel toroid is situated in the barrel region, and two smaller toroidal magnets fit around the end–caps). The muon system is formed by drift tube chambers, these operate similarly to those in the the TRT but differ in material and arrangement [122]. As muons traverse the detector, the magnetic field will bend their trajectory via Lorentz forces. The muon paths are recorded as a sequence of hits in the drift tubes. This trajectory is then used to calculate the muon's momentum.

1.7.8 Trigger

Since the LHC collides protons on average every 25ns, saving data for every bunch–crossing is not practical due to limitations in information storage and recording rate capability. The solution implemented by ATLAS to overcome this problem is to use a trigger system. The system quickly evaluates the properties of a collision by searching for potentially interesting physics characteristics and decides whether to record the event or discard it.

The ATLAS trigger system works in two stages and uses information from the calorimeter and muon systems. The level one (L1) trigger is a system of customised hardware which reads the detectors, using a coarse granularity, in search of “regions of interest” (for example a concentration of energy deposits in the calorimeters [123]). Events passing the L1 trigger are then analysed further by the High Level Trigger (HLT). The HLT is a software based system which performs more complex filters such as requiring finer sampling, b-tagging (checking flavour) of jets and beyond. Events that pass the HLT are finally saved for analysis. The trigger system, records events at an average rate of 1kHz, down from the 40MHz collision rate.

Potentially interesting physics events can have an trigger rate that is too high to record. In such cases, only a fraction of events passing a trigger are recorded. This is referred to as a prescaled trigger. A un–prescaled trigger therefore refers to a filter for which all events that pass are recorded.

Chapter 2

Exotic Higgs Bosons at ATLAS

2.1 Search for a Heavy Higgs Boson Decaying Into a Z Boson and Another Heavy Higgs Boson in the $\ell\ell bb$ and $\ell\ell WW$ Final States in pp Collisions at $\sqrt{s} = 13$ TeV with the ATLAS Detector

After the discovery of a Higgs boson at the LHC [124, 125], detailed measurements of its properties [126–133] have shown excellent compatibility with the SM Higgs boson [22–24, 134–136]. These results indicate that the scalar sector of the theory of the electroweak interaction contains at least a doublet of complex scalar fields. In addition, they constrain the possibilities for additional spin-0 field content in the theory and disfavour parts of the parameter space in models with extended Higgs sectors. These results, however, still allow several extensions of the Higgs sector, such as the 2HDM [34,35], in which large parts of the parameter space are compatible with the existence of a Higgs boson like the one in the SM. In the 2HDM, a second complex doublet of the Higgs fields is added to the single SM Higgs doublet. The model has a weak decoupling limit [137] in which one of its predicted Higgs bosons has couplings to fermions and vector bosons that are the same as those of the SM Higgs boson at lowest order. In addition, a Higgs sector structure with two complex doublets of fields appears in several new physics scenarios, including supersymmetry [138], dark-matter models [41], axion models [139], electroweak baryogenesis [40] and neutrino mass models [42].

The addition of a second Higgs doublet leads to five Higgs bosons after electroweak symmetry breaking. The phenomenology of such a model is very rich and depends on many parameters, such as the ratio of the vacuum expectation values of the two Higgs doublets ($\tan\beta$) and the Yukawa couplings of the scalar sector [35]. When CP conservation is assumed, the model contains two CP-even Higgs bosons, h and H with $m_H > m_h$, one that is CP-odd, A, and two charged scalars, $H^{\pm}$. There have been many searches for a CP-even Higgs boson at the LHC, in channels that include $H \to WW/ZZ$ [140–145] and $H \to hh$ [146, 147], as well as dedicated searches for the heavy CP-odd Higgs boson, as in the $A \to Zh$ channel [148, 149]. Some 2HDM searches are agnostic with respect to whether the heavy Higgs bosons are CP-even or CP-odd, for example searches in the $A/H \to \tau\tau/bb$ [1] channels [150–152]. In the interpretation of this last category of channels it is usually assumed that both heavy Higgs bosons are degenerate in mass, a hypothesis that is motivated in certain

[1] To simplify the notation, antiparticles are not explicitly labelled in this paper.

supersymmetric models [138]. Finally, there have been searches for signatures that explicitly assume different masses for the heavy Higgs bosons, for example searches in the $A \to ZH \to \ell\ell bb/\ell\ell\tau\tau$ channels [153–155].

The case in which the heavy Higgs bosons have different masses, in addition to being in an allowed part of the parameter space, is further motivated by electroweak baryogenesis scenarios in the context of the 2HDM [36–39]. For 2HDM electroweak baryogenesis to occur, the requirement $m_A > m_H$ is favoured [36] for a strong first-order phase transition to take place in the early universe. The A boson mass is also constrained to be less than approximately 800 GeV, whereas the lighter CP-even Higgs boson, h, is required to have properties similar to those of a SM Higgs boson and is assumed to be the Higgs boson with a mass of 125 GeV that was discovered at the LHC [36]. Under such conditions and for large parts of the 2HDM parameter space, the CP-odd Higgs boson, A, decays into ZH [36,156]. At the LHC, the production of the A boson in the relevant 2HDM parameter space proceeds mainly through gluon–gluon fusion and in association with b-quarks (b-associated production).

This search for $A \to ZH$ decays uses proton–proton collision data at $\sqrt{s} = 13$ TeV corresponding to an integrated luminosity of 139 fb^{-1} recorded by the ATLAS detector at the LHC. The search considers $Z \to \ell\ell$, where $\ell = e,\ \mu$, to take advantage of the clean leptonic final state. The H boson is studied in the $H \to bb$ and $H \to WW$ decay channels. The $H \to bb$ channel takes advantage of the high branching ratio in large parts of the 2HDM parameter space, especially in the weak decoupling limit, where the H boson decays into weak vector bosons are suppressed. The $H \to WW$ decay channel is considered in the case where both W bosons decay hadronically. This heavy Higgs boson decay is dominant in parts of the 2HDM parameter space close to, but not exactly at, the weak decoupling limit [36] and it provides a new way to look for $\ell\ell WW$ resonances in a final state that has been less explored by other LHC searches. Both final states considered allow full reconstruction of the A boson's decay kinematics. This search considers both the gluon–gluon fusion (see Figure 2.1a) and b-associated production mechanisms (see Figure 2.1b) for the $A \to ZH \to \ell\ell bb$ channel. For the $A \to ZH \to \ell\ell WW$ channel, only gluon–gluon fusion production is considered (see Figure 2.1c), although the b-associated production is still of interest in this channel.

This article is organised as follows. Section 2.2 introduces the ATLAS detector. A description of the collision and simulated data samples used in this article is given in Section 2.3. The algorithms used to reconstruct the objects used in this search are described in Section 2.4. The event selection and background estimates for the two channels considered and the modelling of the signal are discussed in Sections 2.5 and 2.6, respectively. Section 2.7 is devoted to the description of the systematic uncertainties. The results are discussed in Section 2.8 and the conclusions are given in Section 2.9.

2.2 ATLAS Detector

The ATLAS experiment [157] at the LHC is a general-purpose particle detector with cylindrical geometry and forward–backward symmetry. It includes an inner-detector tracker surrounded by a 2 T superconducting solenoid, electromagnetic and hadronic calorimeters, and a muon spectrometer with a toroidal magnetic field. The inner

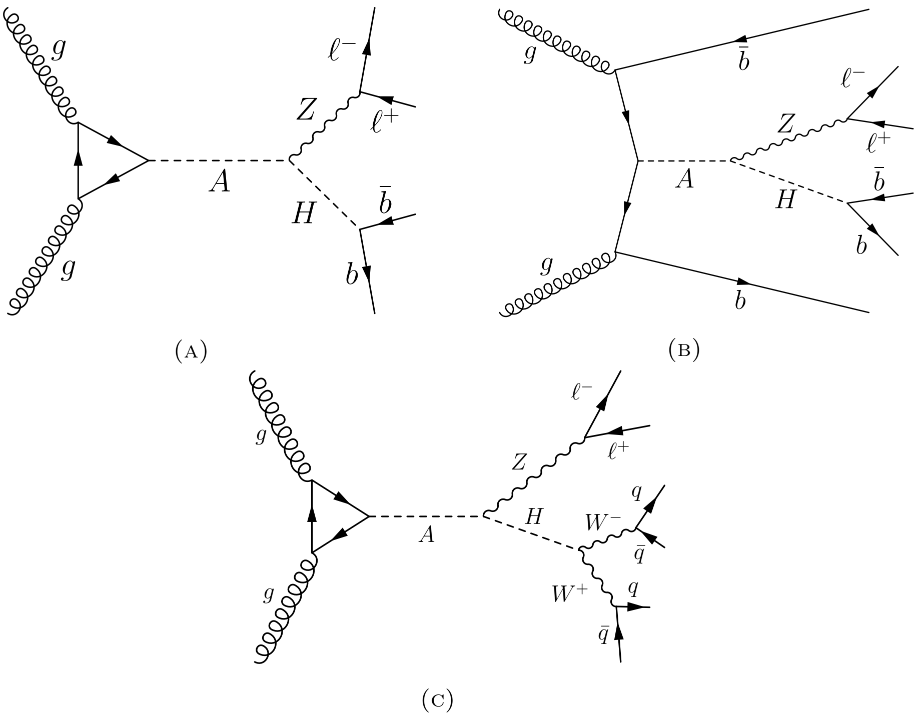

FIGURE 2.1: Example lowest-order Feynman diagrams for (a) gluon–gluon fusion production of A bosons decaying into $ZH \to \ell\ell bb$, (b) b-associated production of A bosons decaying into $ZH \to \ell\ell bb$, and (c) gluon–gluon fusion production of A boson decaying into $ZH \to \ell\ell WW$.

detector consists of a high-granularity silicon pixel detector, including the insertable B-layer [158, 159], a silicon microstrip tracker, and a straw-tube tracker. It provides precision tracking of charged particles with pseudorapidity $|\eta| < 2.5$.[2] The calorimeter system covers the pseudorapidity range $|\eta| < 4.9$. It is composed of sampling calorimeters with either lead/liquid-argon, steel/scintillator-tiles, copper/liquid-argon or tungsten/liquid-argon as the absorber/sensitive material. The muon spectrometer provides muon identification and momentum measurement for $|\eta| < 2.7$. A two-level trigger system [160] is employed to select events to be recorded at an average rate of about 1 kHz for offline analysis.

2.3 Data and Simulated Event Samples

The data used in this search were collected between 2015 and 2018 from $\sqrt{s} = 13$ TeV proton–proton collisions and correspond to an integrated luminosity of 139 fb^{-1} [161–164], which includes only data-taking periods where all relevant detector subsystems were operational [165]. The data sample was collected using a set of single-muon [166]

[2] ATLAS uses a right-handed coordinate system with its origin at the nominal interaction point (IP) in the centre of the detector and the z-axis along the beam pipe. The x-axis points from the IP to the centre of the LHC ring, and the y-axis points upward. Cylindrical coordinates (r,ϕ) are used in the transverse plane, ϕ being the azimuthal angle around the beam pipe. The pseudorapidity is defined in terms of the polar angle, θ, as $\eta = -\ln\tan(\theta/2)$. Transverse momenta are computed from the three-momenta, $\vec{p}$, as $p_{\mathrm{T}} = |\vec{p}|\sin\theta$.

and single-electron triggers [167]. The single-muon triggers had p_T thresholds in the range of 20–26 GeV for isolated muons and 50 GeV for muons without any isolation requirement. The single-electron triggers employed a range of p_T thresholds in the range 24–300 GeV and a combination of quality and isolation requirements depending on the data-taking period and the p_T threshold.

Simulated signal events with A bosons produced by gluon–gluon fusion were generated at leading order (LO) with MadGraph5_aMC@NLO 2.3.3 [168, 169], using Pythia 8.210 [170] with a set of tuned parameters called the A14 tune [171] for parton showering. The decays of $H \to bb$ and WW were considered. Additionally, in the $A \to ZH \to \ell\ell bb$ channel, A bosons produced in association with b-quarks were generated at next-to-leading-order (NLO) with MadGraph5_aMC@NLO 2.1.2 [169, 172, 173] following Ref. [174] together with Pythia 8.212 and the A14 tune for parton showering. The gluon–gluon fusion production used `NNPDF2.3lo` [175] as the parton distribution functions (PDFs), while the b-associated production used `CT10nlo_nf4` [176]. The signal samples were generated for A bosons with masses in the range of 230–800 GeV (300–800 GeV) and widths up to 20% of the A mass, and for narrow-width H bosons with masses in the range of 130–700 GeV (200–700 GeV) for the $\ell\ell bb$ ($\ell\ell WW$) channel.

Background events from the production of W and Z bosons in association with jets were simulated with Sherpa v2.2.1 [177] using NLO matrix elements (ME) for up to two partons, and LO matrix elements for up to four partons calculated with the Comix [178] and OpenLoops [179, 180] libraries. They were matched with the Sherpa parton shower [181] using the MEPS@NLO prescription [182–185] using the set of tuned parameters developed by the Sherpa authors. The `NNPDF3.0nnlo` set of PDFs [186] was used and the samples were normalised to a next-to-next-to-leading-order (NNLO) prediction [187]. Production of WW, ZZ and WZ pairs was simulated using the same generator and parameters as for the W and Z boson samples.

The production of $t\bar{t}$ events was modelled using the Powheg-Box v2 [188–191] generator at NLO with the `NNPDF3.0nlo` [186] PDF set and the h_{damp} parameter[3] set to 1.5 m_{top} [192]. The events were interfaced to Pythia 8.230 to model the parton shower, hadronisation, and underlying event, with parameters set according to the A14 tune and using the `NNPDF2.3lo` set of PDFs. The decays of bottom and charm hadrons were performed by EvtGen v1.6.0 [193]. The associated production of a single top quark and W boson (tW) and single top production in the s-channel were modelled using the Powheg-Box v2 [189–191, 194, 195] generator at NLO in QCD using the five-flavour scheme and the `NNPDF3.0nlo` set of PDFs. The diagram removal scheme [196] was used to remove interference and overlap with $t\bar{t}$ production in the case of tW production. The production of $t\bar{t}V$ events was modelled using the MadGraph5_aMC@NLO v2.3.3 generator at NLO with the `NNPDF3.0nlo` PDF set. The events were interfaced to Pythia 8.210 using the A14 tune and the `NNPDF2.3lo` PDF set. The decays of bottom and charm hadrons were simulated using the EvtGen v1.2.0 program.

Finally, SM Higgs boson production in association with a vector boson was simulated using Powheg [189–191,197] and interfaced with Pythia 8.186 [198] for parton shower and non-perturbative effects. The Powheg prediction is accurate to NLO for

[3]The h_{damp} parameter is a resummation damping factor and one of the parameters that controls the matching of Powheg matrix elements to the parton shower and thus effectively regulates the high-p_T radiation against which the $t\bar{t}$ system recoils.

the Vh boson plus one jet production. The loop-induced $gg \to Zh$ process was generated separately at LO. The PDF4LHC15 PDF set [199] and the AZNLO tune [200] of PYTHIA 8.186 were used. The simulation prediction was normalised to cross sections calculated at NNLO in QCD with NLO electroweak corrections for $q\bar{q}/qg \to Vh$ and at NLO and next-to-leading-logarithm accuracy in QCD for $gg \to Zh$ [201–207].

The effect of multiple interactions in the same and neighbouring bunch crossings (pile-up) was modelled by overlaying the original hard-scattering event with simulated inelastic proton–proton events generated with PYTHIA 8.186 using the `NNPDF2.3lo` set of PDFs and the A3 tune [208]. The simulated events were weighted to reproduce the distribution of the average number of interactions per bunch crossing ($\langle\mu\rangle$) observed in the data. The $\langle\mu\rangle$ value in the simulation was rescaled by a factor of 1.03 ± 0.07 to improve agreement between data and simulation in the visible inelastic proton–proton cross section [209]. All generated background samples were passed through the GEANT4-based [210] detector simulation [211] of the ATLAS detector. The ATLFAST-II simulation [211] was used for the signal samples to allow for the generation of many different A and H boson masses. The simulated events were reconstructed in the same way as the data.

2.4 Object Reconstruction

Selected events are required to contain at least one vertex having at least two associated tracks with $p_{\mathrm{T}} > 500$ MeV, and the primary vertex is chosen to be the vertex reconstructed with the largest Σp_{T}^2 of its associated tracks.

Electrons are reconstructed from energy clusters in the electromagnetic calorimeter that are matched to tracks in the inner detector [212]. Electrons are required to have $|\eta| < 2.47$ and $p_{\mathrm{T}} > 7$ GeV. The associated track must have $|d_0|/\sigma_{d_0} < 5$ and $|z_0|\sin\theta < 0.5$ mm, where d_0 (z_0) is the transverse (longitudinal) impact parameter relative to the primary vertex and σ_{d_0} is the error in d_0. To distinguish electrons from jets, isolation and quality requirements are applied. The quality requirements refer to both the inner detector track and the calorimeter shower shape. The isolation requirements are defined using tracking and calorimeter measurements. Electrons used in this search satisfy the ‘Loose’ quality and isolation requirements.

Muons are reconstructed by matching tracks reconstructed in the inner detector to tracks or track segments in the muon spectrometer [213]. Muons used for this search must have $|\eta| < 2.5$, $p_{\mathrm{T}} > 7$ GeV, $|d_0|/\sigma_{d_0} < 3$, and $|z_0|\sin\theta < 0.5$ mm. They are also required to satisfy ‘Loose’ isolation requirements, similar to those used for electrons, as well as ‘Loose’ quality criteria for tracks in the inner detector and muon spectrometer [214].

Jets are reconstructed from topological clusters in the calorimeter system [215], using the anti-k_t algorithm [216, 217] with radius parameter $R = 0.4$. Candidate jets are required to have $p_{\mathrm{T}} > 20$ GeV ($p_{\mathrm{T}} > 30$ GeV) for $|\eta| < 2.5$ ($2.5 < |\eta| < 4.5$) [218]. Low-p_{T} jets from pile-up are rejected by a multivariate algorithm that uses properties of the reconstructed tracks in the event for jets with $p_{\mathrm{T}} < 60$ GeVand $|\eta| < 2.4$ [219].

Jets containing b-hadrons are identified using a multivariate tagging algorithm (b-tagging) [220, 221], which makes use of track impact parameters and reconstructed secondary vertices. The b-tagging algorithm output is used to define a criterion to select jets originating from b-quark hadronisation for jets with $|\eta| < 2.5$. The jets that are selected in this way are referred to as b-jets in the following. The criterion in use has an average efficiency of 70% for jets from b-quarks in simulated $t\bar{t}$ events, with rejection factors of 8.9, 36 and 300 for jets initiated by c-quarks, hadronically decaying τ-leptons and light-flavour quarks or gluons, respectively [221].

Electrons, muons and jets are reconstructed and identified independently. When those objects are spatially close, these algorithms can lead to ambiguous identifications. An overlap removal procedure [222] is therefore applied to remove ambiguities.

The missing transverse momentum, whose magnitude is denoted by $E_{\mathrm{T}}^{\mathrm{miss}}$, is computed as the negative vectorial sum of the transverse momenta of calibrated leptons and jets, plus an additional soft term constructed from all tracks that originate from the primary vertex but are not associated with any identified lepton or jet [223, 224].

2.5 Event Selection and Background Estimation

The final states for the $A \to ZH \to \ell\ell\ bb/WW$ decays feature a pair of oppositely charged, same-flavour leptons and either two b-jets or four mostly light-flavour jets from the W bosons decays. Three resonances can be formed by combining the selected objects: (i) the Z boson ($\ell\ell$), (ii) the H boson (bb or $WW \to 4j$), and (iii) the A boson (ZH system).

Events are required to contain exactly two muons or two electrons. The two muons must have opposite electric charges. This requirement is not applied to electrons, since they have a non-negligible charge misidentification rate due to conversions of bremsstrahlung photons. The highest-p_{T} lepton must satisfy $p_{\mathrm{T}} > 27$ GeV in the $\ell\ell bb$ final state, to ensure full efficiency of the single-lepton triggers. This requirement is raised to $p_{\mathrm{T}} > 30$ GeV for the $\ell\ell WW$ final state. The invariant mass of the lepton pair, $m_{\ell\ell}$, must be in the range of 80–100 GeV to be compatible with the mass of the Z boson.

Further event selection criteria are channel-specific, and are described separately in the following sections.

2.5.1 The $\ell\ell bb$ Final State

The events that are used for the $A \to ZH \to \ell\ell bb$ search are required to have at least two b-jets, with at least one of them having $p_{\mathrm{T}} > 45$ GeV. The two highest-p_{T} b-jets of the event form the $H \to bb$ system candidate. The A boson candidate is formed by these two b-jets and, in addition, the two leptons that are matched to the Z boson.

The requirement of a same-flavour lepton pair along with several b-jets implies that the signal region is contaminated by Z boson production in association with jets and backgrounds including top quarks, like $t\bar{t}$ production. The presence of neutrinos in semileptonic top-pair production provides a handle to reduce this background by requiring $E_{\mathrm{T}}^{\mathrm{miss}}/\sqrt{H_{\mathrm{T}}} < 3.5\ \mathrm{GeV}^{1/2}$, where H_{T} is the scalar sum of the p_{T} of all jets and leptons in the event. The Z+jets background is reduced by requiring $\sqrt{\Sigma p_{\mathrm{T}}^2}/m_{\ell\ell bb} > 0.4$, where $m_{\ell\ell bb}$ is the four-body invariant mass of the two-lepton, two-b-jet system assigned to the A boson candidate and the summation is performed over the p_{T}^2 of these objects. The distribution of the $\sqrt{\Sigma p_{\mathrm{T}}^2}/m_{\ell\ell bb}$ variable is shown in Figure 2.2 separately for the cases where exactly two b-jets and three or more b-jets are present in the event. The distribution is shown before the $\sqrt{\Sigma p_{\mathrm{T}}^2}/m_{\ell\ell bb} > 0.4$ requirement is applied.

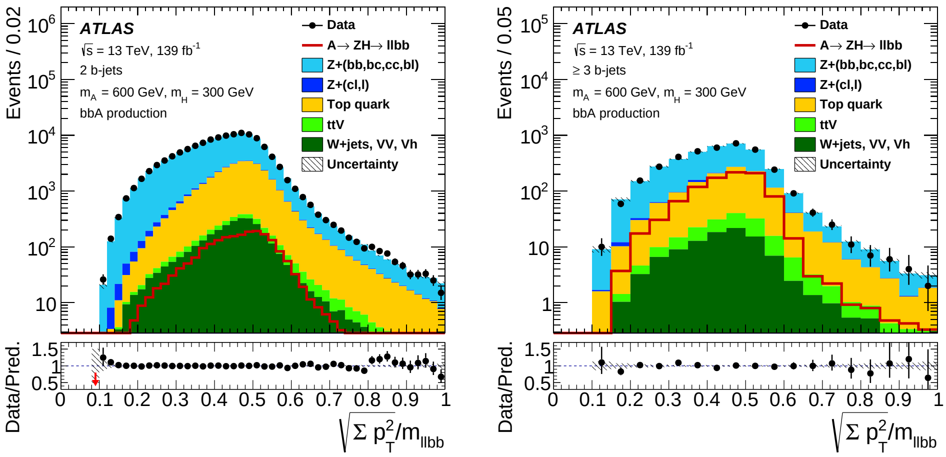

(A) (B)

FIGURE 2.2: The $\sqrt{\Sigma p_{\mathrm{T}}^2}/m_{\ell\ell bb}$ distributions shown before the requirement on this variable is applied for events with (a) exactly two b-jets and (b) three or more b-jets. Corrections from a fit to the data are applied to the simulation, as described in Sections 2.5.1 and 2.8. The signal distribution for $(m_A, m_H) = (600, 300)$ GeV is also shown, and is normalised such that the production cross section times the branching ratios $B(A \to ZH)$ and $B(H \to bb)$ corresponds to 1 pb. The signal shown includes only A bosons produced in association with b-quarks. The lower panel shows the ratio of the data to the background prediction (black filled circles) and the relative uncertainty, which includes both statistical and systematic components, in the background prediction (hatched area). The notations ttV, VV and Vh refer to top-pair production in association with a vector boson, diboson production and SM Higgs boson production in association with a vector boson, respectively. The production of a Z boson in association with jets is split based on jet flavour. The notation Z+(bb,bc,cc,bl) refers to the case where the jets originate from heavy flavour, which includes at least one jet originating from a b-quark or two jets originating from c-quarks, whereas the notation Z+(cl,l) includes all the remaining cases.

The two signal production mechanisms, gluon–gluon fusion and b-associated production, differ mainly in the number of heavy-flavour jets that are produced in association with the A boson. This motivates a categorisation based on the number of b-jets present in the event. In particular, two categories are defined: the $n_b = 2$ category, which contains events with exactly two b-jets, and the $n_b \geq 3$ category, which contains events with three or more b-jets. For gluon–gluon fusion production, more than 95% of the events passing the above selection fall into the $n_b = 2$ category. For b-associated production, only 25–35% of the selected events fall into the $n_b \geq 3$ category, and the others enter the $n_b = 2$ category. This is because of the relatively soft p_{T} spectrum of the associated b-jets and the geometric acceptance of the tracker.

Finally, the invariant mass m_{bb} of the b-jets that are assigned to the H boson must be compatible with the assumed H boson mass. This is ensured by requiring m_{bb} to be within optimised boundaries that depend on the assumed m_H: $0.85 \cdot m_H - 20$ GeV $< m_{bb} < m_H + 20$ GeV for the $n_b = 2$ category, and $0.85 \cdot m_H - 25$ GeV $< m_{bb} < m_H + 50$ GeV for the $n_b \geq 3$ category. The wider window for $n_b \geq 3$ is motivated by a slightly poorer resolution due to potential b-jet misassignments. The b-jets that are matched to the H boson are the highest-p_{T} b-jets in the event and, hence, in the case of b-associated production, where more b-jets are present, may not be the ones that actually come from the $H \to bb$ decay. In b-associated production, the fraction of A bosons for which the correct b-jets are chosen is in the range 50–90% for the $n_b \geq 3$ category and is at least 65% for the $n_b = 2$ category.

The signal efficiency in the $n_b = 2$ category after the m_{bb} window requirement is 5.1–11% (2.5–6.6%) for gluon–gluon fusion (b-associated) production, depending on the m_A and m_H values. Similarly, the efficiency in the $n_b \geq 3$ category after the m_{bb} window requirement is 1.3–3.2% for b-associated production. The quoted numbers refer to the efficiencies for A bosons decaying into ZH, with $Z \to ee/\mu\mu/\tau\tau$ and $H \to bb$, to pass the event selection for each of the categories. The inclusion of $Z \to \tau\tau$ in this definition lowers the quoted signal efficiency because these decays have a very small efficiency to pass in this selection (which aims at $Z \to ee/\mu\mu$). The signal region selection is summarised in Table 2.1.

<table>
<tr><td colspan="3">Single-electron or single-muon trigger
Exactly 2 leptons (e or μ) ($p_{\mathrm{T}} > 7$ GeV) with the leading one having $p_{\mathrm{T}} > 27$ GeV
Opposite electric charge for $\mu\mu$ pairs; 80 GeV $< m_{\ell\ell,\ e\mu} <$ 100 GeV, $\ell = e,\ \mu$
At least 2 b-jets ($p_{\mathrm{T}} > 20$ GeV) with one of them having $p_{\mathrm{T}} > 45$ GeV
$E_{\mathrm{T}}^{\mathrm{miss}}/\sqrt{H_{\mathrm{T}}} < 3.5$ GeV$^{1/2}$, $\sqrt{\Sigma p_{\mathrm{T}}^2}/m_{\ell\ell bb} > 0.4$</td></tr>
<tr><td></td><td>$n_b = 2$ category</td><td>$n_b \geq 3$ category</td></tr>
<tr><td></td><td>Exactly 2 b-tagged jets</td><td>At least 3 b-tagged jets</td></tr>
<tr><td>Signal region</td><td>ee or $\mu\mu$ pair
$0.85 \cdot m_H - 20$ GeV $< m_{bb} < m_H + 20$ GeV</td><td>ee or $\mu\mu$ pair
$0.85 \cdot m_H - 25$ GeV $< m_{bb} < m_H + 50$ GeV</td></tr>
<tr><td>Z+jets control region</td><td>ee or $\mu\mu$ pair
$m_{bb} < 0.85 \cdot m_H - 20$ GeV
or $m_{bb} > m_H + 20$ GeV</td><td>ee or $\mu\mu$ pair
$m_{bb} < 0.85 \cdot m_H - 25$ GeV
or $m_{bb} > m_H + 50$ GeV</td></tr>
<tr><td>Top control region</td><td>$e\mu$ pair
$0.85 \cdot m_H - 20$ GeV $< m_{bb} < m_H + 20$ GeV</td><td>$e\mu$ pair
$0.85 \cdot m_H - 25$ GeV $< m_{bb} < m_H + 50$ GeV</td></tr>
</table>

TABLE 2.1: Summary of the event selection for signal and control regions in the $A \to ZH \to \ell\ell bb$ channel.

The $m_{\ell\ell bb}$ distribution after the m_{bb} requirement is the final discriminating variable, which is fitted to obtain the result of the search in this channel. To improve the $m_{\ell\ell bb}$ resolution, the bb system's four-momentum components are scaled to match the assumed H boson mass and the $\ell\ell$ system's four-momentum components are scaled to match the Z boson mass. This procedure, performed after the event selection, improves the $m_{\ell\ell bb}$ resolution by a factor of two without significantly distorting the background distributions, resulting in an A boson mass resolution that is at best about 1% and up to 4% for gluon–gluon fusion, up to 10% for b-associated production in the $n_b = 2$ category and up to 16% for b-associated production in the $n_b \geq 3$ category, depending on the m_A and m_H values.

Despite the dedicated selection criteria against Z+jets and top-quark production, these background processes dominate the signal region: the Z+jets contribution is ~60–70% depending on the n_b category, while the top-quark contribution is ~30–35%. In the $n_b \geq 3$ category, other processes ($t\bar{t}V$, dibosons, Vh) contribute up to ~5% of the total background, while their contribution to the $n_b = 2$ category is less than 1%. The accurate determination of Z+jets and top-quark contributions is paramount for the sensitivity of this search. Their estimation employs a combination of data-driven corrections to simulated events.

The most abundant background in this channel is from Z+jets production. The normalisation of this process is constrained by a control region defined by inverting the m_{bb} window criterion for each H boson mass hypothesis (see also Table 2.1). The control regions are distinct for the $n_b = 2$ and $n_b \geq 3$ categories, since the accuracy of the background simulation depends on the number of b-jets present in the event. The modelling of the Z+jets simulated events is examined extensively in a number of kinematic variables, including the p_{T} of the Z boson ($p_{\mathrm{T}Z}$), the m_{bb} distribution and the $\sqrt{\Sigma p_{\mathrm{T}}^2}/m_{\ell\ell bb}$ distribution. The simulated distributions are compared against a control region that requires two jets with exactly one of them being a b-jet, as well as an early selection stage, before the m_{bb} window and $\sqrt{\Sigma p_{\mathrm{T}}^2}/m_{\ell\ell bb}$ requirements. For this early selection stage, it was verified that even those signals that were already excluded in Ref. [154] would be washed out by the background and would not bias the results. These regions are not used in the likelihood fit described in Section 2.8 and thus they are not included in Table 2.1. As a result of these studies, corrections to the distributions of $p_{\mathrm{T}Z}$, m_{bb} and $\sqrt{\Sigma p_{\mathrm{T}}^2}/m_{\ell\ell bb}$ in the simulated Z+jets events are applied. The corrections are found to be uncorrelated and they are applied sequentially. The most significant effect on the sensitivity of this search (see also Section 2.7) is due to the corrections to the modelling of the $p_{\mathrm{T}Z}$ distribution, which range from +5% to −10% for most of the Z+jets events. As an example, Figure 2.3 compares the $p_{\mathrm{T}Z}$ distributions in data with the background model after all corrections used in this search for events that satisfy all the requirements of the signal region with the exception of the m_{bb} window requirement, separately for $n_b = 2$ and $n_b \geq 3$ categories.

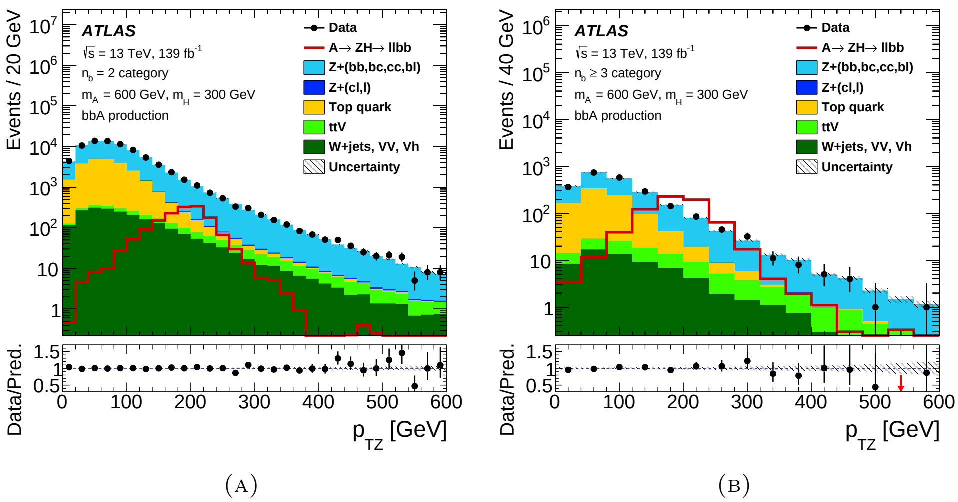

FIGURE 2.3: The $p_{\mathrm{T}Z}$ distributions for (a) the $n_b = 2$ and (b) the $n_b \geq 3$ category. The events are required to satisfy all the signal region criteria with the exception of the m_{bb} window requirement. The same conventions as in Figure 2.2 are used.

Top-quark production is heavily dominated by $t\bar{t}$ production in which both top quarks decay semileptonically. Therefore, it is possible to define a pure top-quark control region by keeping the same selection as discussed previously, apart from an opposite-flavour lepton criterion, i.e. an $e\mu$ pair is required instead of an ee or $\mu\mu$

pair (see also Table 2.1). This region is used for top-pair production normalisation, and also to check that kinematic distributions such as the top-quark p_{T} spectrum are adequately modelled in simulation. Different control regions are used in the $n_b = 2$ and $n_b \geq 3$ categories. This is because in the $n_b \geq 3$ category the top-quark background is dominated by top-quark pair production in association with jets, which is more difficult to model than the inclusive top-quark pair production that dominates the top-quark background in the $n_b = 2$ category. Finally, the m_{bb} window requirement is also applied to the top-quark control region, resulting in a separate control region for each m_H hypothesis tested in the search. Good agreement within uncertainties is observed between data and simulation in the shape of all variables considered.

Backgrounds from diboson, single top-quark, and SM Higgs boson production, as well as $t\bar{t}$ production in association with a vector boson are minor contributions to the total background composition. The shapes of their distributions are taken from simulation, whereas they are normalised using precise inclusive cross sections calculated from theory. The diboson samples are normalised using NNLO cross sections [225–228]. Single-top-quark production and top-quark-pair production in association with vector bosons are normalised to NLO cross sections from Refs. [229–231] and Ref. [169], respectively. The normalisation of SM Higgs boson production in association with a vector boson follows the recommendations of Ref. [174] using NNLO QCD and NLO electroweak corrections.

2.5.2 The $\ell\ell WW$ Final State

The decay $A \to ZH \to \ell\ell WW$ features a pair of electrons or muons and four jets from the hadronic W boson decays. The selected events are required to have at least four jets with the highest- and second-highest-p_{T} jets satisfying $p_{\mathrm{T}} > 40$ GeV and $p_{\mathrm{T}} > 30$ GeV, respectively. In addition, the lowest-p_{T} electrons or muons are required to have $p_{\mathrm{T}} > 15$ GeV.

The selection of the correct jet pairs in the reconstruction of the two W boson candidates is important for improving the signal resolution and suppressing backgrounds. For this task, all possible jet pairs that can be formed by considering up to the five highest-p_{T} jets in the event are taken into account. A set of requirements on kinematic variables, such as the angular distances between the jets within a pair, the jet transverse momenta and the reconstructed masses of the W, H and A boson candidates, is optimised to test the various combinations for compatibility with the signal hypothesis so that the signal efficiency and background rejection are maximised. This procedure results in a signal efficiency that ranges from 50% to 70% depending on m_A and m_H, whereas for background processes the efficiency is about 40%. The fraction of events in which the correct jet pairs are assigned to the W boson candidates after this procedure is in the range from 50% to 70%, depending on the m_A and m_H values.

The main background in this channel is from the production of a Z boson in association with jets. A criterion similar to that in the $\ell\ell bb$ channel is employed to discriminate against it: $\sqrt{\Sigma p_{\mathrm{T}}^2}/m_{2\ell 4q} > 0.3$, where $m_{2\ell 4q}$ is the six-body invariant mass of the two-lepton, four-jet system assigned to the A boson and the summation is performed over the p_{T}^2 of these objects. The distribution of this variable before the requirement is applied is shown in Figure 2.4.

Finally, the invariant mass of the four selected jets, m_{4q}, must be compatible with the assumed H boson mass. This is ensured by requiring m_{4q} to be within optimised

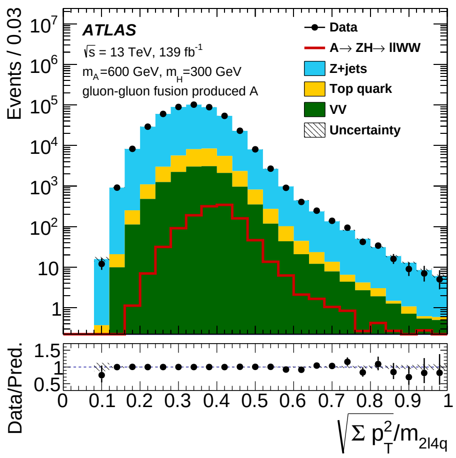

FIGURE 2.4: The $\sqrt{\Sigma p_{\mathrm{T}}^2}/m_{2\ell 4q}$ distribution shown before the requirement on this variable is applied. Corrections from a fit to the data are applied to the simulation, as described in Sections 2.5.2 and 2.8. The notation VV in the legend corresponds to the production of diboson events. The signal distribution for $(m_A, m_H) = (600, 300)$ GeV is also shown, and is normalised such that the production cross section times the branching ratios $B(A \to ZH)$ and $B(H \to WW)$ corresponds to 1 pb. The lower panel shows the ratio of the data to the background prediction (black filled circles) and the relative uncertainty, which includes both statistical and systematic components, in the background prediction (dashed area).

boundaries that depend on m_H: $m_H - 53$ GeV $< m_{4q} < 0.97 \cdot m_H + 54$ GeV. After this requirement the signal efficiency for A bosons decaying into ZH with $Z \to ee/\mu\mu/\tau\tau$ and $H \to WW \to qqqq$ is 6.5–11%, depending on the m_A and m_H values. The signal region selection is summarised in Table 2.2.

Single-electron or single-muon trigger Exactly 2 leptons (e or μ) ($p_{\mathrm{T}} > 15$ GeV) with the leading one having $p_{\mathrm{T}} > 30$ GeV Opposite electric charge for $\mu\mu$ pairs; 80 GeV $< m_{\ell\ell,\ e\mu} < 100$ GeV, $\ell = e,\ \mu$ At least 4 jets ($p_{\mathrm{T}} > 20$ GeV) with leading and second leading jets having $p_{\mathrm{T}} > 40,\ 30$ GeV Jets chosen with a dedicated discriminant $\sqrt{\Sigma p_{\mathrm{T}}^2}/m_{2\ell 4q} > 0.3$	
Signal region	ee or $\mu\mu$ pair $m_H - 53$ GeV $< m_{4q} < 0.97 \cdot m_H + 54$ GeV
Z+jets control region	ee or $\mu\mu$ pair $m_{4q} < m_H - 53$ GeV or $m_{4q} > 0.97 \cdot m_H + 54$ GeV
Top control region	$e\mu$ pair $m_H - 53$ GeV $< m_{4q} < 0.97 \cdot m_H + 54$ GeV

TABLE 2.2: Summary of the event selection for signal and control regions in the $A \to ZH \to \ell\ell WW$ channel.

The $m_{2\ell 4q}$ distribution after the m_{4q} requirement is the final discriminating variable, which is fitted to obtain the results of the search in this channel. To improve the $m_{2\ell 4q}$ resolution, the four-jet system's four-momentum components are scaled to match the assumed H boson mass and the $\ell\ell$ system's four-momentum components are scaled to match the Z boson mass. The final A boson mass resolution is in the range from 1% to 17% of m_A, depending on the m_A and m_H values.

The dominant backgrounds after the event selection are from Z+jets ($\sim$90% of total background), top-quark ($\sim$5%), and diboson ($\sim$5%) production. Smaller backgrounds (W+jets, $t\bar{t}h$, $t\bar{t}V$, and Vh) contribute less than 1% to the total background and are not included in the background composition.

The shape of the Z+jets background is taken from simulation combined with data-driven corrections, and the normalisation is constrained by the control region outside the m_{4q} mass window of each signal region (see Table 2.2), using a procedure similar to that in the $\ell\ell bb$ channel. To address shape differences between distributions of kinematic variables in data and simulated backgrounds, two corrections are applied to the p_{T} of the Z boson candidates and to the leading jet's p_{T}. Those corrections are derived from a control region orthogonal to the signal region, obtained by selecting $\sqrt{\Sigma p_{\mathrm{T}}^2}/m_{2\ell 4q} < 0.3$. This region is not used subsequently in the likelihood fit described in Section 2.8 and therefore it is not included in Table 2.2. The corrections are found to be uncorrelated and they are applied sequentially. The correction to the $p_{\mathrm{T}Z}$ distribution in the simulation is as large as 20% at low $p_{\mathrm{T}Z}$ values and it becomes smaller as $p_{\mathrm{T}Z}$ increases, whereas the correction to the leading jet's p_{T} does not exceed $\pm$10%. The distributions of the p_{T} of the Z boson candidates and of the leading jet's p_{T}, after the reweighting, are shown in Figure 2.5 for events satisfying all requirements for the signal region with the exception of the m_{4q} window cut.

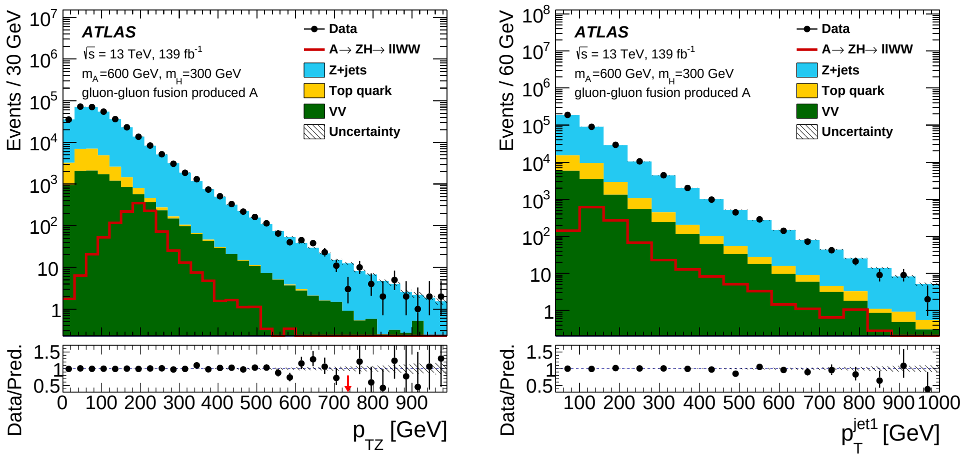

(A) (B)

FIGURE 2.5: The distributions of (a) the p_{T} of the Z boson candidates and (b) the leading jet's p_{T} in the $\ell\ell WW$ channel. The events are required to satisfy all the signal region criteria with the exception of the m_{4q} window requirement. Data-driven corrections are applied, as described in the text. The same conventions as in Figure 2.4 are used.

The top-quark background shape is taken from simulated events. The normalisation is constrained using a high-purity control region defined by keeping the same selection as for the signal region, but replacing the electron or muon pairs by opposite-flavour leptons ($e\mu$ pairs), as indicated in Table 2.2. The single-top-quark, Z+jets and diboson production contributions in this control region are estimated from simulation.

The diboson background shape and normalisation are taken from the simulated samples, using the same cross-section calculation as in the $\ell\ell bb$ channel.

2.6 Signal Modelling

This analysis searches for two new particles, with their mass hypotheses considered in the two-dimensional space m_A–m_H, with good mass resolution of the A and H reconstructed final states. The investigation of the relevant phase space requires a large number of signal mass hypotheses to be tested. In addition, various new physics scenarios which are of interest for this search, like the 2HDM, include A bosons with natural widths comparable to, or larger than, the experimental mass resolution for large parts of the parameter space in which this search has sensitivity. The H bosons are considered to always have negligible natural width, in accordance with the 2HDM scenarios used to interpret this search (see Section 2.8). For these reasons, the $m_{\ell\ell bb}$ and $m_{2\ell 4q}$ distributions can be simulated only for some (m_A, m_H) points and an interpolation using analytic functions is employed for the rest, following a procedure similar to that used in Ref. [154].

In the cases where the natural widths of both the A and H bosons are much smaller than the experimental mass resolution, the modelling of the mass distributions uses two types of parametric functions. First, an *ExpGaussExp* (EGE) function [154, 232] provides a good description of gluon–gluon fusion production of A bosons in the $n_b = 2$ category of the $\ell\ell bb$ channel. Second, a double-Gaussian Crystal Ball (DSCB) function [154, 233] gives a good description of gluon–gluon fusion production in the $\ell\ell WW$ channel and b-associated production in both the $n_b = 2$ and $n_b \geq 3$ categories of the $\ell\ell bb$ channel.

Both the EGE and DSCB functions have a Gaussian core but they differ in the way the tails are treated. The tails of the EGE function are exponential, described by two parameters, whereas DSCB has power-law tails described by four extra parameters. The values of the function parameters are extracted from unbinned maximum-likelihood fits to the simulated $m_{\ell\ell bb}$ and $m_{2\ell 4q}$ distributions. Polynomial functions are used to interpolate the parameters to mass points that were not simulated. These interpolated parametric functions are used to model the signal mass shapes for all the signal assumptions considered in this search. The fit uncertainties of the DSCB and EGE function parameters, as well as the parameters of the polynomial functions used for the interpolation, are used to derive a shape uncertainty for each of the interpolated distributions.

A typical example of the result of the signal parameterisation is shown in Figure 2.6 for the $(m_A, m_H) = (500, 300)$ GeV mass point. The figure shows a comparison of the simulated mass distribution and the interpolated parametric function, as well as the shape variation that is taken as an estimate of the systematic uncertainty from the procedure. In general, the cores of the $m_{\ell\ell bb}$ and $m_{2\ell 4q}$ distributions are well-parameterised by the chosen functional forms. There are some small differences between the function description and the simulated distribution in the tails of the distributions, but those have negligible effects on the final results and they are covered by interpolation uncertainties.

The parameterisation procedure described in the previous paragraph is modified to allow for cases where the width of the A boson is comparable to, or larger than, the

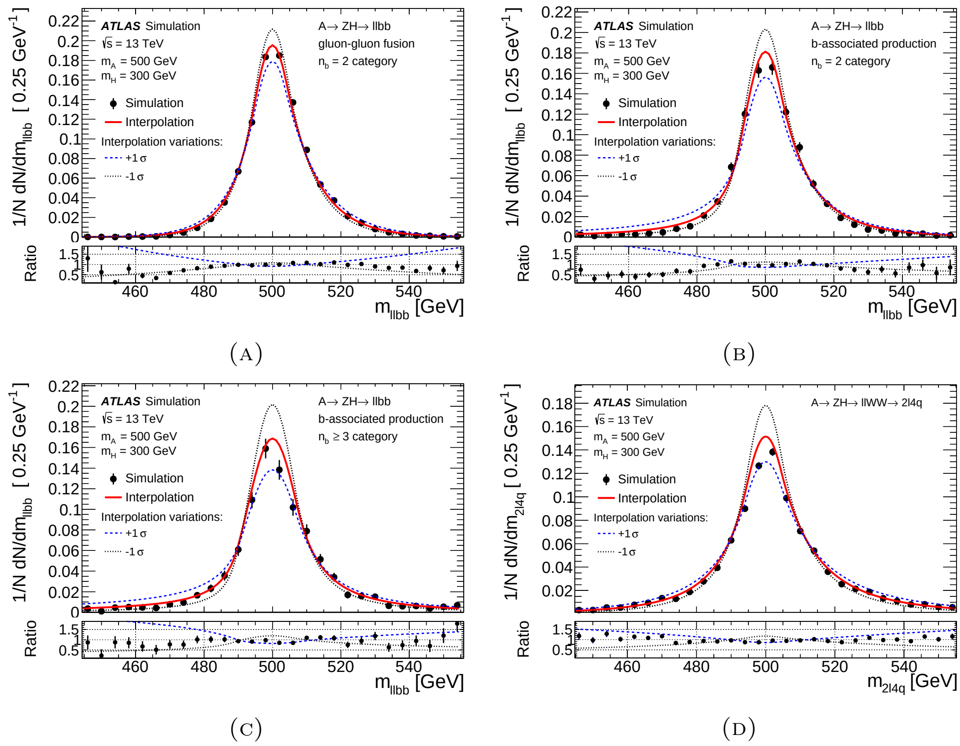

FIGURE 2.6: Signal $m_{\ell\ell bb}$ or $m_{2\ell 4q}$ distributions assuming $m_A = 500$ GeV and $m_H = 300$ GeV for the following cases: $\ell\ell bb$ channel: (a) gluon–gluon fusion in the $n_b = 2$ category, (b) b-associated production in the $n_b = 2$ category, and (c) b-associated production in the $n_b \geq 3$ category; (d) $\ell\ell WW$ channel. In the upper panels, the black filled circles correspond to the simulated distributions, which are compared against the interpolated parameterised signal distributions shown as solid red curves. Also in the same panels, the shape variations of the interpolated parameterised signal distributions are shown in dotted blue ($+1\sigma$) and black (-1σ) lines. In the lower panels, the black filled circles correspond to the ratio of the simulation to the interpolated parameterised curve. The dotted blue (black) line corresponds to the ratio of the $+1\sigma$ (-1σ) shape variation of the interpolated curve to the interpolated curve.

experimental mass resolution. This can be modelled by convolving a modified Breit–Wigner distribution[4] with the EGE or DSCB function. This procedure is valid as long as the width of the H boson remains narrow relative to the experimental resolution, which is the case for the 2HDM scenarios considered in Section 2.8. Widths of up to approximately 20% of the A boson mass are considered, which is the range relevant to the sensitive parameter space of the 2HDM scenarios that are of interest for this search.

Finally, the signal efficiencies for the interpolated mass points are obtained through separate two-dimensional interpolations on the (m_A, m_H) plane using thin-plate splines [234].

2.7 Systematic Uncertainties

Several sources of systematic uncertainty in the signal and background estimates are considered, including experimental and theoretical sources. Experimental uncertainties comprise those in the luminosity measurement [235] (obtained using the LUCID-2 detector [164]), trigger, object identification, energy/momentum scale and resolution as well as underlying-event and pile-up modelling [209, 213, 214, 218]. These uncertainties impact the simulations of signal and background processes.

The signal and background modelling have associated theoretical uncertainties. For the signal modelling, the uncertainties due to the factorisation and renormalisation scale choice, the initial- and final-state radiation treatment and the PDF choice are considered. No additional signal modelling uncertainties related to model-specific cross-section predictions, such as the 2HDM predictions used in Section 2.8, are considered. The renormalisation and factorisation scales are varied up and down separately by a factor of two, and the largest deviation from the nominal signal is taken as the estimated uncertainty. The uncertainties due to initial- and final-state radiation as well as the multiple parton interaction modelling are estimated using a subset of A14 tuning variations [171]. PDF uncertainties are computed using the prescription from PDF4LHC15 [199], which include the envelope of three PDF sets, namely `CT14`, `MMHT2014` and `NNPDF3.0`.

Additional systematic uncertainties are assigned to cover the differences in signal efficiencies and $m_{\ell\ell bb}$ and $m_{\ell\ell WW}$ resolution differences between the interpolations and the simulations, as shown by the dotted blue and black lines in the lower panels of Figure 2.6.

For the background modelling, the most important sources of systematic uncertainty are the modelling of shapes of several kinematic distributions of Z+jets events. In the $\ell\ell bb$ channel, they arise from the shape corrections for the $p_{\mathrm{T}Z}$, $\sqrt{\Sigma p_{\mathrm{T}}^2}/m_{\ell\ell bb}$ and m_{bb} variables described in Section 2.5.1. An uncertainty is estimated by comparing the corrections and the agreement between the background prediction and the data for various variables and among various control regions. For each of the corrections, the applied uncertainty is half the size of the correction in the $n_b = 2$ category, and the full size of the correction in the $n_b \geq 3$ category. In the $\ell\ell WW$ channel, the uncertainties are due to the shapes of the $p_{\mathrm{T}Z}$ and leading-jet p_{T} distributions (Section 2.5.2). The uncertainty is estimated similarly to that in the $\ell\ell bb$ channel and

[4]The modification is the multiplication of the Breit–Wigner distribution with a log-normal distribution to account for the distortion due to the event selection.

is half the size of the correction. For other background processes, modelling uncertainties are obtained by varying the factorisation and renormalisation scales, and the amount of initial- and final-state radiation.

The effect of these systematic uncertainties on the search is studied using a signal-strength parameter μ for hypothesised signal production (see also Section 2.8). The uncertainties found to have the largest impact depend on the choice of (m_A, m_H) signal point. Table 2.3 shows the relative uncertainties in the μ value from the leading sources of systematic uncertainty for two example mass points of gluon–gluon fusion and b-associated production for the $\ell\ell bb$ channel. The uncertainties are evaluated using an Asimov dataset [236] generated with the signal cross section set to the expected limits for the particular (m_A, m_H) signal point, considering a narrow-width A boson. Table 2.4 shows the same information for the $\ell\ell WW$ channel. The leading sources of systematic uncertainty are similar for other mass points studied and for larger A boson widths.

For the $\ell\ell bb$ channel, the most relevant sources of systematic uncertainty are the background modelling, the signal interpolation, and the jet energy scale and resolution. The limited size of the simulated samples has a higher impact at low masses, since at higher masses other sources are more dominant. Other systematic uncertainties with non-negligible impact include those associated with b-tagging and theoretical errors. In the $\ell\ell WW$ channel, the most relevant systematic uncertainties are those related to the jet energy scale and resolution, as expected in a channel with four jets in the final state. The limited size of the simulated samples, the background modelling and the signal interpolation also have a non-negligible impact on the signal-strength parameter. In both channels, the data statistical uncertainties have lower impact at low masses compared to the systematic uncertainties. In addition, the search sensitivity is affected at high masses by the limited size of the data sample, an effect which is more pronounced in the $\ell\ell bb$ channel.

$A \to ZH \to \ell\ell bb$							
Gluon–gluon fusion production				b-associated production			
$(230, 130)$ GeV, 0.31 pb		$(700, 200)$ GeV, 0.017 pb		$(230, 130)$ GeV, 0.16 pb		$(700, 200)$ GeV, 0.018 pb	
Source	$\Delta\mu/\mu$ [%]	Source	$\Delta\mu/\mu$ [%]	Source	$\Delta\mu/\mu$ [%]	Source	$\Delta\mu/\mu$ [%]
Data stat.	28	Data stat.	45	Data stat.	33	Data stat.	46
Total syst.	36	Total syst.	26	Total syst.	33	Total syst.	25
Sim. stat.	19	Sim. stat.	7.2	Sim. stat.	18	Sim. stat.	7.2
Sig. interp.	9.9	Sig. interp.	8.7	Sig. interp.	13	Sig. interp	13
Bkg. model.	19	Bkg. model.	18	Bkg. model.	15	Bkg. model.	16
JES/JER	20	JES/JER	18	JES/JER	14	JES/JER	16
b-tagging	7.5	b-tagging	12	b-tagging	9.5	b-tagging	12
Theory	7.4	Theory	9.5	Theory	5.0	Theory	7.1

TABLE 2.3: The effect of the most important sources of uncertainty on the signal-strength parameter at two example mass points of $(m_A, m_H) = (230, 130)$ GeV and $(m_A, m_H) = (700, 200)$ GeV in the $\ell\ell bb$ channel, for both gluon–gluon fusion and b-associated production of a narrow-width A boson. The signal cross sections are taken to be the expected median upper limits (see Section 2.8) and they correspond to values that are shown next to the indicated mass points. JES and JER stand for jet energy scale and jet energy resolution, 'Sim. stat.' for simulation statistics, 'Sig. interp.' for signal interpolation, and 'Bkg. model.' for the background modelling. 'Theory' refers to theoretical uncertainties in the signal samples due to the PDF choice, factorisation and renormalisation scales, and initial- and final-state radiation.

$A \to ZH \to \ell\ell WW$			
Gluon–gluon fusion production			
(500, 300) GeV, 0.70 pb		(700, 200) GeV, 0.38 pb	
Source	$\Delta\mu/\mu$ [%]	Source	$\Delta\mu/\mu$ [%]
Data stat.	32	Data stat.	33
Total syst.	42	Total stat.	38
Sim. stat.	24	Sim. stat.	19
Sig. interp.	14	Sig. interp.	12
Bkg. model.	14	Bkg. model.	16
JES/JER	30	JES/JER	23
Theory	6.5	Theory	7.6

Table 2.4: The effect of the most important sources of uncertainty on the signal-strength parameter at two example mass points of $(m_A, m_H) = (500, 300)$ GeV and $(m_A, m_H) = (700, 200)$ GeV in the $\ell\ell WW$ channel for gluon–gluon fusion production of a narrow-width A boson. The same notation as in Table 2.3 is used.

2.8 Results

The $m_{\ell\ell bb}$ and $m_{2\ell 4q}$ distributions are expected to exhibit a resonant structure if signal events are present, while background events result in a smoothly falling spectrum. Therefore, those are chosen as the final variables to discriminate between signal and background. The shape differences between the signal and background contributions in the $m_{\ell\ell bb}$ and $m_{2\ell 4q}$ distributions are exploited through binned maximum-likelihood fits of the signal-plus-background hypotheses to extract potential signal contributions. The fits are based on the statistical framework described in Refs. [236–238]. For a given mass hypothesis of (m_A, m_H), the likelihood is constructed as the product of Poisson probabilities for event yields in the $m_{\ell\ell bb}$ or $m_{2\ell 4q}$ bins:

$$L(\mu, \vec{\alpha}, \vec{\theta}|m_A, m_H) = \prod_{i=\text{bins}} \text{Poisson}\left(N_i \middle| \left(\mu \times S_i(m_A, m_H, \vec{\theta}) + B_i(\vec{\alpha}, \vec{\theta})\right)\right) \cdot G(\vec{\theta}) ,$$

where N_i is the number of observed events, and $S_i(m_A, m_H, \vec{\theta})$ and $B_i(\vec{\alpha}, \vec{\theta})$ are the expected number of signal events and estimated number of background events in bin i. The vector $\vec{\alpha}$ represents free background normalisation scale factors (described later) and the vector $\vec{\theta}$ denotes all non-explicitly listed parameters of the likelihood function such as nuisance parameters associated with systematic uncertainties. Systematic uncertainties are incorporated in the likelihood as nuisance parameters with either Gaussian or log-normal constraint terms, denoted by $G(\vec{\theta})$ in the formula above. The parameter of interest, μ, is a multiplicative factor applied to the expected signal rate. The $m_{\ell\ell bb}$ and $m_{2\ell 4q}$ bin widths are chosen according to the expected detector resolution and taking into account the statistical uncertainty in the number of simulated background events. The bin centres are adjusted such that at least 65% of the test signal is contained in one bin.

For each bin, S_i is calculated from the total integrated luminosity, the assumed cross section times branching ratio for the signal and its selection efficiency. The sum of all background contributions in the bin, B_i, is estimated from simulation, which includes the modelling corrections discussed in Sections 2.5.1 and 2.5.2. The number of events in the $t\bar{t}$ and Z+jets control regions is included in the likelihood calculation to constrain their normalisation in the signal regions. This is achieved by introducing two free normalisation scale factors per channel, represented by $\vec{\alpha}$ in the likelihood description earlier in this section. In the $\ell\ell bb$ channel these scale factors apply to the $t\bar{t}$ contribution and the heavy-flavour component of the Z+jets contribution, whereas the rest of the contributions in the control region are estimated from simulation. In the $\ell\ell WW$ channel the scale factors apply to the $t\bar{t}$ contribution and the flavour-inclusive Z+jets contribution. Typical values of the scale factors are close to unity with the exception of Z+jets in the $\ell\ell bb$ channel, which is scaled by a factor of 1.2, and $t\bar{t}$ in the $\ell\ell bb$ $n_b \geq 3$ category, which is typically scaled by a factor of 1.4.

The signals that are fitted in each category are motivated by signal efficiency considerations and the interpretation of the search in the context of the 2HDM. In the $\ell\ell bb$ channel the following fits are performed. First, A bosons produced by gluon–gluon fusion are considered in the $n_b = 2$ category. Second, a combined fit for the b-associated production mechanism in both the $n_b = 2$ and $n_b \geq 3$ categories is performed. Finally, there is a combination of the b-associated production fit with the gluon–gluon fusion fit, which is interpreted in the context of the 2HDM. In the $\ell\ell WW$ channel, only A bosons produced by gluon–gluon fusion are considered and, hence, it is the only fit that is considered.

2.8.1 $A \to ZH \to \ell\ell bb$ Results

The $m_{\ell\ell bb}$ distributions from different m_{bb} mass windows are scanned for potential excesses beyond the background expectations through signal-plus-background fits. The scan is performed in steps of 10 GeV for both the m_A range 230–800 GeV and the m_H range 130–700 GeV, such that $m_A - m_H \geq 100$ GeV. The step sizes are chosen to be compatible with the detector resolution for $m_{\ell\ell bb}$ and m_{bb}. In total, there are 58 m_{bb} windows that are probed for the $n_b = 2$ and $n_b \geq 3$ categories. The overall number of (m_A, m_H) signal hypotheses that are tested is 1711 per category.

Figure 2.7 shows the distribution of the H boson candidate mass m_{bb} before the m_{bb} window requirement in each of the two categories. Typical examples of $m_{\ell\ell bb}$ distributions after the application of the m_{bb} window requirement are shown in Figures 2.8a–2.8d. In particular, the m_{bb} window defined for $m_H = 300$ GeV is shown in Figures 2.8a and 2.8b for the $n_b = 2$ and $n_b \geq 3$ categories, respectively. On the same figures, a signal distribution is shown as well, which corresponds to gluon–gluon fusion production in Figure 2.8a and b-associated production in Figure 2.8b, for the $(m_A, m_H) = (600, 300)$ GeV signal point. Similarly, an m_{bb} window defined for $m_H = 500$ GeV is shown Figures 2.8c and 2.8d for the $n_b = 2$ and $n_b \geq 3$ categories, respectively. The signal distribution for the $(m_A, m_H) = (670, 500)$ GeV signal point is also shown for gluon–gluon fusion production in Figure 2.8c and b-associated production in Figure 2.8d.

In all cases, the data are found to be well described by the background model. The most significant excess for the gluon–gluon fusion production signal assumption is at the $(m_A, m_H) = (610, 290)$ GeV signal point, for which the local (global) significance [239] is 3.1 (1.3) standard deviations. For b-associated production, the most significant excess is at the $(m_A, m_H) = (440, 220)$ GeV signal point, for which the local (global) significance is 3.1 (1.3) standard deviations. The significances are calculated for each production process separately, ignoring the contribution from the other.

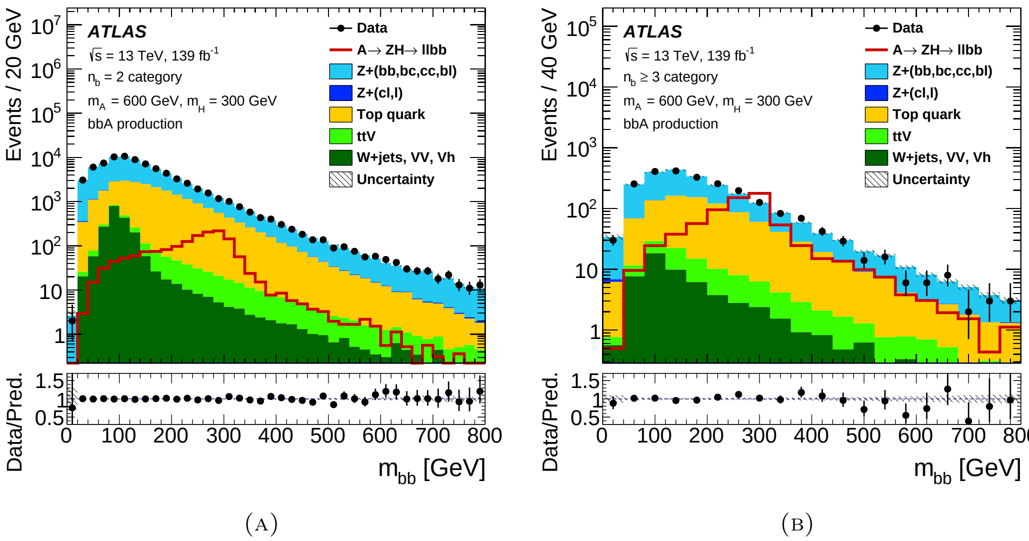

FIGURE 2.7: The m_{bb} distribution before any m_{bb} window cuts for the (a) $n_b = 2$ and (b) $n_b \geq 3$ categories. The signal distribution for $(m_A,\, m_H) = (600,\, 300)$ GeV is also shown, and is normalised such that the production cross section times the branching ratios $B(A \to ZH)$ and $B(H \to bb)$ corresponds to 1 pb. The same conventions as in Figure 2.2 are used.

In the absence of any statistically significant excess, the results of the search in this channel are interpreted as upper limits on the production cross section of an A boson decaying into ZH followed by the $H \to bb$ decay, $\sigma \times B(A \to ZH) \times B(H \to bb)$. The cross-section upper limits consider A bosons that are produced only by a single mechanism, i.e. either gluon–gluon fusion or b-associated production. Modified frequentist [240] 95% confidence level (CL) upper limits on the production cross section of this process are obtained using the asymptotic approximation [236] for the various signal hypotheses that are tested. In particular, expected and observed upper limits for gluon–gluon fusion production of narrow-width A bosons in the $n_b = 2$ category are shown in Figures 2.9a and 2.9b, respectively. For b-associated production of narrow-width A bosons, the expected and observed limits for the combination of the $n_b = 2$ and $n_b \geq 3$ categories are shown in Figures 2.9c and 2.9d, respectively. The upper limits for gluon–gluon fusion vary from 6.2 fb for $(m_A, m_H) = (780, 129)$ GeV to 380 fb for $(m_A, m_H) = (250, 150)$ GeV. This is to be compared with the corresponding expected limits of 15 fb and 240 fb for these two signal hypotheses. For b-associated production the upper limit varies from 6.8 fb for $(m_A, m_H) = (760, 220)$ GeV to 210 fb for $(m_A, m_H) = (230, 130)$ GeV, whereas the corresponding expected limits are 15 fb and 160 fb.

Upper limits are also calculated for signal assumptions where the natural width of the A boson is large in comparison with the experimental mass resolution, which is needed for the interpretation of the search in the context of the 2HDM. The cross-section upper limit decreases as the natural width of the A boson increases. In particular, a gluon–gluon produced A boson with a natural width of 10% of its mass has a cross-section upper limit that is reduced on average by a factor of approximately 3 from the narrow-width case. This factor becomes approximately 4 when the natural

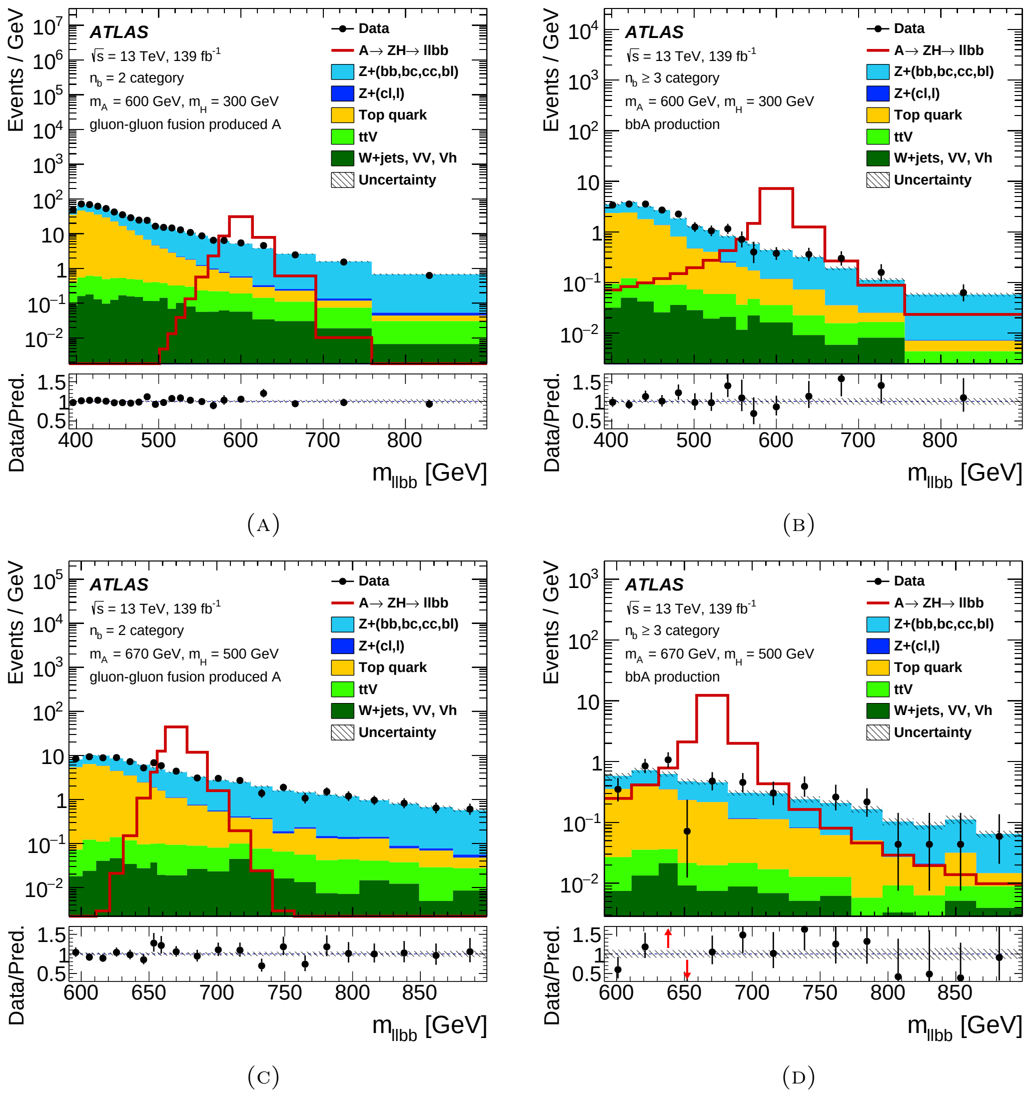

FIGURE 2.8: The $m_{\ell\ell bb}$ mass distribution for the m_{bb} windows defined for $m_H =$ 300 GeV and $m_H = 500$ GeV for (a, c) the $n_b = 2$ and (b, d) the $n_b \geq 3$ category, respectively. Signal distributions with $(m_A, m_H) = (600, 300)$ GeV and $(m_A, m_H) =$ $(670, 500)$ GeV are also shown for gluon–gluon fusion production in (a, c) and b-associated production in (b, d). The number of entries shown in each bin is the number of events in that bin divided by the width of the bin. The same conventions as in Figure 2.2 are used.

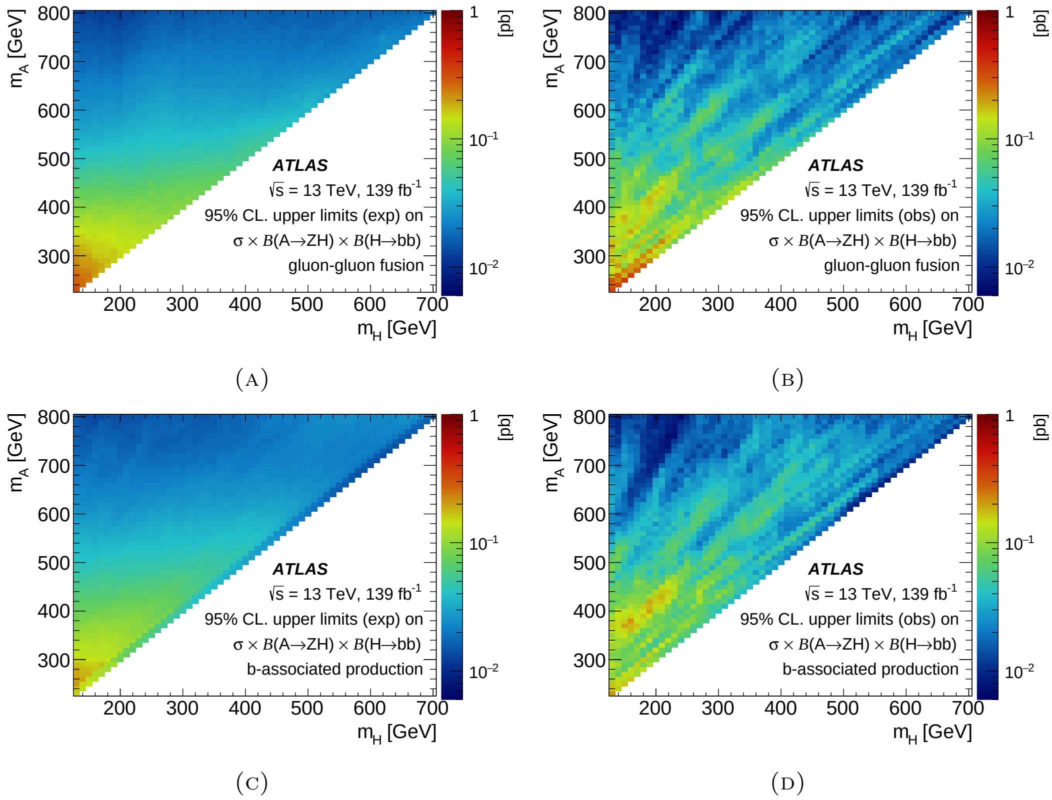

FIGURE 2.9: Upper bounds at 95% CL on the production cross section times the branching ratio $B(A \to ZH) \times B(H \to bb)$ in pb for (a, b) gluon–gluon fusion and (c, d) b-associated production. The expected upper limits are shown in (a) and (c) and the observed upper limits are shown in (b) and (d).

width increases to 20%. The A bosons from b-associated production have worse experimental mass resolution and the deterioration of the limit is on average smaller: the upper limits are reduced by a factor of about 1.9 (2.3) for a natural width of 10% (20%).

The results for A boson natural widths that are comparable to, or larger than, the experimental mass resolution are used for the interpretation of the search in the context of the CP-conserving 2HDM. The 2HDM benchmark against which the search results are compared has three free parameters: m_A, m_H and $\tan\beta$. In addition, there are four ways to assign the Yukawa couplings to fermions, defining type-I, type-II, lepton-specific and flipped 2HDMs. The remaining parameters are fixed. The mass of the lightest Higgs boson in the model is fixed to 125 GeV and its couplings are set to be the same as those of the SM Higgs boson by choosing $\cos(\beta - \alpha) = 0$ [137], which is known as the 2HDM weak decoupling limit. The charged Higgs boson is assumed to have the same mass as the A boson and the potential parameter m_{12}^2 [35] is fixed to $m_A^2 \tan\beta/(1 + \tan^2\beta)$.

The cross sections for A boson production in the 2HDM are calculated using corrections at up to NNLO in QCD for gluon–gluon fusion and b-associated production in the five-flavour scheme as implemented in SusHi [47, 49, 50, 53]. For b-associated production a cross section in the four-flavour scheme is also calculated as described in Refs. [241, 242] and the results are combined with the five-flavour scheme calculation

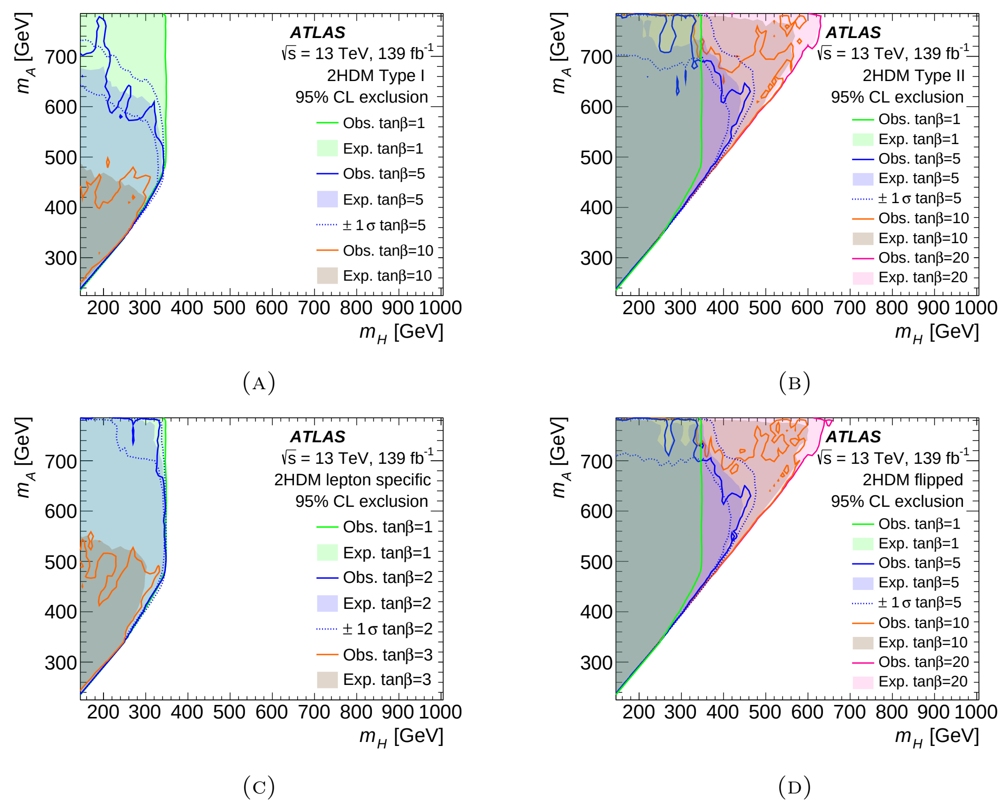

FIGURE 2.10: Observed and expected 95% CL exclusion regions for the $\ell\ell bb$ channel in the (m_H, m_A) plane for various $\tan\beta$ values for the (a) type-I, (b) type-II, (c) lepton-specific and (d) flipped 2HDM, with $\cos(\beta-\alpha)=0$.

following Ref. [243]. The Higgs boson widths and branching ratios are calculated using 2HDMC [244]. The procedure for the calculation of the cross sections and branching ratios, as well as for the choice of 2HDM parameters, follows Ref. [174].

The interpretation of the search in the 2HDM is performed in the (m_H, m_A) plane, as shown in Figure 2.10. In this plot, colour-shaded areas indicate expected and observed exclusions for various $\tan\beta$ values. There is one plot for each of the four 2HDM types. For the type-I and lepton-specific 2HDMs, only gluon–gluon fusion production is relevant. The exclusion region reaches $m_H \lesssim 350$ GeV for $\tan\beta = 1$ and the sensitivity decreases for larger $\tan\beta$ values. In type-I 2HDM for instance, for $\tan\beta = 10$ the exclusion reaches $m_H \lesssim 320$ GeV and $m_A \lesssim 500$ GeV. The limiting value at $m_H \simeq 350$ GeV is due to the drop of the $H \to bb$ branching ratio, which competes with $H \to t\bar{t}$ at larger m_H values. The type-II and flipped 2HDMs are dominated by A bosons from b-associated production as $\tan\beta$ increases, although gluon–gluon fusion is still important for $\tan\beta \approx 1$. Like the type-I and lepton-specific 2HDMs, the type-II and flipped 2HDMs provide similar constraints because they only differ in the lepton Yukawa couplings. The contribution from b-associated signal production increases the sensitivity at large $\tan\beta$ values, excluding $m_H \lesssim 650$ GeV for $\tan\beta = 20$. The search sensitivity deteriorates at lower $\tan\beta$ values, excluding $m_H \lesssim 350$ GeV for $\tan\beta = 1$.

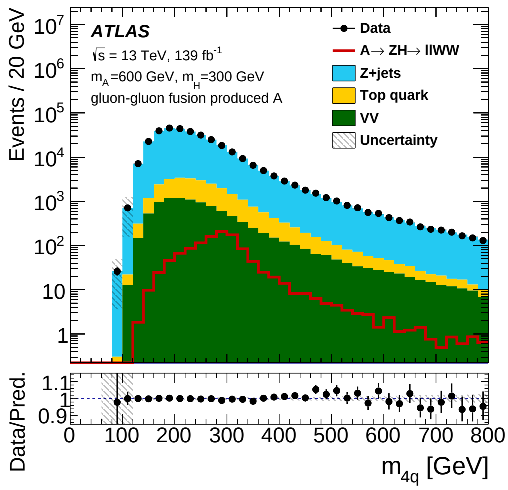

FIGURE 2.11: The m_{4q} distribution before any m_{4q} window cuts. The same conventions as in Figure 2.4 are used.

2.8.2 $A \to ZH \to \ell\ell WW$ Results

The $m_{2\ell 4q}$ distributions from different m_{4q} mass windows are scanned for possible excesses using a procedure similar to the one in the $\ell\ell bb$ channel. The scan is performed in steps of 10 GeV for both the m_A range 300–800 GeV and the m_H range 200–700 GeV, such that $m_A - m_H \geq 100$ GeV. This gives in total 51 m_{4q} mass windows and the overall number of (m_A, m_H) signal hypotheses that are tested is 1326.

Figure 2.11 shows the distribution of the H boson candidate mass m_{4q} before the m_{4q} window requirement. Typical examples of $m_{2\ell 4q}$ distributions after the application of the m_{4q} window requirement are shown in Figures 2.12a and 2.12b, referring to m_{4q} windows defined for $m_H = 300$ GeV and $m_H = 500$ GeV, respectively. Signal distributions corresponding to the $(m_A, m_H) = (600, 300)$ GeV signal point for Figure 2.12a and the $(m_A, m_H) = (670, 500)$ GeV signal point for Figure 2.12b are also shown.

In all cases, the data are found to be well described by the background model. The most significant excess is at the $(m_A, m_H) = (440, 310)$ GeV signal point, for which the local (global) significance is 2.9 (0.82) standard deviations.

Using the same method as for the $\ell\ell bb$ channel, constraints on the production of $A \to ZH$ followed by $H \to WW$ decay are derived. The 95% CL upper limits are shown in Figure 2.13 for a narrow-width A boson produced via gluon–gluon fusion. The upper limit varies from 0.023 pb for the $(m_A, m_H) = (770, 660)$ GeV signal point to 8.9 pb for the $(m_A, m_H) = (340, 220)$ GeV signal point. This is to be compared with the corresponding expected limits of 0.041 pb and 3.6 pb for these two signal points. The upper limits deteriorate when the natural width of the A boson is comparable to, or larger than, the experimental mass resolution. In particular, for a natural width that is 10% of m_A the upper limits decrease on average by a factor of 3. This factor becomes approximately 5 when the natural width increases to 20%.

The sensitivity of the $\ell\ell WW$ channel in the context of the CP-conserving 2HDM was examined. The same 2HDM calculations as in the $\ell\ell bb$ channel are used and the only differences are related to the parameter space of the model that is probed. In

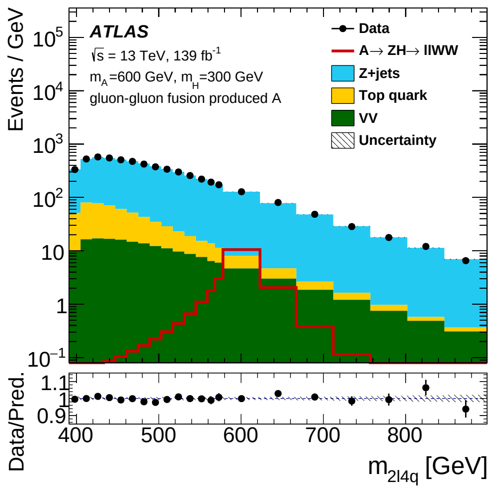

(A)

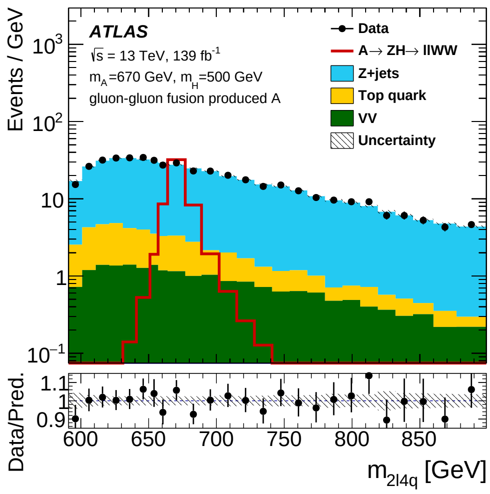

(B)

FIGURE 2.12: The $m_{2\ell 4q}$ mass distribution for the m_{4q} windows defined for (a) $m_H = 300$ GeV and (b) $m_H = 500$ GeV. Signal distributions are also shown with $(m_A, m_H) = (600, 300)$ GeV and $(m_A, m_H) = (670, 500)$ GeV. The number of entries shown in each bin is the number of events in that bin divided by the width of the bin. The same conventions as in Figure 2.4 are used.

particular, because only A bosons produced by gluon–gluon fusion are studied in this search, only type-I and lepton-specific 2HDMs are considered. In addition, the partial width $\Gamma(H \to WW)$ vanishes when $\cos(\beta-\alpha) = 0$ and is maximal at $|\cos(\beta-\alpha)| = 1$, whereas for the partial width $\Gamma(A \to ZH)$ the opposite is true, i.e. it vanishes when $|\cos(\beta-\alpha)| = 1$ and it is maximal when $\cos(\beta-\alpha) = 0$. These observations imply that this channel should be most sensitive between these two extreme values of $|\cos(\beta-\alpha)|$.

The interpretation of the observed and expected upper limits on the cross section times branching ratio in the context of the type-I and lepton-specific 2HDM scenarios show that the $\ell\ell WW$ channel has little sensitivity in regions that are not already excluded by the 125 GeV Higgs boson coupling measurements [126], an analysis that also provides similar limits in this parameter space. In particular, for the m_A range considered in this channel, there is sensitivity up to $m_H < 250$ GeV and for $\tan\beta < 4$. Some examples of 95% CL excluded regions in the plane defined by m_A and $\cos(\beta-\alpha)$ for $m_H = 200$ GeV and $m_H = 240$ GeV are shown in Figure 2.14 for the type-I 2HDM. The results are very similar for the lepton-specific 2HDM, since the only difference between the two 2HDM types is the lepton Yukawa couplings, which only affect the total width.

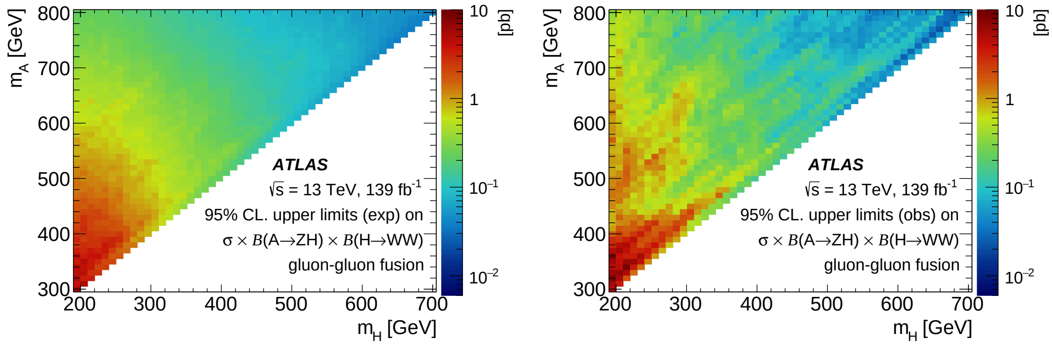

(A) (B)

FIGURE 2.13: Expected (a) and observed (b) upper bounds at 95% CL on the production cross section times the branching ratio $B(A \to ZH) \times B(H \to WW)$ in pb.

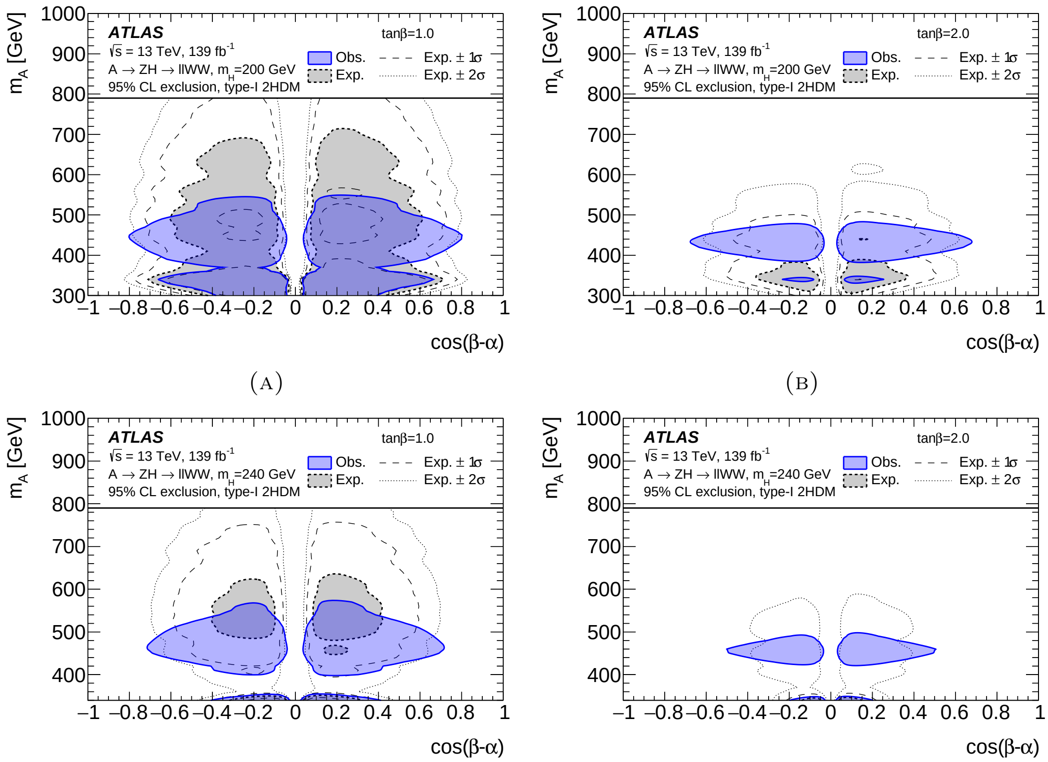

(A) (B) (C) (D)

FIGURE 2.14: Observed and expected 95% CL exclusion regions in the ($\cos(\beta-\alpha)$, m_A) plane for various $\tan\beta$ values for (a,b) $m_H = 200$ GeV and (c,d) $m_H = 240$ GeV in the context of type-I 2HDM for the $\ell\ell WW$ channel.

2.9 Conclusion

Data recorded by the ATLAS experiment at the LHC, corresponding to an integrated luminosity of 139 fb^{-1} from proton–proton collisions at a centre-of-mass energy 13 TeV, are used to search for a heavy Higgs boson, A, decaying into ZH, where H denotes another heavy Higgs boson with mass $m_H > 125$ GeV. Two final states were considered, where the H boson decays into a pair of b-quarks or W bosons, and in both cases the Z boson decays into a pair of electrons or muons. In the $\ell\ell bb$ channel, the A boson is assumed to be produced via either gluon–gluon fusion or b-associated production. In the $\ell\ell WW$ channel, only gluon–gluon fusion production is considered. No significant deviation from the SM background predictions is observed in the $ZH \to \ell\ell bb$ and $ZH \to \ell\ell WW \to \ell\ell qqqq$ final states that are considered in this search. Considering each channel and each production process separately, upper limits are set at the 95% confidence level for $\sigma \times B(A \to ZH) \times B(H \to bb$ or $H \to WW)$. For $\ell\ell bb$, upper limits are set in the range 6.2–380 fb for gluon–gluon fusion and 6.8–210 fb for b-associated production of a narrow A boson in the mass range 230–800 GeV, assuming the H boson is in the mass range 130–700 GeV. For $\ell\ell WW$, the observed upper limits are in the range 0.023–8.9 pb for gluon–gluon fusion production of a narrow A boson in the mass range 300–800 GeV, assuming the H boson is in the mass range 200–700 GeV. Taking into account both production processes, the $\ell\ell bb$ search tightens the constraints on the 2HDM scenario in the case of large mass splittings between its heavier neutral Higgs bosons. The $\ell\ell WW$ channel has not been explored previously at the LHC, and this search explicitly demonstrates its potential to constrain 2HDM parameters away from the weak decoupling limit.

Chapter 3

Phase Transitions in the Early Universe

3.1 Cosmological Bubble Friction in Local Equilibrium

The hot plasma in the early universe may have gone through different phase transitions which contributed to forge the properties of the world around us. Classical examples are the phase transition in QCD and, if the temperature at early times was large enough, the electroweak phase transition. Though both of the former are of the crossover type in the SM [245, 246], first–order phase transitions remain an intriguing possibility which can be realized in SM extensions. Such transitions, which proceed through the nucleation and subsequent expansion of bubbles of the thermodynamically preferred phase, are particularly interesting due to the enhanced deviations from equilibrium during the transition. The loss of spatial homogeneity and isotropy due to the colliding bubble walls can source a stochastic background of gravitational waves [59, 247] (see Ref. [248] for a review) amenable to experimental confirmation by future space-borne interferometers like the Big Bang Observer (BBO) [249], the Deci-hertz Interferometer Gravitational Wave Observatory (DECIGO) [250] and LISA [251]. On the other hand, if the electroweak phase transition were to be of first-order, the former inhomogeneities coupled with novel CP-violating interactions could lead to the generation of the observed baryon asymmetry through the mechanism of electroweak baryogenesis [82] (for a review, see Ref. [252]).

The predictions of the physical effects of a first–order phase transition, such as the power emitted in gravitational waves or the generated baryon asymmetry, crucially depend on the velocity reached by the bubbles expanding through the plasma. While gravitational wave emission is enhanced if the velocity becomes nearly luminal, the generation of the baryon asymmetry requires slow bubbles that allow for the diffusion of the particles reflected in a CP-violating manner by the advancing bubble. This enables the CP excess in front of the bubble wall to be converted into baryon number asymmetry by sphaleron interactions [253].

For these reasons the estimation of bubble velocities has been the subject of intense study, centered on the understanding of the friction effects between the bubbles and the plasma which may slow the advance of the former. Studies based on kinetic theory [66, 254–256], fluctuation-dissipation arguments [257, 258] or non-equilibrium quantum field theory [259] suggest a velocity-dependent friction force caused by deviations from equilibrium interactions in the vicinity of the bubble wall. While most analyses are based on evaluating the rate of momentum transfer integrated across the bubble wall, the ensuing friction force is usually incorporated into the local equation of motion of the scalar field. The kinetic-theory approach or equivalent methods provide first-principle estimates of friction effects by using Boltzmann equations to estimate the out-of-equilibrium effects. Investigations mostly focusing on SM extensions have recently been performed [67, 68, 259–261]. Many studies consider an effective friction term proportional to a phenomenological friction parameter η [70, 71, 262], which is sometimes fixed to match the results from the Boltzmann approach [263–266].

The general expectation is that there is no friction in local equilibrium [267]. Furthermore, it has been argued that the friction force saturates at leading order for high-velocities, such that near-luminal bubble propagation, or "runaway" behaviour is a generic possibility [68, 268]. This was first disputed in [61], in which it was argued that hydrodynamic effects in deflagrations can lead to a heating of the plasma in front of the bubble wall, which affects the force driving the expansion of the bubble. More recently, Ref. [269] showed that in local equilibrium the friction force per unit area follows the relationship

$$\frac{|\vec{F}_{\text{friction}}|}{A} = (\gamma^2(v_w) - 1)\, T\, |\Delta s|, \tag{3.1}$$

where $\gamma(v_w)$ is the Lorentz contraction factor of the asymptotic bubble wall velocity v_w, and Δs the change in entropy density across the bubble. This force keeps growing with the velocity and prevents the bubbles from runaway behaviour.

The analysis of Ref. [269] was based on integrating the stress energy momentum tensor across the bubble wall and assuming a constant temperature and fluid velocity throughout. However, this does not exemplify how friction arises in the local dynamical equations for the scalar field and the plasma, or how to consistently compute both the bubble velocity and the associated entropy change. Furthermore, it was not clarified how the results may be related to the hydrodynamic effects investigated in [61]. In particular, while the latter were expected to only take place in deflagrations, the subluminal speeds found in Ref. [269] are expected regardless of whether the bubbles expand as deflagrations and detonations.

The goal of this work is to confirm that indeed local equilibrium is compatible with subluminal bubble expansion, clarify the local origin of the friction forces and the relation to the hydrodynamic effect of Ref. [61], and provide consistent estimates of bubble velocities. Rather than arising from additional terms in the scalar's equation of motion, the friction-like behaviour in the presence of local equilibrium is caused by the field-dependence of the local entropy and enthalpy density itself, which enters into the hydrodynamic equations of the plasma. As the scalar bubble expands it enforces local entropy and enthalpy changes in the plasma near the bubble wall, and conservation of stress-energy and the total entropy imply that the bubble must slow down. We will illustrate this effect quantitatively in an extension of the SM with additional scalars. We estimate bubble-wall velocities both from time-dependent solutions with radial symmetry, or by finding planar solutions to the static equations in the wall frame and matching them to consistent hydrodynamic profiles away from the wall. The latter allows to make contact with the treatment of Ref. [61], though as a novelty we find profiles corresponding to subluminal detonations, in accordance with the expectations of Ref. [269]

The chapter is organized as follows. In section 3.2 we review the differential equations for the scalar field plus plasma, arising simply from imposing the conservation of the stress-energy tensor. Next, in section 3.3 we introduce the model used to illustrate the friction-like effects. Section 3.4 presents the results for dynamical deflagration solutions with radial symmetry, while finally in sections 3.5 and 3.6 we consider the asymptotic regime of constant velocity expansion and solve for static bubble profiles in the wall frame compatible with consistent deflagration (section 3.5) and detonation (section 3.6) solutions of the plasma equations away from the bubble. Finally, conclusions are drawn in section 3.7.

3.2 Differential Equations for Bubble Propagation

We consider a system involving a real scalar field interacting with a thermal plasma. The stress-energy momentum tensor is given by the sum of contributions from both sectors

$$T^{\mu\nu} = T^{\mu\nu}_{\phi} + T^{\mu\nu}_{p}, \tag{3.2}$$

where ϕ and p denote the scalar field and the plasma respectively. We assume an ordinary scalar with a potential $V(\phi)$ plus a plasma modelled by a perfect fluid, which can be justified as the leading order approximation in an expansion in terms of gradients of the plasma velocity. As such, we have

$$\begin{aligned} T^{\mu\nu}_{\phi} &= \partial^\mu\phi\partial^\nu\phi - \eta^{\mu\nu}\left(\frac{1}{2}\partial_\rho\phi\partial^\rho\phi - V(\phi)\right), \\ T^{\mu\nu}_{p} &= (\rho+p)u^\mu u^\mu - \eta^{\mu\nu}p = \omega\, u^\mu u^\mu - \eta^{\mu\nu}p. \end{aligned} \tag{3.3}$$

In the above equations, u^μ with $\mu = 0, 1, 2, 3$ represents the fluid's four-velocity, while p, ρ and $\omega = \rho + p$ correspond to the pressure, energy density and enthalpy of the plasma. We assume the signature $(+, -, -, -)$ for the Minkowski metric and work in natural units with $c = 1$. In terms of the plasma velocity vector v^i with $i = 1, 2, 3$, its magnitude $v \equiv \sqrt{\sum_i (v^i)^2}$ and the Lorentz factor $\gamma(v) = 1/\sqrt{1-v^2}$, the 4-velocity can be written as $u^\mu = \gamma(v)(1, v^1, v^2, v^3)$. Covariant conservation of the stress-energy momentum tensor in a cosmological background implies $\nabla_\mu T^{\mu\nu} = 0$. Under the typical assumption of a phase transition that proceeds much faster than the Universe's expansion, one may neglect the cosmological scale factor and replace covariant derivatives by ordinary ones. Doing so, the terms in $\nabla_\mu T^{\mu\nu}$ involving $\partial^\nu\phi$ are proportional to the scalar field's equation of motion in the plasma background and must vanish separately. This yields

$$\begin{aligned} \Box\phi + \frac{\partial}{\partial\phi}(V(\phi) - p) &= 0, \\ \partial_\mu(\omega u^\mu u^\nu - \eta^{\mu\nu}p) + \frac{\partial p}{\partial\phi}\partial^\nu\phi &= 0. \end{aligned} \tag{3.4}$$

As initial time boundary conditions for the plasma, a fluid at rest with a temperature given by the nucleation temperature T_{nuc} at which the bubble formation rate overcomes the Hubble expansion should be considered. For the scalar field, a perturbation of the critical bubble that extremizes the three-dimensional integral of the Lagrangian for static fields should be set as an initial condition.

One recognizes the first equation in Eq. (3.4) as the equation of motion of the scalar field at finite temperature. Indeed, under the assumption of local thermal equilibrium with temperature T, the pressure is related to the free energy, which itself is related to the thermal corrections V_T to the effective potential $p = -V_T$. Hence, we may denote $V(\phi) - p = V(\phi, T)$ and recover the standard equation of motion at finite temperature. Equations equivalent to (3.4) were obtained in Ref. [262], where the authors expressed the total pressure as a radiative contribution proportional to T^4 and the additional field dependent terms. We make no such distinction here, thus the simpler notation. Furthermore, the authors of Ref. [262] added a phenomenological friction term without spoiling stress-energy conservation. This corresponds to substituting the r.h.s. of the two equations in (3.4) by $-\eta\, u^\mu \partial_\mu \phi$ and $\eta\, u^\mu \partial_\mu \phi \partial^\nu \phi$, respectively, where η is a friction parameter.

In the second equation of (3.4), it should be noted that the terms involving field derivatives of the pressure cancel, but the terms proportional to $\partial\omega/\partial\phi$ survive. Under local thermal equilibrium, one can relate ω to the entropy density $s = \omega/T$, so that the terms proportional to $\partial\omega/\partial\phi$ account for local entropy changes across the bubble wall. It is precisely these terms which give rise to friction-like effects and subluminal bubble propagation. In fact, this connection to entropy changes across the bubble wall matches the result (3.1) shown in Ref [269]. The former approach directly assumed a steady state expansion, planarity and a common temperature on both sides of the bubble. Our treatment goes beyond the former simplifications by incorporating the friction-like effects at the level of the local field and plasma equations.

We note that standard thermodynamic identities allow the computation of the entropy density in terms of the pressure or equivalently V_T, whose one-loop expression for a general model is a standard result of thermal field theory

$$\omega(\phi, T) = T\, s = T\, \frac{\partial p}{\partial T} = -T\, \frac{\partial V_T(\phi, T)}{\partial T}. \tag{3.5}$$

This considerably simplifies the calculation of backreaction effects under the assumption of local equilibrium, and allows a quick recovery of the lengthier derivations of entropy in e.g. Ref. [269].

It is worth mentioning that the usual friction terms parameterized by η lead to a violation of the conservation of the total entropy of the universe, and thus correspond to out-of-equilibrium, irreversible processes. Indeed, adding the friction term to the second equation in (3.4), contracting with u_ν and using the thermodynamic identities of Eq. (3.5) leads to

$$\partial_\mu (s u^\mu) = \frac{\eta}{T}\, (u^\mu \partial_\mu \phi)^2. \tag{3.6}$$

Integrating the former equation over a region of spacetime between times t_i and t_f, applying the divergence theorem and assuming a fluid at rest at the boundary gives $S(t = t_f) - S(t = t_i) = \int d^4x \frac{\eta}{T}\, (u^\mu \partial_\mu \phi)^2$, where S is the total entropy in the spatial volume.[1] In local equilibrium one expects conservation of S, and thus it is consistent to take $\eta = 0$. Nevertheless, as we will show in the following sections, friction-like behaviour persists. As the expansion is reversible due to the conservation of entropy,

[1] Note that s is the entropy density in the plasma rest frame, and for a general frame one has to account for the Lorentz contraction in the direction of propagation.

the effective force slowing down the bubble is non-dissipative, and we will refer to it as a backreaction as opposed to a friction force. Its effect will be shown in two ways: by solving the dynamical equations (3.4), and by directly looking for solutions of their static limit so as to constrain the possible wall velocities [262]. Indeed, a large bubble propagating with constant speed has a steady profile up to subleading curvature effects. As such, static solutions to (3.4) that capture the field and fluid near the wall can directly be searched for. For a bubble propagating in the z direction with $v^z \equiv \mathfrak{v}$, the static equations can be written as [262]

$$\begin{aligned} &-\phi''(z) + \frac{\partial}{\partial\phi}(V(\phi,T)) = 0, \\ &\omega\gamma^2\mathfrak{v}^2 + \frac{1}{2}\left(\phi'(z)\right)^2 - V(\phi,T) = c_1, \quad \omega\gamma^2\mathfrak{v} = c_2, \end{aligned} \tag{3.7}$$

where c_1, c_2 are constants which can be traded for the temperature T_+ and velocity v_+ in front of the bubble wall. We assume a bubble propagating towards positive z, so that in the wall frame the fluid velocity v_+ is negative. The last two equations in (3.7) can be used to express the temperature and velocity in terms of the Higgs field and its derivatives, which then leaves a single equation for the scalar field with a non-standard potential $\hat{V}(\phi,\phi') = V(\phi,T(\phi,\phi'))$ that depends on $\phi'(z)$. We note that the solutions $T(\phi,\phi'), v(\phi,\phi')$ of the last identities in Eq. (3.7) can be multi-valued, and due to the quadratic dependence on $\mathfrak{v}$ and quartic dependence on T one can expect two branches of physical solutions with $T > 0$, which we will denote with "high" and "low", giving larger or smaller values of $|\mathfrak{v}|$, respectively. Due to the dependence on ϕ', the "energy" function

$$\mathcal{E} \equiv \frac{1}{2}\phi'(z)^2 + \hat{V}_{\text{high,low}}(\phi,\phi') \tag{3.8}$$

is only approximately conserved. The boundary conditions are $\phi'(z) = 0, z \to \pm\infty$, and $\phi \to 0, z \to \infty$. For numerical calculations one may impose analogous boundary conditions at a finite but large z. Given $v_+ < 0$ and T_+, the former boundary conditions can be satisfied only for a specific choice of the value $\phi_-(v_+,T_+)$ of the field behind the wall, leading to a prediction of the fluid velocity $v_-(v_+,T_+)$ behind the bubble. On physical grounds, one expects the field far away from the bubble setting into a minimum of the finite-temperature effective potential. Then from Eq. (3.7) it follows that one should require $\phi''(z) = 0, z \to \pm\infty$, as enforced in Ref. [61]. This reduces the ambiguity of the solutions to a single parameter, e.g. T_+.

The static solutions for the field, velocity and temperature profiles obtained as before have to be matched to time-dependent profiles away from the bubble wall. Far away in front of the wall, one should recover $T = T_{\text{nuc}}$, which fixes the ambiguity of the static solution for the wall once it is matched to a hydrodynamic profile. The time-dependence of the latter is expected because, with the scalar field tending to a constant, the lack of dimensionful scales beyond the temperature in the leading contributions to the plasma equations suggests "self-similar" solutions depending on $xi \equiv |\vec{x}|/t$ [270]. Under this assumption, from the second line in Eq. (3.4) one can derive the equation

$$\begin{aligned}\frac{\xi - v}{\omega}\,\partial_\xi \rho - 2\,\frac{v}{\xi} - (1-\gamma^2 v(\xi - v))\partial_\xi v = 0,\\ \frac{1-v\xi}{\omega}\,\partial_\xi p - \gamma^2(\xi - v)\partial_\xi v = 0.\end{aligned} \tag{3.9}$$

The possible types of solutions of the above relativistic fluid equations are well known [71, 270]. One expects two types of solutions: deflagrations –in which the bubble expands with a velocity below the speed of sound in the plasma $c_s^2 = \partial_T p/\partial_T \rho$, with the fluid heating up and compressing in front of the bubble and at rest behind it– and detonations –in which the expansion velocity is above c_s, the fluid is unperturbed in front of the bubble, but heats up behind it.

For deflagration profiles, since the fluid is expected to be at rest behind the bubble one can obtain the wall velocity v_w in the fluid frame from the static wall solution as $v_w = -v_-$. The fluid velocity in front of the bubble in the fluid frame is then obtained from a Lorentz boost as $v_{\rm fluid,+} = (v_+ - v_-)/(1 - v_+ v_-)$. Together with the temperature T_+, this gives boundary conditions for the plasma equations (3.9) to be solved in front of the bubble, T_+ must be fixed so as to get $T = T_{\rm nuc}$ when the velocity drops to zero in front of the bubble.

For detonation profiles, with the fluid unperturbed in front of the bubble one must impose $T_+ = T_{\rm nuc}$. The static wall solution then gives unique boundary conditions $T = T_-$, $v_{\rm fluid,-} = (v_- - v_+)/(1 - v_+ v_-)$ for Eqs. (3.9) behind the bubble.

Given the approximate conservation of ϵ in Eq. (3.8) and the boundary conditions enforcing that the field reaches the minima of $\hat{V}_{\rm high,low}$ with zero velocity, the task of finding physical solutions can amount to the following: first, one chooses a value of T_+ ($= T_{\rm nuc}$ for detonations) and the value of v_+ is varied until one gets $\hat{V}_{\rm high,low}$ with near degenerate minima, so that solutions with the appropriate physical boundary conditions are allowed. Then one can solve Eqs. (3.9) away from the bubble, and in the case of deflagrations one has to search for the appropriate value of T_+ which allows to recover the nucleation temperature for the fluid at rest.

In a planar approximation the calculation gets simplified because there is no need to solve (3.9). In the planar regime the $1/\xi$ term in Eqs. (3.9) can be dropped and one gets solutions with constant velocity and pressure, which simplifies the treatment. However, satisfying the boundary conditions of fluid at rest far from the wall implies the appearance of discontinuity fronts across which the velocity drops to zero: a shock front in front of the bubble in the case of deflagrations, and a similar discontinuity behind the bubble for detonations. One can relate quantities across the front by imposing continuity of the stress-energy tensor. In the case of deflagrations, equating the fluid velocity between wall and shock front deduced from the solutions of (3.7) and from the shock constraints leads to the condition

$$v_{\rm fluid,+} = \frac{v_+ - v_-}{1 - v_+ v_-} = \frac{\sqrt{3}\,(T_+^4 - T_{\rm nuc}^4)}{\sqrt{(T_{\rm nuc}^4 + 3T_+^4)\,(3T_{\rm nuc}^4 + T_+^4)}}. \tag{3.10}$$

The above can be used to fix the free parameter T_+ for the static wall solution. In the case of detonations, there is no additional constraint as one has $T_+ = T_{\rm nuc}$, but within the planar approximation the temperature $T_{\rm in}$ inside the bubble beyond the detonation front can be obtained from the following equations,

$$v_{\text{fluid},-} = \frac{v_- - v_+}{1 - v_+ v_-} = \frac{\sqrt{3}\left(T_{\text{in}}^4 - T_-^4\right)}{\sqrt{\left(T_{\text{in}}^4 + 3T_-^4\right)\left(3T_-^4 + T_{\text{in}}^4\right)}}. \tag{3.11}$$

To make contact with the results of Ref. [269], let us point out that the friction force (3.1) can be derived directly from the second identity in Eq. (3.7) evaluated at both sides of the wall (where $\phi'(z) = 0$), once one identifies the backreaction pressure $|\vec{F}_{\text{back}}|/A$ with $|\Delta V(\phi, T)|$, and under the approximation of a constant temperature and fluid velocity, the latter identified with $-v_w$. In reality, the situation is more complicated as the temperature and velocity change across the bubble, a more complete result is

$$\frac{|\vec{F}_{\text{back}}|}{A} = |\Delta\{\gamma^2 v^2 \omega\}| = |\Delta\{(\gamma^2 - 1)Ts\}|. \tag{3.12}$$

The planar approximation can be used to gain an intuitive understanding of the reasons behind the subluminal propagation speed. In either deflagration or detonation solutions, the interior of the bubble has lower entropy density than the fluid before the transition. This simply follows from the fact that the phase transition makes some particles massive, while the entropy in the plasma is always dominated by the contribution from the relativistic degrees of freedom. Recall that in thermal plasma, one can write

$$s = \frac{2\pi^2}{45}\, g_{\star s} T^3, \tag{3.13}$$

where $g_{\star s}$ denotes the the number of effective relativistic degrees of freedom. Inside the bubble $g_{\star s}$ drops, and with it s. For the degrees of freedom in local equilibrium, the total entropy has to be conserved. With the entropy decrease due to the presence and expansion of the bubble, there has to be a compensating entropy increase. Given Eq. (3.13), this can be achieved if parts of the fluid heat up. This is precisely what happens in detonations and deflagrations, in which the fluid heats up behind and in front of the bubble respectively. In the planar approximation, one simply expects a detonation/deflagration shell with constant increased temperature T_{shell} –corresponding in the notation above to T_-/T_+ for detonations/deflagrations– and with an additional shell front propagating with constant velocity v_{front} behind/ahead of the bubble wall. The conservation of the total entropy within this approximation then gives

$$v_w = v_{\text{front}} \left(\frac{|\Delta\gamma s|_{\text{front}}}{|\Delta\gamma s|_{\text{wall}}}\right)^{1/3}, \tag{3.14}$$

where we assumed fluid shells with radial symmetry and radii $R_w = v_w t, R_{\text{front}} = v_{\text{front}} t$. Using the stress-energy conservation relations across the front, one can relate v_{front} to the temperatures at each side of the front,

$$v_{\text{front}} = \begin{cases} \frac{1}{\sqrt{3}}\left(\frac{3T_-^4 + T_{\text{in}}^4}{3T_{\text{in}}^4 + T_-^4}\right)^{1/2} & \text{detonations} \\ \frac{1}{\sqrt{3}}\left(\frac{3T_+^4 + T_{\text{nuc}}^4}{3T_{\text{nuc}}^4 + T_+^4}\right)^{1/2} & \text{deflagrations.} \end{cases} \tag{3.15}$$

One can also express the entropy increase across the front in terms of the same temperatures using Eqs. (3.10), (3.11) and (3.13). Subliminal speeds are generally expected for moderate heating in the compression shell.

Above, we related the subluminal propagation speeds to a heating effect associated with the conservation of the entropy of the degrees of freedom in local equilibrium. A heating effect was already connected to subliminal speeds in local equilibrium in the case of deflagrations in Ref. [61], though with different argumentation. It was noted that such a heating in front of the bubble wall could lead to a zero driving force, incorporating the effects of pressure and the zero T potential difference, for the bubble expansion. In view of the arguments provided in Ref. [269] (which, as seen above, follows from the static equations (3.7), which were also solved in Ref. [61]), one does not expect an exactly zero driving force, but a compensation with a backreaction force due to the entropy changes across the bubble. Yet the heating effect first noted in Ref. [61] is definitely connected with subluminal propagation speeds, and can be understood from entropy conservation and extended to detonations.

3.3 Example Model

To illustrate the friction effects, we consider an extension of the SM by an N-dimensional multiplet χ of complex scalar singlets with $U(N)$-preserving couplings, including interactions with the Higgs Φ:

$$\begin{aligned}\mathcal{L} \supset \quad & -m_H^2 \Phi^\dagger \Phi - \frac{\lambda}{2}(\Phi^\dagger\Phi)^2 - m_\chi^2 \chi^\dagger \chi \\ & -\frac{\lambda_\chi}{2}(\chi^\dagger\chi)^2 - \lambda_{H\chi}\Phi^\dagger\Phi\chi^\dagger\chi\,. \end{aligned} \tag{3.16}$$

Now, all that is required for writing down the equations is $p = -V_T$. For simplicity of the numerical implementation we use a high-temperature expansion up to terms of order T, which still captures the nontrivial field dependence

$$\begin{aligned} p(h,T) = {} & \frac{\pi^2 T^4}{90}(g_{*,\mathrm{SM}} + 2N) - T^2\left(h^2\left(\frac{y_b^2}{8} + \frac{3g_1^2}{160}\right.\right. \\ & \left.\left. + \frac{3g_2^2}{32} + \frac{\lambda}{8} + \frac{N\lambda_{H\chi}}{24} + \frac{y_t^2}{8}\right) + \frac{m_H^2}{6} + \frac{Nm_\chi^2}{12}\right) \\ & - \frac{T}{12\pi}\left(-\frac{3}{4}(g_2 h)^3 - \frac{3h^3}{8}\left(\frac{3g_1^2}{5} + g_2^2\right)^{3/2}\right. \\ & - 3\left(\frac{h^2\lambda}{2} + m_H^2\right)^{3/2} - \left(\frac{3h^2\lambda}{2} + m_H^2\right)^{3/2} \\ & \left. -2N\left(\frac{h^2\lambda_{H\chi}}{2} + m_\chi^2\right)^{3/2}\right). \end{aligned} \tag{3.17}$$

In the above equation, we have assumed a background for the neutral component of the Higgs h. $g_{\star,\mathrm{SM}} \sim 106.75$ denotes the number of effective relativistic degrees of freedom in the SM plasma, while g_1 and g_2 are the hypercharge and weak gauge couplings in the normalization compatible with Grand Unification, and y_t, y_b are the bottom and top quark Yukawa couplings respectively. For the couplings and parameters beyond those of the SM we use $N = 4$ or $N = 2$, $m_S^2/m_W^2 = 0.0625$, $\lambda_\chi = 0.085$, $\lambda_{H\chi} = 0.85$. This gives a first–order electroweak phase transition with critical and nucleation temperatures around $T_c = 115.952$GeV, $T_{\rm nuc} = 115.297$GeV for $N = 4$ and $T_c = 126.376$GeV , $T_{\rm nuc} = 126.229$GeV for $N = 2$. The nucleation rate can be estimated by minimizing the three-dimensional integral $S_3[h, T]$ of the finite-temperature action evaluated at static configurations $h(r)$ with radial symmetry, we use the standard criterion for nucleation $S_3[h_{\rm nuc}(r), T_{\rm nuc}]/T_{\rm nuc} \sim 140$, where $h_{\rm nuc}(r)$ is the critical field configuration or bubble.

3.4 Solving for Time-Dependent Solutions with a Neural Network

In this section we focus on solving the time-dependent equations (3.4) for the above parameter choices, with $N = 4$. We assume radial symmetry, with the velocity field having a radial component $v^r \equiv v$, and with v, h, T being functions of r, t. As initial conditions we use $T(r, t = 0) = T_{\rm nuc}, v(r, t = 0) = 0$, while for the Higgs we use the critical bubble perturbed with a nonrelativistic boost (as otherwise the bubble would remain static): $h(r, t = 0) = h_{\rm nuc}(r)$, $\partial_t h(r, t)|_{t=0} = -\delta h'_{\rm nuc}(r)$, with $\delta = 0.2$.

3.4.1 Setup

In order to find time-dependent solutions to Eqs. (3.4) we follow the technique pioneered in Ref. [271] and implement an artificial neural network (NN). The method relies on recasting the partial differential equations (PDEs) as an optimization procedure –for which NN are uniquely suited– of the form $\hat{\mathcal{L}} = 0$, where $\hat{\mathcal{L}}$ is a positive loss function to be minimized by the NN. The network is constructed by considering an initial layer of 2 inputs $\xi_n = (r, t)$ that are to be mapped to a final layer with 3 outputs N_m which are to be approximations of the solutions $\varphi_m = (v, h, T)$ to the differential equations. The inputs are mapped to successive hidden layers of k elements, from the combined action of linear transformations between each layer and the action of a real activation functions, a final linear mapping gives the final outputs. For example, for one hidden layer one has

$$N_m(\vec{\xi}, \{w, b\}) = \sum_{k,n} w^f_{mk} g(w^h_{kn}\xi_n + b^n_k) + b^f_m, \tag{3.18}$$

where g is the activation function, $\omega^h_{mk}, \omega^f_{mk}$ are known as "weights", and b^h, b^f are the "biases". A set of weights and biases which minimize the loss function associated with the system of differential equations are searched for. Writing the latter in the form

$$\mathcal{F}_m(\vec{\xi}, \varphi_n(\vec{\xi}), \partial^p_q \phi_n(\vec{\xi})) = 0, \tag{3.19}$$

with $m, n \in \{1, 2, 3\}$, $p, q \in \{1, 2\}$, and assuming boundary conditions (BCs) for boundary points $\vec{\xi}_b$ of the form

$$\mathcal{B}_a(\vec{\xi}_b, \varphi_n(\vec{\xi}_b), \partial^p_q \phi_n(\vec{\xi}_b)) = 0, \tag{3.20}$$

the loss function is constructed from considering a discrete set of "training points" $\vec{\xi}_i$ including boundary points $\vec{\xi}_{b,j}$, and evaluating $\mathcal{F}_m$ and $\mathcal{B}_a$ on them

$$\begin{aligned}\hat{\mathcal{L}}(\{w,b\}) =& \sum_{i,m} c_m \mathcal{F}_m(\vec{\xi}_i, N_n(\vec{\xi}_i), \partial_k^j N_n(x_i))^2 \\ &+ \sum_{j,a} d_a \mathcal{B}_a(\vec{\xi}_{b,j}, N_n(\vec{\xi}_{b,j}), \partial_k^j N_n(\vec{\xi}_{b,j}))^2. \end{aligned} \tag{3.21}$$

Above, the derivatives of the network outputs can be obtained analytically from (3.18). The coefficients c_m and d_a represent relative weightings for each PDE and BC, required to ensure that all PDEs and BCs contribute comparably to the loss function. We implement the NN with 13 hidden layers with 10 nodes each, with tanh activation functions. We choose the training examples from an evenly spaced 80×80 grid. We use the `pytorch` package along with the `Adam` optimizer for the NN gradient descent. To avoid getting trapped in sub-optimal local minima of the smooth loss function, we take care to reduce the learning rate through cosine annealing with warm restarts. For fast convergence of our solution, we first pretrain the NN with a template solution implemented as a boundary condition for low t. This is obtained using `Wolfram Mathematica`'s PDE solver, which is only able to provide reliable solutions for a small time interval. After the NN is in the correct vicinity of solution, we remove the pretrained template from the loss function and train according to (3.21). This allows reliable solutions for time intervals that cannot be reached with the `Mathematica` solver.

3.4.2 Dynamic Transition Results

From the previous NN setup we were able to obtain solutions in which the individual loss functions $\mathcal{F}_m$ in dimensionless units (obtained by rescaling quantities with appropriate powers of the W mass $m_W \approx 80$GeV) take values $\lesssim 5 \times 10^{-3}$. We show the resulting dynamical profiles of h, T, v in Figure 3.1 as a function of r in dimensionless units for 5 equally spaced timestamps between $t = 0$ and $t = 50/m_W$. We note that the `Mathematica` solver was only able to compute accurate solutions for $t \lesssim 15/m_W$. The scalar profile settles to a slow expansion, while the velocity and temperature profiles show the formation of a faster propagating front, in accordance with the expectations of a deflagration solution with self-similar fluid behaviour. Confirming the latter would require extending the solutions to even later times, a more efficient means is to directly look for static wall solutions with consistent hydrodynamic profiles as we show in the next section. By following points with constant $h(r,t) = 0.5$ we can estimate the bubble's position and velocity, the latter is plotted with a solid line in Figure 3.2, which shows that the bubble's velocity settles to $\lesssim 0.25$. This is in contrast to the result, illustrated with a dashed line, when the terms proportional to $\partial\omega/\partial\phi$ are omitted in Eq. (3.4). In this case the bubble velocity quickly approaches the speed of light. This confirms our observation that the field-dependence of the enthalpy is responsible for the friction-like behaviour.

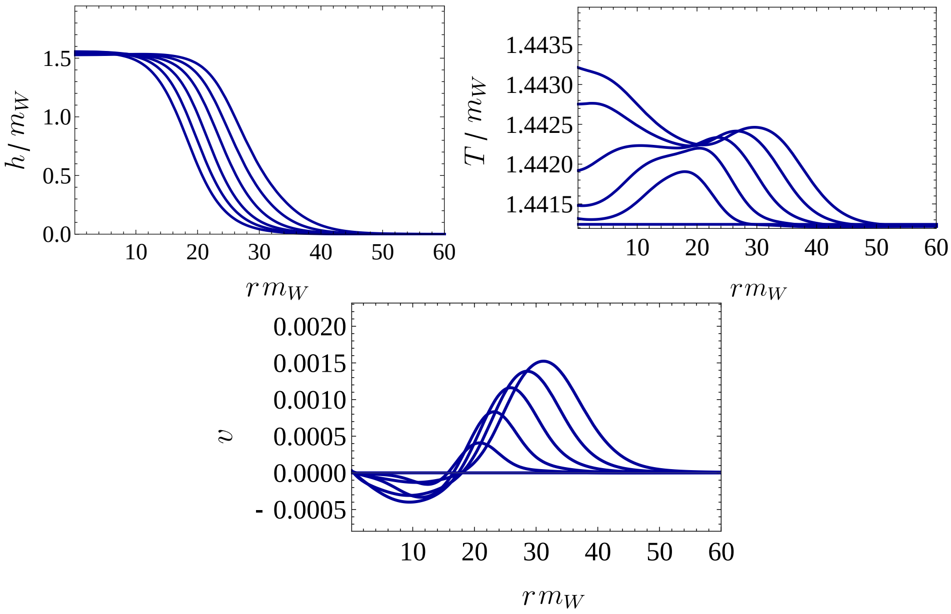

FIGURE 3.1: Dynamical evolution of h, T and v in dimensionless units. The curves from left to right correspond to time steps from $tm_W = [0, 50]$ with $m_W \Delta t = 10$.

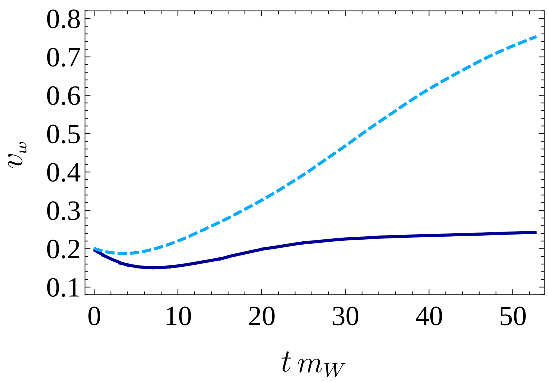

FIGURE 3.2: Bubble velocity versus time in dimensionless units, including the effect of the field dependence of the enthaply (solid line) or without it (dashed line).

3.5 Static Planar Bubble Profiles and Consistent Deflagrations

In this section we report the results of searching for deflagration solutions with the same parameters as in the previous section, assuming a static solution near the bubble wall that solves Eq. (3.7), and either implementing the hydrodynamic constraints of Eqs. (3.10), (3.11) applying in the planar regime, or matching with solutions to the radial hydrodynamic equations (3.9). Without imposing the boundary condition $\phi''(z) \to 0$, we have found a one-parameter branch of solutions satisfying all constraints. These family of configurations corresponds to the "low" branch of solutions for the temperature profiles $T(h, h')$, and when solving Eqs. (3.9) we find acceptable configurations for $T_+ \leq T_+^{\max} = 116.471\text{GeV}$. The upper value of T_+ corresponds to the unique solution satisfying the physical constraint $\phi''(z) \to 0$ at large $|z|$, and having a wall velocity $v_w = 0.496$. We note that with our method it is challenging to exactly recover $\phi''(z_{\min}) = 0$ because we use a finite interval of z, and moreover we find an exponential sensitivity of $\phi''(z_{\min})$ to the value of T_+ near $T_+^{\max}$, with $\phi''(z_{\min})$ approaching zero with a slope that seems to grow towards infinity. The former results are compatible with the dynamical results of the previous section, in which temperatures remained below the above value of $T_+^{\max}$ (see Figure 3.1) and the wall velocity approached 0.25. The lower velocity in the dynamical simulation can be due to the effect of considering a radial expansion, as opposed to the planar approximation used for finding the static wall profile. It could also be that the planar wall velocity is only reached at much later times than the ones covered by the dynamical simulation of the previous section, note that the slope of the wall velocity in Figure 3.2, though very small at later times, seems to be nonzero. The wall velocity v_w, the exact backreaction force of Eq. (3.12) and the approximation of Eq. (3.1) found in Ref. [269] are illustrated in Figure 3.6, which also shows the results when, instead of solving Eqs. (3.9), one imposes the planar constraints of Eq. (3.10). We find qualitative agreement with Eq. (3.1) up to deviations below 70%, which are due to the changes of T and v across the bubble.

In Figure 3.3 we illustrate the pseudopotential $\hat{V}_{\text{low}}(h, h')$ evaluated at constant configurations with $h' = 0$, for three different values of v_+ and the value of $T_+ = 116.471\text{GeV}$ giving the smallest $|\phi''(z_{\min})|$ for $z_{\min} = -25/m_W$. The fact that for this finite interval in z we don't achieve exactly $\phi''(z_{\min}) = 0$ is reflected by the slight non-degeneracy of the minima of the pseudopotential. We illustrate the profiles for solutions near $T_+ = T_+^{\max}$ in Figs. 3.4 and 3.5.

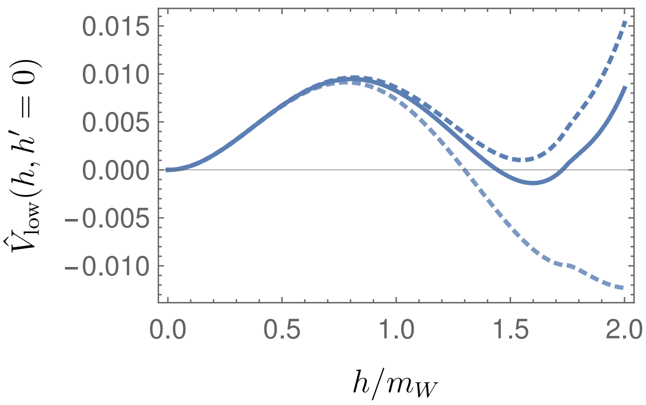

FIGURE 3.3: Pseudopotential $\hat{V}_{\text{low}}(h, h' = 0)$ for $T_+ = 116.471$ GeV, with v_+ taking the values (from top to bottom): -0.47, -0.4809, -0.50. The central choice of v_+ gives a hydrodynamic profile in which $T = T_{\text{nuc}}$ when the fluid velocity drops to zero, and with a minimal value of $|\phi''(z_{\min} = -25/m_W)|$ in our numerical scans.

The physical solution with $\phi''(z) \to 0$ at large $|z|$ would correspond to the solutions that were searched for in Ref. [61]. The solution with a minimal value of $\phi''(z_{\min})$ found here satisfies approximately the constraints derived in the former reference from requiring a zero driving force (although in fact there is a driving force which is exactly compensated by a nonzero $\vec{F}_{\text{back}}$, as illustrated in Figure 3.6). Defining the parameter

$$\alpha_c = \frac{l_c}{4a_+T_c^4}, \tag{3.22}$$

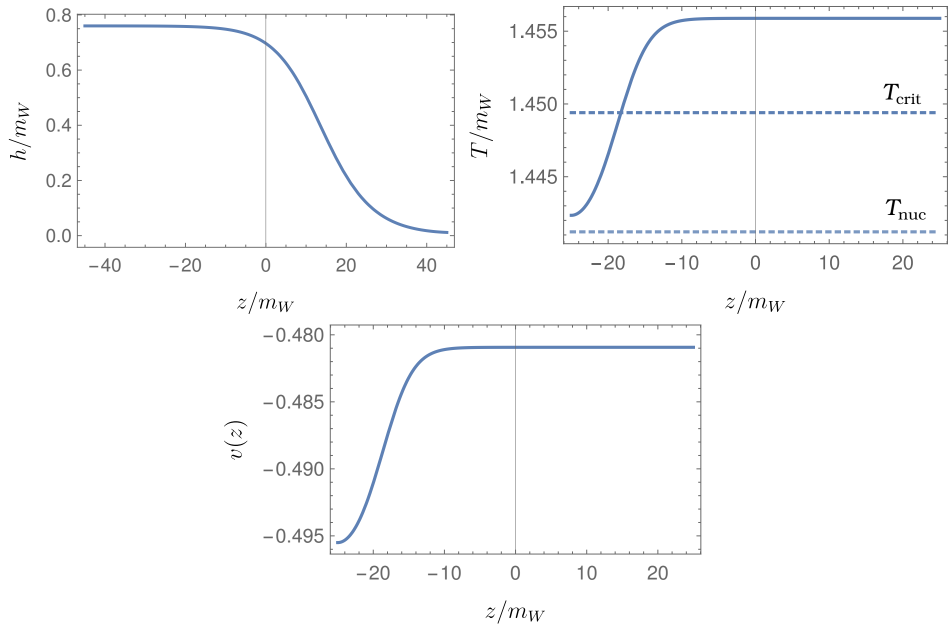

FIGURE 3.4: Deflagration profiles of the Higgs, temperature and velocity across the bubble wall for $T_+ = T_+^{\max}$.

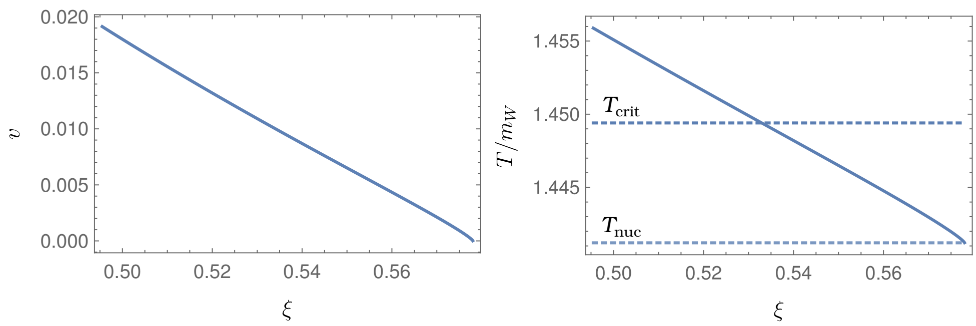

FIGURE 3.5: Hydrodynamic profiles for the fluid temperature and velocity in front of the bubble wall corresponding to the bubble profiles in Figure 3.4.

where $l_c = T\partial_T(V(h_c, T) - V(0, T)|_{T=T_c})$ is the latent heat of the transition (with h_c the nontrivial vev at the critical temperature), and with $a_+ = \pi^2/30(g_{*,SM} + 2N)$ related to the T^4 coefficient of the pressure in Eq. (3.17), the following identities from Ref. [61] are satisfied

$$\begin{aligned} v_w^2 &\sim \frac{1}{6\alpha_c} \log \frac{T_c}{T_{\rm nuc}}, \\ \log \frac{T_c}{T_N} &< \mathcal{O}(1) \left(\sqrt{\frac{\alpha_c}{2}} - \frac{3}{10}\alpha - \frac{1}{5}\alpha^{3/2} \right). \end{aligned} \tag{3.23}$$

The static profiles for the scalar have a typical width as in Figure 3.1, $L \sim 20/m_W \sim 30/T$. The local equilibrium approximation is expected to hold if $L/\gamma(v_w)$ is above the mean free path $\lambda_{\rm mfp}$ of particles in the plasma. With $v_w \lesssim 0.3$ the Lorentz contraction factor is of order one, while Ref. [255] estimated $\lambda_{\rm mfp} \lesssim \hat{m}_W^2(T)/(10\pi\alpha_w^2 T^3)$,

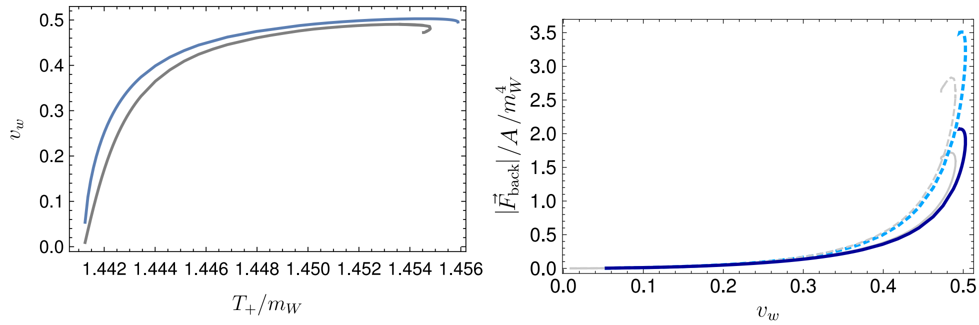

FIGURE 3.6: Upper plot: Bubble velocity as a function of T_+ for the static solutions compatible with consistent deflagrations, and without imposing $\phi''(z) \to 0$ far away from the bubble. The blue curve gives the results when solving the hydrodynamic equations (3.9) away from the bubble, while the grey line gives the results in the planar approximation. Lower plot: Backreaction force as a function of the bubble wall velocity (solid lines) compared to its approximation in Eq. (3.1) (dashed lines). The curves in blue/grey correspond to the hydrodynamic equations with radial/planar symmetry. In both plots, the physical solution with $\phi''(z) \to 0$ at large $|z|$ corresponds to the ending points of the blue curves, or the turning points of the grey curves.

where $\hat{m}_W^2(T)$ is the temperature-dependent W mass, and $\alpha_w = g_2^2/(4\pi)$. In our bubbles, we have $h \lesssim 1.5 m_W \sim T$, giving $\hat{m}_W^2(T) \lesssim T^2/9$ and $\lambda_{\rm mfp} \lesssim 3/T$. Hence the local equilibrium approximation is indeed justified.

3.6 Static Planar Bubble Profiles and Consistent Detonations

In the following we apply the same treatment of the previous section to the search of consistent detonation profiles. Given the inverse proportionality between the wall-velocity and the increase of entropy density across the bubble in Eq. (3.14), one expects higher wall velocities if the phase transition increases the mass of a lower number of particles. This also fits with the proportionality of the backreaction force to the increase in entropy density in Eq. (3.12). As for the choice of couplings described in Section 3.3 we found deflagration solutions for $N = 4$, we hope to find larger wall velocities (and possible detonation solutions) for $N = 2$.

For this choice we find no acceptable deflagration profile with the techniques of the previous section, despite the fact that the parameters satisfy the condition in the second line of Eq. (3.23) derived in Ref. [61] for deflagration profiles in local equilibrium. On the other hand, by choosing the "high" branch of solutions of $T(h, h')$, we find acceptable detonation profiles. The solutions with $|\phi''(z_{\rm min})| \to 0$ are found for $v_+ = -0.723$ (and of course $T_+ = T_{\rm nuc} = 126.229$GeV for $N = 2$), giving a supersonic wall velocity $v_w = 0.723$. This can be connected to a detonation profile behind the wall that solves Eq. (3.9) with the fluid velocity dropping to zero as expected. Figure 3.7 shows the pseudopotential $\hat{V}_{\rm high}(h, h' = 0)$ calculated for three different choices of v_+, the central one giving the physical solution.

The profiles for the Higgs field, the velocity and temperature along the wall are shown in Figure 3.8. Note the heating effect behind the bubble, with the value of

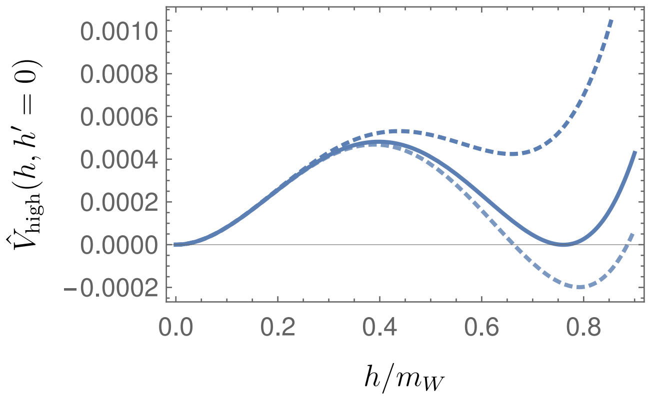

FIGURE 3.7: Pseudopotential $\hat{V}_{\text{high}}(h, h' = 0)$ in the $N = 2$ case for $T_+ = T_{\text{nuc}} =$ 126.229 GeV, with v_+ taking the values (from top to bottom): -0.65, -0.723, -0.80. The central choice of v_+ gives a consistent detonation profile.

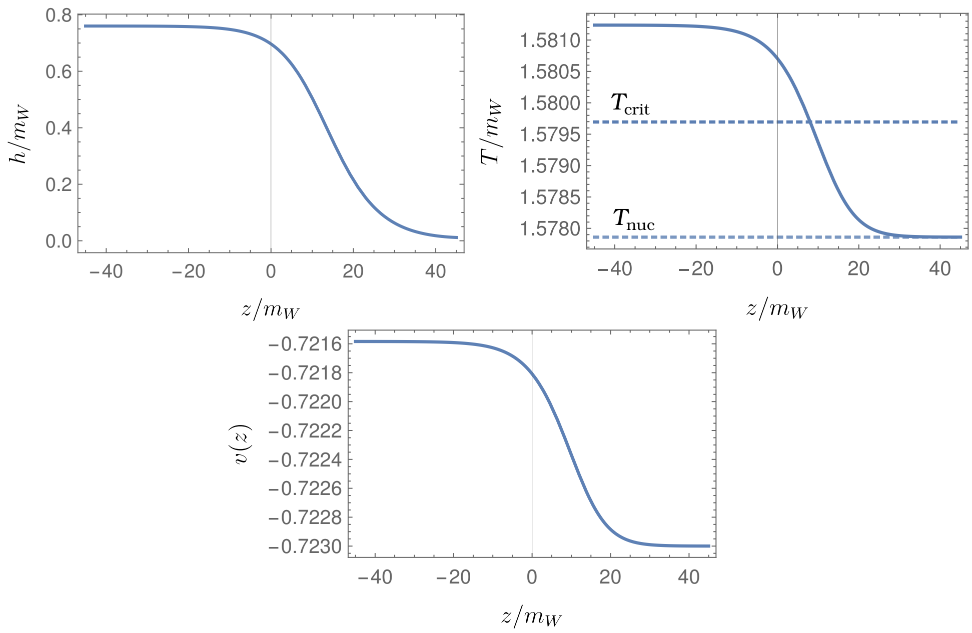

FIGURE 3.8: Detonation profiles of the Higgs, temperature and velocity across the bubble wall. Note how the fluid velocity increases behind the bubble, and the temperature rises. One reaches $T_- > T_c$, but the Higgs is still allowed to be in a metastable minimum. In the hydrodynamic solution far behind the wall, the temperature drops such that the Higgs is stabilized (see Figure 3.9).

T setting onto $T_- = 126.499\,\text{GeV} > T_c = 126.376\text{GeV}$. For this temperature above the critical one there is still a nontrivial Higgs minimum, yet with a higher energy than the minimum at the origin. The physical interpretation is that the fluid heats immediately behind the bubble, driving the Higgs to a metastable minimum.

For solving the hydrodynamic profile behind the bubble, the value of the Higgs can be assumed not to change much i.e. the energy of the Higgs vacuum shifts with temperature, but the relative changes of the vev are small. Then assuming a constant Higgs value one can solve the hydrodynamic equations (3.9) behind the bubble, which

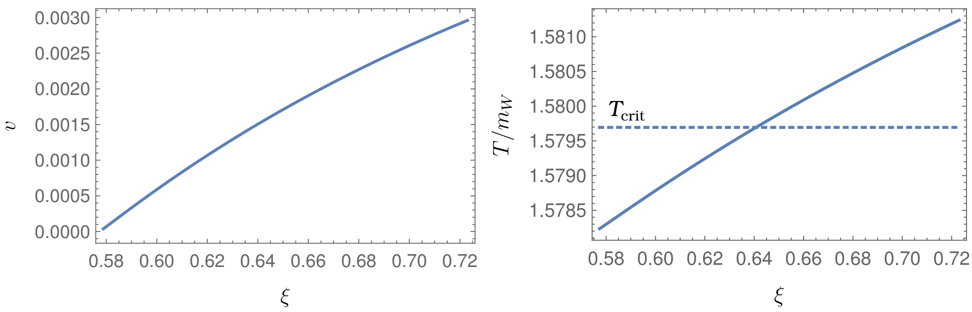

FIGURE 3.9: Hydrodynamic profiles for the fluid temperature and velocity behind the bubble wall, assuming a constant Higgs value.

confirms that the temperature drops to a value $T_{\rm in} = 126.259\,{\rm GeV} < T_c$, so that the Higgs can be stabilized at the absolute minimum of the finite-temperature potential well inside the bubble. The backreaction force computed from Eq. (3.12) is found to be $|\vec{F}_{\rm back}|/A/m_W^4 = 0.648$, while the Eq. (3.1) gives a result which is 3.2 times larger.

3.7 Discussion and Conclusions

In this work we have confirmed and provided new insights on the hydrodynamic effects that give rise to subluminal bubble propagation in first–order phase transitions in which equilibrium is maintained locally. Such subluminal propagation in equilibrium has been proposed for deflagrations in Ref. [61] and for general transitions in [269], and remains in contrast to the common view that links bubble friction with out-of-equilibrium effects. In our work we have provided an understanding of the subliminal propagation as a consequence of the conservation of the total entropy of the degrees of freedom in local equilibrium: in a simplified planar expansion in which detonation or deflagration fronts develop (which typically propagate subluminally) entropy conservation relates the bubble wall and front velocities. We went beyond the work of Ref. [269] by clarifying the origin of the friction forces in the differential equations for the scalar field and the temperature and velocity profiles of the plasma, and by calculating the time-dependent bubble expansion in a SM extension with additional scalars. The slowing down of the bubble arises from terms sensitive to the dependence of the entropy on the scalar field background. These backreaction effects can be accounted for by using conservation of the stress-energy momentum tensor and incorporating the background-field-dependence of the plasma's pressure and enthalpy, which can be derived straightforwardly from the thermal corrections to the effective potential.

We have argued that the conservation of the total entropy of the equilibrated degrees of freedom implies that the fluid must heat up in a region near the bubble, which offers a natural connection with the heating effect that was pointed out in Ref. [61]. That reference analyzed bubble profiles by considering the equations in the static limit, while accounting for consistent hydrodynamic deflagration profiles away from the bubble. We have done analogous computations and found that, while the effect pointed out in Ref. [61] was assumed to be restricted to deflagrations, one can also get consistent detonation solutions with subluminal wall velocities, as expected from the results of Ref. [269].

The computations of the static wall profiles allowed us to estimate the resulting backreaction force, computed from Eq. (3.12), against the results (3.1) of Ref. [269], which excludes runaway bubbles. We found qualitative agreement up to $\mathcal{O}(1)$ effects related to the change of velocity and temperature across the wall.

In our calculations we considered a scenario in which the hypothesis of local equilibrium seems to be justified. Nevertheless, in general settings in which some species remain out of equilbrium, we expect as pointed out in Ref. [269] that the backreaction force from the equilibrated plasma will still play an important role, as the conservation of the total entropy of the degrees of freedom in equilibrium will typically require subluminal speeds. This effect should be accounted for properly in such cases.

Chapter 4

CP Violation

4.1 CP Violation and Circular Polarisation in Neutrino Radiative Decay

For decades, studies of neutrinos have deepened our understanding of nature [75]. Although their very small but non-zero masses (for at least two of their generations) and lepton flavour mixing have been observed and verified by neutrino oscillation experiments, some fundamental questions about neutrinos such as their electromagnetic properties, CP violation, whether they are Dirac or Majorana fermions and if they have additional species existing in nature remain unknown.

The studies of neutrino radiative decays dates back fourty years [272–274] and beyond. Assuming neutrinos are electrically neutral fermions (Dirac or Majorana), their electromagnetic dipole moments (EDMs) can be generated at various loop levels and neutrino radiative decays $\nu_{\mathbf{i}} \to \nu_{\mathbf{f}} + \gamma$ are induced by off-diagonal parts of the EDMs [275–280]. Charged current interaction contributions in the SM have previously been calculated at one-loop level in [275–279] and later studied in detail in [281, 282]. However, these contributions are tiny due to the large mass hierarchy between the active neutrinos and the W boson and there is currently no positive experimental indication in favour of their existence. Neutrino electromagnetic interactions therefore provide a tantalising probe for new physics (NP) beyond the SM (see [283] for a comprehensive review).

If more massive neutrinos exist, then these heavy neutrinos may decay to the lighter active neutrinos radiatively. These heavier neutrinos will consequently have a larger decay width due to the existence of such decay channels. Various hypothetical heavier neutrinos have been historically introduced, motivated by a combination of theoretical and phenomenological reasons. Some of the most famous ones are those introduced in the type-I seesaw mechanism [284–289], which was proposed in order to address the origin of sub-eV left-handed neutrino masses. Phenomenological motivations have suggested keV sterile neutrinos as dark matter (DM) candidates to explain the detection of a 3.5 keV X-ray line in [290, 291] (for some representative reviews, see [292–294]). Very heavy DM was also proposed [295, 296] in order to explain the IceCube data [297, 298]. Radiative decays of such heavy particles may be more significant than those of active neutrinos due to their very large relative mass. Hence, radiative decay is typically a major channel of importance in detecting possible keV sterile neutrino DM.

CP violation may exist in various processes involving neutrinos. At low energy, neutrino oscillations provide the best way to clarify its existence in the neutrino sector.

Combined analysis of current accelerator neutrino oscillation data [299] supports large CP violation in the appearance channel of neutrino oscillations [300, 301]. The next-generation neutrino oscillation experiments DUNE and T2HK are projected to observe CP violation in the near future [302–304]. At high energy, the most well-studied process involving CP violation is the very heavy right-handed neutrino decaying into SM leptons and the Higgs boson. This effect is the source of the so-called thermal leptogenesis phenomenon, which can explain the observed matter-antimatter asymmetry in our universe [81]. On the other hand, if these heavy neutrinos have lighter masses, specifically around the GeV scale, CP violation may appear in right-handed neutrino oscillations, which provides an alternative mechanism for leptogenesis [305] (See [306, 307] for some reviews).

In this work we study CP violation in radiative decays of both Dirac and Majorana neutrinos. Whilst neutrino radiative decays have been extensively studied for some mass regions of neutrinos, CP violation in these processes has not been studied for a more general spectrum of mass scales with very few exceptions e.g. [308]. Recently, it was suggested in [309] that a net circular polarisation, specifically an asymmetry between two circularly polarised photons γ_+ and γ_-, can be generated if CP is violated in neutrino radiative decays. Therefore, the circular polarisation of photons provides a potentially crucial probe to prove the existence of CP violation in the neutrino and DM sectors.

This work builds a formulation to describe both CP violation in neutrino radiative decays and also the resulting asymmetry between the produced photons γ_+ and γ_-. In Section 4.1.1, we outline the most general formalism of CP violation and circular polarisation in terms of form factors where the result is independent of the neutrino model or mass scale. In Section 4.1.5, we discuss CP violation based on a simplified neutrino model. We begin this section with a discussion about the size of CP asymmetry for the SM contribution and then consider how CP violation can be enhanced via new interactions. A comprehensive analytical calculation of CP asymmetry based on Yukawa type NP interactions is then performed in Section 4.1.7, this type of simple interaction has a wide ensemble of phenomenological applications which is shown in Section 4.1.8. Finally, we summarise our results in Section 4.1.12.

4.1.1 The Framework

In this section we shall set up the framework for computation of CP violation in neutrino radiative decays and the general connection with circular polarisation generated by such processes. Discussion in this section is fully independent of neutrino interactions and thus is applicable to any other electrically neutral fermion with mass at any scale.

Discussions in Section 4.1.2 and 4.1.3 assume neutrinos are Dirac fermions. The extension to Majorana neutrinos will be given in Section 4.1.4.

4.1.2 Matrix Element for Polarised Particles

Assuming fermions are Dirac particles, the amplitude for the process $\nu_{\mathbf{i}} \to \nu_{\mathbf{f}} + \gamma_\pm$ is given by

$$i\mathcal{M}(\nu_{\mathbf{i}} \to \nu_{\mathbf{f}} + \gamma_\pm) = i\bar{u}(p_{\mathbf{f}})\Gamma^\mu_{\mathbf{fi}}(q^2)u(p_{\mathbf{i}})\varepsilon^*_{\pm,\mu}(q)\,. \tag{4.1}$$

Here, $u(p_{\mathbf{i}})$ and $u(p_{\mathbf{f}})$ are spinors for the initial $\nu_{\mathbf{i}}$ and final $\nu_{\mathbf{f}}$ state neutrinos respectively. By momentum conservation, the photon momentum is $q = p_{\mathbf{i}} - p_{\mathbf{f}}$. The spinors include the spin polarisation of the fermions, this will be discussed in more detail in the next subsection in a specified inertial reference frame. The transition form factor is then parametrised as per [278–280, 310]

$$\Gamma^{\mu}_{\mathbf{fi}}(q^2) = f^{\mathrm{Q}}_{\mathbf{fi}}(q^2)\gamma^{\mu} - f^{\mathrm{M}}_{\mathbf{fi}}(q^2) i\sigma^{\mu\nu}q_{\nu} + f^{\mathrm{E}}_{\mathbf{fi}}(q^2)\sigma^{\mu\nu}q_{\nu}\gamma_5 + f^{\mathrm{A}}_{\mathbf{fi}}(q^2)(q^2\gamma^{\mu} - q^{\mu}\not{q})\gamma_5 \quad (4.2)$$

We will not consider electrically charged neutrinos, namely we require that $f^Q = 0$. The modification to the result in the case of non-zero f^Q will be mentioned at the end of this section. By requiring the photon to be on-shell $q^2 = 0$ and choosing the Lorenz gauge $q \cdot \varepsilon_p = 0$, the anapole does not contribute. In this case, only the electromagnetic dipole moment contributes to the neutrino radiative decay. We then rewrite the form factor as

$$\Gamma^{\mu}_{\mathbf{fi}}(q^2) = i\sigma^{\mu\nu}q_{\nu}[f^{\mathrm{L}}_{\mathbf{fi}}(q^2)P_{\mathrm{L}} + f^{\mathrm{R}}_{\mathbf{fi}}(q^2)P_{\mathrm{R}}]\,, \quad (4.3)$$

where $f^{\mathrm{L,R}}_{\mathbf{fi}} = -f^{\mathrm{M}}_{\mathbf{fi}} \pm i f^{\mathrm{E}}_{\mathbf{fi}}$ and the chiral projection operators are defined as $P_{\mathrm{L,R}} = \frac{1}{2}(1 \mp \gamma_5)$. The decay widths for $\nu_{\mathbf{i}} \to \nu_{\mathbf{f}} + \gamma_{\pm}$ are then given by

$$\Gamma(\nu_{\mathbf{i}} \to \nu_{\mathbf{f}} + \gamma_{\pm}) = \frac{m_{\mathbf{i}}^2 - m_{\mathbf{f}}^2}{16\pi m_{\mathbf{i}}^3}|\mathcal{M}(\nu_{\mathbf{i}} \to \nu_{\mathbf{f}} + \gamma_{\pm})|^2\,. \quad (4.4)$$

The amplitudes $\mathcal{M}(\nu_{\mathbf{i}} \to \nu_{\mathbf{f}} + \gamma_{\pm})$ are directly correlated with the coefficients

$$\begin{aligned}\mathcal{M}(\nu_{\mathbf{i}} \to \nu_{\mathbf{f}} + \gamma_{+}) &= +\sqrt{2} f^{\mathrm{L}}_{\mathbf{fi}}(m_{\mathbf{i}}^2 - m_{\mathbf{f}}^2)\,,\\ \mathcal{M}(\nu_{\mathbf{i}} \to \nu_{\mathbf{f}} + \gamma_{-}) &= -\sqrt{2} f^{\mathrm{R}}_{\mathbf{fi}}(m_{\mathbf{i}}^2 - m_{\mathbf{f}}^2)\,.\end{aligned} \quad (4.5)$$

which are derived in detail in Appendix B.1. The sum of the decay widths for $\nu_{\mathbf{i}} \to \nu_{\mathbf{f}} + \gamma_{+}$ and $\nu_{\mathbf{i}} \to \nu_{\mathbf{f}} + \gamma_{-}$ yields the total radiative decay width $\Gamma(\nu_{\mathbf{i}} \to \nu_{\mathbf{f}} + \gamma)$.

Again, if we only consider radiative decay for an electrically neutral antineutrino, the amplitudes of radiative decay $\bar{\nu}_{\mathbf{i}} \to \bar{\nu}_{\mathbf{f}} + \gamma_{\pm}$ are then given by

$$i\mathcal{M}(\bar{\nu}_{\mathbf{i}} \to \bar{\nu}_{\mathbf{f}} + \gamma_{\pm}) = i\bar{v}(p_{\mathbf{i}})\bar{\Gamma}^{\mu}_{\mathbf{if}}(q^2)v(p_{\mathbf{f}})\varepsilon^{*}_{\pm,\mu}(q)\,, \quad (4.6)$$

where $v(p_{\mathbf{i}})$ and $v(p_{\mathbf{f}})$ are antineutrino spinors. The decay width for $\bar{\nu}_{\mathbf{i}} \to \bar{\nu}_{\mathbf{f},s'} + \gamma_l$ is

$$\Gamma(\bar{\nu}_{\mathbf{i}} \to \bar{\nu}_{\mathbf{f}} + \gamma_{\pm}) = \frac{m_{\mathbf{i}}^2 - m_{\mathbf{f}}^2}{16\pi m_{\mathbf{i}}^3}|\mathcal{M}(\bar{\nu}_{\mathbf{i}} \to \bar{\nu}_{\mathbf{f}} + \gamma_{\pm})|^2\,. \quad (4.7)$$

By parametrising the form factor in a similar form to before, we have

$$\bar{\Gamma}^{\mu}_{\mathbf{if}}(q^2) = i\sigma^{\mu\nu}q_{\nu}[\bar{f}^{\mathrm{L}}_{\mathbf{if}}(q^2)P_{\mathrm{L}} + \bar{f}^{\mathrm{R}}_{\mathbf{if}}(q^2)P_{\mathrm{R}}]\,, \quad (4.8)$$

with $\bar{f}^{\mathrm{L,R}}_{\mathbf{if}} = -\bar{f}^{\mathrm{M}}_{\mathbf{if}} \pm i\bar{f}^{\mathrm{E}}_{\mathbf{if}}$. Therefore, the amplitudes can be written in a similar fashion following Eq. (4.5), i.e. by replacing $f^{\mathrm{L}}_{\mathbf{fi}}$ and $f^{\mathrm{R}}_{\mathbf{fi}}$ by $\bar{f}^{\mathrm{L}}_{\mathbf{if}}$ and $\bar{f}^{\mathrm{R}}_{\mathbf{if}}$ respectively (see the proof in Appendix (B.1)). These formulae can be further simplified with the help of the *CPT* theorem, which is satisfied in all Lorentz invariant local quantum field theories with a Hermitian Hamiltonian. Due to *CPT* invariance, $\bar{\nu}_{\mathbf{i}} \to \bar{\nu}_{\mathbf{f}} + \gamma_{\mp}$ and $\nu_{\mathbf{f}} + \gamma_{\pm} \to \nu_{\mathbf{i}}$ have the same amplitude, and thus $\bar{f}^{\mathrm{M,E}}_{\mathbf{if}}(q^2) = -f^{\mathrm{M,E}}_{\mathbf{if}}(q^2)$ is satisfied [283], leading to

$$\bar{f}^{\rm L}_{\bf if}(q^2) = -f^{\rm L}_{\bf if}(q^2)\,, \quad \bar{f}^{\rm R}_{\bf if}(q^2) = -f^{\rm R}_{\bf if}(q^2)\,. \tag{4.9}$$

Hence, amplitudes $\mathcal{M}(\bar{\nu}_{\bf i} \to \bar{\nu}_{\bf f} + \gamma_+)$ can be simplified to

$$\begin{aligned}\mathcal{M}(\bar{\nu}_{\bf i} \to \bar{\nu}_{\bf f} + \gamma_+) &= +\sqrt{2} f^{\rm L}_{\bf if}(m_{\bf i}^2 - m_{\bf f}^2)\,, \\ \mathcal{M}(\bar{\nu}_{\bf i} \to \bar{\nu}_{\bf f} + \gamma_-) &= -\sqrt{2} f^{\rm R}_{\bf if}(m_{\bf i}^2 - m_{\bf f}^2)\,.\end{aligned} \tag{4.10}$$

Physical neutrinos and antineutrinos are related by a CP transformation which interchanges particles with antiparticles and replaces momentum by its parity conjugate $\tilde{p} = (p_0, -\vec{p})$. The CP transformation reverses the momentum but preserves angular momentum. As a consequence, the polarisation is reversed. Performing a CP transformation for $\nu_{\bf i}(p_{\bf i}) \to \nu_{\bf f}(p_{\bf f}) + \gamma_\pm(q)$ gives rise to antineutrino channels with reversed 3D momentum and reversed photon polarisations in the final states $\bar{\nu}_{\bf i}(\tilde{p}_{\bf i}) \to \bar{\nu}_{\bf f}(\tilde{p}_{\bf f}) + \gamma_\mp(\tilde{q})$. Since the amplitude is parity-invariant, the amplitude of the process is equivalent to $\bar{\nu}_{\bf i}(p_{\bf i}) \to \bar{\nu}_{\bf f}(p_{\bf f}) + \gamma_\mp(q)$. Therefore, the radiative decay of antineutrinos can be represented as a CP conjugate of the decay of neutrinos

$$i\mathcal{M}(\bar{\nu}_{\bf i} \to \bar{\nu}_{\bf f} + \gamma_\pm) = i\mathcal{M}^{CP}(\nu_{\bf i} \to \nu_{\bf f} + \gamma_\mp)\,. \tag{4.11}$$

In the case of CP conservation, both $f^{\rm E}_{\bf if}(q^2)$ and $f^{\rm M}_{\bf if}(q^2)$ are Hermitian i.e. $f^{\rm M,E}_{\bf if}(q^2) = [f^{\rm M,E}_{\bf fi}(q^2)]^*$. This leads to $f^{\rm L,R}_{\bf if}(q^2) = [f^{\rm R,L}_{\bf fi}(q^2)]^*$, namely, $\bar{f}^{\rm L,R}_{\bf if}(q^2) = -[f^{\rm R,L}_{\bf fi}(q^2)]^*$ [283, 311]. And eventually, we arrive at the identity

$$\Gamma(\nu_{\bf i} \to \nu_{\bf f} + \gamma_\pm) - \Gamma(\bar{\nu}_{\bf i} \to \bar{\nu}_{\bf f} + \gamma_\mp) \propto |\mathcal{M}(\nu_{\bf i} \to \nu_{\bf f} + \gamma_\pm)|^2 - |\mathcal{M}^{CP}(\nu_{\bf i} \to \nu_{\bf f} + \gamma_\pm)|^2 = 0\,. \tag{4.12}$$

However, a CP violating source in the interaction may contribute at loop level and break this equality.

4.1.3 Correlation Between CP Asymmetry and Circular Polarisation

We define the CP asymmetry between the radiative decay $\nu_{\bf i} \to \nu_{\bf f} + \gamma_+$ and its CP conjugate process $\bar{\nu}_{\bf i} \to \bar{\nu}_{\bf f} + \gamma_-$ as

$$\Delta_{CP,+} = \frac{\Gamma(\nu_{\bf i} \to \nu_{\bf f} + \gamma_+) - \Gamma(\bar{\nu}_{\bf i} \to \bar{\nu}_{\bf f} + \gamma_-)}{\Gamma(\nu_{\bf i} \to \nu_{\bf f} + \gamma) + \Gamma(\bar{\nu}_{\bf i} \to \bar{\nu}_{\bf f} + \gamma)}\,. \tag{4.13}$$

The CP asymmetry between $\nu_{\bf i} \to \nu_{\bf f} + \gamma_-$ and its CP conjugate process $\bar{\nu}_{\bf i} \to \bar{\nu}_{\bf f} + \gamma_+$, $\Delta_{CP,-}$, is defined by exchanging $+$ and $-$ signs. The photon polarisation independent CP asymmetry is obtained by summing $\Delta_{CP,+}$ and $\Delta_{CP,-}$ together which yields

$$\Delta_{CP} = \frac{\Gamma(\nu_{\bf i} \to \nu_{\bf f} + \gamma_+) - \Gamma(\bar{\nu}_{\bf i} \to \bar{\nu}_{\bf f} + \gamma_-) + \Gamma(\nu_{\bf i} \to \nu_{\bf f} + \gamma_-) - \Gamma(\bar{\nu}_{\bf i} \to \bar{\nu}_{\bf f} + \gamma_+)}{\Gamma(\nu_{\bf i} \to \nu_{\bf f} + \gamma) + \Gamma(\bar{\nu}_{\bf i} \to \bar{\nu}_{\bf f} + \gamma)}\,. \tag{4.14}$$

It is also convenient to define the asymmetry between the radiated photons γ_+ and γ_- as

$$\Delta_{+-} = \frac{\Gamma(\nu_{\mathbf{i}} \to \nu_{\mathbf{f}} + \gamma_+) + \Gamma(\bar{\nu}_{\mathbf{i}} \to \bar{\nu}_{\mathbf{f}} + \gamma_+) - \Gamma(\nu_{\mathbf{i}} \to \nu_{\mathbf{f}} + \gamma_-) - \Gamma(\bar{\nu}_{\mathbf{i}} \to \bar{\nu}_{\mathbf{f}} + \gamma_-)}{\Gamma(\nu_{\mathbf{i}} \to \nu_{\mathbf{f}} + \gamma) + \Gamma(\bar{\nu}_{\mathbf{i}} \to \bar{\nu}_{\mathbf{f}} + \gamma)} . \tag{4.15}$$

Given equal numbers for initial neutrinos and antineutrinos, Δ_{+-} represents the fraction $(\mathrm{N}_{\gamma_+} - \mathrm{N}_{\gamma_-})/(\mathrm{N}_{\gamma_+} + \mathrm{N}_{\gamma_-})$, where N_{γ_+} and N_{γ_-} are the number of polarised photons γ_+ and γ_- produced by the radiative decays respectively. It is this source that generates circular polarisation for the radiated photons giving rise to a non-zero Stokes parameter V.

Therefore, a non-zero Δ_{+-} is a source of circular polarisation for the photon produced by the radiative decay. Since the phase spaces are the same for neutrino and antineutrino channels, these formulae can be simplified to

$$\begin{aligned}
\Delta_{CP,+} &= \frac{|f^{\mathrm{L}}_{\mathbf{fi}}|^2 - |f^{\mathrm{R}}_{\mathbf{if}}|^2}{|f^{\mathrm{L}}_{\mathbf{fi}}|^2 + |f^{\mathrm{R}}_{\mathbf{fi}}|^2 + |f^{\mathrm{R}}_{\mathbf{if}}|^2 + |f^{\mathrm{L}}_{\mathbf{if}}|^2} , \\
\Delta_{CP,-} &= \frac{|f^{\mathrm{R}}_{\mathbf{fi}}|^2 - |f^{\mathrm{L}}_{\mathbf{if}}|^2}{|f^{\mathrm{L}}_{\mathbf{fi}}|^2 + |f^{\mathrm{R}}_{\mathbf{fi}}|^2 + |f^{\mathrm{R}}_{\mathbf{if}}|^2 + |f^{\mathrm{L}}_{\mathbf{if}}|^2} ,
\end{aligned} \tag{4.16}$$

as well as

$$\begin{aligned}
\Delta_{CP} &= \frac{|f^{\mathrm{L}}_{\mathbf{fi}}|^2 + |f^{\mathrm{R}}_{\mathbf{fi}}|^2 - |f^{\mathrm{R}}_{\mathbf{if}}|^2 - |f^{\mathrm{L}}_{\mathbf{if}}|^2}{|f^{\mathrm{L}}_{\mathbf{fi}}|^2 + |f^{\mathrm{R}}_{\mathbf{fi}}|^2 + |f^{\mathrm{R}}_{\mathbf{if}}|^2 + |f^{\mathrm{L}}_{\mathbf{if}}|^2} , \\
\Delta_{+-} &= \frac{|f^{\mathrm{L}}_{\mathbf{fi}}|^2 - |f^{\mathrm{R}}_{\mathbf{fi}}|^2 - |f^{\mathrm{R}}_{\mathbf{if}}|^2 + |f^{\mathrm{L}}_{\mathbf{if}}|^2}{|f^{\mathrm{L}}_{\mathbf{fi}}|^2 + |f^{\mathrm{R}}_{\mathbf{fi}}|^2 + |f^{\mathrm{R}}_{\mathbf{if}}|^2 + |f^{\mathrm{L}}_{\mathbf{if}}|^2} .
\end{aligned} \tag{4.17}$$

The total CP asymmetry and the asymmetry between γ_+ and γ_- follows simple relations with $\Delta_{CP,+}$ and $\Delta_{CP,-}$ as

$$\begin{aligned}
\Delta_{CP} &= \Delta_{CP,+} + \Delta_{CP,-} , \\
\Delta_{+-} &= \Delta_{CP,+} - \Delta_{CP,-} .
\end{aligned} \tag{4.18}$$

Therefore, we arrive at an important result that the generation of circular polarisation is essentially dependent upon CP asymmetry between neutrino radiative decay and its CP conjugate process. Note that we have not included any details related to the Lagrangian or interactions yet. Given any neutral fermion, its radiative decay can always be parametrised by the electromagnetic dipole moments with coefficients $f^{\mathrm{L}}_{\mathbf{fi}}$ and $f^{\mathrm{R}}_{\mathbf{fi}}$ (as well as $\bar{f}^{\mathrm{L}}_{\mathbf{if}}$ and $\bar{f}^{\mathrm{R}}_{\mathbf{if}}$ for its antiparticle), we then arrive at the correlations between CP violation and circular polarisation in Eq. (4.18) with their definitions in Eqs. (4.16) and (4.17).

Another source of asymmetry between polarised photons is the existence of an initial number asymmetry between neutrinos and antineutrinos [309]. There may be some other CP violating sources in particle physics which can induce this condition [312]. On the other hand, this kind of asymmetry is more likely to be generated in extreme astrophysical environments. For example, in supernovae explosions, the asymmetry between sterile neutrinos and antineutrinos may be generated because of the different matter effects during neutrino and antineutrino propagation [313, 314].

In the rest of this section, we will only consider circular polarisation directly produced by the CP violating decays between neutrinos and antineutrinos.

Now we may turn our attention to obtaining non-zero CP violation for the radiative decay. For $\nu_{\mathbf{i}} \to \nu_{\mathbf{f}} + \gamma_+$ and $\nu_{\mathbf{i}} \to \nu_{\mathbf{f}} + \gamma_-$, we parametrise the effective coefficients $f^{\rm L}_{\mathbf{fi}}$ and $f^{\rm R}_{\mathbf{fi}}$, these should be obtained from the relevant loop calculations in the form

$$f^{\rm L}_{\mathbf{fi}} = \sum_l C_l K^{\rm L}_l \,, \quad f^{\rm R}_{\mathbf{fi}} = \sum_l C_l K^{\rm R}_l , \tag{4.19}$$

without loss of generality. Here, we have used l to classify the different categories of loop contributions. For each loop category l, C_l factorises out all coefficients of operators contributing to the diagram. $K^{\rm L}_l$ and $K^{\rm R}_l$ represents the pure loop kinematics after coefficients are extracted out. As a consequence, $\bar{f}^{\rm L}_{\mathbf{if}}$ and $\bar{f}^{\rm R}_{\mathbf{if}}$ (namely $-f^{\rm L}_{\mathbf{if}}$ and $-f^{\rm R}_{\mathbf{if}}$) corresponding to the effective parameters for $\bar{\nu}_{\mathbf{i}} \to \bar{\nu}_{\mathbf{f}} + \gamma_\pm$, can always be represented in the form [1]

$$f^{\rm L}_{\mathbf{if}} = \sum_l C^*_l K^{\rm R}_l \,, \quad f^{\rm R}_{\mathbf{if}} = \sum_l C^*_l K^{\rm L}_l \,. \tag{4.20}$$

The CP asymmetries with respect to the photon polarisations can then be simplified to

$$\begin{aligned}
\Delta_{CP,+} \propto |f^{\rm L}_{\mathbf{fi}}| - |\bar{f}^{\rm R}_{\mathbf{if}}| &= -4 \sum_{l \neq l'} {\rm Im}(C_l C^*_{l'}) {\rm Im}(K^{\rm L}_l K^{\rm L}_{l'}{}^*) \,, \\
\Delta_{CP,-} \propto |f^{\rm R}_{\mathbf{fi}}| - |\bar{f}^{\rm L}_{\mathbf{if}}| &= -4 \sum_{l \neq l'} {\rm Im}(C_l C^*_{l'}) {\rm Im}(K^{\rm R}_l K^{\rm R}_{l'}{}^*) \,.
\end{aligned} \tag{4.21}$$

Therefore, a non-zero CP asymmetry is determined by non-vanishing ${\rm Im}(C_l C^*_{l'})$ and non-vanishing ${\rm Im}(K^{\rm L}_l K^{\rm L}_{l'}{}^*)$ (or ${\rm Im}(K^{\rm R}_l K^{\rm R}_{l'}{}^*)$) from loops l and l'.

While the imaginary part of ${\rm Im}(C_l C^*_{l'})$ is straightforwardly obtained from the relevant terms in the Lagrangian, the main task is to compute the imaginary parts of $K^{\rm L}_l K^{\rm L}_{l'}{}^*$ and $K^{\rm R}_l K^{\rm L}_{l'}{}^*$. In order to achieve non-zero values of these imaginary parts, one may apply the optical theorem which can be expressed as

$${\rm Im}\mathcal{M}(a \to b) = \frac{1}{2} \sum_c \int d\Pi_c \, \mathcal{M}^*(b \to c) \mathcal{M}(a \to c) \,, \tag{4.22}$$

where the sum runs over all possible sets c of final-state particles [315]. Fixing $a = \nu_{\mathbf{i}}$ and $b = \nu_{\mathbf{f}} + \gamma$, c has to include an odd number of fermions plus arbitrary bosons. All particles heavier than $\nu_{\mathbf{i}}$ cannot be included in c since this would violate energy-momentum conservation. In the next section, we will explicitly show how to derive

[1] To clarify how this parametrisation is valid, we write out the subscripts explicitly, $f^{\rm L}_{\mathbf{fi}} = \sum_l (C_l)_{\mathbf{fi}} (K^{\rm L}_l)_{\mathbf{fi}}$ and $f^{\rm R}_{\mathbf{fi}} = \sum_l (C_l)_{\mathbf{fi}} (K^{\rm R}_l)_{\mathbf{fi}}$. Similarly, we can write out $f^{\rm L}_{\mathbf{if}} = \sum_l (C_l)_{\mathbf{if}} (K^{\rm L}_l)_{\mathbf{if}}$ and $f^{\rm R}_{\mathbf{if}} = \sum_l (C_l)_{\mathbf{if}} (K^{\rm R}_l)_{\mathbf{if}}$. One can simplify $f^{\rm L}_{\mathbf{if}}$ and $f^{\rm R}_{\mathbf{if}}$ in the following steps. 1) The coefficient $(C_l)_{\mathbf{if}}$ must be the complex conjugate of $(C_l)_{\mathbf{fi}}$ since both processes are CP conjugates of one another. 2) $(K^{\rm L}_l)_{\mathbf{if}}$ and $(K^{\rm R}_l)_{\mathbf{if}}$, as pure kinetic terms, must satisfy T parity, namely they must be invariant under the interchange of the initial and final state neutrinos $\nu_{\mathbf{i}} \leftrightarrow \nu_{\mathbf{f}}$, the chiralities must also be interchanged L $\leftrightarrow$ R, namely, $(K^{\rm L}_l)_{\mathbf{if}} = (K^{\rm R}_l)_{\mathbf{fi}}$ and $(K^{\rm R}_l)_{\mathbf{if}} = (K^{\rm L}_l)_{\mathbf{fi}}$. Therefore, $f^{\rm L}_{\mathbf{if}}$ and $f^{\rm R}_{\mathbf{if}}$ can be re-written to be $f^{\rm L}_{\mathbf{if}} = \sum_l (C_l)^*_{\mathbf{fi}} (K^{\rm R}_l)_{\mathbf{fi}}$ and $f^{\rm R}_{\mathbf{if}} = \sum_l (C_l)^*_{\mathbf{fi}} (K^{\rm L}_l)_{\mathbf{fi}}$.

a non-zero analytical result for $\mathrm{Im}(K_l^{\mathrm{R}} K_{l'}^{\mathrm{R}\,*})$ based on a simplified NP model where $\mathrm{Im}(K_l^{\mathrm{L}} K_{l'}^{\mathrm{L}\,*})$ is negligibly small.

4.1.4 *CP* Violation in Majorana Neutrino Radiative Decay

The above discussion is only limited to Dirac neutrinos. However, neutrinos may also be Majorana particles i.e. where the neutrino is identical to the antineutrino but with potentially different kinematics. In this case, both the neutrino and antineutrino modes must be considered together. The amplitude is then given by $i\mathcal{M}^{\mathrm{M}}(\nu_{\mathbf{i}} \to \nu_{\mathbf{f}} + \gamma_\pm) = i\mathcal{M}(\nu_{\mathbf{i}} \to \nu_{\mathbf{f}} + \gamma_\pm) + i\mathcal{M}(\bar{\nu}_{\mathbf{i}} \to \bar{\nu}_{\mathbf{f}} + \gamma_\pm)$. Taking the explicit formulas for the amplitudes given in Eq (4.5) and (4.10), we obtain results with definite spins in the initial and final states as

$$\begin{aligned} \mathcal{M}^{\mathrm{M}}(\nu_{\mathbf{i}} \to \nu_{\mathbf{f}} + \gamma_+) &= +\sqrt{2}[f_{\mathbf{fi}}^{\mathrm{L}} - f_{\mathbf{if}}^{\mathrm{L}}](m_{\mathbf{i}}^2 - m_{\mathbf{f}}^2)\,, \\ \mathcal{M}^{\mathrm{M}}(\nu_{\mathbf{i}} \to \nu_{\mathbf{f}} + \gamma_-) &= -\sqrt{2}[f_{\mathbf{fi}}^{\mathrm{R}} - f_{\mathbf{if}}^{\mathrm{R}}](m_{\mathbf{i}}^2 - m_{\mathbf{f}}^2)\,, \end{aligned} \tag{4.23}$$

The decay width $\Gamma^{\mathrm{M}}(\nu_{\mathbf{i}} \to \nu_{\mathbf{f}} + \gamma_\pm)$ is still written in the form shown in Eq. (4.4).

For Majorana fermions, the *CP* violation is identical to that obtained from *P* violation alone i.e. the *CP* asymmetry is essentially the same as the asymmetry between the two polarised photons Δ_{+-}^{M}

$$\Delta_{CP,+}^{\mathrm{M}} = -\Delta_{CP,-}^{\mathrm{M}} = \Delta_{+-}^{\mathrm{M}} = \frac{\Gamma^{\mathrm{M}}(\nu_{\mathbf{i}} \to \nu_{\mathbf{f}} + \gamma_+) - \Gamma^{\mathrm{M}}(\nu_{\mathbf{i}} \to \nu_{\mathbf{f}} + \gamma_-)}{\Gamma^{\mathrm{M}}(\nu_{\mathbf{i}} \to \nu_{\mathbf{f}} + \gamma)}\,. \tag{4.24}$$

The *CP* asymmetry without considering the polarisation of the radiated photon is zero, namely, $\Delta_{CP}^{\mathrm{M}} = \Delta_{CP,+}^{\mathrm{M}} + \Delta_{CP,-}^{\mathrm{M}} = 0$. With the help of Eq. (4.23), we can express Δ_{+-}^{M} in the form of electromagnetc dipole parameters as

$$\Delta_{+-}^{\mathrm{M}} = \frac{|f_{\mathbf{fi}}^{\mathrm{L}} - f_{\mathbf{if}}^{\mathrm{L}}|^2 - |f_{\mathbf{fi}}^{\mathrm{R}} - f_{\mathbf{if}}^{\mathrm{R}}|^2}{|f_{\mathbf{fi}}^{\mathrm{L}} - f_{\mathbf{if}}^{\mathrm{L}}|^2 + |f_{\mathbf{fi}}^{\mathrm{R}} - f_{\mathbf{if}}^{\mathrm{R}}|^2}\,. \tag{4.25}$$

We will not discuss the Majorana case further here since the asymmetries are similarly straightforward to obtain once coefficients of the transition dipole moment are ascertained.

At the end of this section, we comment on *CP* violation in electrically charged neutrino decay. In this scenario, the magnitudes of the neutrino and antineutrino decay modes are modified to

$$\begin{aligned} \mathcal{M}(\nu_{\mathbf{i}} \to \nu_{\mathbf{f}} + \gamma_+) &= +\sqrt{2} f_{\mathbf{fi}}^{\mathrm{L}}(m_{\mathbf{i}}^2 - m_{\mathbf{f}}^2) - \sqrt{2} f_{\mathbf{fi}}^{Q}(m_{\mathbf{i}} - m_{\mathbf{f}})\,, \\ \mathcal{M}(\nu_{\mathbf{i}} \to \nu_{\mathbf{f}} + \gamma_-) &= -\sqrt{2} f_{\mathbf{fi}}^{\mathrm{R}}(m_{\mathbf{i}}^2 - m_{\mathbf{f}}^2) + \sqrt{2} f_{\mathbf{fi}}^{Q}(m_{\mathbf{i}} - m_{\mathbf{f}})\,, \\ \mathcal{M}(\bar{\nu}_{\mathbf{i}} \to \bar{\nu}_{\mathbf{f}} + \gamma_+) &= +\sqrt{2} f_{\mathbf{if}}^{\mathrm{L}}(m_{\mathbf{i}}^2 - m_{\mathbf{f}}^2) - \sqrt{2} f_{\mathbf{if}}^{Q}(m_{\mathbf{i}} - m_{\mathbf{f}})\,, \\ \mathcal{M}(\bar{\nu}_{\mathbf{i}} \to \bar{\nu}_{\mathbf{f}} + \gamma_-) &= -\sqrt{2} f_{\mathbf{if}}^{\mathrm{R}}(m_{\mathbf{i}}^2 - m_{\mathbf{f}}^2) + \sqrt{2} f_{\mathbf{if}}^{Q}(m_{\mathbf{i}} - m_{\mathbf{f}})\,, \end{aligned} \tag{4.26}$$

where, according to the CPT theorem, $\bar{f}_{\mathbf{if}}^{Q} = -f_{\mathbf{if}}^{Q}$ has been used. The modified amplitudes are equivalent to shifting coefficients f^{L} and f^{R} in Eqs. (4.5) and (4.10) to $f^{\mathrm{L}\prime} = f^{\mathrm{L}} - f^{Q}/(m_{\mathbf{i}} + m_{\mathbf{f}})$ and $f^{\mathrm{R}\prime} = f^{\mathrm{R}} - f^{Q}/(m_{\mathbf{i}} + m_{\mathbf{f}})$ respectively. *CP* asymmetries $\Delta_{CP,+}$, $\Delta_{CP,-}$, Δ_{CP} and the asymmetry between polarised photons Δ_{+-}

(Dirac neutrino), as well as $\Delta^{\rm M}_{+-}$ (Majorana neutrino), are obtained following the same coefficient shifts.

4.1.5 Calculating CP Violation in Radiative Decay

Having provided a very general discussion on CP violation and circular polarisation for neutrino radiative decay in a mass scale and model independent way in the previous section, in the following sections, we will concentrate on a simplified example where a sterile neutrino radiatively decays $\nu_s \to \nu_i + \gamma$ and show how to obtain the exact form of the CP asymmetry and circular polarisation for the radiated photon. In this example, the initial and final state neutrinos are specified as $\nu_{\bf i} = \nu_s$ and $\nu_{\bf f} = \nu_i$ respectively. In this simplified case, we consider only one sterile neutrino generation and the three active neutrino generations with both ν_s and ν_i (for $i = 1, 2, 3$) being mass eigenstates. Extensions to multiple sterile neutrino generations are straightforward, and thus, will not be discussed here.

We will apply the above formulation in the following way. First, we estimate the size of CP violation from the SM contribution alone i.e. via the charged current interaction mediated by the W boson. Then, we consider the enhancement of CP violation by including NP Yukawa interactions for sterile neutrinos. Such Yukawa interactions have a wide array of applications with theoretical and phenomenological utility which we will outline in the following section. Finally, we list the simplified analytical result for CP violation and circular polarisation generated from the decay at the end of this section.

4.1.6 The Standard Model Contribution

It is well known that the radiative decay can happen via one-loop corrections induced by SM weak interactions with SM particles (specifically with charged lepton ℓ_α for $\alpha = e, \mu, \tau$ and the W boson) in the loop. The crucial operator is the charged-current interaction is

$$\mathcal{L}_{\rm c.c.} = \sum_{\alpha=e,\mu,\tau} \sum_{m=1,2,3,s} \frac{g}{\sqrt{2}} U_{\alpha m}\, \bar{\ell}_\alpha \gamma^\mu P_{\rm L} \nu_m W^-_\mu + {\rm h.c.}\,, \tag{4.27}$$

where g is the EW gauge coupling constant and $U_{\alpha m}$ represent the lepton flavour mixing. Here we have $m = i, s$ (where $i = 1, 2, 3$) representing the active light neutrino mass eigenstate ν_i and the sterile neutrino mass eigenstate ν_s.

The one-loop Feynman diagrams for the radiative decay via the SM charged current interaction are shown in Figure 4.1.[2] In the limit $m_s^2/m_W^2 \ll a_\alpha \equiv m_\alpha^2/m_W^2$, where m_α and m_W are the charged lepton and W boson masses respectively, we have the result for $\Gamma^\mu_{\bf fi}$ given as

$$\Gamma^\mu_{is} = \frac{ieG_{\rm F}\sigma^{\mu\nu}q_\nu}{4\pi^2\sqrt{2}} \sum_{\alpha=e,\mu,\tau} U^*_{\alpha i} U_{\alpha s} F_\alpha (m_s P_{\rm R} + m_i P_{\rm L})\,, \tag{4.28}$$

[2]In the Feynman gauge, additional diagrams involving unphysical Goldstone bosons and ghosts should also be included, note that these are not shown in the figure. In addition, the one-loop $\gamma - Z$ self-energy diagrams are essential to include to eliminate divergences in the presence of the sterile neutrino [316].

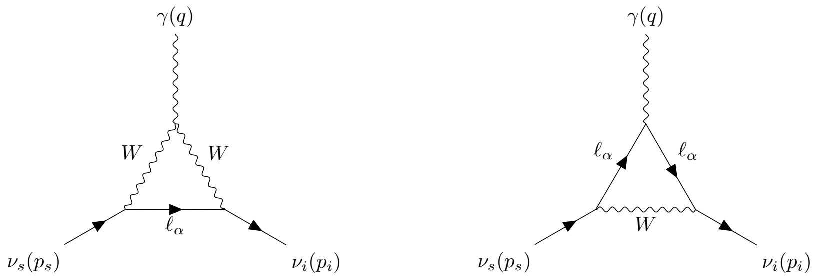

FIGURE 4.1: The Feynman diagrams for the one-loop Standard Model contributions from charged current interactions are shown above for radiative decay of a sterile neutrino. Diagrams involving unphysical Goldstone bosons and ghosts are omitted for the sake of brevity.

where F_α is a function obtained from the loop integrals and the Fermi constant is defined $G_{\rm F} = \dfrac{g^2}{4\sqrt{2}m_W^2}$. If $m_{\bf i}$ is much smaller than the charged lepton masses, we arrive at the classic result [276, 278]

$$F_\alpha = \frac{3}{4}\left(\frac{2-a_\alpha}{1-a_\alpha} - \frac{2a_\alpha}{(1-a_\alpha)^2} - \frac{2a_\alpha^2 \ln a_\alpha}{(1-a_\alpha)^3}\right) \approx \frac{3}{2} - \frac{3}{4}a_\alpha\,, \tag{4.29}$$

which is insensitive to neutrino masses. A more general neutrino mass-dependent result for F_α with $m_{\bf i}$, $m_{\bf f}$ up to the W boson mass has been given in [281, 282]. In general, for $m_{\bf i} < m_W$, F_α is always positive, this is consistent with the optical theorem.

From the above formulae, we obtain results for $f^{\rm L}_{\bf fi}$ and $f^{\rm R}_{\bf fi}$ given as

$$f^{\rm L}_{is} = e\frac{g^2}{2}\frac{1}{16\pi^2 m_W^2}\sum_{\alpha=e,\mu,\tau} U^*_{\alpha i}U_{\alpha s}F_\alpha m_i\,,\quad f^{\rm R}_{is} = e\frac{g^2}{2}\frac{1}{16\pi^2 m_W^2}\sum_{\alpha=e,\mu,\tau} U^*_{\alpha i}U_{\alpha s}F_\alpha m_s\,, \tag{4.30}$$

factorising the SM contribution into a coefficient part and a purely kinetic part yields

$$f^{\rm L}_{\bf fi,SM} = \sum_\alpha C_\alpha K^{\rm L}_\alpha\,,\quad f^{\rm R}_{\bf fi,SM} = \sum_\alpha C_\alpha K^{\rm R}_\alpha \tag{4.31}$$

with

$$(C_\alpha)_{is} \;=\; e\frac{g^2}{2}U^*_{\alpha i}U_{\alpha s}\,, \tag{4.32}$$

and

$$(K^{\rm L}_\alpha)_{is} = \frac{1}{16\pi^2 m_W^2}F_\alpha m_i\,,\quad (K^{\rm R}_\alpha)_{is} = \frac{1}{16\pi^2 m_W^2}F_\alpha m_s\,, \tag{4.33}$$

with flavour index $\alpha = e,\mu,\tau$. Since F_α is real, both ${\rm Im}(K^{\rm L}_\alpha K^{\rm L\,*}_\beta)$ and ${\rm Im}(K^{\rm R}_\alpha K^{\rm R\,*}_\beta)$ vanish for any flacours $\alpha,\beta = e,\mu,\tau$. In addition, by interchanging $i \leftrightarrow s$ we notice that the one-loop SM contribution exactly satisfies $f^{\rm L}_{\bf fi} = \bar{f}^{\rm R}_{\bf if}$ and $f^{\rm R}_{\bf fi} = \bar{f}^{\rm L}_{\bf if}$. Therefore, there is no CP violation coming from these diagrams.

For a sterile neutrino with mass smaller than the W boson mass, we comment that a non-zero CP violation can in principle be obtained after considering higher-loop SM contributions. We analyse this by applying the optical theorem once again. In order to generate an imaginary part for the kinetic loop contribution, the requirement of on-shell intermediate states has to be satisfied. Thus only neutrinos and photons are left in the intermediate state c. There are typically three cases with intermediate states given by (a) $c = \nu_j + \gamma$,[3] (b) $\nu_j + \nu_k + \bar{\nu}_k$, and (c) $\nu_j + \alpha + \bar{\alpha}$ for $\alpha = e, \mu, \tau$. They correspond to four-, three- and two-loop diagrams respectively. Case (c) applies only if $m_s > 2m_\alpha$, these contributions are in general very small. In order to obtain large CP violation, additional loop contributions from NP have to be considered.

Namely, if the sterile neutrino is heavier than the W boson, an imaginary part can be obtained directly from the SM one-loop diagram, we will discuss this case in some of the following sections.

4.1.7 Enhancement by New Physics

In order to enhance the CP violation in the radiative decay of the sterile neutrino, we include NP contributions. We being by introducing two new particles, one fermion ψ and one scalar ϕ with opposite electric charges Q and $-Q$ respectively. Their couplings with neutrinos and the sterile neutrino are described by the following Yukawa interaction

$$-\mathcal{L}_{\mathrm{NP}} \supset \sum_{m=1,2,3,s} \lambda_m \bar{\psi} \phi^* P_{\mathrm{L}} \nu_m + \lambda_m^* \bar{\nu}_m \phi P_{\mathrm{R}} \psi \,, \tag{4.34}$$

where λ_m, with $m = i, s$ (for $i = 1, 2, 3$), are complex coefficients to ν_i and ν_s, which are the active and sterile neutrino mass eigenstates respectively. Here, we only included one generation of ϕ and ψ respectively. The extension to more generations is straightforward and will be mentioned as necessary. Neither ψ or ϕ are supposed to be a specific DM candidate in this work and they can annihilate with their antiparticles due to their opposite electric charges.

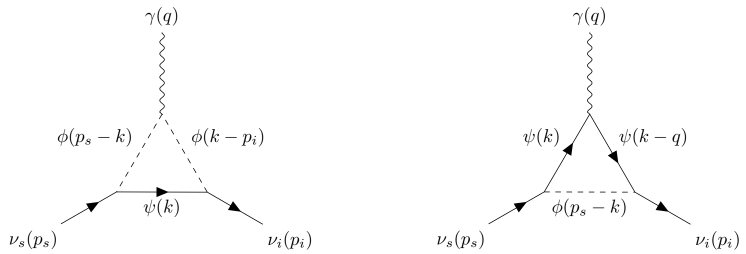

FIGURE 4.2: Feynman diagrams for the new physics one-loop contributions to the radiative decay of a sterile neutrino. We denote amplitudes for the two diagrams as $\mathcal{M}_1^{\mathrm{NP}}$ and $\mathcal{M}_2^{\mathrm{NP}}$. For $\mathcal{M}_1^{\mathrm{NP}}$ we make the momenta assignments $p_1 = p_s - k$, $p_2 = k - p_i$ and for $\mathcal{M}_2^{\mathrm{NP}}$, we assign $k' = k - q$. In both diagrams $p_s = p_i + q$.

[3] CP violation for this case has been calculated in [308]

The full amplitude including the NP contribution for $\nu_s \to \nu_i + \gamma$ can then be written

$$\mathcal{M} = \sum_{\alpha} \mathcal{M}_{\alpha}^{\rm SM} + \sum_{l_{\rm NP}} \mathcal{M}_{l_{\rm NP}}^{\rm NP}\,, \tag{4.35}$$

where we have flavour index $\alpha = e, \mu, \tau$ and $l_{\rm NP}$ represents one-loop NP contributions. Since $U(1)_Q$ is explicitly conserved and no electric charges are assigned for neutrinos at tree level, they keep free of electric charges after loop corrections are included. Thus, radiative decays are induced only via the electromagnetic transition dipole moments. The coefficients $f_{\bf fi}^{\rm L}$, $f_{\bf fi}^{\rm R}$ and $f_{\bf if}^{\rm L}$, $f_{\bf if}^{\rm R}$, including NP, are now written as

$$\begin{aligned} f_{\bf fi}^{\rm L} &= \sum_{\alpha} C_\alpha K_\alpha^{\rm L} + \sum_{l_{\rm NP}} C_{l_{\rm NP}} K_{l_{\rm NP}}^{\rm L}\,, \qquad & f_{\bf fi}^{\rm R} &= \sum_{\alpha} C_\alpha K_\alpha^{\rm R} + \sum_{l_{\rm NP}} C_{l_{\rm NP}} K_{l_{\rm NP}}^{\rm R}\,, \\ f_{\bf if}^{\rm L} &= \sum_{\alpha} C_\alpha K_\alpha^{\rm R} + \sum_{l_{\rm NP}} C_{l_{\rm NP}} K_{l_{\rm NP}}^{\rm R}\,, \qquad & f_{\bf if}^{\rm R} &= \sum_{\alpha} C_\alpha K_\alpha^{\rm L} + \sum_{l_{\rm NP}} C_{l_{\rm NP}} K_{l_{\rm NP}}^{\rm L}\,. \end{aligned} \tag{4.36}$$

From Eq. (4.36), we have the necessary expressions to compute the CP violation and asymmetry between the radiated photons γ_+ and γ_-. As an example, we take $\Delta_{CP,-}$ to demonstrate an explicit calculation. The definition of $\Delta_{CP,-}$ has been given in Eq. (4.16) where $\Delta_{CP,-} \propto |f_{\bf fi}^{\rm R}|^2 - |f_{\bf if}^{\rm L}|^2$. With the help of the parametrisation in Eq. (4.36) and assuming $|K_l^{\rm R}| = |\bar{K}_l^{\rm L}|$ for any loop l, we obtain

$$|f_{\bf fi}^{\rm R}|^2 - |f_{\bf if}^{\rm L}|^2 = -4 \sum_{\alpha, l_{\rm NP}} {\rm Im}(C_\alpha C_{l_{\rm NP}}^*) {\rm Im}(K_\alpha^{\rm R} K_{l_{\rm NP}}^{{\rm R}\,*}) - 2 \sum_{l_{\rm NP} \neq l'_{\rm NP}} {\rm Im}(C_{l_{\rm NP}} C_{l'_{\rm NP}}^*) {\rm Im}(K_{l_{\rm NP}}^{\rm R} K_{l'_{\rm NP}}^{{\rm R}\,*}). \tag{4.37}$$

For the two NP diagrams shown in Figure 4.2, where a photon is radiated via the interaction between scalars ϕ and fermions ψ respectively, the amplitudes can be explicitly written as

$$\begin{aligned} i\mathcal{M}_1^{\rm NP} &= -Qe\lambda_s\lambda_i^* \int \frac{d^4k}{(2\pi)^4} \frac{\overline{u}(p_i) P_{\rm R} (\not{k} + m_\psi)(p_1 - p_2)^\mu P_{\rm L} u(p_s) \varepsilon_{-,\mu}^*(q)}{(k^2 - m_\psi^2 + i\epsilon)((k - p_s)^2 - m_\phi^2 + i\epsilon)((k - p_i)^2 - m_\phi^2 + i\epsilon)}\,, \\ i\mathcal{M}_2^{\rm NP} &= +Qe\lambda_s\lambda_i^* \int \frac{d^4k}{(2\pi)^4} \frac{\overline{u}(p_i) P_{\rm R} (\not{k}' + m_\psi)\gamma^\mu (\not{k} + m_\psi) P_{\rm L} u(p_s) \varepsilon_{-,\mu}^*(q)}{((k - p_s)^2 - m_\phi^2 + i\epsilon)(k'^2 - m_\psi^2 + i\epsilon)(k^2 - m_\psi^2 + i\epsilon)}\,. \end{aligned} \tag{4.38}$$

The coefficients $C_{l_{\rm NP}}$ (for $l_{\rm NP} = 1, 2$) are then simply obtained from inspection to be

$$C_1 \;=\; -C_2 = -Qe\lambda_s\lambda_i^*\,. \tag{4.39}$$

In this case, ${\rm Im}(C_1 C_2^*) = 0$ and the second part of Eq. (4.37) vanishes. On the other hand the imaginary part is given by

$${\rm Im}(C_\alpha C_1^*) = -{\rm Im}(C_\alpha C_2^*) = -\frac{Q}{2} e^2 g^2\, {\rm Im}(U_{\alpha s} U_{\alpha i}^* \lambda_i \lambda_s^*)\,. \tag{4.40}$$

We now turn to the loop contributions. $\mathrm{Im}(K_1^{\mathrm{R}} K_2^{\mathrm{R}*})$ does not need to be calculated since $\mathrm{Im}(C_1 C_2^*)$ vanishes explicitly. Hence, the remaining term to be computed is $\mathrm{Im}(K_\alpha^{\mathrm{R}} K_{l_{\mathrm{NP}}}^{\mathrm{R}*})$. Furthermore, since the SM contributions are always real, $\mathrm{Im}(K_\alpha^{\mathrm{R}} K_{l_{\mathrm{NP}}}^{\mathrm{R}*}) = -K_\alpha^{\mathrm{R}} \mathrm{Im}(K_{l_{\mathrm{NP}}}^{\mathrm{R}})$.

In order to obtain CP violation between the radiative decay $\nu_s \to \nu_i + \gamma_-$ and its CP conjugate channel $\bar{\nu}_s \to \bar{\nu}_i + \gamma_+$ for a Dirac-type sterile neutrino, a non-vanishing imaginary part $\mathrm{Im}(K_{l_{\mathrm{NP}}}^{\mathrm{R}})$ is required, this can be summarised

$$|f_{\mathbf{fi}}^{\mathrm{R}}|^2 - |f_{\mathbf{if}}^{\mathrm{L}}|^2 = +4 \sum_{\alpha, l_{\mathrm{NP}}} \mathrm{Im}(C_\alpha C_{l_{\mathrm{NP}}}^*) K_\alpha^{\mathrm{R}} \mathrm{Im}(K_{l_{\mathrm{NP}}}^{\mathrm{R}}) \,. \tag{4.41}$$

Following a similar approach to determine CP violation between $\nu_s \to \nu_i + \gamma_+$ and its CP conjugate process $\bar{\nu}_s \to \bar{\nu}_i + \gamma_-$, we obtain

$$|f_{\mathbf{fi}}^{\mathrm{L}}|^2 - |f_{\mathbf{if}}^{\mathrm{R}}|^2 = +4 \sum_{\alpha, l_{\mathrm{NP}}} \mathrm{Im}(C_\alpha C_{l_{\mathrm{NP}}}^*) K_\alpha^{\mathrm{L}} \mathrm{Im}(K_{l_{\mathrm{NP}}}^{\mathrm{L}}) \,. \tag{4.42}$$

Due to the optical theorem, non-zero $\mathrm{Im}(K_{l_{\mathrm{NP}}}^{\mathrm{L}})$ and $\mathrm{Im}(K_{l_{\mathrm{NP}}}^{\mathrm{R}})$ can only be achieved if the sterile neutrino mass is larger than the sum of the charged scalar and the charged fermion masses, $m_s > m_\phi + m_\psi$. In the remainder of this section, our aim will be to compute these quantities.

Here, the loop integrals for the relevant diagrams shown in Figure 4.2 will be calculated. Starting from the general form of the amplitude for sterile neutrino radiative decay $\nu_s \to \nu_i + \gamma_\pm$ given in Eq. (4.1), we extract the purely kinetic terms $K_{l_{\mathrm{NP}}}^{\mathrm{L}}$ and $K_{l_{\mathrm{NP}}}^{\mathrm{R}}$ for $l_{\mathrm{NP}} = 1, 2$ as [4]

$$\begin{aligned}
K_1^{\mathrm{L}} &= \frac{m_i}{16\pi^2} \int_0^1 \mathrm{d}x \mathrm{d}y \mathrm{d}z \frac{\delta(x+y+z-1)\, z}{\Delta_{\phi\psi}(x,y,z)} \,, \\
K_1^{\mathrm{R}} &= \frac{m_s}{16\pi^2} \int_0^1 \mathrm{d}x \mathrm{d}y \mathrm{d}z \frac{\delta(x+y+z-1)\, y}{\Delta_{\phi\psi}(x,y,z)} \,, \\
K_2^{\mathrm{L}} &= \frac{m_i}{16\pi^2} \int_0^1 \mathrm{d}x \mathrm{d}y \mathrm{d}z \frac{\delta(x+y+z-1)\, xz}{\Delta_{\psi\phi}(x,y,z)} \,, \\
K_2^{\mathrm{R}} &= \frac{m_s}{16\pi^2} \int_0^1 \mathrm{d}x \mathrm{d}y \mathrm{d}z \frac{\delta(x+y+z-1)\, xy}{\Delta_{\psi\phi}(x,y,z)} \,,
\end{aligned} \tag{4.43}$$

where

$$\begin{aligned}
\Delta_{\phi\psi}(x,y,z) &= m_\phi^2(1-x) + x m_\psi^2 - x(y m_s^2 + z m_i^2) \\
\Delta_{\psi\phi}(x,y,z) &= m_\psi^2(1-x) + x m_\phi^2 - x(y m_s^2 + z m_i^2) \,.
\end{aligned} \tag{4.44}$$

The above results are obtained without any approximations. In order to derive further simplified analytical formulae, we consider the large mass hierarchy between ν_s and ν_i where $m_i \ll m_s$, and may therefore take the limit $m_i \to 0$. In this case, $K_{l_{\mathrm{NP}}}^{\mathrm{L}} = 0$

[4] Here, $K_{l_{\mathrm{NP}}}^{\mathrm{L}}$ and $K_{l_{\mathrm{NP}}}^{\mathrm{R}}$ represent $(K_{l_{\mathrm{NP}}}^{\mathrm{L}})_{is}$ and $(K_{l_{\mathrm{NP}}}^{\mathrm{R}})_{is}$, respectively. Exchanging i with s, we obtain $(K_{l_{\mathrm{NP}}}^{\mathrm{L}})_{si} = (K_{l_{\mathrm{NP}}}^{\mathrm{R}})_{is}$ and $(K_{l_{\mathrm{NP}}}^{\mathrm{R}})_{si} = 0$, this is compatible with our previous statement that $(K_l^{\mathrm{L}})_{\mathbf{if}} = (K_l^{\mathrm{R}})_{\mathbf{fi}}$ and $(K_l^{\mathrm{R}})_{\mathbf{if}} = (K_l^{\mathrm{L}})_{\mathbf{fi}}$.

and after integrating over Feynman parameters z and x, $K^{\mathrm{R}}_{l_{\mathrm{NP}}}$ can be written as

$$K^{\mathrm{R}}_1 = \frac{m_s}{16\pi^2}\int_0^1 \mathrm{d}y \frac{y}{m_s^2 y - m_\psi^2 + m_\phi^2}\log\left(\frac{\Delta_{\phi\psi}(y)}{m_\phi^2}\right),$$
$$K^{\mathrm{R}}_2 = \frac{m_s}{16\pi^2}\left[\int_0^1 \mathrm{d}y \frac{-m_\psi^2 y}{(m_s^2 y + m_\psi^2 - m_\phi^2)^2}\log\left(\frac{\Delta_{\psi\phi}(y)}{m_\psi^2}\right) + \int_0^1 \mathrm{d}y \frac{y(y-1)}{m_s^2 y + m_\psi^2 - m_\phi^2}\right], \tag{4.45}$$

where

$$\begin{aligned}\Delta_{\phi\psi}(y) &= y\left(m_s^2(y-1) + m_\phi^2\right) - m_\psi^2(y-1)\,,\\ \Delta_{\psi\phi}(y) &= y\left(m_s^2(y-1) + m_\psi^2\right) - m_\phi^2(y-1)\,.\end{aligned} \tag{4.46}$$

$K^{\mathrm{R}}_{l_{\mathrm{NP}}}$ may have both real parts and imaginary parts. The real part $\mathrm{Re}(K^{\mathrm{R}}_{l_{\mathrm{NP}}})$ is directly obtained by replacing $\Delta_{\phi\psi}$ and $\Delta_{\psi\phi}$ with there absolute values, therefore simple analytical expressions for $\mathrm{Re}(K^{\mathrm{R}}_{l_{\mathrm{NP}}})$ are difficult to obtain. However, in the hierarchical case $m_s \gg m_\phi, m_\psi$ approximate analytical expressions can be derived by expanding in powers of m_ϕ^2/m_s^2 and m_ψ^2/m_s^2. Specifically, the leading-order results are given by

$$\begin{aligned}\mathrm{Re}(K^{\mathrm{R}}_1) &\approx \frac{1}{16\pi^2 m_s}\left[\log\left(\frac{m_s^2}{m_\phi^2}\right) - 2\right],\\ \mathrm{Re}(K^{\mathrm{R}}_2) &\approx \frac{1}{16\pi^2 m_s}\times\frac{-1}{2}\,.\end{aligned} \tag{4.47}$$

Since we are chiefly interested in the CP violating component, we will focus on how to obtain and simplify the imaginary parts of $K^{\mathrm{R}}_{l_{\mathrm{NP}}}$.

Since $m_\phi^2, m_\psi^2 \geq 0$, the imaginary and thus CP violating component in Eq. (4.45) factorises when the argument of the logarithm is negative, by inspection we can see this occurs when

$$\begin{aligned}\Delta_{\phi\psi}(y) &< 0\,,\\ \Delta_{\psi\phi}(y) &< 0\,.\end{aligned} \tag{4.48}$$

Solutions at the boundaries of the CP violation conditions $\Delta_{\phi\psi}(y) = 0$ and $\Delta_{\psi\phi}(y) = 0$ are $y_{1,2}(m_\phi, m_\psi)$ and $y_{1,2}(m_\psi, m_\phi)$ respectively. Therefore the conditions in Eq. (4.48) in terms of y are fulfilled when $y_1(m_\phi, m_\psi) \leq y \leq y_2(m_\phi, m_\psi)$ and $y_1(m_\psi, m_\phi) \leq y \leq y_2(m_\psi, m_\phi)$ for the two diagrams respectively, where

$$\begin{aligned}y_{1,2}(m_\phi, m_\psi) &= \frac{1}{2} + \frac{m_\psi^2 - m_\phi^2 \mp \mu^2}{2m_s^2}\,,\\ y_{1,2}(m_\psi, m_\phi) &= \frac{1}{2} + \frac{m_\phi^2 - m_\psi^2 \mp \mu^2}{2m_s^2}\,,\end{aligned} \tag{4.49}$$

and μ^2 is defined as

$$\mu^2 = \sqrt{m_s^4 + m_\phi^4 + m_\psi^4 - 2m_s^2 m_\phi^2 - 2m_s^2 m_\psi^2 - 2m_\phi^2 m_\psi^2}\,. \tag{4.50}$$

It should be noted that in both cases $0 < y_1 < y_2 < 1$ is necessarily satisfied.

Hence, the imaginary component of Eq. (4.45) can now be written according to the complex logarithm definition as

$$\begin{aligned}
\mathrm{Im}(K_1^{\mathrm{R}}) &= \frac{m_s}{16\pi^2} \times \pi \int_{y_1(m_\phi,m_\psi)}^{y_2(m_\phi,m_\psi)} \mathrm{d}y \frac{y}{m_s^2 y - m_\psi^2 + m_\phi^2}\,, \\
\mathrm{Im}(K_2^{\mathrm{R}}) &= \frac{m_s}{16\pi^2} \times \pi \int_{y_1(m_\psi,m_\phi)}^{y_2(m_\psi,m_\phi)} \mathrm{d}y \frac{-m_\psi^2 y}{(m_s^2 y + m_\psi^2 - m_\phi^2)^2}\,.
\end{aligned} \tag{4.51}$$

Finally, integrating over the final Feynman parameter y leads to

$$\begin{aligned}
\mathrm{Im}(K_1^{\mathrm{R}}) &= \frac{m_s}{16\pi^2}\frac{-\pi}{m_s^2}\left[\frac{\mu^2}{m_s^2} + \frac{m_\phi^2 - m_\psi^2}{m_s^2}\log\left(\frac{m_s^2 + m_\phi^2 - m_\psi^2 - \mu^2}{m_s^2 + m_\phi^2 - m_\psi^2 + \mu^2}\right)\right]\,, \\
\mathrm{Im}(K_2^{\mathrm{R}}) &= \frac{m_s}{16\pi^2}\frac{+\pi}{m_s^2}\left[\frac{\mu^2(m_\psi^2 - m_\phi^2)}{m_s^4} + \frac{m_\psi^2}{m_s^2}\log\left(\frac{m_s^2 + m_\psi^2 - m_\phi^2 - \mu^2}{m_s^2 + m_\psi^2 - m_\phi^2 + \mu^2}\right)\right]\,.
\end{aligned} \tag{4.52}$$

The requirement $m_s > m_\phi + m_\psi$ leads to a positive μ^2. In the mass-degenerate limit $m_s = m_\phi + m_\psi$, $\mu^2 = 0$ and after some simplifications, it can be shown for this case that $\mathrm{Im}(K_1^{\mathrm{R}}) = \mathrm{Im}(K_2^{\mathrm{R}}) = 0$. In the massless limit $m_\phi, m_\psi \to 0$, these imaginary parts are approximately given by $\mathrm{Im}(K_1^{\mathrm{R}}) \to -1/(16\pi m_s)$ and $\mathrm{Im}(K_2^{\mathrm{R}}) \to 0$.

Since we need to compute $\Delta_{CP,-}$ to calculate CP violation, we apply Eq. (4.41), which in this example can be written explicitly as $|f_{\mathbf{fi}}^{\mathrm{R}}|^2 - |f_{\mathbf{if}}^{\mathrm{L}}|^2 = +4\sum_\alpha \mathrm{Im}(C_\alpha C_1^*) \times K_\alpha^{\mathrm{R}}[\mathrm{Im}(K_1^{\mathrm{R}} - K_2^{\mathrm{R}})]$, therefore we obtain

$$|f_{\mathbf{fi}}^{\mathrm{R}}|^2 - |f_{\mathbf{if}}^{\mathrm{L}}|^2 = \frac{2\pi Q e^2 g^2}{(16\pi^2)^2 m_W^2} \sum_\alpha \mathrm{Im}(U_{\alpha s} U_{\alpha i}^* \lambda_i \lambda_s^*)\, F_\alpha\, I_{\phi\psi}\,. \tag{4.53}$$

For $\Delta_{CP,+}$, $|f_{\mathbf{fi}}^{\mathrm{R}}|^2 - |f_{\mathbf{if}}^{\mathrm{L}}|^2$ is obtained by multiplying by a factor m_i^2/m_s^2 which is strongly suppressed by the light active neutrino mass.

Here, we have defined $I_{\phi\psi}$, an order one normalised parameter which is defined via $\mathrm{Im}(K_2^{\mathrm{R}} - K_1^{\mathrm{R}}) = \dfrac{m_s}{16\pi^2}\dfrac{\pi}{m_s^2} I_{\phi\psi}$ and explicitly given by

$$\begin{aligned}
I_{\phi\psi} = \frac{\mu^2(m_s^2 + m_\psi^2 - m_\phi^2)}{m_s^4} &+ \frac{m_\phi^2 - m_\psi^2}{m_s^2}\log\left(\frac{m_s^2 + m_\phi^2 - m_\psi^2 - \mu^2}{m_s^2 + m_\phi^2 - m_\psi^2 + \mu^2}\right) \\
&+ \frac{m_\psi^2}{m_s^2}\log\left(\frac{m_s^2 + m_\psi^2 - m_\phi^2 - \mu^2}{m_s^2 + m_\psi^2 - m_\phi^2 + \mu^2}\right)\,.
\end{aligned} \tag{4.54}$$

See Appendix B.2 for more details regarding the calculation of the imaginary part of the loop diagrams.

In this example, we may safely ignore the $f_{\mathbf{fi}}^{\mathrm{L}}$ and $f_{\mathbf{if}}^{\mathrm{R}}$ terms since $f_{\mathbf{fi}}^{\mathrm{L}} \sim f_{\mathbf{if}}^{\mathrm{R}} \sim \frac{m_i}{m_s} f_{\mathbf{if}}^{\mathrm{L}} \sim \frac{m_i}{m_s} f_{\mathbf{fi}}^{\mathrm{R}}$, thus the asymmetries, defined in Eqs. (4.16) and (4.17) are approximately given by

$$-\Delta_{CP,-} \approx -\Delta_{CP} \approx \Delta_{+-} \approx \frac{|f_{\mathbf{if}}^{\mathrm{L}}|^2 - |f_{\mathbf{fi}}^{\mathrm{R}}|^2}{|f_{\mathbf{if}}^{\mathrm{L}}|^2 + |f_{\mathbf{fi}}^{\mathrm{R}}|^2} \tag{4.55}$$

and $\Delta_{CP,+}$ is negligibly small. This result works for the Dirac neutrino case. In the Majorana neutrino case, from Eq. (4.25), it is straightforward to apply a similar procedure and obtain

$$\Delta^{\mathrm{M}}_{CP,+} = -\Delta^{\mathrm{M}}_{CP,-} = \Delta^{\mathrm{M}}_{+-} \approx \frac{|f^{\mathrm{L}}_{\mathbf{if}}|^2 - |f^{\mathrm{R}}_{\mathbf{fi}}|^2}{|f^{\mathrm{L}}_{\mathbf{if}}|^2 + |f^{\mathrm{R}}_{\mathbf{fi}}|^2} \tag{4.56}$$

and $\Delta_{CP} = 0$. Regardless of whether the neutrinos are Dirac or Majorana particles $\Delta_{CP,-} \approx -\Delta_{+-}$ is satisfied. This is true in general if $f^{\mathrm{L}}_{\mathbf{fi}}, f^{\mathrm{R}}_{\mathbf{if}} \ll f^{\mathrm{L}}_{\mathbf{if}}, f^{\mathrm{R}}_{\mathbf{fi}}$.

4.1.8 Phenomenological Applications of the Formulation

We are now ready to discuss possible phenomenological implications of this suggested sterile neutrino model which has CP violation generated at one-loop level for radiative decays. The formulation based on the simplified example above has a wide array of possible applications. One direct application is the study of CP violation in keV neutrino DM radiative decay. We can also apply it to the general type-I seesaw mechanism where right-handed neutrinos are much heavier than the electroweak scale in order to recover light active neutrino masses. It is also of interest to consider its application for heavy neutrino DM motivated by the IceCube data.

4.1.9 keV Sterile Neutrino Dark Matter

The keV-scale sterile neutrino has been discussed extensively as a DM candidate (for example models, see [317–321]). Following the discussion in Section 4.1.6, it is clear that the SM contribution at one-loop level cannot generate CP violation in keV neutrino radiative decay and a non-zero CP asymmetry can only be obtained at four-loop level. Therefore, we consider Yukawa interactions as shown in Eq. (4.34).

We give a brief discussion on constraints to the sterile neutrino ν_s and the new charged particles ϕ and ψ. Since ν_s is assumed to be a DM candidate, the decay channel $\nu_s \to \phi\psi$ introduced by the new interaction with ϕ and ψ must be controlled. The width of this channel is around

$$\Gamma_{\mathrm{NP}} = c_\nu \frac{|\lambda_s|^2}{8\pi} m_s \,, \tag{4.57}$$

where $c_\nu = 1$ for a Dirac neutrino and $c_\nu = 2$ for a Majorana neutrino. We require the width to be at least as small as the decay width of the SM Γ_{SM}. We approximate Γ_{SM} to the width of the dominant channels $\nu_s \to \nu_i \nu_j \bar{\nu}_i$ for any active neutrinos ν_i and ν_j [276, 317, 322] namely

$$\Gamma_{\mathrm{SM}} \approx c_\nu \frac{G_F^2 m_s^5}{192\pi^3} \sum_{i=1,2,3} |(U^\dagger U)_{is}|^2 \,, \tag{4.58}$$

where $(U^\dagger U)_{is} = \sum_{\alpha=e,\mu,\tau} U^*_{\alpha i} U_{\alpha s}$. By introducing a parameter η representing the ratio of the two decay widths $\eta = \Gamma_{\mathrm{NP}}/\Gamma_{\mathrm{SM}}$, we can express $|\lambda_s|$ by η as $|\lambda_s| \approx \frac{1}{2\sqrt{6}\pi}\sqrt{\eta}\, G_F m_s^2 \sqrt{\sum_i |(U^\dagger U)_{is}|^2}$, namely, an extremely small value for λ_s is required.[5] The charged particles ϕ and ψ as in our previous formulation are assumed to be

[5] Note that $G_F m_s^2 \sim 10^{-16}$ for keV sterile neutrino DM.

lighter than the sterile neutrino. Thus, they have to be at most millicharged to avoid significant modification to the precisely measured QED interactions at low energy. The Lamb shift imposes an upper bound for the millicharge $Q \lesssim 10^{-4}e$ [323], which is valid for a scalar or fermion with a mass less than 1 keV.

Considering these bounds, we can roughly estimate the size of CP violation of ν_s radiative decay. We also recall that the SM decay channel dominates the DM radiative decay while $\eta < 1$.

In this case, we can approximate both $f^{\rm R}_{\bf fi}$ and $f^{\rm L}_{\bf if}$ in the denominator by $f^{\rm R}_{{\bf fi},{\rm SM}}$ and it then follows that

$$\Delta_{CP,-} \approx \Delta_{CP} \approx -\Delta_{+-} \approx \frac{|f^{\rm R}_{\bf fi}|^2 - |f^{\rm L}_{\bf if}|^2}{2|f^{\rm R}_{{\bf fi},{\rm SM}}|^2}\,. \tag{4.59}$$

Therefore, we obtain the analytical result of the CP asymmmetry as

$$\begin{aligned} \Delta_{CP,-} &\approx \frac{8\pi}{3}\frac{Qm_W^2}{g^2m_s^2}\frac{{\rm Im}(\lambda_i(U^\dagger U)_{is}\lambda_s^*)}{(U^\dagger U)_{is}}I_{\phi\psi} \\ &\approx \frac{\sqrt{\eta}Q}{6\sqrt{3}}|\lambda_i|I_{\phi\psi}\sin\delta_{is}\frac{\sqrt{|(U^\dagger U)_{1s}|^2+|(U^\dagger U)_{2s}|^2+|(U^\dagger U)_{3s}|^2}}{(U^\dagger U)_{is}} \end{aligned} \tag{4.60}$$

where we have made the approximations $F_\alpha \approx 3/2$ since $m_\alpha \ll m_W$, and denoted the phase of $\lambda_i(U^\dagger U)_{is}\lambda_s^*$ as δ_{is}. In the limits $m_s \gg m_\phi, m_\psi$, we have $I_{\phi\psi} \approx 1$, and thus arrive at $\Delta_{CP,-} \sim 10^{-1}\sqrt{\eta}Q|\lambda_i|$, which is small due to the suppression by the millicharge Q. Enhancement can be achieved by considering a different parameter space. For example, by assuming $m_s, m_\psi \gg m_\phi$, we have $I_{\phi\psi} \approx \frac{m_\psi^2}{m_s^2}\log\frac{(m_s^2-m_\psi^2)^2}{m_s^2m_\phi^2}$, and thus the enhancement by an order of magnitude is easily obtained from $I_{\phi\psi}$. By assuming a typical value of the millicharge $Q \sim 10^{-4}e$, the coupling $\lambda_i \sim 10^{-1}$ and $\eta \sim 1$, we arrive at $\Delta_{CP,-} \sim 10^{-5}$. Other enhancements could be realised by considering the hierarchical mixing of the sterile neutrino with different active neutrinos.

4.1.10 Seesaw Mechanism and Leptogenesis

Our discussion thus far can also be generalised to the case of very heavy neutrinos. Heavy neutrinos with masses much higher than the EW scale are introduced in the seesaw mechanism to explain the tiny observed active neutrino masses. The heavy neutrinos are assumed to be Majorana particles in the mechanism. These particles, as originally proposed in [81], provide a class of scenarios where matter-antimatter asymmetry of the universe is generated by the decays of heavy neutrinos by a process termed leptogenesis.

Yukawa interactions involving heavy neutrinos provide the necessary source of CP violation between the decay $N_I \to L_\alpha H$ and its CP conjugate $N_I \to \bar{L}_\alpha H^\dagger$ in leptogenesis. We address the fact that these interactions can also generate CP violation between the radiative decay $N_I \to N_J\gamma_+$ and its CP conjugate process $N_I \to N_J\gamma_-$.[6] The CP asymmetry can be simply estimated with the help of the analytical result obtained in the last subsection. In order to achieve this, we first

[6]Neutrinos are Majorana particles in the seesaw mechanism framework.

present the Yukawa interactions in the form

$$-\mathcal{L}_Y \supset \sum_{\alpha,I} \lambda_{\alpha I}\bar{L}_\alpha \tilde{H} P_{\rm R} N_I + \lambda^*_{\alpha I}\bar{N}_I \tilde{H}^\dagger P_{\rm L} L_\alpha = \sum_{\alpha,I} \lambda_{\alpha I}\bar{N}^c_I \tilde{H}^T P_{\rm R} L^c_\alpha + \lambda^*_{\alpha I}\bar{L}^c_\alpha \tilde{H}^* P_{\rm L} N^c_I\,, \tag{4.61}$$

where $\tilde{H} = i\sigma_2 H^*$. Since we consider right-handed neutrinos to be much heavier than the W boson mass, the Goldstone-boson equivalence theorem can be applied. The main contributions to $N_I \to N_J\gamma$ are those loops involving charged leptons ℓ_α and the Goldstone boson H^+. Therefore, we can simply apply the formulation in Section 4.1.7 by replacing masses m_ψ and m_ϕ with m_α and m_W respectively. Here, it is necessary to keep the charged lepton masses as we will see later that it is essential to generate CP asymmetry. In this case, $f^{\rm L}_{\rm fi}$ and $f^{\rm R}_{\rm fi}$ are approximatively given by $f^{\rm L}_{JI} \approx \sum_\alpha C_\alpha K^{\rm L}_\alpha$ and $f^{\rm R}_{JI} \approx \sum_\alpha C_\alpha K^{\rm R}_\alpha$ with C_α and $K^{\rm L,R}_\alpha$ given by

$$\begin{aligned} C_\alpha &= -e\lambda_{\alpha I}\lambda^*_{\alpha J}\,, \\ K^{\rm L}_\alpha &= K^{\rm L}_{1,\alpha} - K^{\rm L}_{2,\alpha}\,, \quad K^{\rm R}_\alpha = K^{\rm R}_{1,\alpha} - K^{\rm R}_{2,\alpha} \end{aligned} \tag{4.62}$$

with $K^{\rm R}_{1,\alpha}$ and $K^{\rm R}_{2,\alpha}$ given by $K^{\rm R}_1$ and $K^{\rm R}_2$ in Eq. (4.43) with masses m_s, m_i, m_ϕ, m_ψ replaced by M_I, M_J, m_α and m_W respectively. Assuming right–handed neutrino masses $M_I \gg M_J$, we can safely ignore the $K^{\rm L}_\alpha$ contribution and arrive at the approximation of CP asymmetry shown in Eq. (4.56).

The CP violation requires both non-zero values for ${\rm Im}(C_\alpha C^*_\beta)$ and ${\rm Im}(K^{\rm R}_\alpha K^{{\rm R}\,*}_\beta)$. The former term given by ${\rm Im}(C_\alpha C^*_\beta) = e^2{\rm Im}(\lambda_{\alpha I}\lambda^*_{\alpha J}\lambda_{\beta J}\lambda^*_{\beta I})$ is usually non-zero based on the complex Yukawa couplings which are necessary for leptogenesis. For the latter term, without considering the difference between charged lepton masses $K^{\rm R}_\alpha = K^{\rm R}_\beta$ and ${\rm Im}(K^{\rm R}_\alpha K^{{\rm R}\,*}_\beta) = 0$ holds explicitly. Taking charged lepton masses into account and considering the hierarchy $m_\alpha \ll m_W \ll M_I$, we obtain the leading contribution (c.f. Eq. (4.45) and Eq. (4.52))

$$ {\rm Im}(K^{\rm R}_\alpha K^{{\rm R}\,*}_\beta) \approx \frac{-\pi}{(16\pi^2 M_I)^2}\log\left(\frac{m_W^2}{M_I^2}\right)\left[\frac{m_\alpha^2}{M_I^2}\log\left(\frac{m_\alpha^2}{M_I^2}\right) - \frac{m_\beta^2}{M_I^2}\log\left(\frac{m_\beta^2}{M_I^2}\right)\right]. \tag{4.63}$$

Eventually, we arrive at the CP asymmetry as

$$\Delta_{CP,-} \approx \frac{-\pi e^2}{|[\lambda^\dagger\lambda]_{IJ}|^2}\,{\rm Im}(\lambda_{\tau I}[\lambda^\dagger\lambda]_{IJ}\lambda^*_{\tau J})\,\frac{m_\tau^2}{M_I^2}\log\left(\frac{m_\tau^2}{M_I^2}\right)\Big/\log\left(\frac{m_W^2}{M_I^2}\right), \tag{4.64}$$

where for charged leptons, only the dominant τ mass has been considered. This formula takes a similar structure as the CP asymmetry of the $N \to L_\tau H$ decay in thermal leptogenesis (see e.g., in [307]), namely, the coefficient combination, ${\rm Im}(\lambda_{\tau I}[\lambda^\dagger\lambda]_{IJ}\lambda^*_{\tau J})$. The difference is that, while the asymmetry in thermal leptogenesis is suppressed by a loop factor,[7] the asymmetry here is not, but rather strongly suppressed by the mass hierarchy m_τ^2/M_I^2.

Furthermore, we comment that the CP violation for heavy neutrino radiative decays are very hard to observe since the only way to access this quantity is to measure the circular polarisation of photons radiated from the decay. This is not possible to

[7] The leading order contribution of the $N \to L_\tau H$ decay is at tree level and the CP violation appears at one-loop level.

measure currently due to the very small size of Δ_{+-}. What presents an even larger challenge is that these processes happen in the very early stages of the evolution of the universe. Thus, even if there is a large fraction of polarised photons produced, the asymmetry will be washed out by ubiquitous Compton scattering processes [324].

A possible way to enhance the CP asymmetry may be by considering a low-energy seesaw mechanism. For example, in the GeV sterile neutrino seesaw, there is no severe mass suppression between right-handed neutrino masses and the τ lepton mass to significantly reduce the CP asymmetry. Neutrinos at such a scale can explain baryon asymmetry based on a different leptogenesis mechanism, specifically the Akhmedov-Rubakov-Smirnov mechanism [305]. Another advantage is that these neutrinos can be tested at the SHiP experiment [325]. The disadvantage is that since the neutrino mass is lower than the W boson mass, CP violation of the radiative decay cannot be generated at one-loop, but rather at two-loop level. Thus, a more complicated calculation is required for this case.

4.1.11 Heavy Dark Matter and IceCube

Very heavy neutrinos could also be DM candidates. In fact, a heavy neutrino DM $N_{\rm DM}$ with mass around 10^2TeV – PeV scale as a DM candidate [295,296] is motivated by the high energy neutrino component in excess of the well-known atmospheric events [297,326] by the IceCube experiment (see [327,328] for recent progresses and [329,330] for analysis combining with other experimental data). Examples of typical heavy neutrino DM models explaining these observations have been shown in [331–335]. At low energy, they may induce very weak effective Yukawa interactions between the DM neutrino with other fermions.

Since radiative decay of a DM candidate can proceed very slowly until the present day, the washout by Compton scattering in the early stage of universe can be avoided. Given a sufficiently small Yukawa coupling $\lambda_{\alpha\text{-DM}}\bar{L}_\alpha \tilde{H} N_{\rm DM}$,[8] we may easily estimate the size of CP asymmetry in the DM radiative decay. The tree-level decay to νZ is induced and is one of the main decay channels being tested at IceCube. On the other hand, this coupling also induces the radiative decay $N_{\rm DM} \to \nu\gamma$ which may result in CP violation. The CP violation, as discussed in the last subsection, would be suppressed by the ratio $m_\tau^2/M_{\rm DM}^2 \lesssim 10^{-6}$.

4.1.12 Conclusion

In this work, we built a general framework for CP violation in neutrino radiative decays. CP violation in such processes produces an asymmetry between the circularly polarised radiated photons and provides an important source of net circular polarisation that can be observed in particle and astroparticle physics experiments.

The formulation between CP violation in neutrino radiative decays and the neutrino electromagnetic dipole moment at the form factor level is developed for both

[8]This Yukawa coupling may be effectively induced. For example, in the Higgs induced RHiNo DM model [331, 335, 336], it is the dimension-five operator $\frac{1}{\Lambda}\bar{N}_I^c N_{\rm DM} H^\dagger H$ with the thermal effect enhancing the mixing between DM with source neutrino N_I which eventually enhances the DM production. This operator, together with the Yukawa coupling Eq. (4.61) induces a very weak Yukawa coupling with coefficient $\lambda_{\alpha\text{-DM}} \sim y_{\alpha I}\frac{v_H M_I}{\Lambda M_{\rm DM}}$ in the limit $M_{\rm DM} \gg M_I$ where v_H is the Higgs VEV.

Dirac and Majorana neutrinos. We observed the model-independent connection between the decays and photon circular polarisation produced by these processes and concluded that CP violation directly determines the circular polarisation. Specifically in the Majorana neutrino case, the CP asymmetry is identical to the asymmetry of photon polarisations up to an overall sign difference. The contribution of a non-zero electric charge to neutrino decays is also discussed for completeness.

We then discussed how to generate non-vanishing CP violation through a generic new physics Yukawa interaction extension consisting of electrically charged scalar and fermion states. Without introducing any source of electric charge for the neutrinos, these particles can decay only via the electromagnetic transition dipole moment. The explicit analytical result of CP violation for this model was derived and presented. This fundamental result is applicable when determining circular polarisation for both Dirac and Majorana fermions and can be exported for use in any models that generate radiative decays of this type.

Finally, we included some brief discussion pertaining to the phenomenological implications of neutrinos at various mass scales. Firstly, the fomalism was applied to keV sterile neutrinos which are popular DM candidates and found CP violation and circular polarisation of the resulting radiated X-ray. We also considered the implications for much heavier sterile neutrinos of scale $\gtrsim$ 1TeV which are required for the seesaw mechanism and leptogenesis. We argue that the CP source in the Yukawa coupling, which is essential for leptogenesis, can trigger CP violation for heavy neutrino radiative decays. The case of weakly interacting sterile neutrinos at a mass comparable to the electroweak scale is also interesting as it could produce exotic collider signatures as well as circular polarisation. We plan to compute the CP violation from such a process in future work. We also discussed the circular polarisation of γ-rays released from the radiative decay of the PeV scale dark matter motivated by IceCube data, however the size of this effect is too small to observe at current experimental sensitivities.

4.2 CP Violation in the Neutral Lepton Transition Dipole Moment

Since the discovery of neutrino oscillations [337–340], it has been well understood that neutrinos have tiny masses and that their flavour eigenstates are different from, but merely superpositions of their mass eigenstates. The mismatch between the flavour and mass basis is described by lepton flavour mixing. The most important lepton flavour question mixing remaining is whether CP is violated. A large CP violation is supported by the combined analysis of current accelerator neutrino oscillation data [299] in the appearance channel of neutrino oscillations [300, 301]. The next-generation large-scale neutrino experiments DUNE and T2HK are projected to observe CP violation in the near future [302–304].

On the theoretical side, the origin of finite but tiny neutrino masses is still unknown. The canonical seesaw mechanism [284–289] and its numerous variations are proposed to solve this problem. The basic idea is that the small masses of left-handed neutrinos are attributed to the existence of much heavier right-handed Majorana neutrinos. In this elegant picture the flavour states are dominantly superpositions of massless left-handed neutrinos but also, to a smaller degree, their heavy right-handed counterparts. The minimal seesaw model [341] is a simplified version of the canonical seesaw mechanism with only two right-handed neutrinos, which has been studied in depth [342]. The seesaw mechanism induces new sources of CP violation in the heavy neutrino sector, providing the so-called leptogenesis, as one of the most popular mechanisms to explain the observed matter-antimatter asymmetry in our universe [81].

Neutrinos are usually considered as electrically neutral particles which do not participate in tree-level electromagnetic interactions. However, they may have electric and magnetic dipole moments appearing at loop level. The study of the neutrino dipole moment dates back four decades [272, 273, 343, 344]. In the SM, weak charged current interactions contribute in the loops and induce non-zero dipole moment for neutrinos [275–280, 345], see also in [281, 282, 316]. A *transition* dipole moment between two different neutrino mass eigenstates can trigger a heavier neutrino radiatively decaying to a lighter neutrino through the release of a photon. In fact, if neutrinos are Majorana particles, the property that Majorana fermions are their own antiparticles implies that neutrinos have only a transitional component to their dipole moment [346].

In various studies of the neutrino dipole moment in the literature, CP symmetry is always considered as an explicit symmetry for the relevant mass regions of neutrinos. However, a CP violating dipole moment has many interesting phenomenological applications. It may contribute to leptogenesis to explain the observed baryon-antibaryon asymmetry in our universe [308]. It also provides a source of a circular polarisation of photons in the sky for a suitable range of neutrino masses, [309]. In Ref. [3], the general conditions required to generate CP violation in the dipole moment was elucidated as well as the CP asymmetry based on a widely studied Yukawa interaction. The latter was applied to both left- and right-handed neutrino radiative decay scenarios as well as searches for dark matter via direct detection and collider signatures.

This work will focus on discussing CP violation in the neutrino dipole moment with right-handed neutrinos. We will provide the one-loop calculation of the CP asymmetry of the neutrino transition dipole moment in full detail in the framework of the SM with the addition of $SU(2)_L$-singlet right-handed neutrinos. In Section 4.2.1, we review the model-independent neutrino dipole moment written in terms of form factors producing CP violation. Section 4.2.4 contributes to a comprehensive analytical one-loop calculation of form factors. Finally, a numerical scan of the CP asymmetry with inputs of current neutrino oscillation data is performed in Section 4.2.5. We summarise our results in Section 4.2.6.

4.2.1 Neutrino Electromagnetic Dipole Moment with CP Violation

In this section we give a brief review of the framework for CP violation in neutrino radiative decays. We refer to our former paper Ref. [3] for the detailed derivation. Discussions in Section 4.2.2 assumes neutrinos are Dirac particles. The extension to Majorana neutrinos will be given in Section 4.2.3.

4.2.2 Form Factors for Dirac Neutrino

Assuming the decaying fermion is a Dirac particle, amplitudes for the processes $\nu_{\mathbf{i}} \to \nu_{\mathbf{f}}\gamma_+$ and $\nu_{\mathbf{i}} \to \nu_{\mathbf{f}}\gamma_-$, with respect to the photon polarisation $+$ and $-$ are given by

$$i\mathcal{M}(\nu_{\mathbf{i}} \to \nu_{\mathbf{f}}\gamma_\pm) = i\bar{u}(p_{\mathbf{f}})\Gamma^\mu_{\mathbf{fi}}(q^2)u(p_{\mathbf{i}})\varepsilon^*_{\pm,\mu}(q)\,, \tag{4.65}$$

where $u(p_{\mathbf{i}})$ and $u(p_{\mathbf{f}})$ are spinors for the initial $\nu_{\mathbf{i}}$ and final $\nu_{\mathbf{f}}$ state neutrinos respectively, and the photon momentum $q = p_{\mathbf{i}} - p_{\mathbf{f}}$. The vertex function $\Gamma^\mu_{\mathbf{fi}}(q^2)$ can in general be decomposed into four terms, electric charge, magnetic dipole moment, electric dipole moment and the anapole form factors [278–280, 310]. Without introducing a source for the electric charge, the neutrino will remain electrically neutral forever. By requiring the photon to be on-shell $q^2 = 0$ and choosing the Lorenz gauge $q \cdot \varepsilon_p = 0$, the anapole does not contribute to $\Gamma^\mu_{\mathbf{fi}}$. Therefore, the vertex function is simplified to [278–280, 310]

$$\Gamma^\mu_{\mathbf{fi}}(q^2 = 0) \;\;=\;\; -f^{\mathrm{M}}_{\mathbf{fi}}(i\sigma^{\mu\nu}q_\nu) + f^{\mathrm{E}}_{\mathbf{fi}}(i\sigma^{\mu\nu}q_\nu\gamma_5)\,, \tag{4.66}$$

where $f^{\mathrm{E}}_{\mathbf{fi}}$ and $f^{\mathrm{M}}_{\mathbf{fi}}$ are the electric and magnetic transition dipole moments of $\nu_{\mathbf{i}} \to \nu_{\mathbf{f}}\gamma$ respectively. It is helpful to rewrite it in the chiral form

$$\Gamma^\mu_{\mathbf{fi}}(0) \;\;=\;\; i\sigma^{\mu\nu}q_\nu[f^{\mathrm{L}}_{\mathbf{fi}}P_{\mathrm{L}} + f^{\mathrm{R}}_{\mathbf{fi}}P_{\mathrm{R}}]\,, \tag{4.67}$$

where $f^{\mathrm{L,R}}_{\mathbf{fi}} = -f^{\mathrm{M}}_{\mathbf{fi}} \pm i f^{\mathrm{E}}_{\mathbf{fi}}$ and the chiral projection operators are defined as $P_{\mathrm{L,R}} = \frac{1}{2}(1 \mp \gamma_5)$ [3]. The amplitudes $\mathcal{M}(\nu_{\mathbf{i}} \to \nu_{\mathbf{f}}\gamma_\pm)$ are directly correlated with the coefficients as [3]

$$\mathcal{M}(\nu_{\mathbf{i}} \to \nu_{\mathbf{f}}\gamma_+) = \sqrt{2}f^{\mathrm{L}}_{\mathbf{fi}}(m^2_{\mathbf{i}} - m^2_{\mathbf{f}})\,, \quad \mathcal{M}(\nu_{\mathbf{i}} \to \nu_{\mathbf{f}}\gamma_-) = -\sqrt{2}f^{\mathrm{R}}_{\mathbf{fi}}(m^2_{\mathbf{i}} - m^2_{\mathbf{f}})\,. \tag{4.68}$$

With the above justification, decay widths for $\nu_{\mathbf{i}} \to \nu_{\mathbf{f}}\gamma_\pm$, after averaging over the spin for the initial neutrino, can be written in a simple form

$$\Gamma(\nu_{\mathbf{i}} \to \nu_{\mathbf{f}}\gamma_+) = \mathcal{A}|f^{\mathrm{L}}_{\mathbf{fi}}|^2\,, \quad \Gamma(\nu_{\mathbf{i}} \to \nu_{\mathbf{f}}\gamma_-) = \mathcal{A}|f^{\mathrm{R}}_{\mathbf{fi}}|^2\,, \tag{4.69}$$

with $\mathcal{A} = (m^2_{\mathbf{i}} - m^2_{\mathbf{f}})^3/(16\pi m^3_{\mathbf{i}})$. The total radiative decay width $\Gamma(\nu_{\mathbf{i}} \to \nu_{\mathbf{f}}\gamma)$ is obtained by summing the decay widths for $\nu_{\mathbf{i}} \to \nu_{\mathbf{f}}\gamma_+$ and $\nu_{\mathbf{i}} \to \nu_{\mathbf{f}}\gamma_-$.

For antineutrinos, amplitudes for $\bar{\nu}_{\mathbf{i}} \to \bar{\nu}_{\mathbf{f}}\gamma_+$ and $\bar{\nu}_{\mathbf{i}} \to \bar{\nu}_{\mathbf{f}}\gamma_-$ are given by

$$i\mathcal{M}(\bar{\nu}_{\mathbf{i}} \to \bar{\nu}_{\mathbf{f}}\gamma_\pm) \;\;=\;\; i\bar{v}(p_{\mathbf{i}})\bar{\Gamma}^\mu_{\mathbf{if}}(q^2)v(p_{\mathbf{f}})\varepsilon^*_{\pm,\mu}(q)\,, \tag{4.70}$$

respectively, where $v(p_{\mathbf{i}})$ and $v(p_{\mathbf{f}})$ are antineutrino spinors. The vertex function $\bar{\Gamma}^\mu_{\mathbf{if}}$ when the photon is on-shell is consequently written in a similar form as shown in Eq. (4.67),

$$\bar{\Gamma}^\mu_{\mathbf{if}}(0) \;\;=\;\; i\sigma^{\mu\nu}q_\nu[\bar{f}^{\mathrm{L}}_{\mathbf{if}}P_{\mathrm{L}} + \bar{f}^{\mathrm{R}}_{\mathbf{if}}P_{\mathrm{R}}]\,. \tag{4.71}$$

Where CPT invariance ensures $\bar{f}^{\mathrm{L}}_{\mathbf{if}} = -f^{\mathrm{L}}_{\mathbf{if}}$, and $\bar{f}^{\mathrm{R}}_{\mathbf{if}} = -f^{\mathrm{R}}_{\mathbf{if}}$ [283]. Hence, amplitudes $\mathcal{M}(\bar{\nu}_{\mathbf{i}} \to \bar{\nu}_{\mathbf{f}}\gamma_+)$ are simplified to [3]

$$\mathcal{M}(\bar{\nu}_{\mathbf{i}} \to \bar{\nu}_{\mathbf{f}}\gamma_+) = \sqrt{2}f^{\mathrm{L}}_{\mathbf{if}}(m^2_{\mathbf{i}} - m^2_{\mathbf{f}})\,, \quad \mathcal{M}(\bar{\nu}_{\mathbf{i}} \to \bar{\nu}_{\mathbf{f}}\gamma_-) = -\sqrt{2}f^{\mathrm{R}}_{\mathbf{if}}(m^2_{\mathbf{i}} - m^2_{\mathbf{f}})\,. \tag{4.72}$$

The antineutrino decay widths are then given by $\Gamma(\bar{\nu}_{\mathbf{i}} \to \bar{\nu}_{\mathbf{f}}\gamma_+) = \mathcal{A}\left|f^{\rm L}_{\mathbf{if}}\right|^2$ and $\Gamma(\bar{\nu}_{\mathbf{i}} \to \bar{\nu}_{\mathbf{f}}\gamma_-) = \mathcal{A}\left|f^{\rm R}_{\mathbf{if}}\right|^2$.

In [3], we have defined a set of CP asymmetries between neutrino radiative decay and antineutrino radiative decay. In terms of ratios specifying photon polarisations, we may write

$$\begin{aligned}\Delta_{CP,+} =& \frac{\Gamma(\nu_{\mathbf{i}} \to \nu_{\mathbf{f}}\gamma_+) - \Gamma(\bar{\nu}_{\mathbf{i}} \to \bar{\nu}_{\mathbf{f}}\gamma_-)}{\Gamma(\nu_{\mathbf{i}} \to \nu_{\mathbf{f}}\gamma) + \Gamma(\bar{\nu}_{\mathbf{i}} \to \bar{\nu}_{\mathbf{f}}\gamma)}\,,\\ \Delta_{CP,-} =& \frac{\Gamma(\nu_{\mathbf{i}} \to \nu_{\mathbf{f}}\gamma_-) - \Gamma(\bar{\nu}_{\mathbf{i}} \to \bar{\nu}_{\mathbf{f}}\gamma_+)}{\Gamma(\nu_{\mathbf{i}} \to \nu_{\mathbf{f}}\gamma) + \Gamma(\bar{\nu}_{\mathbf{i}} \to \bar{\nu}_{\mathbf{f}}\gamma)}\,,\end{aligned} \tag{4.73}$$

which can further be simplified to

$$\begin{aligned}\Delta_{CP,+} =& \frac{|f^{\rm L}_{\mathbf{fi}}|^2 - |f^{\rm R}_{\mathbf{if}}|^2}{|f^{\rm L}_{\mathbf{fi}}|^2 + |f^{\rm R}_{\mathbf{fi}}|^2 + |f^{\rm R}_{\mathbf{if}}|^2 + |f^{\rm L}_{\mathbf{if}}|^2}\,,\\ \Delta_{CP,-} =& \frac{|f^{\rm R}_{\mathbf{fi}}|^2 - |f^{\rm L}_{\mathbf{if}}|^2}{|f^{\rm L}_{\mathbf{fi}}|^2 + |f^{\rm R}_{\mathbf{fi}}|^2 + |f^{\rm R}_{\mathbf{if}}|^2 + |f^{\rm L}_{\mathbf{if}}|^2}\,.\end{aligned} \tag{4.74}$$

In the case of CP conservation, $f^{\rm L,R}_{\mathbf{if}} = [f^{\rm R,L}_{\mathbf{fi}}]^*$, we arrive at vanishing CP asymmetries $\Delta_{CP,+} = \Delta_{CP,-} = 0$.

4.2.3 Form Factors for Majorana Neutrinos

We now extend the discussion to Majorana neutrinos. The Majorana field satisfies $\nu = C\overline{\nu}^T$, where C is the charge-conjugation matrix. Compared with the Dirac field which contains independent left-handed and right-handed components $\nu_{\rm L} \equiv P_{\rm L}\nu$ and $\nu_{\rm R} \equiv P_{\rm R}\nu$, the Majorana field enforces the right-handed component to be the charge conjugation of the left-handed component, i.e., $P_{\rm R}\nu = C\overline{\nu_{\rm L}}^T$, leading to the quantisation in the form $\nu \sim au(p)e^{-ip\cdot x} + a^\dagger v(p)e^{ip\cdot x}$. Taking this into account and applying the parametrisation in Eqs. (4.65) and (4.70), the amplitude for $\nu_{\mathbf{i}} \to \nu_{\mathbf{f}}\gamma_\pm$ is proven to be

$$i\mathcal{M}^{\rm M}(\nu_{\mathbf{i}} \to \nu_{\mathbf{f}}\gamma_\pm) = i\bar{u}(p_{\mathbf{f}})\Gamma^\mu_{\mathbf{fi}}(q^2)u(p_{\mathbf{i}})\varepsilon^*_{\pm,\mu}(q) - i\bar{v}(p_{\mathbf{i}})\Gamma^\mu_{\mathbf{if}}(q^2)v(p_{\mathbf{f}})\varepsilon^*_{\pm,\mu}(q) \tag{4.75}$$

in the Majorana case [283]. It can be explained as the sum of amplitudes of the Dirac neutrino radiative decay and antineutrino radiative decay channels, i.e., $i\mathcal{M}^{\rm M}(\nu_{\mathbf{i}} \to \nu_{\mathbf{f}}\gamma_\pm) = i\mathcal{M}(\nu_{\mathbf{i}} \to \nu_{\mathbf{f}}\gamma_\pm) + i\mathcal{M}(\bar{\nu}_{\mathbf{i}} \to \bar{\nu}_{\mathbf{f}}\gamma_\pm)$. Taking the explicit formulas for the amplitudes given in Eq. (4.68) and Eq. (4.72), we obtain results with definite spins in the initial and final states as

$$\begin{aligned}\mathcal{M}^{\rm M}(\nu_{\mathbf{i}} \to \nu_{\mathbf{f}}\gamma_+) &= +\sqrt{2}[f^{\rm L}_{\mathbf{fi}} - f^{\rm L}_{\mathbf{if}}](m^2_{\mathbf{i}} - m^2_{\mathbf{f}})\,,\\ \mathcal{M}^{\rm M}(\nu_{\mathbf{i}} \to \nu_{\mathbf{f}}\gamma_-) &= -\sqrt{2}[f^{\rm R}_{\mathbf{fi}} - f^{\rm R}_{\mathbf{if}}](m^2_{\mathbf{i}} - m^2_{\mathbf{f}})\,.\end{aligned} \tag{4.76}$$

The decay widths are given by $\Gamma^{\rm M}(\nu_{\mathbf{i}} \to \nu_{\mathbf{f}}\gamma_+) = \mathcal{A}|f^{\rm L}_{\mathbf{fi}} - f^{\rm L}_{\mathbf{if}}|^2$ and $\Gamma^{\rm M}(\nu_{\mathbf{i}} \to \nu_{\mathbf{f}}\gamma_-) = \mathcal{A}|f^{\rm R}_{\mathbf{fi}} - f^{\rm R}_{\mathbf{if}}|^2$.

For Majorana fermions, the CP violation is identical to that obtained from P-violation alone i.e. the CP asymmetry is essentially the same as the asymmetry between the two polarised photons. Hence, we have

$$\begin{aligned}\Delta^{\rm M}_{CP,+} = -\Delta^{\rm M}_{CP,-} &= \frac{\Gamma^{\rm M}(\nu_{\mathbf{i}} \to \nu_{\mathbf{f}}\gamma_+) - \Gamma^{\rm M}(\nu_{\mathbf{i}} \to \nu_{\mathbf{f}}\gamma_-)}{\Gamma^{\rm M}(\nu_{\mathbf{i}} \to \nu_{\mathbf{f}} + \gamma)} \\ &= \frac{|f^{\rm L}_{\mathbf{fi}} - f^{\rm L}_{\mathbf{if}}|^2 - |f^{\rm R}_{\mathbf{fi}} - f^{\rm R}_{\mathbf{if}}|^2}{|f^{\rm L}_{\mathbf{fi}} - f^{\rm L}_{\mathbf{if}}|^2 + |f^{\rm R}_{\mathbf{fi}} - f^{\rm R}_{\mathbf{if}}|^2}\,. \end{aligned} \tag{4.77}$$

For simplicity, we make the assignment $\Delta_{CP} \equiv \Delta^{\rm M}_{CP,+}$ for use in the following phenomenological discussions.

4.2.4 CP Violating Form Factors Induced by Charged-Current Interactions

We present below, the one-loop calculation of neutrino radiative decay $\nu_{\mathbf{i}} \to \nu_{\mathbf{f}}\gamma$ for massive neutrinos with the existence of CP violation. We work in the framework of the SM extended with an arbitrary number of $SU(2)_L$-singlet right-handed neutrinos in the Feynman gauge. The crucial operator for the charged-current interaction is

$$\mathcal{L}_{\rm c.c.} = \sum_{\alpha,m} \frac{g}{\sqrt{2}} \mathcal{U}_{\alpha m}\, \bar{\ell}_\alpha \gamma^\mu P_{\rm L} \nu_m W^-_\mu + {\rm h.c.}\,, \tag{4.78}$$

where g is the electroweak gauge coupling constant, α is an index that represents charged lepton flavours $\alpha = e, \mu, \tau$ and m is an index that represents the neutrino mass eigenstates. In particular, $\nu_m = \nu_1, \nu_2, \nu_3$ represent three light neutrino mass eigenstates and $\nu_m = N_1, N_2, \dots$ representing heavy neutrino mass eigenstates. The matrix $\mathcal{U}_{\alpha m}$ denotes the lepton flavour mixing accounting for heavy neutrino mass eigenstates.

The one-loop Feynman diagrams for the radiative decay via the SM charged current interaction are shown in Figure 4.3. The vertex functions of each proper vertex diagram in Figure 1 is given by

$$\begin{aligned}
\Gamma^{\mu,(1)}_{\mathbf{fi},\alpha} &= C \int \frac{d^4p}{(2\pi)^4} \frac{\gamma_\nu P_{\rm L}(\not{p}_{\mathbf{f}} - \not{p} + m_\alpha)\gamma^\mu(\not{p}_{\mathbf{i}} - \not{p} + m_\alpha)\gamma^\nu P_{\rm L}}{[(p_{\mathbf{f}}-p)^2 - m_\alpha^2][(p_{\mathbf{i}}-p)^2 - m_\alpha^2][p^2 - m_W^2]}\,, \\
\Gamma^{\mu,(2)}_{\mathbf{fi},\alpha} &= C \int \frac{d^4p}{(2\pi)^4} \frac{(m_{\mathbf{f}}P_{\rm L} - m_\alpha P_{\rm R})(\not{p}_{\mathbf{f}} - \not{p} + m_\alpha)\gamma^\mu(\not{p}_{\mathbf{i}} - \not{p} + m_\alpha)(m_\alpha P_{\rm L} - m_{\mathbf{i}} P_{\rm R})}{m_W^2[(p_{\mathbf{f}}-p)^2 - m_\alpha^2][(p_{\mathbf{i}}-p)^2 - m_\alpha^2][p^2 - m_W^2]}\,, \\
\Gamma^{\mu,(3)}_{\mathbf{fi},\alpha} &= C \int \frac{d^4p}{(2\pi)^4} \frac{\gamma_\rho P_{\rm L}(\not{p} + m_\alpha)\gamma_\nu P_{\rm L} V^{\mu\nu\rho}}{[(p_{\mathbf{f}}-p)^2 - m_W^2][(p_{\mathbf{i}}-p)^2 - m_W^2][p^2 - m_\alpha^2]}\,, \\
\Gamma^{\mu,(4)}_{\mathbf{fi},\alpha} &= C \int \frac{d^4p}{(2\pi)^4} \frac{(2p - p_{\mathbf{i}} - p_{\mathbf{f}})^\mu (m_{\mathbf{f}}P_{\rm L} - m_\alpha P_{\rm R})(\not{p} + m_\alpha)(m_\alpha P_{\rm L} - m_{\mathbf{i}} P_{\rm R})}{m_W^2[(p_{\mathbf{f}}-p)^2 - m_W^2][(p_{\mathbf{i}}-p)^2 - m_W^2][p^2 - m_\alpha^2]}\,, \\
\Gamma^{\mu,(5)}_{\mathbf{fi},\alpha} &= C \int \frac{d^4p}{(2\pi)^4} \frac{\gamma^\mu P_{\rm L}(\not{p} + m_\alpha)(m_\alpha P_{\rm L} - m_{\mathbf{i}} P_{\rm R})}{[(p_{\mathbf{f}}-p)^2 - m_W^2][(p_{\mathbf{i}}-p)^2 - m_W^2][p^2 - m_\alpha^2]}\,, \\
\Gamma^{\mu,(6)}_{\mathbf{fi},\alpha} &= C \int \frac{d^4p}{(2\pi)^4} \frac{(m_\alpha P_{\rm R} - m_{\mathbf{f}} P_{\rm L})(\not{p} + m_\alpha)\gamma^\mu P_{\rm L}}{[(p_{\mathbf{f}}-p)^2 - m_W^2][(p_{\mathbf{i}}-p)^2 - m_W^2][p^2 - m_\alpha^2]}\,,
\end{aligned} \tag{4.79}$$

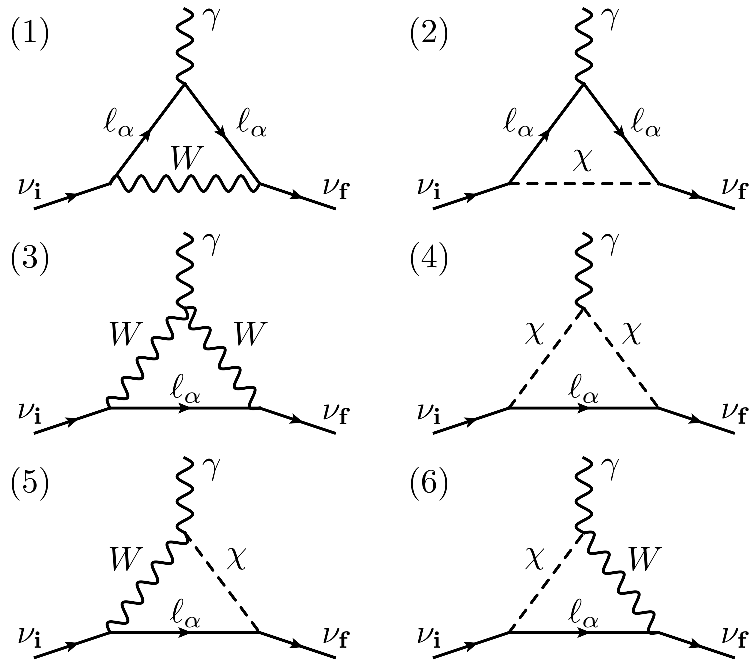

FIGURE 4.3: All Feynman diagrams contributing to the neutrino electromagnetic transition dipole moment, where χ is the charged Goldstone boson.

where

$$V^{\mu\nu\rho} \;=\; g^{\mu\nu}(2p_{\mathbf{i}} - p - p_{\mathbf{f}})^{\rho} + g^{\rho\mu}(2p_{\mathbf{f}} - p - p_{\mathbf{i}})^{\nu} + g^{\nu\rho}(2p - p_{\mathbf{i}} - p_{\mathbf{f}})^{\mu}\,. \tag{4.80}$$

and

$$C = i\frac{eg^2}{2}\mathcal{U}_{\alpha\mathbf{i}}\mathcal{U}^*_{\alpha\mathbf{f}} \tag{4.81}$$

The non-vanishing CP asymmetry requires two conditions. Namely, a CP violating contribution from coefficients of tree-level vertices and an imaginary part coming purely from loop kinematics [3]. In the present work, the first condition is satisfied by the complex phases in the lepton flavour mixing matrix $\mathcal{U}$ and will be discussed in more detail in subsequent sections. Here, we first contend with the second condition by completing the loop calculation and deriving its imaginary part analytically.

We follow the standard procedure to integrate the loop momenta with the help of the Feynman parametrisation. Then, we apply the Gordon decomposition taking chirality into consideration, and factorise dipole moment terms with coefficients as

$$\Gamma^{\mu,(\mathrm{k})}_{\mathbf{fi},\alpha} \;=\; \frac{eg^2}{4(4\pi)^2}\mathcal{U}_{\alpha\mathbf{i}}\mathcal{U}^*_{\alpha\mathbf{f}} i\sigma^{\mu\nu}q_\nu \int_0^1 \mathrm{d}x\mathrm{d}y\mathrm{d}z\,\delta(x+y+z-1)\,\mathcal{P}^{(\mathrm{k})}\,, \tag{4.82}$$

where

$$
\begin{aligned}
\mathcal{P}^{(1)} &= \frac{-2x(x+z)m_{\mathbf{i}}P_{\mathrm{R}} - 2x(x+y)m_{\mathbf{f}}P_{\mathrm{L}}}{\Delta_{\alpha W}(x,y,z)}\,, \\
\mathcal{P}^{(2)} &= \frac{[xzm_{\mathbf{f}}^2 - ((1-x)^2+xz)m_\alpha^2]m_{\mathbf{i}}P_{\mathrm{R}} + [xym_{\mathbf{i}}^2 - ((1-x)^2+xy)m_\alpha^2]m_{\mathbf{f}}P_{\mathrm{L}}}{m_W^2\Delta_{\alpha W}(x,y,z)}\,, \\
\mathcal{P}^{(3)} &= \frac{[(1-2x)z - 2(1-x)^2]m_{\mathbf{i}}P_{\mathrm{R}} + [(1-2x)y - 2(1-x)^2]m_{\mathbf{f}}P_{\mathrm{L}}}{\Delta_{W\alpha}(x,y,z)}\,, \\
\mathcal{P}^{(4)} &= \frac{[xzm_{\mathbf{f}}^2 - x(x+z)m_\alpha^2]m_{\mathbf{i}}P_{\mathrm{R}} + [xym_{\mathbf{i}}^2 - x(x+y)m_\alpha^2]m_{\mathbf{f}}P_{\mathrm{L}}}{m_W^2\Delta_{W\alpha}(x,y,z)}\,, \\
\mathcal{P}^{(5)} &= \frac{-zm_{\mathbf{i}}P_{\mathrm{R}}}{\Delta_{W\alpha}(x,y,z)}\,, \\
\mathcal{P}^{(6)} &= \frac{-ym_{\mathbf{f}}P_{\mathrm{L}}}{\Delta_{W\alpha}(x,y,z)}\,,
\end{aligned}
\tag{4.83}
$$

and

$$
\begin{aligned}
\Delta_{W\alpha}(x,y,z) &= m_W^2(1-x) + xm_\alpha^2 - x(ym_{\mathbf{i}}^2 + zm_{\mathbf{f}}^2)\,, \\
\Delta_{\alpha W}(x,y,z) &= m_\alpha^2(1-x) + xm_W^2 - x(ym_{\mathbf{i}}^2 + zm_{\mathbf{f}}^2)\,.
\end{aligned}
\tag{4.84}
$$

Eq. (4.82) can be further simplified to

$$
\Gamma^{\mu,(\mathrm{k})}_{\mathbf{fi},\alpha} = \frac{eG_{\mathrm{F}}}{4\sqrt{2}\pi^2}\mathcal{U}_{\alpha\mathbf{i}}\mathcal{U}^*_{\alpha\mathbf{f}}i\sigma^{\mu\nu}q_\nu(\mathcal{F}_{\mathbf{fi},\alpha}m_{\mathbf{i}}P_{\mathrm{R}} + \mathcal{F}_{\mathbf{if},\alpha}m_{\mathbf{f}}P_{\mathrm{L}})\,. \tag{4.85}
$$

Here, $\mathcal{F}$ is derived from the sum of the integrals $\mathcal{P}^{(k)}$

$$
\begin{aligned}
\mathcal{F}_{\mathbf{fi},\alpha} = \int_0^1 \mathrm{d}x \Bigg\{ & \frac{\left(m_{\mathbf{i}}^2 - m_\alpha^2 - 2m_W^2\right)\left(m_\alpha^2 + m_{\mathbf{f}}^2x^2\right) + m_{\mathbf{fi},\alpha}^4 x}{\left(m_{\mathbf{i}}^2 - m_{\mathbf{f}}^2\right)^2 x} \times \\
& \times \log\left(\frac{m_\alpha^2 + \left(m_W^2 - m_\alpha^2 - m_{\mathbf{i}}^2\right)x + m_{\mathbf{i}}^2x^2}{m_\alpha^2 + \left(m_W^2 - m_\alpha^2 - m_{\mathbf{f}}^2\right)x + m_{\mathbf{f}}^2x^2}\right) \\
& + \frac{\left(m_{\mathbf{i}}^2 - m_\alpha^2 - 2m_W^2\right)\left(m_\alpha^2 + m_{\mathbf{f}}^2(1-x)^2\right) + m_{\mathbf{fi},\alpha}^4(1-x)}{\left(m_{\mathbf{i}}^2 - m_{\mathbf{f}}^2\right)^2 x} \times \\
& \times \log\left(\frac{m_W^2 + \left(m_\alpha^2 - m_W^2 - m_{\mathbf{i}}^2\right)x + m_{\mathbf{i}}^2x^2}{m_W^2 + \left(m_\alpha^2 - m_W^2 - m_{\mathbf{f}}^2\right)x + m_{\mathbf{f}}^2x^2}\right)\Bigg\} + \frac{m_{\mathbf{f}}^2 - m_\alpha^2 - 2m_W^2}{m_{\mathbf{i}}^2 - m_{\mathbf{f}}^2}\,,
\end{aligned}
\tag{4.86}
$$

where we define $m_{\mathbf{fi},\alpha}^4 = -(m_{\mathbf{i}}^2 - m_\alpha^2 - m_W^2)(m_{\mathbf{f}}^2 + m_\alpha^2 - 2m_W^2) + 2m_\alpha^2 m_W^2$, and $\mathcal{F}_{\mathbf{if},\alpha}$ is obtained by exchanging $m_{\mathbf{i}}$ and $m_{\mathbf{f}}$. Therefore, we obtain the coefficients $f^{\mathrm{L}}_{\mathbf{fi}}$, $f^{\mathrm{L}}_{\mathbf{if}}$, $f^{\mathrm{R}}_{\mathbf{fi}}$ and $f^{\mathrm{R}}_{\mathbf{if}}$ as

$$
\begin{aligned}
f^{\mathrm{L}}_{\mathbf{fi}} &= \frac{eG_{\mathrm{F}}}{4\sqrt{2}\pi^2}\mathcal{U}_{\alpha\mathbf{i}}\mathcal{U}^*_{\alpha\mathbf{f}}\mathcal{F}_{\mathbf{if},\alpha}m_{\mathbf{f}}\,, \quad & f^{\mathrm{R}}_{\mathbf{fi}} &= \frac{eG_{\mathrm{F}}}{4\sqrt{2}\pi^2}\mathcal{U}_{\alpha\mathbf{i}}\mathcal{U}^*_{\alpha\mathbf{f}}\mathcal{F}_{\mathbf{fi},\alpha}m_{\mathbf{i}}\,, \\
f^{\mathrm{L}}_{\mathbf{if}} &= \frac{eG_{\mathrm{F}}}{4\sqrt{2}\pi^2}\mathcal{U}_{\alpha\mathbf{f}}\mathcal{U}^*_{\alpha\mathbf{i}}\mathcal{F}_{\mathbf{fi},\alpha}m_{\mathbf{i}}\,, \quad & f^{\mathrm{R}}_{\mathbf{if}} &= \frac{eG_{\mathrm{F}}}{4\sqrt{2}\pi^2}\mathcal{U}_{\alpha\mathbf{f}}\mathcal{U}^*_{\alpha\mathbf{i}}\mathcal{F}_{\mathbf{if},\alpha}m_{\mathbf{f}}\,.
\end{aligned}
\tag{4.87}
$$

The integrals $\mathcal{F}_{\mathbf{fi},\alpha}$ and $\mathcal{F}_{\mathbf{if},\alpha}$ in Eq. (4.86) can be further simplified when the limit of small neutrino masses, i.e., $m_{\mathbf{i}}^2, m_{\mathbf{f}}^2 \ll m_\alpha^2, m_W^2$ is considered. In this case, the logarithm terms can be expanded in a series of $m_{\mathbf{i}}^2$ and $m_{\mathbf{f}}^2$, and after a straightforward calculation, we prove that both $\mathcal{F}_{\mathbf{fi},\alpha}$ and $\mathcal{F}_{\mathbf{if},\alpha}$ are identical to $F(m_\alpha^2/m_W^2)$, where

$$F(a) = \frac{3}{4}\left(\frac{2-a}{1-a} - \frac{2a}{(1-a)^2} - \frac{2a^2\log a}{(1-a)^3}\right) \tag{4.88}$$

which is a well known result for the loop factor obtained in the studies of neutrino dipole moments and radiative decays [276, 278].

We now outline how to obtain non-zero imaginary parts for $\mathcal{F}_{\mathbf{fi},\alpha}$ and $\mathcal{F}_{\mathbf{if},\alpha}$ when neutrinos have large masses. They include integral terms of the form $\int_0^1 \mathrm{d}x f(x)\log g(x)$, where $g(x)$ is not always positive in the domain $(0,1)$. Instead, one can prove that there is an interval $(x_1, x_2) \subset (0,1)$ where $g(x) < 0$ is satisfied, and x_1 and x_2 are solutions of $g(x) = 0$. The real and imaginary parts in the integral can then be split into

$$\int_0^1 \mathrm{d}x f(x)\log g(x) = \int_0^1 \mathrm{d}x f(x)\log|g(x)| + i\pi\int_{x_1}^{x_2} \mathrm{d}x f(x)\,. \tag{4.89}$$

The imaginary part of $\int_{x_1}^{x_2} \mathrm{d}x f(x)$ can then be analytical obtained. In this way, we derive the analytical expression for the imaginary part of $\mathcal{F}_{\mathbf{fi},\alpha}$ as

$$\begin{aligned}
\mathrm{Im}(\mathcal{F}_{\mathbf{fi},\alpha}) = \pi\vartheta_{\mathbf{i}} \Bigg\{ & \frac{m_{\mathbf{i}}^2 - m_\alpha^2 - 2m_W^2}{\left(m_{\mathbf{i}}^2 - m_{\mathbf{f}}^2\right)^2}\left[-\mu_{\mathbf{i}}^2\frac{m_{\mathbf{f}}^2}{m_{\mathbf{i}}^2} + m_\alpha^2\log\left(\frac{m_{\mathbf{i}}^2 + m_\alpha^2 - m_W^2 + \mu_{\mathbf{i}}^2}{m_{\mathbf{i}}^2 + m_\alpha^2 - m_W^2 - \mu_{\mathbf{i}}^2}\right)\right] \\
& + \frac{\left(2m_{\mathbf{i}}^2 - m_{\mathbf{f}}^2 - m_\alpha^2 - 2m_W^2\right)m_W^2}{\left(m_{\mathbf{i}}^2 - m_{\mathbf{f}}^2\right)^2}\log\left(\frac{m_{\mathbf{i}}^2 - m_\alpha^2 + m_W^2 + \mu_{\mathbf{i}}^2}{m_{\mathbf{i}}^2 - m_\alpha^2 + m_W^2 - \mu_{\mathbf{i}}^2}\right)\Bigg\} \\
+\pi\vartheta_{\mathbf{f}} \Bigg\{ & -\frac{m_{\mathbf{i}}^2 - m_\alpha^2 - 2m_W^2}{\left(m_{\mathbf{i}}^2 - m_{\mathbf{f}}^2\right)^2}\left[-\mu_{\mathbf{f}}^2 + m_\alpha^2\log\left(\frac{m_{\mathbf{f}}^2 + m_\alpha^2 - m_W^2 + \mu_{\mathbf{f}}^2}{m_{\mathbf{f}}^2 + m_\alpha^2 - m_W^2 - \mu_{\mathbf{f}}^2}\right)\right] \\
& + \frac{\left(2m_{\mathbf{i}}^2 - m_{\mathbf{f}}^2 - m_\alpha^2 - 2m_W^2\right)m_W^2}{\left(m_{\mathbf{i}}^2 - m_{\mathbf{f}}^2\right)^2}\log\left(\frac{m_{\mathbf{f}}^2 - m_\alpha^2 + m_W^2 + \mu_{\mathbf{f}}^2}{m_{\mathbf{f}}^2 - m_\alpha^2 + m_W^2 - \mu_{\mathbf{f}}^2}\right)\Bigg\}\,,
\end{aligned} \tag{4.90}$$

where $\vartheta_{\mathbf{i},\mathbf{f}} \equiv \vartheta(m_{\mathbf{i},\mathbf{f}} - m_W - m_\alpha)$ is the Heaviside step function, and

$$\begin{aligned}
\mu_{\mathbf{i}}^2 &= \sqrt{m_{\mathbf{i}}^4 + m_\alpha^4 + m_W^4 - 2m_{\mathbf{i}}^2 m_\alpha^2 - 2m_{\mathbf{i}}^2 m_W^2 - 2m_\alpha^2 m_W^2}\,, \\
\mu_{\mathbf{f}}^2 &= \sqrt{m_{\mathbf{f}}^4 + m_\alpha^4 + m_W^4 - 2m_{\mathbf{f}}^2 m_\alpha^2 - 2m_{\mathbf{f}}^2 m_W^2 - 2m_\alpha^2 m_W^2}\,.
\end{aligned} \tag{4.91}$$

Again, $\mathrm{Im}(\mathcal{F}_{\mathbf{if},\alpha})$ is obtained from $\mathrm{Im}(\mathcal{F}_{\mathbf{fi},\alpha})$ by exchanging $m_{\mathbf{i}}$ and $m_{\mathbf{f}}$. Some comments on the imaginary part of $\mathcal{F}_{\mathbf{fi},\alpha}$ are

- In order to generate a non-zero imaginary part in the loop integration, a threshold condition for the initial neutrino mass is required. That is $m_{\mathbf{i}} > m_W + m_\alpha$, namely, initial neutrino mass larger than the sum of the W-boson mass and the charged lepton mass. This is consistent with optical theorem as discussed in Ref. [3].

- Taking the charged lepton flavour to be the electron, $\alpha = e$, the threshold condition for initial neutrino masses is simplified to $m_{\mathbf{i}} > m_W + m_e \approx m_W$.
- There is a second contribution to the imaginary part of $\mathcal{F}_{\mathbf{fi},\alpha}$ if the neutrino in the final state satisfies the threshold condition, $m_{\mathbf{f}} > m_W + m_\alpha$. Due to the sign difference, it partly cancels with the first contribution.

With the above results, we are now able to obtain the most general result for CP asymmetries in neutrino radiative decays. For Dirac neutrinos, recall Eq. (4.74). We derive the CP asymmetry between $\nu_{\mathbf{i}} \to \nu_{\mathbf{f}}\gamma_+$ and $\bar{\nu}_{\mathbf{i}} \to \bar{\nu}_{\mathbf{f}}\gamma_-$ and between $\nu_{\mathbf{i}} \to \nu_{\mathbf{f}}\gamma_-$ and $\bar{\nu}_{\mathbf{i}} \to \bar{\nu}_{\mathbf{f}}\gamma_+$ as

$$\begin{aligned} \Delta^{\rm D}_{CP,+} &= \frac{-\sum_{\alpha,\beta}\mathcal{J}^{\mathbf{if}}_{\alpha\beta}{\rm Im}(\mathcal{F}_{\mathbf{if},\alpha}\mathcal{F}^*_{\mathbf{if},\beta})m_{\mathbf{f}}^2}{\sum_{\alpha,\beta}\mathcal{R}^{\mathbf{if}}_{\alpha\beta}\left[{\rm Re}(\mathcal{F}_{\mathbf{fi},\alpha}\mathcal{F}^*_{\mathbf{fi},\beta})m_{\mathbf{i}}^2 + {\rm Re}(\mathcal{F}_{\mathbf{if},\alpha}\mathcal{F}^*_{\mathbf{if},\beta})m_{\mathbf{f}}^2\right]}\,, \\ \Delta^{\rm D}_{CP,-} &= \frac{-\sum_{\alpha,\beta}\mathcal{J}^{\mathbf{if}}_{\alpha\beta}{\rm Im}(\mathcal{F}_{\mathbf{fi},\alpha}\mathcal{F}^*_{\mathbf{fi},\beta})m_{\mathbf{i}}^2}{\sum_{\alpha,\beta}\mathcal{R}^{\mathbf{if}}_{\alpha\beta}\left[{\rm Re}(\mathcal{F}_{\mathbf{fi},\alpha}\mathcal{F}^*_{\mathbf{fi},\beta})m_{\mathbf{i}}^2 + {\rm Re}(\mathcal{F}_{\mathbf{if},\alpha}\mathcal{F}^*_{\mathbf{if},\beta})m_{\mathbf{f}}^2\right]}\,, \end{aligned} \tag{4.92}$$

where α, β run for charged lepton flavours e, μ, τ and

$$\mathcal{J}^{\mathbf{if}}_{\alpha\beta} = {\rm Im}(\mathcal{U}_{\alpha\mathbf{i}}\mathcal{U}^*_{\alpha\mathbf{f}}\mathcal{U}^*_{\beta\mathbf{i}}\mathcal{U}_{\beta\mathbf{f}})\,, \qquad \mathcal{R}^{\mathbf{if}}_{\alpha\beta} = {\rm Re}(\mathcal{U}_{\alpha\mathbf{i}}\mathcal{U}^*_{\alpha\mathbf{f}}\mathcal{U}^*_{\beta\mathbf{i}}\mathcal{U}_{\beta\mathbf{f}})\,. \tag{4.93}$$

We now outline the contribution of coefficients to the tree-level vertices. We have introduced a set of Jarlskog-like parameters $\mathcal{J}^{\mathbf{if}}_{\alpha\beta}$ to describe the CP violation from the vertex contribution. This parametrisation follows the famous definition of the Jarlskog invariant used to describe CP violation in neutrino oscillations [347, 348]. The Jarlskog-like parameters are invariant under any phase rotation of charged leptons and neutrinos. If the Jarlskog-like parameters vanish, no CP violation is generated in the neutrino transition dipole moment.

For Majorana neutrinos, the relevant CP asymmetries, via Eq. (4.77), are given by

$$\begin{aligned} \Delta^{\rm M}_{CP,+} =& -\Delta^{\rm M}_{CP,-} \\ =& \frac{\sum_{\alpha,\beta}\mathcal{J}^{\mathbf{if}}_{\alpha\beta}\left[{\rm Im}(\mathcal{F}_{\mathbf{fi},\alpha}\mathcal{F}^*_{\mathbf{fi},\beta})m_{\mathbf{i}}^2 - {\rm Im}(\mathcal{F}_{\mathbf{if},\alpha}\mathcal{F}^*_{\mathbf{if},\beta})m_{\mathbf{f}}^2\right] - 2\mathcal{V}^{\mathbf{if}}_{\alpha\beta}{\rm Im}(\mathcal{F}_{\mathbf{fi},\alpha}\mathcal{F}^*_{\mathbf{if},\beta})m_{\mathbf{i}}m_{\mathbf{f}}}{\sum_{\alpha,\beta}\mathcal{R}^{\mathbf{if}}_{\alpha\beta}\left[{\rm Re}(\mathcal{F}_{\mathbf{fi},\alpha}\mathcal{F}^*_{\mathbf{fi},\beta})m_{\mathbf{i}}^2 + {\rm Re}(\mathcal{F}_{\mathbf{if},\alpha}\mathcal{F}^*_{\mathbf{if},\beta})m_{\mathbf{f}}^2\right] - 2\mathcal{C}^{\mathbf{if}}_{\alpha\beta}{\rm Re}(\mathcal{F}_{\mathbf{fi},\alpha}\mathcal{F}^*_{\mathbf{if},\beta})m_{\mathbf{i}}m_{\mathbf{f}}} \end{aligned} \tag{4.94}$$

where

$$\mathcal{V}^{\mathbf{if}}_{\alpha\beta} = {\rm Im}(\mathcal{U}_{\alpha\mathbf{i}}\mathcal{U}^*_{\alpha\mathbf{f}}\mathcal{U}_{\beta\mathbf{i}}\mathcal{U}^*_{\beta\mathbf{f}})\,, \qquad \mathcal{C}^{\mathbf{if}}_{\alpha\beta} = {\rm Re}(\mathcal{U}_{\alpha\mathbf{i}}\mathcal{U}^*_{\alpha\mathbf{f}}\mathcal{U}_{\beta\mathbf{i}}\mathcal{U}^*_{\beta\mathbf{f}})\,. \tag{4.95}$$

$\mathcal{V}^{\mathbf{if}}_{\alpha\beta}$ is another type of Jarlskog-like parameters which appears only for Majorana neutrinos. It was first defined in the study of neutrino-antineutrino oscillations in the context of only three light neutrinos [349]. They are invariant under phase rotations for charged lepton but not for neutrinos.

4.2.5 CP Violation in Heavy Neutrino Radiative Decays

In the rest of this paper, we will discuss the CP violating radiative decay in the seesaw model, where the tiny masses for left-handed neutrinos are generated due to the suppression of heavy right-handed neutrinos. We recall that the notation $\Delta_{CP} = \Delta^{\rm M}_{CP,+}$ for Majorana neutrinos is used.

We consider the minimal seesaw model where only two copies of right-handed neutrinos are introduced [341]. This is the minimal number required to generate two non-zero mass square differences i.e. $\Delta m^2_{21} \equiv m_2^2 - m_1^2$ and $\Delta m^2_{31} \equiv m_3^2 - m_1^2$. We denote two right-handed neutrino mass eigenstates as N_I for $I = 1, 2$, with masses $M_1 < M_2$. The following discussion is straightforwardly generalised to a canonical seesaw model with three right-handed neutrinos. Including more copies of right-handed neutrinos just increases the number of free model parameters.

The minimal seesaw model predicts one massless neutrino $m_1 = 0$ in the normal mass ordering ($m_1 < m_2 < m_3$) and $m_3 = 0$ in the inverted mass ordering ($m_3 < m_1 < m_2$) schemes. In this section, we will only consider the normal mass ordering as we don't expect the inverted mass ordering to make a significant difference. Moreover, the inverted ordering is slightly disfavoured ($\Delta\chi^2 = 6.2$) by the current neutrino oscillation global fit data [350]. We take the best fit (in the 3σ ranges) of mass square differences in the normal ordering scheme [350], this is

$$\begin{aligned} m_2 &= \sqrt{\Delta m^2_{21}} = 8.60\ (8.24 \to 8.95)\ \text{meV}\,, \\ m_3 &= \sqrt{\Delta m^2_{31}} = 50.2\ (49.3 \to 51.2)\ \text{meV}\,. \end{aligned} \tag{4.96}$$

We recall once again the lepton charged-current interaction in Eq. (4.78). The three light neutrino mixing is represented by the first 3×3 submatrix of $\mathcal{U}$, i.e., $\mathcal{U}_{\alpha i}$ for $\alpha = e, \mu, \tau$ and $i = 1, 2, 3$. In the case of negligible non-unitary effect, $\mathcal{U}_{\alpha i}$ is parametrised as

$$U \equiv \begin{pmatrix} c_{12}c_{13} & c_{13}s_{12} & s_{13}e^{-i\delta} \\ -c_{23}s_{12} - c_{12}s_{13}s_{23}e^{i\delta} & c_{12}c_{23} - s_{12}s_{13}s_{23}e^{i\delta} & c_{13}s_{23} \\ s_{12}s_{23} - c_{12}c_{23}s_{13}e^{i\delta} & -c_{12}s_{23} - c_{23}s_{12}s_{13}e^{i\delta} & c_{13}c_{23} \end{pmatrix} \begin{pmatrix} e^{i\rho} & 0 & 0 \\ 0 & e^{i\sigma} & 0 \\ 0 & 0 & 1 \end{pmatrix}, \tag{4.97}$$

where $c_{ij} = \cos\theta_{ij}$, $s_{ij} = \sin\theta_{ij}$, θ_{ij} (for $ij = 12, 13, 23$) are three mixing angles, δ is the Dirac-type CP violating phase and ρ and σ are two Majorana-type CP violating phases. U is a 3×3 unitary matrix, $U^\dagger U = UU^\dagger = \mathbf{1}_{3\times 3}$. The three mixing angles and the Dirac CP violating phase for normal mass ordering are measured to be

$$\begin{aligned} \theta_{13} &= 8.61^\circ \quad (8.22^\circ \to 8.99^\circ)\,, \\ \theta_{12} &= 33.82^\circ\ (31.61^\circ \to 36.27^\circ)\,, \\ \theta_{23} &= 48.3^\circ \quad (40.8^\circ \to 51.3^\circ)\,, \\ \delta &= 222^\circ \qquad (141^\circ \to 370^\circ) \end{aligned} \tag{4.98}$$

at the best fit (in the 3σ ranges) [350]. As we work in the minimal seesaw model where the lightest neutrino mass $m_1 = 0$ is massless, ρ is unphysical and will not be considered below. We are left with two CP violating phases δ and σ from the mixing of light neutrinos.

Accounting for the non-unitary effect, namely, the fraction of heavy neutrinos contributing to the flavour mixing $\mathcal{U}_{\alpha(I+3)}$, which we denote as $R_{\alpha I}$ from now on. $\mathcal{U}_{\alpha i}$ is only approximately equal to $U_{\alpha i}$, $\mathcal{U}_{\alpha i} = U_{\alpha i} + \mathcal{O}(RR^\dagger)$. $RR^\dagger$ is constrained to be maximally at milli-level [351, 352]. Therefore, $\mathcal{U}_{\alpha i} \approx U_{\alpha i}$ is still a very good approximation.

The charged-current interaction for leptons in the mass eigenstates is now written as

$$\mathcal{L}_{\text{c.c.}} = \sum_{\alpha=e,\mu,\tau} \frac{g}{\sqrt{2}}\, \bar{\ell}_\alpha \gamma^\mu P_{\text{L}} \Big(\sum_{i=1,2,3} U_{\alpha i}\nu_i + \sum_{I=1,2} R_{\alpha I} N_I \Big) W_\mu^- + \mathcal{O}(RR^\dagger) + \text{h.c.}\,. \quad (4.99)$$

We use the Casas-Ibarra parametrisation [353] to express R in the form

$$R_{\alpha I} = \sum_{i=1,2} U_{\alpha i}\Omega_{iI}\sqrt{\frac{m_{i+1}}{M_I}}\,. \quad (4.100)$$

Here, Ω is a 2×2 complex orthogonal matrix satisfying $\Omega^T\Omega = \Omega\Omega^T = \mathbf{1}$.[9] We parametrise it as

$$\Omega = \begin{pmatrix} \cos\omega & \sin\omega \\ -\zeta\sin\omega & \zeta\cos\omega \end{pmatrix}, \quad (4.101)$$

where ω is a complex parameter and $\zeta = \pm 1$. The two possible values of ζ correspond to two distinct branches of Ω [335, 354]. The Yukawa coupling Y between lepton doublets and right-handed neutrinos are directly connected with R via $Y_{\alpha I} = R_{\alpha I} M_I / v_H$ [355].

In the whole model, three CP violating parameters are induced, δ, σ and $\text{Im}[\omega]$, if $\delta = 0$, $\sigma = 0$ or $\pi/2$ and $\text{Im}[\omega] = 0$, no CP violation can be generated.

The CP violation in the neutrino transition dipole moment can be checked by the study of the CP asymmetry of neutrino radiative decay. There are three channels of interest, $\nu_i \to \nu_j\gamma$, $N_I \to \nu_i\gamma$ and $N_2 \to N_1\gamma$. For the first channel, since the light neutrinos have masses much lighter than the W boson, no CP violation can be generated. The CP asymmetry for $N_I \to \nu_i\gamma$ is non-zero if N_I has a mass $M_I > m_W + m_e \approx m_W$. Note that in this case, masses of three light neutrinos ν_i for $i = 1, 2, 3$ are negligible and photons released in the relevant three channels are indistinguishable, so we sum these channels together and calculate the overall CP asymmetry [cf. Eq. (4.94)]

$$\Delta_{CP}(N_I \to \nu\gamma) = \frac{\sum_i \sum_{\alpha,\beta} \mathcal{J}_{\alpha\beta}^{(I+3)i} \text{Im}(\mathcal{F}_{i(I+3),\alpha}\mathcal{F}^*_{i(I+3),\beta})}{\sum_i \sum_{\alpha,\beta} \mathcal{R}_{\alpha\beta}^{(I+3)i} \text{Re}(\mathcal{F}_{i(I+3),\alpha}\mathcal{F}^*_{i(I+3),\beta})}\,. \quad (4.102)$$

[9] In the case of three copies of right-handed neutrinos, Ω is a 3×3 matrix, this leads to each entry in $R_{\alpha I}$ for $I = 1, 2, 3$ to be expressed as

$$R_{\alpha I} = \sum_{i=1,2,3} U_{\alpha i}\Omega_{iI}\sqrt{\frac{m_i}{M_I}}\,.$$

This parameter is tiny, numerically confirmed to be maximally $\lesssim 10^{-17}$. The reason why it is so small can be understood as follows.Since m_i is negligible,

$$\mathcal{F}_{i(I+3),\alpha} = \mathcal{F}_{1(I+3),\alpha} \tag{4.103}$$

and

$$\begin{aligned}\Delta_{CP}(N_I \to \nu\gamma) \propto \sum_i \sum_{\alpha,\beta} \mathcal{J}^{(I+3)i}_{\alpha\beta} &= \sum_i \sum_{\alpha,\beta} \mathrm{Im}(\mathcal{U}_{\alpha(I+3)}\mathcal{U}^*_{\alpha i}\mathcal{U}^*_{\beta(I+3)}\mathcal{U}_{\beta i}) \\ &\approx \sum_i \sum_{\alpha} \mathrm{Im}(\mathcal{U}_{\alpha(I+3)}\mathcal{U}^*_{\alpha(I+3)}) = 0. \end{aligned} \tag{4.104}$$

Finally, we focus on the CP asymmetry in $N_2 \to N_1\gamma$, which is given by

$$\Delta_{CP} = \frac{\mathcal{J}^{54}_{\alpha\beta}\left[\mathrm{Im}(\mathcal{F}_{45,\alpha}\mathcal{F}^*_{45,\beta})M_2^2 - \mathrm{Im}(\mathcal{F}_{54,\alpha}\mathcal{F}^*_{54,\beta})M_1^2\right] - 2\mathcal{V}^{54}_{\alpha\beta}\mathrm{Im}(\mathcal{F}_{45,\alpha}\mathcal{F}^*_{54,\beta})M_2M_1}{\mathcal{R}^{54}_{\alpha\beta}\left[\mathrm{Re}(\mathcal{F}_{45,\alpha}\mathcal{F}^*_{45,\beta})M_2^2 + \mathrm{Re}(\mathcal{F}_{54,\alpha}\mathcal{F}^*_{54,\beta})M_1^2\right] - 2\mathcal{C}^{54}_{\alpha\beta}\mathrm{Re}(\mathcal{F}_{45,\alpha}\mathcal{F}^*_{54,\beta})M_2M_1}.$$

Here, we are doing the sum $\sum_{\alpha,\beta}$ in the numerator and denominator, and $\mathcal{C}^{\mathbf{if}}_{\alpha\beta}$ and $\mathcal{V}^{\mathbf{if}}_{\alpha\beta}$ were defined in Eq. (4.95) and the Jarlskog-like parameters are given by $\mathcal{J}^{54}_{\alpha\beta} = \mathrm{Im}(R_{\alpha 2}R^*_{\alpha 1}R^*_{\beta 2}R_{\beta 1})$ and $\mathcal{V}^{54}_{\alpha\beta} = \mathrm{Im}(R_{\alpha 2}R^*_{\alpha 1}R_{\beta 2}R^*_{\beta 1})$.

The behaviour of the CP asymmetry as a function of the right-handed neutrino mass M_2 is shown in Figure 4.4. We can see that the CP asymmetry of this channel is much larger than that in $N \to \nu\gamma$. In this figure, we vary M_2 from 0.1 to 10 TeV and consider three benchmark scenarios where the mass ratio M_1/M_2 is fixed to 0.2, 0.5 and 0.8 respectively. In all plots, we fix $\zeta = 1$ and the Majorana phase $\sigma = \pi/2$. Therefore, no Majorana-type CP violation is induced. We use the best-fit oscillation data as inputs which include a large CP violating value for δ. In the top panel, we fix ω to be real, $\omega = 5$. Therefore, δ is the only source of CP violation. We note that a large CP asymmetry ratio $|\Delta_{CP}| \sim 10^{-5}$-$10^{-3}$ is easily generated. Peaks of $|\Delta_{CP}|$ are generated due to the enhancement in the log term of $\mathrm{Im}(\mathcal{F}_{\mathbf{fi},\alpha})$ around $M_2 \approx m_W$ (cf. Eq.(4.90)). Sharp changes refer to cancellations occurring in Δ_{CP} due to the selected values of inputs. In the bottom panel, $\omega = 5 - 5i$, both δ and ω contribute to the CP violation. The constraints on $|RR^\dagger|$ from the non-unitarity effect has been included [351].

We also show the branching ratio $\mathcal{B}(N_2 \to N_1\gamma) = \Gamma(N_2 \to N_1\gamma)/\Gamma_{N_2}$. In the total decay width Γ_{N_2}, we include five main decay channels $N_2 \to \ell^- W^+_{L,T}$, $\nu Z_{L,T}$ and νH [356]. Although the CP asymmetry is large, the branching ratio is suppressed as shown in the right panel of Figure 4.4, leading to very small $\Delta_{CP} \times \mathcal{B}$. We note that there is particularly interesting phenomenology for $\omega = 5 - 5i$ as the branching ratio is greatly enhanced when assigning an imaginary part to ω. This is because the mixing R is enhanced by $\sin\omega$ and $\cos\omega$, which are both $\sim e^{|\mathrm{Im}[\omega]|}$. One can further increase the branching ratio to be much larger than 10^{-13} by enlarging the imaginary part of ω, hence the combination $\Delta_{CP} \times \mathcal{B}$ is also enhanced. Another feature of the right panels is that, in spite of the different orders of magnitude, the shape profiles of the curves are almost the same between $\omega = 5$ and $5 - 5i$. This is because the inclusion of an imaginary part for ω simply changes the size of $R_{\alpha I}$ but rarely changes

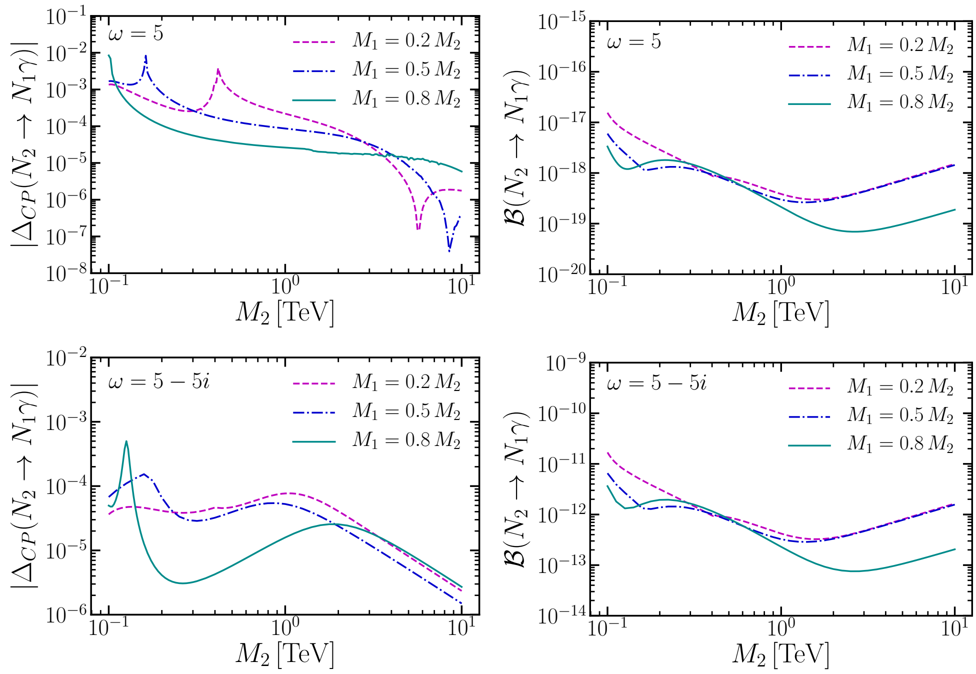

FIGURE 4.4: The CP asymmetry (left panel) and branching ratio (right panel) for the radiative decay process $N_2 \to N_1\gamma$ as a function of the heavy neutrino mass M_2. Four different benchmarks for the lightest right-handed neutrino $M_1 = 0.2M_2, 0.5M_2, 0.8M_2$ are considered as per the respective plot legends. Values of ω are fixed at $\omega = 5$ (top panel) and $5 - 5i$ (bottom panel), respectively. In all cases, we use the best-fit oscillation data as inputs while we set $\zeta = 1$ with a Majorana phase $\sigma = \pi/2$.

the correlation between the decay width and right-handed neutrino masses.

In Figure 4.5 we show a numerical scan performed for M_2 in the same range. We sample M_2 logarithmically in the range [0.1, 10] TeV and the ratio M_1/M_2 in the range [0.1, 1). The blue points refer to purely real ω randomly sampled from $[0, 2\pi)$. In this case, only two of the CP violating phases δ and σ contribute to the CP violation. the CP asymmetry Δ_{CP} shows a roughly linear correlation with M_2^{-1}. Most points of Δ_{CP} are located in the regimes (10^{-3}, 10^{-5}) for $M_2 \simeq 0.1$ TeV, (10^{-4}, 10^{-6}) for $M_2 \simeq 1$ TeV and (10^{-5}, 10^{-7}) for $M_2 \simeq 10$ TeV. However, the branching ratio of the decay is tiny, between (10^{-20}, 10^{-15}), which makes the CP asymmetry unobservable in experiments. For the red points, we allow an imaginary part for ω as well, namely, $\mathrm{Im}[\omega] \in [-5, 5]$. A CP asymmetry of order one is then easily achieved. The branching ratio of the radiative decay can maximally reach $\sim 10^{-11}$. We have also checked that the combination $\Delta_{CP} \times \mathcal{B}$ can maximally reach 4×10^{-15}. Note that considering a larger imaginary part of ω could further enhance the branching ratio and $\Delta_{CP} \times \mathcal{B}$. However, as this process happens at one loop and there are constraints on the non-unitary effect, the branching ratio is always suppressed by $(16\pi^2)^{-2}|RR^\dagger|^2/|RR^\dagger|$. By taking $RR^\dagger \sim 10^{-3}$, we obtain a branching ratio which maximally reaches $\sim 10^{-7}$ and is therefore challenging to probe in future experiments.

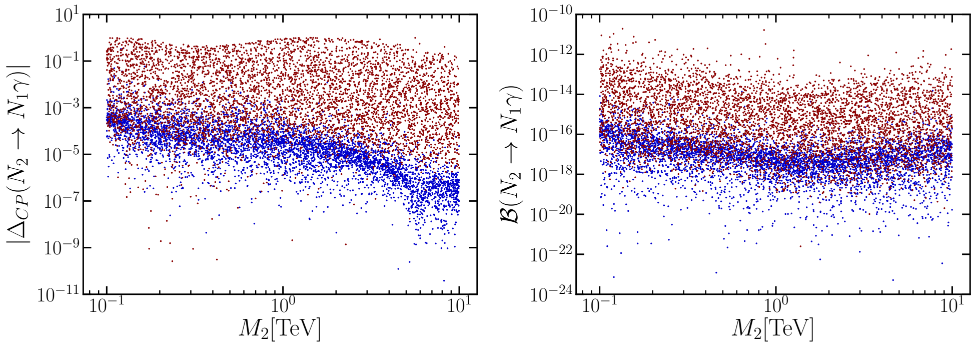

FIGURE 4.5: The CP asymmetry parameter Δ_{CP} (left) and branching ratio (right) scanned in the region M_2 in $[0.1, 10]$ TeV and the ratio M_1/M_2 in $[0.1,\ 1)$, where both masses are scanned in the logarithmic scale. The red region refers to $\omega = [0, 2\pi] + i[-5, 5]$ while the blue region is the smaller $\omega = [0, 2\pi]$. All oscillation parameters are scanned in the 3σ ranges, $\omega = [0, 2\pi]$ and $\zeta = +1$ are used. The scan performed for the $\zeta = -1$ branch gives the same distribution and is thus omitted.

4.2.6 Conclusion

We study the CP violation in the neutrino electromagnetic dipole moment. A full one-loop calculation of the transition dipole moment is performed in the context of the Standard Model with an arbitrary number of right-handed singlet neutrinos. The CP asymmetry is analytically derived in terms of the leptonic mixing matrix accounting for heavy neutrino mass eigenstates. A detailed explanation of how to generate a non-vanishing CP asymmetry in the neutrino transition dipole moment is provided. This requires a threshold condition for the initial neutrino mass being larger than the sum of W-boson mass and the charged leptons runnning in the loop and a CP violating phase in the lepton flavour mixing matrix. The threshold condition is necessary to generate a non-zero imaginary part for the loop function. An analytical formulation of this loop integral imaginary component is derived. The lepton flavour mixing for vertex contributions has been parametrised in terms of Jarlskog-like parameters. For Majorana particles, the CP asymmetry is identical to the asymmetry of circularly-polarised photons released from the radiative decay.

The formulation is then applied to a minimal seesaw model where two right-handed neutrinos N_1 and N_2 are introduced with the mass ordering $M_1 < M_2$. A complete study of CP asymmetry in all radiative decay channels was performed, where the mass range 0.1 TeV $< M_2 <$ 10 TeV is considered. The CP asymmetry in $N_{1,2} \to \nu\gamma$ is very small, maximally reaching 10^{-17}. In the $N_2 \to N_1\gamma$ channel, the CP asymmetry is significantly enhanced, with Δ_{CP} achieving 10^{-5}-10^{-3}, even with the Dirac phase δ being the only source of CP violation. There is a significant correlation between the CP violation in radiative decay and that coming from oscillation experiments. We performed a parameter scan of the CP asymmetry with oscillation data in 3σ ranges taken as inputs and found that the CP asymmetry can maximally reach order one.

4.3 CP Asymmetries in the Rare Top Decays $t \to c\gamma$ and $t \to cg$

The study of radiative decays has been of interest for many decades because they provide an experimentally clean probe for new physics [357]. The electromagnetic dipole moment of heavy quarks can be generated at various loop levels and their radiative decays are induced by the off diagonal parts of the dipole moments analogously to the lepton sector [3, 4]. Precision measurements of electromagnetic interactions provide a tantalising probe for new physics beyond the SM [4]. This is particularly relevant due to the presence of current top factories such as the LHC which provide an unprecedented increase in top quark statistics, thereby enabling radical improvement in the understanding of heavy quark properties [357]. Of particular importance are precision studies of the various rare top quark decays. These include flavour-changing neutral (FCN) decays $t \to cZ$ as well as $t \to c\gamma$ and $t \to cg$ [358]. The radiative decays of heavy fermions are more significant than those of light fermions due to their larger partial widths resulting from their much higher relative mass. Hence, such clean channels are of major importance in testing precise theoretical predictions for particle properties and searching for tensions with the SM.

Within the SM, these processes are mediated at lowest order in perturbation theory by penguin diagrams with charged down-type quarks running loops. However, due to the large hierarchy in the down-type quark masses relative to the W bosons in the loop, these decays are suppressed by the GIM mechanism. This is in contrast with processes such as $b \to s\gamma$, which contain the much heavier top quark in the loop. This extra suppression resulted in branching ratios being computed at $\lesssim 10^{-10}$ or smaller [359–362]. These were later estimated with more precision in Ref. [358], using the the b-quark running mass at the top mass scale in the $\overline{\text{MS}}$ scheme. The use of the running b-quark mass represents a more rigorous treatment for the calculation as the top quark decays at its pole mass.

In this work, we focus primarily on a precise computation of the SM branching ratios for the radiative top decays with the current CKM best fit values and particle masses extracted from Ref. [75]. Additionally, we pay particular interest to the computation of the CP asymmetry resulting from the imaginary part of the loop integrals that imply $\Gamma(t \to c\gamma) \neq \Gamma(\bar{t} \to \bar{c}\gamma)$. We provide the closed form analytical formulation for the kinetic loop terms and their imaginary parts that generate the CP asymmetry. Here we note that by kinetic loop term, we refer to the contribution coming explicitly from the particles running in the loop and not the vertex contributions which can be factorized separately. We will continue with this nomenclature for the rest of this work. This is in contrast to previous studies which are limited to numerical estimations of the loop functions derived from generic Passarino-Veltman functions [358]. Although in the SM, the radiative process branching ratios are currently unobservable due to the aforementioned large GIM suppression, the above results can be easily applied to a host of beyond the SM theories which we briefly outline below.

A notable application of the formulation shown could be beyond the SM extensions with heavy VLQs [358, 363] e.g. heavy t' and b' states with extended CKM matrices. Many of which provide an improved global fit to data compared to the SM when considering several flavour physics observables and precision electroweak measurements [364–366]. A comprehensive review of the various types of VLQs can be found in Ref. [367] and there is some related discussion in Ref. [368]. The addition of quark singlets to the SM particle content represents the simplest way to break the GIM mechanism and can thereby enable large radiative decay widths. These models typically contain a non-unitary higher dimensional CKM matrix and contain FCNC couplings to the Z boson at tree-level since the new heavy quarks are not $SU(2)_L$ doublets.

Moreover, there are other SM extensions that can enhance branching ratios for top decays by many orders of magnitude thereby yielding compelling phenomenology. For instance, in 2HDMs we find that $\mathcal{B}(t \to cZ) \sim 10^{-6}$, $\mathcal{B}(t \to c\gamma) \sim 10^{-7}$, $\mathcal{B}(t \to cg) \sim 10^{-5}$ can be achieved [360]. More recently, it was shown that in the type-III 2HDM one could expect up to $N(t \to c\gamma) = 100$ events at the LHC with an integrated luminosity of $300fb^{-1}$ in certain parameter regions [369]. The rare top quark decays at one-loop with FCNCs coming from additional fermions and gauge bosons has been studied in several extensions of the SM such as the minimal super-symmetric model, Left-Right symmetry models, top colour assisted technicolour and two Higgs doublets with four generations of quarks [360, 369–375]. There is also potential for similar radiative processes to occur in models with leptoquarks such as light versions of the ones shown in [6, 7].

These applications are of particular interest, since it was recently shown that a net circular polarisation, specifically an asymmetry between two circularly polarised photons γ_+ and γ_-, is generated if CP is violated in neutrino radiative decays [309]. The same CP effect is induced for top quarks or new VLQs and therefore polarisation measurements on the resulting photons are a crucial and experimentally clean probe for new physics.

The outline of the section is as follows, we first show the full radiative process calculation in Section 4.3.1. This section is further divided into an overview of the interaction Lagrangian, computation of the relevant amplitudes, analytical evaluation of the kinetic terms and most importantly their imaginary parts (which are responsible for generating CP asymmetry), followed by showing the computation for the CP asymmetry itself. This is accompanied by Section 4.3.5 which contains an overview of the process to calculate the radiative branching fractions and decay widths for the various channels as well as the main numerical results. Finally, we briefly discuss the applications of the formalism to beyond the SM theories in Section 4.3.8 via inclusion of heavy VLQs and the 2HDM.

4.3.1 Calculation of Radiative Processes

4.3.2 Calculation of Lorentz Invariant Amplitudes

In this work we first overview the interaction Lagrangian relating the mass eigenstates of the up and down-type quarks via the SM charge current interaction. We denote the up-type quarks as $u_\beta = (u, c, t)$ and the down-type quarks as $d_\alpha = (d, s, b)$. The corresponding interaction Lagrangian is then given by

$$\mathcal{L}_{int} = -\frac{g}{\sqrt{2}} \left[\bar{u}_\beta \gamma^\mu P_L V_{\beta\alpha} d_\alpha\right] W^+_\mu + h.c. \tag{4.105}$$

Where V is the SM 3×3 CKM matrix and g is the usual weak interaction gauge coupling constant and P_L is the left-chiral projection operator.

We focus firstly on the contributions to the rare photon radiative top decay mediated by SM interactions as given in Figure 4.6. In this work, we are primarily interested in top decays, hence we denote the initial state t and the final state quark to be generically $u_\beta = (u, c)$ and $d_\alpha = (d, s, b)$. Hence we may write the corresponding $t \to u_\beta \gamma$ process amplitudes in full generality as follows

$$i\mathcal{M}(t \to u_\beta + \gamma_\pm) = i\bar{u}(p_{\mathbf{f}})\Gamma^\mu_{\mathbf{fi}}(q^2)u(p_{\mathbf{i}})\varepsilon^*_{\pm,\mu}(q)\,. \tag{4.106}$$

More explicitly, for each Feynman diagram shown in Figure 4.6, we have

$$\begin{aligned}
i\mathcal{M}_1 &= i\frac{eg^2}{6}V_{t\alpha}V^*_{\beta\alpha}\int\frac{d^4p}{(2\pi)^4}\frac{\overline{u}(p_{\mathbf{f}})\gamma_\mu P_L(\not{p}_{\mathbf{f}} - \not{p} + m_d)\gamma^\rho(\not{p}_{\mathbf{i}} - \not{p} + m_d)\gamma^\mu P_L u(p_{\mathbf{i}})\epsilon^*_\rho(q)}{[(p_{\mathbf{f}} - p)^2 - m_d^2][p^2 - m_W^2][(p_{\mathbf{i}} - p)^2 - m_d^2]},\\
i\mathcal{M}_2 &= i\frac{eg^2}{6m_W^2}V_{t\alpha}V^*_{\beta\alpha}\int\frac{d^4p}{(2\pi)^4}\frac{\overline{u}(p_{\mathbf{f}})\mathcal{N}_2 u(p_{\mathbf{i}})\epsilon^*_\rho(q)}{[(p_{\mathbf{f}} - p)^2 - m_d^2][(p_{\mathbf{i}} - p)^2 - m_d^2][p^2 - m_W^2]},\\
i\mathcal{M}_3 &= i\frac{eg^2}{2}V_{t\alpha}V^*_{\beta\alpha}\int\frac{d^4p}{(2\pi)^4}\frac{\overline{u}(p_{\mathbf{f}})\gamma_\nu P_L(\not{p} + m_d)\gamma_\mu P_L V(p_{\mathbf{i}}, p_{\mathbf{f}}, p)^{\mu\nu\rho}u(p_{\mathbf{i}})\epsilon^*_\rho(q)}{[(p_{\mathbf{f}} - p)^2 - m_W^2][p^2 - m_d^2][(p_{\mathbf{i}} - p)^2 - m_W^2]},\\
i\mathcal{M}_4 &= i\frac{eg^2}{2m_W^2}V_{t\alpha}V^*_{\beta\alpha}\int\frac{d^4p}{(2\pi)^4}\frac{\overline{u}(p_{\mathbf{f}})\mathcal{N}_4 u(p_{\mathbf{i}})\epsilon^*_\rho(q)}{[(p_{\mathbf{f}} - p)^2 - m_W^2][p^2 - m_d^2][(p_{\mathbf{i}} - p)^2 - m_W^2]},\\
i\mathcal{M}_{5+6} &= i\frac{eg^2}{2}V_{t\alpha}V^*_{\beta\alpha}\int\frac{d^4p}{(2\pi)^4}\overline{u}(p_{\mathbf{f}})\left[\frac{\gamma^\rho P_L(\not{p} + m_d)(m_d P_L - m_{\mathbf{i}} P_R)}{(p^2 - m_d^2)((p_{\mathbf{f}} - p)^2 - m_W^2)((p_{\mathbf{i}} - p)^2 - m_W^2)}\right.\\
&\quad \left. - \frac{(m_\beta P_L - m_d P_R)(\not{p} + m_d)\gamma^\rho P_L}{(p^2 - m_d^2)((p_{\mathbf{i}} - p)^2 - m_W^2)((p_{\mathbf{f}} - p)^2 - m_W^2)}\right]u(p_{\mathbf{i}})\epsilon^*_\rho(q).
\end{aligned} \tag{4.107}$$

where for compactness, the numerators are defined

$$\begin{aligned}
\mathcal{N}_2 &= (m_\beta P_L - m_d P_R)(\not{p}_{\mathbf{f}} - \not{p} + m_d)\gamma^\rho(\not{p}_{\mathbf{i}} - \not{p} + m_d)(m_d P_L - m_{\mathbf{i}} P_R),\\
\mathcal{N}_4 &= (m_{\mathbf{f}} P_L - m_d P_R)(\not{p} + m_d)(m_d P_L - m_{\mathbf{i}} P_R)(2p - p_{\mathbf{i}} - p_{\mathbf{f}})^\rho,
\end{aligned} \tag{4.108}$$

and the contribution from the triple gauge boson vertex is given

$$V^{\mu\nu\rho} = g^{\mu\nu}(2p_{\mathbf{i}} - p - p_{\mathbf{f}})^\rho + g^{\rho\mu}(2p_{\mathbf{f}} - p - p_{\mathbf{i}})^\nu + g^{\nu\rho}(2p - p_{\mathbf{i}} - p_{\mathbf{f}})^\mu\,, \tag{4.109}$$

and e refers to the usual $U(1)$ Abelian electromagnetic charge. We denote the initial state momentum of the top quark as $p_{\mathbf{i}}$ and the final state up-type quark as $p_{\mathbf{f}}$. The 't Hooft–Feynman gauge is chosen to simplify the amplitude calculations and the scalar χ refers to the unphysical charged Goldstone boson. We apply the Gordon decomposition as well as Ward identity $q_\mu\mathcal{M}^\mu = 0$ and ignore all vector terms proportional to γ^μ, since these are simply vertex corrections to the overall electric charge, we need only consider tensor-like terms within the current Γ_μ to determine the transition form factor resulting from these diagrams.

We follow the standard procedure to integrate over all internal momenta p in the loop with the help of the Feynman parametrisation. We take the initial and final state chiralities into account followed by factorising the electromagnetic dipole

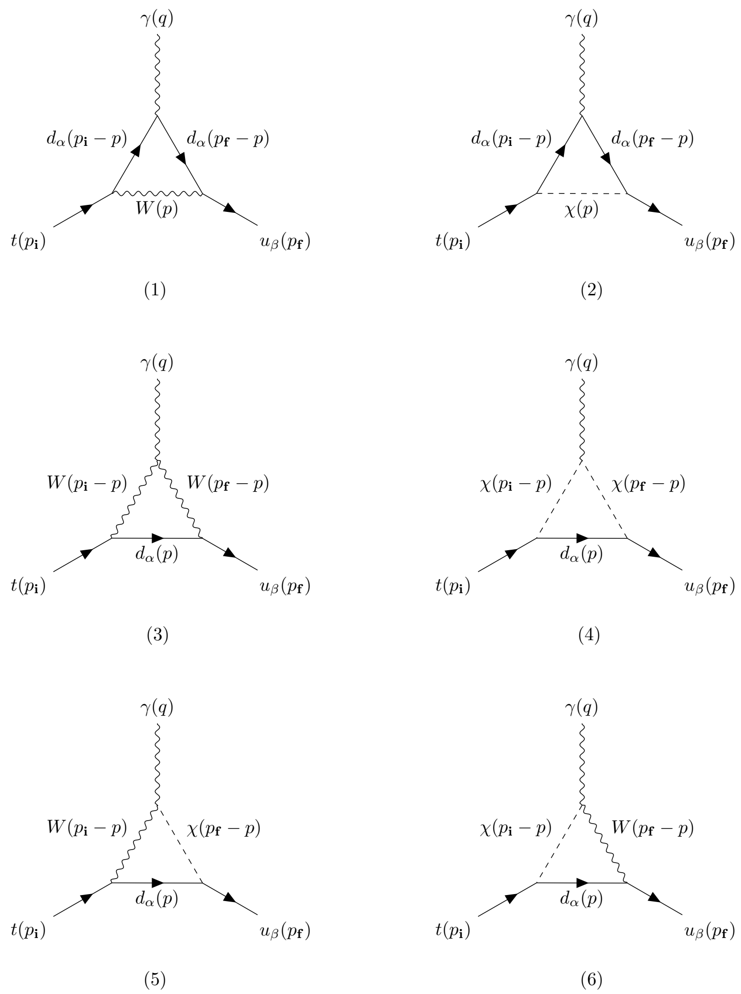

FIGURE 4.6: Feynman Diagrams for the one-loop radiative top decay $t \to u_\beta\gamma$ induced by SM weak interactions with SM fields. We denote the amplitudes for the six diagrams as $\mathcal{M}_1 - \mathcal{M}_6$ accordingly. For the gluon channel, $t \to u_\beta g$, only the first two diagrams contribute and the photon is replaced with a gluon. In all cases, external radiated gauge boson momenta is denoted $q = p_\mathbf{f} - p_\mathbf{i}$ while the internal momenta that are integrated over in the loop calculations are denoted p.

moment terms with coefficients as

$$\Gamma^{\mu,(\mathrm{k})}_{\mathbf{fi},\alpha} = \frac{eg^2}{4(4\pi)^2} V_{\mathbf{i}\alpha} V^*_{\mathbf{f}\alpha} i\sigma^{\mu\nu} q_\nu \int_0^1 \mathrm{d}x\mathrm{d}y\mathrm{d}z\, \delta(x+y+z-1)\, \mathcal{P}^{(\mathrm{k})} . \quad (4.110)$$

where each loop contribution is given by

$$\begin{aligned}
\mathcal{P}^{(1)} &= \frac{-2x(x+z)m_{\mathbf{i}}P_{\mathrm{R}} - 2x(x+y)m_{\mathbf{f}}P_{\mathrm{L}}}{3\Delta_{\alpha W}(x,y,z)}\,, \\
\mathcal{P}^{(2)} &= \frac{[xzm_{\mathbf{f}}^2 - ((1-x)^2+xz)m_d^2]m_{\mathbf{i}}P_{\mathrm{R}} + [xym_{\mathbf{i}}^2 - ((1-x)^2+xy)m_d^2]m_{\mathbf{f}}P_{\mathrm{L}}}{3m_W^2\Delta_{\alpha W}(x,y,z)}\,, \\
\mathcal{P}^{(3)} &= \frac{[(1-2x)z - 2(1-x)^2]m_{\mathbf{i}}P_{\mathrm{R}} + [(1-2x)y - 2(1-x)^2]m_{\mathbf{f}}P_{\mathrm{L}}}{\Delta_{W\alpha}(x,y,z)}\,, \\
\mathcal{P}^{(4)} &= \frac{[xzm_{\mathbf{f}}^2 - x(x+z)m_d^2]m_{\mathbf{i}}P_{\mathrm{R}} + [xym_{\mathbf{i}}^2 - x(x+y)m_d^2]m_{\mathbf{f}}P_{\mathrm{L}}}{m_W^2\Delta_{W\alpha}(x,y,z)}\,, \\
\mathcal{P}^{(5)} &= \frac{-zm_{\mathbf{i}}P_{\mathrm{R}}}{\Delta_{W\alpha}(x,y,z)}\,, \\
\mathcal{P}^{(6)} &= \frac{-ym_{\mathbf{f}}P_{\mathrm{L}}}{\Delta_{W\alpha}(x,y,z)}\,,
\end{aligned} \tag{4.111}$$

where it is convenient to define the function in the denominator in terms of the Feynman parameters as

$$\begin{aligned}
\Delta_{W\alpha}(x,y,z) &= m_W^2(1-x) + xm_d^2 - x(ym_{\mathbf{i}}^2 + zm_{\mathbf{f}}^2), \\
\Delta_{\alpha W}(x,y,z) &= m_d^2(1-x) + xm_W^2 - x(ym_{\mathbf{i}}^2 + zm_{\mathbf{f}}^2)\,.
\end{aligned} \tag{4.112}$$

We note that for $t \to u_\beta g$, the structure of amplitudes are largely the same, but we only require $3\mathcal{P}^{(1)}$ and $3\mathcal{P}^{(2)}$ (because the down-quark electric charge prefactor of $Q = \frac{1}{3}$ doesn't appear at the highest vertex) along with the gauge coupling replacement $e \to g_s$ in Eq. (4.110) due to the presence of gluon emission.

4.3.3 Derivation of the Total Kinetic Contribution

We are now ready to compute the total kinetic contribution for both $t \to u_\beta\gamma$ and $t \to u_\beta g$ channels. From Ref. [3], it was shown we could rewrite Eqs. (4.110), (4.111) and (4.112) in terms of the dimensionless kinetic term $\mathcal{F}^\gamma$ such that

$$\Gamma^{\mu,(\mathrm{k})}_{\mathbf{fi},\alpha} = \frac{eG_{\mathrm{F}}}{4\sqrt{2}\pi^2}V_{\mathbf{i}\alpha}V^*_{\mathbf{f}\alpha}i\sigma^{\mu\nu}q_\nu(\mathcal{F}^\gamma_{\mathbf{fi},\alpha}m_{\mathbf{i}}P_{\mathrm{R}} + \mathcal{F}^\gamma_{\mathbf{if},\alpha}m_{\mathbf{f}}P_{\mathrm{L}})\,. \tag{4.113}$$

In the case of a gluon being radiated instead of a photon (which is otherwise identical to the first two diagrams in Figure 4.6), we simply make the coupling replacement $e \to g_s$ in the above expression as well as $\mathcal{F}^\gamma \to \mathcal{F}^g$. Performing the loop integrals using the same approach shown in Ref. [4] and summing the kinetic contribution for each individual diagram $\sum_{k=1}^{5} \mathcal{P}^{(k)}$ with a radiated photon results in

$$\mathcal{F}^{\gamma}_{\mathbf{fi},d} = \int_0^1 \mathrm{d}x \left\{ \frac{(m_{\mathbf{i}}^2 - m_d^2 - 2m_W^2)(m_d^2 + m_{\mathbf{f}}^2 x^2) + x m^4_{\mathbf{fi},d}}{3(m_{\mathbf{f}}^2 - m_{\mathbf{i}}^2)^2 x} \times \right.$$

$$\times \log\left(\frac{m_d^2 + x(m_W^2 - m_d^2 - m_{\mathbf{i}}^2) + m_{\mathbf{i}}^2 x^2}{m_d^2 + x(m_W^2 - m_d^2 - m_{\mathbf{f}}^2) + m_{\mathbf{f}}^2 x^2} \right)$$

$$+ \frac{(m_{\mathbf{i}}^2 - m_d^2 - 2m_W^2)(m_d^2 + m_{\mathbf{f}}^2 (x-1)^2) + (1-x) m^4_{\mathbf{fi},d}}{(m_{\mathbf{i}}^2 - m_{\mathbf{f}}^2)^2 x} \times$$

$$\left. \times \log\left(\frac{m_W^2 + (m_d^2 - m_W^2 - m_{\mathbf{i}}^2)x + m_{\mathbf{i}}^2}{m_W^2 + (m_d^2 - m_W^2 - m_{\mathbf{f}}^2)x + m_{\mathbf{f}}^2} \right) \right\}$$

$$+ \frac{2(m_d^2 - m_{\mathbf{f}}^2 + 2m_W^2)}{3(m_{\mathbf{f}}^2 - m_{\mathbf{i}}^2)}. \tag{4.114}$$

We also consider the case where a gluon is radiated which only corresponds to the first two diagrams i.e. $\sum_{k=1,2} 3\mathcal{P}^{(k)}$ where, as mentioned earlier, the pre-factor of three is required since the down-quark electric charge $Q = \frac{1}{3}$ does not appear at the quark-quark-gluon vertex, therefore we may write $\mathcal{F}^g$ as

$$\mathcal{F}^{g}_{\mathbf{fi},d} = \int_0^1 \mathrm{d}x \left\{ \frac{(m_{\mathbf{f}}^2 - 2m_W^2 - m_d^2)(x-1)x}{(m_{\mathbf{f}}^2 - m_{\mathbf{i}}^2)x} \right.$$

$$\left. + \frac{(m_{\mathbf{i}}^2 - m_d^2 - 2m_W^2)(m_d^2 + m_{\mathbf{f}}^2 x^2) + x m^4_{\mathbf{fi},d}}{(m_{\mathbf{i}}^2 - m_{\mathbf{f}}^2)^2 x} \log\left(\frac{m_d^2 + (m_W^2 - m_d^2 - m_{\mathbf{i}}^2)x + m_{\mathbf{i}}^2}{m_d^2 + (m_W^2 - m_d^2 - m_{\mathbf{f}}^2)x + m_{\mathbf{f}}^2} \right) \right\}, \tag{4.115}$$

where in both cases we make the assignment

$$m^4_{\mathbf{fi},d} = 2m_W^2 m_d^2 - (m_d^2 + m_{\mathbf{f}}^2 - 2m_W^2)(m_{\mathbf{i}}^2 - m_d^2 - m_W^2). \tag{4.116}$$

We note that in Eq. (4.114) and Eq. (4.115) the sub-index d denotes each flavour of down-type quark that can run in the loop, this will later have to be summed over when computing branching ratios and CP observables.

The non-zero imaginary parts for $\mathcal{F}^{\gamma,g}_{\mathbf{fi},\alpha}$ and $\mathcal{F}^{\gamma,g}_{\mathbf{if},\alpha}$ can now be obtained. Since, they include integral terms of the form $\int_0^1 \mathrm{d}x f(x) \log g(x)$, where $g(x)$ is not positive definite in $(0,1)$. One can instead use the fact that there is an interval $(x_1, x_2) \subset (0,1)$ where $g(x) < 0$ is satisfied, and x_1 and x_2 are solutions of $g(x) = 0$. The real and imaginary parts in the integration can then be split into

$$\int_0^1 \mathrm{d}x f(x) \log g(x) = \int_0^1 \mathrm{d}x f(x) \log |g(x)| + i\pi \int_{x_1}^{x_2} \mathrm{d}x f(x)\,. \tag{4.117}$$

Now the imaginary part given by $\int_{x_1}^{x_2} \mathrm{d}x f(x)$ can be analytical obtained. In this way, we derive the following key analytical expressions

$$\begin{aligned}\mathrm{Im}[\mathcal{F}^{\gamma}_{\mathbf{fi},d}] = &\left\{\frac{\pi\vartheta_{\mathbf{i}}}{3(m_{\mathbf{f}}^2-m_{\mathbf{i}}^2)^2}\left[\frac{\mu_{\mathbf{i}}^2}{m_{\mathbf{i}}^4}\rho^6 + m_d^2\left(m_{\mathbf{i}}^2-m_d^2-2m_W^2\right)\log\left(\frac{m_{\mathbf{i}}^2+m_d^2-m_W^2+\mu_{\mathbf{i}}^2}{m_{\mathbf{i}}^2+m_d^2-m_W^2-\mu_{\mathbf{i}}^2}\right)\right.\right.\\ &\left.\left.-3m_W^2\left(m_d^2+m_{\mathbf{f}}^2-2m_{\mathbf{i}}^2+2m_W^2\right)\log\left(\frac{m_{\mathbf{i}}^2+m_W^2-m_d^2+\mu_{\mathbf{i}}^2}{m_{\mathbf{i}}^2+m_W^2-m_d^2-\mu_{\mathbf{i}}^2}\right)\right]\right\}\\ &+\left\{\frac{\pi\vartheta_{\mathbf{f}}}{3(m_{\mathbf{f}}^2-m_{\mathbf{i}}^2)^2}\left[\frac{\mu_{\mathbf{f}}^2}{m_{\mathbf{f}}^2}\sigma^4 - m_d^2(m_{\mathbf{i}}^2-m_d^2-2m_W^2)\log\left(\frac{m_{\mathbf{f}}^2+m_d^2-m_W^2-\mu_{\mathbf{f}}^2}{m_{\mathbf{f}}^2+m_d^2-m_W^2+\mu_{\mathbf{f}}^2}\right)\right.\right.\\ &\left.\left.+3m_W^2\left(m_d^2+m_{\mathbf{f}}^2-2m_{\mathbf{i}}^2+2m_W^2\right)\log\left(\frac{m_{\mathbf{f}}^2+m_W^2-m_d^2-\mu_{\mathbf{f}}^2}{m_{\mathbf{f}}^2+m_W^2-m_d^2+\mu_{\mathbf{f}}^2}\right)\right]\right\},\end{aligned} \tag{4.118}$$

and similarly

$$\begin{aligned}\mathrm{Im}[\mathcal{F}^{g}_{\mathbf{fi},d}] = &\frac{\pi}{2(m_{\mathbf{f}}^2-m_{\mathbf{i}}^2)^2}\times\\ &\times\left\{\vartheta_{\mathbf{i}}\left[\frac{\mu_{\mathbf{i}}^2}{m_{\mathbf{i}}^4}\xi^6 - 2m_d^2(m_d^2-m_{\mathbf{i}}^2+2m_W^2)\log\left(\frac{m_{\mathbf{i}}^2+m_d^2-m_W^2+\mu_{\mathbf{i}}^2}{m_{\mathbf{i}}^2+m_d^2-m_W^2-\mu_{\mathbf{i}}^2}\right)\right]\right\}\\ &+\left\{\vartheta_{\mathbf{f}}\left[\frac{\mu_{\mathbf{f}}^2}{m_{\mathbf{f}}^2}\eta^4 - 2m_d^2(m_d^2-m_{\mathbf{i}}^2+2m_W^2)\log\left(\frac{m_{\mathbf{f}}^2+m_d^2-m_W^2+\mu_{\mathbf{f}}^2}{m_{\mathbf{f}}^2+m_d^2-m_W^2-\mu_{\mathbf{f}}^2}\right)\right]\right\},\end{aligned} \tag{4.119}$$

where the following mass dimension parameters ρ, σ, ξ and η are introduced as

$$\begin{aligned}\rho^6 =& \left(m_d^2-m_{\mathbf{i}}^2\right)\left(m_d^2\left(m_{\mathbf{f}}^2-2m_{\mathbf{i}}^2\right)+2m_{\mathbf{f}}^2m_{\mathbf{i}}^2\right)\\ &+m_W^2\left(m_d^2\left(m_{\mathbf{f}}^2-2m_{\mathbf{i}}^2\right)+7m_{\mathbf{f}}^2m_{\mathbf{i}}^2-4m_{\mathbf{i}}^4\right)-2m_W^4\left(m_{\mathbf{f}}^2-2m_{\mathbf{i}}^2\right),\\ \sigma^4 =&2m_{\mathbf{f}}^2\left(m_d^2-m_{\mathbf{i}}^2+3m_W^2\right)+m_{\mathbf{i}}^2\left(m_d^2-3m_W^2\right)+\left(m_W^2-m_d^2\right)\left(m_d^2+2m_W^2\right),\\ \xi^6 =&(m_d^2-m_{\mathbf{i}}^2)((2m_d^2+m_{\mathbf{f}}^2)m_{\mathbf{i}}^2-m_d^2m_{\mathbf{f}}^2)\\ &-(m_{\mathbf{f}}^2m_{\mathbf{i}}^2-4m_{\mathbf{i}}^4+m_d^2(m_{\mathbf{f}}^2-2m_{\mathbf{i}}^2))m_W^2+2(m_{\mathbf{f}}^2-2m_{\mathbf{i}}^2)m_W^4,\\ \eta^4 =&(m_d^2+m_{\mathbf{f}}^2)(m_d^2-m_{\mathbf{i}}^2)+(m_d^2+3m_{\mathbf{i}}^2)m_W^2-2m_W^4,\end{aligned} \tag{4.120}$$

$\vartheta_{\mathbf{i},\mathbf{f}}(x) \equiv (m_{\mathbf{i},\mathbf{f}} - m_W - m_d)$ is the Heaviside step function, and

$$\begin{aligned}\mu_{\mathbf{i}}^2 &= \sqrt{m_{\mathbf{i}}^4+m_d^4+m_W^4-2m_{\mathbf{i}}^2m_d^2-2m_{\mathbf{i}}^2m_W^2-2m_d^2m_W^2}\,,\\ \mu_{\mathbf{f}}^2 &= \sqrt{m_{\mathbf{f}}^4+m_d^4+m_W^4-2m_{\mathbf{f}}^2m_d^2-2m_{\mathbf{f}}^2m_W^2-2m_d^2m_W^2}\,.\end{aligned} \tag{4.121}$$

It should be noted that $\mathrm{Im}[\mathcal{F}_{\mathbf{if},d}]$ is obtained by exchanging the masses $m_{\mathbf{i}}$ and $m_{\mathbf{f}}$ in $\mathrm{Im}[\mathcal{F}_{\mathbf{fi},d}]$. We note the important feature of $\mathrm{Im}[\mathcal{F}_{\mathbf{fi},d}] \neq 0$ being generated only in the branches where the particle mass conditions $m_{\mathbf{i}} > m_W + m_d$ or $m_{\mathbf{f}} > m_W + m_d$ is recovered. This important threshold mass condition required to generate kinetic CP asymmetry at loop level is ameliorated further in Ref. [3]. We note that we keep the initial and final state quark masses general in the above discussion, however in the special case where the top quark decays into light flavour quarks, only the first bracketed terms in Eq. (4.118) and Eq. (4.119) respectively survive because the mass condition $m_t > m_W + m_d$ is satisfied.

4.3.4 Derivation of CP Asymmetry

For Dirac particles, we state the CP asymmetry between the initial and final state fermions as $u_{\mathbf{i}} \to u_{\mathbf{f}}\gamma_+$ and $\bar{u}_{\mathbf{i}} \to \bar{u}_{\mathbf{f}}\gamma_-$ and between $u_{\mathbf{i}} \to u_{\mathbf{f}}\gamma_-$ and $\bar{u}_{\mathbf{i}} \to \bar{u}_{\mathbf{f}}\gamma_+$, following similar notation to Ref. [3]. These can be written in terms of the photon polarisations (analogous replacements used for the gluon case) as

$$\Delta_{CP,+} = \frac{\Gamma(u_{\mathbf{i}} \to u_{\mathbf{f}}\gamma_+) - \Gamma(\bar{u}_{\mathbf{i}} \to \bar{u}_{\mathbf{f}}\gamma_-)}{\Gamma(u_{\mathbf{i}} \to u_{\mathbf{f}}\gamma) + \Gamma(\bar{u}_{\mathbf{i}} \to \bar{u}_{\mathbf{f}}\gamma)}\,, \quad \Delta_{CP,-} = \frac{\Gamma(u_{\mathbf{i}} \to u_{\mathbf{f}}\gamma_-) - \Gamma(\bar{u}_{\mathbf{i}} \to \bar{u}_{\mathbf{f}}\gamma_+)}{\Gamma(u_{\mathbf{i}} \to u_{\mathbf{f}}\gamma) + \Gamma(\bar{u}_{\mathbf{i}} \to \bar{u}_{\mathbf{f}}\gamma)}\,, \tag{4.122}$$

and it then follows according to Ref. [4] that the CP asymmetries can be written in terms of particle masses, CKM mixing and the loop functions $\mathcal{F}$ as

$$\begin{aligned}
\Delta_{CP,+} &= \frac{-\sum_{\alpha,\beta}\mathcal{J}^{\mathbf{if}}_{\alpha\beta}\mathrm{Im}(\mathcal{F}_{\mathbf{if},\alpha}\mathcal{F}^*_{\mathbf{if},\beta})m_{\mathbf{f}}^2}{\sum_{\alpha,\beta}\mathcal{R}^{\mathbf{if}}_{\alpha\beta}\left[\mathrm{Re}(\mathcal{F}_{\mathbf{fi},\alpha}\mathcal{F}^*_{\mathbf{fi},\beta})m_{\mathbf{i}}^2 + \mathrm{Re}(\mathcal{F}_{\mathbf{if},\alpha}\mathcal{F}^*_{\mathbf{if},\beta})m_{\mathbf{f}}^2\right]}\,, \\
\Delta_{CP,-} &= \frac{-\sum_{\alpha,\beta}\mathcal{J}^{\mathbf{if}}_{\alpha\beta}\mathrm{Im}(\mathcal{F}_{\mathbf{fi},\alpha}\mathcal{F}^*_{\mathbf{fi},\beta})m_{\mathbf{i}}^2}{\sum_{\alpha,\beta}\mathcal{R}^{\mathbf{if}}_{\alpha\beta}\left[\mathrm{Re}(\mathcal{F}_{\mathbf{fi},\alpha}\mathcal{F}^*_{\mathbf{fi},\beta})m_{\mathbf{i}}^2 + \mathrm{Re}(\mathcal{F}_{\mathbf{if},\alpha}\mathcal{F}^*_{\mathbf{if},\beta})m_{\mathbf{f}}^2\right]}\,.
\end{aligned} \tag{4.123}$$

where α, β run for charged down-quark flavours d, s, b and

$$\mathcal{J}^{\mathbf{if}}_{\alpha\beta} = \mathrm{Im}(V_{\mathbf{i}\alpha}V^*_{\mathbf{f}\alpha}V^*_{\mathbf{i}\beta}V_{\mathbf{f}\beta})\,, \qquad \mathcal{R}^{\mathbf{if}}_{\alpha\beta} = \mathrm{Re}(V_{\mathbf{i}\alpha}V^*_{\mathbf{f}\alpha}V^*_{\mathbf{i}\beta}V_{\mathbf{f}\beta})\,. \tag{4.124}$$

Here the classic Jarlskog-like parameters $\mathcal{J}^{\mathbf{if}}_{\alpha\beta}$ are utilised to describe the CP violation [347,348]. These parameters are invariant under any phase rotation of charged up and down-type quarks.

4.3.5 Results

4.3.6 Branching Ratios and Decay Widths

In the SM, we may write the expression for the polarised radiative decay width in terms of functions denoted A and B for each channel as [3]

$$\begin{aligned}
\Gamma(t \to u_\beta\gamma_+) &= \frac{1}{\pi}\left(\frac{m_t^2 - m_u^2}{2m_t}\right)^3 |A^\gamma - B^\gamma|^2 \\
\Gamma(t \to u_\beta\gamma_-) &= \frac{1}{\pi}\left(\frac{m_t^2 - m_u^2}{2m_t}\right)^3 |A^\gamma + B^\gamma|^2, \\
\Gamma(t \to u_\beta g_+) &= \frac{C_F}{\pi}\left(\frac{m_t^2 - m_u^2}{2m_t}\right)^3 |A^g - B^g|^2\,, \\
\Gamma(t \to u_\beta g_-) &= \frac{C_F}{\pi}\left(\frac{m_t^2 - m_u^2}{2m_t}\right)^3 |A^g + B^g|^2.
\end{aligned} \tag{4.125}$$

Then it follows that the total unpolarised radiative width is given by summing the two polarisation channels and averaging over the two initial state spins so $\Gamma(t \to u_\beta\gamma) =$

$\frac{1}{2}[\Gamma(t \to u_\beta \gamma_+) + \Gamma(t \to u_\beta \gamma_-)]$, which yields

$$\Gamma(t \to u_\beta \gamma) = \frac{1}{\pi}\left(\frac{m_t^2 - m_u^2}{2m_t}\right)^3 \left(|A^\gamma|^2 + |B^\gamma|^2\right) ,$$
$$\Gamma(t \to u_\beta g) = \frac{C_F}{\pi}\left(\frac{m_t^2 - m_u^2}{2m_t}\right)^3 \left(|A^g|^2 + |B^g|^2\right) . \tag{4.126}$$

where $C_F = 4/3$ is the standard colour factor [358]. We note that the usual Lorentz invariant amplitude can be separated into terms proportional and not proportional to γ_5 as

$$\mathcal{M}(t \to u_\beta + \gamma) = i\bar{u}(p_\beta)\sigma^{\mu\nu}(A^\gamma + B^\gamma\gamma_5)q_\nu u(p_t)\varepsilon^*_{\pm,\mu}(q) , \tag{4.127}$$

by comparing coefficients between Eq. (4.113) and Eq. (4.127), it follows

$$A^\gamma = \frac{eG_F}{8\sqrt{2}\pi^2}V_{td}V_{ud}^*(\mathcal{F}^\gamma_{ut,d}m_t + \mathcal{F}^\gamma_{tu,d}m_u) , \quad B^\gamma = \frac{eG_F}{8\sqrt{2}\pi^2}V_{td}V_{ud}^*(\mathcal{F}^\gamma_{ut,d}m_t - \mathcal{F}^\gamma_{tu,d}m_u), \tag{4.128}$$

where $u = (u, c)$ depending on the final state and the above expressions must be summed over $d = (d, s, b)$ as shown in Eq. (4.123) with each of their individual contributions. The corresponding parameters for gluon radiation, A^g and B^g , are obtained by simply performing the gauge coupling replacement $e \to g_s$ and $\mathcal{F}^\gamma \to \mathcal{F}^g$. We may also explicitly write the relations between the magnetic and electric transition dipole moments in terms of A and B as $f^M = -A^\gamma$ and $f^E = iB^\gamma$ [3], the chromodynamic transition dipole moments are analogous except with the replacements A^g and B^g respectively.

The leading order SM top decay width is dominated by the tree level decay $t \to bW^+$ and given as [358]

$$\Gamma(t \to bW^+) = \frac{g^2}{64\pi}|V_{tb}|^2\frac{m_t^3}{m_W^2}\left(1 - 3\frac{m_W^4}{m_t^4} + 2\frac{m_W^6}{m_t^6}\right) . \tag{4.129}$$

We avoid using the next to leading order width as it makes a negligible difference numerically and our other calculations are performed at leading order. The branching ratios for the radiative processes are then simply given by

$$\mathcal{B}(t \to u_\beta\gamma) = \frac{\Gamma(t \to u_\beta\gamma)}{\Gamma(t \to bW^+)}, \tag{4.130}$$

where the analogous replacement $\Gamma(t \to u_\beta g)$ is performed in the numerator when computing $\mathcal{B}(t \to u_\beta g)$.

4.3.7 Numerical Results and Discussion

We compute the branching ratios and CP asymmetries according to Eq. (4.130) and Eq. (4.123) respectively. In this work, we use the standard parametrisation for the CKM matrix with angles $\theta_{12} = 13.04 \pm 0.05°$, $\theta_{13} = 0.201 \pm 0.011°$, $\theta_{23} = 2.38 \pm 0.06°$ and $\delta_{cp} = 1.20 \pm 0.08$ [75]. Additionally, we take the b-quark mass to be be the three loop $\overline{\text{MS}}$ scheme value evaluated at the top mass $m_b(m_t) = 2.681 \pm 0.003$ [376]. We take pole masses of $(m_t, m_c, m_u) = (173.21, 1.275, 2.30 \times 10^{-3})$GeV for the external quarks. It should be noted that the running mass for the down-type quarks is not a fundamental parameter of the SM Lagrangian, but rather a product of the running Yukawa coupling $y_b = m_b/v$ and the Higgs vacuum expectation value v. Firstly, it is first of interest to directly calculate the central polarised widths which we obtain directly from Eq. (4.125) as

Decay Channel	Decay Width GeV	Decay Channel	Decay Width GeV
$t \to u\gamma_+$	2.714×10^{-21}	$t \to ug_+$	5.418×10^{-19}
$t \to u\gamma_-$	9.781×10^{-16}	$t \to ug_-$	1.142×10^{-13}
$t \to c\gamma_+$	1.520×10^{-18}	$t \to cg_+$	3.031×10^{-16}
$t \to c\gamma_-$	1.364×10^{-13}	$t \to cg_-$	1.592×10^{-11}

TABLE 4.1: Results for the polarised decay widths for the radiative channels $t \to u\gamma$, $t \to c\gamma$, $t \to ug$ and $t \to cg$.

The total unpolarised branching ratios can then be computed from Eq. (4.126), which are shown in Table 4.2 and are approximately one order of magnitude smaller compared to the ones quoted in Ref. [359]. This is expected as they used the internal b-quark pole mass in their calculation ($m_b = 5$GeV is assumed). In the more recent Ref. [358], they compute

$$\begin{aligned} &\mathcal{B}(t \to u\gamma) \simeq 3.7 \times 10^{-16}\,, \qquad &&\mathcal{B}(t \to c\gamma) \simeq 4.6 \times 10^{-14}, \\ &\mathcal{B}(t \to ug) \simeq 3.7 \times 10^{-14}\,, \qquad &&\mathcal{B}(t \to cg) \simeq 4.6 \times 10^{-12}, \end{aligned} \tag{4.131}$$

which is comparable to those shown in Table 4.2, the marginal differences observed are well within the one sigma uncertainties they quote and can be attributed to the fact that they use a now superseded running mass for the b-quark of $m_b(m_t) = 2.74 \pm 0.17$GeV as well as an external line c-quark mass of $m_c = 1.5$GeV. As previously noted in the same work, the uncertainty in the top quark mass does not affect the results shown, since the partial widths of $t \to c\gamma$, $t \to cg$ are proportional to m_t^3, it follows that the leading dependence on m_t gets cancelled when branching ratios and CP asymmetries are computed, meaning the uncertainty in m_t has a negligible effect on the final result.

In Ref. [358], they also provide an order of magnitude estimate for the CP asymmetries

$$\Delta_{CP,-}(t \to c\gamma) \sim -5 \times 10^{-6}\,, \qquad \Delta_{CP,-}(t \to cg) \sim -6 \times 10^{-6}, \tag{4.132}$$

in the SM case[10]. This is about a factor of two smaller than the result we compute in Table 4.2. This is an unsurprising discrepancy as the result shown in this work includes all of the kinetic terms, appropriate quark running masses and current CKM parameters. Here we see that the ratio for branching fractions and the CP-asymmetries can be approximated $\frac{\mathcal{B}(t\to c\gamma(g))}{\mathcal{B}(t\to u\gamma(g))} \simeq \left(\frac{|V_{cb}|}{|V_{ub}|}\right)^2$, $\frac{\Delta_{CP,-}(t\to c\gamma(g))}{\Delta_{CP,-}(t\to u\gamma(g))} \simeq -\left(\frac{|V_{ub}|}{|V_{cb}|}\right)^2$ $\frac{\Delta_{CP,+}(t\to c\gamma(g))}{\Delta_{CP,+}(t\to u\gamma(g))} \simeq \frac{|V_{cb}|}{|V_{ub}|}\frac{m_c}{m_u}$ while the hierarchy $\Delta_{CP,+} \ll \Delta_{CP,-}$ is a direct consequence

[10]We note that the CP asymmetries are denoted a_γ and a_g in Ref. [358], corresponds to $\Delta_{CP} = \Delta_{CP,+} + \Delta_{CP,-}$. In this work $\Delta_{CP,+} \ll \Delta_{CP,-}$ and so $\Delta_{CP} \simeq \Delta_{CP,-}$

of angular momentum conservation and the fact that the weak interaction is parity violating.

Decay Channel	Branching Ratio	$\Delta_{CP,+}$	$\Delta_{CP,-}$
$t \to u\gamma$	$(3.262 \pm 0.341) \times 10^{-16}$	$-(7.142 \pm 0.668) \times 10^{-14}$	$(1.612 \pm 0.151) \times 10^{-3}$
$t \to c\gamma$	$(4.550 \pm 0.234) \times 10^{-14}$	$-(6.232 \pm 0.605) \times 10^{-10}$	$-(1.150 \pm 0.112) \times 10^{-5}$
$t \to ug$	$(3.810 \pm 0.340) \times 10^{-14}$	$-(4.521 \pm 0.424) \times 10^{-14}$	$(1.617 \pm 0.152) \times 10^{-3}$
$t \to cg$	$(5.310 \pm 0.271) \times 10^{-12}$	$-(6.245 \pm 0.605) \times 10^{-10}$	$-(1.153 \pm 0.112) \times 10^{-5}$

TABLE 4.2: Results for the branching ratio and CP asymmetries for the radiative channels $t \to u\gamma$, $t \to c\gamma$, $t \to ug$ and $t \to cg$. The quoted uncertainty is propagated from the one sigma CKM angle uncertainties and running bottom quark mass at the top quark mass scale using the $\overline{\text{MS}}$ scheme.

4.3.8 Application to Selected New Physics Models

We do not focus on beyond the SM physics scenarios in this work, however there are numerous potential applications of the results shown in this section to beyond the SM theories. The most direct of these is likely the aforementioned extension of the SM via VLQs. This is motivated, namely by a recent more precise evaluation of V_{ud} and V_{us}, which places the unitarity condition of the first row in the CKM matrix $|V_{ud}|^2 + |V_{us}|^2 + |V_{ub}|^2 = 0.99798 \pm 0.00038$ at a deviation more than 4σ from unity [377, 378]. Furthermore, a mild excess in the overall Higgs signal strength appears at about 2σ above the standard model (SM) prediction [131]. Additionally, there is the long-lasting discrepancy in the forward-backward asymmetry $\mathcal{A}^b_{FB}$ in $Z \to b\bar{b}$ at LEP [75]. There have been models motivated by explaining the above three anomalies via extension of the SM quark sector via down-type VLQs which alleviate the tension among these datasets such as the one shown in Ref. [379].

There are also direct searches for the down-type VLQs at the LHC [380–382]. Inclusion of these down-type quarks b' and b'' realise improved agreement to data compared to the SM [379]. The results shown in Section 4.3.3 in conjunction with Section 4.3.4 can be used to predict polarised photons observables resulting from the CP asymmetries for processes such as $b' \to d_\beta\gamma$ and $b'' \to d_\beta\gamma$. It should be noted that these VLQs are experimentally favoured over previously studied fourth generation models such as in Ref. [383] due to precision Higgs measurements at the LHC [384]. The main addition to the results shown in this work for a complete description of these decays would be the inclusion of FCNC diagrams with Z, h and unphysical scalar χ bosons appearing in the penguin diagrams. However, it should be noted that these amplitudes share similar Lorentz structure to the results shown in this section. Hence, this class of models represent a relatively straightforward extension. We plan to show this explicitly in a future work. Experimental interest in such models is high and there has been many detailed searches performed for these down-type VLQs at the LHC [380–382, 385, 386]. Similarly, in Ref. [364], the inclusion of new vector iso-singlet up-type quarks is discussed in detail with a 4×3 CKM matrix. ATLAS searches have also already been conducted to try and find these new up-type quarks, which are often referred to as t' or T in the literature [387, 388].

Additionally, the mass hierarchy between the up-type and down-type quarks observed in nature motivates consideration of models with two complex $SU(2)_L$ doublet scalar fields which comprise the 2HDM. In the so called type III 2HDM both doublets simultaneously give masses to all quark types. In these 2HDM variants, it has been shown that $\mathcal{B}(t \to c\gamma)$ can reach about 10^{-8} [362], 10^{-6} [389, 390] and recently it has even been suggested that parameter regions exist where it can be enhanced to about 10^{-5}. The dominant contributions for the rare radiative top decay $t \to c\gamma$ at one-loop in 2HDM come from neutral and charged Higgs bosons running in the loop analogous to the third diagram in Figure 4.6 but with the W bosons replaced with the charged Higgs H^+ and the second diagram where the unphysical scalar χ is replaced with the physical SM-like Higgs h. Therefore, it is clear that the result for the CP asymmetry shown in this section can easily exported for use in the 2HDM as well. We note that the previous focus in the literature of these rare decays has primarily been on photon radiation rather than gluon radiation. The latter of which, we have studied in this work and would be expected to have a much larger branching fraction albeit a less experimentally clean probe of new physics in hadron colliders due to large QCD backgrounds.

4.3.9 Conclusion

The rare radiative flavour changing loop level top decays $t \to c\gamma$, $t \to cg$, $t \to u\gamma$ and $t \to ug$ branching ratios and corresponding CP asymmetries are computed in full detail. These signatures exist due to imaginary components of the loop functions and the CKM matrix and provide a potentially clean probe of new physics or further validation of the SM. A full analytical formulation for the CP asymmetry resulting from the loop functions as well as a revised numerical computation of the SM branching fractions is provided. The branching fractions are comparable to the values quoted in the literature while the CP asymmetry is computed to a higher degree of precision and is about a factor of two larger than the previously stated order of magnitude estimates [358]. These rare radiative processes are suppressed in the SM by the GIM mechanism, however, the kinetic terms and loop functions presented can easily be adapted for use with minimal modification in extensions of the SM via vector-like quarks or in Two-Higgs-Doublet models. These extensions can enhance the same channels of interest by many orders of magnitude relative to the SM, even reaching branching ratios up to 10^{-5} or higher, due to the presence of an extended CKM matrix, FCNC at tree level or new scalar field content respectively. Several of these extensions have been studied in detail recently and comprise an active area of research since they can provide improved global fits to several recent flavour physics measurements. Studying the phenomenology of radiative decays produced in these beyond the SM models by application of the formulae detailed is intended to be performed as a future work.

Chapter 5

Lepton Flavour Universality Violation in B Decays

5.1 A Chiral $SU(4)$ Explanation of the $b \to s$ Anomalies

There is mounting evidence for a violation of LFU in FCNC processes $b \to s\bar{\mu}\mu$ in recent measurements of B decays [94, 391–396]. The theoretically cleanest probes are the LFU ratios

$$R_{K^{(*)}} = \frac{\Gamma(\bar{B} \to \bar{K}^{(*)}\mu^+\mu^-)}{\Gamma(\bar{B} \to \bar{K}^{(*)}e^+e^-)} \tag{5.1}$$

which compare the decay rate $b \to s\bar{\ell}\ell$ ratio between muons and electrons respectively. Hadronic uncertainties cancel out in the ratios as long as new physics effects are small [397–399]. The current experimental data shown in Table 5.1 indicates deviations of more than 2σ for both LFU ratios $R_{K^{(*)}}$ separately. An effective field theory analysis including all $b \to s\bar{\ell}\ell$ data in fact shows that the introduction of operators

$$O_9 = [\bar{s}\gamma^\mu P_L b][\bar{\mu}\gamma_\mu\mu] \qquad\qquad O_{10} = [\bar{s}\gamma^\mu P_L b][\bar{\mu}\gamma_\mu\gamma_5\mu] \tag{5.2}$$

may improve the global fit by $4-5\sigma$ [399–404]. In addition to the R_K anomaly, there is some evidence for a deviation from SM predictions in the muon $g-2$ measurements (see e.g. Ref. [405]) and also in charged-current semi-leptonic decays $b \to c\ell\bar{\nu}$ (R_D anomaly) see e.g. Ref. [406]. The leading SM contributions to $b \to c\ell\bar{\nu}$ arise at tree level, while the contributions to the muon $g-2$ and $b \to s\bar{\ell}\ell$ arise at one-loop level. Although new physics contributions to the muon $g-2$ arise at loop level, there may be new physics contributions to $b \to c\ell\bar{\nu}$ and $b \to s\bar{\ell}\ell$ at tree level. It follows that the $b \to s$ processes are expected to provide a more sensitive probe of deviations from the SM. The experimental sensitivity is expected to significantly improve in the next few years: LHCb will acquire more data and the Belle II experiment is anticipated to start collecting data with the full detector soon and will measure $R_{K^{(*)}}$ with a precision of 3.6% (3.2%).

	observed	SM	q^2 range
R_K	$0.745^{+0.090}_{-0.074} \pm 0.036$ [94]	1.0003 ± 0.0001 [407]	$1\,\mathrm{GeV}^2 < q^2 < 6\,\mathrm{GeV}^2$
R_{K^*}	$0.69^{+0.11}_{-0.07} \pm 0.05$ [391]	1.00 ± 0.01 [93]	$1.1\,\mathrm{GeV}^2 < q^2 < 6\,\mathrm{GeV}^2$

Table 5.1: LFU ratios $R_{K^{(*)}}$, where we first list the statistical error and then the systematic.

The possibility that some or even all of these deviations might be a harbinger of new physics has been entertained in the literature, e.g. by introducing a new effective interaction of third-generation weak eigenstates [408], models of Z' gauge bosons e.g. [409–411] and leptoquarks e.g. [412, 413]. In this section we consider a rather particular kind of Pati-Salam inspired $SU(4)$ gauge model, with chiral gauge interactions with quarks and leptons. In this scheme, the $b \to s$ anomaly is explained via tree level leptoquark gauge bosons with mass $m_{W'} \gtrsim 10$TeV. Although various kinds of $SU(4)$ models have also been considered in the context of the B-physics anomalies in several papers [414–423], the proposal identified in this section appears to have escaped attention in the literature. Our model provides a very simple and predictive scheme, describing the $b \to s$ anomaly with only two parameters, $m_{W'}$ and a CKM-type mixing angle, θ. The leptoquark gauge boson does not contribute significantly to the R_D anomaly. If both R_D and R_K anomalies are confirmed then the R_K anomaly could be explained in terms of chiral Pati-Salam gauge bosons as described here, with R_D explained, potentially, via scalar leptoquarks incorporated in simple extensions of the proposed model.

The section is organised as follows. In Sec. 5.1.1 we introduce the model and discuss the relevant effective operators in Sec. 5.1.2. Our results are presented in Sec. 5.1.3 and we conclude in Sec. 5.1.4.

5.1.1 The Model

The Pati-Salam model [424] is a left-right symmetric model based on the gauge group $SU(4)_C \times SU(2)_L \times SU(2)_R$ where both chiral left- and right-handed leptons are interpreted as the fourth colour of $(4, 2, 1), (4, 1, 2)$ fermion multiplets (the other three colours representing the quarks). In the original version of the model, quite stringent limits on the $SU(4)$ symmetry breaking scale arises from various processes, especially two-body leptonic decays of mesons: $K \to \bar{\mu}e$, $B \to \bar{\mu}e$ etc.. These two-body rare decays are effectively enhanced over three-body processes because the $SU(4)$ leptoquark gauge bosons couple in a vector-like manner to the charged leptons, eliminating any helicity suppression.

It was noticed some time ago [425, 426] that variants of the Pati-Salam model can easily be constructed whereby the $SU(4)$ leptoquark gauge bosons couple in a chiral fashion to the quarks and leptons. Such chiral $SU(4)_C$ models are less constrained than the original Pati-Salam model, and $SU(4)$ symmetry breaking at the TeV scale can be envisaged. The particular model studied in Refs. [425,426] featured leptoquark gauge bosons coupling to chiral right-handed quarks and leptons, a circumstance which is not well suited to explaining the R_K anomaly. Here we aim to construct the simplest chiral $SU(4)$ model in which the leptoquark gauge bosons couple to quarks and leptons in a predominately left-handed manner.

The gauge symmetry of the model is $SU(4)_C \times SU(2)_L \times U(1)_{Y'}$, and the fermion/scalar particle content is listed in Table 5.2. The $SU(4)$ symmetry is broken by the vacuum expectation value (vev) of the scalar χ at a high scale ($\langle\chi\rangle \equiv w \gtrsim 10$TeV), while the electroweak symmetry is broken by the vevs of the scalars ϕ and Δ, with $\sqrt{v^2 + u^2} \simeq 174$ GeV where $\langle\phi\rangle \equiv v$ and $\langle\Delta\rangle \equiv u$.[1] The symmetry breaking pattern

[1] The vev u also breaks $SU(4)_C \times U(1)_{Y'}$, but its effects are suppressed, since we assume $u \ll w$.

fermion	$(SU(4)_C, SU(2)_L, U(1)_{Y'})$	scalar	$(SU(4)_C, SU(2)_L, U(1)_{Y'})$
$\mathbf{Q}_L$	$(4,2,0)$	ϕ	$(1,2,1)$
$\mathbf{u}_R$	$(4,1,1)$	χ	$(4,1,1)$
$\mathbf{d}_R$	$(4,1,-1)$	Δ	$(4,2,2)$
E_L	$(1,1,-2)$		
e_R	$(1,1,-2)$		
N_L	$(1,1,0)$		

TABLE 5.2: Particle content

that results is

$$\begin{gathered} SU(4)_C \times SU(2)_L \times U(1)_{Y'} \\ \downarrow \langle\chi\rangle \\ SU(3) \times SU(2)_L \times U(1)_Y \\ \downarrow \langle\phi\rangle\,, \langle\Delta\rangle \\ SU(3) \times U(1)_Q \end{gathered} \tag{5.3}$$

Here hypercharge $Y = T + Y'$ and electric charge $Q = I_3 + \frac{Y}{2}$. If we use the gauge symmetry to rotate the vev of χ to the fourth component, then T is the diagonal traceless $SU(4)$ generator with elements $(\frac{1}{3}, \frac{1}{3}, \frac{1}{3}, -1)$.

The Yukawa Lagrangian is

$$\begin{aligned} \mathcal{L} = {} & Y_u \bar{\mathbf{Q}}_L \tilde{\phi} \mathbf{u}_R + Y_d \bar{\mathbf{Q}}_L \phi \mathbf{d}_R + Y_N \bar{\mathbf{u}}_R \chi N_L + Y_E \bar{\mathbf{d}}_R \chi E_L + Y_e \bar{\mathbf{Q}}_L \Delta e_R \\ & + m_1 \bar{E}_L e_R + \frac{1}{2} m_N \bar{N}_L^c N_L + h.c.\,, \end{aligned} \tag{5.4}$$

where $\tilde{\phi} \equiv i\tau_2 \phi^*$, and we have used bold face notation to label $SU(4)_C$ $\underline{4}$ multiplets which contain the usual quarks plus a leptonic component. The generation index has been suppressed, and it is implicit that each of these components comes in three generations, i.e. $u_R \equiv u_R^i = (u_R, c_R, t_R)$, $d_R \equiv d_R^i = (d_R, s_R, b_R)$, etc.. The χ field gives mass to the charged ($\frac{2}{3}e$) W' and neutral Z' gauge bosons along with the exotic charged $E^-_{L,R}$ and neutral $N_{L,R}$ fermions. The SM fields acquire mass via the ϕ and Δ fields.

The quark mass matrices are given by $m_u = Y_u v$ and $m_d = Y_d v$, while the charged and neutral lepton mass matrices are

$$M_{e,E} = \begin{pmatrix} Y_e u & m_d \\ m_1 & Y_E^\dagger w \end{pmatrix} \qquad\qquad M_N = \begin{pmatrix} 0 & m_u & 0 \\ m_u^T & 0 & Y_N w \\ 0 & Y_N^T w & m_N \end{pmatrix}\,. \tag{5.5}$$

In defining these matrices we have adopted a basis $(e, E)_{L,R}$ and (ν_L, N_R^c, N_L) where e_L, ν_L are the fourth components of $\mathbf{Q}_L$ and E_R, N_R are the fourth components of $\mathbf{d}_R$, $\mathbf{u}_R$. In the limit $w \gg m_1, m_d$ (assumed in this section) the charged lepton masses reduce to $m_e \simeq Y_e u$, while the exotic charged leptons have mass $M_E \simeq Y_E^\dagger w$. Also, the W' leptoquark $SU(4)$ gauge bosons couple chirally to the SM quarks and leptons. It is beneficial to explicitly write out the fermion multiplets. For the first generation we have

$$\mathbf{Q}_L = \begin{pmatrix} u_r & d_r \\ u_g & d_g \\ u_b & d_b \\ \nu & e \end{pmatrix}_L \qquad \mathbf{d}_R = \begin{pmatrix} d_r \\ d_g \\ d_b \\ E \end{pmatrix}_R \qquad \mathbf{u}_R = \begin{pmatrix} u_r \\ u_g \\ u_b \\ N \end{pmatrix}_R \qquad E_L \qquad e_R \qquad N_L \; . \tag{5.6}$$

Note that the active neutrino masses are generated via an inverse seesaw, and their observed sub-eV mass scale is compatible with a TeV scale vev w.

In this model the masses of the charged leptons arise from the vev of the Δ scalar, while the masses of the quarks result from the vev of ϕ. In such a situation, consistent Higgs phenomenology requires the existence of a decoupling limit where the LHC Higgs-like scalar is identified with the lightest neutral scalar in the model. To see how this can arise consider the Higgs potential terms

$$V(\chi, \phi, \Delta) = \lambda_1(\chi^\dagger\chi - w^2)^2 + \lambda_2(\phi^\dagger\phi - v^2)^2 + m_\Delta^2\Delta^\dagger\Delta - m_{123}\Delta^\dagger\phi\chi - m_{123}^*\chi^\dagger\phi^\dagger\Delta \; . \tag{5.7}$$

Here m_{123} is a trilinear coupling of dimensions of mass which, without loss of generality, we can take to be real. For $\lambda_1, \lambda_2, m_\Delta > 0$, and considering initially $m_{123} = 0$, the potential is minimised when $\langle\chi^\dagger\chi\rangle = w^2$, $\langle\phi^\dagger\phi\rangle = v^2$, and $\langle\Delta\rangle = 0$. Taking advantage of the gauge symmetry, the vevs can be rotated into the real part of one of the complex components of χ and ϕ: $\langle Re : \chi_0\rangle = w$, $\langle Re : \phi_0\rangle = v$. In the non-trivial case where $m_{123} \neq 0$, a vev is induced for the real part of Δ_0

$$\langle Re : \Delta_0\rangle \equiv u \simeq \frac{m_{123}wv}{m_\Delta^2} \; . \tag{5.8}$$

In such a manner, $u \ll v$ can naturally arise if $m_{123}w/m_\Delta^2 \ll 1$.

The physical scalar content consists of electrically charged 5/3 and 2/3 coloured leptoquark scalars, a singly charged scalar, Δ^+, three neutral scalars, $\tilde{\chi}_0/\sqrt{2} = Re : \chi_0$, $\tilde{\phi}_0/\sqrt{2} = Re : \phi_0$, $\tilde{\Delta}_0/\sqrt{2} = Re : \Delta_0$, and a pseudo scalar, $\tilde{\Delta}_0'/\sqrt{2} = Im : \Delta_0$. In the limit $w^2 \gg v^2$, the $\tilde{\chi}_0$ scalar decouples and the two remaining neutral scalars mix so that their physical mass eigenstates take the form

$$\begin{aligned} h &= \cos\beta\tilde{\phi}_0 + \sin\beta\tilde{\Delta}_0 \\ H &= -\sin\beta\tilde{\phi}_0 + \cos\beta\tilde{\Delta}_0 \end{aligned} \tag{5.9}$$

where $\sin\beta \simeq m_{123}w/(m_\Delta^2) = u/v$ in the decoupling limit $m_\Delta^2 \gg m_{123}w$. In this limit it is easy to check that the lightest scalar, h, has Higgs-like coupling to the SM particles. This result would hold for the most general Higgs potential so long as a decoupling regime as described is considered [427]. The scalar h can thus be identified with the Higgs-like scalar discovered at the LHC [428, 429].

Finally, the model features an unbroken global $U(1)_B$ baryon number symmetry. As with the standard model, this global symmetry is not imposed but appears as an accidental symmetry of the Lagrangian. However, unlike the standard model, the unbroken baryon global symmetry does not commute with the gauge symmetries, and is generated by

$$B = \frac{B' + T}{4} \; . \tag{5.10}$$

Here, we have introduced the generator, B', which commutes with the gauge symmetries, and is defined by the charges: $B'(\mathbf{Q}_L, \mathbf{u}_R, \mathbf{d}_R, \chi, \Delta) = 1$, $B'(E_L, e_R, N_L, \phi, \mathcal{G}) = 0$ ($\mathcal{G}$ is the set of gauge fields). With B defined as above, one can easily check that $U(1)_B$ is an unbroken symmetry of the Lagrangian (i.e. $B\langle\chi\rangle = B\langle\Delta\rangle = B\langle\phi\rangle = 0$). The $U(1)_{B'}$ is also a symmetry of the Lagrangian, but is not independent of the gauge symmetries and $U(1)_B$.

5.1.2 Effective Operators

The relevant new physics contributions to the anomalies and possible constraints are most efficiently described by the effective Lagrangian

$$\mathcal{L}_{eff} = \frac{4G_F}{\sqrt{2}}\frac{\alpha_{em}}{4\pi}\sum_{q,q',\ell,\ell'} V_{tq}V^*_{tq'}\sum_{i=9,10}(C_i^{qq'\ell\ell'}O_i^{qq'\ell\ell'} + C_i^{\prime qq'\ell\ell'}O_i^{\prime qq'\ell\ell'}) + \text{h.c.}\,, \tag{5.11}$$

where O_i denotes operators with two down-type quarks and two charged leptons

$$\begin{aligned} O_9^{qq'\ell\ell'} &= (\bar{q}\gamma_\mu P_L q')(\bar{\ell}\gamma^\mu\ell') & O_9^{\prime qq'\ell\ell'} &= (\bar{q}\gamma_\mu P_R q')(\bar{\ell}\gamma^\mu\ell') \\ O_{10}^{qq'\ell\ell'} &= (\bar{q}\gamma_\mu P_L q')(\bar{\ell}\gamma^\mu\gamma_5\ell') & O_{10}^{\prime qq'\ell\ell'} &= (\bar{q}\gamma_\mu P_R q')(\bar{\ell}\gamma^\mu\gamma_5\ell')\,. \end{aligned} \tag{5.12}$$

In the above, G_F denotes the Fermi constant, $\alpha_{em} = 1/127.9$ the fine-structure constant evaluated at the electroweak scale, V_{ij} are CKM mixing matrix elements, $q^{(\prime)}$ are down-type quark fields, $\ell^{(\prime)}$ denotes charged leptons and $P_{L,R} = (1 \pm \gamma_5)/2$ are the chiral projection operators.

The relevant $SU(4)$ gauge interactions with the fermions, together with the leptoquark gauge boson mass term, are given by

$$\mathcal{L} = \frac{g_s}{\sqrt{2}}K_{ij}W'_\mu\bar{d}_i\gamma^\mu P_L\ell_j + \frac{g_s}{\sqrt{2}}K^*_{ji}W'^*_\mu\bar{\ell}_i\gamma^\mu P_L d_j - m^2_{W'}W'^*_\mu W'^\mu \tag{5.13}$$

where g_s is the $SU(4)$ gauge coupling constant. Here we have defined ℓ to include the three charged SM leptons and the three heavy exotic charged lepton mass eigenstates, i.e. $\ell = e, E$. This means that K_{ij} is in general a 3×6 matrix which satisfies the unitarity condition $KK^\dagger = 1_{3\times3}$, where $1_{3\times3}$ is the 3×3 unit matrix.

In this model the Wilson coefficients for the effective four-fermion interaction after integrating out the heavy W' mediator and using the appropriate Fierz rearrangement to collect quark and lepton bilinears are

$$C_9^{qq'\ell\ell'} = -C_{10}^{qq'\ell\ell'} = \frac{\sqrt{2}\pi^2\alpha_s}{V_{tq}V^*_{tq'}\alpha_{em}}\frac{K_{q\ell'}K^*_{q'\ell}}{G_F m^2_{W'}} \tag{5.14}$$

where $\alpha_s = g_s^2(m^2_{W'})/4\pi$. Typically, limits from lepton flavour violating Kaon decays are more stringent then those from B meson decays, and this constrains the possible flavour structure of the theory. In order to satisfy these constraints, and to explain the $R_{K^{(*)}}$ anomaly, a particular structure of the K matrix is suggested. Considering only the first 3 columns of the general K matrix, i.e. the part relevant to quark-SM lepton interactions, we adopt the limiting case:

$$K = \begin{pmatrix} 0 & 0 & 1 \\ \cos\theta & \sin\theta & 0 \\ -\sin\theta & \cos\theta & 0 \end{pmatrix} . \tag{5.15}$$

In general, the zero elements need not be exactly zero, but for the $m_{W'}$, θ values of interest for the $R_{K^{(*)}}$ measurements are constrained from lepton flavour violating Kaon decays to be relatively small ($\lesssim 0.1$).

5.1.3 Results & Discussion

With the ansatz Eq. (5.15) it is straightforward to evaluate the W' leptoquark gauge boson contributions to the $R_{K^{(*)}}$ anomaly. The model has the distinctive feature that both $b \to s\bar{e}e$ and $b \to s\bar{\mu}\mu$ processes receive corrections of approximately the same magnitude, but with opposite sign. One consequence of this is that modifications to the angular distributions are anticipated in both muon and electron channels. However, it is noteworthy that the muon channel is experimentally advantageous over the electron channel due to improved resolution.

The favoured region of parameter space for the model is identified using the `flavio` package [430] and tree-level analytical estimations where appropriate. The $\bar{B} \to \bar{K}^{(*)}\mu^+\mu^-$, $\bar{B} \to \bar{K}^{(*)}e^+e^-$ rates are used to determine the R_K and R_{K^*} ratios for a given $m_{W'}$ leptoquark mass and θ mixing angle, with the C_9 and C_{10} coefficients detailed in Eq. (5.14). Additionally, we calculate $BR(B^+ \to K^+\mu^-e^+)$ and $BR(B^+ \to K^+e^-\mu^+)$ values. The 1σ and [90% C.L.] favoured parameter region is defined by the $m_{W'}, \theta$ values which satisfy $R_K = 0.745 \pm 0.097$ [$R_K = 0.745 \pm 0.159$], $R_{K^*} = 0.69 \pm 0.12$ [$R_{K^*} = 0.69 \pm 0.20$] and also satisfy the current 90% C.L. experimental limits $BR(B^+ \to K^+\mu^-e^+) < 1.3 \times 10^{-7}$ and $BR(B^+ \to K^+e^-\mu^+) < 9.1 \times 10^{-8}$ [75]. It turns out that the favoured region, defined in the way we have done, is not currently constrained by any other process.

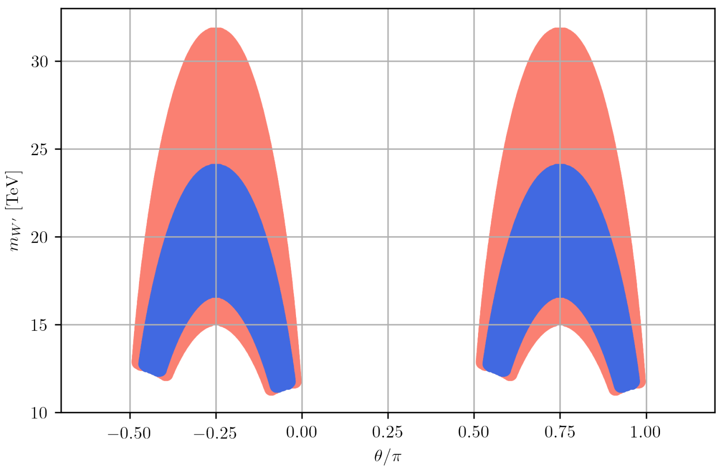

FIGURE 5.1: The favoured parameter regions compatible with the current experimental limits from $B^+ \to K^+\mu^-e^+$, $B^+ \to K^+e^-\mu^+$. Shown are the 1σ (blue) and 90% confidence level (red) bands suggested by the measured R_K and R_{K*} ratios.

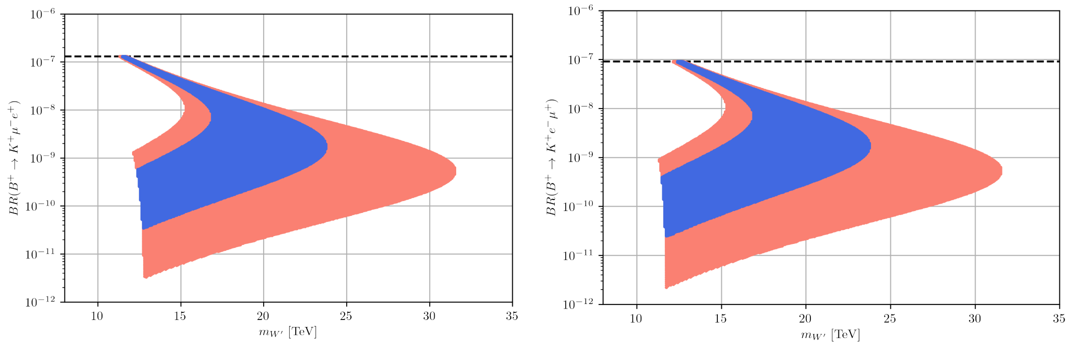

(A) (B)

FIGURE 5.2: Expectation for (a) $BR(B^+ \to K^+\mu^-e^+)$ (b) $BR(B^+ \to K^+e^-\mu^+)$ for the favoured parameter region identified in Figure 5.1. The black dashed lines correspond to the current experimental 90% C.L. upper bounds on these branching fractions.

A plot of the allowed model parameters is shown in Figure 5.1. From that figure it is clear that the favoured range of θ is approximately between $[-\frac{\pi}{2}, 0]$ or $[\frac{\pi}{2}, \pi]$ and $m_{W'}/\text{TeV}$ between $[12, 31]$. The identical nature of the two adjacent regions can be understood as follows. Under the transformation $\theta \to \theta + \pi$, $\sin\theta \to -\sin\theta, \cos\theta \to -\cos\theta$, and the leading order amplitudes for $b \to s\bar{\ell}\ell$ (which are proportional to $\sin\theta\cos\theta$) are invariant. Also the amplitudes for the decay processes, $B^+ \to K^+\mu^-e^+$, $B^+ \to K^+e^-\mu^+$, are proportional to $\sin^2\theta$ and $\cos^2\theta$ respectively, and are also invariant under $\theta \to \theta + \pi$. It should be noted that the $R_{K^{(*)}}$ anomalies on their own can potentially have $m_{W'} < 12$TeV, but the low mass cut-off is acquired due to the $B^+ \to K^+e^\mp\mu^\pm$ decay constraints.

For each point in the favoured region shown in Figure 5.1 we can calculate the expected rates for the rare $B^+ \to K^+\mu^-e^+$ and $B^+ \to K^+e^-\mu^+$ processes. The result of this exercise is shown in Figure 5.2. Note that $B^+ \to K^+\mu^-e^+$ probes $\sin^2\theta \approx 1$, while $B^+ \to K^+\mu^+e^-$ probes $\cos^2\theta \approx 1$, and thus these two decay channels are complimentary. Using the first $9\,\text{fb}^{-1}$ LHCb is expected to be sensitive to the branching ratio of $B^+ \to K^+e^\pm\mu^\mp$ at the level of 10^{-9} and scale almost linearly with integrated luminosity. [431]

In addition to further improvements to $B^+ \to K^+\mu^\pm e^\mp$ there are a number of other ways to test this model. In the remainder of this section we focus on making predictions for various rare decays that directly involve the new physics invoked in explaining the $R_{K^{(*)}}$ anomalies. We first consider the rare tau lepton decays: $\tau \to K_s\ell$, $\ell = e, \mu$. The decay rate for the $\tau \to K_s\ell$ process is calculated to be

$$\Gamma(\tau \to K_s\ell) = \frac{f_K^2\alpha_s^2\pi(m_\tau^2 - m_K^2)^2[|K_{s\ell}|^2|K_{d\tau}|^2 + |K_{s\tau}|^2|K_{d\ell}|^2]}{64m_{W'}^4 m_\tau}\,. \tag{5.16}$$

Here, $m_K \simeq 497.7$MeV and $f_K \simeq 156.1$MeV are the K_s meson mass and decay constant respectively, and we have set the final state lepton mass to zero in the above calculation. With the ansatz, Eq. (5.15), we have $K_{se} = \cos\theta$, $K_{s\mu} = \sin\theta$, $K_{d\tau} = 1$, $K_{d\ell} = 0$. Using the experimentally observed decay width, $\Gamma(\tau \to \text{all}) \simeq 2.27 \times 10^{-12}$GeV, the branching fraction, $BR(\tau \to K_s\ell) = \Gamma(\tau \to K_s\ell)/\Gamma(\tau \to \text{all})$,

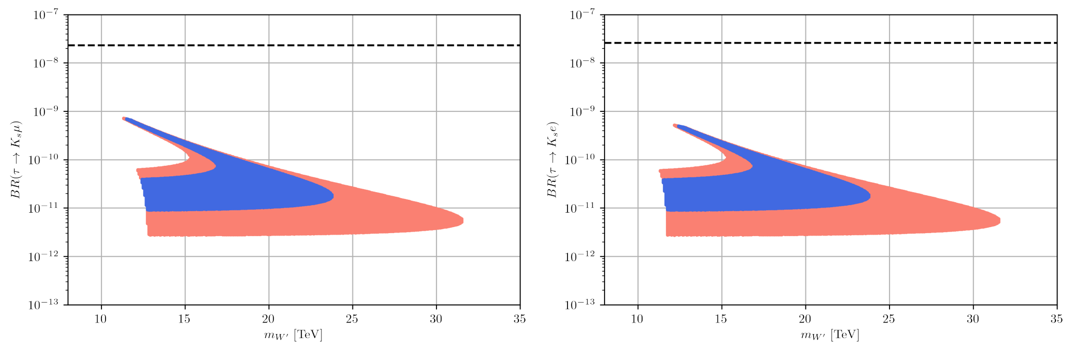

(A) (B)

FIGURE 5.3: Expectation for (a) $BR(\tau \to K_s\mu)$ (b) $BR(\tau \to K_s e)$ for the favoured parameter region identified in Figure 5.1. The black dashed lines correspond to the current experimental 90% C.L. upper bounds on these branching fractions.

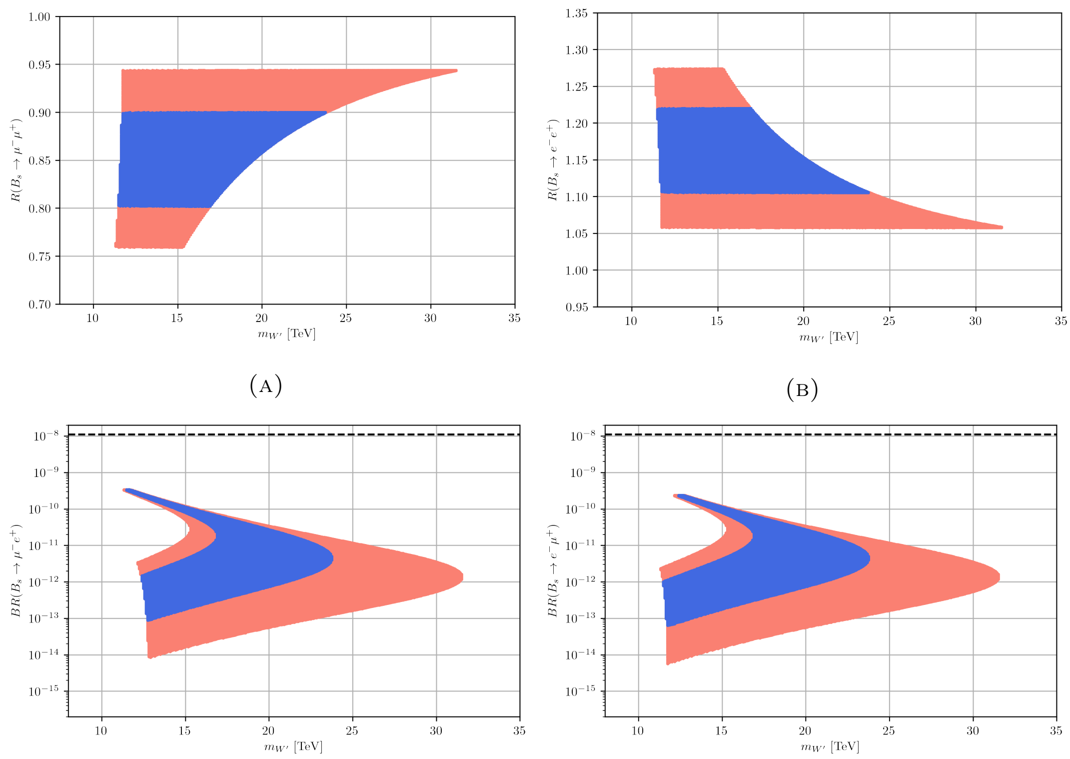

(A) (B) (C) (D)

FIGURE 5.4: Expectation for (a) $R(B_s \to \mu^-\mu^+)$ (b) $R(B_s \to e^-e^+)$ (c) $BR(B_s \to \mu^-e^+)$ (d) $BR(B_s \to e^-\mu^+)$ for the favoured region of parameter space identified in Figure 5.1.

can then be obtained. Our results are shown in Figure 5.3. The Belle II experiment will search for $\tau \to K_s\ell$ decays with an improved sensitivity of 5×10^{-10} (4×10^{-10}) for $\tau \to K_s e$ ($\tau \to K_s\mu$). [432]

The effective Lagrangian that induces modifications to the R_K ratio also modifies the two-body B_s decays: $B_s \to \mu^-\mu^+$ and $B_s \to e^-e^+$. These decays also arise in the standard model, and so it is useful to compute the ratio

$$R(B_s \to \ell^-\ell^+) \equiv \frac{\Gamma(B_s \to \ell^-\ell^+)}{\Gamma_{SM}(B_s \to \ell^-\ell^+)} \tag{5.17}$$

where the numerator, $\Gamma(B_s \to \ell^-\ell^+)$, includes the new physics (W') contributions as well as the standard model contribution. In this model we expect $R(B_s \to \mu^-\mu^+) \simeq (1+R_K)/2$, and $R(B_s \to e^-e^+) \simeq (3-R_K)/2$. In Figure 5.4 we have calculated the predictions for $R(B_s \to \ell^-\ell^+)$. A comparison of the experimental values [75] with the SM predictions [433] shows that the $R(B_s \to \mu^-\mu^+)$ ratio inferred from measurement is $R(B_s \to \mu^-\mu^+) = 0.7 \pm 0.3$. This value is consistent with what we would expect given the central values of R_K and R_{K^*}, but of course the current error is too large to rigorously test this model. In Figure 5.4 we have also shown the predicted branching ratios $BR(B_s \to \mu^-e^+)$ and $BR(B_s \to e^-\mu^+)$, together with the 90% C.L. upper bound $BR(B_s \to e^\pm\mu^\mp) < 1.1 \times 10^{-8}$.

The vector leptoquark also modifies the two lepton univerality ratios $R_D^{\mu/e} = \Gamma(B \to D\mu\bar{\nu})/\Gamma(B \to De\bar{\nu})$ and $R_{D^*}^{e/\mu} = \Gamma(B \to D^*e\bar{\nu})/\Gamma(B \to D^*\mu\bar{\nu})$ via its couplings to up-type quarks and neutrinos. These ratios have been measured by the Belle experiment: $R_D^{\mu/e} = 0.995 \pm 0.022 \pm 0.039$ [434] and $R_{D^*}^{e/\mu} = 1.04 \pm 0.05 \pm 0.01$ [435], where the first and second uncertainties are statistical and systematic respectively. To leading order in the contribution of the vector leptoquark the lepton universality ratios are given by

$$\begin{aligned} R_D^{\mu/e} &\simeq R_{D,SM}^{\mu/e}\left(1 + \frac{\sqrt{2}\pi\alpha_s \cos\theta_c \sin 2\theta}{V_{cb}G_F m_{W'}^2}\right), \\ R_{D^*}^{e/\mu} &\simeq R_{D^*,SM}^{e/\mu}\left(1 - \frac{\sqrt{2}\pi\alpha_s \cos\theta_c \sin 2\theta}{V_{cb}G_F m_{W'}^2}\right), \end{aligned} \tag{5.18}$$

where θ_c denotes the Cabibbo angle. For the region of interest the deviation from the SM value is about one order of magnitude smaller than the experimental sensitivity of Belle and hence does not currently pose a new constraint.

We have briefly looked at the $\mu \to e\gamma$ radiative decay. This decay arises at one-loop level, with virtual down-type quarks and W' gauge boson propagators in the loop. Making use of the general calculation given in Ref. [436], we show that the first two terms in the $m_b^2/m_{W'}^2$ expansion vanish: the first one due to unitarity and the second one

$$\Gamma(\mu \to e\gamma) \simeq \frac{9\,\alpha_{em}\alpha_s^2 m_b^4 m_\mu^5\,(2Q_b + Q_{W'})^2 \sin^2\theta \cos^2\theta}{256 m_{W'}^8} \tag{5.19}$$

is proportional to $(2Q_b + Q_{W'})^2$ and thus vanishes as the charge assignments in this model satisfy $Q_b = -1/3$ and $Q_{W'} = 2/3$. Hence we do not expect the $\mu \to e\gamma$ process to be important in this model.

A similar conclusion holds for $\mu \to eee$ and $\mu \to e$ conversion in nuclei, because due to dipole dominance the decay width $\Gamma(\mu \to eee)$ and the conversion rate $CR(\mu N \to eN)$ are directly proportional to $\Gamma(\mu \to e\gamma)$. In particular, there are no tree-level contributions to $\mu \to e$ conversion for the K matrix in Eq. (5.15).

5.1.4 Conclusion

We have proposed a Pati-Salam variant $SU(4)$ theory, with gauge group $SU(4)_C \times SU(2)_L \times U(1)_{Y'}$, which is capable of explaining the R_K and R_{K^*} anomalies via new gauge interactions. The model is consistent with experimental constraints, including the stringent limits on $B^+ \to K^+\mu^-e^+$ and $B^+ \to K^+e^-\mu^+$ decays. In this model, the chiral left-handed fermions are arranged in a similar fashion to the original Pati-Salam model, i.e. with leptons making up the fourth colour, while the chiral right-handed fermions are treated quite differently. The model features $SU(4)$ symmetry breaking via the introduction of a $SU(4)$ scalar multiplet χ with a vev $w \gtrsim 10$TeV and electroweak symmetry breaking via scalars ϕ and Δ with vevs that satisfy $\sqrt{v^2+u^2} \simeq 174$ GeV. In addition to new scalar particles, the model contains new charged $(\frac{2}{3}e)$ W' and neutral Z' gauge bosons along with heavy exotic charged $E^-_{L,R}$ and neutral $N_{L,R}$ fermions. The charged leptoquark gauge bosons W' couple in a chiral manner to the familiar quarks and leptons and can thereby interfere with SM weak processes. The theory makes predictions for $B^+ \to K^+\mu^-e^+$, $B^+ \to K^+e^-\mu^+$, $\tau \to K_s\ell$, $B_s \to \mu^-\mu^+$, as well as the highly suppressed $B_s \to \mu^-e^+$ and $B_s \to e^-\mu^+$ processes. For instance, for the leptonic $B_s \to \mu^-\mu^+$ decay channel the rate is predicted to satisfy: $\Gamma(B_s \to \mu^-\mu^+)/\Gamma_{SM}(B_s \to \mu^-\mu^+) = (1+R_K)/2$. These predictions can be tested at the LHCb and Belle II experiments when increased statistics become available.

The leptoquark gauge boson phenomenology of the chiral $SU(4)$ Pati-Salam model considered will be relevant for more general chiral $SU(4)$ models. In particular, the model can easily be extended to the full Pati-Salam gauge group: $SU(4) \otimes SU(2)_L \otimes SU(2)_R$. In this case, the three $SU(4)$ singlet fermions in Table 5.2 unify into a $SU(2)_R$ triplet, that is the fermion content of each generation have gauge transformation: $Q_L \sim (4,2,1), Q_R \sim (4,1,2), F_R \sim (1,1,3)$. The $SU(4)$ leptoquark gauge bosons of such extended models can explain the measured R_K deviations in the same manner as discussed here. However, since such models typically require more scalar degrees of freedom, there are more observable signatures of new physics, including the possibility of explaining the R_D anomalies via scalar leptoquarks. Although very interesting and topical in light of the tantalizing experimental hints, we leave further investigations along these lines for future work.

5.2 Unified $SU(4)$ Theory for the $R_{D^{(*)}}$ and $R_{K^{(*)}}$ Anomalies

The SM of particle physics with the inclusion of neutrino masses describes nature with unprecedented precision and has so far withstood all experimental tests. However, recently several hints for a violation of LFU in recent measurements of semileptonic B meson decays [94, 391–396, 437] have emerged. The theoretically cleanest probes are the LFU ratios

$$R_{K^{(*)}} = \frac{\Gamma(\bar{B} \to \bar{K}^{(*)}\mu^+\mu^-)}{\Gamma(\bar{B} \to \bar{K}^{(*)}e^+e^-)} \qquad \text{and} \qquad R_{D^{(*)}} = \frac{\Gamma(B \to D^{(*)}\tau\bar{\nu})}{\Gamma(B \to D^{(*)}\ell\bar{\nu})}\,, \tag{5.20}$$

where ℓ is a light lepton $\ell = e, \mu$, because hadronic uncertainties cancel out in the LFU ratios [397]. Their current experimental measurements and SM predictions are summarized in Table 5.3. While the LFU ratios $R_{K^{(*)}}$ point to a smaller decay rate with final state muons compared to electrons in the neutral current process $b \to s\ell^+\ell^-$, the LFU ratios $R_{D^{(*)}}$ indicate an enhanced rate for the charged current process $b \to c\tau\bar{\nu}$ compared to light charged leptons in the final state. The significance of the anomalies in semileptonic B meson decays is at the level of 2.5σ for both R_K and R_{K^*} ratios, while the significance for the combined measurement of the LFU ratios R_D and R_{D^*} exceeds 3σ.

	Observed	SM	q^2 range
R_K	$0.846^{+0.060+0.016}_{-0.054-0.014}$ [437]	1.0003 ± 0.0001 [407]	$1\,\mathrm{GeV}^2 < q^2 < 6\,\mathrm{GeV}^2$
R_{K^*}	$0.685^{+0.113}_{-0.069} \pm 0.047$ [391]	1.00 ± 0.01 [93]	$1.1\,\mathrm{GeV}^2 < q^2 < 6\,\mathrm{GeV}^2$
R_D	$0.340 \pm 0.027 \pm 0.013$ [89]	0.299 ± 0.011 [438]	Full
R_{D^*}	$0.295 \pm 0.012 \pm 0.008$ [89]	0.252 ± 0.003 [439]	Full

Table 5.3: Experimental results and standard model theory predictions for the LFU ratios $R_{K^{(*)}}$ and $R_{D^{(*)}}$. Statistical uncertainties are listed first and systematic uncertainties second. In the case of the LFU ratios $R_{K^{(*)}}$, the data are binned in the invariant mass q^2 of the final state lepton pair, in order to avoid the J/ψ and other resonances. The relevant q^2 range is indicated in the last column.

The experimental anomalies in R_D and R_{D^*} are supported by a similar deviation in the LFU ratio $R_{J/\psi} = \Gamma(B_c^+ \to J/\psi\tau^+\nu)/\Gamma(B_c^+ \to J/\psi\mu^+\nu)$ which analogously points to a larger branching fraction to tau leptons compared to muons, although still being consistent with the SM at the 2σ level due to large experimental uncertainties [440]. Also, there are deviations in the angular observable P_5' [409, 441] and more generally data from several measurements of $b \to s\mu^+\mu^-$ [442] that suggest a suppression of the decays $b \to s\mu^+\mu^-$ compared to the SM expectation, while being consistent with the experimentally observed value of the LFU ratios $R_{K^{(*)}}$. However, as these other channels currently have fewer clean signals due to large hadronic uncertainties in absolute branching ratio measurements and due to the difficulty of estimating a signal for P_5' [441] along with other experimental uncertainties, we instead focus on the LFU ratios introduced in Eq. (5.20) in the following discussion.

The possibility that some or even all of these deviations might be a harbinger of new physics has been entertained in the literature. In particular, several $SU(4)$ models [6, 414–423, 443] have been proposed. Most of these models simultaneously explain the B physics anomalies via a massive vector leptoquark $W' \sim (3, 1, 4/3)$[2], which is predicted by the breaking of $SU(4)_C \to SU(3)_C$. In particular chiral $SU(4)$ models [6, 443, 445] are phenomenologically motivated, because they avoid constraints from lepton-flavor-violating pseudoscalar meson decays like $K_L \to e^\pm\mu^\mp$, which place stringent constraints on the $SU(4)$-breaking scale [446–451]. The authors of Ref. [452] find that minimal models with a single vector leptoquark and a unitary quark-lepton mixing matrix are generally disfavored due to strong constraints from charged lepton-flavor-violating processes.

We pursue a different approach and build on our previously suggested Pati-Salam inspired chiral $SU(4)$ gauge model [6], where the $b \to s$ anomaly is explained via the vector leptoquark W' with purely left-handed couplings. The explanation of $R_{K^{(*)}}$ is predictive and depends on only two parameters, the mass of the vector leptoquark and a CKM-type mixing angle between left-handed down-type quarks and charged leptons. One interesting feature of the model is the simultaneous modification of both

[2] W' is the U_1 vector leptoquark in the nomenclature of Ref. [444].

the decay to muons, $b \to s\mu^+\mu^-$, and electrons[3], $b \to se^+e^-$, in opposite directions by an equal amount. Here, we consider a simple extension of the model with a larger gauge group $SU(4)_C \times SU(2)_L \times SU(2)_R$ which further unifies the right-handed matter fields. This allows explanation of the $R_{D^{(*)}}$ anomalies with a new scalar leptoquark $\tilde{\chi} \sim (3, 1, -2/3)$[4], which is part of the scalar breaking of the Pati-Salam gauge group to the SM gauge group. The $\tilde{\chi}$ leptoquark is well known as an explanation for $R_{D^{(*)}}$ [455,456] and other hints of new physics (see e.g. Refs. [457–461]). Here, the $\tilde{\chi}$ leptoquark features purely right-handed couplings and thus mediates $b_R \to c_R\tau_R\nu$ with right-handed charged fermions, where ν is a new light sterile neutrino. The sterile neutrino can be searched for and provides a smoking-gun signature of the explanation of the observed measurement of $R_{D^{(*)}}$.

The paper is structured as follows. In Sec. 5.2.1 we introduce the model and discuss the scalar potential and fermion masses. New contributions to the B physics anomalies are discussed in Sec. 5.2.4 and relevant constraints in Sec. 5.2.7. In Sec. 5.2.12 we present our results before concluding in Sec. 5.2.16. The decomposition of the particle content in terms of SM multiplets is shown in the appendix.

5.2.1 Model

We propose a model based on the gauge group $SU(4)_C \times SU(2)_L \times SU(2)_R$ and assign the particle content such that the $SU(4)$ leptoquark gauge boson couples to the quarks and leptons in a chiral fashion. This naturally avoids strong constraints from charged lepton-flavor-violating leptonic neutral meson decays such as $K_L \to e^\pm\mu^\mp$ and $B \to e^\pm\mu^\mp$. The particle content of the model is listed in Table 5.4. Apart from the

Fermion	$(SU(4)_C, SU(2)_L, SU(2)_R)$	Generations	Scalar	$(SU(4)_C, SU(2)_L, SU(2)_R)$
$\mathbf{Q}_L$	$(4, 2, 1)$	3	ϕ	$(1, 2, 2)$
$\mathbf{Q}_R$	$(4, 1, 2)$	3	χ	$(4, 1, 2)$
$\mathbf{f}_R$	$(1, 1, 3)$	3	Δ	$(4, 2, 3)$
S_L	$(1, 1, 1)$	1		

Table 5.4: Particle content

usual matter fields $\mathbf{Q}_{R,L}$ in the fundamental representation of $SU(4)_C$, there are three generations of right-handed triplet fermions $\mathbf{f}_R$ and a left-handed total singlet fermion S_L. The scalar sector consists of a bidoublet ϕ and two fields in the fundamental representation of $SU(4)_C$, χ and Δ.

The $SU(4)_C \times SU(2)_R$ symmetry is broken by the vacuum expectation value (vev) of the scalar χ at a high scale, $\langle\chi_{41}\rangle \equiv w \gtrsim 20$TeV, where the first (second) index refers to the fundamental representation of $SU(4)_C$ ($SU(2)_R$). Electroweak symmetry is broken by the scalar ϕ with $v \equiv \sqrt{|v_{12}|^2 + |v_{21}|^2} \simeq (2\sqrt{2}G_F)^{-1/2} \simeq 174$ GeV where $v_{12} \equiv \langle\phi_{12}\rangle$ and $v_{21} \equiv \langle\phi_{21}\rangle$ refer to the vevs in the $(I_{3L}, I_{3R}) = (\frac{1}{2}, -\frac{1}{2})$ and $(I_{3L}, I_{3R}) = (-\frac{1}{2}, \frac{1}{2})$ components. The combination of the vevs of χ and ϕ induces small vevs for Δ, $\langle\Delta_{41(12)}\rangle = u_1$ and $\langle\Delta_{42(11)}\rangle = u_2$. The first index refers to the fundamental representation of $SU(4)_C$, the second refers to the fundamental representation of $SU(2)_L$ and the last two in round brackets are two indices in the

[3]Modifications to electrons have been suggested in Ref. [453] and also realized in the simultaneous explanation of both anomalies using the R_2 leptoquark [454].

[4]$\tilde{\chi}$ corresponds to the conjugate of the S_1 leptoquark in the nomenclature of Ref. [444].

fundamental representation of $SU(2)_R$ which are symmetrized as indicated by the round brackets, $T_{(ab)} = \frac{1}{2}(T_{ab} + T_{ba})$. Thus the following symmetry-breaking pattern emerges $|u_1|^2 + |u_2|^2 \ll |v_{12}|^2 + |v_{21}|^2 \ll |w|^2$

$$\begin{gathered} SU(4)_C \times SU(2)_L \times SU(2)_R \\ \downarrow \langle\chi\rangle \\ SU(3) \times SU(2)_L \times U(1)_Y \\ \downarrow \langle\phi\rangle\,,\langle\Delta\rangle \\ SU(3) \times U(1)_Q \end{gathered} \tag{5.21}$$

Here weak hypercharge Y and electric charge Q are related to the generators in $SU(4)_C \times SU(2)_L \times SU(2)_R$ by $Y = T + 2I_{3R}$ and $Q = \frac{T}{2} + I_{3L} + I_{3R} = I_{3L} + Y/2$, respectively. If we use the gauge symmetry to rotate the vev of χ to the fourth component, then T is the diagonal traceless $SU(4)$ generator with elements $(\frac{1}{3}, \frac{1}{3}, \frac{1}{3}, -1)$.

5.2.2 Yukawa Sector

Given the particle content in Table 5.4 the full Yukawa Lagrangian is given by

$$\begin{aligned} \mathcal{L} =& Y_1 \bar{\mathbf{Q}}_L^{ia} \phi_{a\beta} (\mathbf{Q}_R)_{i\gamma} \varepsilon^{\beta\gamma} + Y_2 \bar{\mathbf{Q}}_L^{ia} \tilde{\phi}_{a\beta} (\mathbf{Q}_R)_{i\gamma} \varepsilon^{\beta\gamma} - Y_3 \bar{\mathbf{Q}}_R^{i\alpha} \chi_{i\alpha} S_L + Y_4 \bar{\mathbf{Q}}_R^{i\alpha} \chi_{i\beta} (\mathbf{f}_R^c)_{(\alpha\gamma)} \varepsilon^{\beta\gamma} \\ &+ Y_5 \bar{\mathbf{Q}}_L^{ia} \Delta_{ia(\alpha\beta)} (\mathbf{f}_R)_{(\gamma\delta)} \varepsilon^{\alpha\gamma} \varepsilon^{\beta\delta} + \frac{1}{2} m (\bar{\mathbf{f}}_R^c)^{(\alpha\beta)} (\mathbf{f}_R)_{(\alpha\beta)} - \frac{1}{2} m_S S_L^T \hat{\mathbf{C}} S_L + h.c.\,, \end{aligned} \tag{5.22}$$

where flavor indices are suppressed, but indices for the gauge groups are explicitly shown.[5] The Yukawa couplings are matrices in flavor space; rows (columns) are labeled by the first (second) fermion in the fermion bilinear. Indices in fundamental representation of $SU(4)_C$ are labeled by roman letters $i, j, \ldots$, indices in the fundamental representation of $SU(2)_L$ are labeled by greek letters $\alpha, \beta, \ldots$ and indices in the fundamental representation of $SU(2)_R$ are labeled by roman letters $a, b, \ldots$. In the above expression we used the charge-conjugate fields $\tilde{\phi}_{\alpha a} = \epsilon_{\alpha\beta}\epsilon_{ab}\phi^{*\beta b}$ and $(f_R^c)_{\alpha\beta} = \epsilon_{\alpha\alpha'}\epsilon_{\beta\beta'}\hat{\mathbf{C}}\gamma^0 f_R^{*\alpha'\beta'}$ with $\hat{\mathbf{C}} = i\gamma^2\gamma^0$. From the Yukawa Lagrangian (5.22) we obtain the Lagrangian of the quark masses

$$\mathcal{L} = -\bar{\mathbf{u}}_L m_u \mathbf{u}_R - \bar{\mathbf{d}}_L m_d \mathbf{d}_R + h.c. \tag{5.23}$$

with the quark mass matrices

$$m_u = Y_1 v_{12} + Y_2 v_{21}^* \qquad\qquad m_d = -Y_1 v_{21} - Y_2 v_{12}^*\,. \tag{5.24}$$

[5] Lower indices refer to the fundamental representation and upper indices refer to the antifundamental representation. Fields ψ with lower indices transform as $\psi_i \to (U\psi)_i \equiv U_i^j \psi_j$.

The charged and neutral lepton mass matrices can be written in the basis

$$\mathcal{L} = -\frac{1}{2}\mathcal{N}^T\hat{\mathbf{C}}M_{\nu,N}\mathcal{N} - \left(\bar{\mathcal{E}}_L M_{e,E}\mathcal{E}_R + h.c.\right) \quad \mathcal{E}_L \equiv \begin{pmatrix}\mathbf{e}_L \\ \mathbf{E}_L\end{pmatrix} \quad \mathcal{E}_R \equiv \begin{pmatrix}\mathbf{e}_R \\ \mathbf{E}_R\end{pmatrix} \quad \mathcal{N} \equiv \begin{pmatrix}\nu_L \\ \nu_R^c \\ \mathbf{N}_R^c \\ S_L\end{pmatrix} \tag{5.25}$$

with the mass matrices

$$M_{e,E} = \begin{pmatrix}-Y_5 u_2 & m_d \\ -m & -Y_4^\dagger w^*\end{pmatrix} \qquad M_{\nu,N} = \begin{pmatrix}0 & m_u^* & \sqrt{2}Y_5^* u_1^* & 0 \\ . & 0 & -\frac{Y_4 w}{\sqrt{2}} & Y_3 w \\ . & . & -m^* & 0 \\ . & . & . & m_S\end{pmatrix} \tag{5.26}$$

A viable mass spectrum for the charged leptons is obtained for $m_d, m \ll Y_4 w$. More precisely, we take the eigenvalues of m to be less than $\simeq 1$ GeV and the eigenvalues of $Y_4 w$ to be larger than $\simeq 1$TeV. In this case the new charged fermions $E_{L,R}$ decouple and their masses are determined by $M_E \approx -Y_4^\dagger w^*$, while the light charged lepton masses are determined by $M_e \approx -Y_5 u_2$. The contribution from mixing with $E_{L,R}$ can be neglected because of the assumed relative sizes of m, m_d and $Y_4 w$. In the basis of a diagonal Y_5 the SM charged lepton mass eigenstates are approximately given by the weak interaction eigenstates. We thus denote them by $e_{L,R}$. Neutrino mass eigenstates are labeled by n_i. Hence in this basis the leptonic mixing matrix is determined by the neutrino mass matrix up to subpercent-level corrections from mixing with the heavy charged leptons.

The neutrino oscillation data and the existence of a fourth light sterile neutrino with $m_4 \lesssim 1$GeV requires $u_1 \ll u_2$ and $Y_4 w, Y_3 w \gg m, m_S$ to be satisfied. For the remainder of this work we focus exclusively on the limit $u_1 \to 0$ in order to recover the experimentally observed active neutrino mass spectrum and the leptonic mixing angles. In this limit, three pseudo-Dirac pairs obtain masses of order $Y_{3,4}w$ and decouple from four light neutrinos. A minimal phenomenologically viable texture for the neutrino mass matrix is given by

$$Y_3 = \begin{pmatrix}0 \\ 0 \\ y_3\end{pmatrix} \qquad Y_4 = \begin{pmatrix}Y_{ue} & 0 & 0 \\ 0 & 0 & Y_{c\tau} \\ 0 & Y_{t\mu} & 0\end{pmatrix}. \tag{5.27}$$

The large off-diagonal entries $Y_{c\tau}$ and $Y_{t\mu}$ are required for the $b \to c$ anomalies. The entries of the Majorana mass matrices m and m_S have to be small $\lesssim 1$ GeV in order to kinematically allow $R_{D^{(*)}}$ from the relevant $b \to c\tau n_4$ process.

5.2.3 Scalar Potential

In this model, the masses of the charged leptons arise from the vev of the Δ scalar, while the masses of the quarks result from the vevs of the bidoublet ϕ. In such a situation, consistent Higgs phenomenology requires a decoupling limit where the LHC Higgs-like scalar is identified with the lightest neutral scalar in the model. The decoupling limit works analogously to the one shown in Refs. [6, 427] and thus, we do not repeat the whole discussion, but instead focus only on the pertinent differences in the following.

In order to achieve the desired symmetry-breaking pattern, we first neglect the scalar Δ and focus on the scalars χ and ϕ. In this case the possible invariants which enter the scalar potential are

$$\begin{aligned} I_1 &= \chi^{*i\alpha}\chi_{i\alpha} - w^2, & I_2 &= \chi_{i\alpha}\chi_{j\beta}\chi_{k\gamma}\chi_{l\delta}\epsilon^{ijkl}(\epsilon^{\alpha\beta}\epsilon^{\gamma\delta} + \epsilon^{\alpha\gamma}\epsilon^{\delta\beta} + \epsilon^{\alpha\delta}\epsilon^{\beta\gamma}) + \text{h.c.} \\ J_1 &= \phi^{*a\beta}\phi_{a\beta} - (|v_{12}|^2 + |v_{21}|^2), & J_2 &= \frac{1}{4}(\phi_{a\alpha}\phi_{b\beta}\epsilon^{ab}\epsilon^{\alpha\beta} + \text{h.c.}) + \text{Re}(v_{12}v_{21}) \\ K_1 &= \left(\chi^{*i\alpha}\chi_{i\beta} - w^2\right)\left(\phi_{a\alpha}\phi^{*a\beta} - |v_{21}|^2\right), & J_3 &= \frac{1}{4i}(\phi_{a\alpha}\phi_{b\beta}\epsilon^{ab}\epsilon^{\alpha\beta} - \text{h.c.}) + \text{Im}(v_{12}v_{21}), \end{aligned} \tag{5.28}$$

where we have subtracted the vevs from each invariant such that the invariants vanish in the vacuum. The vev of χ can always be chosen to be real by using a suitable global $SU(4)_C \times SU(2)_R$ rotation. The terms I_1, J_1 and K_1 respect an accidental $U(1)_\chi \times U(1)_\phi$ symmetry. $U(1)_\chi$ is broken by I_2 and $U(1)_\phi$ is broken by $J_{2,3}$. The invariants I_1, J_1 and K_1 are non-negative, while the others may become negative and thus terms involving these have to be sufficiently small to ensure vacuum stability. As the discussion of the B physics anomalies is mostly independent to the exact form of the scalar potential, we only comment on how to obtain the correct vacuum structure. The scalar potential in terms of invariants is given by

$$V(\chi,\phi) = \lambda_1 I_1^2 + \lambda_2 I_2 + \frac{1}{2}\sum_{i=1}^{3}\sum_{j=1}^{i}\lambda_{ij}J_iJ_j + \sum_{i=1}^{3}\lambda_i' I_1 J_i + \lambda_4' K_1\ . \tag{5.29}$$

The coefficients λ_i' parametrize interactions between the χ and ϕ fields. Most of the scalar potential is invariant under a larger symmetry group $SU(4)_C \times SU(2)_L \times SU(2)_{R,\chi} \times SU(2)_{R,\phi}$ with two separate $SU(2)_R$ symmetries for each of the two scalars χ and ϕ. It is only broken to the diagonal subgroup by the last term $\lambda_4' K_1$. The couplings in the scalar potential can be chosen real due to the invariants in Eq. (5.28) being Hermitian. We also restrict ourselves to real vevs. This potential allows the vev hierarchy $w \gg v_{21} \gg v_{12} = 0$ to emerge, which leads to the correct quark mass spectrum with $Y_2 = m_u/v_{21}^*$ and $Y_1 = -m_d/v_{21}$ as mentioned in the previous section. The scalar doublet in the bidoublet which does not obtain a vev induces flavor changing neutral currents [462–465] which poses a lower bound on its mass scale of $\mathcal{O}(20)$TeV [466].

There are many terms in the scalar potential which couple the scalar field Δ to other scalar fields. However most of them are not relevant for the induced vevs of Δ. The most important term is linear in Δ

$$V(\Delta,\phi,\chi) = m_{123}\,(\Delta^{*ia(\alpha\beta)}\,\phi_{a\alpha}\,\chi_{i\beta} + \text{h.c.}) = \sqrt{2}m_{123}\,v_{21}\,w\,h_3 + \dots\ , \tag{5.30}$$

where we have absorbed the phase of m_{123} by rephasing Δ and defined the electrically neutral scalar $h_3 \equiv \sqrt{2}\text{Re}(\Delta_{42(11)})$. In order to calculate the induced vev of the scalar Δ it is sufficient to consider terms quadratic in h_3, because the induced vev is much smaller compared to all other scales. Thus we obtain

$$u_2 \equiv \langle \mathrm{Re}(\Delta_{42(11)}) \rangle = \frac{\langle h_3 \rangle}{\sqrt{2}} = -\frac{m_{123}\, v_{21}\, w}{m_{h_3}^2} , \tag{5.31}$$

where m_{h_3} is the mass of h_3. In the limit $w^2 \gg v_{21}^2$ the observed Higgs boson h is a linear combination of $h_1 \equiv \sqrt{2}\mathrm{Re}(\phi_{21})$ and h_3

$$h = \cos\beta\, h_1 + \sin\beta\, h_3 . \tag{5.32}$$

The mixing arises from the term in Eq. (5.30) and indirectly from terms quadratic in Δ and ϕ, after Δ obtains a vev u_2. Generally the mixing angle is given by $\sin\beta \sim m_{123} w / m_{h_3}^2 = u_2/v_{21}$ and thus the Higgs h features SM-like couplings, as discussed in Refs. [6, 427].

5.2.4 New Contributions to Semileptonic B Decays

In Ref. [6], we showed that the experimentally observed values of R_K and R_{K^*} can be explained via the exchange of the massive leptoquark gauge boson W' in $SU(4)_C$. There has been a recent measurement of R_K by the LHCb experiment [437] (see Table 5.3) and the LHCb experiment also published a new stronger limit [467] on the branching ratio of the semileptonic charged lepton flavor violating decay $B \to K e^\pm \mu^\mp$: $\mathrm{BR}(B^+ \to K^+ \mu^- e^+) < 7.0 \times 10^{-9}$ and $\mathrm{BR}(B^+ \to K^+ \mu^+ e^-) < 6.4 \times 10^{-9}$ at 90% C.L. Hence we briefly summarize the relevant definitions in Sec. 5.2.5 and update the analysis with the latest measurements in Sec. 5.2.7.

The aforementioned vector leptoquark W' cannot explain the measurement of R_D and R_{D^*} due to its chiral couplings. This model also features several scalar leptoquarks which also contribute to $R_{D^{(*)}}$: (i) The scalar Δ contains two leptoquarks $\Delta_{i\alpha 11}$ and $\Delta_{i\alpha(12)}$, denoted by R_2 and $\tilde{R}_2$ in the nomenclature of Ref. [444]. However these two leptoquarks have chiral couplings and either couple to charged leptons or neutrinos, but not both simultaneously. Although their electric charge 2/3 components mix and thus in general contribute to $R_{D^{(*)}}$, their contribution is suppressed due to the small mixing and thus cannot account for the observed deviation in $R_{D^{(*)}}$. (ii) The scalar χ also contains a leptoquark $\tilde{\chi}_i = \chi_{i2} \sim (3, 1, -2/3)$. We discuss its contributions to $R_{D^{(*)}}$ in Sec. 5.2.6.

5.2.5 Neutral Current Process: $c \to s\ell\ell$

We briefly outline the most important points from the study in Ref. [6] and refer the interested reader to the publication for further details. The relevant $SU(4)$ gauge interactions with the fermions are given by

$$\mathcal{L} = \frac{g_s}{\sqrt{2}} K_{ij} W'_\mu \bar{d}_i \gamma^\mu P_L \ell_j + \frac{g_s}{\sqrt{2}} K^*_{ji} W'^*_\mu \bar{\ell}_i \gamma^\mu P_L d_j \tag{5.33}$$

where g_s is the $SU(4)_C$ gauge coupling constant and K is the mixing matrix between left-handed charged leptons and down-type quarks as shown in Ref. [6]. As quantum chromodynamics $SU(3)_C$ is embedded in $SU(4)_C$, the coupling g_s is directly defined by the strong gauge coupling. Here we have defined ℓ to include the three charged SM leptons and the three heavy exotic charged lepton mass eigenstates, i.e. $\ell = e, E$.

After integrating out the heavy W' mediator with mass $m_{W'}$ there are new contributions to the Wilson coefficients of $b \to s\ell\ell'$,

$$C_9^{sb\ell\ell'} = -C_{10}^{sb\ell\ell'} = \frac{\sqrt{2}\pi^2\alpha_s}{V_{ts}V_{tb}^*\alpha_{em}} \frac{K_{s\ell'}K_{b\ell}^*}{G_F m_{W'}^2} \,. \tag{5.34}$$

In the above $\alpha_s = g_s^2(m_{W'})/4\pi$ is the running strong coupling constant and $\alpha_{em} = 1/127.9$ denotes the fine-structure constant evaluated at the electroweak scale. K_{ij} are the elements of a CKM-type quark-lepton mixing matrix. The Wilson coefficients are defined by the effective Lagrangian

$$\mathcal{L}_{eff} = \frac{4G_F}{\sqrt{2}} \frac{\alpha_{em}}{4\pi} \sum_{\ell,\ell'} V_{ts}V_{tb}^* \sum_{i=9,10} C_i^{sb\ell\ell'} O_i^{sb\ell\ell'} + \text{h.c.} \,, \tag{5.35}$$

where O_i denotes operators with a strange and bottom quark and two charged leptons

$$O_9^{sb\ell\ell'} = (\bar{s}\gamma_\mu P_L b)(\bar{\ell}\gamma^\mu \ell') \qquad O_{10}^{sb\ell\ell'} = (\bar{s}\gamma_\mu P_L b)(\bar{\ell}\gamma^\mu\gamma_5 \ell') \,. \tag{5.36}$$

In order to explain the $R_{K^{(*)}}$ anomalies and to avoid stringent constraints from the lepton-flavor-violating $K_L \to e^\pm\mu^\mp$ decays among others, a particular off-diagonal structure of the CKM-type quark-lepton mixing K matrix is suggested. Considering only the first three columns of the general K matrix, i.e. the part relevant to quark-SM lepton interactions, we adopt the limiting case [6]

$$K = \begin{pmatrix} 0 & 0 & 1 \\ \cos\theta & \sin\theta & 0 \\ -\sin\theta & \cos\theta & 0 \end{pmatrix} \,. \tag{5.37}$$

5.2.6 Charged Current Process: $b \to c\tau\bar{\nu}$

The leptoquark $\tilde{\chi}$ couples to both charged leptons and neutrinos

$$\mathcal{L} = -Y_3 \bar{\mathbf{d}}_R \tilde{\chi} S_L - Y_4 \bar{\mathbf{u}}_R \tilde{\chi} \mathbf{e}_R^c - \frac{Y_4}{\sqrt{2}} \bar{\mathbf{d}}_R \tilde{\chi} (\mathbf{N}_R^c) + h.c. \tag{5.38}$$

Starting from this interaction Lagrangian we derive the Wilson coefficients. The neutrino mass eigenstate n_4 mixes with the flavor eigenstates $(N_R^c)_\beta = U_{N_\beta 4} n_4 + \dots$ and $S_L = U_{S4} n_4 + \dots$ where U denotes the matrix diagonalizing the neutral fermion mass matrix $U^T M_{\nu,N} U = \text{diag}(m_1, \dots, m_{10})$. The masses of the neutrino mass eigenstates n_i are denoted m_i, $i = 1, \dots, 10$, where $m_{1,2,3}$ denotes the masses of the three active neutrinos, m_4 is the mass of the fourth mass eigenstate n_4 and $m_{5,\dots,10}$ labels the masses of the mostly heavy sterile neutrinos. We work in the basis where the right-handed charged leptons and the right-handed up-type quarks are given by their mass eigenstates. Then the relevant part of the interaction Lagrangian for $\tilde{\chi}$ reads

$$\mathcal{L} = -\left(Y_{d4} \bar{\mathbf{d}}'_R n_4 + Y_4 \bar{\mathbf{u}}'_R \mathbf{e}'^c_R\right) \tilde{\chi} + h.c. \tag{5.39}$$

[6] In general (K_{ij}) is a 3×6 matrix which satisfies the unitarity condition $KK^\dagger = 1_{3\times3}$, where $1_{3\times3}$ is the 3×3 unit matrix.

with $Y_{d4} = (R_d)^*_{\alpha d}\left[(Y_3)_\alpha U_{S4} + \frac{(Y_4)_{\alpha\beta}}{\sqrt{2}} U_{N_\beta 4}\right]$, where R_d relates the weak interaction eigenstates $\mathbf{d}_R = R_d \mathbf{d}'_R$ with the mass eigenstate $\mathbf{d}'_R$. In the following we use $R_d = 1$ and drop the primes from the mass eigenstates. Integrating out scalar $\tilde{\chi}$ results in

$$\mathcal{L} = \frac{Y_{b4} Y^*_{c\tau}}{4 m^2_{\tilde{\chi}}} (\mathcal{O}^{cb\tau 4}_{VR} + \mathcal{O}^{cb\tau 4}_{AR}) \tag{5.40}$$

among other operators. The effective vector $\mathcal{O}^{cb\ell\nu}_{VR}$ and axial-vector $\mathcal{O}^{cb\ell\nu}_{AR}$ operators for a lepton ℓ and right-handed neutrino ν are defined according to Ref. [468] as

$$\mathcal{O}^{cb\ell\nu}_{VR} = (\bar{c}\gamma_\mu b)(\bar{\ell}\gamma^\mu P_R \nu) \qquad \mathcal{O}^{cb\ell\nu}_{AR} = (\bar{c}\gamma_\mu \gamma_5 b)(\bar{\ell}\gamma^\mu P_R \nu) \tag{5.41}$$

and enter the effective Lagrangian

$$\mathcal{L}_{eff} = \frac{2 G_F V_{cb}}{\sqrt{2}} \left(C^{cb\ell\nu}_{VR} \mathcal{O}^{cb\ell\nu}_{VR} + C^{cb\ell\nu}_{AR} \mathcal{O}^{cb\ell\nu}_{AR} \right) , \tag{5.42}$$

We may then simply compute the relevant Wilson coefficients required to compute $R_{D^{(*)}}$ which are given by

$$C^{cb\tau 4}_{VR} = C^{cb\tau 4}_{AR} = \frac{1}{4\sqrt{2} V_{cb} G_F m^2_{\tilde{\chi}}} \left(y_3 U_{S4} + \frac{Y_{t\mu}}{\sqrt{2}} U_{N_\mu 4} \right) Y^*_{c\tau} , \tag{5.43}$$

where we expressed Y_{b4} in terms of the entries of the minimal Yukawa matrix structure defined in Eq. (5.27) and the matrix elements of U.

Considering the aforementioned limit where $Y_{ue} w, Y_{c\tau} w, Y_{t\mu} w \gg m_t, m^*, m_S$, we may compute the mixing angles U_{S4} and $U_{N_\alpha 4}$ for the fourth neutrino state n_4

$$U_{S4} = \frac{1}{\sqrt{1 + 2|\frac{y_3}{Y_{t\mu}}|^2}} \quad U_{N_e 4} = 0 \quad U_{N_\mu 4} = \frac{\sqrt{2} y_3}{Y_{t\mu}} \frac{1}{\sqrt{1 + 2|\frac{y_3}{Y_{t\mu}}|^2}} \quad U_{N_\tau 4} = 0 \tag{5.44}$$

to leading order. So we note that with the selected Yukawa structure, the neutrino that participates in the $R_{D^{(*)}}$ anomalies is dominantly a mixture of the singlet S_L and the second state N_μ in $\mathbf{N}^c_R$. Substituting the above mixing angles into (5.43) results in

$$C^{cb\tau 4}_{VR} = C^{cb\tau 4}_{AR} \approx \frac{1}{2\sqrt{2} V_{cb} G_F m^2_{\tilde{\chi}}} \frac{y_3 Y^*_{c\tau}}{\sqrt{1 + 2|\frac{y_3}{Y_{t\mu}}|^2}} . \tag{5.45}$$

As the decay rates are summed over all polarizations and spins, the expressions for the LFU ratios should be invariant after replacing all Wilson coefficients for left-handed currents by right-handed ones and vice versa [469]. Hence, we may use the literature result for left-handed neutrinos [468] and map them directly to right-handed neutrinos since there is no interference between left- and right-handed operators. The resulting 1σ (90%C.L.) bounds on $R_{D^{(*)}}$ from Table 5.3 can be directly converted to constraints on the right-handed neutrino current Wilson coefficient

$$-0.33(-0.37) \leq C^{cb\tau 4}_{VR} \leq -0.25(-0.19) . \tag{5.46}$$

5.2.7 Constraints

Several measurements already place constraints on the favored parameter region. In particular Z boson decays to charged leptons, semihadronic B-meson decays, and collider constraints for the leptoquark, cosmological, astrophysical and direct search constraints on the sterile neutrino n_4.

5.2.8 Z Decay Constraints

The new leptoquark $\tilde{\chi}$ modifies the Z decay width to muons at one-loop level due to the presence of a large Yukawa coupling $Y_{t\mu}$. Contributions to other leptonic decays of the Z boson are generally small in this model. As the leptoquark $\tilde{\chi}$ only couples to right-handed charged leptons, its contribution can be parametrized by

$$\mathcal{L} = \frac{g}{\cos\theta_w}\left[\sin^2\theta_w + \delta g_{\mu,R}\right]\bar{\mu}_R Z_\mu \gamma^\mu \mu_R \tag{5.47}$$

following Ref. [470], where g is the $SU(2)_L$ gauge coupling and θ_w the weak mixing angle. For $m_t \ll m_{\tilde{\chi}}$ the contribution of the leptoquark $\tilde{\chi}$ can simply be written as

$$\delta g_{\mu,R} = 3\frac{|Y_{t\mu}|^2}{32\pi^2} x_t(1+\log x_t) \tag{5.48}$$

to leading order, where $x_t = m_t^2/m_{\tilde{\chi}}^2$. The current best experimental bound from precision electroweak physics comes from the LEP experiments [471]. We demand that the Z-boson coupling to muons is not changed by more than the experimental uncertainty at (1σ) [90% C.L.], i.e. $|\delta g_{\mu,R}| < \delta g_{\mu,R}^{\mathrm{exp}} = (1.3)[2.1]\times 10^{-3}$, and thus we obtain the constraint

$$|Y_{t\mu}| \leq \frac{4\pi\sqrt{2\delta g_{\mu R}^{\mathrm{exp}}}}{\sqrt{3x_t\,(1+\log x_t)}}\ . \tag{5.49}$$

5.2.9 $B \to K\nu\bar{\nu}$

Another constraint Comes from $B \to K\nu\bar{\nu}$ which is modified by the leptoquark $\tilde{\chi}$. It is described by effective operators of the form [472]

$$\mathcal{L} = 2\sqrt{2}G_F V_{tb}V_{ts}^* \frac{\alpha_{em}}{4\pi}\sum_{X=L,R} C_{\nu,X}\,\bar{s}\gamma_\mu P_X b\bar{\nu}(1-\gamma_5)\nu\ . \tag{5.50}$$

Integrating out $\tilde{\chi}$ as before we obtain

$$\mathcal{L} = \frac{(\sqrt{2}y_3 U_{S4} + Y_{t\mu}U_{N_\mu 4})^* Y_{c\tau}U_{N_\tau 4}}{4m_{\tilde{\chi}}^2}(\bar{s}\gamma^\mu P_R b)(\bar{n}_4\gamma_\mu P_L n_4)\ . \tag{5.51}$$

As $|U_{N_\tau 4}| \ll 1$ we find that the new physics contribution $C_{\nu,R}^{\mathrm{NP}}$ is very small compared to the SM contribution $C_{\nu,R}^{\mathrm{SM}} = -6.38 \pm 0.06$ and thus $B \to K\nu\bar{\nu}$ does not provide any competitive constraint. Similarly, new contributions from the exchange of $\tilde{\chi}$ to $B \to \pi\nu\bar{\nu}$ and $K \to \pi\nu\bar{\nu}$ decay rates are very suppressed due to the assumed Yukawa coupling structure.

5.2.10 Collider Constraints

There currently does not exist a plethora of dedicated searches at colliders for the leptoquark $\tilde{\chi}$ since the chosen Yukawa texture by construction couples only second-generation quarks with third-generation leptons and vice versa. The most common LHC searches are for single generation leptoquarks [473, 474, 474–478]. The searches are commonly separated into single leptoquark and pair production. The latter is generally independent of the absolute magnitude of the leptoquark Yukawa coupling, because the leptoquarks are produced via strong interactions in a hadron collider, unless the Yukawa couplings are large and substantially contribute to the leptoquark production, while single leptoquark production depends on the Yukawa coupling.

The model parameter space can be most economically constrained by searches with τc or μt final states. The $\tilde{\chi}$ particle can also decay into $b\nu$ due to the coupling y_3 being nonzero, but searches for final states with missing transverse energy are typically less sensitive. For the chosen mass range of the scalar leptoquark $\tilde{\chi}$ imposing the constraints from searches with third-generation scalar leptoquarks decaying into a tau lepton and a b quark such as the analysis in Ref. [474] does not pose any additional constraint on the parameter space over the Z decay constraint, although the sensitivity on the quark is markedly improved due to b tagging of the final state jets. However, a mixed 1-3 generation leptoquark search with final states μt analogous to the third-generation search in Ref. [479] could strengthen the limits on the $Y_{t\mu}$ coupling significantly in the future. Of course more complicated Yukawa textures for Y_3 and Y_4 (particularly the diagonal entries), can be chosen and constrained with the aforementioned single generations searches, however we do not consider these more complicated parametrizations in this work for the sake of brevity.

Finally there are constraints from the single τ-lepton + MET searches. The authors of Ref. [480] reinterpreted the searches for a heavy charged gauge boson from sequential SM (SSM) resonance searches of the ATLAS [481] and CMS [482] experiments as constraints on models explaining $R_{D^{(*)}}$. In particular, the leptoquark $\tilde{\chi}$ with purely right-handed couplings has been studied and the study finds that leptoquark masses above 2TeV are excluded at more than 2σ. At face value this constrains the leptoquark $m_{\tilde{\chi}}$ to be lighter than 2TeV. As the study was based on an older best fit to the $R_{D^{(*)}}$ anomalies further away from the SM, the current constraint for heavy charged gauge bosons from SSM resonance searches is relaxed and heavier masses are allowed. However, the precise value of the current constraint requires a new study. In the following results discussion, we thus consider leptoquark masses up to 3TeV and caution the reader that the SSM resonance search poses a constraint on the heaviest allowable leptoquark masses according to the study shown in Ref. [480].

5.2.11 Constraints on the Sterile Neutrino

The sterile neutrino n_4 as defined would be produced in the early Universe. The dominant decay modes are $n_4 \to \nu_\alpha f \bar{f}$ with $f = \nu_\beta, e^-, \mu^-$ for masses $m_4 \leq 1$ GeV. These decays are mediated by the Z boson and thus the decay rate depends quadratically on the $\nu_\alpha - n_4$ mixing matrix element $|U_{\alpha 4}|^2$. In the limit of vanishing final state lepton masses, the decay rate of $n_4 \to \nu_\alpha \bar{f} f$ is given by [276, 322, 344]

$$\Gamma(n_4 \to \nu_\alpha \bar{f} f) = \frac{G_F^2 m_4^5}{96\pi^3} |U_{\alpha 4}|^2 \ . \tag{5.52}$$

For $2m_\mu \geq m_4 \gg 2m_e$ the lifetime is given

$$\tau = \Gamma(n_4 \to \nu \bar{f} f)^{-1} = \frac{96\pi^3}{4G_F^2 m_4^5 \sum_\alpha |U_{\alpha 4}|^2} \simeq 0.04s \left(\frac{100\text{MeV}}{m_4}\right)^5 \left(\frac{10^{-5}}{\sum_\alpha |U_{\alpha 4}|^2}\right) . \tag{5.53}$$

Big bang nucleosynthesis (BBN) poses a constraint on the lifetime of n_4, since the abundances of the light elements agree well with the standard cosmological model. Thus in order to avoid any changes to the standard BBN, the sterile neutrino n_4 has to decay and its decay products thermalize, before BBN. If the lifetime of n_4 is shorter than $\tau < 0.1s$, this condition can be satisfied as it has been shown in Refs. [483, 484]. This translates into a bound

$$m_4 \gtrsim 87\,\text{MeV} \left(\frac{10^{-5}}{\sum_\alpha |U_{\alpha 4}|^2}\right)^{1/5} . \tag{5.54}$$

Similarly, sterile neutrinos can be produced in supernovae. The arguments of Ref. [483] imply that the duration of the SN 1987A neutrino burst excludes mixing angles $3 \times 10^{-8} < \sin^2 2\theta < 0.1$ for sterile neutrinos $m_4 \lesssim 100$MeV.

Finally, sterile neutrinos can be searched for at terrestrial experiments. In particular the fixed-target experiments NOMAD [485] and CHARM [486] placed limits on the mixing angle of sterile neutrinos with τ neutrinos, which further constrains the allowed parameter space, as discussed in Sec. 5.2.12.

Together this puts a lower bound on the sterile neutrino mass of $m_4 \geq 100$MeV.

5.2.12 Results

As the explanations for the $R_{K^{(*)}}$ and $R_{D^{(*)}}$ anomalies are mostly independent, we first discuss the explanation of $R_{K^{(*)}}$, which sets the scale of the $SU(4)_C \times SU(2)_L \times SU(2)_R$ symmetry breaking. As a second step, we present the favored region for the anomalies $R_{D^{(*)}}$, before finally discussing its predictions for the sterile neutrino n_4 in the process $b \to c\tau n_4$.

5.2.13 $R_{K^{(*)}}$

We follow our previous analysis [6] and identify the favored region of parameter space for the model using the `flavio` package [430] and tree-level analytical estimations where appropriate. The 1σ (90% C.L.) favored parameter region is defined by the values of the vector leptoquark mass $m_{W'}$ and the quark-SM lepton mixing angle θ [see Eq. (5.37) for its definition] which satisfy $R_K = 0.846^{+0.062}_{-0.056}$ ($R_K = 0.846^{+0.102}_{-0.091}$), $R_{K^*} = 0.685^{+0.122}_{-0.083}$ ($R_{K^*} = 0.685^{+0.201}_{-0.137}$) and also satisfy the current 90% C.L. experimental limits $BR(B^+ \to K^+\mu^- e^+) < 7 \times 10^{-9}$ and $BR(B^+ \to K^+ e^- \mu^+) < 6.4 \times 10^{-9}$ [75]. Other processes currently do not constrain the parameter region as we discussed in Ref. [6].

Figure 5.5 shows the favored region of parameter space in the $m_{W'}$ leptoquark mass versus the θ mixing angle plane. Compared to Ref. [6] the mass of W' is larger, because the experimentally observed value of R_K has since moved closer to the SM prediction with smaller error bars and therefore the 1σ region is smaller. The favored range of θ is approximately between $[-\frac{\pi}{2}, 0]$ or $[\frac{\pi}{2}, \pi]$ and $m_{W'}$ between $[20, 31]$TeV . The identical nature of the two adjacent regions can be understood from the invariance

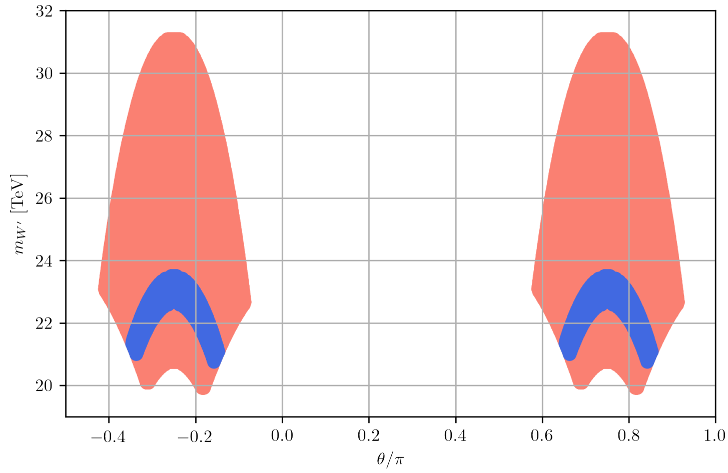

FIGURE 5.5: The favored parameter regions compatible with the current experimental limits from $B^+ \to K^+\mu^-e^+$, $B^+ \to K^+e^-\mu^+$. Shown are the 1σ (blue) and 90% confidence level (red) bands suggested by the measured R_K and R_{K^*} ratios.

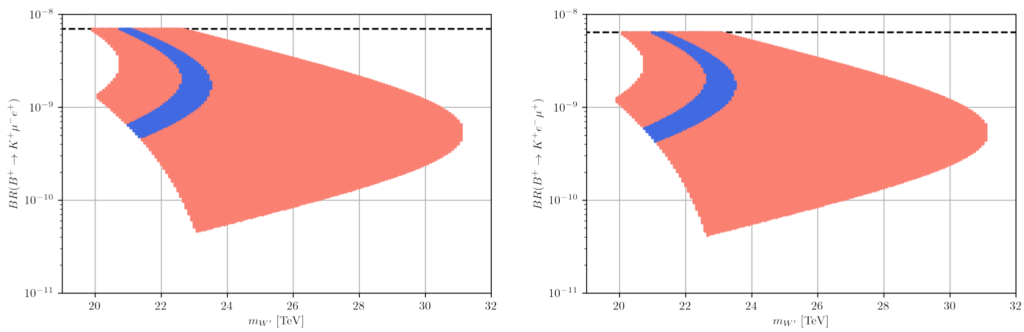

FIGURE 5.6: Expectation for $BR(B^+ \to K^+\mu^-e^+)$ (left) and $BR(B^+ \to K^+e^-\mu^+)$ (right) for the favored parameter region identified in Figure 5.5. The black dashed lines correspond to the current experimental 90% confidence-level upper bounds on these branching fractions.

of the relevant branching ratios under the transformation $\theta \to \theta + \pi$. The constraints from $B \to Ke^\pm\mu^\mp$ lead to the wedge-shape form at the bottom of each favored region.

Figure 5.6 shows the predicted range for the branching ratios of the lepton-flavor-violating rare decays $B^+ \to K^+\mu^-e^+$ and $B^+ \to K^+e^-\mu^+$ processes. The two processes probe different ranges of θ values and are thus complementary: While $B^+ \to K^+\mu^-e^+$ is sensitive to $\sin^2\theta \approx 1$, $B^+ \to K^+\mu^+e^-$ is sensitive to $\cos^2\theta \approx 1$. LHCb is expected to further improve its sensitivity and to probe the two branching ratios of $B^+ \to K^+e^\pm\mu^\mp$ at the level of 10^{-9} [431].

In addition to further improvements to $B^+ \to K^+\mu^\pm e^\mp$ this leptoquark contributes to lepton-flavor-violating rare tau lepton decays such as $\tau \to K_s\ell$, $\ell = e, \mu$ and the leptonic B_s decays $B_s \to \ell^-\ell'^+$, $\ell, \ell' = e, \mu$ as shown in Ref. [6]. However, the additional contributions are below the current experimental sensitivity and thus we do not show these predictions for the sake of brevity and refer the interested reader to Ref. [6] for further details.

5.2.14 $R_{D^{(*)}}$

Using Eq. (5.45) along with the 1σ and 90% C.L. $R_{D^{(*)}}$ constraints on the Wilson coefficient $C_{VR}^{cb\tau 4}$ we may derive the allowable parameter region for the model which satisfies the anomalies. We restrict ourselves to placing bounds on the 1σ and 90% C.L. $R_{D^{(*)}}$ region. Choosing the minimal Yukawa texture described in Sec. 5.2.2 for Y_3 and Y_4 constrains the parameter region in $Y_{c\tau}$, $Y_{t\mu}$, y_3 and $m_{\tilde{\chi}}$ space.

We limit $Y_{ue} \simeq 0.1$ for our parameter scans to ensure that the lightest flavor exotic charged lepton E mass is larger than $\simeq$ TeV for scales larger than $w \simeq 10$TeV, and this coupling does not affect the neutrino states S and N_μ that participate in the anomaly and is therefore not important in constraining the model's allowable region. The Yukawa couplings of interest must also satisfy perturbativity requirements such that $0 \leq Y_{c\tau} \leq 4\pi$, $0 \leq Y_{t\mu} \leq 4\pi$ while $-4\pi \leq y_3 \leq 0$ in order to obtain Wilson coefficient $C_{VR}^{cb\tau 4}$ with the correct sign. The vev $w = 26.7$TeV was chosen for our parameter scans as this is a favoured central value for the $m_{W'} \simeq 23$TeV gauge boson mass scale which explains the $R_{K^{(*)}}$ anomalies. This fixes the lightest exotic vectorlike lepton mass to $Y_{ue}w \simeq 2.7$TeV which easily evades the LEP constraints for heavy charged leptons [75].

We also set $m_S = 2m_\mu$ as this acts as an upper bound on the fourth neutrino mass participating in $b \to c\tau\nu$. This value is chosen because it ensures that the sterile neutrino n_4 decays before BBN. The analytical approximation for the mixing angles U_{S4} and $U_{N_\mu 4}$ in Eq. (5.44) and subsequently Eq. (5.45) is respected as well as ensuring that the new neutrino mass is light enough that it does not introduce too much phase space suppression in the decay $b \to c\tau n_4$. Consequently in our parameter scan we find the fourth neutrino mass to be lighter than the $2m_\mu$, but heavier than 100MeV after imposing all constraints, which ensures that it is still significantly heavier than the active neutrinos but sufficiently lighter than the B meson. The parameter ranges of the relevant new physics parameters detailed above are summarized in Table 5.5 for convenience.

Parameter	Value
u_1	0
v_{12}	0
$u_2^2 + v_{21}^2$	$1/(2\sqrt{2}G_F) \simeq (174\text{GeV})^2$
w	26.7TeV
$m_{\tilde{\chi}}$	$[0.8, 3]$TeV
m_S	$2m_\mu$
y_3	$[-4\pi, 0]$
$Y_{ue}, Y_{c\tau}, Y_{t\mu}$	0.1, $[0, 4\pi]$, $[0, 4\pi]$

TABLE 5.5: Parameter ranges for the new physics model parameters used in the numerical scans.

We also ensure that the leptonic mixing parameters and the neutrino mass squared differences satisfy the 3σ ranges from the latest global fit by the NuFIT collaboration [350]: $0.275 \leq \sin^2\theta_{12} \leq 0.350$, $0.427 \leq \sin^2\theta_{23} \leq 0.609$, $0.02046 \leq \sin^2\theta_{13} \leq 0.02440$ and the solar and atmospheric mass squared differences $6.79 \leq \frac{\Delta m_{21}^2}{10^{-5}eV^2} \leq 8.01$, $2.432 \leq \frac{\Delta m_{3\ell}^2}{10^{-3}eV^2} \leq 2.618$. We also impose the 3σ unitarity deviation bound derived

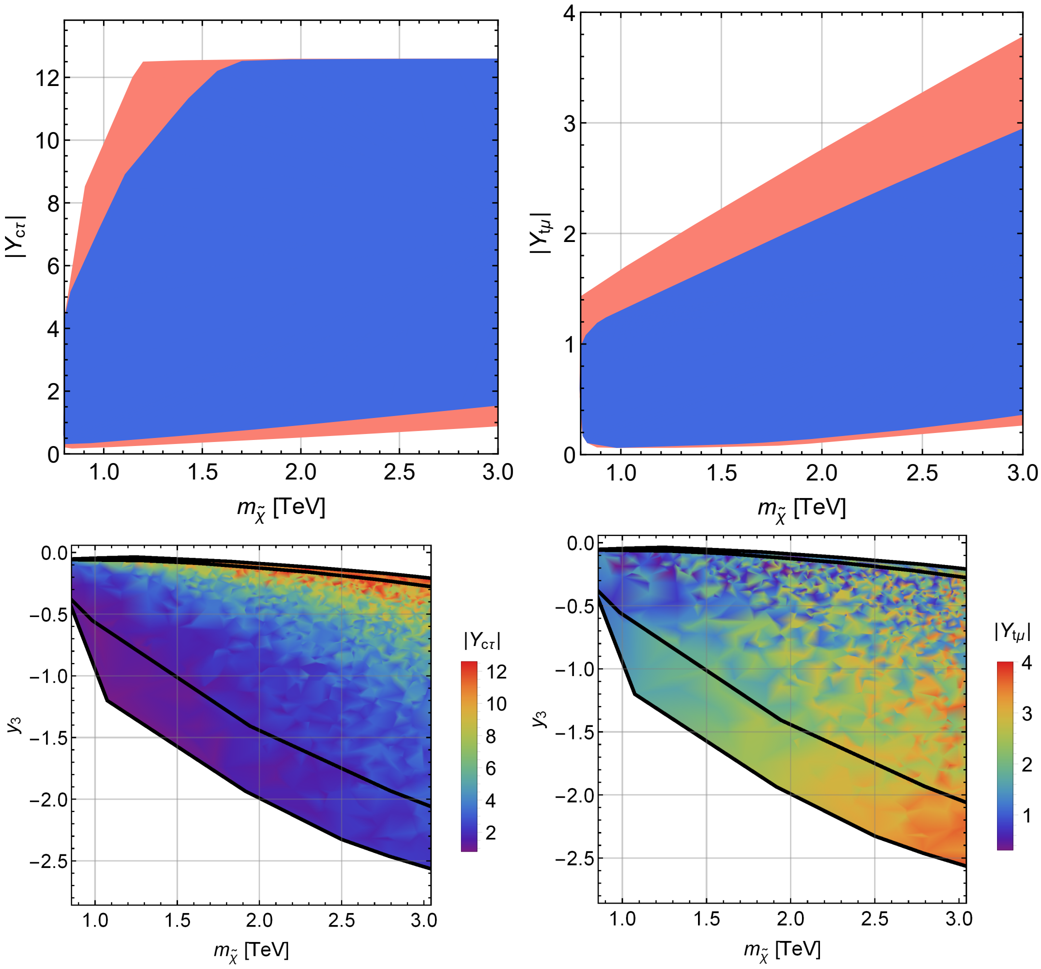

FIGURE 5.7: The top two panels show the allowable $R_{D^{(*)}}$ 1σ (blue) and 90% confidence level (red) parameter regions for the Yukawa couplings $Y_{c\tau}$ (top left) and $Y_{t\mu}$ (top right). The parameter region is displayed over the $0.8 \leq m_{\tilde{\chi}} \leq 3$ TeV range, which is of immediate interest in current and future TeV scale collider searches. The Yukawa couplings are also restricted to be $\leq 4\pi$ to remain in the perturbative regime. The $Z \to \mu\mu$ 1σ and 90% confidence new physics coupling correction $\delta g_{\mu R}$ constraints also enforce an important upper cutoff on $Y_{t\mu}$ as seen in the right-hand side allowable regions. In the lower panels we show density plots which are a result of our numerical scan with the additional BBN constraint shown in Eq. (5.54) and the SN 1987A [483, 484] and CHARM [486] neutrino mixing constraints, where y_3 is a function of $m_{\tilde{\chi}}$, $Y_{c\tau}$ (bottom left) and $Y_{t\mu}$ (bottom right). The region contained within the inner and outer black boundaries corresponds to the 1σ and 90% confidence level regions respectively. Note that the sharp edges and color discontinuities are due to limitations in numerical sampling and not physical effects.

from $|2\eta_{\alpha\beta}|$ as shown in Ref. [487] on $|UU^\dagger|$. The allowed regions are then constrained by the combination of Yukawa coupling ranges in conjunction with the $Z \to \mu\mu$ constraint in Eq. (5.49) and the $C_{VR}^{cb\tau 4}$ constraint in Eq. (5.45), which can be easily plotted analytically along with the perturbative boundaries.

Figure 5.7 shows the viable parameter ranges for the Yukawa couplings $Y_{c\tau}$, $Y_{t\mu}$, and y_3 as a function of the leptoquark mass $m_{\tilde{\chi}}$. We find that for small $Y_{t\mu}$ we require large $Y_{c\tau}$ and vice versa which is what we expect from inspecting Eq. (5.45). It should be noted that more complicated Yukawa textures for Y_4 and Y_3 are indeed permissible as mentioned earlier. But our selection is motivated by maintaining simplicity and reducing the number of free parameters in the theory. If the $R_{D^{(*)}}$ anomalies persist and new stronger constraints become available reducing the parameter space of this chosen texture, other more elaborate ones can indeed be explored.

5.2.15 Prediction for Neutrino Mixing and Mass of n_4

We may additionally predict the mixing of the fourth neutrino mass eigenstate n_4 with the active neutrinos. In our numerical scan we find that the mixing matrix elements U_{e4} and $U_{\mu 4}$ are negligibly small, $|U_{e4}|^2 \lesssim 10^{-11}$ and $|U_{\mu 4}|^2 \lesssim 10^{-10}$, due to y_3 being the only nonzero element in the chosen texture for Y_3. In Figure 5.8 we show the allowable region of parameter space as a function of $|U_{\tau 4}|^2$ vs the sterile neutrino mass m_4. The BBN constraint from Eq. (5.54) results in a lower bound on the mixing matrix element $|U_{\tau 4}|^2$ as a function of the sterile neutrino mass. The duration of the neutrino burst of SN 1987A imposes a lower bound on the sterile neutrino mass $m_4 \geq 100$MeV and thus we only show sterile neutrino masses heavier than 100MeV.

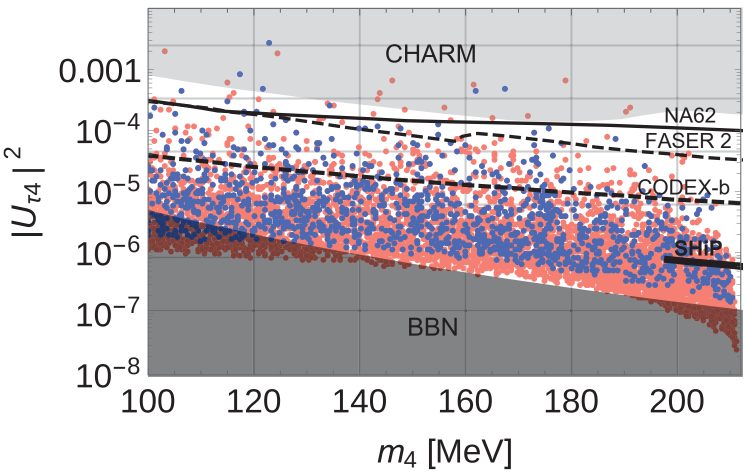

FIGURE 5.8: Prediction for the mixing between the fourth neutrino mass eigenstate n_4 participating in the $R_{D^{(*)}}$ anomalies with the dominant active neutrino flavor τ as a function of its mass m_4. The blue and red regions correspond to the 1σ and 90% confidence level regions respectively while the bottom black shaded region corresponds to the BBN exclusion bound shown in Eq. (5.54) and the top bound shown in gray comes from the CHARM experiment. The lines show projected upper bounds for the NA62 (black), FASER 2 (dashed black), CODEX-b (thick dashed black) and SHiP (thick black) experiments from top to bottom respectively.

In this study, we focus on light sterile neutrino masses satisfying $m_4 \leq 2m_\mu$, because the contribution to $R_{D^{(*)}}$ is phase space suppressed for a heavy sterile neutrino n_4. Indeed larger neutrino masses could still be kinematically accessible and interesting to study in the light of the MiniBooNE excess as proposed in Ref. [488]. However we do not analyze such cases in this work. There are additional constraints coming from the NOMAD [485] and CHARM [486] fixed-target experiments, the stronger of which comes from the CHARM experiment which we also show in Figure 5.8. It is also of interest to compare the projected experimental sensitivities for n_4, i.e. a sterile neutrino which almost exclusively mixes with ν_τ, with proposals of future experiments including NA62 [489], FASER [490], CODEX-b [491] and SHiP [492]. The contours have been extracted from Ref. [493]. We note that the SHiP contour only starts at around $m_4 \simeq 191$MeV coinciding with the mass splitting between the $D_s^\pm$ meson mother and tau lepton daughter.

5.2.16 Conclusion

We have proposed a chiral Pati-Salam theory with gauge group $SU(4)_C \times SU(2)_L \times SU(2)_R$ which is capable of explaining the $R_{D^{(*)}}$ anomalies with new scalar leptoquarks and the R_{K^*} anomalies via $SU(4)$ gauge boson leptoquarks. The model is consistent with experimental constraints, including the fermion mass spectrum, modifications to leptonic Z-boson decays via the new scalar leptoquark, $B \to K\nu\bar{\nu}$ as well as the best available LHC constraints for single and pair production searches of leptoquarks at the LHC and other new particles. New physics coming from the gauge sector via a spectrum of colored leptoquarks with charge $\frac{2}{3}e$ also satisfies the best available constraints from lepton number violating searches such as $B^+ \to K^+\mu^\mp e^\pm$. These gauge bosons couple in a chiral manner to the familiar quarks and leptons and interfere with standard model weak processes.

Both the scalar and massive vector leptoquarks originate from one scalar multiplet χ which breaks the Pati-Salam group to the SM group, $SU(4)_C \times SU(2)_R \to SU(3)_C \times U(1)_Y$, at a scale of $\langle\chi_{41}\rangle \equiv w \gtrsim 20$TeV. As already discussed in Ref. [6] the explanation of the $b \to s\ell\ell$ anomalies originates from an equal and opposite tree-level correction to muons and electrons and thus can be tested at the LHCb and Belle II experiments by measuring both lepton flavor-conserving and lepton flavor-violating processes $b \to s\ell\ell'$ and similarly $B_s \to \ell\ell'$, when increased statistics become available. The $R_{D^{(*)}}$ anomalies can be explained using a simple Yukawa texture with only three free parameters, although more complex Yukawa structures are also feasible. There is an intricate relation between the lepton mass spectrum, particularly neutrino mass spectrum, and the $R_{D^{(*)}}$ anomalies. One of the striking signatures is a light sterile neutrino with dominant mixing with tau neutrinos. We constrain the model parameter space using the strong bounds on active-sterile neutrino mixing from big bang nucleosynthesis in conjunction with the supernova SN 1987A and CHARM experiments. Additionally, we make predictions for the sterile neutrino properties which can be probed in future searches such as the proposed NA62, FASER, CODEX-b and SHiP experiments.

Chapter 6

Conclusion

In this thesis we have explored solutions to some of the most pertinent problems in particle physics. We have paid particular attention to resolving fundamental questions, with emphasis on searches for new Higgs bosons, phase transitions in the early universe, new sources of CP violation, explanations for neutrino mass, mechanisms for matter-antimatter asymmetry, hitherto unexplored electromagnetic properties of fermions and finally, violation of flavour universality in the lepton sector.

In Chapter 2 [1], we outlined our search for one the most popular classes of extended Higgs theory, the Two-Higgs-Doublet model. We presented a search for a heavy CP odd Higgs boson, A, decaying to another heavy CP even Higgs boson, H, and a Z boson, which subsequently decay to $\ell\ell bb$ and $\ell\ell WW$ ($\ell\ell qqqq$) final states. We showed results for data recorded by the ATLAS experiment at the LHC, corresponding to an integrated luminosity of 139 fb^{-1} from proton–proton collisions at a centre-of-mass energy 13TeV. The A boson was assumed to be produced via either gluon–gluon fusion or b-associated production. In the $\ell\ell WW$ channel, only gluon–gluon fusion production was considered. No significant deviation from the SM background predictions was observed in any of the channels considered in this search. Considering each channel and each production process separately, upper limits are set at the 95% confidence level for $\sigma \times B(A \to ZH) \times B(H \to bb$ or $H \to WW)$. For $\ell\ell bb$, upper limits were set in the range 6.2–380 fb for gluon–gluon fusion and 6.8–210 fb for b-associated production of a narrow A boson in the mass range 230–800 GeV, assuming the H boson was in the mass range 130–700 GeV. For $\ell\ell WW$, the observed upper limits were in the range 0.023–8.9 pb for gluon–gluon fusion production of a narrow A boson in the mass range 300–800 GeV, assuming the H boson was in the mass range 200–700 GeV. Taking into account both production processes, the $\ell\ell bb$ search tightened the constraints on the 2HDM scenario in the case of large mass splittings between its heavier neutral Higgs bosons. The $\ell\ell WW$ channel was not previously explored at the LHC, and this search explicitly demonstrates its potential to constrain 2HDM parameters away from the weak decoupling limit.

In Chapter 3 [2], we explored first–order cosmological phase transitions, similar to the ones that arise from the scalar sector outlined in Chapter 2. This is an important area of study since the asymptotic velocity of expanding bubbles is of crucial relevance for predicting observables like the spectrum of stochastic gravitational waves, or for establishing the viability of mechanisms explaining fundamental properties of the universe such as the observed baryon asymmetry. In these dynamic phase transitions, it was generally accepted that subluminal bubble expansion requires out-of-equilibrium interactions with the plasma which are captured by friction terms in the equations of motion for the scalar field. This has been disputed in works pointing out subluminal velocities in local equilibrium arising either from hydrodynamic effects in transitions of deflagration type or from the entropy change across the bubble wall in general situations. In this chapter, we explored both effects and their relations which can be understood from the conservation of the entropy of the degrees of freedom in local equilibrium. This naturally lead to subluminal speeds for both deflagration and detonation type transitions. The friction effects arising from the background field dependence of the entropy density in the plasma were studied and accounted for considering local conservation of stress-energy and including field dependent thermal contributions to the effective potential. Furthermore, we illustrated these effects with explicit calculations of dynamic and static bubbles for a first–order electroweak transition in a SM extension with additional scalar fields. The results were compared with recent analysis linking friction forces in local equilibrium with entropy changes across the bubble. We outlined novel corrections from the temperature and velocity gradients.

In Chapter 4 , we explored novel sources of CP violation and potential signals of new physics. The radiative decay of charged and neutral fermions has been studied for decades but we focused on CP violation in such processes explicitly. CP violation in the radiative decay of neutral leptons such as neutrinos can produce an net polarisation asymmetry for the radiated light and produces an important source of net circular polarisation in particle and astroparticle physics observables.

In Section 4.1 [3], we built a general framework for CP violation in neutrino radiative decays. CP violation in such processes produces an asymmetry between the circularly polarised radiated photons and provides an important source of net circular polarisation that can be observed in particle and astroparticle physics experiments. The formulation between CP violation in neutrino radiative decays and the neutrino electromagnetic dipole moment at the form factor level was developed for both Dirac and Majorana neutrinos. We observed a model independent connection between the decays and photon circular polarisation produced by these processes and concluded that CP violation directly determines the circular polarisation. Specifically in the case of Majorana neutrino, the CP asymmetry is identical to the asymmetry of photon polarisations up to an overall sign difference. The contribution of a nonzero electric charge to neutrino decays is also discussed for completeness.

We subsequently showed how to generate non-vanishing CP violation through a generic new physics Yukawa interaction extension consisting of electrically charged scalar and fermion states. Without adding any new source of electric charge for the neutrinos, these particles can decay only via the electromagnetic transition dipole moment. The explicit analytical result of CP violation for this model was derived and presented. This result is applicable when computing polarisation observables for both Dirac and Majorana fermions and can be directly used in any models that generate radiative decays of this type.

We also included some brief discussion pertaining to the phenomenological implications for neutrinos at different mass scales. We, applied the formalism to keV sterile neutrinos which are popular DM candidates and found CP violation and circular polarisation of the resulting radiated X-rays. We also considered the implications for much heavier sterile neutrinos of scale $\gtrsim 1$TeV which are required for the seesaw mechanism and leptogenesis. We argued that the CP source in the Yukawa coupling, which is essential for leptogenesis, can trigger CP violation for heavy neutrino radiative decays. The case of weakly interacting sterile neutrinos at a mass comparable to the electroweak scale is also interesting as it could produce exotic collider signatures as well as circular polarisation. We also discussed the circular polarisation of γ-rays released from the radiative decay of the PeV scale dark matter motivated by IceCube data, however we conclude that the size of this effect is too small to observe at current experiments.

In Section 4.2 [4], we studied CP violation in the neutrino electromagnetic dipole moment. A full one-loop calculation of the transition dipole moment in particular was performed in the context of the Standard Model with an arbitrary number of right-handed singlet neutrinos. The CP asymmetry was analytically derived in terms of the leptonic mixing matrix accounting for heavy neutrino mass eigenstates. A detailed explanation of how to generate a non-vanishing CP asymmetry in the neutrino transition dipole moment was provided. This requires a threshold condition for the initial neutrino mass being larger than the sum of W boson mass and the charged leptons running in the loop and a CP violating phase in the lepton flavour mixing matrix. The threshold condition is necessary to generate a non-zero imaginary part for the loop function. An analytical formulation of this loop integral imaginary component was derived. The lepton flavour mixing for vertex contributions was parametrised in terms of Jarlskog-like parameters. For Majorana particles, the CP asymmetry is identical to the asymmetry of circularly-polarised photons released from the radiative decay.

We then applied the formulation to a minimal seesaw model where two right-handed neutrinos N_1 and N_2 were introduced with mass ordering $M_1 < M_2$. A complete study of CP asymmetry in all radiative decay channels was performed, where the mass range $0.1\text{TeV} < M_2 < 10\text{TeV}$ was considered. The CP asymmetry in $N_{1,2} \to \nu\gamma$ was found to be very small, maximally reaching 10^{-17}. However, in the $N_2 \to N_1\gamma$ channel, the CP asymmetry was significantly enhanced, with Δ_{CP} achieving 10^{-5}-10^{-3}, even with the Dirac phase δ being the only source of CP violation. There is a significant correlation between the CP violation in radiative decay and that coming from oscillation experiments. Additionally, we performed a parameter scan of the CP asymmetry with oscillation data in 3σ ranges taken as inputs and found that the CP asymmetry can maximally reach order one which is phenomenologically very interesting.

In Section 4.3 [5], we explored fundamental properties of the top quark through the CP properties of its flavour violating decays. The rare radiative flavour changing top decays $t \to c\gamma$ and $t \to cg$ (and the even rarer $t \to u\gamma$ and $t \to ug$) have been processes of interest for decades as they offer a key probe for studying top quark properties. However an explicit analytical study of the branching ratios and CP asymmetries resulting from these loop level processes had thus far evaded attention. In this section, we provided the formulation for the CP asymmetry resulting from the total kinetic contribution of the loop integrals and their imaginary parts, as well as an updated numerical computation of the predicted SM branching fractions. These rare processes are suppressed in the SM by the GIM mechanism. The results presented here can easily be exported for use in minimal extensions of the SM including vector-like quarks or in 2HDMs such as the one described in Chapter 2, where radiative fermionic decay processes can be enhanced relative to the SM by several orders of magnitude. Such processes provide an experimentally clean signature for new fundamental physics and can potentially be tested by current collider experiments. These topical beyond the SM theories are an elegant means to provide improved global fits to the latest results emerging from flavour physics, Cabibbo–Kobayashi–Maskawa matrix and precision electroweak measurements.

In Chapter 5, we studied the B physics anomalies which suggest a strong hint in favour of violation of lepton flavour universality and possible beyond the SM explanations. We first discuss a variant of the famous unified Pati-Salam model, with gauge group $SU(4)_C \times SU(2)_L \times U(1)_{Y'}$ in Section 5.1 [6], wherein chiral left–handed quarks and leptons are unified into a $\underline{4}$ of $SU(4)_C$, while the right–handed quarks and leptons have quite a distinct treatment. The model introduces particles that couple to both quarks and leptons called leptoquarks.

The model features $SU(4)$ symmetry breaking via the introduction of a $SU(4)$ scalar multiplet χ with a vev $w \gtrsim 10$TeV and electroweak symmetry breaking via scalars ϕ and Δ with vevs that satisfy $\sqrt{v^2 + u^2} \simeq 174$ GeV. In addition to new scalar particles, the model contains new charged $(\frac{2}{3}e)$ W' and neutral Z' gauge bosons along with heavy exotic charged $E^-_{L,R}$ and neutral $N_{L,R}$ fermions. The charged leptoquark gauge bosons W' couple in a chiral manner to the familiar quarks and leptons and can thereby interfere with SM weak processes. The theory makes predictions for $B^+ \to K^+\mu^-e^+$, $B^+ \to K^+e^-\mu^+$, $\tau \to K_s\ell$, $B_s \to \mu^-\mu^+$, as well as the highly suppressed $B_s \to \mu^-e^+$ and $B_s \to e^-\mu^+$ processes. For instance, for the leptonic $B_s \to \mu^-\mu^+$ decay channel the rate is predicted to satisfy: $\Gamma(B_s \to \mu^-\mu^+)/\Gamma_{SM}(B_s \to \mu^-\mu^+) = (1+R_K)/2$. The leptoquark gauge boson phenomenology of the chiral $SU(4)$ Pati-Salam model considered will be relevant for more general chiral $SU(4)$ models.

In Section 5.2 [7] we proposed a similar Pati-Salam theory as in Section 5.1 with gauge group $SU(4)_C \times SU(2)_L \times SU(2)_R$ which explain the $R_{D^{(*)}}$ anomalies with new scalar leptoquarks and the R_{K^*} anomalies with the same $SU(4)$ gauge boson leptoquarks. The model satisfies all available experimental constraints, including the fermion mass spectrum, modifications to leptonic Z boson decays via the new scalar leptoquark, $B \to K\nu\bar{\nu}$ as well as LHC constraints for single and pair production searches of leptoquarks at the LHC and other new particles. Beyond the SM physics coming from the gauge sector via a spectrum of coloured leptoquarks with charge $\frac{2}{3}e$ also satisfies the best available constraints from lepton number violating searches such as $B^+ \to K^+\mu^\mp e^\pm$.

Both the massive scalar and vector leptoquarks originate from one scalar multiplet χ which breaks the Pati-Salam group to the SM group, $SU(4)_C \times SU(2)_R \to SU(3)_C \times U(1)_Y$, at a scale of $\langle\chi_{41}\rangle \equiv w \gtrsim 20$TeV. As already discussed in Chapter 5.1, the explanation of the $b \to s\ell\ell$ anomalies originates from an equal and opposite tree-level correction to muons and electrons and can therefore be tested at the LHCb and Belle II experiments by measuring both lepton flavor-conserving and lepton flavor-violating processes $b \to s\ell\ell'$ and similarly $B_s \to \ell\ell'$, when increased statistics become available. The $R_{D^{(*)}}$ anomalies were explained using a simple Yukawa texture with only three free parameters, although more complex Yukawa structures are also permissible. We found an intricate relation between the lepton mass spectrum, particularly neutrino mass spectrum, and the $R_{D^{(*)}}$ anomalies. One of the noteworthy predictions of the model is a light sterile neutrino with dominant mixing to tau neutrinos. The model parameter space was constrained using the strong bounds on active-sterile neutrino mixing from big bang nucleosynthesis in conjunction with the supernova SN 1987A and CHARM experiments. Additionally, we made several predictions for the sterile neutrino properties which can be probed in future searches such as the proposed NA62, FASER, CODEX-b and SHiP experiments.

In conclusion, this doctoral thesis has presented new findings for a set of fundamental problems facing the field of particle physics. These include the potential existence of extended scalar sectors including direct searches for new Higgs particles at the CERN ATLAS experiment as well as intricate calculations of phase transitions that could arise from these beyond the SM potentials. We also studied the theoretical and phenomenological implications of CP violation, which we have explored in the context of heavy neutrinos and other fermions such as the top quark. Finally, we developed two unified field theories that could explain the strongest experimental anomalies in the flavour sector.

Appendix A

Auxiliary Material for Chapter 2

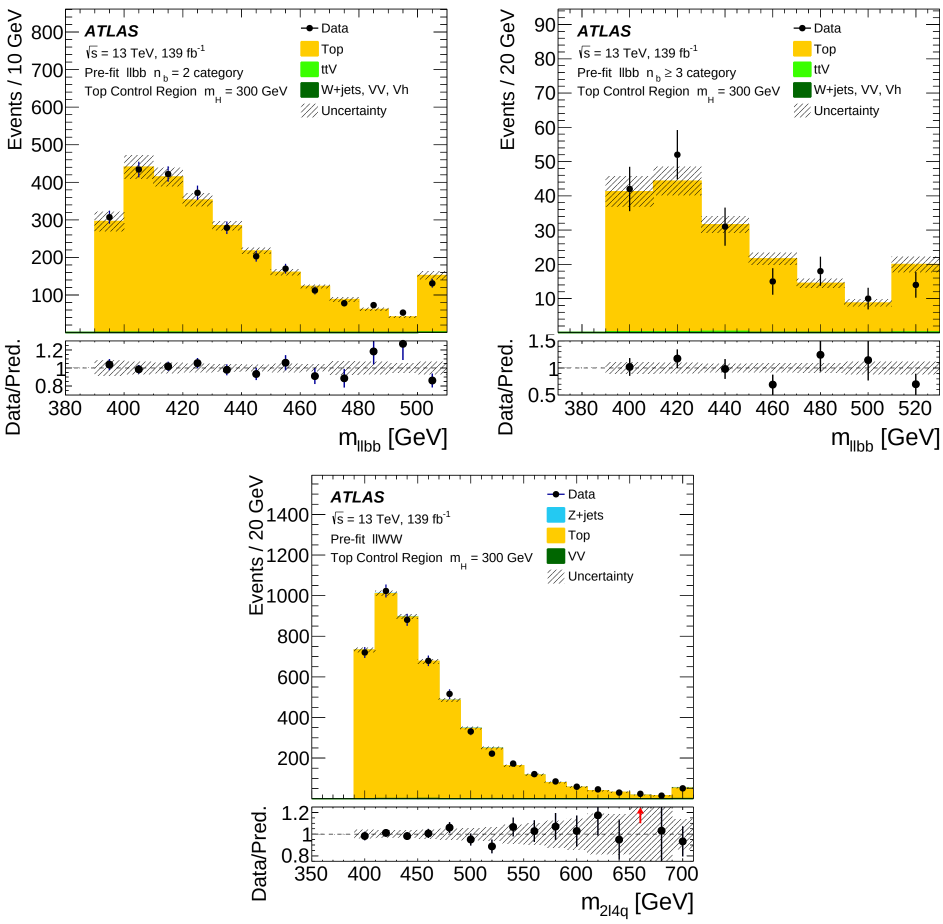

FIGURE A.1: The reconstructed A boson mass distributions for the top-quark control region for the m_{bb} and m_{4q} windows centred at $m_H = 300$ GeV for (a) $\ell\ell bb$ channel, $n_b = 2$ category, (b) $\ell\ell bb$ channel, $n_b \geq 3$ category, and (c) $\ell\ell WW$ channel. The plots are before the fit that is used to extract the signal. The number of events in the top-quark pair production simulated sample is normalized to the number of the observed data events in the control region. Overflows are included in the last bin of the distributions.

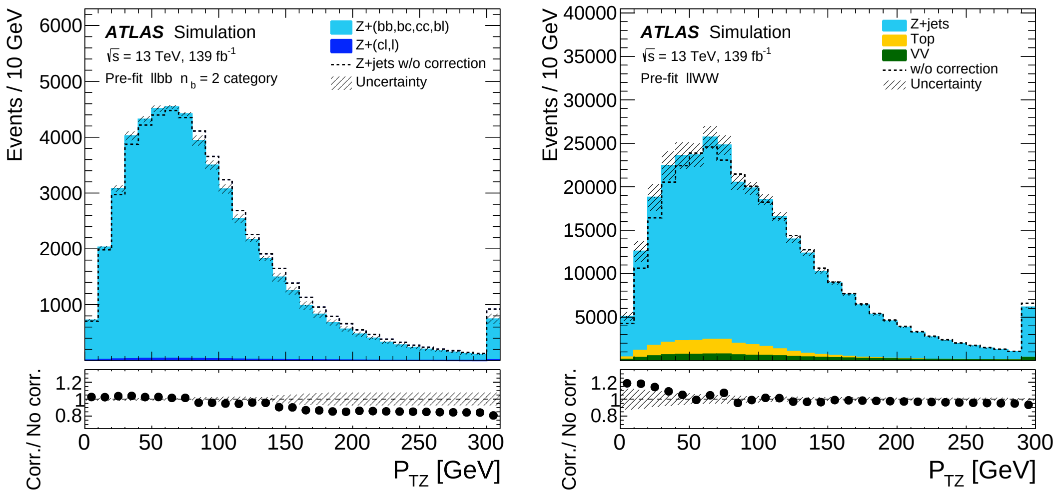

FIGURE A.2: The p_{TZ} distributions in simulation with and without correction in (a) $\ell\ell bb$ channel, $n_b = 2$ category, and (b) $\ell\ell WW$ channel. The distributions are for events that pass all the selection criteria with the exception of the m_{bb} or m_{4q} mass window requirements. Only simulated samples for which the correction is applied to are shown. The plots are before the fit that is used to extract the signal. The uncertainty shown in the plots refer to the uncertainty of the p_{TZ} correction and the uncertainty due to the limited number of events in the simulated samples. Overflows are included in the last bin of the distributions.

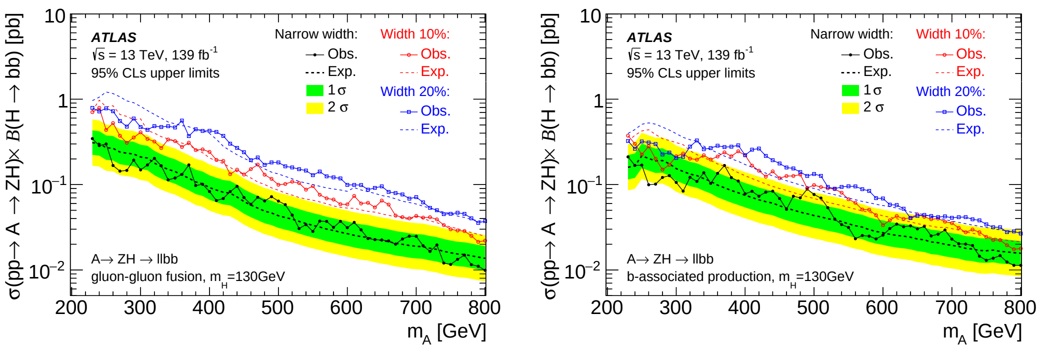

FIGURE A.3: Observed and expected upper limits at 95% CL on the production cross section times the branching ratio $B(A \to ZH) \times B(H \to bb)$ in pb as a function of m_A for a fixed choice of $m_H = 130$ GeV. The upper limits are shown for an A boson with narrow width with respect to the experimental mass resolution, and for a natural width of 10% and 20% with respect with its mass. The plots refer to an A boson produced via (a) gluon–gluon fusion and (b) b-associated production.

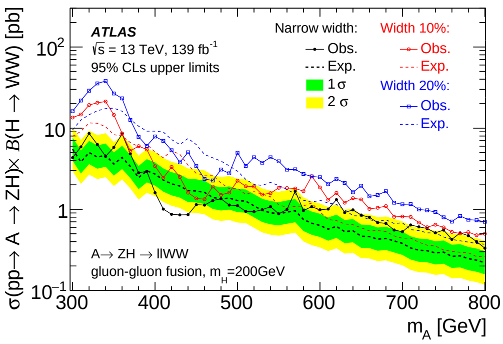

FIGURE A.4: Observed and expected upper limits at 95% CL on the production cross section times the branching ratio $B(A \to ZH) \times B(H \to WW)$ in pb as a function of m_A for a fixed choice of $m_H = 200$ GeV. The upper limits are shown for an A boson with narrow width with respect to the experimental mass resolution, and for a natural width of 10% and 20% with respect with its mass. The A boson is produced via gluon–gluon fusion.

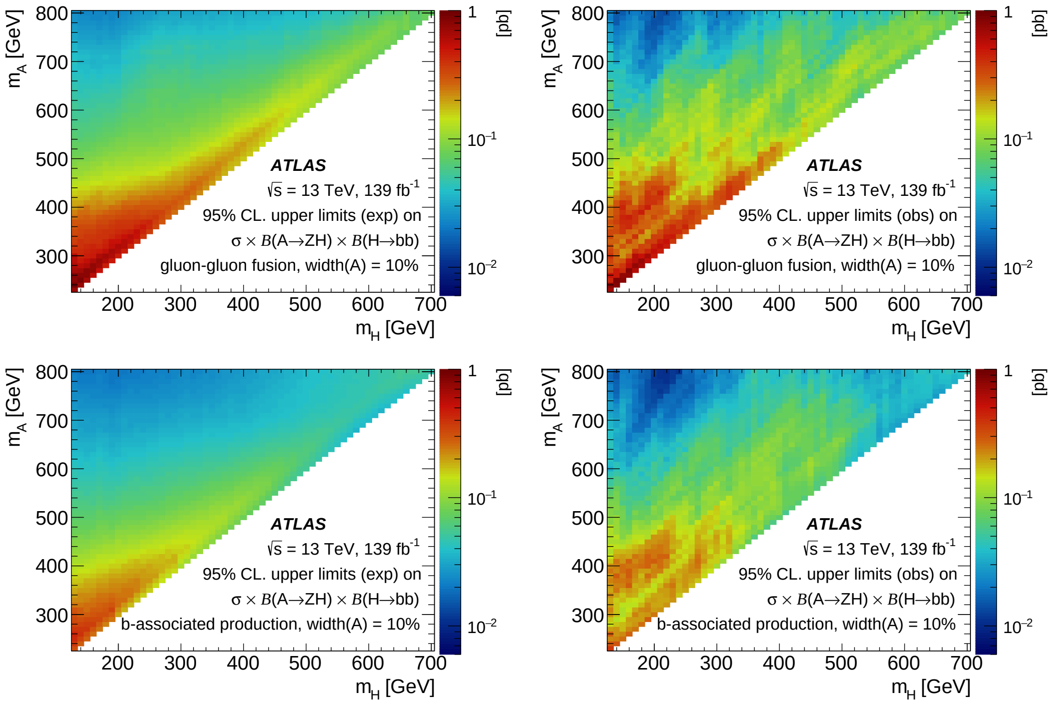

FIGURE A.5: Upper bounds at 95% CL on the production cross section times the branching ratio $B(A \to ZH) \times B(H \to bb)$ in pb for an A boson with natural width that is 10% with respect to its mass. The plots refer to an A boson produced via (a, b) gluon–gluon fusion and (c, d) b-associated production. The expected upper limits are shown in (a) and (c) and the observed upper limits are shown in (b) and (d).

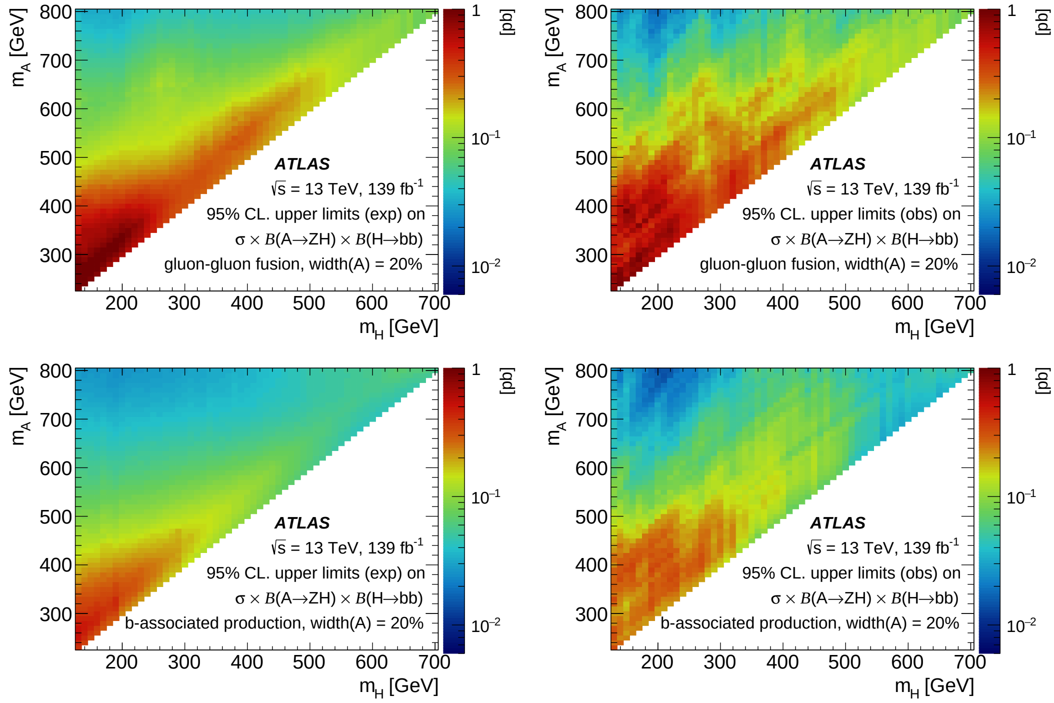

FIGURE A.6: Upper bounds at 95% CL on the production cross section times the branching ratio $\mathcal{B}(A \to ZH) \times \mathcal{B}(H \to bb)$ in pb for an A boson with natural width that is 20% with respect to its mass. The plots refer to an A boson produced via (a, b) gluon–gluon fusion and (c, d) b-associated production. The expected upper limits are shown in (a) and (c) and the observed upper limits are shown in (b) and (d).

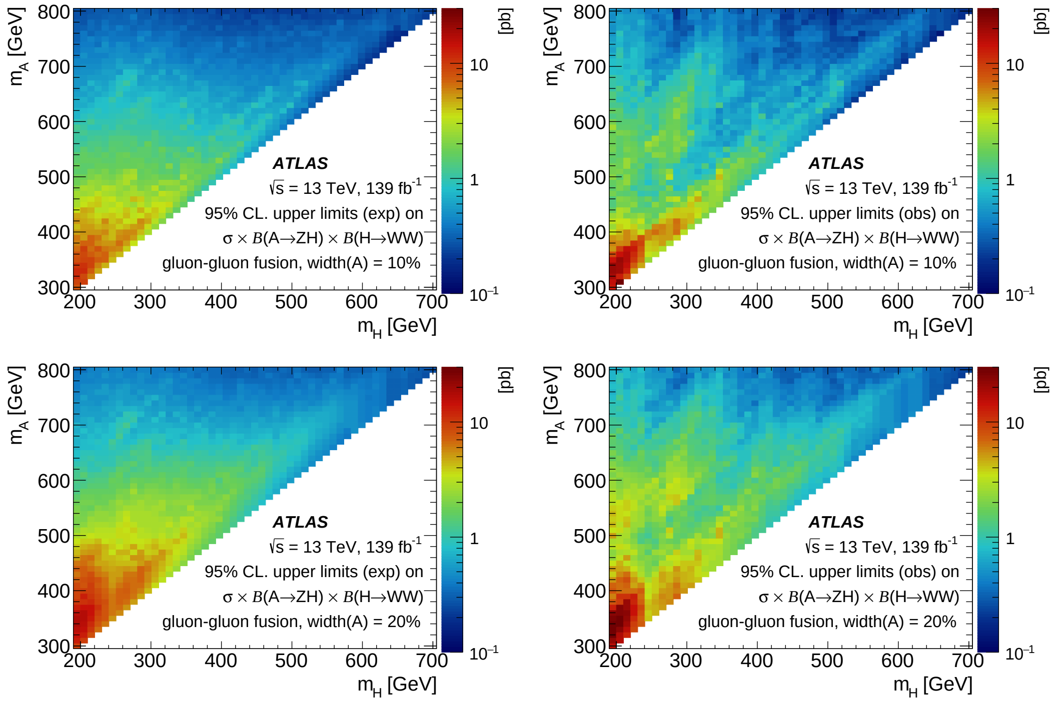

FIGURE A.7: Upper bounds at 95% CL on the production cross section times the branching ratio $B(A \to ZH) \times B(H \to WW)$ in pb for a gluon–gluon fusion produced A boson with natural width that is (a, b) 10% and (c, d) 20% with respect to its mass. The expected upper limits are shown in (a) and (c) and the observed upper limits are shown in (b) and (d).

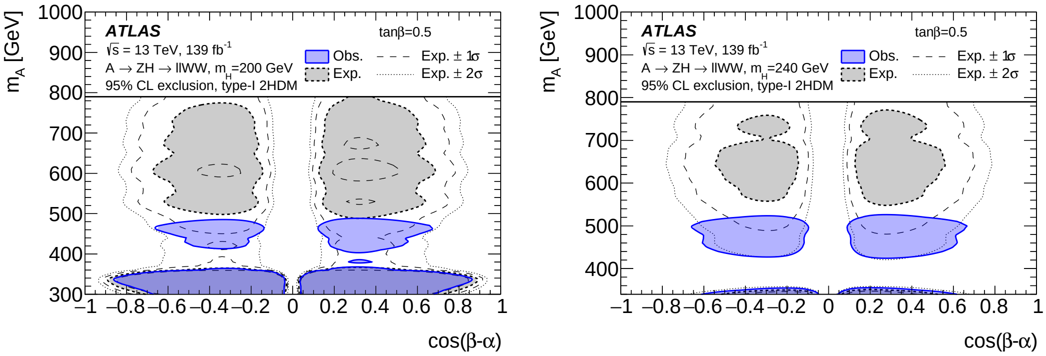

FIGURE A.8: Observed and expected 95% CL exclusion regions in the (m_A, $\cos(\beta-\alpha)$) plane for $\tan\beta = 0.5$ for (a) $m_H = 200$ GeV and (b) $m_H = 240$ GeV in the context of type-I 2HDM for the $\ell\ell WW$ channel.

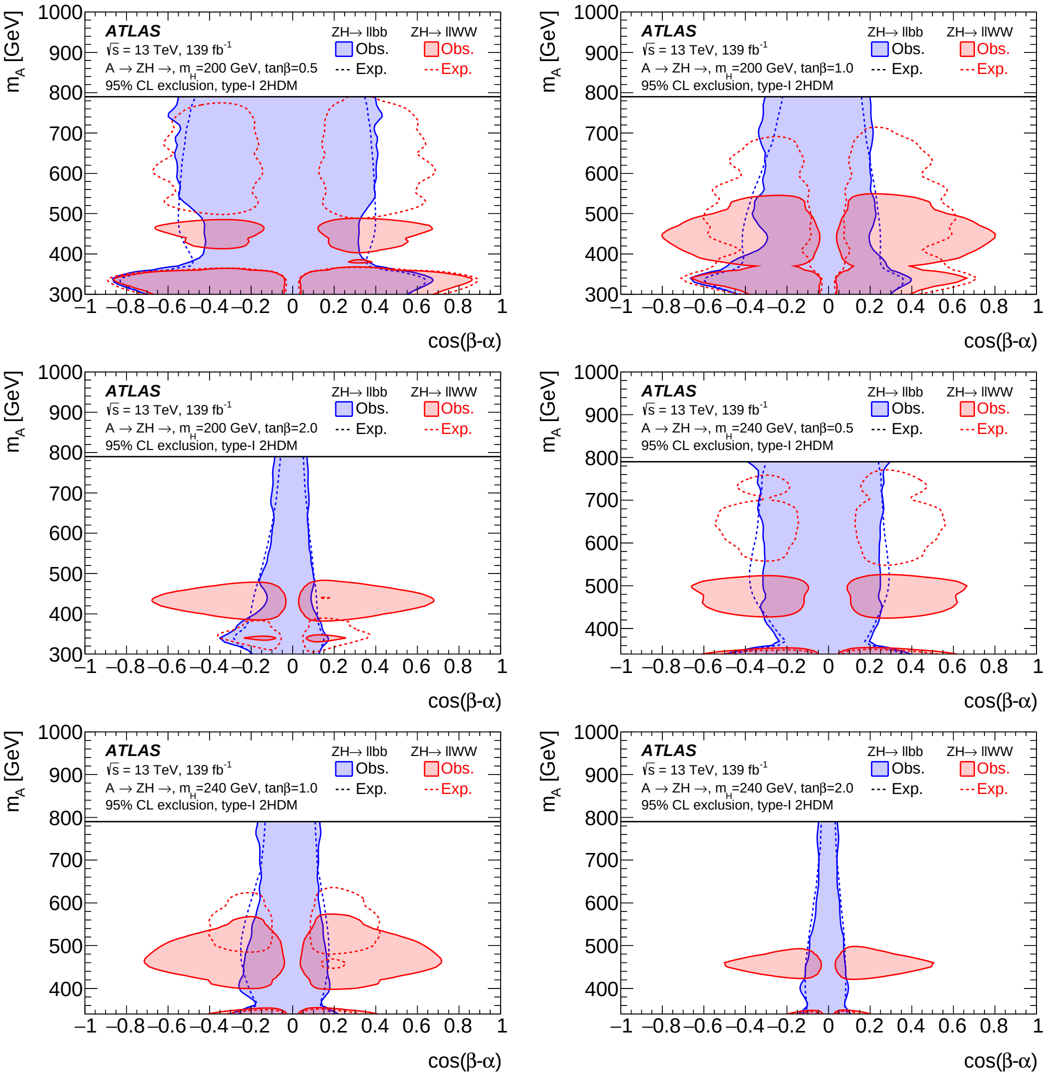

FIGURE A.9: Comparison of the observed and expected 95% CL exclusion regions in the $(m_A, \cos(\beta-\alpha))$ plane of $\ell\ell bb$ and $\ell\ell WW$ channels for various $\tan\beta$ values for (a,b,c) $m_H = 200$ GeV and (c,d,e) $m_H = 240$ GeV in the context of type-I 2HDM.

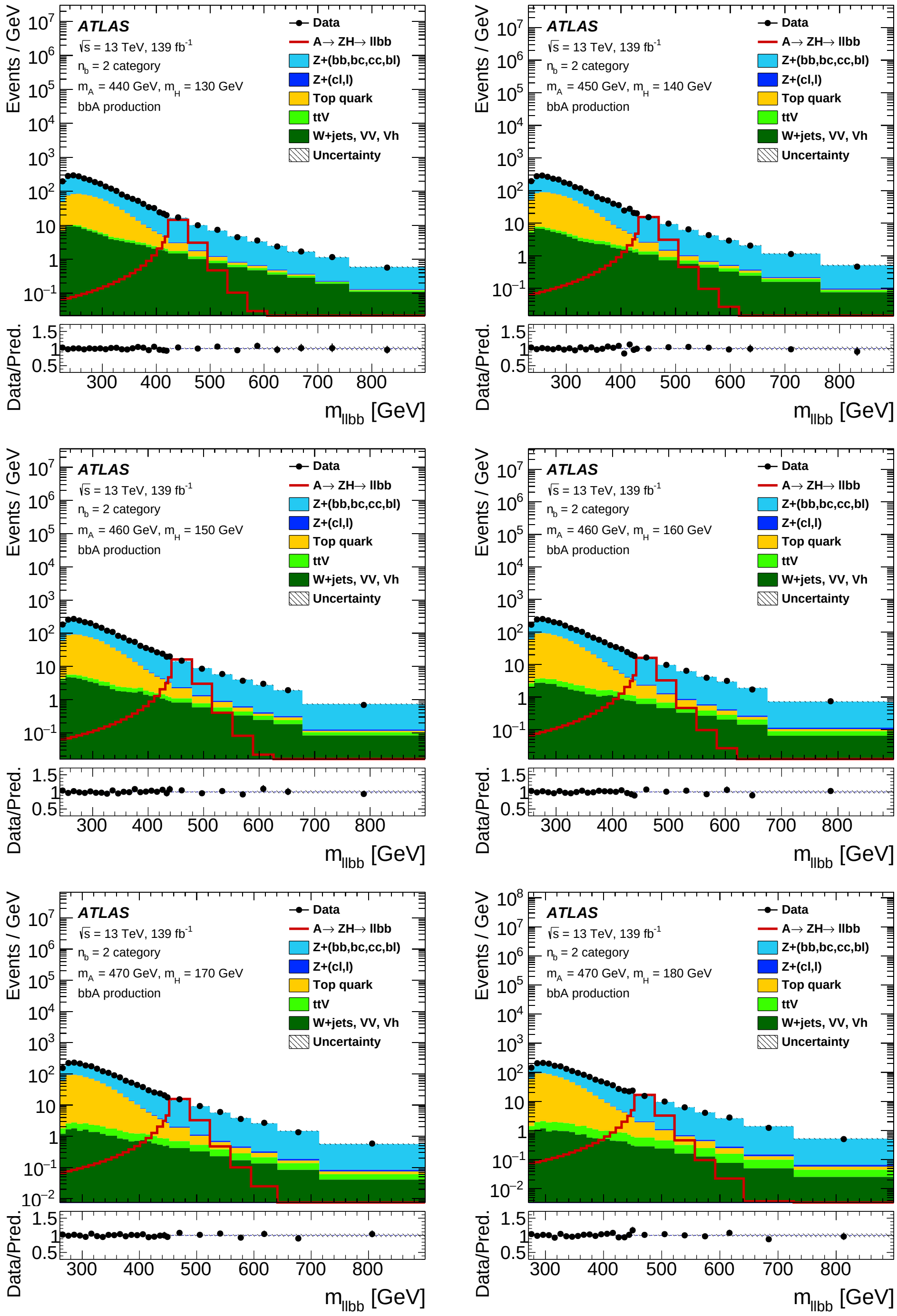

FIGURE A.10: The $m_{\ell\ell bb}$ mass distribution for the various m_{bb} windows and all the categories considered in the $\ell\ell bb$ channel. The number of entries shown in each bin is the number of events in that bin divided by the width of the bin. The same conventions as in Figure 2.2 are used.

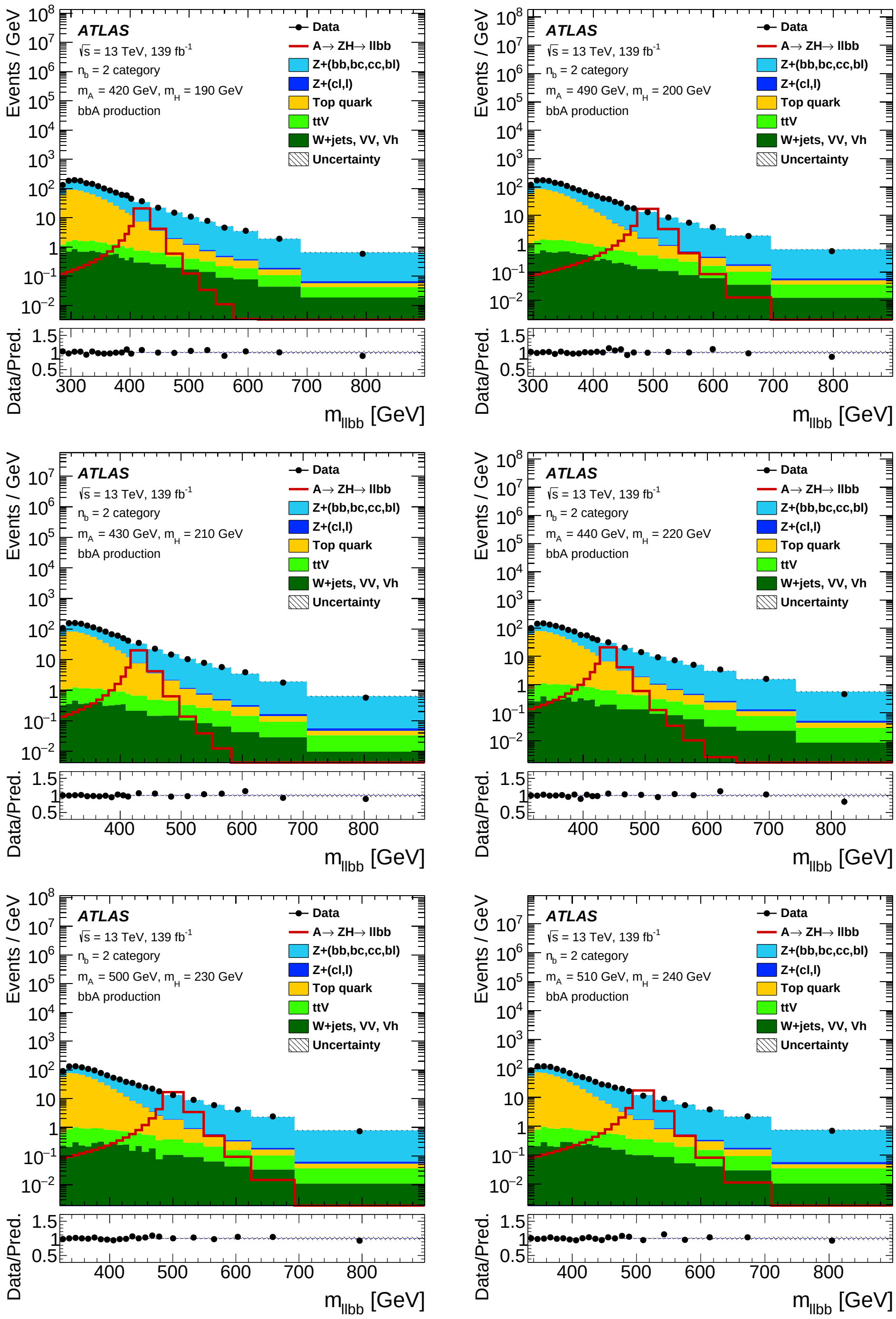

FIGURE A.11: The $m_{\ell\ell bb}$ mass distribution for the various m_{bb} windows and all the categories considered in the $\ell\ell bb$ channel. The number of entries shown in each bin is the number of events in that bin divided by the width of the bin. The same conventions as in Figure 2.2 are used.

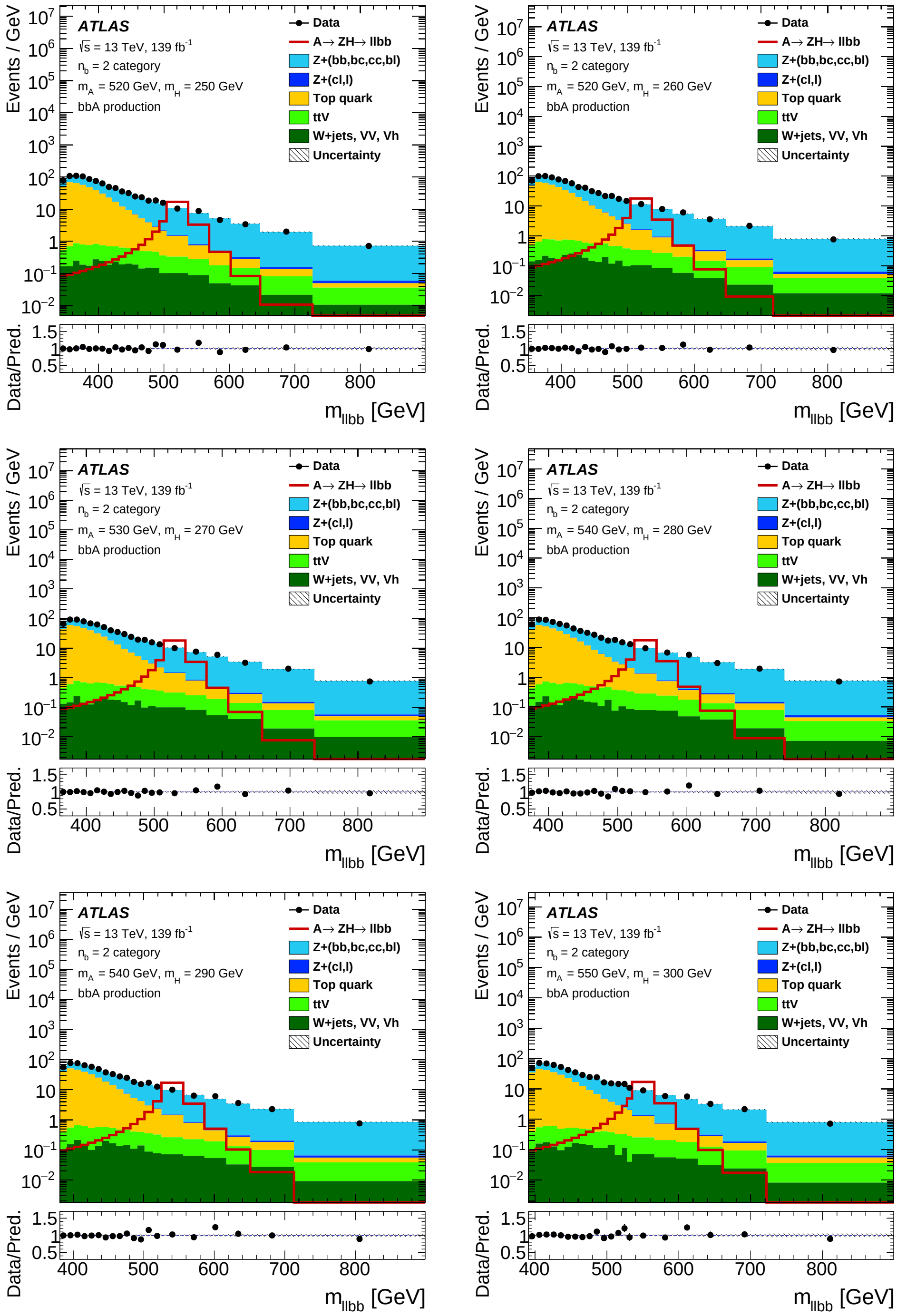

FIGURE A.12: The $m_{\ell\ell bb}$ mass distribution for the various m_{bb} windows and all the categories considered in the $\ell\ell bb$ channel. The number of entries shown in each bin is the number of events in that bin divided by the width of the bin. The same conventions as in Figure 2.2 are used.

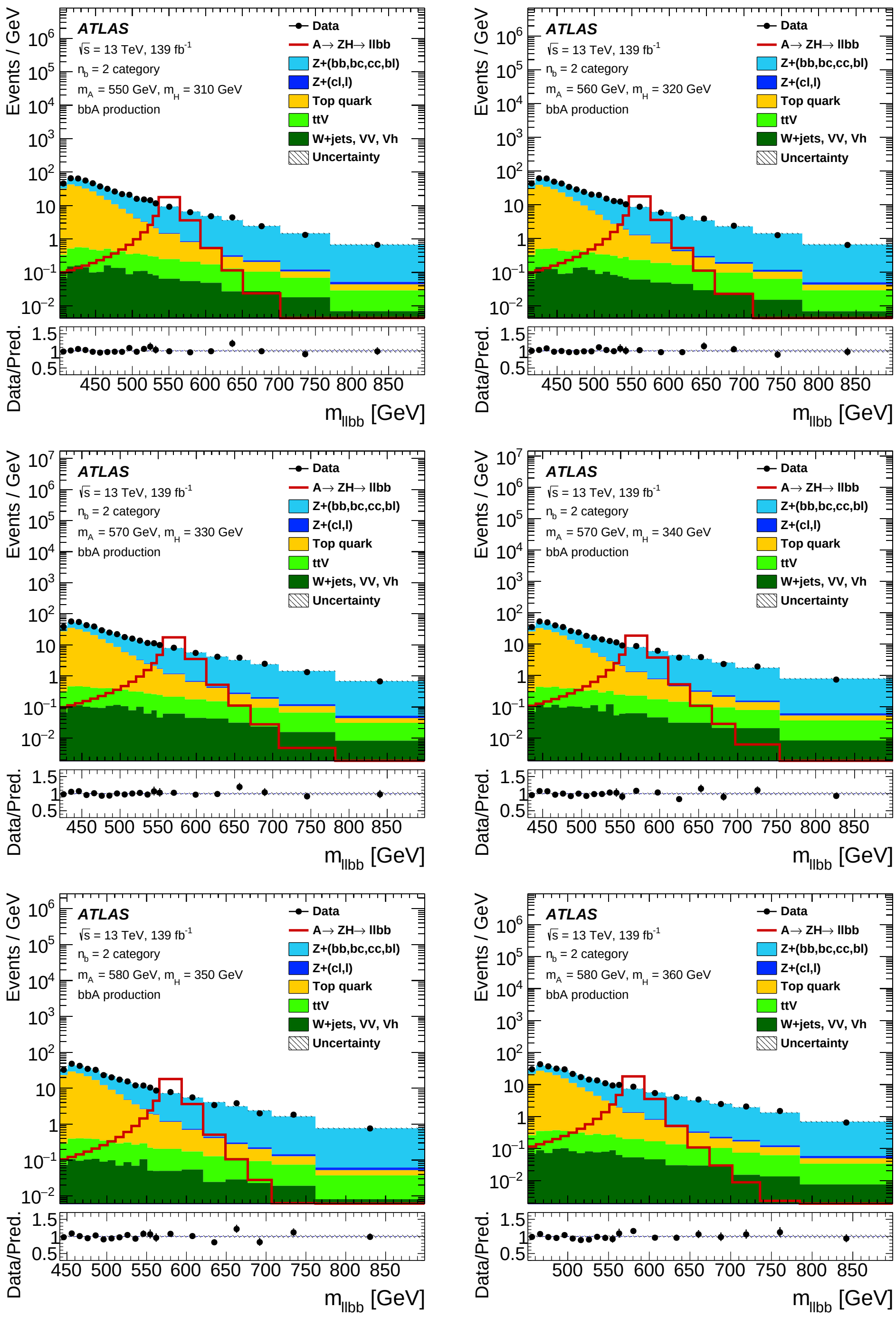

FIGURE A.13: The $m_{\ell\ell bb}$ mass distribution for the various m_{bb} windows and all the categories considered in the $\ell\ell bb$ channel. The number of entries shown in each bin is the number of events in that bin divided by the width of the bin. The same conventions as in Figure 2.2 are used.

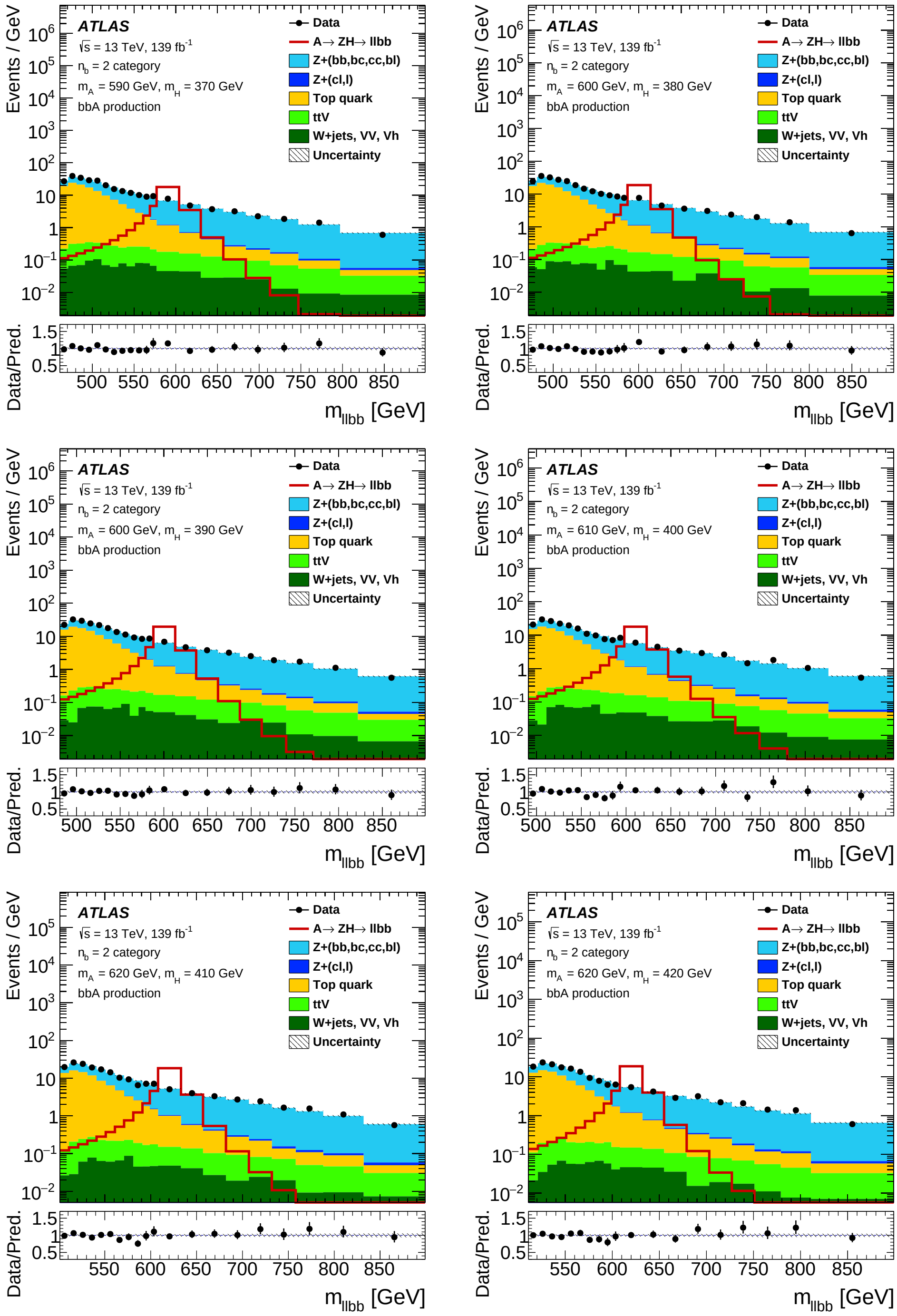

FIGURE A.14: The $m_{\ell\ell bb}$ mass distribution for the various m_{bb} windows and all the categories considered in the $\ell\ell bb$ channel. The number of entries shown in each bin is the number of events in that bin divided by the width of the bin. The same conventions as in Figure 2.2 are used.

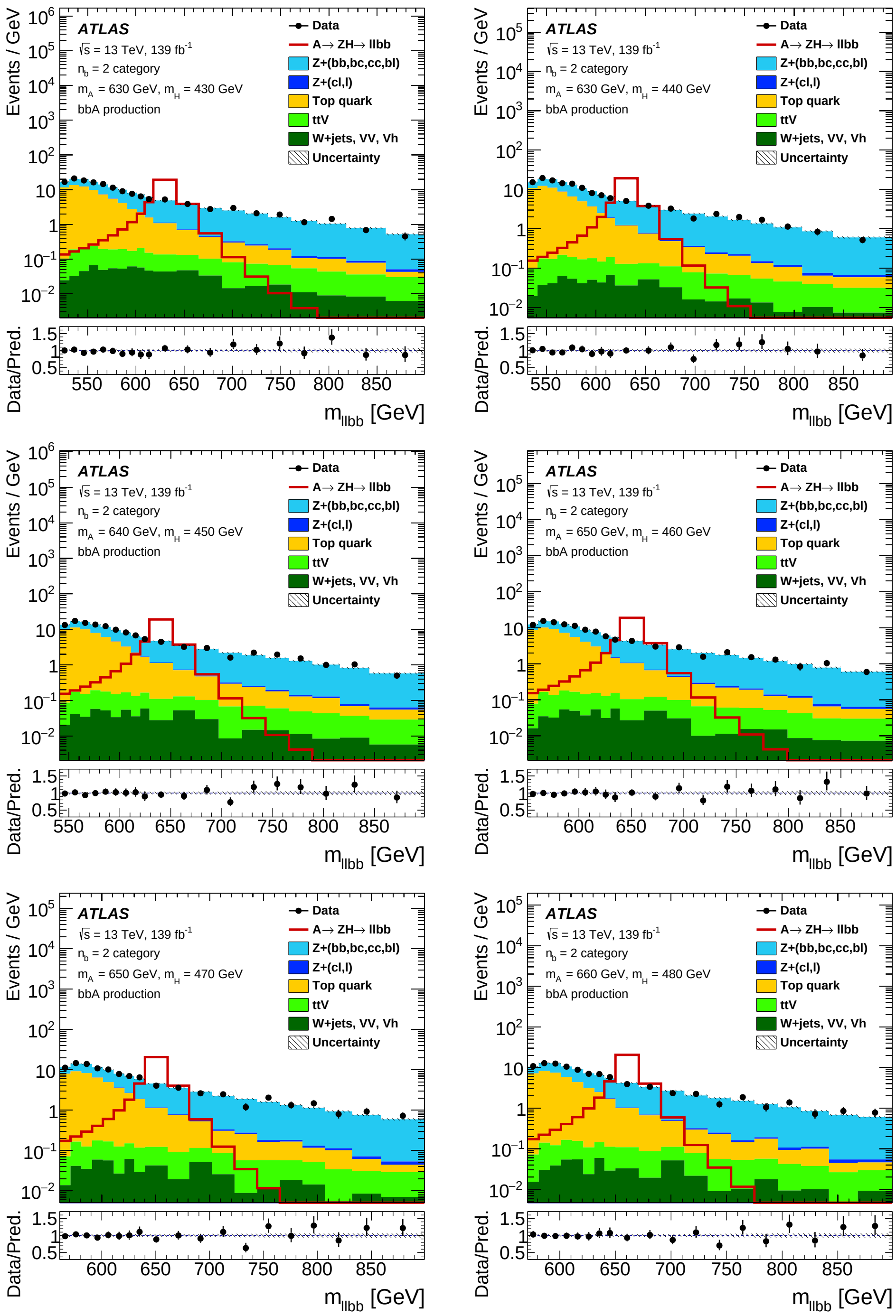

FIGURE A.15: The $m_{\ell\ell bb}$ mass distribution for the various m_{bb} windows and all the categories considered in the $\ell\ell bb$ channel. The number of entries shown in each bin is the number of events in that bin divided by the width of the bin. The same conventions as in Figure 2.2 are used.

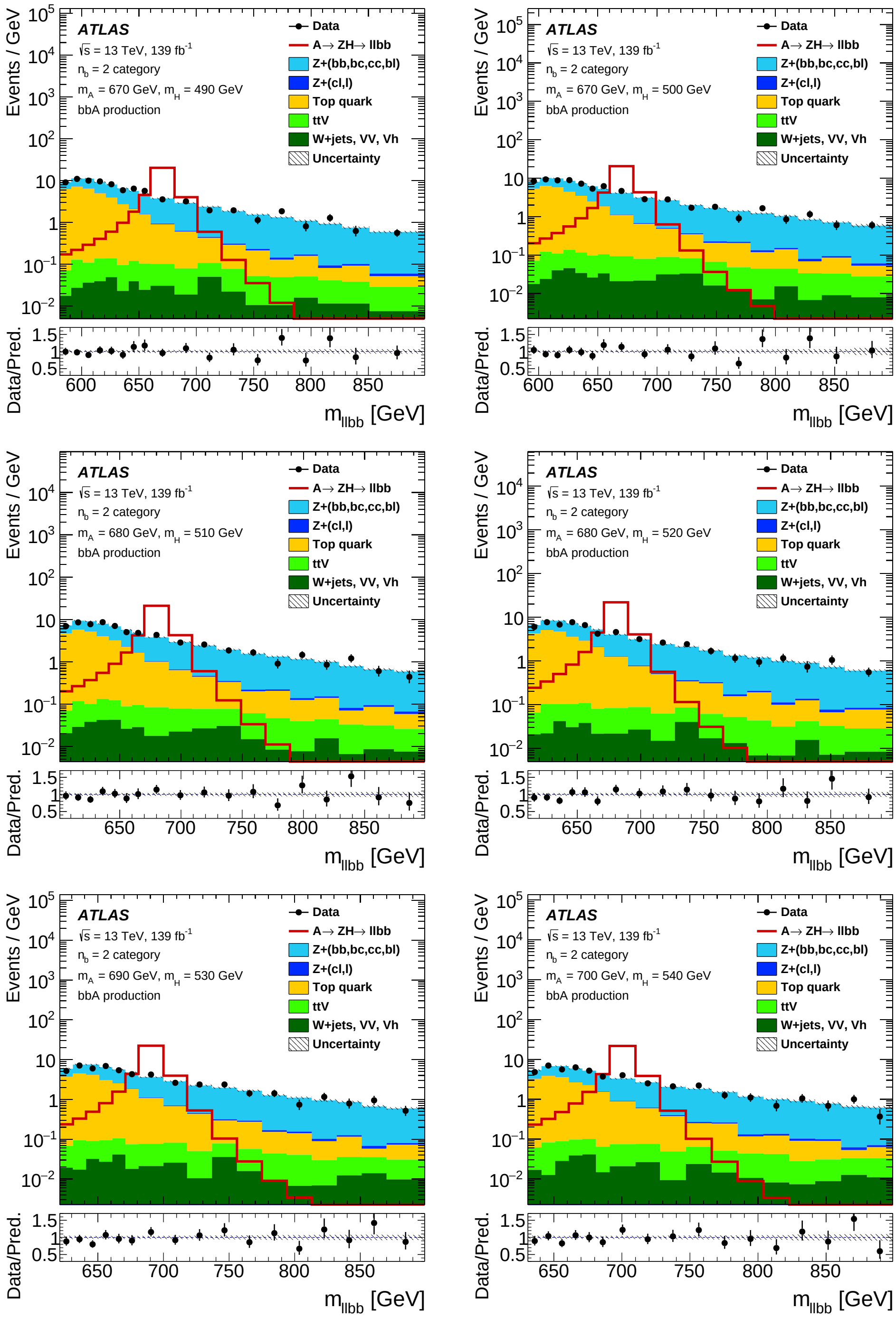

FIGURE A.16: The $m_{\ell\ell bb}$ mass distribution for the various m_{bb} windows and all the categories considered in the $\ell\ell bb$ channel. The number of entries shown in each bin is the number of events in that bin divided by the width of the bin. The same conventions as in Figure 2.2 are used.

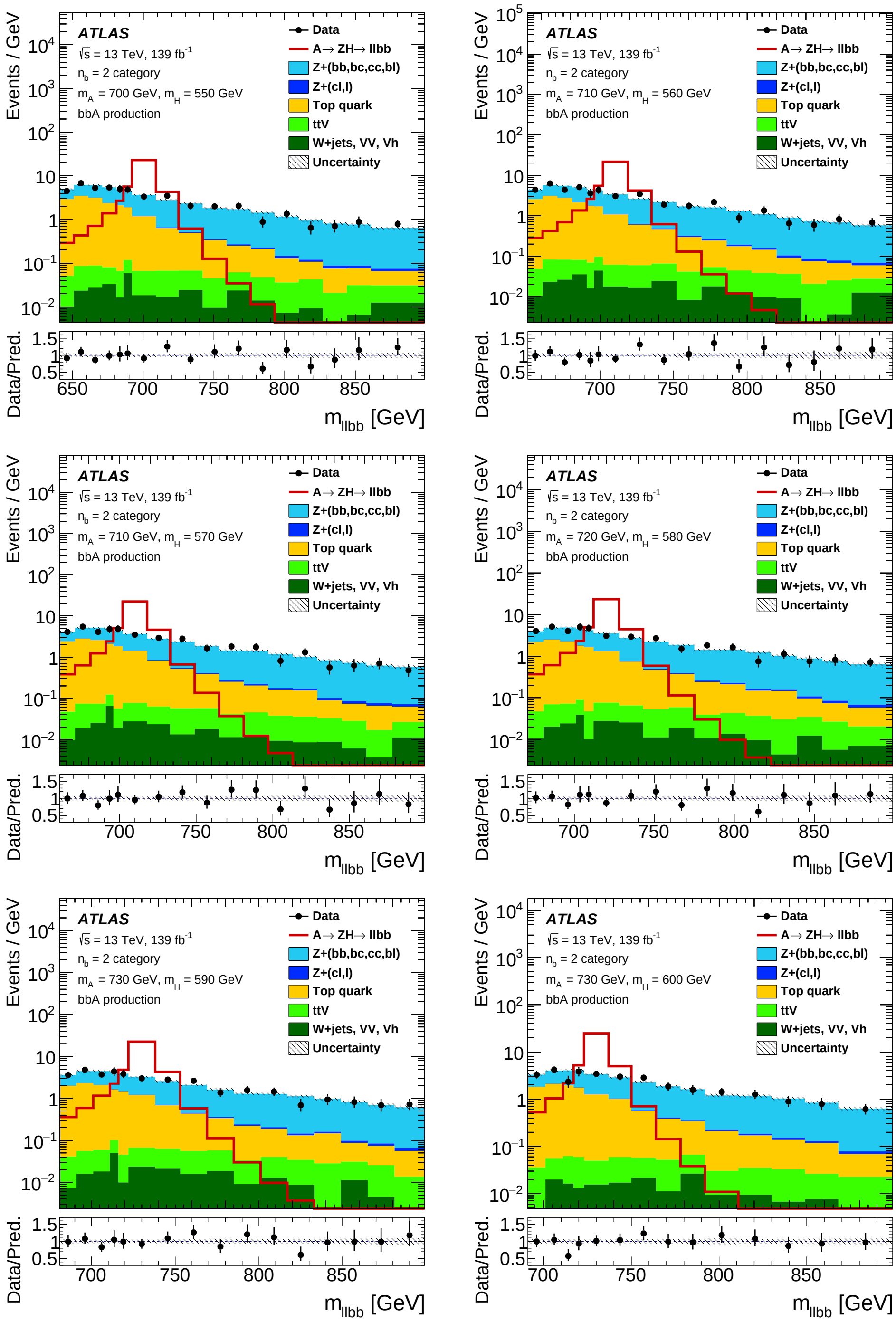

FIGURE A.17: The $m_{\ell\ell bb}$ mass distribution for the various m_{bb} windows and all the categories considered in the $\ell\ell bb$ channel. The number of entries shown in each bin is the number of events in that bin divided by the width of the bin. The same conventions as in Figure 2.2 are used.

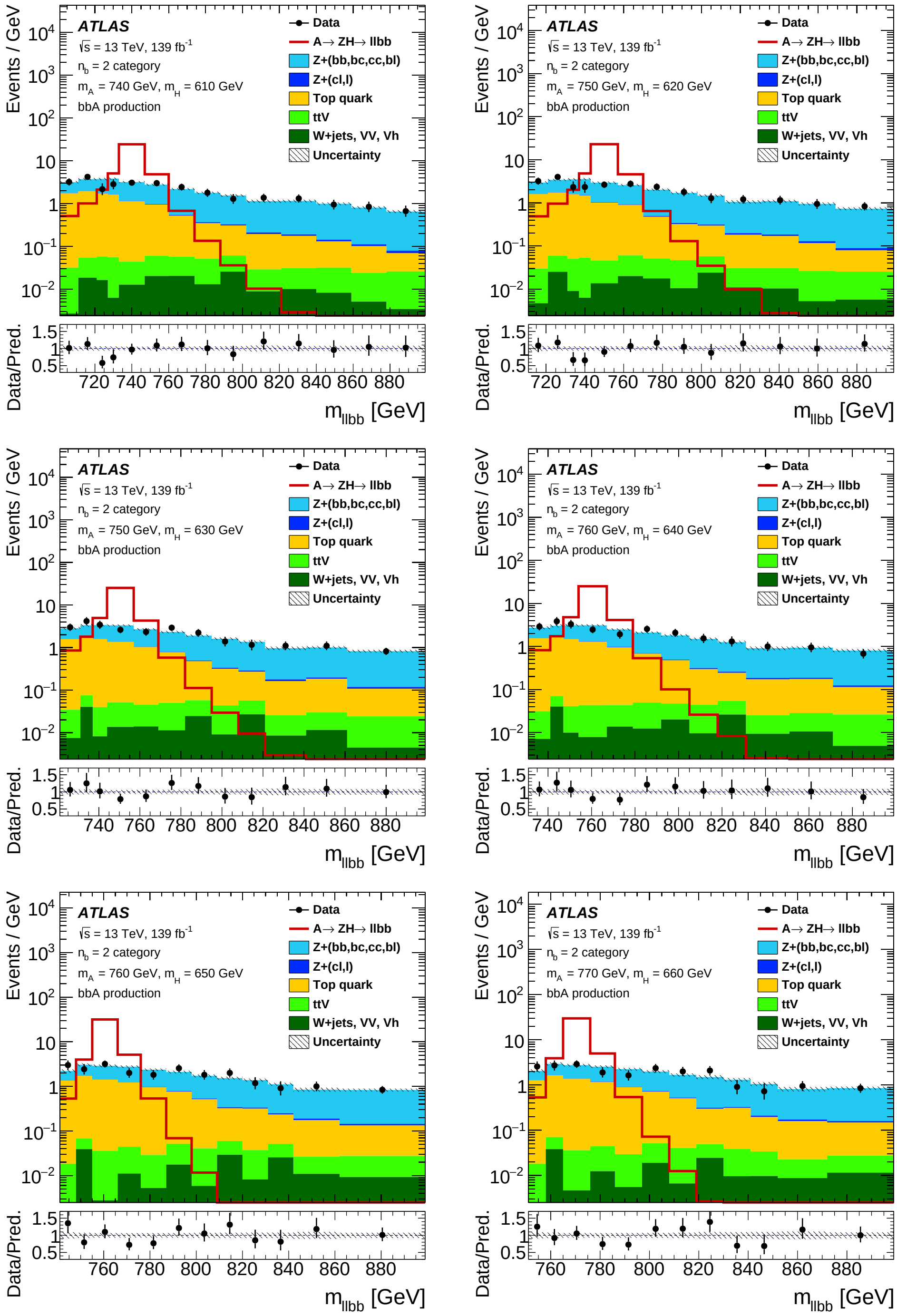

FIGURE A.18: The $m_{\ell\ell bb}$ mass distribution for the various m_{bb} windows and all the categories considered in the $\ell\ell bb$ channel. The number of entries shown in each bin is the number of events in that bin divided by the width of the bin. The same conventions as in Figure 2.2 are used.

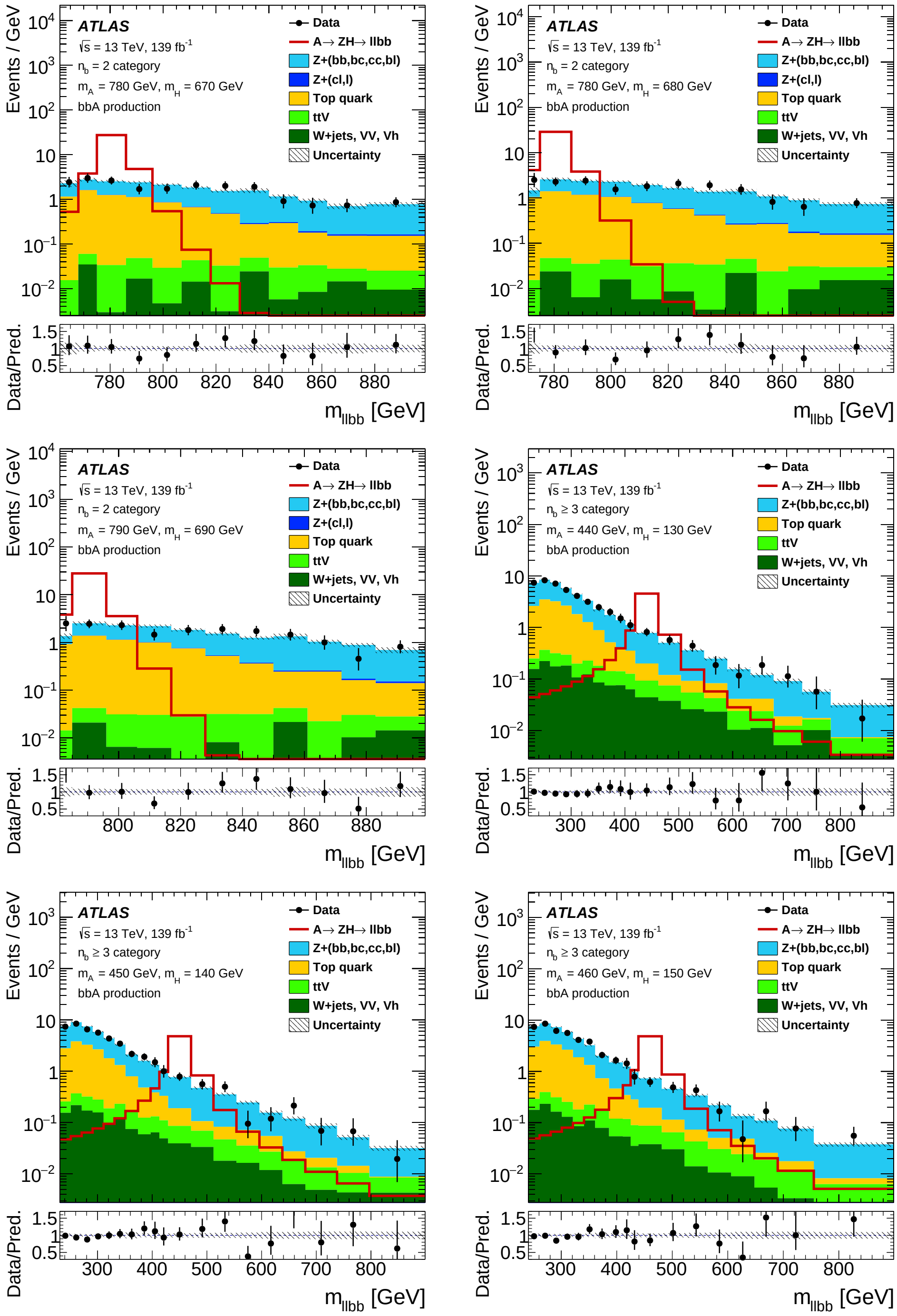

FIGURE A.19: The $m_{\ell\ell bb}$ mass distribution for the various m_{bb} windows and all the categories considered in the $\ell\ell bb$ channel. The number of entries shown in each bin is the number of events in that bin divided by the width of the bin. The same conventions as in Figure 2.2 are used.

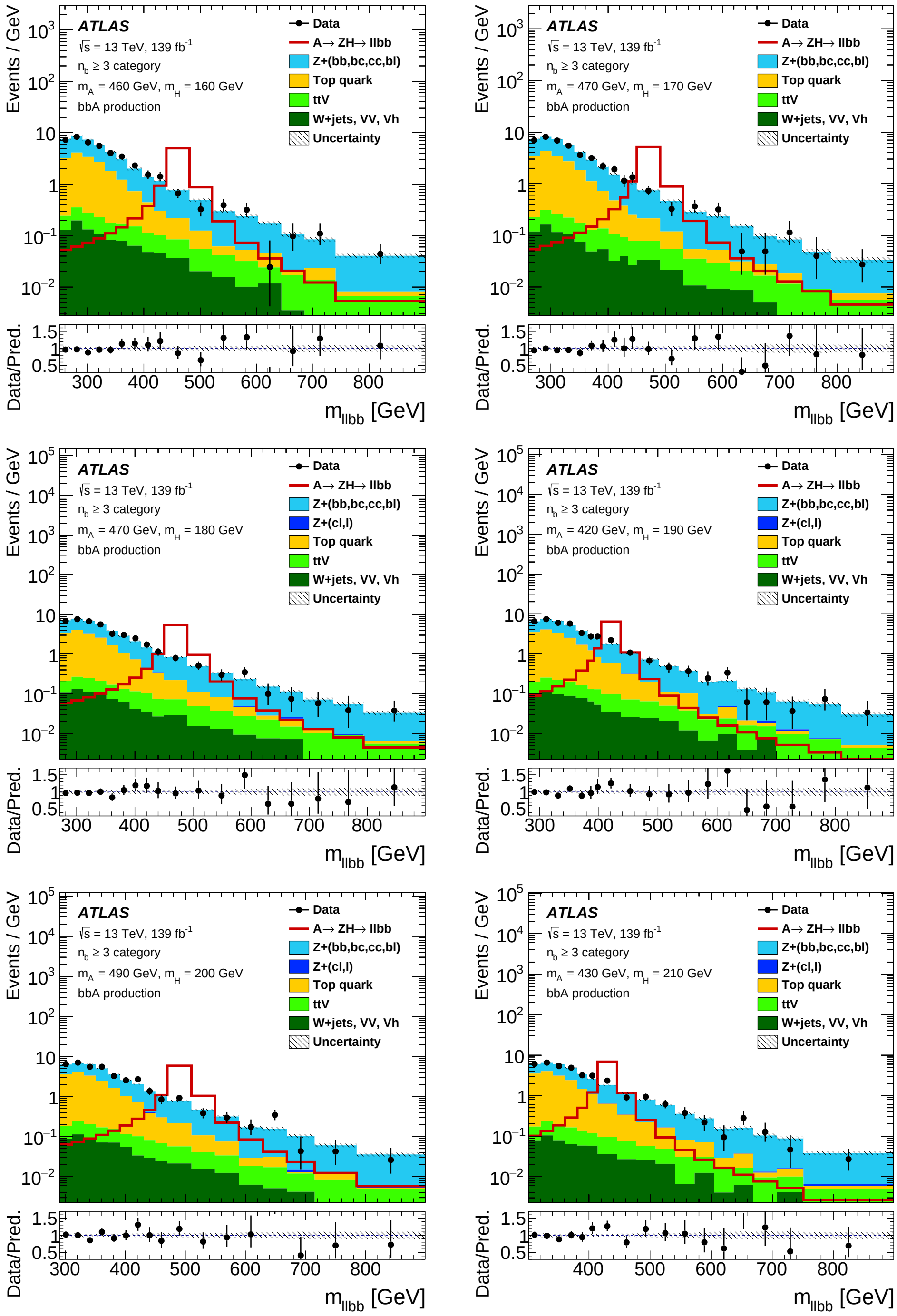

FIGURE A.20: The $m_{\ell\ell bb}$ mass distribution for the various m_{bb} windows and all the categories considered in the $\ell\ell bb$ channel. The number of entries shown in each bin is the number of events in that bin divided by the width of the bin. The same conventions as in Figure 2.2 are used.

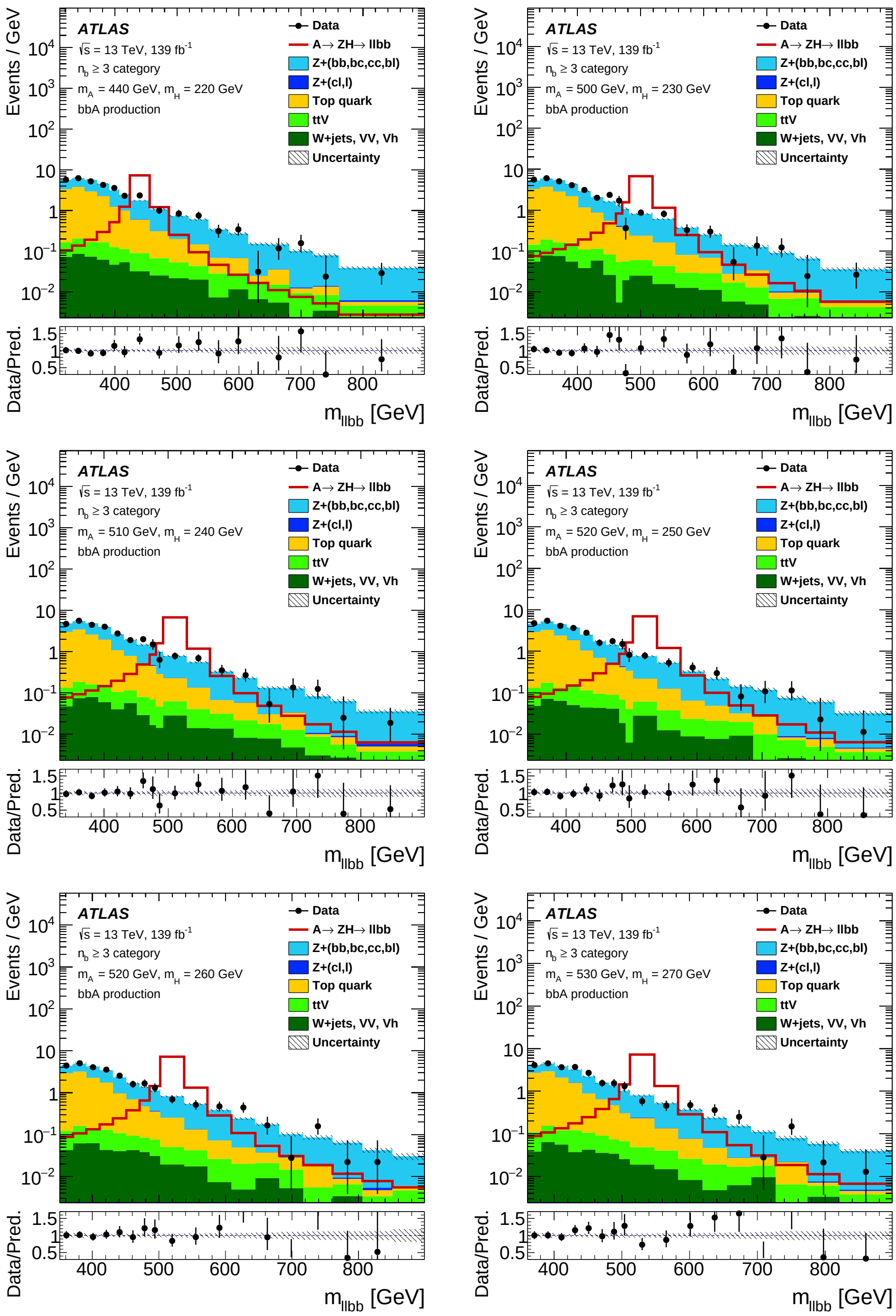

FIGURE A.21: The $m_{\ell\ell bb}$ mass distribution for the various m_{bb} windows and all the categories considered in the $\ell\ell bb$ channel. The number of entries shown in each bin is the number of events in that bin divided by the width of the bin. The same conventions as in Figure 2.2 are used.

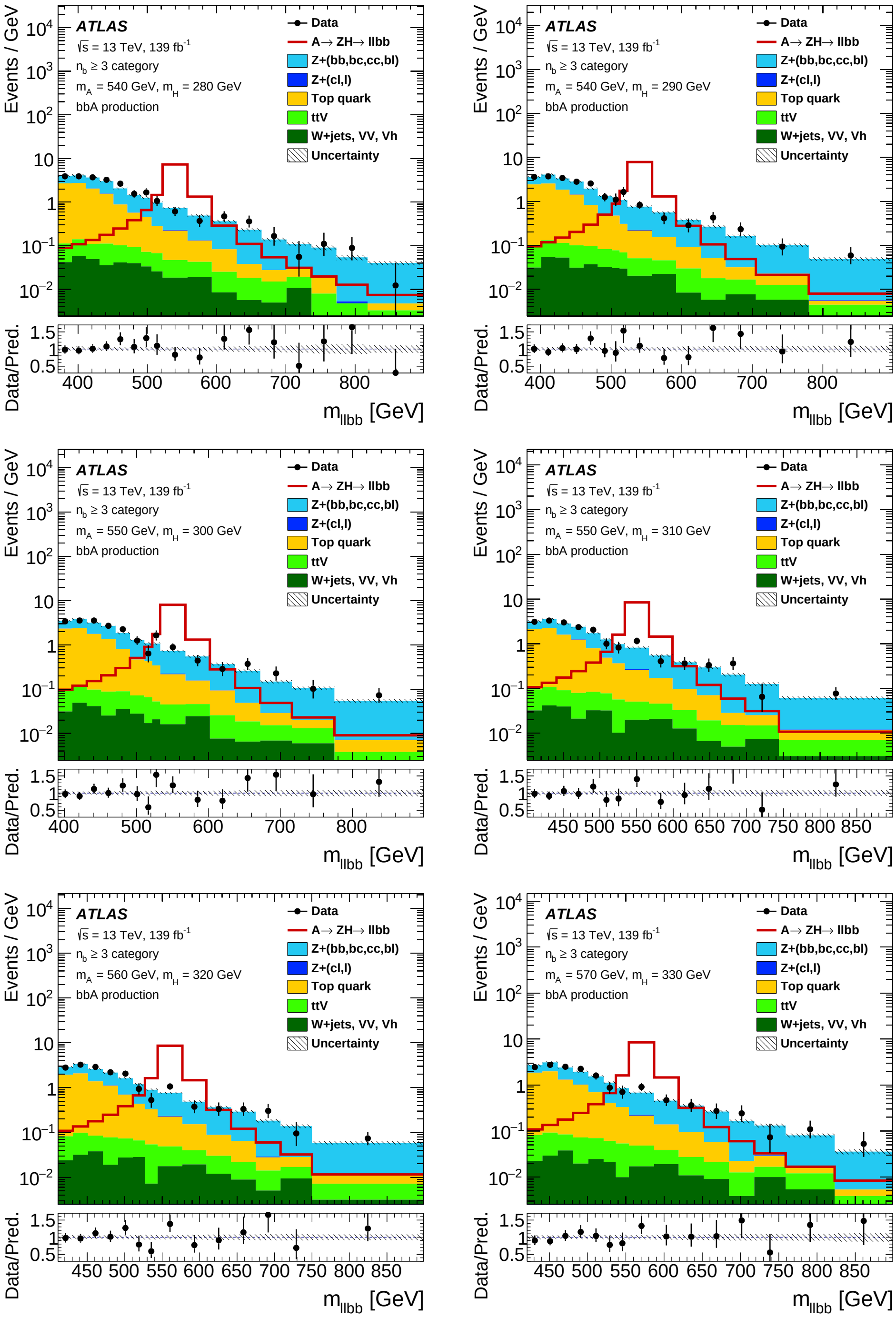

FIGURE A.22: The $m_{\ell\ell bb}$ mass distribution for the various m_{bb} windows and all the categories considered in the $\ell\ell bb$ channel. The number of entries shown in each bin is the number of events in that bin divided by the width of the bin. The same conventions as in Figure 2.2 are used.

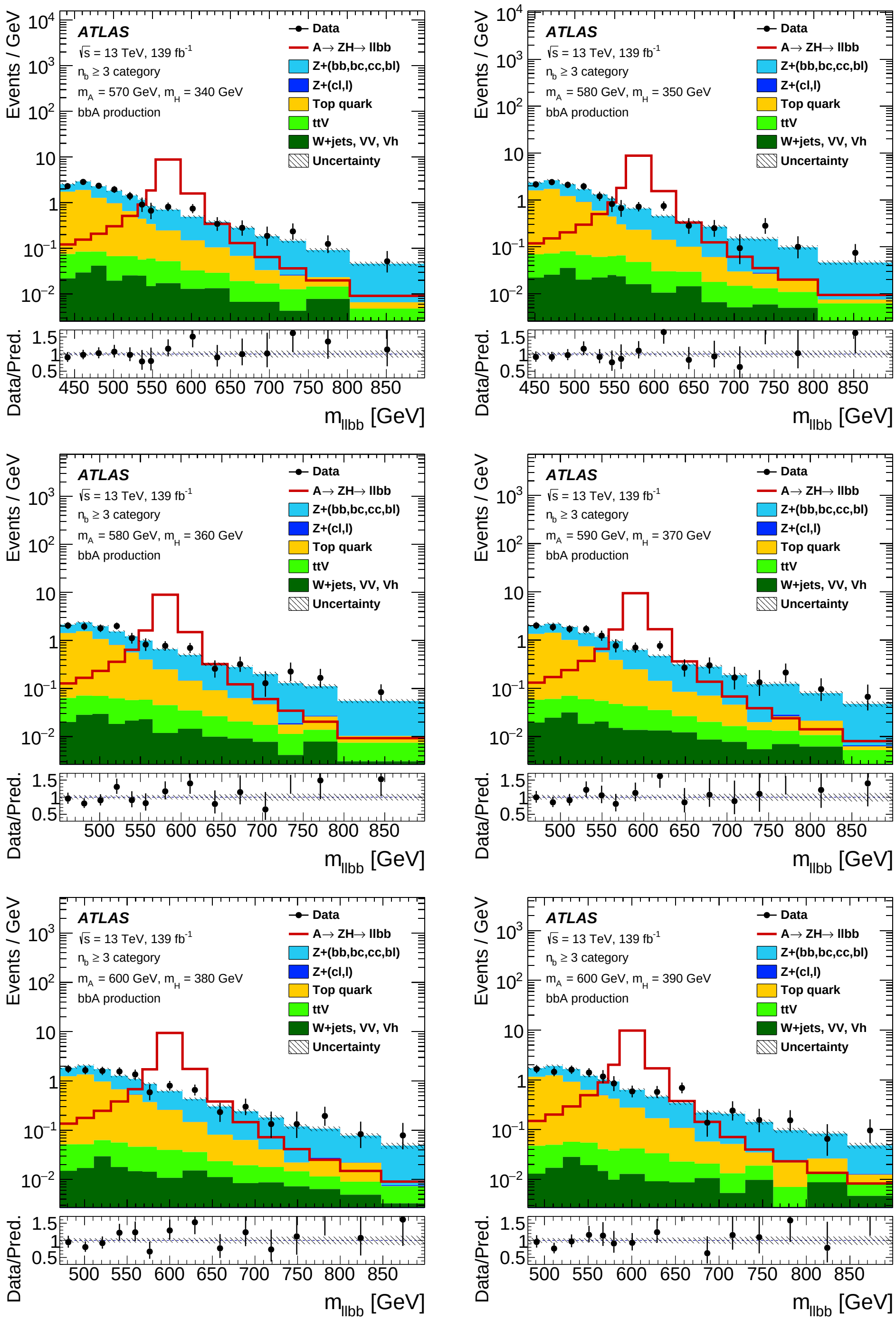

FIGURE A.23: The $m_{\ell\ell bb}$ mass distribution for the various m_{bb} windows and all the categories considered in the $\ell\ell bb$ channel. The number of entries shown in each bin is the number of events in that bin divided by the width of the bin. The same conventions as in Figure 2.2 are used.

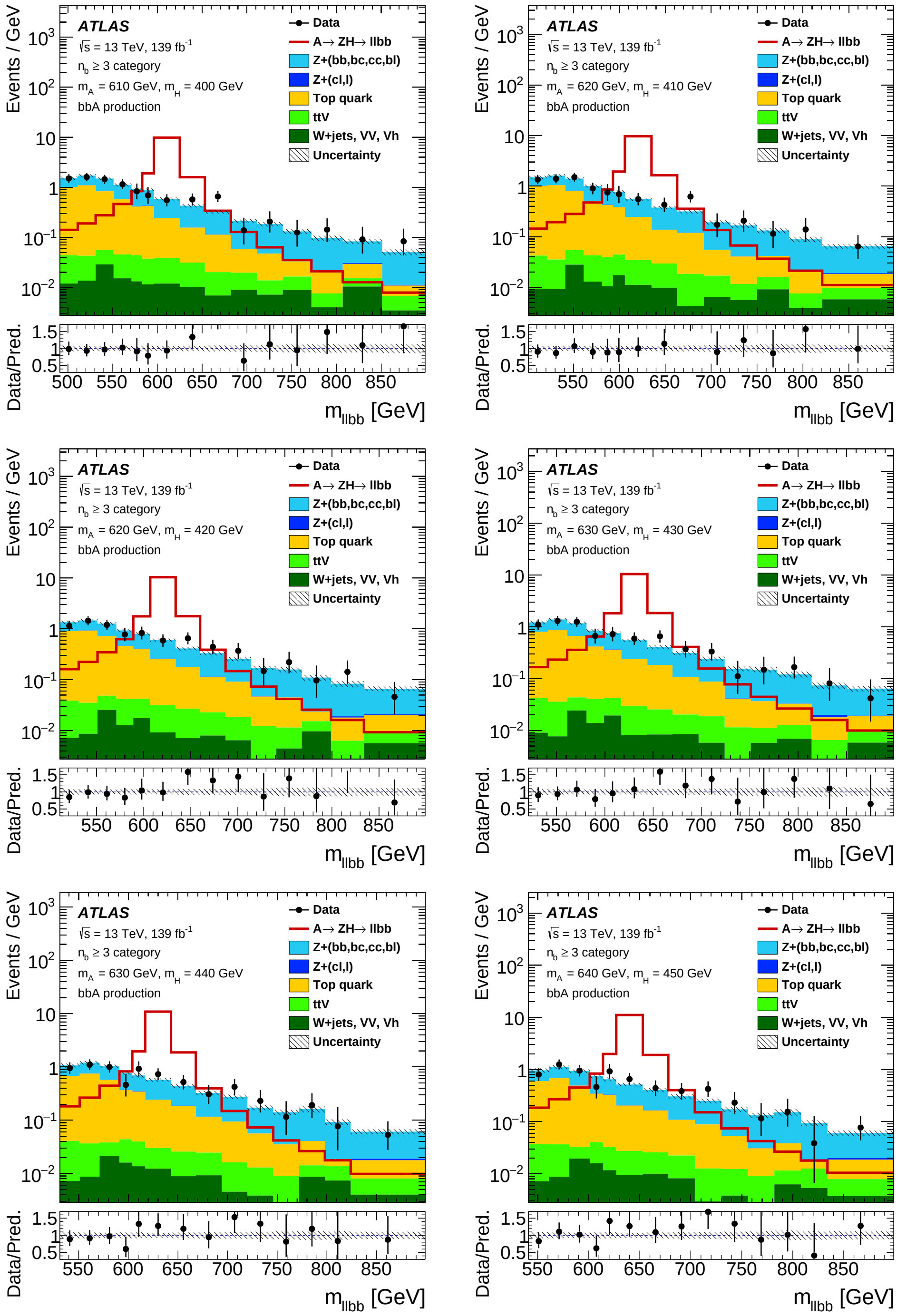

FIGURE A.24: The $m_{\ell\ell bb}$ mass distribution for the various m_{bb} windows and all the categories considered in the $\ell\ell bb$ channel. The number of entries shown in each bin is the number of events in that bin divided by the width of the bin. The same conventions as in Figure 2.2 are used.

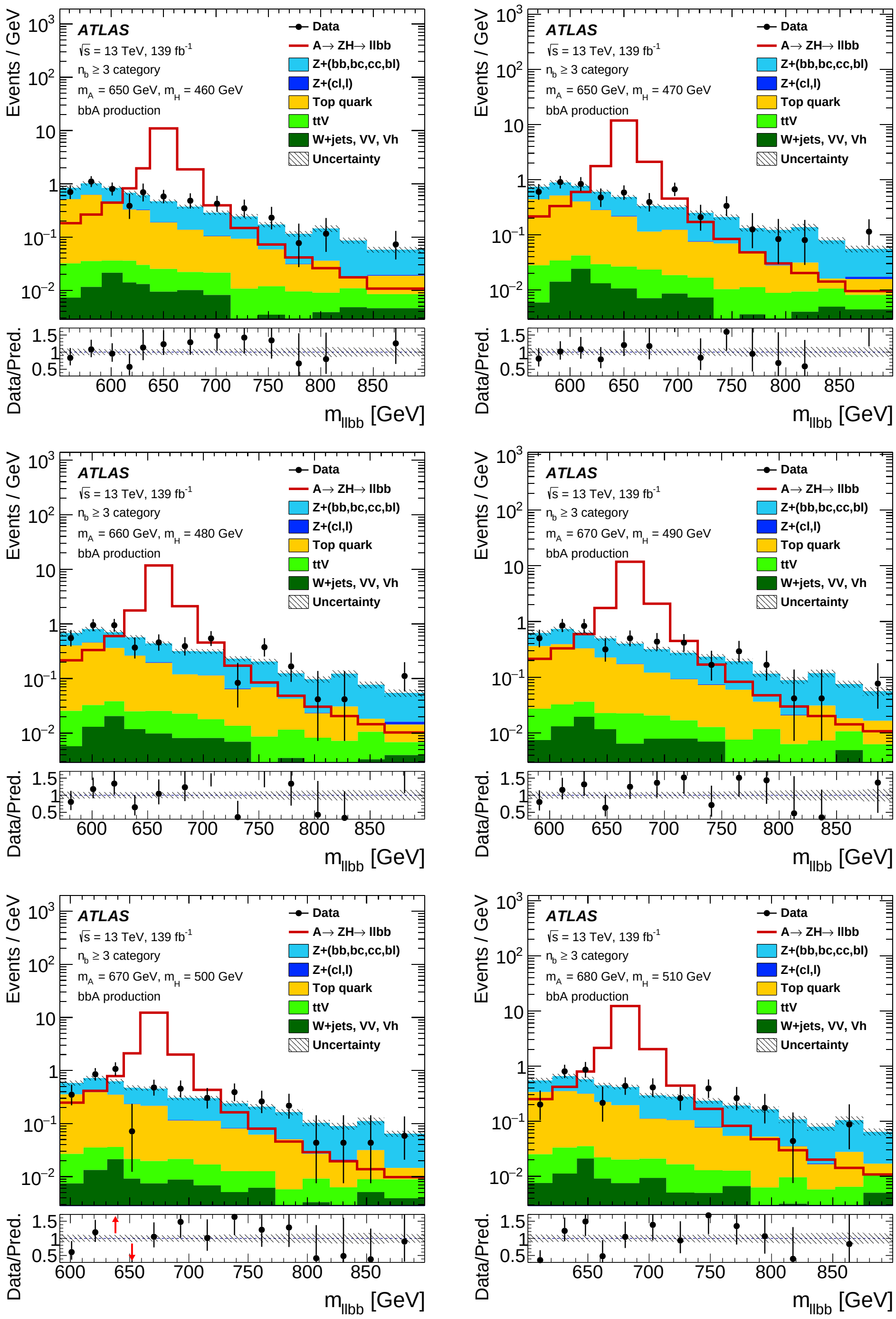

FIGURE A.25: The $m_{\ell\ell bb}$ mass distribution for the various m_{bb} windows and all the categories considered in the $\ell\ell bb$ channel. The number of entries shown in each bin is the number of events in that bin divided by the width of the bin. The same conventions as in Figure 2.2 are used.

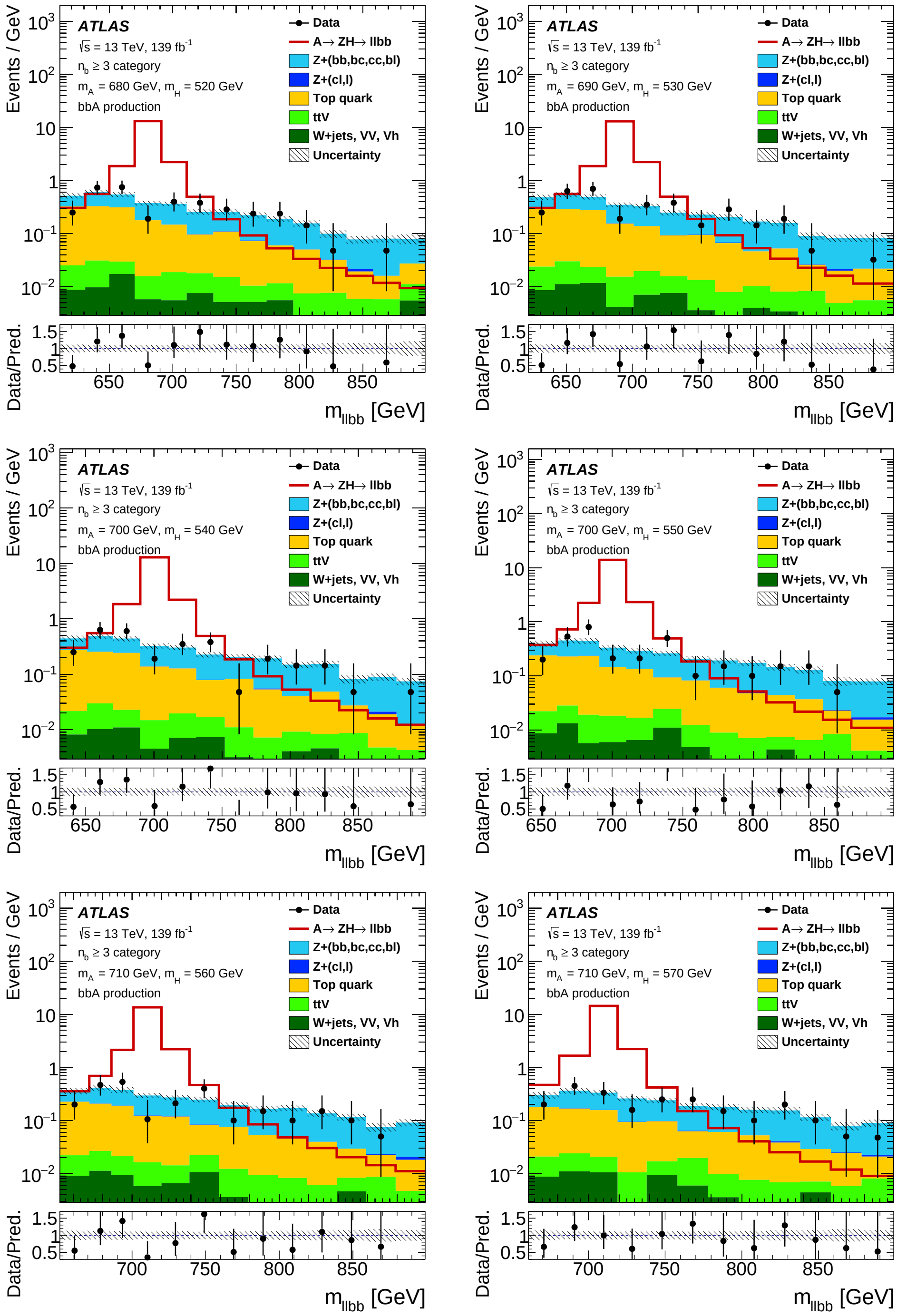

FIGURE A.26: The $m_{\ell\ell bb}$ mass distribution for the various m_{bb} windows and all the categories considered in the $\ell\ell bb$ channel. The number of entries shown in each bin is the number of events in that bin divided by the width of the bin. The same conventions as in Figure 2.2 are used.

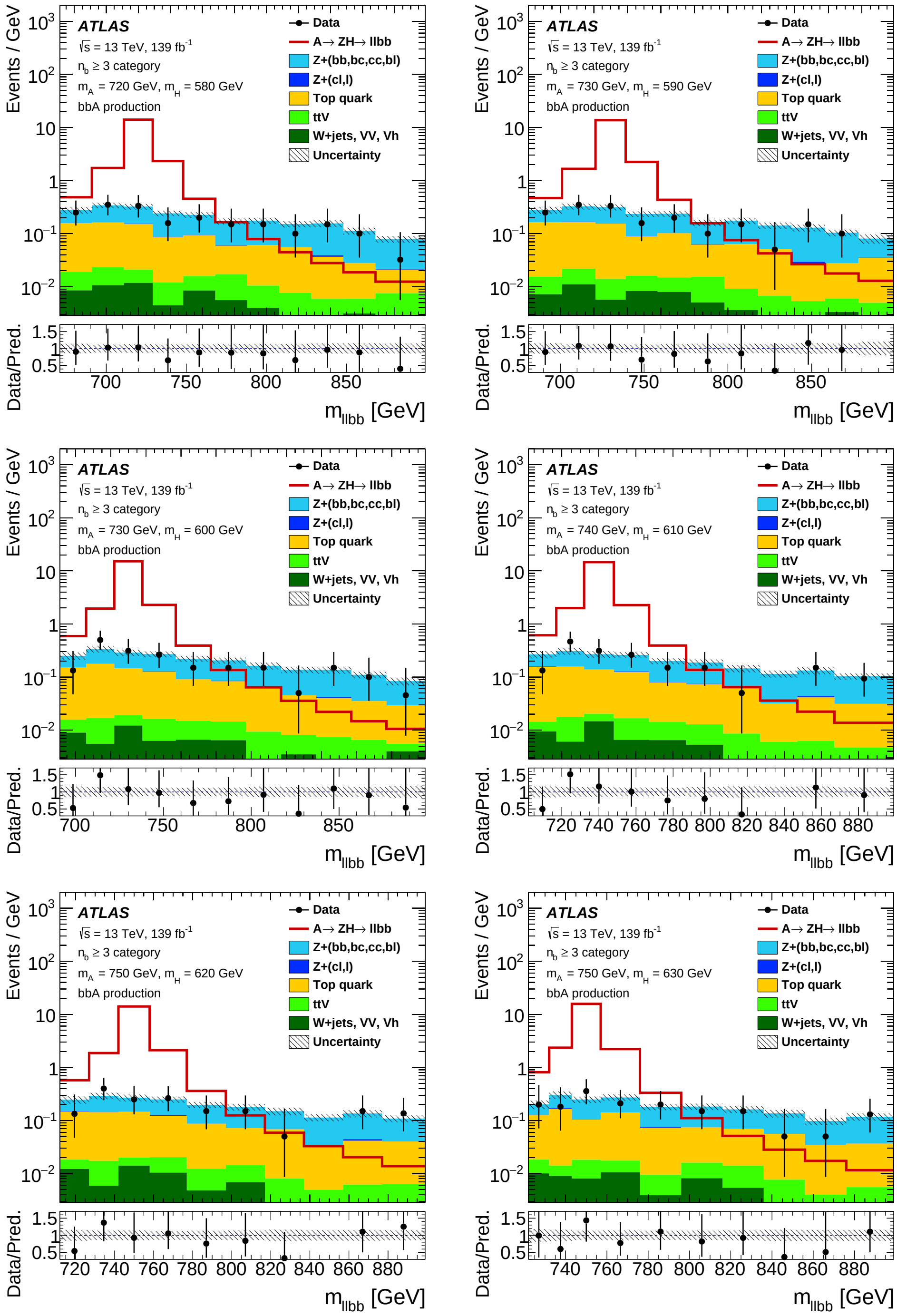

FIGURE A.27: The $m_{\ell\ell bb}$ mass distribution for the various m_{bb} windows and all the categories considered in the $\ell\ell bb$ channel. The number of entries shown in each bin is the number of events in that bin divided by the width of the bin. The same conventions as in Figure 2.2 are used.

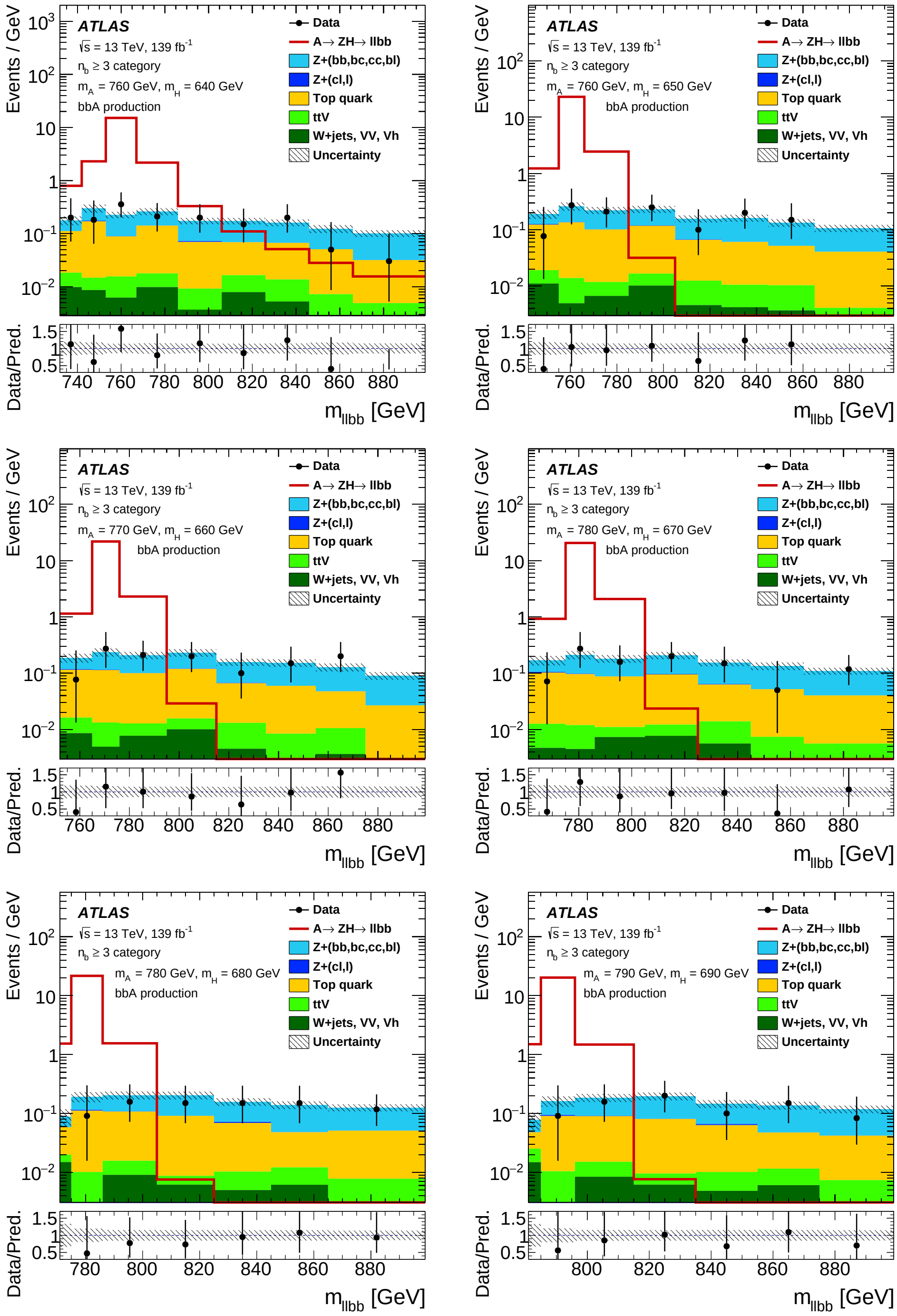

FIGURE A.28: The $m_{\ell\ell bb}$ mass distribution for the various m_{bb} windows and all the categories considered in the $\ell\ell bb$ channel. The number of entries shown in each bin is the number of events in that bin divided by the width of the bin. The same conventions as in Figure 2.2 are used.

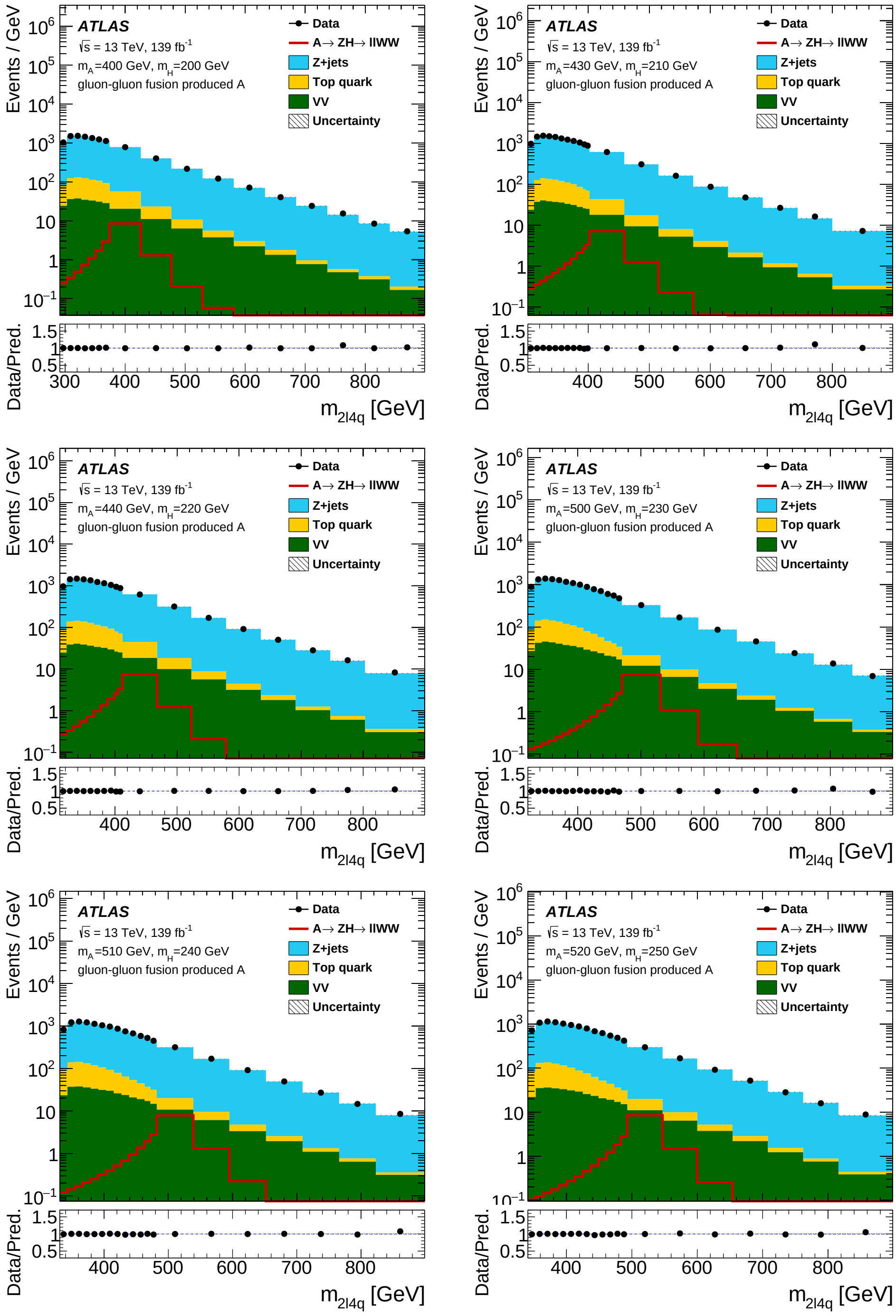

FIGURE A.29: The $m_{2\ell 4q}$ mass distribution for the various m_{4q} windows considered in the $\ell\ell WW$ channel. The number of entries shown in each bin is the number of events in that bin divided by the width of the bin. The same conventions as in Figure 2.4 are used.

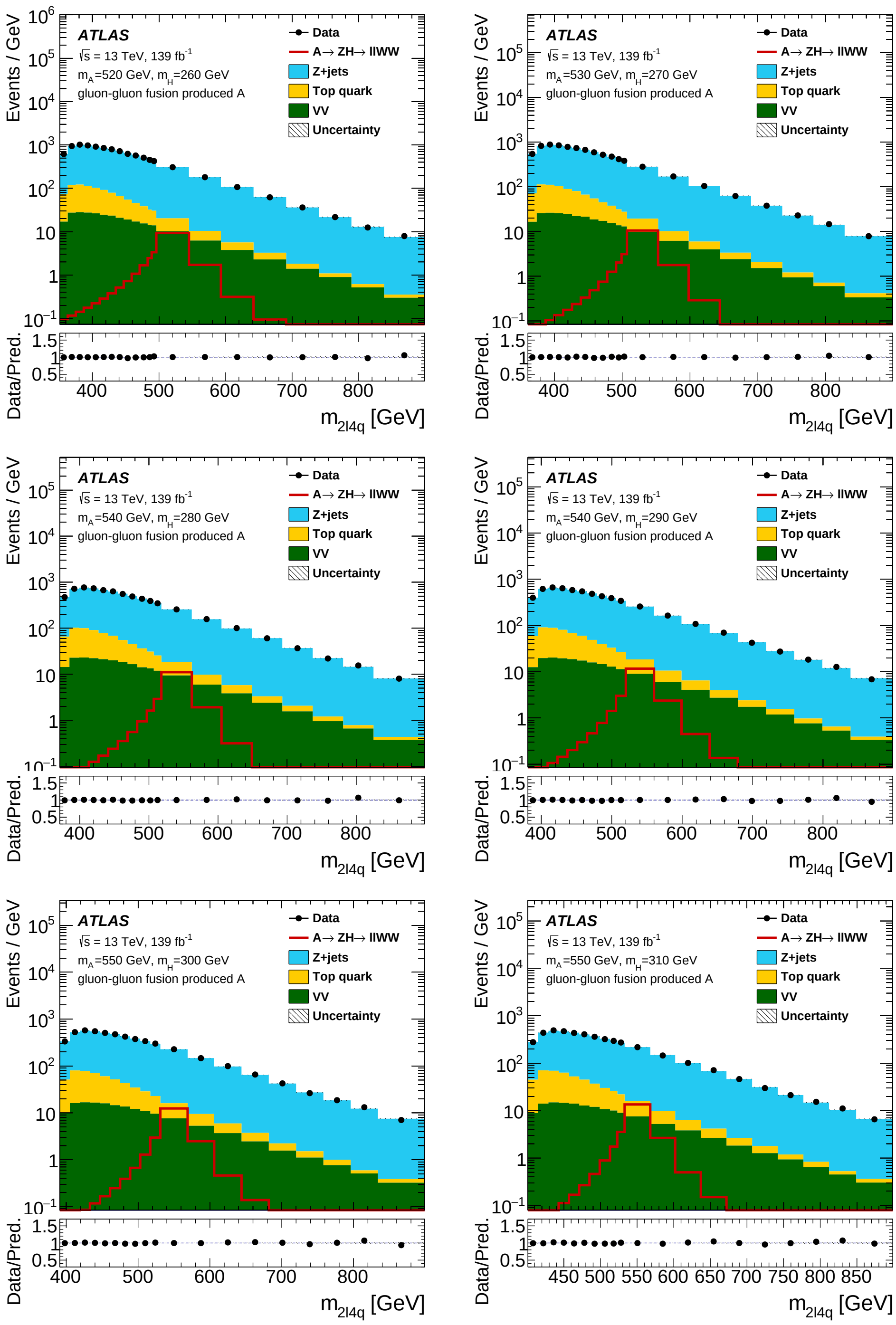

FIGURE A.30: The $m_{2\ell 4q}$ mass distribution for the various m_{4q} windows considered in the $\ell\ell WW$ channel. The number of entries shown in each bin is the number of events in that bin divided by the width of the bin. The same conventions as in Figure 2.4 are used.

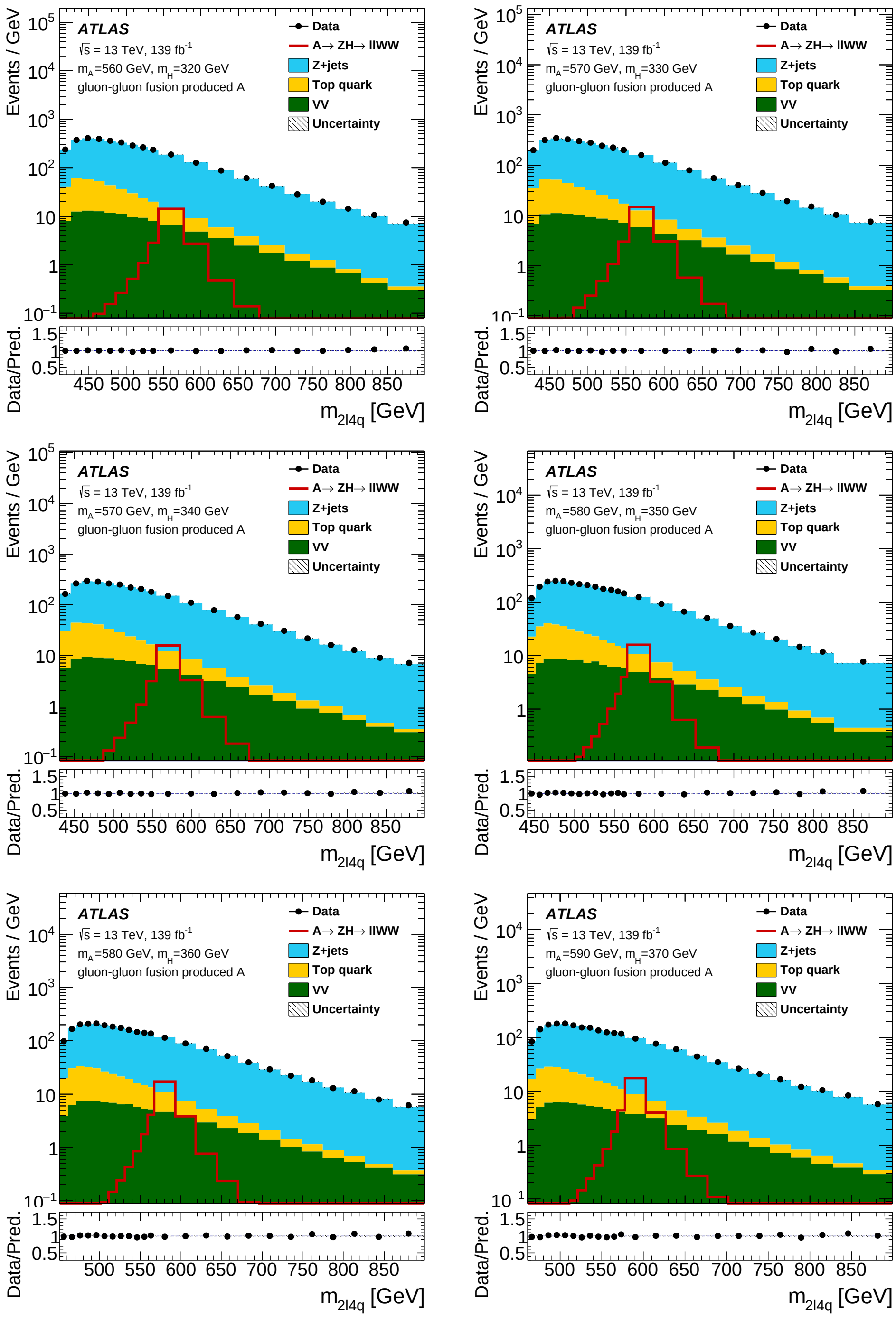

FIGURE A.31: The $m_{2\ell 4q}$ mass distribution for the various m_{4q} windows considered in the $\ell\ell WW$ channel. The number of entries shown in each bin is the number of events in that bin divided by the width of the bin. The same conventions as in Figure 2.4 are used.

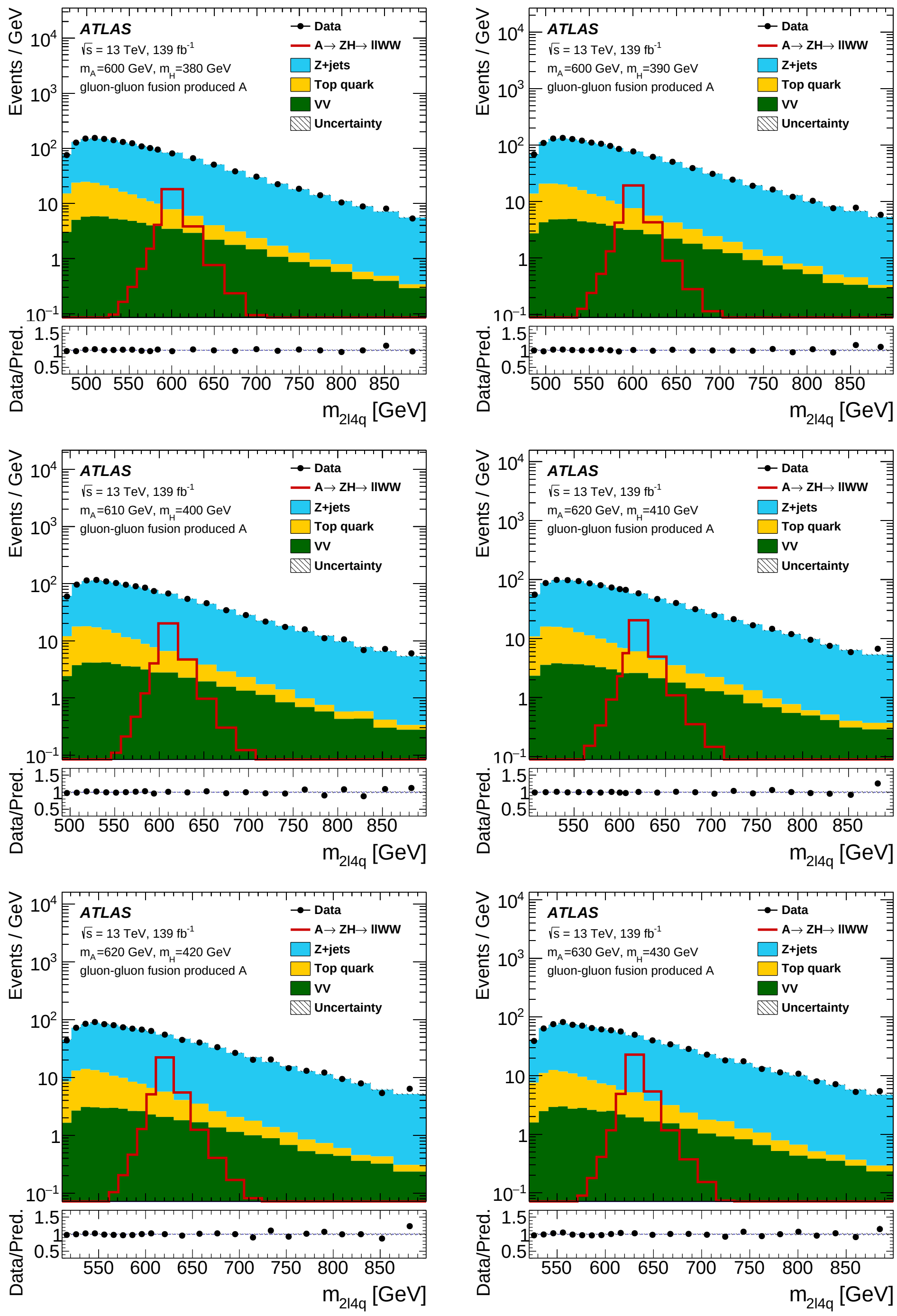

FIGURE A.32: The $m_{2\ell 4q}$ mass distribution for the various m_{4q} windows considered in the $\ell\ell WW$ channel. The number of entries shown in each bin is the number of events in that bin divided by the width of the bin. The same conventions as in Figure 2.4 are used.

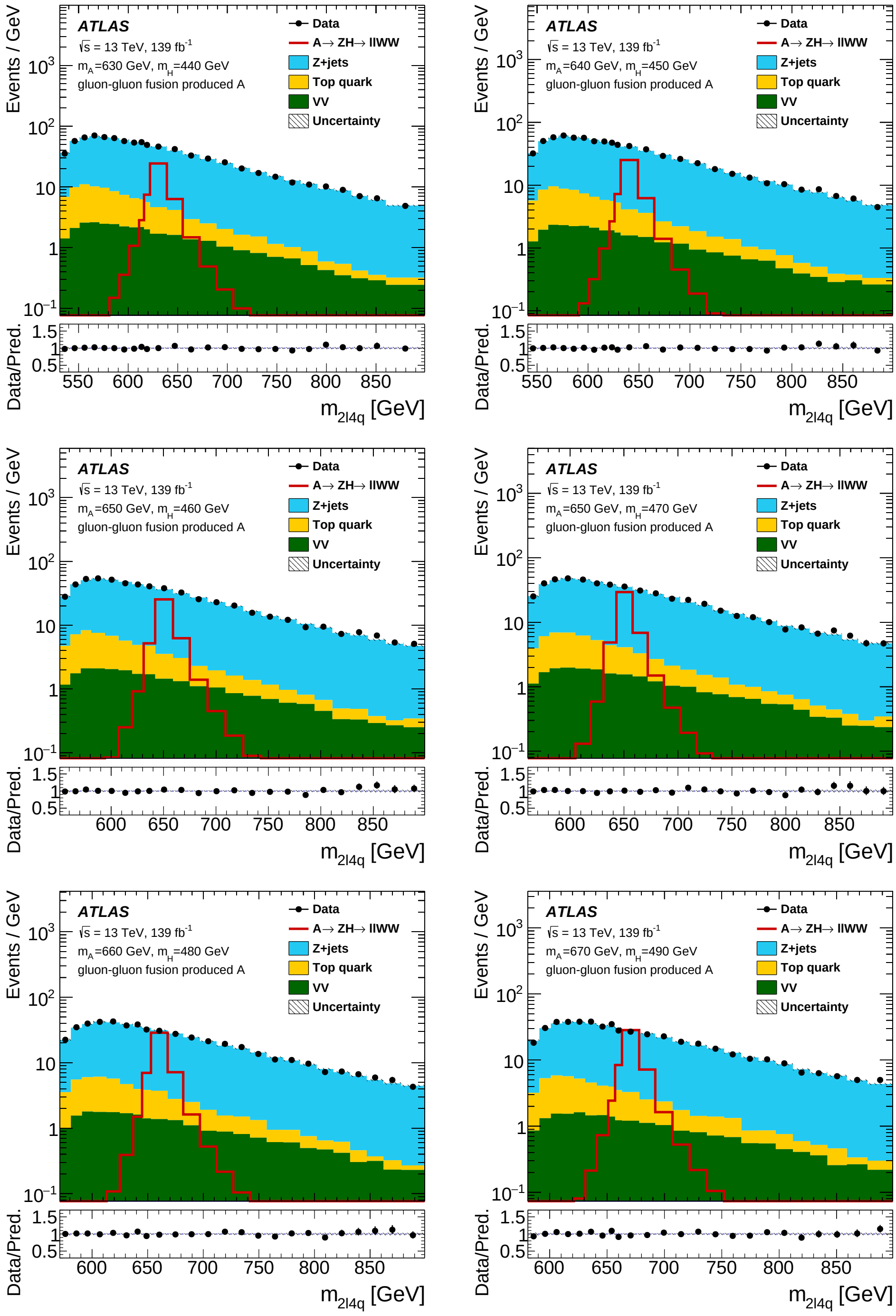

FIGURE A.33: The $m_{2\ell 4q}$ mass distribution for the various m_{4q} windows considered in the $\ell\ell WW$ channel. The number of entries shown in each bin is the number of events in that bin divided by the width of the bin. The same conventions as in Figure 2.4 are used.

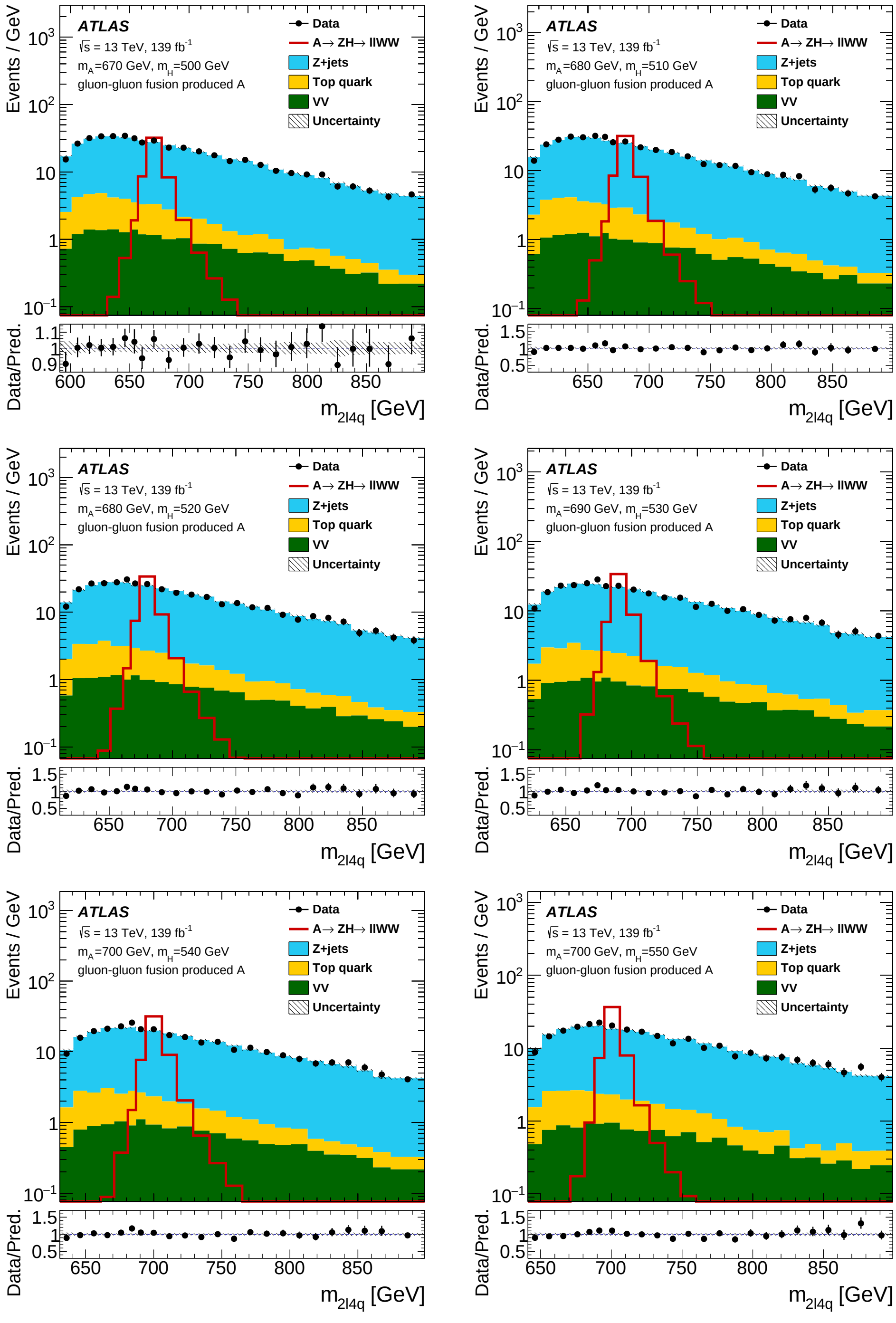

FIGURE A.34: The $m_{2\ell 4q}$ mass distribution for the various m_{4q} windows considered in the $\ell\ell WW$ channel. The number of entries shown in each bin is the number of events in that bin divided by the width of the bin. The same conventions as in Figure 2.4 are used.

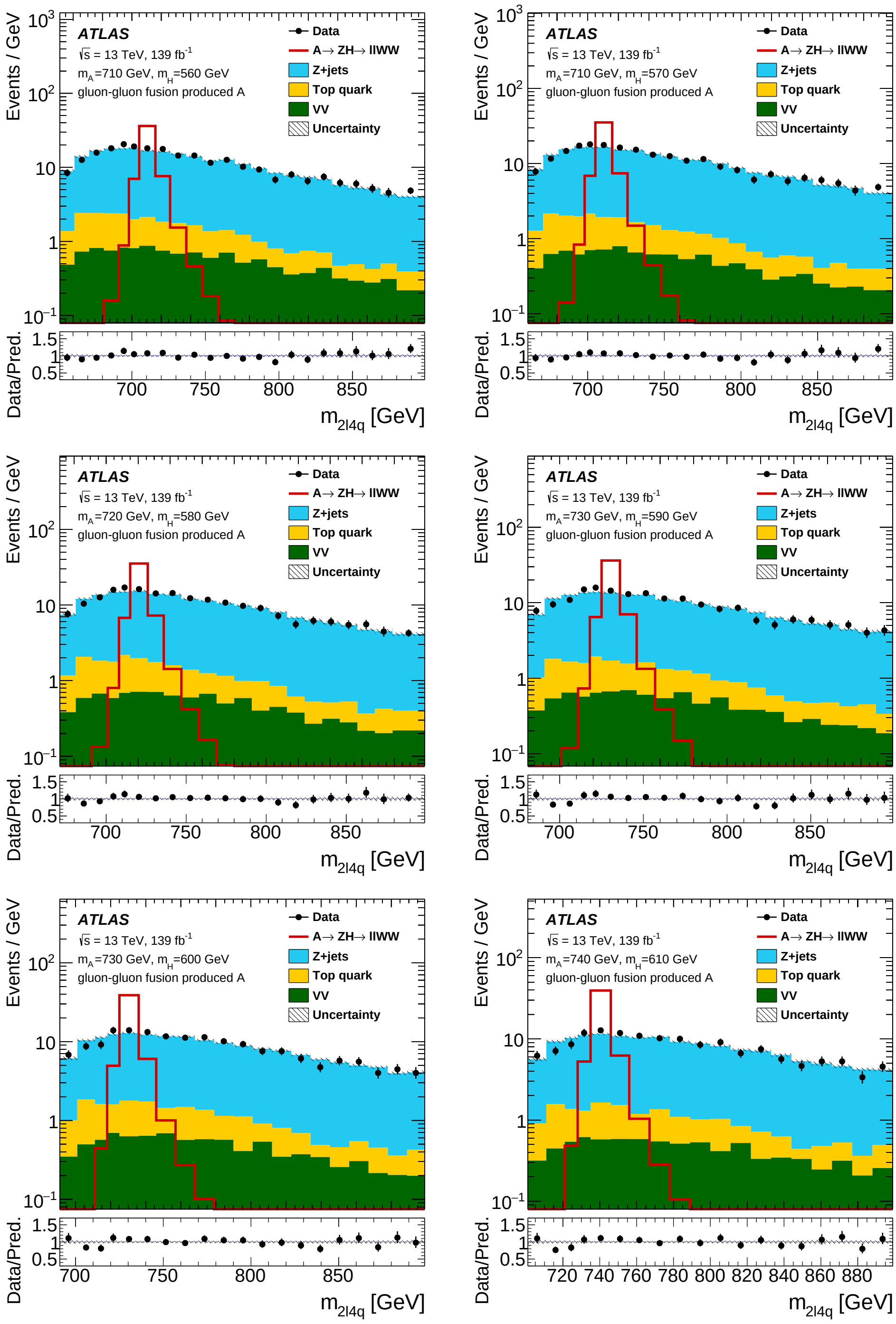

FIGURE A.35: The $m_{2\ell 4q}$ mass distribution for the various m_{4q} windows considered in the $\ell\ell WW$ channel. The number of entries shown in each bin is the number of events in that bin divided by the width of the bin. The same conventions as in Figure 2.4 are used.

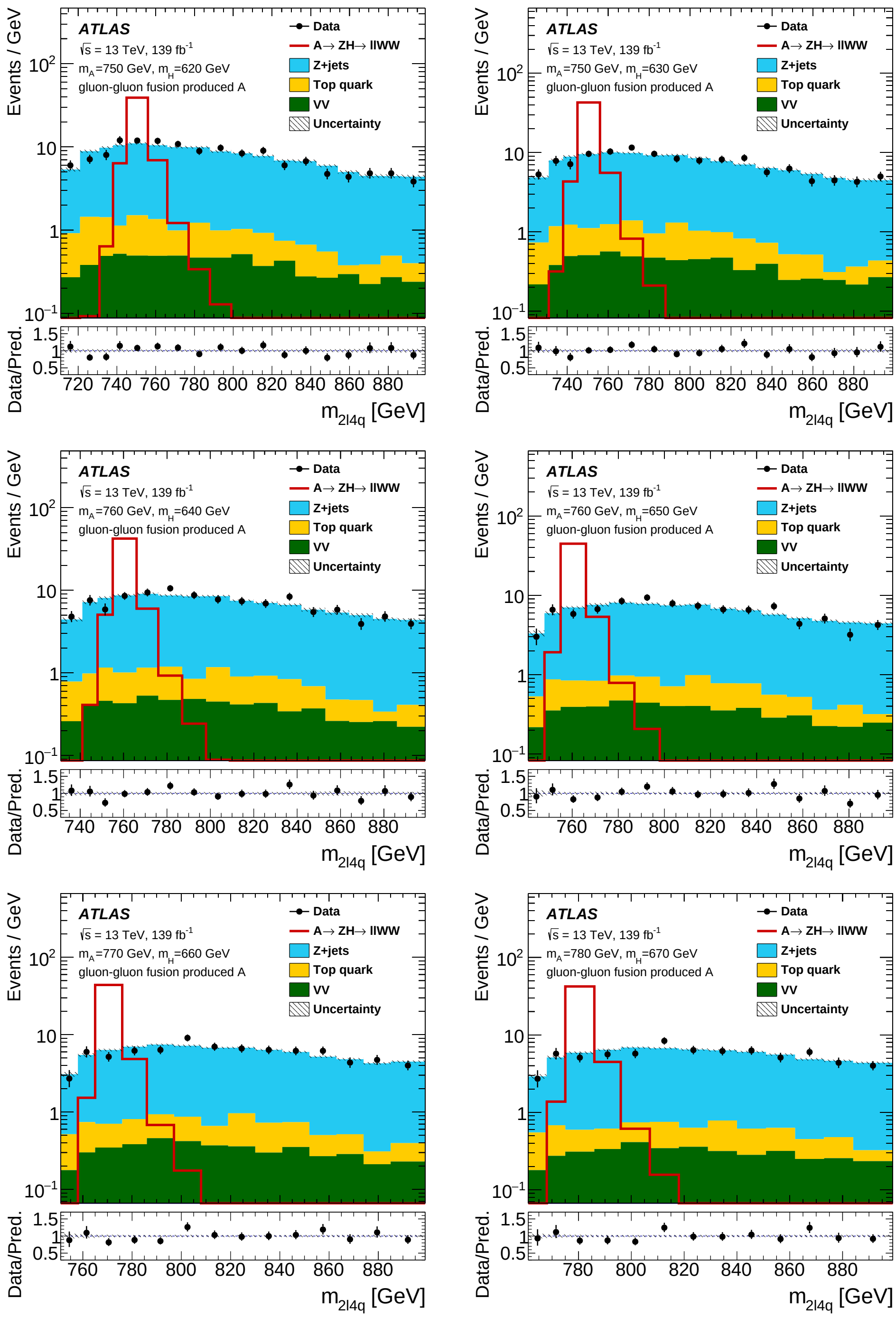

FIGURE A.36: The $m_{2\ell 4q}$ mass distribution for the various m_{4q} windows considered in the $\ell\ell WW$ channel. The number of entries shown in each bin is the number of events in that bin divided by the width of the bin. The same conventions as in Figure 2.4 are used.

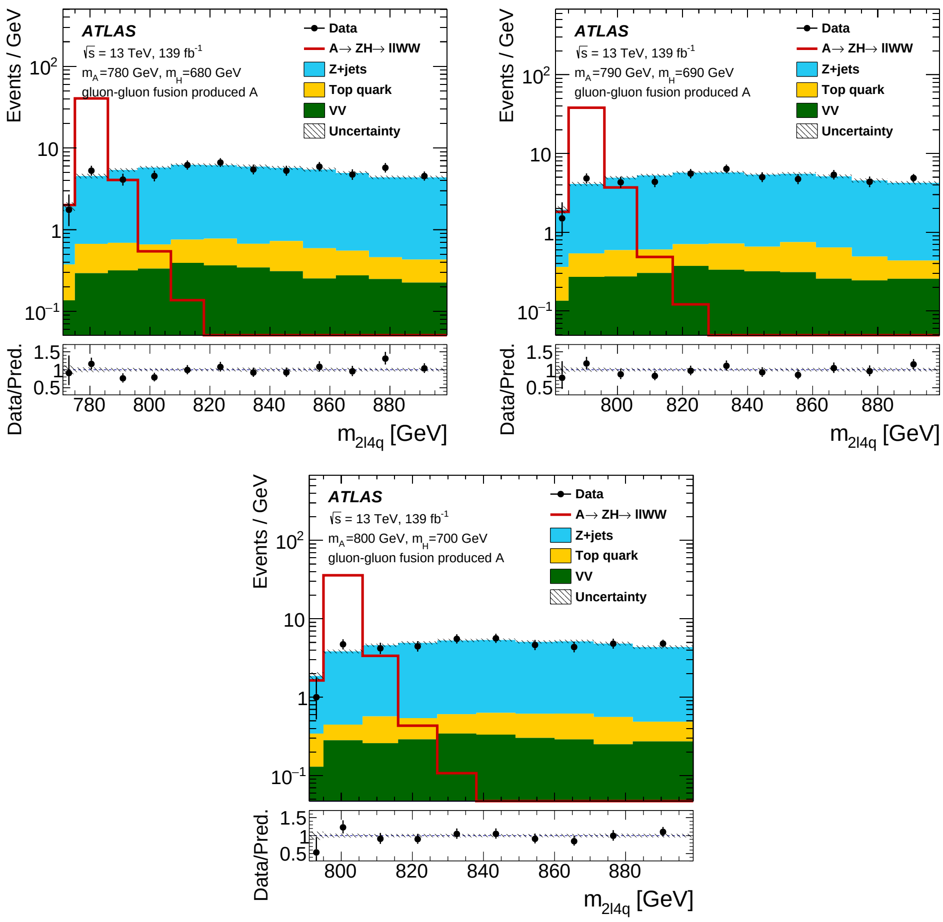

FIGURE A.37: The $m_{2\ell 4q}$ mass distribution for the various m_{4q} windows considered in the $\ell\ell WW$ channel. The number of entries shown in each bin is the number of events in that bin divided by the width of the bin. The same conventions as in Figure 2.4 are used.

Appendix B

Auxiliary Material for Section 4.1

B.1 Polarisation-Dependent Amplitudes

We may derive the amplitudes of neutrino and antineutrino radiative decays specifying the photon polarisation in the final state, $\mathcal{M}(\nu_\mathbf{i} \to \nu_\mathbf{f} + \gamma_\pm)$ and $\mathcal{M}(\bar{\nu}_\mathbf{i} \to \bar{\nu}_\mathbf{f} + \gamma_\pm)$.

We apply the chiral representation, where the γ matrices are given by

$$\gamma^\mu = \begin{pmatrix} 0 & \sigma^\mu \\ \bar{\sigma}^\mu & 0 \end{pmatrix}, \ \sigma^{\mu\nu} = \frac{i}{2}[\gamma^\mu, \gamma^\nu], \ \gamma_5 \equiv i\gamma^0\gamma^1\gamma^2\gamma^3 = \begin{pmatrix} -\mathbf{1} & 0 \\ 0 & \mathbf{1} \end{pmatrix}, \ P_{\mathrm{L,R}} = \frac{1 \mp \gamma_5}{2}, \tag{B.1}$$

and $\sigma^\mu = (\mathbf{1}, \sigma^1, \sigma^2, \sigma^3)$ and $\bar{\sigma}^\mu = (\mathbf{1}, -\sigma^1, -\sigma^2, -\sigma^3)$ and σ^i are Pauli matrices. Given momentum $p = (p_0, \vec{p})$, the normalised particle and antiparticle Dirac spinors are represented by

$$u_S(p) = \begin{pmatrix} \sqrt{p \cdot \sigma}\ \xi_S \\ \sqrt{p \cdot \bar{\sigma}}\ \xi_S \end{pmatrix}, \quad v_S(p) = \begin{pmatrix} \sqrt{p \cdot \sigma}\ \eta_S \\ \sqrt{-p \cdot \bar{\sigma}}\ \eta_S \end{pmatrix}, \tag{B.2}$$

where ξ_S and η_S are two-component spinors normalised to unity. Here, we include the polarisation index S for two independent spinors.

To simplify the derivation, we prefer to work in the rest frame. Frame-independent results can be obtained straightforwardly from this case. In the rest frame, the initial sterile neutrino $\nu_\mathbf{i}$ is at rest $p_\mathbf{i}^\mu = (m_\mathbf{i}, 0, 0, 0)^T$, and the photon is released in the $+z$ direction with momentum $q^\mu = (q, 0, 0, q)^T$. Conservation of momentum requires $p_\mathbf{f}^\mu = (E_\mathbf{f}, 0, 0, -q)^T$ with $q = (m_\mathbf{i}^2 - m_\mathbf{f}^2)/(2m_\mathbf{i})$ and $E_\mathbf{f} = (m_\mathbf{i}^2 + m_\mathbf{f}^2)/(2m_\mathbf{i})$. In this frame, S denotes spin along the $+z$ direction i.e. S_z, which takes values $\pm\frac{1}{2}$. This geometry is shown in Fig. B.1.

The angular momentum along the z direction is conserved $S_z(\nu_\mathbf{i}) = S_z(\nu_\mathbf{f}) + S_z(\gamma)$. For a fermion, $S_z = \pm 1/2$ and for a massless photon, $S_z = \pm 1$. Given the initial state $\nu_\mathbf{i}$ with spin $S_z(\nu_\mathbf{i}) = +1/2(-1/2)$, the only solution for spins in final states is $S_z(\nu_\mathbf{f}) = -1/2(+1/2)$ and $S_z(\gamma) = +1(-1)$. In other words, the released photon is the right-handed γ_+ (left-handed γ_-).

For the photon moving in the $+z$ direction, the polarisation vectors are as defined in [315]

$$\varepsilon_+^\mu = \frac{1}{\sqrt{2}}(0, 1, i, 0), \quad \varepsilon_-^\mu = \frac{1}{\sqrt{2}}(0, 1, -i, 0) \tag{B.3}$$

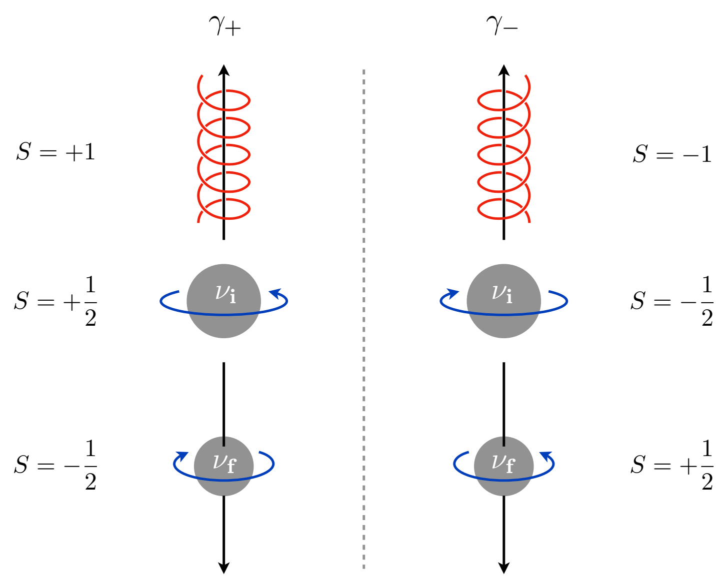

FIGURE B.1: Polarisation for neutrino radiative decay in the rest frame.

correspond to spin $S_z = +1$ and -1, respectively.[1]

In this frame, for the neutrino $\nu_\mathbf{f}$ moving in the $-z$ direction, the spinors $u_S(p)$ and $v_S(p)$ with spin $\pm\frac{1}{2}$ are simplified to

$$\begin{aligned} u_{+\frac{1}{2}}(p_\mathbf{f}) &= \begin{pmatrix} \sqrt{E+q}\;\xi_{+\frac{1}{2}} \\ \sqrt{E-q}\;\xi_{+\frac{1}{2}} \end{pmatrix}, \qquad u_{-\frac{1}{2}}(p_\mathbf{f}) = \begin{pmatrix} \sqrt{E-q}\;\xi_{-\frac{1}{2}} \\ \sqrt{E+q}\;\xi_{-\frac{1}{2}} \end{pmatrix}, \\ v_{+\frac{1}{2}}(p_\mathbf{f}) &= \begin{pmatrix} \sqrt{E+q}\;\eta_{+\frac{1}{2}} \\ -\sqrt{E-q}\;\eta_{+\frac{1}{2}} \end{pmatrix}, \quad v_{-\frac{1}{2}}(p_\mathbf{f}) = \begin{pmatrix} \sqrt{E-q}\;\eta_{-\frac{1}{2}} \\ -\sqrt{E+q}\;\eta_{-\frac{1}{2}} \end{pmatrix}, \end{aligned} \tag{B.4}$$

with

$$\xi_{+\frac{1}{2}} = \eta_{-\frac{1}{2}} = \begin{pmatrix} 1 \\ 0 \end{pmatrix}, \quad \xi_{-\frac{1}{2}} = \eta_{+\frac{1}{2}} = \begin{pmatrix} 0 \\ 1 \end{pmatrix}. \tag{B.5}$$

In the massless case, $u_{+\frac{1}{2}}$ and $u_{-\frac{1}{2}}$ are purely left- and right-handed respectively (because we have assumed $\nu_\mathbf{f}$ is moving in the $-z$ direction). Spinors for initial neutrino $\nu_\mathbf{i}$ and antineutrino $\bar{\nu}_\mathbf{i}$ are given by

$$\begin{aligned} u_{+\frac{1}{2}}(p_\mathbf{i}) &= \sqrt{E}\begin{pmatrix} \xi_{+\frac{1}{2}} \\ \xi_{+\frac{1}{2}} \end{pmatrix}, \qquad u_{-\frac{1}{2}}(p_\mathbf{i}) = \sqrt{E}\begin{pmatrix} \xi_{-\frac{1}{2}} \\ \xi_{-\frac{1}{2}} \end{pmatrix}, \\ v_{+\frac{1}{2}}(p_\mathbf{i}) &= \sqrt{E}\begin{pmatrix} \eta_{+\frac{1}{2}} \\ -\eta_{+\frac{1}{2}} \end{pmatrix}, \quad v_{-\frac{1}{2}}(p_\mathbf{i}) = \sqrt{E}\begin{pmatrix} \eta_{-\frac{1}{2}} \\ -\eta_{-\frac{1}{2}} \end{pmatrix}, \end{aligned} \tag{B.6}$$

[1]Here we apply the convention in the textbook [315]. The definition of ϵ_+ in this convention has a sign difference from the one shown in [309]. Using the convention in [309] leads to a sign difference for $i\mathcal{M}(\nu_{\mathbf{i},+\frac{1}{2}} \to \nu_{\mathbf{f},-\frac{1}{2}} + \gamma_+)$ and $i\mathcal{M}(\bar{\nu}_{\mathbf{i},+\frac{1}{2}} \to \bar{\nu}_{\mathbf{f},-\frac{1}{2}} + \gamma_+)$ in Eqs. (4.5) and (4.10) and $i\mathcal{M}^{\mathrm{M}}(\nu_{\mathbf{i},+\frac{1}{2}} \to \nu_{\mathbf{f},-\frac{1}{2}} + \gamma_+)$ in Eq. (4.23).

The amplitudes with definite spins in the initial and final states are then given by

$$
\begin{aligned}
\mathcal{M}(\nu_{\mathbf{i},+\frac{1}{2}} \to \nu_{\mathbf{f},-\frac{1}{2}} + \gamma_+) &= +\sqrt{2} f^{\mathrm{L}}_{\mathbf{fi}} (m^2_{\mathbf{i}} - m^2_{\mathbf{f}}) \,, \\
\mathcal{M}(\nu_{\mathbf{i},-\frac{1}{2}} \to \nu_{\mathbf{f},+\frac{1}{2}} + \gamma_-) &= -\sqrt{2} f^{\mathrm{R}}_{\mathbf{fi}} (m^2_{\mathbf{i}} - m^2_{\mathbf{f}}) \,, \\
\mathcal{M}(\bar{\nu}_{\mathbf{i},+\frac{1}{2}} \to \bar{\nu}_{\mathbf{f},-\frac{1}{2}} + \gamma_+) &= -\sqrt{2} \bar{f}^{\mathrm{L}}_{\mathbf{if}} (m^2_{\mathbf{i}} - m^2_{\mathbf{f}}) \,, \\
\mathcal{M}(\bar{\nu}_{\mathbf{i},-\frac{1}{2}} \to \bar{\nu}_{\mathbf{f},+\frac{1}{2}} + \gamma_-) &= +\sqrt{2} \bar{f}^{\mathrm{R}}_{\mathbf{if}} (m^2_{\mathbf{i}} - m^2_{\mathbf{f}}) \,,
\end{aligned} \tag{B.7}
$$

Here, $\nu_{\mathbf{i},+\frac{1}{2}} \to \nu_{\mathbf{f},-\frac{1}{2}} + \gamma_+$ and $\bar{\nu}_{\mathbf{i},-\frac{1}{2}} \to \bar{\nu}_{\mathbf{f},+\frac{1}{2}} + \gamma_-$ are CP conjugates, while $\nu_{\mathbf{i},-\frac{1}{2}} \to \nu_{\mathbf{f},+\frac{1}{2}} + \gamma_-$ and $\bar{\nu}_{\mathbf{i},+\frac{1}{2}} \to \bar{\nu}_{\mathbf{f},-\frac{1}{2}} + \gamma_+$ are CP conjugates. The other channels have vanishing amplitudes, consistent with angular momentum conservation.

We can generalise the result in Eq. (B.7) to any inertial reference frame via spatial rotations and Lorentz boosts. These transformations change spins for fermions but leave photon polarisation invariant. Eventually, we obtain the Lorentz-invariant amplitudes $\mathcal{M}(\nu_{\mathbf{i}} \to \nu_{\mathbf{f}} + \gamma_\pm)$ and $\mathcal{M}(\bar{\nu}_{\mathbf{i}} \to \bar{\nu}_{\mathbf{f}} + \gamma_\pm)$ taking the same result as Eq. (B.7) in any reference frame. Using the CPT-invariance property, namely, $\bar{f}^{\mathrm{R,L}}_{\mathbf{if}} = -f^{\mathrm{R,L}}_{\mathbf{if}}$, we eventually arrive at Eqs. (4.5) and (4.10). These are the most general results independent of either particle model or reference frame.

B.2 Derivation of Imaginary Parts of the Loop Integrals

The two NP contributions to the sterile neutrino radiative decay given by the new proposed interactions are shown in Fig. 4.2. In order to compute their respective matrix elements, we use the couplings of the new particles ϕ and ψ with neutrinos and sterile neutrinos shown in Section 4.1.7.

In general, we have

$$
i\mathcal{M}(\nu_s \to \nu_i + \gamma_\pm) = i\overline{u}(p_i)\Gamma^\mu_{is}(q^2)u(p_s)\varepsilon^*_{\pm,\mu}(q) \tag{B.8}
$$

and the matrix elements for each loop contribution, $\mathcal{M}_j \equiv \mathcal{M}_j(\nu_s \to \nu_i + \gamma_\pm)$, shown in Fig. 4.2 take the form

$$
\begin{aligned}
i\mathcal{M}_1 &= -Qe\lambda_s\lambda_i^* \int \frac{d^4k}{(2\pi)^4} \frac{\overline{u}(p_i)P_{\mathrm{R}}(\not{k} + m_\psi)(p_1 - p_2)^\mu P_{\mathrm{L}} u(p_s)\varepsilon^*_{\pm,\mu}(q)}{(k^2 - m^2_\psi + i\epsilon)((k-p_s)^2 - m^2_\phi + i\epsilon)((k-p_i)^2 - m^2_\phi + i\epsilon)} \,, \\
i\mathcal{M}_2 &= +Qe\lambda_s\lambda_i^* \int \frac{d^4k}{(2\pi)^4} \frac{\overline{u}(p_i)P_{\mathrm{R}}(\not{k}' + m_\psi)\gamma^\mu(\not{k} + m_\psi)P_{\mathrm{L}} u(p_s)\varepsilon^*_{\pm,\mu}(q)}{((k-p_s)^2 - m^2_\phi + i\epsilon)(k'^2 - m^2_\psi + i\epsilon)(k^2 - m^2_\psi + i\epsilon)} \,.
\end{aligned} \tag{B.9}
$$

Due to the projection operators, the matrix elements reduce to

$$
\begin{aligned}
i\mathcal{M}_1 &= -Qe\lambda_s\lambda_i^* \int \frac{d^4k}{(2\pi)^4} \frac{\overline{u}(p_i)\not{k}(p_1 - p_2)^\mu P_{\mathrm{L}} u(p_s)\varepsilon^*_{\pm,\mu}(q)}{(k^2 - m^2_\psi + i\epsilon)((k-p_s)^2 - m^2_\phi + i\epsilon)((k-p_i)^2 - m^2_\phi + i\epsilon)} \\
i\mathcal{M}_2 &= +Qe\lambda_s\lambda_i^* \int \frac{d^4k}{(2\pi)^4} \frac{\overline{u}(p_i)\not{k}'\gamma^\mu\not{k}P_{\mathrm{L}} u(p_s)\varepsilon^*_{\pm,\mu}(q)}{((k-p_s)^2 - m^2_\phi + i\epsilon)(k'^2 - m^2_\psi + i\epsilon)(k^2 - m^2_\psi + i\epsilon)} \,.
\end{aligned} \tag{B.10}
$$

In order to perform dimensional regularisation to Eq. (B.10), we must substitute the denominator with the relevant Feynman parameters, therefore, we perform the loop momentum shifts $\ell = k - (xp_s + zp_i)$ and $\ell = k - (xp_s + zq)$ for the two diagrams respectively. This leads to

$$
\begin{aligned}
i\mathcal{M}_1 &= -Qe\lambda_s\lambda_i^* \int \frac{d^d\ell}{(2\pi)^d} \int dxdydz\delta(x+y+z-1)\times \\
&\times \frac{\overline{u}(p_i)[-2\ell^\mu \not{\ell} + (p_s+p_i)^\mu(\not{p}_s y + \not{p}_i z) - 2(p_s y + p_i z)^\mu(\not{p}_s y + \not{p}_i z)]P_\mathrm{L} u(p_s)\varepsilon^*_{\pm,\mu}(q)}{(\ell^2 - \Delta_{\phi\psi}(x,y,z))^3}\,, \\
i\mathcal{M}_2 &= +Qe\lambda_s\lambda_i^* \int \frac{d^d\ell}{(2\pi)^d} \int dxdydz\delta(x+y+z-1)\times \\
&\times \frac{\overline{u}(p_i)[\not{\ell}\gamma^\mu\not{\ell} + (\not{q}(z-1) + \not{p}_s x)\gamma^\mu(\not{q}z + \not{p}_s x)]P_\mathrm{L} u(p_s)\varepsilon^*_{\pm,\mu}(q)}{(\ell^2 - \Delta_{\psi\phi}(x,y,z))^3}\,, \qquad \text{(B.11)}
\end{aligned}
$$

where $\Delta_{\phi\psi}(x,y,z)$ and $\Delta_{\psi\phi}(x,y,z)$ have been defined in Eq. (4.84). We ignore linear terms of ℓ since these terms vanish after integration. We use the following results from [315] for d-dimensional integrals over ℓ in Minkowski space

$$
\begin{aligned}
\int \frac{d^d\ell}{(2\pi)^d}\frac{1}{(\ell^2-\Delta)^n} &= \frac{(-1)^n}{(4\pi)^{d/2}}\frac{\Gamma(n-d/2)}{\Gamma(n)}\left(\frac{1}{\Delta}\right)^{n-\frac{d}{2}} \\
\int \frac{d^d\ell}{(2\pi)^d}\frac{\ell^\alpha\ell^\beta}{(\ell^2-\Delta)^n} &= i\frac{(-1)^{n-1}}{(4\pi)^{d/2}}\frac{g^{\alpha\beta}}{2}\frac{\Gamma(n-d/2-1)}{\Gamma(n)}\left(\frac{1}{\Delta}\right)^{n-\frac{d}{2}-1}. \qquad \text{(B.12)}
\end{aligned}
$$

After dimensional regularisation, we set $d = 4-\epsilon$, therefore the amplitudes acquire the following general form

$$
\begin{aligned}
i\mathcal{M}_1 =& \frac{-iQe\lambda_s\lambda_i^*}{(4\pi)^2}\int dxdydz\delta(x+y+z-1)\overline{u}(p_i)\times \\
&\times\left[\left(-\frac{2}{\epsilon} + \log\frac{\Delta_{\phi\psi}(x,y,z)}{4\pi} + \gamma_\epsilon + \mathcal{O}(\epsilon)\right)\gamma^\mu\right. \\
&\left.-\frac{(p_s+p_i)^\mu(\not{p}_s y + \not{p}_i z) - 2(p_s y + p_i z)^\mu(\not{p}_s y + \not{p}_i z)]}{\Delta_{\phi\psi}(x,y,z)}\right]P_\mathrm{L}u(p_s)\varepsilon^*_{\pm,\mu}(q)\,, \\
i\mathcal{M}_2 =& \frac{+iQe\lambda_s\lambda_i^*}{(4\pi)^2}\int dxdydz\delta(x+y+z-1)\overline{u}(p_i)\times \\
&\times\left[\left(-\frac{2}{\epsilon} + 1 + \log\frac{\Delta_{\psi\phi}(x,y,z)}{4\pi} + \gamma_\epsilon + \mathcal{O}(\epsilon)\right)\gamma^\mu\right. \\
&\left.-\frac{(\not{q}(z-1)+\not{p}_s x)\gamma^\mu(\not{q}z + \not{p}_s x)}{\Delta_{\psi\phi}(x,y,z)}\right]P_\mathrm{L}u(p_s)\varepsilon^*_{\pm,\mu}(q). \qquad \text{(B.13)}
\end{aligned}
$$

We simplify the above expressions by making use of the following identities

$$
\begin{aligned}
\overline{u}(p_i)(p_s+p_i)^\mu P_\mathrm{L}u(p_s) &= \overline{u}(p_i)[\gamma^\mu(m_sP_\mathrm{R} + m_iP_\mathrm{L}) + i\sigma^{\mu\nu}q_\nu P_\mathrm{L}]u(p_s)\,, \\
\overline{u}(p_i)(\not{p}_s + \not{p}_i)\gamma^\mu P_\mathrm{L}u(p_s) &= \overline{u}(p_i)[2m_i\gamma^\mu P_\mathrm{L} + i\sigma^{\mu\nu}q_\nu P_\mathrm{L} + q^\mu P_\mathrm{L}]u(p_s)\,, \\
\overline{u}(p_i)\gamma^\mu(\not{p}_s + \not{p}_i)P_\mathrm{L}u(p_s) &= \overline{u}(p_i)[2m_s\gamma^\mu P_\mathrm{R} + i\sigma^{\mu\nu}q_\nu P_\mathrm{L} - q^\mu P_\mathrm{L}]u(p_s)\,. \qquad \text{(B.14)}
\end{aligned}
$$

Finally, applying the Ward identity $q^\mu \mathcal{M}_\mu = 0$ and ignoring terms proportional to γ^μ, since these are simply vertex corrections to the overall electric charge,[2] we only need to consider the tensor-like terms within Γ^μ_{is} to determine the form factor resulting from these diagrams. These are given by

$$\begin{aligned}
\Gamma^\mu_{is,1} &= -\frac{Qe\lambda_s\lambda_i^*}{(4\pi)^2} i\sigma^{\mu\nu}q_\nu \int_0^1 \mathrm{d}x\mathrm{d}y\mathrm{d}z\delta(x+y+z-1)\frac{(m_s y P_\mathrm{R} + m_i z P_\mathrm{L})}{\Delta_{\phi\psi}(x,y,z)} \\
\Gamma^\mu_{is,2} &= +\frac{Qe\lambda_s\lambda_i^*}{(4\pi)^2} i\sigma^{\mu\nu}q_\nu \int_0^1 \mathrm{d}x\mathrm{d}y\mathrm{d}z\delta(x+y+z-1)\frac{(m_s xy P_\mathrm{R} + m_i xz P_\mathrm{L})}{\Delta_{\psi\phi}(x,y,z)} .
\end{aligned} \tag{B.15}$$

Setting $m_i \to 0$ for the active neutrino mass in Eq. (B.15) and integrating over z yields

$$\begin{aligned}
\Gamma^\mu_{is,1} &= \frac{C_1}{(4\pi)^2} i\sigma^{\mu\nu}q_\nu \int_0^1 \int_0^{1-y} \mathrm{d}x\mathrm{d}y \frac{m_s y P_\mathrm{R}}{m_\phi^2(1-x) + x m_\psi^2 - xy m_s^2} \\
\Gamma^\mu_{is,2} &= \frac{C_2}{(4\pi)^2} i\sigma^{\mu\nu}q_\nu \int_0^1 \int_0^{1-y} \mathrm{d}x\mathrm{d}y \frac{m_s xy P_\mathrm{R}}{m_\psi^2(1-x) + x m_\phi^2 - xy m_s^2} .
\end{aligned} \tag{B.16}$$

From these last expressions, we can identify the factors $K^\mathrm{L}_{1,2}$ and $K^\mathrm{R}_{1,2}$ given in Eq. (4.43) and then integrate over the remaining Feynman parameters x and y as shown in Eq. (4.45).

[2] Notice that when both contributions are added the divergent terms cancel out.

Bibliography

[1] ATLAS collaboration, G. Aad et al., *Search for a heavy Higgs boson decaying into a Z boson and another heavy Higgs boson in the $\ell\ell bb$ and $\ell\ell WW$ final states in pp collisions at $\sqrt{s} = 13$ TeV with the ATLAS detector*, 2011.05639.

[2] S. Balaji, M. Spannowsky and C. Tamarit, *Cosmological bubble friction in local equilibrium*, *Journal of Cosmology and Astroparticle Physics* **2021** (mar, 2021) 051.

[3] S. Balaji, M. Ramirez-Quezada and Y.-L. Zhou, *CP violation and circular polarisation in neutrino radiative decay*, *JHEP* **04** (2020) 178, [1910.08558].

[4] S. Balaji, M. Ramirez-Quezada and Y.-L. Zhou, *CP violation in neutral lepton transition dipole moment*, *JHEP* **12** (2020) 090, [2008.12795].

[5] S. Balaji, *CP asymmetries in the rare top decays $t \to c\gamma$ and $t \to cg$*, *Phys. Rev. D* **102** (2020) 113010, [2009.03315].

[6] S. Balaji, R. Foot and M. A. Schmidt, *Chiral SU(4) explanation of the $b \to s$ anomalies*, *Phys. Rev.* **D99** (2019) 015029, [1809.07562].

[7] S. Balaji and M. A. Schmidt, *Unified SU(4) theory for the $R_{D^{(*)}}$ and $R_{K^{(*)}}$ anomalies*, *Phys. Rev. D* **101** (2020) 015026, [1911.08873].

[8] S. Tomonaga, *On a relativistically invariant formulation of the quantum theory of wave fields*, *Prog. Theor. Phys.* **1** (1946) 27–42.

[9] J. S. Schwinger, *On Quantum electrodynamics and the magnetic moment of the electron*, *Phys. Rev.* **73** (1948) 416–417.

[10] J. S. Schwinger, *Quantum electrodynamics. I A covariant formulation*, *Phys. Rev.* **74** (1948) 1439.

[11] R. P. Feynman, *Space - time approach to quantum electrodynamics*, *Phys. Rev.* **76** (1949) 769–789.

[12] R. P. Feynman, *The Theory of positrons*, *Phys. Rev.* **76** (1949) 749–759.

[13] R. P. Feynman, *Mathematical formulation of the quantum theory of electromagnetic interaction*, *Phys. Rev.* **80** (1950) 440–457.

[14] S. Weinberg, *A Model of Leptons*, *Phys. Rev. Lett.* **19** (1967) 1264–1266.

[15] A. Salam, *Weak and Electromagnetic Interactions*, *Conf. Proc. C* **680519** (1968) 367–377.

[16] A. Pich, *Aspects of quantum chromodynamics*, in *ICTP Summer School in Particle Physics*, pp. 53–102, 6, 1999, `hep-ph/0001118`.

[17] D. S. Nielsen, *In search of new Higgs bosons*, Ph.D. thesis, Niels Bohn Institute.

[18] G. Arnison, A. Astbury, B. Aubert, C. Bacci, G. Bauer, A. Bézaguet et al., *Experimental observation of isolated large transverse energy electrons with associated missing energy at s=540 gev*, *Physics Letters B* **122** (1983) 103 – 116.

[19] M. Banner, R. Battiston, P. Bloch, F. Bonaudi, K. Borer, M. Borghini et al., *Observation of single isolated electrons of high transverse momentum in events with missing transverse energy at the cern pp collider*, *Physics Letters B* **122** (1983) 476 – 485.

[20] G. Arnison, A. Astbury, B. Aubert, C. Bacci, G. Bauer, A. Bézaguet et al., *Experimental observation of lepton pairs of invariant mass around 95 gev/c2 at the cern sps collider*, *Physics Letters B* **126** (1983) 398 – 410.

[21] P. Bagnaia, M. Banner, R. Battiston, P. Bloch, F. Bonaudi, K. Borer et al., *Evidence for z0→e+e at the cern pp collider*, *Physics Letters B* **129** (1983) 130 – 140.

[22] G. S. Guralnik, C. R. Hagen and T. W. B. Kibble, *Global conservation laws and massless particles*, *Phys. Rev. Lett.* **13** (Nov, 1964) 585–587.

[23] F. Englert and R. Brout, *Broken symmetry and the mass of gauge vector mesons*, *Phys. Rev. Lett.* **13** (Aug, 1964) 321–323.

[24] P. W. Higgs, *Broken symmetries and the masses of gauge bosons*, *Phys. Rev. Lett.* **13** (Oct, 1964) 508–509.

[25] Particle Data Group collaboration, K. Olive et al., *Review of Particle Physics*, *Chin. Phys. C* **38** (2014) 090001.

[26] Particle Data Group Collaboration, J. Beringer et al., *Review of particle physics*, *Phys. Rev. D* **86** (2012) 010001.

[27] N. Cabibbo, *Unitary Symmetry and Leptonic Decays*, *Phys. Rev. Lett.* **10** (1963) 531–533.

[28] L.-L. Chau and W.-Y. Keung, *Comments on the parametrization of the kobayashi-maskawa matrix*, *Phys. Rev. Lett.* **53** (Nov, 1984) 1802–1805.

[29] M. Kobayashi and T. Maskawa, *CP Violation in the Renormalizable Theory of Weak Interaction*, *Prog. Theor. Phys.* **49** (1973) 652–657.

[30] J. H. Christenson, J. W. Cronin, V. L. Fitch and R. Turlay, *Evidence for the 2π decay of the k_2^0 meson*, *Phys. Rev. Lett.* **13** (Jul, 1964) 138–140.

[31] A. D. Sakharov, *Violation of CP Invariance, C asymmetry, and baryon asymmetry of the universe*, *Sov. Phys. Usp.* **34** (1991) 392–393.

[32] S. Bruggisser, *Flavour cosmology: Electroweak baryogenesis from varying Yukawas*, Ph.D. thesis, Hamburg U., Hamburg, 2018. 10.3204/PUBDB-2019-01768.

[33] M. Thomson, *Modern particle physics.* Cambridge University Press, New York, 2013.

[34] T. D. Lee, *A Theory of Spontaneous T Violation*, *Phys. Rev. D* **8** (1973) 1226–1239.

[35] G. C. Branco et al., *Theory and phenomenology of two-Higgs-doublet models*, *Phys. Rept.* **516** (2012) 1, [1106.0034].

[36] G. C. Dorsch, S. J. Huber, K. Mimasu and J. M. No, *Echoes of the Electroweak Phase Transition: Discovering a second Higgs doublet through* $A_0 \to ZH_0$, *Phys. Rev. Lett.* **113** (2014) 211802, [1405.5537].

[37] N. Turok and J. Zadrozny, *Electroweak baryogenesis in the two-doublet model*, *Nucl. Phys. B* **358** (1991) 471–493.

[38] L. Fromme, S. J. Huber and M. Seniuch, *Baryogenesis in the two-Higgs doublet model*, *JHEP* **11** (2006) 038, [hep-ph/0605242].

[39] P. Basler, M. Krause, M. Mühlleitner, J. Wittbrodt and A. Wlotzka, *Strong first order electroweak phase transition in the CP-conserving 2HDM revisited*, *JHEP* **02** (2017) 121, [1612.04086].

[40] A. G. Cohen, D. B. Kaplan and A. E. Nelson, *Progress in electroweak baryogenesis*, *Ann. Rev. Nucl. Part. Sci.* **43** (1993) 27–70, [hep-ph/9302210].

[41] J. Abdallah et al., *Simplified models for dark matter searches at the LHC*, *Phys. Dark Univ.* **9-10** (2015) 8–23, [1506.03116].

[42] S. F. King, *Neutrino mass models*, *Rept. Prog. Phys.* **67** (2004) 107–158, [hep-ph/0310204].

[43] R. D. Peccei and H. R. Quinn, *Constraints Imposed by CP Conservation in the Presence of Instantons*, *Phys. Rev. D* **16** (1977) 1791–1797.

[44] M. Carena and H. E. Haber, *Higgs Boson Theory and Phenomenology*, *Prog. Part. Nucl. Phys.* **50** (2003) 63–152, [hep-ph/0208209].

[45] D. Kominis, *The Phenomenology of the CP odd scalar in two doublet models*, *Nucl. Phys. B* **427** (1994) 575–613, [hep-ph/9402339].

[46] ATLAS collaboration, M. Aaboud et al., *Search for Heavy Higgs Bosons A/H Decaying to a Top Quark Pair in pp Collisions at* $\sqrt{s} = 8$ TeV *with the ATLAS Detector*, *Phys. Rev. Lett.* **119** (2017) 191803, [1707.06025].

[47] R. V. Harlander, S. Liebler and H. Mantler, *SusHi: A program for the calculation of Higgs production in gluon fusion and bottom-quark annihilation in the Standard Model and the MSSM*, *Comp. Phys. Commun.* **184** (2013) 1605, [1212.3249].

[48] R. V. Harlander, S. Liebler and H. Mantler, *SusHi Bento: Beyond NNLO and the heavy-top limit*, *Comput. Phys. Commun.* **212** (2017) 239–257, [1605.03190].

[49] R. V. Harlander and W. B. Kilgore, *Next-to-Next-to-Leading Order Higgs Production at Hadron Colliders*, *Phys. Rev. Lett.* **88** (2002) 201801, [hep-ph/0201206].

[50] R. Harlander and W. B. Kilgore, *Higgs boson production in bottom quark fusion at next-to-next-to-leading order*, *Phys. Rev. D* **68** (2003) 013001, [hep-ph/0304035].

[51] U. Aglietti, R. Bonciani, G. Degrassi and A. Vicini, *Two loop light fermion contribution to Higgs production and decays*, *Phys. Lett. B* **595** (2004) 432, [hep-ph/0404071].

[52] R. Bonciani, G. Degrassi and A. Vicini, *On the Generalized Harmonic Polylogarithms of One Complex Variable*, *Comput. Phys. Commun.* **182** (2011) 1253, [1007.1891].

[53] R. Harlander and P. Kant, *Higgs production and decay: Analytic results at next-to-leading order QCD*, *JHEP* **12** (2005) 015, [hep-ph/0509189].

[54] A. Buckley, J. Ferrando, S. Lloyd, K. Nordstr, B. Page, M. Renacht et al., *LHAPDF6: parton density access in the LHC precision era*, *Eur. Phys. J. C* **75** (2015) 132, [1412.7420].

[55] D. Eriksson, J. Rathsman and O. Stal, *2HDMC: Two-Higgs-doublet model calculator*, *Comput. Phys. Commun.* **181** (2010) 833–834.

[56] ATLAS collaboration, M. Aaboud et al., *Search for a heavy Higgs boson decaying into a Z boson and another heavy Higgs boson in the $\ell\ell bb$ final state in pp collisions at $\sqrt{s} = 13$ TeV with the ATLAS detector*, *Phys. Lett. B* **783** (2018) 392–414, [1804.01126].

[57] J. Haller, A. Hoecker, R. Kogler, K. Mönig, T. Peiffer and J. Stelzer, *Update of the global electroweak fit and constraints on two-Higgs-doublet models*, *Eur. Phys. J. C* **78** (2018) 675, [1803.01853].

[58] ATLAS collaboration, G. Aad et al., *Combined measurements of Higgs boson production and decay using up to 80 fb^{-1} of proton-proton collision data at $\sqrt{s} = 13$ TeV collected with the ATLAS experiment*, *Phys. Rev. D* **101** (2020) 012002, [1909.02845].

[59] E. Witten, *Cosmic Separation of Phases*, *Phys. Rev. D* **30** (1984) 272–285.

[60] M. Kamionkowski, A. Kosowsky and M. S. Turner, *Gravitational radiation from first order phase transitions*, *Phys. Rev. D* **49** (1994) 2837–2851, [astro-ph/9310044].

[61] T. Konstandin and J. M. No, *Hydrodynamic obstruction to bubble expansion*, *JCAP* **02** (2011) 008, [1011.3735].

[62] A. Kosowsky and M. S. Turner, *Gravitational radiation from colliding vacuum bubbles: envelope approximation to many bubble collisions*, *Phys. Rev. D* **47** (1993) 4372–4391, [astro-ph/9211004].

[63] C. Caprini, R. Durrer, T. Konstandin and G. Servant, *General Properties of the Gravitational Wave Spectrum from Phase Transitions*, *Phys. Rev. D* **79** (2009) 083519, [0901.1661].

[64] G. Gogoberidze, T. Kahniashvili and A. Kosowsky, *The Spectrum of Gravitational Radiation from Primordial Turbulence*, *Phys. Rev. D* **76** (2007) 083002, [0705.1733].

[65] C. Caprini, R. Durrer and G. Servant, *The stochastic gravitational wave background from turbulence and magnetic fields generated by a first-order phase transition*, *JCAP* **12** (2009) 024, [0909.0622].

[66] G. D. Moore and T. Prokopec, *How fast can the wall move? A Study of the electroweak phase transition dynamics*, *Phys. Rev. D* **52** (1995) 7182–7204, [hep-ph/9506475].

[67] P. John and M. G. Schmidt, *Do stops slow down electroweak bubble walls?*, *Nucl. Phys. B* **598** (2001) 291–305, [hep-ph/0002050].

[68] D. Bodeker and G. D. Moore, *Can electroweak bubble walls run away?*, *JCAP* **05** (2009) 009, [0903.4099].

[69] D. J. Weir, *Gravitational waves from a first order electroweak phase transition: a brief review*, *Phil. Trans. Roy. Soc. Lond. A* **376** (2018) 20170126, [1705.01783].

[70] H. Kurki-Suonio and M. Laine, *Real time history of the cosmological electroweak phase transition*, *Phys. Rev. Lett.* **77** (1996) 3951–3954, [hep-ph/9607382].

[71] J. R. Espinosa, T. Konstandin, J. M. No and G. Servant, *Energy Budget of Cosmological First-order Phase Transitions*, *JCAP* **06** (2010) 028, [1004.4187].

[72] I. Affleck, *Quantum Statistical Metastability*, *Phys. Rev. Lett.* **46** (1981) 388.

[73] Z. Maki, M. Nakagawa and S. Sakata, *Remarks on the unified model of elementary particles*, *Prog. Theor. Phys.* **28** (1962) 870–880.

[74] B. Pontecorvo, *Inverse beta processes and nonconservation of lepton charge*, *Sov. Phys. JETP* **7** (1958) 172–173.

[75] Particle Data Group collaboration, M. Tanabashi et al., *Review of Particle Physics*, *Phys. Rev. D* **98** (2018) 030001.

[76] E. Majorana, *Teoria simmetrica dell'elettrone e del positrone*, *Il Nuovo Cimento* **14** (Apr., 1937) 171–184.

[77] B. Pontecorvo, *Inverse beta processes and nonconservation of lepton charge*, *Zhur. Eksptl'. i Teoret. Fiz.* **Vol: 34** (1, 1958) .

[78] V. Gribov and B. Pontecorvo, *Neutrino astronomy and lepton charge*, *Physics Letters B* **28** (1969) 493 – 496.

[79] C. Giunti and C. W. Kim, *Fundamentals of Neutrino Physics and Astrophysics.* 4, 2007.

[80] R. Zukanovich Funchal, B. Schmauch and G. Giesen, *The Physics of Neutrinos*, 1308.1029.

[81] M. Fukugita and T. Yanagida, *Baryogenesis Without Grand Unification (leptogenesis)*, *Phys. Lett.* **B174** (1986) 45–47.

[82] V. Kuzmin, V. Rubakov and M. Shaposhnikov, *On the Anomalous Electroweak Baryon Number Nonconservation in the Early Universe*, *Phys. Lett. B* **155** (1985) 36.

[83] BaBar collaboration, J. P. Lees et al., *Evidence for an excess of $\bar{B} \to D^{(*)}\tau^-\bar{\nu}_\tau$ decays*, *Phys. Rev. Lett.* **109** (2012) 101802, [1205.5442].

[84] Belle collaboration, M. Huschle et al., *Measurement of the branching ratio of $\bar{B} \to D^{(*)}\tau^-\bar{\nu}_\tau$ relative to $\bar{B} \to D^{(*)}\ell^-\bar{\nu}_\ell$ decays with hadronic tagging at Belle*, *Phys. Rev. D* **92** (2015) 072014, [1507.03233].

[85] Belle collaboration, S. Hirose et al., *Measurement of the τ lepton polarization and $R(D^*)$ in the decay $\bar{B} \to D^*\tau^-\bar{\nu}_\tau$*, *Phys. Rev. Lett.* **118** (2017) 211801, [1612.00529].

[86] Belle collaboration, G. Caria et al., *Measurement of $\mathcal{R}(D)$ and $\mathcal{R}(D^*)$ with a semileptonic tagging method*, *Phys. Rev. Lett.* **124** (2020) 161803, [1910.05864].

[87] LHCb collaboration, R. Aaij et al., *Measurement of the ratio of branching fractions $\mathcal{B}(\bar{B}^0 \to D^{*+}\tau^-\bar{\nu}_\tau)/\mathcal{B}(\bar{B}^0 \to D^{*+}\mu^-\bar{\nu}_\mu)$*, *Phys. Rev. Lett.* **115** (2015) 111803, [1506.08614].

[88] LHCb collaboration, R. Aaij et al., *Measurement of the ratio of the $B^0 \to D^{*-}\tau^+\nu_\tau$ and $B^0 \to D^{*-}\mu^+\nu_\mu$ branching fractions using three-prong τ-lepton decays*, *Phys. Rev. Lett.* **120** (2018) 171802, [1708.08856].

[89] Heavy Flavor Averaging Group collaboration, Y. Amhis et al., *Averages of b-hadron, c-hadron, and τ-lepton properties as of summer 2018*, 1909.12524.

[90] F. U. Bernlochner, Z. Ligeti, M. Papucci and D. J. Robinson, *Combined analysis of semileptonic B decays to D and D^*: $R(D^{(*)})$, $|V_{cb}|$, and new physics*, *Phys. Rev. D* **95** (2017) 115008, [1703.05330].

[91] S. Jaiswal, S. Nandi and S. K. Patra, *Extraction of $|V_{cb}|$ from $B \to D^{(*)}\ell\nu_\ell$ and the Standard Model predictions of $R(D^{(*)})$*, *JHEP* **12** (2017) 060, [1707.09977].

[92] D. Bigi, P. Gambino and S. Schacht, *$R(D^*)$, $|V_{cb}|$, and the Heavy Quark Symmetry relations between form factors*, *JHEP* **11** (2017) 061, [1707.09509].

[93] M. Bordone, G. Isidori and A. Pattori, *On the Standard Model predictions for R_K and R_{K^*}*, *Eur. Phys. J.* **C76** (2016) 440, [1605.07633].

[94] LHCb collaboration, R. Aaij et al., *Test of lepton universality using $B^+ \to K^+\ell^+\ell^-$ decays*, *Phys. Rev. Lett.* **113** (2014) 151601, [1406.6482].

[95] Belle collaboration, A. Abdesselam et al., *Test of lepton flavor universality in $B \to K^*\ell^+\ell^-$ decays at Belle*, 1904.02440.

[96] Belle collaboration, A. Abdesselam et al., *Test of lepton flavor universality in $B \to K\ell^+\ell^-$ decays*, 1908.01848.

[97] C. J. E. Suster, *Cross-section measurements of the electroweak production of a single top quark in association with a W boson at s = 13 TeV with the ATLAS detector*, doctor of philosophy ph.d., 2019-07-01.

[98] A. D. Martin et al., *Parton distributions for the LHC*, *Eur. Phys. J. C* **63** (2009) 189, [0901.0002].

[99] S. Catani, *Aspects of QCD, from the Tevatron to the LHC*, in *1st Les Houches Workshop on Physics at TeV Colliders*, pp. 4–33, 5, 2000, hep-ph/0005233.

[100] G. Avoni, M. Bruschi, G. Cabras, D. Caforio, N. Dehghanian, A. Floderus et al., *The new LUCID-2 detector for luminosity measurement and monitoring in ATLAS*, *Journal of Instrumentation* **13** (jul, 2018) P07017–P07017.

[101] S. Marzani, G. Soyez and M. Spannowsky, *Looking inside jets: an introduction to jet substructure and boosted-object phenomenology*, vol. 958. Springer, 2019, 10.1007/978-3-030-15709-8.

[102] A. J. Larkoski, D. Neill and J. Thaler, *Jet Shapes with the Broadening Axis*, *JHEP* **04** (2014) 017, [1401.2158].

[103] G. P. Salam, *Towards Jetography*, *Eur. Phys. J. C* **67** (2010) 637–686, [0906.1833].

[104] T. C. collaboration, *Missing transverse energy performance of the cms detector*, *Journal of Instrumentation* **6** (Sep, 2011) P09001–P09001.

[105] S. Agostinelli, *Geant4—a simulation toolkit*, *Nuclear Instruments and Methods in Physics Research Section A: Accelerators, Spectrometers, Detectors and Associated Equipment* **506** (2003) 250–303.

[106] ATLAS Collaboration, "The simulation principle and performance of the ATLAS fast calorimeter simulation FastCaloSim." ATL-PHYS-PUB-2010-013, 2010.

[107] ATLAS collaboration, *The ATLAS Experiment at the CERN Large Hadron Collider*, *JINST* **3** (2008) S08003.

[108] ALICE collaboration, K. Aamodt et al., *The ALICE experiment at the CERN LHC*, *JINST* **3** (2008) S08002.

[109] CMS collaboration, S. Chatrchyan et al., *The CMS Experiment at the CERN LHC*, *JINST* **3** (2008) S08004.

[110] LHCb collaboration, A. A. Alves, Jr. et al., *The LHCb Detector at the LHC*, *JINST* **3** (2008) S08005.

[111] E. Mobs, *The CERN accelerator complex - 2019. Complexe des accélérateurs du CERN - 2019*, .

[112] ATLAS collaboration, G. Aad et al., *Improved luminosity determination in pp collisions at sqrt(s) = 7 TeV using the ATLAS detector at the LHC*, *Eur. Phys. J. C* **73** (2013) 2518, [1302.4393].

[113] ATLAS collaboration, M. Aaboud et al., *Luminosity determination in pp collisions at* $\sqrt{s} = 8$ *TeV using the ATLAS detector at the LHC*, *Eur. Phys. J. C* **76** (2016) 653, [1608.03953].

[114] ATLAS Collaboration collaboration, *ATLAS inner detector: Technical Design Report, 1.* Technical design report. ATLAS. CERN, Geneva, 1997.

[115] E. Simas, J. M. Seixas and L. Caloba, *Self-organized mapping of calorimetry information for high efficient online electron / jet identification in ATLAS*, *PoS* **ACAT** (2007) 055.

[116] G. Barr, R. Devenish, R. Walczak and T. Weidberg, *Particle physics in the LHC era.* Oxford master series in particle physics, astrophysics, and cosmology. Oxford University Press, Oxford, 2016, 10.1093/acprof:oso/9780198748557.001.0001.

[117] S. Paredes Saenz, *Search for new physics through Higgs-boson-pair production at the LHC and beyond*, Ph.D. thesis, University of Oxford.

[118] ATLAS Collaboration collaboration, *Technical Design Report for the ATLAS Inner Tracker Strip Detector*, Tech. Rep. CERN-LHCC-2017-005. ATLAS-TDR-025, CERN, Geneva, Apr, 2017.

[119] A. Vogel, *ATLAS Transition Radiation Tracker (TRT): Straw Tube Gaseous Detectors at High Rates*, Tech. Rep. ATL-INDET-PROC-2013-005, CERN, Geneva, Apr, 2013.

[120] ATLAS Collaboration collaboration, *ATLAS tile calorimeter: Technical Design Report.* Technical design report. ATLAS. CERN, Geneva, 1996.

[121] ATLAS Collaboration collaboration, *ATLAS liquid-argon calorimeter: Technical Design Report.* Technical design report. ATLAS. CERN, Geneva, 1996.

[122] ATLAS Collaboration collaboration, *ATLAS muon spectrometer: Technical Design Report.* Technical design report. ATLAS. CERN, Geneva, 1997.

[123] M. z. Nedden, *The LHC Run 2 ATLAS trigger system: design, performance and plans*, *JINST* **12** (2017) C03024.

[124] ATLAS Collaboration, *Observation of a new particle in the search for the Standard Model Higgs boson with the ATLAS detector at the LHC*, *Phys. Lett. B* **716** (2012) 1, [1207.7214].

[125] CMS Collaboration, *Observation of a new boson at a mass of 125 GeV with the CMS experiment at the LHC*, *Phys. Lett. B* **716** (2012) 30, [1207.7235].

[126] ATLAS Collaboration, *Combined measurements of Higgs boson production and decay using up to* $80\,fb^{-1}$ *of proton–proton collision data at* $\sqrt{s} = 13$ *TeV collected with the ATLAS experiment*, *Phys. Rev. D* **101** (2020) 012002, [1909.02845].

[127] ATLAS Collaboration, *CP Properties of Higgs Boson Interactions with Top Quarks in the* $t\bar{t}H$ *and* tH *Processes Using* $H \to \gamma\gamma$ *with the ATLAS Detector*, *Phys. Rev. Lett.* **125** (2020) 061802, [2004.04545].

[128] ATLAS Collaboration, *Test of CP invariance in vector-boson fusion production of the Higgs boson in the* $H \to \tau\tau$ *channel in proton–proton collisions at* $\sqrt{s} = 13$ *TeV with the ATLAS detector*, *Phys. Lett. B* **805** (2020) 135426, [2002.05315].

[129] ATLAS Collaboration, *Study of the spin and parity of the Higgs boson in diboson decays with the ATLAS detector*, *Eur. Phys. J. C* **75** (2015) 476, [1506.05669].

[130] CMS collaboration, CMS Collaboration, *Measurement and interpretation of differential cross sections for Higgs boson production at* $\sqrt{s} =$ *13 TeV*, *Phys. Lett. B* **792** (2019) 369–396, [1812.06504].

[131] CMS collaboration, A. M. Sirunyan et al., *Combined measurements of Higgs boson couplings in proton–proton collisions at* $\sqrt{s} = 13$ *TeV*, *Eur. Phys. J. C* **79** (2019) 421, [1809.10733].

[132] CMS collaboration, CMS Collaboration, *Measurements of* $\mathrm{t\bar{t}}H$ *production and the CP structure of the Yukawa interaction between the Higgs boson and top quark in the diphoton decay channel*, *Phys. Rev. Lett.* **125** (2020) 061801, [2003.10866].

[133] ATLAS, CMS collaboration, ATLAS and CMS Collaborations, *Measurements of the Higgs boson production and decay rates and constraints on its couplings from a combined ATLAS and CMS analysis of the LHC pp collision data at* $\sqrt{s} =$ *7 and 8 TeV*, 1606.02266.

[134] P. W. Higgs, *Broken symmetries, massless particles and gauge fields*, *Phys. Lett.* **12** (1964) 132 – 133.

[135] P. W. Higgs, *Spontaneous symmetry breakdown without massless bosons*, *Phys. Rev.* **145** (May, 1966) 1156–1163.

[136] T. W. B. Kibble, *Symmetry breaking in non-abelian gauge theories*, *Phys. Rev.* **155** (Mar, 1967) 1554–1561.

[137] J. F. Gunion and H. E. Haber, *Cp-conserving two-higgs-doublet model: The approach to the decoupling limit*, *Phys. Rev. D* **67** (Apr, 2003) 075019.

[138] A. Djouadi, *The Anatomy of electro-weak symmetry breaking. II. The Higgs bosons in the minimal supersymmetric model*, Phys. Rept. **459** (2008) 1, [hep-ph/0503173].

[139] J. E. Kim and G. Carosi, *Axions and the strong CP problem*, Rev. Mod. Phys. **82** (2010) 557–602, [0807.3125].

[140] ATLAS Collaboration, *Searches for heavy ZZ and ZW resonances in the $\ell\ell qq$ and $\nu\nu qq$ final states in pp collisions at $\sqrt{s} = 13$ TeV with the ATLAS detector*, JHEP **03** (2018) 009, [1708.09638].

[141] ATLAS Collaboration, *Search for WW/WZ resonance production in $\ell\nu qq$ final states in pp collisions at $\sqrt{s} = 13$ TeV with the ATLAS detector*, JHEP **03** (2018) 042, [1710.07235].

[142] ATLAS Collaboration, *Search for heavy diboson resonances in semileptonic final states in pp collisions at $\sqrt{s} = 13$ TeV with the ATLAS detector*, 2004.14636.

[143] ATLAS Collaboration, *Search for diboson resonances in hadronic final states in 139 fb^{-1} of pp collisions at $\sqrt{s} = 13$ TeV with the ATLAS detector*, JHEP **09** (2019) 091, [1906.08589].

[144] CMS Collaboration, *Search for a heavy Higgs boson decaying to a pair of W bosons in proton–proton collisions at $\sqrt{s} = 13$ TeV*, JHEP **03** (2020) 034, [1912.01594].

[145] CMS Collaboration, *Search for a new scalar resonance decaying to a pair of Z bosons in proton–proton collisions at $\sqrt{s} = 13$ TeV*, JHEP **06** (2018) 127, [1804.01939].

[146] ATLAS Collaboration, *Combination of searches for Higgs boson pairs in pp collisions at $\sqrt{s} = 13$ TeV with the ATLAS detector*, Phys. Lett. B **800** (2020) 135103, [1906.02025].

[147] CMS Collaboration, *Combination of Searches for Higgs Boson Pair Production in Proton–Proton Collisions at $\sqrt{s} = 13$ TeV*, Phys. Rev. Lett. **122** (2019) 121803, [1811.09689].

[148] ATLAS Collaboration, *Search for heavy resonances decaying into a W or Z boson and a Higgs boson in final states with leptons and b-jets in 36 fb^{-1} of $\sqrt{s} = 13$ TeV pp collisions with the ATLAS detector*, JHEP **03** (2018) 174, [1712.06518].

[149] CMS Collaboration, *Search for a heavy pseudoscalar Higgs boson decaying into a 125 GeV Higgs boson and a Z boson in final states with two tau and two light leptons at $\sqrt{s} = 13$ TeV*, JHEP **03** (2020) 065, [1910.11634].

[150] ATLAS Collaboration, *Search for Heavy Higgs Bosons Decaying into Two Tau Leptons with the ATLAS Detector Using pp Collisions at $\sqrt{s} = 13$ TeV*, Phys. Rev. Lett. **125** (2020) 051801, [2002.12223].

[151] CMS Collaboration, *Search for beyond the standard model Higgs bosons decaying into a $b\bar{b}$ pair in pp collisions at $\sqrt{s} = 13$ TeV*, *JHEP* **08** (2018) 113, [1805.12191].

[152] CMS Collaboration, *Search for additional neutral MSSM Higgs bosons in the $\tau\tau$ final state in proton–proton collisions at $\sqrt{s} = 13$ TeV*, *JHEP* **09** (2018) 007, [1803.06553].

[153] CMS Collaboration, *Search for neutral resonances decaying into a Z boson and a pair of b jets or τ leptons*, *Phys. Lett. B* **759** (2016) 369, [1603.02991].

[154] ATLAS Collaboration, *Search for a heavy Higgs boson decaying into a Z boson and another heavy Higgs boson in the $\ell\ell bb$ final state in pp collisions at $\sqrt{s} = 13$ TeV with the ATLAS detector*, *Phys. Lett. B* **783** (2018) 392, [1804.01126].

[155] CMS Collaboration, *Search for new neutral Higgs bosons through the $H \to ZA \to \ell^+\ell^- b\bar{b}$ process in pp collisions at $\sqrt{s} = 13$ TeV*, *JHEP* **03** (2020) 055, [1911.03781].

[156] B. Coleppa, F. Kling and S. Su, *Exotic decays of a heavy neutral Higgs through HZ/AZ channel*, *JHEP* **09** (2014) 161, [1404.1922].

[157] ATLAS Collaboration, *The ATLAS Experiment at the CERN Large Hadron Collider*, *JINST* **3** (2008) S08003.

[158] ATLAS collaboration, ATLAS Collaboration, *ATLAS Insertable B-Layer Technical Design Report Addendum*, .

[159] B. Abbott et al, *Production and Integration of the ATLAS Insertable B-Layer*, *JINST* **13** (2018) T05008, [1803.00844].

[160] ATLAS Collaboration, *Performance of the ATLAS trigger system in 2015*, *Eur. Phys. J. C* **77** (2017) 317, [1611.09661].

[161] ATLAS Collaboration, *Luminosity determination in pp collisions at $\sqrt{s} = 7$ TeV using the ATLAS detector at the LHC*, *Eur. Phys. J. C* **71** (2011) 1630, [1101.2185].

[162] ATLAS Collaboration, *Improved luminosity determination in pp collisions at $\sqrt{s} = 7$ TeV using the ATLAS detector at the LHC*, *Eur. Phys. J. C* **73** (2013) 2518, [1302.4393].

[163] ATLAS Collaboration, *Luminosity determination in pp collisions at $\sqrt{s} = 8$ TeV using the ATLAS detector at the LHC*, *Eur. Phys. J. C* **76** (2016) 653, [1608.03953].

[164] G. Avoni et al., *The new lucid-2 detector for luminosity measurement and monitoring in atlas*, *JINST* **13** (2018) P07017.

[165] ATLAS Collaboration, *ATLAS data quality operations and performance for 2015–2018 data-taking*, *JINST* **15** (2020) P04003, [1911.04632].

[166] ATLAS collaboration, ATLAS Collaboration, *Performance of the ATLAS muon triggers in Run 2*, *JINST* **15** (2020) P09015, [2004.13447].

[167] ATLAS Collaboration, *Performance of electron and photon triggers in ATLAS during LHC Run 2*, *Eur. Phys. J. C* **80** (2020) 47, [1909.00761].

[168] J. Alwall, M. Herquet, F. Maltoni, O. Mattelaer and T. Stelzer, *MadGraph 5 : Going Beyond*, *JHEP* **1106** (2011) 128, [1106.0522].

[169] J. Alwall, R. Frederix, S. Frixione, V. Hirschi, F. Maltoni et al., *The automated computation of tree-level and next-to-leading order differential cross sections, and their matching to parton shower simulations*, *JHEP* **07** (2014) 079, [1405.0301].

[170] T. Sjöstrand, S. Ask, J. R. Christiansen, R. Corke, N. Desai, P. Ilten et al., *An introduction to PYTHIA 8.2*, *Comput. Phys. Commun.* **191** (2015) 159, [1410.3012].

[171] ATLAS Collaboration, "ATLAS Run 1 Pythia8 tunes." ATL-PHYS-PUB-2014-021, 2014.

[172] S. Frixione and B. R. Webber, *Matching NLO QCD computations and parton shower simulations*, *JHEP* **06** (2002) 029, [hep-ph/0204244].

[173] M. Wiesemann, R. Frederix, S. Frixione, V. Hirschi, F. Maltoni and P. Torrielli, *Higgs production in association with bottom quarks*, *JHEP* **02** (2015) 132, [1409.5301].

[174] LHC Higgs Cross Section Working Group collaboration, D. de Florian et al., *Handbook of LHC Higgs Cross Sections: 4. Deciphering the Nature of the Higgs Sector*, 1610.07922.

[175] R. D. Ball et al., *Parton distributions with LHC data*, *Nucl. Phys. B* **867** (2013) 244–289, [1207.1303].

[176] H.-L. Lai et al., *New parton distributions for collider physics*, *Phys. Rev. D* **82** (2010) 074024, [1007.2241].

[177] E. Bothmann et al., *Event generation with Sherpa 2.2*, *SciPost Phys.* **7** (2019) 034, [1905.09127].

[178] T. Gleisberg and S. Höche, *Comix, a new matrix element generator*, *JHEP* **12** (2008) 039, [0808.3674].

[179] F. Cascioli, P. Maierhofer and S. Pozzorini, *Scattering Amplitudes with Open Loops*, *Phys. Rev. Lett.* **108** (2012) 111601, [1111.5206].

[180] A. Denner, S. Dittmaier and L. Hofer, Collier*: A fortran-based complex one-loop library in extended regularizations*, *Comput. Phys. Commun.* **212** (2017) 220–238, [1604.06792].

[181] S. Schumann and F. Krauss, *A Parton shower algorithm based on Catani-Seymour dipole factorisation*, *JHEP* **03** (2008) 038, [0709.1027].

[182] S. Höche, F. Krauss, M. Schönherr and F. Siegert, *A critical appraisal of NLO+PS matching methods*, *JHEP* **09** (2012) 049, [1111.1220].

[183] S. Höche, F. Krauss, M. Schönherr and F. Siegert, *QCD matrix elements + parton showers: The NLO case*, *JHEP* **04** (2013) 027, [1207.5030].

[184] S. Catani, F. Krauss, R. Kuhn and B. R. Webber, *QCD Matrix Elements + Parton Showers*, *JHEP* **11** (2001) 063, [hep-ph/0109231].

[185] S. Höche, F. Krauss, S. Schumann and F. Siegert, *QCD matrix elements and truncated showers*, *JHEP* **05** (2009) 053, [0903.1219].

[186] NNPDF collaboration, R. D. Ball et al., *Parton distributions for the LHC Run II*, *JHEP* **04** (2015) 040, [1410.8849].

[187] C. Anastasiou, L. J. Dixon, K. Melnikov and F. Petriello, *High precision QCD at hadron colliders: Electroweak gauge boson rapidity distributions at NNLO*, *Phys. Rev. D* **69** (2004) 094008, [hep-ph/0312266].

[188] S. Frixione, P. Nason and G. Ridolfi, *A positive-weight next-to-leading-order Monte Carlo for heavy flavour hadroproduction*, *JHEP* **09** (2007) 126, [0707.3088].

[189] P. Nason, *A New method for combining NLO QCD with shower Monte Carlo algorithms*, *JHEP* **11** (2004) 040, [hep-ph/0409146].

[190] S. Frixione, P. Nason and C. Oleari, *Matching NLO QCD computations with Parton Shower simulations: the POWHEG method*, *JHEP* **11** (2007) 070, [0709.2092].

[191] S. Alioli, P. Nason, C. Oleari and E. Re, *A general framework for implementing NLO calculations in shower Monte Carlo programs: the POWHEG BOX*, *JHEP* **1006** (2010) 043, [1002.2581].

[192] ATLAS Collaboration, "Studies on top-quark Monte Carlo modelling for Top2016." ATL-PHYS-PUB-2016-020, 2016.

[193] D. J. Lange, *The EvtGen particle decay simulation package*, *Nucl. Instrum. Meth. A* **462** (2001) 152.

[194] E. Re, *Single-top Wt-channel production matched with parton showers using the POWHEG method*, *Eur. Phys. J. C* **71** (2011) 1547, [1009.2450].

[195] S. Alioli, P. Nason, C. Oleari and E. Re, *NLO single-top production matched with shower in POWHEG: s- and t-channel contributions*, *JHEP* **09** (2009) 111, [0907.4076].

[196] S. Frixione, E. Laenen, P. Motylinski, C. White and B. R. Webber, *Single-top hadroproduction in association with a W boson*, *JHEP* **07** (2008) 029, [0805.3067].

[197] P. Nason and C. Oleari, *NLO Higgs boson production via vector-boson fusion matched with shower in POWHEG*, *JHEP* **02** (2010) 037, [0911.5299].

[198] T. Sjostrand, S. Mrenna and P. Z. Skands, *A Brief Introduction to PYTHIA 8.1*, *Comput.Phys.Commun.* **178** (2008) 852–867, [0710.3820].

[199] J. Butterworth et al., *PDF4LHC recommendations for LHC Run II*, 1510.03865.

[200] ATLAS Collaboration, *Measurement of the Z/γ^* boson transverse momentum distribution in pp collisions at $\sqrt{s} = 7$ TeV with the ATLAS detector*, *JHEP* **09** (2014) 145, [1406.3660].

[201] M. L. Ciccolini, S. Dittmaier and M. Krämer, *Electroweak radiative corrections to associated WH and ZH production at hadron colliders*, *Phys. Rev. D* **68** (2003) 073003, [hep-ph/0306234].

[202] O. Brein, A. Djouadi and R. Harlander, *NNLO QCD corrections to the Higgs-strahlung processes at hadron colliders*, *Phys. Lett. B* **579** (2004) 149–156, [hep-ph/0307206].

[203] O. Brein, R. Harlander, M. Wiesemann and T. Zirke, *Top-Quark Mediated Effects in Hadronic Higgs-Strahlung*, *Eur. Phys. J. C* **72** (2012) 1868, [1111.0761].

[204] L. Altenkamp, S. Dittmaier, R. V. Harlander, H. Rzehak and T. J. E. Zirke, *Gluon-induced Higgs-strahlung at next-to-leading order QCD*, *JHEP* **02** (2013) 078, [1211.5015].

[205] A. Denner, S. Dittmaier, S. Kallweit and A. Mück, *HAWK 2.0: A Monte Carlo program for Higgs production in vector-boson fusion and Higgs strahlung at hadron colliders*, *Comput. Phys. Commun.* **195** (2015) 161–171, [1412.5390].

[206] O. Brein, R. V. Harlander and T. J. E. Zirke, *vh@nnlo – Higgs Strahlung at hadron colliders*, *Comput. Phys. Commun.* **184** (2013) 998–1003, [1210.5347].

[207] R. V. Harlander, A. Kulesza, V. Theeuwes and T. Zirke, *Soft gluon resummation for gluon-induced Higgs Strahlung*, *JHEP* **11** (2014) 082, [1410.0217].

[208] ATLAS Collaboration, "The Pythia 8 A3 tune description of ATLAS minimum bias and inelastic measurements incorporating the Donnachie–Landshoff diffractive model." ATL-PHYS-PUB-2016-017, 2016.

[209] ATLAS Collaboration, *Measurement of the Inelastic Proton–Proton Cross Section at $\sqrt{s} = 13$ TeV with the ATLAS Detector at the LHC*, *Phys. Rev. Lett.* **117** (2016) 182002, [1606.02625].

[210] S. Agostinelli et al., GEANT4 – *a simulation toolkit*, *Nucl. Instrum. Meth. A* **506** (2003) 250.

[211] ATLAS Collaboration, *The ATLAS Simulation Infrastructure*, *Eur. Phys. J. C* **70** (2010) 823, [1005.4568].

[212] ATLAS collaboration, ATLAS Collaboration, *Electron and photon performance measurements with the ATLAS detector using the 2015-2017 LHC proton-proton collision data*, *JINST* **14** (2019) P12006, [1908.00005].

[213] ATLAS Collaboration, *Muon reconstruction performance of the ATLAS detector in proton–proton collision data at $\sqrt{s} = 13$ TeV*, *Eur. Phys. J. C* **76** (2016) 292, [1603.05598].

[214] ATLAS Collaboration, "Muon reconstruction and identification efficiency in ATLAS using the full Run 2 *pp* collision data set at $\sqrt{s} = 13\,\text{TeV}$." ATLAS-CONF-2020-030, 2020.

[215] ATLAS Collaboration, *Topological cell clustering in the ATLAS calorimeters and its performance in LHC Run 1*, *Eur. Phys. J. C* **77** (2017) 490, [1603.02934].

[216] M. Cacciari, G. P. Salam and G. Soyez, *The Anti-k_t jet clustering algorithm*, *JHEP* **04** (2008) 063, [0802.1189].

[217] M. Cacciari, G. P. Salam and G. Soyez, *FastJet user manual*, *Eur. Phys. J. C* **72** (2012) 1896, [1111.6097].

[218] ATLAS collaboration, ATLAS Collaboration, *Jet energy scale and resolution measured in proton-proton collisions at $\sqrt{s} = 13$ TeV with the ATLAS detector*, 2007.02645.

[219] ATLAS Collaboration, *Performance of pile-up mitigation techniques for jets in pp collisions at $\sqrt{s} = 8$ TeV using the ATLAS detector*, *Eur. Phys. J. C* **76** (2016) 581, [1510.03823].

[220] ATLAS Collaboration, "Optimisation and performance studies of the ATLAS b-tagging algorithms for the 2017-18 LHC run." ATL-PHYS-PUB-2017-013, 2017.

[221] ATLAS Collaboration, *ATLAS b-jet identification performance and efficiency measurement with $t\bar{t}$ events in pp collisions at $\sqrt{s} = 13$ TeV*, *Eur. Phys. J. C* **79** (2019) 970, [1907.05120].

[222] ATLAS Collaboration, *Evidence for the $H \to b\bar{b}$ decay with the ATLAS detector*, *JHEP* **12** (2017) 024, [1708.03299].

[223] ATLAS Collaboration, *Performance of missing transverse momentum reconstruction with the ATLAS detector using proton–proton collisions at $\sqrt{s} = 13$ TeV*, *Eur. Phys. J. C* **78** (2018) 903, [1802.08168].

[224] ATLAS Collaboration, "$E_{\mathrm{T}}^{\mathrm{miss}}$ performance in the ATLAS detector using 2015–2016 LHC *pp* collisions." ATLAS-CONF-2018-023, 2018.

[225] T. Gehrmann, M. Grazzini, S. Kallweit, P. Maierhöfer, A. von Manteuffel, S. Pozzorini et al., *W^+W^- Production at Hadron Colliders in Next to Next to Leading Order QCD*, *Phys. Rev. Lett.* **113** (2014) 212001, [1408.5243].

[226] M. Grazzini, S. Kallweit, D. Rathlev and M. Wiesemann, *$W^{\pm}Z$ production at hadron colliders in NNLO QCD*, *Phys. Lett. B* **761** (2016) 179–183, [1604.08576].

[227] M. Grazzini, S. Kallweit and D. Rathlev, *ZZ production at the LHC: Fiducial cross sections and distributions in NNLO QCD*, *Phys. Lett. B* **750** (2015) 407–410, [1507.06257].

[228] F. Cascioli, T. Gehrmann, M. Grazzini, S. Kallweit, P. Maierhöfer, A. von Manteuffel et al., *ZZ production at hadron colliders in NNLO QCD*, *Phys. Lett. B* **735** (2014) 311–313, [1405.2219].

[229] N. Kidonakis, *NNLL resummation for s-channel single top quark production*, *Phys. Rev. D* **81** (2010) 054028, [1001.5034].

[230] N. Kidonakis, *Next-to-next-to-leading-order collinear and soft gluon corrections for t-channel single top quark production*, *Phys. Rev. D* **83** (2011) 091503, [1103.2792].

[231] N. Kidonakis, *Two-loop soft anomalous dimensions for single top quark associated production with a W- or H-*, *Phys. Rev. D* **82** (2010) 054018, [1005.4451].

[232] S. Das, *A simple alternative to the Crystal Ball function*, 1603.08591.

[233] M. Oreglia, *A Study of the Reactions $\psi' \to \gamma\gamma\psi$*, Ph.D. thesis, SLAC, 1980.

[234] J. Duchon, *Interpolation des fonctions de deux variables suivant le principe de la flexion des plaques minces*, *ESAIM: Mathematical Modelling and Numerical Analysis - Modélisation Mathématique et Analyse Numérique* **10** (1976) 5–12.

[235] ATLAS Collaboration, "Luminosity determination in pp collisions at $\sqrt{s} = 13$ TeV using the ATLAS detector at the LHC." ATLAS-CONF-2019-021, 2019.

[236] G. Cowan, K. Cranmer, E. Gross and O. Vitells, *Asymptotic formulae for likelihood-based tests of new physics*, *Eur. Phys. J. C* **71** (2011) 1554, [1007.1727].

[237] L. Moneta, K. Belasco, K. S. Cranmer, S. Kreiss, A. Lazzaro, D. Piparo et al., *The RooStats Project*, *PoS* **ACAT2010** (2010) 057, [1009.1003].

[238] W. Verkerke and D. Kirkby, *The RooFit toolkit for data modeling*, 2003.

[239] O. Vitells and E. Gross, *Estimating the significance of a signal in a multi-dimensional search*, *Astropart. Phys.* **35** (2011) 230–234, [1105.4355].

[240] A. L. Read, *Presentation of search results: the CL_S technique*, *J. Phys. G* **28** (2002) 2693.

[241] S. Dawson, C. B. Jackson, L. Reina and D. Wackeroth, *Exclusive Higgs boson production with bottom quarks at hadron colliders*, *Phys. Rev. D* **69** (2004) 074027, [hep-ph/0311067].

[242] S. Dittmaier, M. Krämer and M. Spira, *Higgs radiation off bottom quarks at the Tevatron and the LHC*, *Phys. Rev. D* **70** (2004) 074010, [hep-ph/0309204].

[243] R. Harlander, M. Krämer and M. Schumacher, *Bottom-quark associated Higgs-boson production: reconciling the four- and five-flavour scheme approach*, 1112.3478.

[244] D. Eriksson, J. Rathsman and O. Stål, *2HDMC - two-Higgs-doublet model calculator physics and manual*, *Comput. Phys. Commun.* **181** (2010) 189–205, [0902.0851].

[245] Y. Aoki, G. Endrodi, Z. Fodor, S. Katz and K. Szabo, *The Order of the quantum chromodynamics transition predicted by the standard model of particle physics*, *Nature* **443** (2006) 675–678, [hep-lat/0611014].

[246] K. Kajantie, M. Laine, K. Rummukainen and M. E. Shaposhnikov, *Is there a hot electroweak phase transition at m(H) larger or equal to m(W)?*, *Phys. Rev. Lett.* **77** (1996) 2887–2890, [hep-ph/9605288].

[247] C. Hogan, *Gravitational radiation from cosmological phase transitions*, *Mon. Not. Roy. Astron. Soc.* **218** (1986) 629–636.

[248] C. Caprini and D. G. Figueroa, *Cosmological Backgrounds of Gravitational Waves*, *Class. Quant. Grav.* **35** (2018) 163001, [1801.04268].

[249] J. Crowder and N. J. Cornish, *Beyond LISA: Exploring future gravitational wave missions*, *Phys. Rev. D* **72** (2005) 083005, [gr-qc/0506015].

[250] N. Seto, S. Kawamura and T. Nakamura, *Possibility of direct measurement of the acceleration of the universe using 0.1-Hz band laser interferometer gravitational wave antenna in space*, *Phys. Rev. Lett.* **87** (2001) 221103, [astro-ph/0108011].

[251] LISA collaboration, P. Amaro-Seoane et al., *Laser Interferometer Space Antenna*, 1702.00786.

[252] B. Garbrecht, *Why is there more matter than antimatter? Calculational methods for leptogenesis and electroweak baryogenesis*, *Prog. Part. Nucl. Phys.* **110** (2020) 103727, [1812.02651].

[253] A. F. Heckler, *The Effects of electroweak phase transition dynamics on baryogenesis and primordial nucleosynthesis*, *Phys. Rev. D* **51** (1995) 405–428, [astro-ph/9407064].

[254] M. Dine, R. G. Leigh, P. Y. Huet, A. D. Linde and D. A. Linde, *Towards the theory of the electroweak phase transition*, *Phys. Rev. D* **46** (1992) 550–571, [hep-ph/9203203].

[255] B.-H. Liu, L. D. McLerran and N. Turok, *Bubble nucleation and growth at a baryon number producing electroweak phase transition*, *Phys. Rev. D* **46** (1992) 2668–2688.

[256] G. D. Moore and T. Prokopec, *Bubble wall velocity in a first order electroweak phase transition*, *Phys. Rev. Lett.* **75** (1995) 777–780, [hep-ph/9503296].

[257] S. Khlebnikov, *Fluctuation - dissipation formula for bubble wall velocity*, *Phys. Rev. D* **46** (1992) 3223–3226.

[258] P. B. Arnold, *One loop fluctuation - dissipation formula for bubble wall velocity*, *Phys. Rev. D* **48** (1993) 1539–1545, [hep-ph/9302258].

[259] T. Konstandin, G. Nardini and I. Rues, *From Boltzmann equations to steady wall velocities*, *JCAP* **09** (2014) 028, [1407.3132].

[260] J. Kozaczuk, *Bubble Expansion and the Viability of Singlet-Driven Electroweak Baryogenesis*, *JHEP* **10** (2015) 135, [1506.04741].

[261] S. Höche, J. Kozaczuk, A. J. Long, J. Turner and Y. Wang, *Towards an all-orders calculation of the electroweak bubble wall velocity*, 2007.10343.

[262] J. Ignatius, K. Kajantie, H. Kurki-Suonio and M. Laine, *The growth of bubbles in cosmological phase transitions*, *Phys. Rev. D* **49** (1994) 3854–3868, [astro-ph/9309059].

[263] A. Megevand and A. D. Sanchez, *Detonations and deflagrations in cosmological phase transitions*, *Nucl. Phys. B* **820** (2009) 47–74, [0904.1753].

[264] A. Megevand and A. D. Sanchez, *Velocity of electroweak bubble walls*, *Nucl. Phys. B* **825** (2010) 151–176, [0908.3663].

[265] S. J. Huber and M. Sopena, *The bubble wall velocity in the minimal supersymmetric light stop scenario*, *Phys. Rev. D* **85** (2012) 103507, [1112.1888].

[266] S. J. Huber and M. Sopena, *An efficient approach to electroweak bubble velocities*, 1302.1044.

[267] N. Turok, *Electroweak bubbles: Nucleation and growth*, *Phys. Rev. Lett.* **68** (1992) 1803–1806.

[268] D. Bodeker and G. D. Moore, *Electroweak Bubble Wall Speed Limit*, *JCAP* **05** (2017) 025, [1703.08215].

[269] M. Barroso Mancha, T. Prokopec and B. Swiezewska, *Field theoretic derivation of bubble wall force*, 2005.10875.

[270] M. Gyulassy, K. Kajantie, H. Kurki-Suonio and L. D. McLerran, *Deflagrations and Detonations as a Mechanism of Hadron Bubble Growth in Supercooled Quark Gluon Plasma*, *Nucl. Phys. B* **237** (1984) 477–501.

[271] M. L. Piscopo, M. Spannowsky and P. Waite, *Solving differential equations with neural networks: Applications to the calculation of cosmological phase transitions*, *Phys. Rev.* **D100** (2019) 016002, [1902.05563].

[272] R. Shrock, *Decay l0 —> nu(lepton) gamma in gauge theories of weak and electromagnetic interactions*, *Phys. Rev. D* **9** (1974) 743–748.

[273] S. Petcov, *The Processes $\mu \to e + \gamma, \mu \to e + \overline{e}, \nu' \to \nu + \gamma$ in the Weinberg-Salam Model with Neutrino Mixing*, *Sov. J. Nucl. Phys.* **25** (1977) 340.

[274] J. T. Goldman and G. J. Stephenson, Jr., *Limits on the Mass of the Muon-neutrino in the Absence of Muon Lepton Number Conservation*, *Phys. Rev.* **D16** (1977) 2256.

[275] J. Schechter and J. Valle, *Majorana Neutrinos and Magnetic Fields*, *Phys. Rev. D* **24** (1981) 1883–1889.

[276] P. B. Pal and L. Wolfenstein, *Radiative Decays of Massive Neutrinos*, *Phys. Rev. D* **25** (1982) 766.

[277] J. Schechter and J. Valle, *Neutrino Decay and Spontaneous Violation of Lepton Number*, *Phys. Rev. D* **25** (1982) 774.

[278] R. E. Shrock, *Electromagnetic Properties and Decays of Dirac and Majorana Neutrinos in a General Class of Gauge Theories*, *Nucl. Phys. B* **206** (1982) 359–379.

[279] J. F. Nieves, *Electromagnetic Properties of Majorana Neutrinos*, *Phys. Rev.* **D26** (1982) 3152.

[280] B. Kayser, *Majorana Neutrinos and their Electromagnetic Properties*, *Phys. Rev. D* **26** (1982) 1662.

[281] M. Dvornikov and A. Studenikin, *Electric charge and magnetic moment of massive neutrino*, *Phys. Rev. D* **69** (2004) 073001, [hep-ph/0305206].

[282] M. S. Dvornikov and A. I. Studenikin, *Electromagnetic form-factors of a massive neutrino*, *J. Exp. Theor. Phys.* **99** (2004) 254–269, [hep-ph/0411085].

[283] C. Giunti and A. Studenikin, *Neutrino electromagnetic interactions: a window to new physics*, *Rev. Mod. Phys.* **87** (2015) 531, [1403.6344].

[284] P. Minkowski, *$\mu \to e\gamma$ at a Rate of One Out of 10^9 Muon Decays?*, *Phys. Lett. B* **67** (1977) 421–428.

[285] T. Yanagida, *Horizontal gauge symmetry and masses of neutrinos*, *Conf. Proc.* **C7902131** (1979) 95–99.

[286] M. Gell-Mann, P. Ramond and R. Slansky, *Complex Spinors and Unified Theories*, *Conf. Proc.* **C790927** (1979) 315–321, [1306.4669].

[287] S. L. Glashow, *The Future of Elementary Particle Physics*, *NATO Sci. Ser. B* **61** (1980) 687.

[288] R. N. Mohapatra and G. Senjanovic, *Neutrino Mass and Spontaneous Parity Nonconservation*, *Phys. Rev. Lett.* **44** (1980) 912.

[289] J. Schechter and J. W. F. Valle, *Neutrino Masses in SU(2) x U(1) Theories*, *Phys. Rev.* **D22** (1980) 2227.

[290] E. Bulbul, M. Markevitch, A. Foster, R. K. Smith, M. Loewenstein and S. W. Randall, *Detection of An Unidentified Emission Line in the Stacked X-ray spectrum of Galaxy Clusters*, *Astrophys. J.* **789** (2014) 13, [1402.2301].

[291] A. Boyarsky, O. Ruchayskiy, D. Iakubovskyi and J. Franse, *Unidentified Line in X-Ray Spectra of the Andromeda Galaxy and Perseus Galaxy Cluster*, *Phys. Rev. Lett.* **113** (2014) 251301, [1402.4119].

[292] S. Gariazzo, C. Giunti, M. Laveder, Y. F. Li and E. M. Zavanin, *Light sterile neutrinos*, *J. Phys.* **G43** (2016) 033001, [1507.08204].

[293] M. Drewes et al., *A White Paper on keV Sterile Neutrino Dark Matter*, *JCAP* **1701** (2017) 025, [1602.04816].

[294] Z.-z. Xing, *Flavor structures of charged fermions and massive neutrinos*, 1909.09610.

[295] M. Chianese, G. Miele, S. Morisi and E. Vitagliano, *Low energy IceCube data and a possible Dark Matter related excess*, *Phys. Lett.* **B757** (2016) 251–256, [1601.02934].

[296] IceCube collaboration, M. G. Aartsen et al., *Search for neutrinos from decaying dark matter with IceCube*, *Eur. Phys. J.* **C78** (2018) 831, [1804.03848].

[297] IceCube collaboration, M. G. Aartsen et al., *First observation of PeV-energy neutrinos with IceCube*, *Phys. Rev. Lett.* **111** (2013) 021103, [1304.5356].

[298] IceCube collaboration, M. G. Aartsen et al., *Observation and Characterization of a Cosmic Muon Neutrino Flux from the Northern Hemisphere using six years of IceCube data*, *Astrophys. J.* **833** (2016) 3, [1607.08006].

[299] T2K collaboration, K. Abe et al., *Search for CP Violation in Neutrino and Antineutrino Oscillations by the T2K Experiment with* 2.2×10^{21} *Protons on Target*, *Phys. Rev. Lett.* **121** (2018) 171802, [1807.07891].

[300] T2K collaboration, K. Abe et al., *Combined Analysis of Neutrino and Antineutrino Oscillations at T2K*, *Phys. Rev. Lett.* **118** (2017) 151801, [1701.00432].

[301] NOvA collaboration, P. Adamson et al., *Constraints on Oscillation Parameters from* ν_e *Appearance and* ν_μ *Disappearance in NOvA*, *Phys. Rev. Lett.* **118** (2017) 231801, [1703.03328].

[302] DUNE collaboration, B. Abi et al., *The DUNE Far Detector Interim Design Report, Volume 2: Single-Phase Module*, 1807.10327.

[303] Hyper-Kamiokande Proto-Collaboration collaboration, K. Abe et al., *Physics potential of a long-baseline neutrino oscillation experiment using a J-PARC neutrino beam and Hyper-Kamiokande*, *PTEP* **2015** (2015) 053C02, [1502.05199].

[304] Hyper-Kamiokande collaboration, K. Abe et al., *Physics potentials with the second Hyper-Kamiokande detector in Korea*, *PTEP* **2018** (2018) 063C01, [1611.06118].

[305] E. K. Akhmedov, V. A. Rubakov and A. Yu. Smirnov, *Baryogenesis via neutrino oscillations*, *Phys. Rev. Lett.* **81** (1998) 1359–1362, [hep-ph/9803255].

[306] W. Buchmuller, P. Di Bari and M. Plumacher, *Leptogenesis for pedestrians*, *Annals Phys.* **315** (2005) 305–351, [hep-ph/0401240].

[307] S. Davidson, E. Nardi and Y. Nir, *Leptogenesis*, *Phys. Rept.* **466** (2008) 105–177, [0802.2962].

[308] N. F. Bell, B. Kayser and S. S. C. Law, *Electromagnetic Leptogenesis*, *Phys. Rev.* **D78** (2008) 085024, [0806.3307].

[309] C. Boehm, C. Degrande, O. Mattelaer and A. C. Vincent, *Circular polarisation: a new probe of dark matter and neutrinos in the sky*, *JCAP* **1705** (2017) 043, [1701.02754].

[310] B. Kayser, *CPT, CP, and c Phases and their Effects in Majorana Particle Processes*, *Phys. Rev. D* **30** (1984) 1023.

[311] C. Broggini, C. Giunti and A. Studenikin, *Electromagnetic Properties of Neutrinos*, *Adv. High Energy Phys.* **2012** (2012) 459526, [1207.3980].

[312] W. Bonivento, D. Gorbunov, M. Shaposhnikov and A. Tokareva, *Polarization of photons emitted by decaying dark matter*, *Phys. Lett.* **B765** (2017) 127–131, [1610.04532].

[313] X. Shi and G. Sigl, *A Type II supernovae constraint on electron-neutrino - sterile-neutrino mixing*, *Phys. Lett. B* **323** (1994) 360–366, [hep-ph/9312247].

[314] G. G. Raffelt and S. Zhou, *Supernova bound on keV-mass sterile neutrinos reexamined*, *Phys. Rev. D* **83** (2011) 093014, [1102.5124].

[315] M. E. Peskin and D. V. Schroeder, *An Introduction to quantum field theory.* Addison-Wesley, Reading, USA, 1995.

[316] Z.-z. Xing and Y.-L. Zhou, *Enhanced Electromagnetic Transition Dipole Moments and Radiative Decays of Massive Neutrinos due to the Seesaw-induced Non-unitary Effects*, *Phys. Lett. B* **715** (2012) 178–182, [1201.2543].

[317] Y. F. Li and Z.-z. Xing, *Possible Capture of keV Sterile Neutrino Dark Matter on Radioactive β-decaying Nuclei*, *Phys. Lett.* **B695** (2011) 205–210, [1009.5870].

[318] T. Araki and Y. F. Li, *Q6 flavor symmetry model for the extension of the minimal standard model by three right-handed sterile neutrinos*, *Phys. Rev.* **D85** (2012) 065016, [1112.5819].

[319] K. N. Abazajian, *Resonantly Produced 7Â keV Sterile Neutrino Dark Matter Models and the Properties of Milky Way Satellites*, *Phys. Rev. Lett.* **112** (2014) 161303, [1403.0954].

[320] A. C. Vincent, E. F. Martinez, P. Hernndez, M. Lattanzi and O. Mena, *Revisiting cosmological bounds on sterile neutrinos*, *JCAP* **1504** (2015) 006, [1408.1956].

[321] A. Harada and A. Kamada, *Structure formation in a mixed dark matter model with decaying sterile neutrino: the 3.5 keV X-ray line and the Galactic substructure*, *JCAP* **1601** (2016) 031, [1412.1592].

[322] V. D. Barger, R. J. N. Phillips and S. Sarkar, *Remarks on the karmen anomaly*, *Phys. Lett.* **B352** (1995) 365–371, [hep-ph/9503295].

[323] M. Gluck, S. Rakshit and E. Reya, *The Lamb shift contribution of very light milli-charged fermions*, *Phys. Rev.* **D76** (2007) 091701, [hep-ph/0703140].

[324] C. Boehm, A. Olivares-Del Campo, M. Ramirez-Quezada and Y.-L. Zhou, *Polarisation of high energy gamma-rays after scattering*, 1903.11074.

[325] SHiP collaboration, M. Anelli et al., *A facility to Search for Hidden Particles (SHiP) at the CERN SPS*, 1504.04956.

[326] IceCube collaboration, M. G. Aartsen et al., *Evidence for Astrophysical Muon Neutrinos from the Northern Sky with IceCube*, *Phys. Rev. Lett.* **115** (2015) 081102, [1507.04005].

[327] IceCube collaboration, J. Stettner, *Measurement of the Diffuse Astrophysical Muon-Neutrino Spectrum with Ten Years of IceCube Data*, in *HAWC Contributions to the 36th International Cosmic Ray Conference (ICRC2019)*, 2019, 1908.09551.

[328] M. Chianese, D. F. G. Fiorillo, G. Miele, S. Morisi and O. Pisanti, *Decaying dark matter at IceCube and its signature on High Energy gamma experiments*, 1907.11222.

[329] Y. Sui and P. S. Bhupal Dev, *A Combined Astrophysical and Dark Matter Interpretation of the IceCube HESE and Throughgoing Muon Events*, *JCAP* **1807** (2018) 020, [1804.04919].

[330] M. Chianese and A. Merle, *A consistent theory of decaying dark matter connecting IceCube to the sesame street*, *Journal of Cosmology and Astroparticle Physics* **2017** (apr, 2017) 017–017.

[331] P. Di Bari, P. O. Ludl and S. Palomares-Ruiz, *Unifying leptogenesis, dark matter and high-energy neutrinos with right-handed neutrino mixing via Higgs portal*, *JCAP* **1611** (2016) 044, [1606.06238].

[332] M. Re Fiorentin, V. Niro and N. Fornengo, *A consistent model for leptogenesis, dark matter and the IceCube signal*, *JHEP* **11** (2016) 022, [1606.04445].

[333] M. Chianese and A. Merle, *A Consistent Theory of Decaying Dark Matter Connecting IceCube to the Sesame Street*, *JCAP* **1704** (2017) 017, [1607.05283].

[334] N. Hiroshima, R. Kitano, K. Kohri and K. Murase, *High-energy neutrinos from multibody decaying dark matter*, *Phys. Rev.* **D97** (2018) 023006, [1705.04419].

[335] P. Di Bari, K. Farrag, R. Samanta and Y. L. Zhou, *Density matrix calculation of the dark matter abundance in the Higgs induced right-handed neutrino mixing model*, 1908.00521.

[336] A. Anisimov and P. Di Bari, *Cold Dark Matter from heavy Right-Handed neutrino mixing*, *Phys. Rev.* **D80** (2009) 073017, [0812.5085].

[337] Super-Kamiokande collaboration, Y. Fukuda et al., *Evidence for oscillation of atmospheric neutrinos*, *Phys. Rev. Lett.* **81** (1998) 1562–1567, [hep-ex/9807003].

[338] Super-Kamiokande collaboration, S. Fukuda et al., *Solar B-8 and hep neutrino measurements from 1258 days of Super-Kamiokande data*, *Phys. Rev. Lett.* **86** (2001) 5651–5655, [hep-ex/0103032].

[339] SNO collaboration, Q. Ahmad et al., *Measurement of the rate of $\nu_e + d \to p + p + e^-$ interactions produced by ^8B solar neutrinos at the Sudbury Neutrino Observatory*, *Phys. Rev. Lett.* **87** (2001) 071301, [nucl-ex/0106015].

[340] SNO collaboration, Q. Ahmad et al., *Direct evidence for neutrino flavor transformation from neutral current interactions in the Sudbury Neutrino Observatory*, *Phys. Rev. Lett.* **89** (2002) 011301, [nucl-ex/0204008].

[341] P. Frampton, S. Glashow and T. Yanagida, *Cosmological sign of neutrino CP violation*, *Phys. Lett. B* **548** (2002) 119–121, [hep-ph/0208157].

[342] Z.-z. Xing and Z.-h. Zhao, *The minimal seesaw and leptogenesis models*, 2008.12090.

[343] W. Marciano and A. Sanda, *Exotic Decays of the Muon and Heavy Leptons in Gauge Theories*, *Phys. Lett. B* **67** (1977) 303–305.

[344] B. W. Lee and R. E. Shrock, *Natural Suppression of Symmetry Violation in Gauge Theories: Muon - Lepton and Electron Lepton Number Nonconservation*, *Phys. Rev.* **D16** (1977) 1444.

[345] K. Fujikawa and R. Shrock, *The Magnetic Moment of a Massive Neutrino and Neutrino Spin Rotation*, *Phys. Rev. Lett.* **45** (1980) 963.

[346] Z.-z. Xing and S. Zhou, *Neutrinos in particle physics, astronomy and cosmology*. 5, 2011.

[347] C. Jarlskog, *Commutator of the Quark Mass Matrices in the Standard Electroweak Model and a Measure of Maximal CP Violation*, *Phys. Rev. Lett.* **55** (1985) 1039.

[348] D.-d. Wu, *The Rephasing Invariants and CP*, *Phys. Rev. D* **33** (1986) 860.

[349] Z.-z. Xing and Y.-L. Zhou, *Majorana CP-violating phases in neutrino-antineutrino oscillations and other lepton-number-violating processes*, *Phys. Rev. D* **88** (2013) 033002, [1305.5718].

[350] I. Esteban, M. C. Gonzalez-Garcia, A. Hernandez-Cabezudo, M. Maltoni and T. Schwetz, *Global analysis of three-flavour neutrino oscillations: synergies and tensions in the determination of $\theta_2 3, \delta_C P$, and the mass ordering*, *JHEP* **01** (2019) 106, [1811.05487].

[351] E. Fernandez-Martinez, J. Hernandez-Garcia and J. Lopez-Pavon, *Global constraints on heavy neutrino mixing*, *JHEP* **08** (2016) 033, [1605.08774].

[352] A. M. Coutinho, A. Crivellin and C. A. Manzari, *Global Fit to Modified Neutrino Couplings and the Cabibbo-Angle Anomaly*, *Phys. Rev. Lett.* **125** (2020) 071802, [1912.08823].

[353] J. Casas and A. Ibarra, *Oscillating neutrinos and $\mu \to e, \gamma$*, *Nucl. Phys. B* **618** (2001) 171–204, [hep-ph/0103065].

[354] S. Antusch, P. Di Bari, D. Jones and S. King, *Leptogenesis in the Two Right-Handed Neutrino Model Revisited*, *Phys. Rev. D* **86** (2012) 023516, [1107.6002].

[355] A. Ibarra and G. G. Ross, *Neutrino phenomenology: The Case of two right-handed neutrinos*, *Phys. Lett. B* **591** (2004) 285–296, [hep-ph/0312138].

[356] A. Atre, T. Han, S. Pascoli and B. Zhang, *The Search for Heavy Majorana Neutrinos*, *JHEP* **05** (2009) 030, [0901.3589].

[357] M. Beneke et al., *Top quark physics*, in *Workshop on Standard Model Physics (and more) at the LHC (First Plenary Meeting)*, pp. 419–529, 3, 2000, hep-ph/0003033.

[358] J. Aguilar-Saavedra and B. Nobre, *Rare top decays t —> c gamma, t —> cg and CKM unitarity*, *Phys. Lett. B* **553** (2003) 251–260, [hep-ph/0210360].

[359] G. Eilam, J. Hewett and A. Soni, *Rare decays of the top quark in the standard and two Higgs doublet models*, *Phys. Rev. D* **44** (1991) 1473–1484.

[360] D. Atwood, L. Reina and A. Soni, *Phenomenology of two Higgs doublet models with flavor changing neutral currents*, *Phys. Rev. D* **55** (1997) 3156–3176, [hep-ph/9609279].

[361] B. Grzadkowski, J. Gunion and P. Krawczyk, *Neutral current flavor changing decays for the Z boson and the top quark in two Higgs doublet models*, *Phys. Lett. B* **268** (1991) 106–111.

[362] M. E. Luke and M. J. Savage, *Flavor changing neutral currents in the Higgs sector and rare top decays*, *Phys. Lett. B* **307** (1993) 387–393, [hep-ph/9303249].

[363] J. Aguilar-Saavedra, *Effects of mixing with quark singlets*, *Phys. Rev. D* **67** (2003) 035003, [hep-ph/0210112].

[364] A. K. Alok, S. Banerjee, D. Kumar, S. U. Sankar and D. London, *New-physics signals of a model with a vector-singlet up-type quark*, *Phys. Rev. D* **92** (2015) 013002, [1504.00517].

[365] A. K. Alok, S. Banerjee, D. Kumar, S. U. Sankar and D. London, *New-physics signals of a model with an isosinglet vector-like t' quark*, *PoS* **EPS-HEP2015** (2015) 579.

[366] A. K. Alok, S. Banerjee, D. Kumar and S. Uma Sankar, *Flavor signatures of isosinglet vector-like down quark model*, *Nucl. Phys. B* **906** (2016) 321–341, [1402.1023].

[367] J. Aguilar-Saavedra, R. Benbrik, S. Heinemeyer and M. Pérez-Victoria, *Handbook of vectorlike quarks: Mixing and single production*, *Phys. Rev. D* **88** (2013) 094010, [1306.0572].

[368] C. Boehm and P. Fayet, *Scalar dark matter candidates*, *Nucl. Phys. B* **683** (2004) 219–263, [hep-ph/0305261].

[369] R. Gaitán, J. H. Montes de Oca, E. A. Garcés and R. Martinez, *Rare top decay $t \to c\gamma$ with flavor changing neutral scalar interactions in two Higgs doublet model*, *Phys. Rev. D* **94** (2016) 094038, [1503.04391].

[370] A. Dedes, M. Paraskevas, J. Rosiek, K. Suxho and K. Tamvakis, *Rare Top-quark Decays to Higgs boson in MSSM*, *JHEP* **11** (2014) 137, [1409.6546].

[371] C. T. Hill, *Topcolor assisted technicolor*, *Phys. Lett. B* **345** (1995) 483–489, [hep-ph/9411426].

[372] A. Arhrib, *Top and Higgs flavor changing neutral couplings in two Higgs doublets model*, *Phys. Rev. D* **72** (2005) 075016, [hep-ph/0510107].

[373] J. Diaz-Cruz, R. Martinez, M. Perez and A. Rosado, *Flavor Changing Radiative Decay of Thf T Quark*, *Phys. Rev. D* **41** (1990) 891–894.

[374] D. Atwood, L. Reina and A. Soni, *Probing flavor changing top - charm - scalar interactions in e^+e^- collisions*, *Phys. Rev. D* **53** (1996) 1199–1201, [hep-ph/9506243].

[375] D. Atwood, L. Reina and A. Soni, *Flavor changing neutral scalar currents at $\mu^+\mu^-$ colliders*, *Phys. Rev. Lett.* **75** (1995) 3800–3803, [hep-ph/9507416].

[376] A. Bednyakov, B. Kniehl, A. Pikelner and O. Veretin, *On the b-quark running mass in QCD and the SM*, *Nucl. Phys. B* **916** (2017) 463–483, [1612.00660].

[377] B. Belfatto, R. Beradze and Z. Berezhiani, *The CKM unitarity problem: A trace of new physics at the TeV scale?*, *Eur. Phys. J. C* **80** (2020) 149, [1906.02714].

[378] C.-Y. Seng, M. Gorchtein, H. H. Patel and M. J. Ramsey-Musolf, *Reduced Hadronic Uncertainty in the Determination of V_{ud}*, *Phys. Rev. Lett.* **121** (2018) 241804, [1807.10197].

[379] K. Cheung, W.-Y. Keung, C.-T. Lu and P.-Y. Tseng, *Vector-like Quark Interpretation for the CKM Unitarity Violation, Excess in Higgs Signal Strength, and Bottom Quark Forward-Backward Asymmetry*, *JHEP* **05** (2020) 117, [2001.02853].

[380] ATLAS collaboration, M. Aaboud et al., *Combination of the searches for pair-produced vector-like partners of the third-generation quarks at $\sqrt{s} = 13$ TeV with the ATLAS detector*, *Phys. Rev. Lett.* **121** (2018) 211801, [1808.02343].

[381] CMS collaboration, A. M. Sirunyan et al., *Search for vector-like quarks in events with two oppositely charged leptons and jets in proton-proton collisions at $\sqrt{s} = 13$ TeV*, *Eur. Phys. J. C* **79** (2019) 364, [1812.09768].

[382] CMS collaboration, A. M. Sirunyan et al., *Search for pair production of vectorlike quarks in the fully hadronic final state*, *Phys. Rev. D* **100** (2019) 072001, [1906.11903].

[383] G. Eilam, B. Melic and J. Trampetic, *CP violation and the 4th generation*, *Phys. Rev. D* **80** (2009) 116003, [0909.3227].

[384] J. Erler and P. Langacker, *Precision Constraints on Extra Fermion Generations*, *Phys. Rev. Lett.* **105** (2010) 031801, [1003.3211].

[385] CMS collaboration, A. M. Sirunyan et al., *Search for pair production of vector-like quarks in the $bW\overline{b}W$ channel from proton-proton collisions at $\sqrt{s} = 13$ TeV*, *Phys. Lett. B* **779** (2018) 82–106, [1710.01539].

[386] ATLAS collaboration, M. Aaboud et al., *Search for single production of vector-like quarks decaying into Wb in pp collisions at $\sqrt{s} = 13$ TeV with the ATLAS detector*, *JHEP* **05** (2019) 164, [1812.07343].

[387] CMS collaboration, S. Chatrchyan et al., *Combined Search for the Quarks of a Sequential Fourth Generation*, *Phys. Rev. D* **86** (2012) 112003, [1209.1062].

[388] CMS collaboration, S. Chatrchyan et al., *Inclusive Search for a Vector-Like T Quark with Charge $\frac{2}{3}$ in pp Collisions at $\sqrt{s} = 8$ TeV*, *Phys. Lett. B* **729** (2014) 149–171, [1311.7667].

[389] R. A. Diaz, R. Martinez and J. Alexis Rodriguez, *The Rare decay $t \to c\gamma$ in the general 2 HDM type III*, hep-ph/0103307.

[390] R. Gaitan-Lozano, R. Martinez and J. H. M. de Oca, *Rare top decay $t \to c\gamma$ in general THDM-III*, 1407.3318.

[391] LHCb collaboration, R. Aaij et al., *Test of lepton universality with $B^0 \to K^{*0}\ell^+\ell^-$ decays*, *JHEP* **08** (2017) 055, [1705.05802].

[392] LHCb collaboration, R. Aaij et al., *Measurement of Form-Factor-Independent Observables in the Decay $B^0 \to K^{*0}\mu^+\mu^-$*, *Phys. Rev. Lett.* **111** (2013) 191801, [1308.1707].

[393] LHCb collaboration, R. Aaij et al., *Angular analysis of the $B^0 \to K^{*0}\mu^+\mu^-$ decay using 3 fb^{-1} of integrated luminosity*, *JHEP* **02** (2016) 104, [1512.04442].

[394] Belle collaboration, S. Wehle et al., *Lepton-Flavor-Dependent Angular Analysis of $B \to K^*\ell^+\ell^-$*, *Phys. Rev. Lett.* **118** (2017) 111801, [1612.05014].

[395] LHCb collaboration, R. Aaij et al., *Differential branching fractions and isospin asymmetries of $B \to K^{(*)}\mu^+\mu^-$ decays*, *JHEP* **06** (2014) 133, [1403.8044].

[396] LHCb collaboration, R. Aaij et al., *Angular analysis and differential branching fraction of the decay $B_s^0 \to \phi\mu^+\mu^-$*, *JHEP* **09** (2015) 179, [1506.08777].

[397] G. Hiller and F. Kruger, *More model-independent analysis of $b \to s$ processes*, *Phys. Rev.* **D69** (2004) 074020, [hep-ph/0310219].

[398] B. Capdevila, S. Descotes-Genon, J. Matias and J. Virto, *Assessing lepton-flavour non-universality from $B \to K^*\ell\ell$ angular analyses*, *JHEP* **10** (2016) 075, [1605.03156].

[399] B. Capdevila, A. Crivellin, S. Descotes-Genon, J. Matias and J. Virto, *Patterns of New Physics in $b \to s\ell^+\ell^-$ transitions in the light of recent data*, *JHEP* **01** (2018) 093, [1704.05340].

[400] W. Altmannshofer, P. Stangl and D. M. Straub, *Interpreting Hints for Lepton Flavor Universality Violation*, *Phys. Rev.* **D96** (2017) 055008, [1704.05435].

[401] G. D'Amico, M. Nardecchia, P. Panci, F. Sannino, A. Strumia, R. Torre et al., *Flavour anomalies after the R_{K^*} measurement*, *JHEP* **09** (2017) 010, [1704.05438].

[402] G. Hiller and I. Nisandzic, *R_K and R_{K^*} beyond the standard model*, *Phys. Rev.* **D96** (2017) 035003, [1704.05444].

[403] L.-S. Geng, B. Grinstein, S. Jäger, J. Martin Camalich, X.-L. Ren and R.-X. Shi, *Towards the discovery of new physics with lepton-universality ratios of $b \to s\ell\ell$ decays*, *Phys. Rev.* **D96** (2017) 093006, [1704.05446].

[404] M. Ciuchini, A. M. Coutinho, M. Fedele, E. Franco, A. Paul, L. Silvestrini et al., *On Flavourful Easter eggs for New Physics hunger and Lepton Flavour Universality violation*, *Eur. Phys. J.* **C77** (2017) 688, [1704.05447].

[405] T. Blum, A. Denig, I. Logashenko, E. de Rafael, B. Lee Roberts, T. Teubner et al., *The Muon (g-2) Theory Value: Present and Future*, 1311.2198.

[406] S. Bifani, S. Descotes-Genon, A. Romero Vidal and M.-H. Schune, *Review of Lepton Universality tests in B decays*, 1809.06229.

[407] C. Bobeth, G. Hiller and G. Piranishvili, *Angular distributions of $\bar{B} \to \bar{K}\ell^+\ell^-$ decays*, *JHEP* **12** (2007) 040, [0709.4174].

[408] S. L. Glashow, D. Guadagnoli and K. Lane, *Lepton Flavor Violation in B Decays?*, *Phys. Rev. Lett.* **114** (2015) 091801, [1411.0565].

[409] S. Descotes-Genon, J. Matias and J. Virto, *Understanding the $B \to K^*\mu^+\mu^-$ Anomaly*, *Phys. Rev.* **D88** (2013) 074002, [1307.5683].

[410] R. Gauld, F. Goertz and U. Haisch, *On minimal Z' explanations of the $B \to K^*\mu^+\mu^-$ anomaly*, *Phys. Rev.* **D89** (2014) 015005, [1308.1959].

[411] C.-W. Chiang, X.-G. He and G. Valencia, *Z' model for $b \to s\ell\bar{\ell}$ flavor anomalies*, *Phys. Rev.* **D93** (2016) 074003, [1601.07328].

[412] A. Datta, M. Duraisamy and D. Ghosh, *Explaining the $B \to K^*\mu^+\mu^-$ data with scalar interactions*, *Phys. Rev.* **D89** (2014) 071501, [1310.1937].

[413] G. Hiller and M. Schmaltz, *R_K and future $b \to s\ell\ell$ physics beyond the standard model opportunities*, *Phys. Rev.* **D90** (2014) 054014, [1408.1627].

[414] N. Assad, B. Fornal and B. Grinstein, *Baryon Number and Lepton Universality Violation in Leptoquark and Diquark Models*, *Phys. Lett.* **B777** (2018) 324–331, [1708.06350].

[415] L. Di Luzio, A. Greljo and M. Nardecchia, *Gauge leptoquark as the origin of B-physics anomalies*, *Phys. Rev.* **D96** (2017) 115011, [1708.08450].

[416] L. Calibbi, A. Crivellin and T. Li, *A model of vector leptoquarks in view of the B-physics anomalies*, 1709.00692.

[417] M. Bordone, C. Cornella, J. Fuentes-Martin and G. Isidori, *A three-site gauge model for flavor hierarchies and flavor anomalies*, *Phys. Lett.* **B779** (2018) 317–323, [1712.01368].

[418] R. Barbieri and A. Tesi, *B-decay anomalies in Pati-Salam SU(4)*, *Eur. Phys. J.* **C78** (2018) 193, [1712.06844].

[419] M. Blanke and A. Crivellin, *B Meson Anomalies in a Pati-Salam Model within the Randall-Sundrum Background*, *Phys. Rev. Lett.* **121** (2018) 011801, [1801.07256].

[420] A. Greljo and B. A. Stefanek, *Third family quark–lepton unification at the TeV scale*, *Phys. Lett.* **B782** (2018) 131–138, [1802.04274].

[421] M. Bordone, C. Cornella, J. Fuentes-Martín and G. Isidori, *Low-energy signatures of the* PS^3 *model: from B-physics anomalies to LFV*, 1805.09328.

[422] T. Faber, M. Hudec, M. Malinský, P. Meinzinger, W. Porod and F. Staub, *A unified leptoquark model confronted with lepton non-universality in B-meson decays*, 1808.05511.

[423] J. Heeck and D. Teresi, *Pati-Salam explanations of the B-meson anomalies*, 1808.07492.

[424] J. C. Pati and A. Salam, *Lepton Number as the Fourth Color*, *Phys. Rev.* **D10** (1974) 275–289.

[425] R. Foot, *An Alternative $SU(4) \times SU(2)_L \times SU(2)_R$ model*, *Phys. Lett.* **B420** (1998) 333–339, [hep-ph/9708205].

[426] R. Foot and G. Filewood, *Implications of TeV scale $SU(4) \times SU(2)_L \times SU(2)_R$ quark lepton-lepton unification*, *Phys. Rev.* **D60** (1999) 115002, [hep-ph/9903374].

[427] H. E. Haber and Y. Nir, *Multiscalar models with a high-energy scale*, *Nucl. Phys.* **B335** (1990) 363–394.

[428] ATLAS collaboration, ATLAS Collaboration, *Observation of a new particle in the search for the Standard Model Higgs boson with the ATLAS detector at the LHC*, *Phys. Lett. B* **716** (2012) 1–29, [1207.7214].

[429] CMS Collaboration, *Observation of a new boson at a mass of 125 GeV with the CMS experiment at the LHC*, *Phys. Lett. B* **716** (2012) 30–61, [1207.7235].

[430] D. Straub, P. Stangl, C. Niehoff, E. Gürler, Z. Wang, J. Kumar et al., *flav-io/flavio v0.29.1*, Aug., 2018. 10.5281/zenodo.1326349.

[431] LHCb collaboration, R. Aaij et al., *Physics case for an LHCb Upgrade II - Opportunities in flavour physics, and beyond, in the HL-LHC era*, 1808.08865.

[432] Belle II collaboration, E. Kou et al., *The Belle II Physics Book*, 1808.10567.

[433] C. Bobeth, M. Gorbahn, T. Hermann, M. Misiak, E. Stamou and M. Steinhauser, *$B_{s,d} \to l^+l^-$ in the Standard Model with Reduced Theoretical Uncertainty*, *Phys. Rev. Lett.* **112** (2014) 101801, [1311.0903].

[434] Belle collaboration, R. Glattauer et al., *Measurement of the decay $B \to D\ell\nu_\ell$ in fully reconstructed events and determination of the Cabibbo-Kobayashi-Maskawa matrix element $|V_{cb}|$*, *Phys. Rev.* **D93** (2016) 032006, [1510.03657].

[435] Belle collaboration, A. Abdesselam et al., *Precise determination of the CKM matrix element $|V_{cb}|$ with $\bar{B}^0 \to D^{*+}\,\ell^-\,\bar{\nu}_\ell$ decays with hadronic tagging at Belle*, 1702.01521.

[436] L. Lavoura, *General formulae for f(1) $\to$ f(2) gamma*, *Eur. Phys. J.* **C29** (2003) 191–195, [hep-ph/0302221].

[437] LHCb collaboration, R. Aaij et al., *Search for lepton-universality violation in $B^+ \to K^+\ell^+\ell^-$ decays*, *Phys. Rev. Lett.* **122** (2019) 191801, [1903.09252].

[438] MILC collaboration, J. A. Bailey et al., *$B{\to}D\ell\nu$ form factors at nonzero recoil and $|V_{cb}|$ from 2+1-flavor lattice QCD*, *Phys. Rev. D* **92** (2015) 034506, [1503.07237].

[439] S. Fajfer, J. F. Kamenik and I. Nisandzic, *On the $B \to D^*\tau\bar{\nu}_\tau$ Sensitivity to New Physics*, *Phys. Rev.* **D85** (2012) 094025, [1203.2654].

[440] LHCb collaboration, R. Aaij et al., *Measurement of the ratio of branching fractions $\mathcal{B}(B_c^+ \to J/\psi\tau^+\nu_\tau)/\mathcal{B}(B_c^+ \to J/\psi\mu^+\nu_\mu)$*, 1711.05623.

[441] D. Guadagnoli, *Flavor anomalies on the eve of the Run-2 verdict*, *Mod. Phys. Lett.* **A32** (2017) 1730006, [1703.02804].

[442] S. Descotes-Genon, L. Hofer, J. Matias and J. Virto, *Global analysis of $b \to s\ell\ell$ anomalies*, *JHEP* **06** (2016) 092, [1510.04239].

[443] B. Fornal, S. A. Gadam and B. Grinstein, *Left-Right SU(4) Vector Leptoquark Model for Flavor Anomalies*, *Phys. Rev.* **D99** (2019) 055025, [1812.01603].

[444] W. Buchmuller, R. Ruckl and D. Wyler, *Leptoquarks in Lepton - Quark Collisions*, *Phys. Lett.* **B191** (1987) 442–448.

[445] D. Buttazzo, A. Greljo, G. Isidori and D. Marzocca, *B-physics anomalies: a guide to combined explanations*, *JHEP* **11** (2017) 044, [1706.07808].

[446] P. Q. Hung, A. J. Buras and J. D. Bjorken, *Petite Unification of Quarks and Leptons*, *Phys. Rev.* **D25** (1982) 805.

[447] G. Valencia and S. Willenbrock, *Quark - lepton unification and rare meson decays*, *Phys. Rev.* **D50** (1994) 6843–6848, [hep-ph/9409201].

[448] A. Smirnov, *Mass limits for scalar and gauge leptoquarks from K(L)0 —> e-+ mu+-, B0 —> e-+ tau+- decays*, *Mod. Phys. Lett. A* **22** (2007) 2353–2363, [0705.0308].

[449] A. V. Kuznetsov, N. V. Mikheev and A. V. Serghienko, *The third type of fermion mixing in the lepton and quark interactions with leptoquarks*, *Int. J. Mod. Phys.* **A27** (2012) 1250062, [1203.0196].

[450] M. Carpentier and S. Davidson, *Constraints on two-lepton, two quark operators*, *Eur. Phys. J.* **C70** (2010) 1071–1090, [1008.0280].

[451] A. D. Smirnov, *Vector leptoquark mass limits and branching ratios of $K^0_L, B^0, B_s \to l_i^+ l_j^-$ decays with account of fermion mixing in leptoquark currents*, *Mod. Phys. Lett.* **A33** (2018) 1850019, [1801.02895].

[452] C. Hati, J. Kriewald, J. Orloff and A. M. Teixeira, *A nonunitary interpretation for a single vector leptoquark combined explanation to the B-decay anomalies*, 1907.05511.

[453] G. Hiller and M. Schmaltz, *Diagnosing lepton-nonuniversality in $b \to s\ell\ell$*, *JHEP* **02** (2015) 055, [1411.4773].

[454] O. Popov, M. A. Schmidt and G. White, *R_2 as a single leptoquark solution to $R_{D^{(*)}}$ and $R_{K^{(*)}}$*, *Phys. Rev.* **D100** (2019) 035028, [1905.06339].

[455] Y. Sakaki, M. Tanaka, A. Tayduganov and R. Watanabe, *Testing leptoquark models in $\bar{B} \to D^{(*)}\tau\bar{\nu}$*, *Phys. Rev.* **D88** (2013) 094012, [1309.0301].

[456] M. Freytsis, Z. Ligeti and J. T. Ruderman, *Flavor models for $\bar{B} \to D^{(*)}\tau\bar{\nu}$*, *Phys. Rev.* **D92** (2015) 054018, [1506.08896].

[457] M. Bauer and M. Neubert, *Minimal Leptoquark Explanation for the $R_{D^{(*)}}$, R_K , and $(g-2)_g$ Anomalies*, *Phys. Rev. Lett.* **116** (2016) 141802, [1511.01900].

[458] O. Popov and G. A. White, *One Leptoquark to unify them? Neutrino masses and unification in the light of $(g-2)_\mu$, $R_{D^{(*)}}$ and R_K anomalies*, *Nucl. Phys.* **B923** (2017) 324–338, [1611.04566].

[459] Y. Cai, J. Gargalionis, M. A. Schmidt and R. R. Volkas, *Reconsidering the One Leptoquark solution: flavor anomalies and neutrino mass*, *JHEP* **10** (2017) 047, [1704.05849].

[460] A. Azatov, D. Barducci, D. Ghosh, D. Marzocca and L. Ubaldi, *Combined explanations of B-physics anomalies: the sterile neutrino solution*, *JHEP* **10** (2018) 092, [1807.10745].

[461] I. Bigaran, J. Gargalionis and R. R. Volkas, *A near-minimal leptoquark model for reconciling flavour anomalies and generating radiative neutrino masses*, *JHEP* **10** (2019) 106, [1906.01870].

[462] R. N. Mohapatra, G. Senjanovic and M. D. Tran, *Strangeness Changing Processes and the Limit on the Right-handed Gauge Boson Mass*, *Phys. Rev.* **D28** (1983) 546.

[463] F. J. Gilman and M. H. Reno, *Restrictions From the Neutral K and B Meson Systems on Left-right Symmetric Gauge Theories*, *Phys. Rev.* **D29** (1984) 937.

[464] F. J. Gilman and M. H. Reno, *Restrictions on Left-right Symmetric Gauge Theories From the Neutral Kaon System and B Decays*, *Phys. Lett.* **127B** (1983) 426–428.

[465] G. Ecker, W. Grimus and H. Neufeld, *Higgs Induced Flavor Changing Neutral Interactions in SU(2)-l X SU(2)-r X U(1)*, *Phys. Lett.* **127B** (1983) 365.

[466] S. Bertolini, A. Maiezza and F. Nesti, *Present and Future K and B Meson Mixing Constraints on TeV Scale Left-Right Symmetry*, *Phys. Rev.* **D89** (2014) 095028, [1403.7112].

[467] LHCb collaboration, R. Aaij et al., *Search for the lepton-flavour violating decays $B^+ \to K^+\mu^\pm e^\mp$*, 1909.01010.

[468] D. Bardhan, P. Byakti and D. Ghosh, *A closer look at the R_D and R_{D^*} anomalies*, *JHEP* **01** (2017) 125, [1610.03038].

[469] P. Asadi, M. R. Buckley and D. Shih, *It's all right(-handed neutrinos): a new W model for the $R_{D^{(*)}}$ anomaly*, *JHEP* **09** (2018) 010, [1804.04135].

[470] P. Arnan, D. Becirevic, F. Mescia and O. Sumensari, *Probing low energy scalar leptoquarks by the leptonic W and Z couplings*, *JHEP* **02** (2019) 109, [1901.06315].

[471] ALEPH, DELPHI, L3, OPAL, SLD, LEP Electroweak Working Group, SLD Electroweak Group, SLD Heavy Flavour Group collaboration, S. Schael et al., *Precision electroweak measurements on the Z resonance*, *Phys. Rept.* **427** (2006) 257–454, [hep-ex/0509008].

[472] A. J. Buras, J. Girrbach-Noe, C. Niehoff and D. M. Straub, *$B \to K^{(*)} \nu \overline{\nu}$ decays in the Standard Model and beyond*, *JHEP* **02** (2015) 184, [1409.4557].

[473] CMS collaboration, A. M. Sirunyan et al., *Search for heavy neutrinos and third-generation leptoquarks in hadronic states of two τ leptons and two jets in proton-proton collisions at $\sqrt{s} = 13$ TeV*, *JHEP* **03** (2019) 170, [1811.00806].

[474] CMS collaboration, A. M. Sirunyan et al., *Search for a singly produced third-generation scalar leptoquark decaying to a τ lepton and a bottom quark in proton-proton collisions at $\sqrt{s} = 13$ TeV*, *JHEP* **07** (2018) 115, [1806.03472].

[475] CMS collaboration, V. Khachatryan et al., *Search for heavy neutrinos or third-generation leptoquarks in final states with two hadronically decaying τ leptons and two jets in proton-proton collisions at $\sqrt{s} = 13$ TeV*, *JHEP* **03** (2017) 077, [1612.01190].

[476] CMS collaboration, V. Khachatryan et al., *Search for pair production of third-generation scalar leptoquarks and top squarks in proton–proton collisions at $\sqrt{s}$=8 TeV*, *Phys. Lett.* **B739** (2014) 229–249, [1408.0806].

[477] CMS collaboration, S. Chatrchyan et al., *Search for Third-Generation Leptoquarks and Scalar Bottom Quarks in pp Collisions at $\sqrt{s} = 7$ TeV*, *JHEP* **12** (2012) 055, [1210.5627].

[478] CMS collaboration, S. Chatrchyan et al., *Search for Pair Production of Third-Generation Leptoquarks and Top Squarks in pp Collisions at $\sqrt{s} = 7$ TeV*, *Phys. Rev. Lett.* **110** (2013) 081801, [1210.5629].

[479] CMS collaboration, V. Khachatryan et al., *Search for Third-Generation Scalar Leptoquarks in the $t\tau$ Channel in Proton-Proton Collisions at $\sqrt{s} = 8$ TeV*, *JHEP* **07** (2015) 042, [1503.09049].

[480] A. Greljo, J. Martin Camalich and J. D. Ruiz-Álvarez, *Mono-τ Signatures at the LHC Constrain Explanations of B-decay Anomalies*, *Phys. Rev. Lett.* **122** (2019) 131803, [1811.07920].

[481] ATLAS collaboration, M. Aaboud et al., *Search for High-Mass Resonances Decaying to $\tau\nu$ in pp Collisions at $\sqrt{s}$=13 TeV with the ATLAS Detector*, *Phys. Rev. Lett.* **120** (2018) 161802, [1801.06992].

[482] CMS collaboration, A. M. Sirunyan et al., *Search for a W' boson decaying to a τ lepton and a neutrino in proton-proton collisions at $\sqrt{s} = 13$ TeV*, *Phys. Lett.* **B792** (2019) 107–131, [1807.11421].

[483] A. D. Dolgov, S. H. Hansen, G. Raffelt and D. V. Semikoz, *Cosmological and astrophysical bounds on a heavy sterile neutrino and the KARMEN anomaly*, *Nucl. Phys.* **B580** (2000) 331–351, [hep-ph/0002223].

[484] A. D. Dolgov, S. H. Hansen, G. Raffelt and D. V. Semikoz, *Heavy sterile neutrinos: Bounds from big bang nucleosynthesis and SN1987A*, *Nucl. Phys.* **B590** (2000) 562–574, [hep-ph/0008138].

[485] NOMAD collaboration, P. Astier et al., *Search for heavy neutrinos mixing with tau neutrinos*, *Phys. Lett.* **B506** (2001) 27–38, [hep-ex/0101041].

[486] J. Orloff, A. N. Rozanov and C. Santoni, *Limits on the mixing of tau neutrino to heavy neutrinos*, *Phys. Lett.* **B550** (2002) 8–15, [hep-ph/0208075].

[487] N. R. Agostinho, G. C. Branco, P. M. F. Pereira, M. N. Rebelo and J. I. Silva-Marcos, *Can one have significant deviations from leptonic 3 × 3 unitarity in the framework of type I seesaw mechanism?*, *Eur. Phys. J.* **C78** (2018) 895, [1711.06229].

[488] O. Fischer, A. Hernandez-Cabezudo and T. Schwetz, *Explaining the MiniBooNE excess by a decaying sterile neutrino with mass in the 250 MeV range*, 1909.09561.

[489] NA62 collaboration, B. Döbrich, *Dark Sectors at fixed targets: The example of NA62*, *Frascati Phys. Ser.* **66** (2018) 312–327, [1807.10170].

[490] J. L. Feng, I. Galon, F. Kling and S. Trojanowski, *ForwArd Search ExpeRiment at the LHC*, *Phys. Rev.* **D97** (2018) 035001, [1708.09389].

[491] V. V. Gligorov, S. Knapen, M. Papucci and D. J. Robinson, *Searching for Long-lived Particles: A Compact Detector for Exotics at LHCb*, *Phys. Rev.* **D97** (2018) 015023, [1708.09395].

[492] W. Bonivento et al., *Proposal to Search for Heavy Neutral Leptons at the SPS*, 1310.1762.

[493] FASER collaboration, A. Ariga et al., *FASER's physics reach for long-lived particles*, *Phys. Rev.* **D99** (2019) 095011, [1811.12522].